IntechOpen

Wind Turbines

Design, Control and Applications

Edited by Abdel Ghani Aissaoui and Ahmed Tahour

WIND TURBINES - DESIGN, CONTROL AND APPLICATIONS

Edited by **Abdel Ghani Aissaoui** and **Ahmed Tahour**

Wind Turbines - Design, Control and Applications
http://dx.doi.org/10.5772/61672
Edited by Abdel Ghani Aissaoui and Ahmed Tahour

Contributors

Ranjan Vepa, Daniel Micallef, Tonio Sant, Adam Chehouri, Ahmad Reza Ghasemi, Masood Mohandes, Nicolae Florin Jurca, Ahmed El-Naggar, Ayodeji S.O. Ogunjuyigbe, Temitope Raphael Ayodele, Bukola Babatunde Adetokun, Abdul-Ganiyu Adisa Jimoh, Jean Patric Da Costa, Emerson Giovani Carati, Carlos Marcelo De Oliveira Stein, Rafael Cardoso, Diana Martinello, Victor Maldonado, Jakub Bukala, Krzysztof Damaziak, Jerzy Malachowski, Tomasz Szafranski, Hamid Reza Karimi, Krzysztof Jozwik, Maciej Karczewski, Krzysztof Sobczak, Michal Tomaszewski, Karim Belmokhtar, Hussein Ibrahim, Mamadou Lamine Doumbia, Wei Jun Zhu, Pablo Castro, Alberto Arroyo, Juan Carcedo, Ramon Lecuna, Mario Manana, Raquel Martinez, Adrian Ilinca, Oloufemi Fakorede, Jean Perron

First published in Croatia, 2016 by INTECH d.o.o.
eBook (PDF) Published by IN TECH d.o.o.
Place and year of publication of eBook (PDF): Rijeka, 2019.
IntechOpen is the global imprint of IN TECH d.o.o.
Printed in Croatia

Legal deposit, Croatia: National and University Library in Zagreb

Additional hard and PDF copies can be obtained from orders@intechopen.com

Wind Turbines - Design, Control and Applications
Edited by Abdel Ghani Aissaoui and Ahmed Tahour
p. cm.
Print ISBN 978-953-51-2495-5
Online ISBN 978-953-51-2496-2
eBook (PDF) ISBN 978-953-51-6664-1

Meet the editors

Abdel Ghani Aissaoui is a full Professor of electrical engineering at the University of Bechar (Algeria). He was born in 1969 in Naama, Algeria. He received his BS degree in 1993, the MS degree in 1997 and the PhD degree in 2007 from the Electrical Engineering Institute of Djilali Liabes University of Sidi Bel Abbes (Algeria). He is an active member of IRECOM (Interaction Réseaux Electriques – COnvertisseurs Machines) Laboratory and IEEE senior member. He is an editor member and a reviewer in many international journals. He serves as a member in technical committee (TPC) and as a reviewer in international conferences (CHUSER 2011, SHUSER 2012, PECON 2012, SAI 2013, SCSE 2013, SDM 2014, SEB 2014, PEMC 2014, PEAM 2014, SEB [2014, 2015], ICRERA 2015, etc.). His current research interest includes power electronics, control of electrical machines, artificial intelligence and renewable energies.

Ahmed Tahour was born in 1972 in ouled mimoun, Tlemcen, Algeria. He received his BS degree in electrical engineering in 1996, the MS degree in 1999 and the PhD in 2007 from the Electrical Engineering Institute of the University of Sidi Bel Abbes (Algeria). He is currently a full Professor of electrical engineering at University of Mascara (Algeria). His current research interest includes power electronics, control of electrical machines and renewable energies.

Contents

Preface

Renewable energies constitute excellent solutions to both the increase of energy consumption and environment problems. They are clean and present an alternative to meet the needs of today's society. These energies neglected in the past, find their proper place through researches and studies that are increasingly diverse and multidisciplinary.

Several sources of renewable energy are subject of great interest for scientific research. In this work, we focus on wind energy. Use of this energy has become competitive due to three main factors:

- Wind energy is clean, renewable and naturally replenished by nature.
- The development of the wind turbines industry.
- The evolution of semiconductor technology and new methodologies for control of variable wind turbines speed.

The wind source of energy is the subject of advanced research; the aim is to develop techniques for extracting power with high reliability, lower cost and increased energy efficiency.

In the development of wind turbine, the design of its different structures is very important. It becomes complicated depending on the levels of the generated power and on locations chosen: onshore, offshore, mountains, desert, cold area, etc. In the design of a wind turbine, we have to ensure: the robustness of all systems, the energy efficiency, the optimal cost and the high reliability.

The control part is very important; it allows having a good functioning of the system. The use of advanced techniques of control and the new technology products brings the system in its optimal operating mode. Different strategies of control can be applied on generators, converters, systems relating to blades, etc. in order to extract maximal power from the wind in safety conditions, to respect the governmental rules on environment and to preserve the identity of the regional landscapes.

The goal of this book is to present recent works on design, control and applications in wind energy conversion systems (WECS). The developments in this field are rapid, accompanied with many difficulties which required solutions. Different solutions are proposed based on new techniques of control and advanced technology products in the field of wind turbine. This allows to maximize the energy production in such systems and to increase their economic attractiveness.

This book is divided in two parts. The first part is devoted to the design of different elements of the wind turbine:

• In the first chapter, four main topics in composite blades of wind turbines including design, stress analysis, aeroelasticity and fatigue are studied.

• In the second chapter, the fundamental physics of horizontal axis wind turbine (HAWT) aerodynamics in yaw is reviewed with reference to some of the latest scientific research covering both measurements and numerical modeling. The purpose of this chapter is to enable a concise overview of the aerodynamics in rotors.

• The third chapter describes the design and the optimization of low noise airfoil and wind turbines. The airfoils and wind turbine blades are designed with the objective of high power performance. The aerodynamic noise is one of the important constraints for the optimization. The power coefficient of an airfoil is computed with the blade element momentum theory.

• In the fourth chapter, we consider various aspects of small wind turbines (SWTs) design and operation. The literature review and series of coupled numerical simulations investigate the impact of the chosen design solutions on small wind turbine operation. It allowed objective evaluation of different design solutions of SWTs: horizontal axis wind turbines (HAWTs) and vertical axis wind turbines (VAWTs), the rotor position in relation to the tower (upwind vs. downwind) and diffusor-augmented wind turbine (DAWT).

• The fifth chapter deals with the theoretical analysis of two configurations of low cost permanent synchronous generator (PMSG), suitable for small rating, such as small and microscale wind power plants. The first structure is a permanent magnet claw pole synchronous generator (PMCPSG) to be used in an isolated micro wind power plant with installed power around few hundred watts. A permanent magnet synchronous machine with outer rotor (PMSMOR) is the second presented structure, suitable for small wind system with installed power between 2 and 5 kW.

• In the sixth chapter, we present the fundamental principles of multi-objective optimization in wind turbine design and solve a classic multi-objective wind turbine optimization problem by using a genetic algorithm technique.

• The seventh chapter describes a new methodology to increase the efficiency of small wind turbines. This is done by considering the interaction between various components, such as wind rotors, electrical generators, rectifiers and inverters.

The second part is dedicated to control and implementation in wind turbine

• The eighth chapter presents the modeling, simulation and emulation for small wind turbine systems. The main objective of the emulation system is to reproduce the wind turbine dynamic torque behavior in the generator shaft, which must be similar to the real horizontal wind turbine used for distributed generation.

• The ninth chapter deals with a comprehensive overview of the direct-driven permanent magnet synchronous generator (PMSG) for wind energy generation system for stand-alone applications. The dynamic model of PMSG is presented and different maximum power point tracking (MPPT) algorithms have been realized in the aim to compare their performances.

• The tenth chapter presents the dynamic performance of an isolated wind-driven self-excited reluctance generator (WDSERG) for rural electrification application.

• In the eleventh chapter, the design of a nonlinear rotor-side controller is described for a variable pitch wind turbine based on nonlinear H_2 optimal control theory. A nonlinear estimation technique is proposed to improve the dynamic control of the system.

• In the twelfth chapter, the fault current contribution of doubly fed induction generator–based wind turbines (DFIG-WTs) is dictated by a combination of factors, including the electrical parameters of the machine and the converter controller configuration. A detailed analysis of the DFIG-WT fault response was introduced considering all controller parameters and configurations.

• In the thirteenth chapter, the active flow control technique is used to improve the fluid dynamics of an aerodynamic body utilizing an active actuator and energy input. The main focus is to regulate unsteady aerodynamic blade loads and vibration by controlling the localized flow along the blade.

• In the last chapter, electrothermal anti-icing is used in ice mitigation and its energy consumption for wind turbines has been numerically investigated and validated experimentally. We determine the energy consumption for anti-icing systems based solely on experimental investigations.

The chapters in this book present recent works in the design, control and applications in wind turbines. Contributions reveal the importance of the treated subject. We aim by this book to give new trends of the researches in wind turbines areas, and to present the new challenges in the implementation of such renewable source of energy. We hope that the readers will find this book a unique and significant source of knowledge and reference for the future years.

Prof. Dr. Abdel Ghani AISSAOUI
Electrical Department, Faculty of Technology
University Tahri Mohamed of Bechar (UTMB), Algeria

Prof. Dr. Ahmed TAHOUR
Electrical Department, Faculty of Technology
University of Mascara, Algeria

Section 1

Design of Wind Turbines

Chapter 1

Composite Blades of Wind Turbine: Design, Stress Analysis, Aeroelasticity, and Fatigue

Ahmad Reza Ghasemi and Masood Mohandes

Additional information is available at the end of the chapter

http://dx.doi.org/10.5772/63446

Abstract

In this chapter, four main topics in composite blades of wind turbines including design, stress analysis, aeroelasticity, and fatigue are studied. For static analysis, finite element method (FEM) is applied and the critical zone is extracted. Moreover, geometry, layup, and loading of the turbine blades made of laminated composites are calculated and evaluated. Then, according to the stress analysis, critical layer is specified and safety factor is studied based on Tsai-Wu failure criterion. Aeroelasticity is the main source of instability in structures that are subjected to aerodynamic forces. One of the major reasons of instability is the coupling of bending and torsional vibration of flexible bodies, which is known as flutter and considered in this study. Numerical and analytical methods are applied for considering the flutter phenomenon of the blades. For numerical method, the FEM and Joint Aviation Requirements (JAR-23) standard and for analytical method, two-degree freedom flutter and Lagrange's equations are utilized. Also, lifetime prediction of a horizontal axis wind turbine composite blade is investigated. Accumulated fatigue damage modeling is employed as a damage estimation rule based on generalized material property degradation.

Keywords: wind turbine, composite blade, aeroelasticity, fatigue, finite element method

1. Introduction

1.1. Wind turbine

Using wind turbine as electricity generator has some advantages and disadvantages. Some advantages of using wind turbines for electricity generation are electricity generation without

any pollution, fast installation and commissioning, and also low expense for maintenance. Although electricity generation by the wind turbine has some advantages, it has some disadvantages, too that its main disadvantage is the temporary nature of wind flow. Therefore, utilizing efficient equipment is necessary in order to get as much as energy from wind during the limited period of time that it flows strongly.

1.2. Composite blades

One of the most important components of a wind turbine is blade. A beam model of a wind turbine blade is generally suitable for structural-dynamic analysis. It will differ from the small-deflection theory beam models used in conventional analyses of non-rotating structures, and it is more like the beam-column representations used in elastic stability analysis. Four main topics in blade of the wind turbines that should be considered are designing, stress analysis, aeroelasticity, and fatigue.

1.3. Literature review

Development and application of wind turbines and the related issues such as structural design, aerodynamic design, and material selection as well as manufacturing issues, including fatigue, optimization, and aeroelastic stability have attracted researchers' attention. Jureczko et al. [1] presented a model for the design and optimization of wind turbine blades and development an ANSYS program that implements a modified genetic algorithm enables optimization of various objective functions subjective to various constraints such as thicknesses and main dimensions of the model blade. Guo [2] studied weight optimization and aeroelasticity of aircraft wing structure analytically and numerically and compared the results with experimental results. Veers et al. [3] considered the design, manufacture, and evaluation of wind turbine blades. They also verified and improved blade design with detailed stress analysis. Baumgart [4] presented a mathematical model for an elastic wind turbine blade and compared analytical and experimental results. Nonlinear rotor dynamic stimulation of wind turbine by parametric excitation of both linear and nonlinear terms caused by centrifugal and Coriolis forces was investigated by Larsen and Nielsen [5].

The fundamental aspects and the major issues related to the design of offshore wind turbines were outlined by Petrini et al. [6]. They considered the decomposition of these structural systems, the required performance, and the acting loads. Lee et al. [7] numerically investigated the load reduction of large wind turbine blades using active aerodynamic load control devices, namely trailing edge flaps. Tenguria et al. [8] studied the design and analysis of large horizontal axis wind turbine, and NACA airfoils were taken for the blade from root to tip.

Every structure under the influence of aerodynamic forces has specific performance that can change its properties and structure constants such as stiffness coefficient and natural frequencies. Therefore, the structure is faced with strong instabilities that cannot be prevented even by increasing the reliability of the design. This destruction has been created due to a specific force, and this value of force is created because of a specific relative velocity of flow that is called flutter phenomenon, and the fluid speed destruction is called flutter speed [9]. Recog-

http://dx.doi.org/10.5772/63446

nizing the flutter speed, we can ensure the safety of structure under aerodynamic forces. In structures such as a plane, flutter speed is considered as the limiting velocity. Limiting velocity is the velocity which must not be reached by an aircraft under any circumstances.

To ensure the safety of aerospace structures against aeroelastic instability, the Joint Aviation Requirements (JAR) [10] standard is used. Based on JAR-23, preventing flutter in the vicinity of fluid velocity can be ensured, if natural frequencies of the bending and torsion are isolated. Shokrieh and Taheri [11] conducted a numerical and experimental study of aeroelastic stability of composite blades of aircrafts based on this standard. Baxevanou et al. [12] described a new aeroelastic numerical model, which combines a Navier-Stokes CFD solver with an elastic model and two coupling schemes for the study of the aeroelastic behavior of wind turbine blades undergoing classical flutter. Fazelzadeh et al. [13] studied the coupling of bending-torsional flutter of a wing containing an arbitrarily placed mass under a driving force. Results are indicative of the important influence of the location and magnitude of the mass and the driving force on the flutter speed and the frequency of the aircraft wing. Lee et al. [14] investigated the performance and aeroelastic characteristics of wind turbine blades based on flexible multibody dynamics, a new aerodynamic model, and the fluid-structure interaction approach. They proposed a new aerodynamic model based on modified strip theory (MST).

Some researches have been done on the fatigue phenomenon of the blades. In the most of them, in the first step, load spectra obtained by digital sampling of strain gauges which read the strain at a specific location near the root of blade has been used. In the second one, the weight of each load spectrum is obtained by its rate of occurrence. Finally, total load spectrum, which is obtained by the summation of all weighted load spectra, is used to estimate fatigue damage in the blade using Miner's rule [15]. This rule has some defects that linear nature is its main weakness. Investigations have shown that Miner's rule is not proper for fatigue consideration in both metals and composites [16]. Also, another shortcoming of this rule lies in simulation of the load sequence and history of load events which is seen in the difference of predicted lifetimes of blades with two orders of magnitudes for two load cases with different load sequences [15]. Admittedly many researches have considered the fatigue simulation of the composite blades, but the most of them have focused on the deterministic approach. Furthermore, there are other problems for fatigue in the blades by these methods such as recognizing a place to install the strain gauges in order to extract the load spectrum and also using a massive and high-cost material fatigue database.

The main reason to create fatigue in the wind turbine blades is cyclic loads. Variation of wind speed, annual gust, rotation of rotor, and variation of weight vector direction toward the local position of the blade [17] are the production sources of the cyclic loads. These sources have different effects on the cyclic load. The two first sources change the total amount of the load. Also, rotation of rotor produces fluctuating load with a frequency identical to the rotor rotation frequency. Last one is the effect of wind shear which arises from change of wind speed by changing in height.

Considering the effect of wind shear in the design process is not necessary, because its influence on the fatigue damage is negligible [18]. Moreover, gust phenomenon is studied annually based on the Germnaschier Lloyds standard [19]. During gust occurrence, vibration is created

in the blade due to the gust impact effect, which arises the linear combination of its mode shapes. Eggleston and Stoddard [20] investigated engineering design of wind turbine. The results of their study showed that the first mode shape had the most significant role in displacements. Furthermore, the effect of wind direction on the turbine blades is not considerable, because the turbine always stays upwind and with changing the wind direction, the active yaw control system will adapt the turbine with new direction of wind vector as quickly as possible. Therefore, after defining cyclic loading sources, all corresponding applied stresses are derived from full range static analyses covering all events [17].

Designing, stress analysis, aeroelasticity, and fatigue of a composite blade wind turbine are investigated in this chapter. First, the geometry of blades is designed using the finite element method (FEM) for considered materials and layups. Then, using the static and dynamic analyses of the blades, the critical zone and flutter phenomenon are considered. Also, the damage is estimated utilizing accumulated fatigue damage modeling.

2. Problem description

Designing of the blades to get the maximum energy from the wind flow is an essential topic which is according to a refined aerodynamic science. Stiffness and strength to weight ratios are two important parameters to design the blades. Blades of horizontal axis are now completely made of composite materials that not only have they lower weight and appropriate stiffness, but also providing good resistance to the static, dynamic, and fatigue loadings. To attain the highest possible power output from the wind turbine under specified atmospheric conditions, changing two parameters are necessary. The first is change of the dynamic and mechanical properties of the wind turbine blade which modify the composite material, which the blade is made of it, and the second is changing shape of the blade. Admittedly change of the shape of blade modifies the stiffness and stability, but it may influence aerodynamic efficiency of wind turbine. Therefore, specifying the optimal shape of blade and optimal composite material are an important and complex problem. Nevertheless, selection of airfoil and also calculating the loading are two significant topics to design the composite blade.

3. Design of the blade

3.1. Finite element modeling

For finite element (FE), analysis of the turbine blade, the ANSYS commercial software is used. The FEM is provided according to dimensions of 660 kW composite wind turbine blades, and an airfoil is selected appropriately, as well as most popular design methods [14, 21]. Geometric dimensions of the blade structure are shown in **Table 1**. To carry aerodynamic forces, the weight of the blade, bending moment in blade and other forces, two beams (main beam and spar) are used in the length of the blade, as shown in **Figure 1**.

Length	Attack degree	Chord length (m)		Twist	Distance end section to hub	Airfoil type
(m)	(O)	Root	Tip	(m)	(O)	(NACA)
21	14	2	0.4	15	3.50	*NACA* 63_2 – 415

Table 1. Geometric dimensions of 660 kW wind turbine blades.

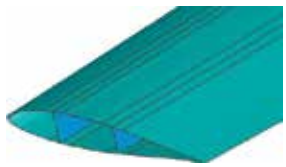

Figure 1. Section of two beams in the length of blade.

Section of the blade has taper as well as twist in the length of the blade in which the amount of twist in the tip of the blade as compared to the root is 15° (**Figure 2**). According to the physics and geometry of the blade, in order to have the layup ability of the structure, the Shell99 element for meshing is selected. To simulate the structure of the blade, it is divided into five distinct regions, including shell, three parts of the main beam, and the spar, and the special layup is used for each part. The number of extractions of optimal elements carried out for analysis of the blade is known as convergence analysis. The number of optimal element of the structure is about 33,200. Three-dimensional FEM of turbine blade is shown in **Figure 3**.

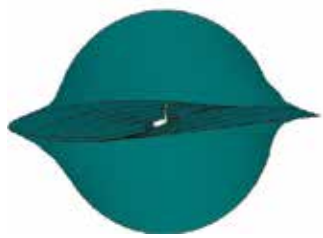

Figure 2. Twist of the airfoil tip of the blade in relation to its root.

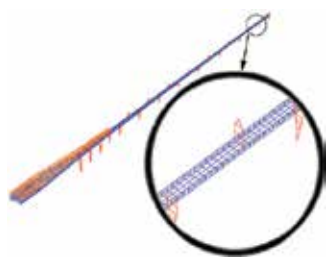

Figure 3. Three-dimensional FEM of the turbine blade.

3.2. Aerodynamic loading

The resultant of the aerodynamic forces into an airfoil section is generally shown as the lift and drag forces. By using lift and drag forces, the force F_Q that causes creation of a useful torque in the direction of rotor's rotation, and the force F_T that applies an axial force to the blades, are calculated. By integration of the moment ΔQ and the thrust ΔQ in the length of the blade, bending moment M_T and rotation moment M_Q can be obtained. The value of the torque and thrust axial force for each section from Glauert vortex theory is determined [20–22].

$$\begin{aligned} \Delta Q &= 0.5\rho\omega^2 r(C_l \sin\varphi - C_d \cos\varphi)C\Delta r \\ \Delta T &= 0.5\rho\omega^2 r(C_l \cos\varphi + C_d \sin\varphi)C\Delta r \end{aligned} \tag{1}$$

$$\begin{aligned} F_Q &= L\sin\varphi - D\cos\varphi \\ F_T &= L\cos\varphi + D\sin\varphi \end{aligned} \tag{2}$$

where C is chord length, r is radius, ω is angular speed, and ρ is air density. The C_l, C_d, L, and D indicate the lift and drag coefficients, and lift and drag forces, respectively. The diagram of these forces is shown in **Figure 4**. In this figure, W indicates the relative effective wind speed on the blades and the Ø is the angle between the relative wind speed and the axis perpendicular to the rotation axis, which consists of the attack angle (α) and the airfoil torsion (θ) [20–22]. Using MATLAB software, a computer code was developed which is able to calculate the values of the forces and moments in Eqs. (1) and (2), for the blade 660 kW and are shown in **Table 2**. The above forces and moments are entered at the center of each section.

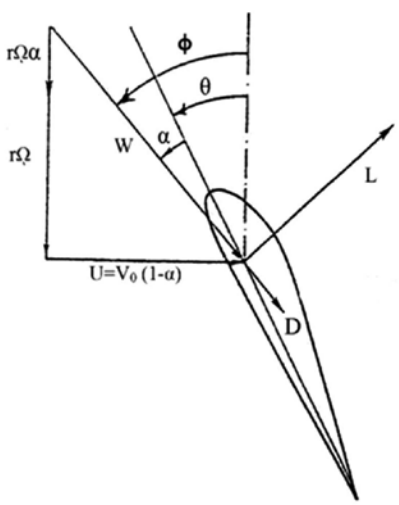

Figure 4. Aerodynamic forces acting on the turbine blade.

Rotation forces (F_Q)	Axial forces (F_T)	Rotation moment (M_Q)	Bending moment (M_T)
13,262 (N)	90,177 (N)	174,015 (N m)	1,291,914 (N.m)

Table 2. Total forces and moments on the 660 (kW) turbine blades.

3.3. Centrifugal force

The value of centrifugal force caused by rotor rotation with angular speed (ω) that in the plate rotation as tensile load, is calculated using equation $F_{centrifugal} = mr\omega^2$. This force depends on the angular speed of the blade and the radius rotation which is the distance from the axis of rotation to the center of mass. Angular speed of the blade is 4.45 radian per second, and hub radius of 0.8 m is considered.

4. Finite element analysis of the composite blade

4.1. Layup design

For different parts of the blade according to the applied loads, proper arrangement of the glass/epoxy laminates and foam was used [23]. The high stiffness, low density, and good fatigue performance are important for composite wind turbine blades. In **Table 3**, ρ is density, E_x and E_y are the stiffness, G_{xy} is the shear stiffness, and ν_{xy} and ν_{yx} are the Poisson's ratios. The thickness of each layer of composite was 0.3 mm, and the thickness of the foam was 3 mm.

E_x (GPa)	E_y (GPa)	E_{xy} (GPa)	ν_{xy} (GPa)
76	10.3	7.17	0.28

Table 3. Elastic constants of glass/epoxy unidirectional ply [23].

Based on the decrease in bending moment from root to tip of the blade, there is no need to have a uniform thickness throughout the length of the beam. Therefore, it is necessary to reduce the thickness by dropping the number of composite ply in order to decline weight of the structure and to optimize the model.

Since the arrangement of the composite laminates, it should be noted that the flange beam bears the bending forces and the web section transfers the shear stress. Therefore, stacking sequences in the flange in the zero layers and layup in the web section have ±45 angle relative to the longitudinal axis of the blade. The results of the analysis of the metal model confirm this result, and the direction of the principle stresses in the metal model indicates the layup of laminate in the composite blade [21]. Stacking sequences of the shell is $[\pm 54_5 / C / \pm 45_5]$, and its thickness is 6 mm. The main and the secondary beam layup are shown in **Table 4**.

Main beam	Stacking sequences in web	Thickness in web	Stacking sequences in flange	Thickness in flange (mm)
Root to 7 m	$[\pm 54_{10} / C / \pm 45_{10}]$	9	$[0]_{46}$	13.8
From 7 to 14 m	$[\pm 54_{9} / C / \pm 45_{9}]$	8.4	$[0]_{36}$	10.8
From 14 to 21 m	$[\pm 54_{8} / C / \pm 45_{8}]$	7.8	$[0]_{20}$	6
Spar	$[\pm 54_{7} / C / \pm 45_{7}]$	7.2	$[0]_{20}$	6

Table 4. Layup design of beam and spar for 660 kW turbine blades.

4.2. Stress analysis

Stress analysis is a major topic in the wind turbine blades which is performed by software program. The stress and strain at different directions are considered in order to control the safety factor of the blade against applied loads. The most important parameter in the stress analysis of the blades is the maximum stresses and critical values. For a composite blade, the normal and shear stresses are calculated initially and then the stresses are analyzed based on the Tsai-Wu failure criterion. Moreover, stress contour must be studied in the critical layer because the possibility of failure is highest in the whole structure.

From the theoretical point of view, the stress in the area of the blade root which is under the influence of aerodynamic forces, weight force, and maximum bending moment is higher than other parts of the blade.

Figure 5(a)

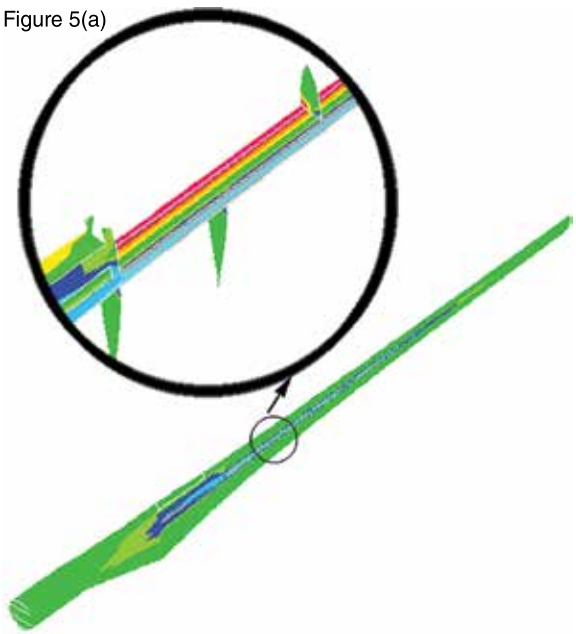

http://dx.doi.org/10.5772/63446

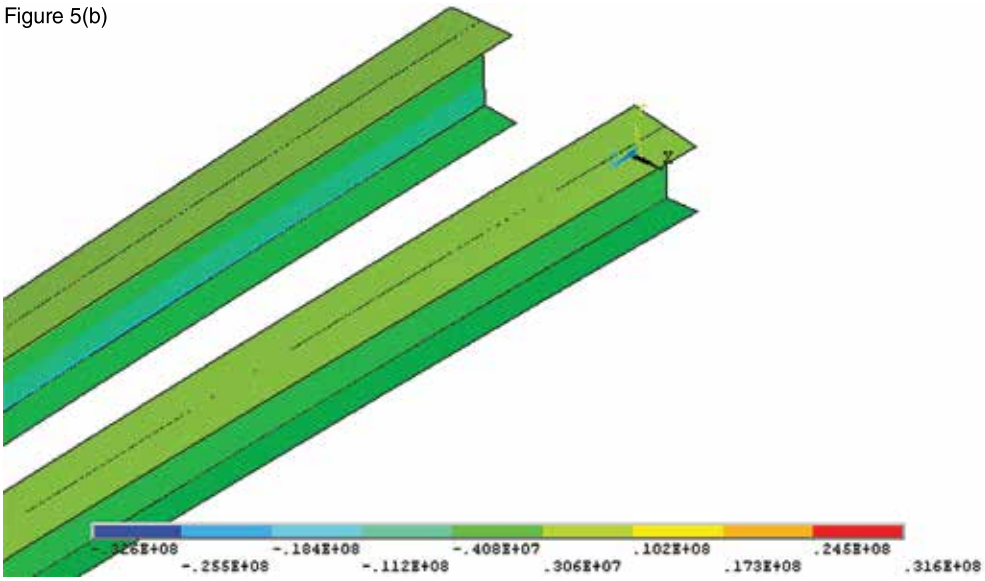

Figure 5. The stress contours in the critical layer of main beam: (a) stress in fiber direction (b) stress in transverse direction.

Furthermore, according to the layer properties of the composites, it is necessary that stress contour in the critical layer in which the possibility of failure is highest in the whole structure be studied. In this study, the critical values are extracted by investigating the stress in fiber direction, perpendicular to fiber (transverse) direction, and the shear stress. The stress contours in the beam and spar critical layer with maximum failure stress number is shown in **Figure 5**.

Figure 6. Deflection of the 660 kW turbine blades.

In order to study the safety factor of static design, Tsai-Wu failure criterion was used. Minimum safety factor for destruction in the critical layer is obtained equal to 4. Also, during rotor performance, the maximum displacement of the blades is 1.4 m where the angle of the blade is 3.81° deflection at the tip [21]. This indicates a considerable improvement over similar models. The deflection of composite wind turbine blade is shown in **Figure 6**. The minimizing blade tip deflection and the sufficient distance between blade and tower in critical conditions are very important.

4.3. Vibration analysis

Dynamic effects in mechanism of the wind turbine due to frequency of aerodynamic loads during normal rotation are significant. In structural engineering, modal analysis uses the overall mass and stiffness of a structure to find the various periods at which it will naturally resonate. The modal analysis for structural mechanics is performed in order to obtain the natural mode shapes and frequencies of a structure. This analysis is carried out by the FEM. In order to do aeroelastic analysis and ensure the non-occurrence of flutter phenomenon, modal analysis of composite structures, natural frequencies with their mode shapes are studied. The results of modal analysis of structure using FEM up to 10 natural frequencies are expressed in **Table 5**.

Number mode	**1**	**2**	**3**	**4**	**5**	**6**	**7**	**8**	**9**	**10**
Natural frequency (Hz)	0.89	2.52	2.98	5.44	8.51	9.41	10.63	14.82	15.72	16.35

Table 5. Natural frequencies of the 660 kW composite wind turbine blade.

5. Aeroelastic analysis

One of the important topics for designing of the wind turbines blades is aeroelasticity phenomenon, because it is the major source of instability in the blades. Flutter is the coupling between bending and torsional vibration of the flexible bodies which is one of the instability factors. There are different models to analyze the flutter such as simple, spring restrained, and rigid wing that in the rigid wing model, the discrete springs would reflect the wing structural bending and torsional stiffnesses, and the reference point would represent the elastic axis [24]. To prevent the aeroelasticity instability due to the flutter in the blades, JAR-23 [2] standard is proposed. Using the JAR-23 and isolating the natural frequencies of the bending and torsional, the blade can be protected against flutter in the close of fluid velocity.

5.1. Numerical aeroelastic of a blade

The bending and torsion modes related to these frequencies should be identified and separated by finding the values of natural frequencies.

According to JAR-23 standard, flutter phenomenon occurs when both bending and torsion sequential modes are overlapped. Therefore, flutter safety factor of blades equals the ratio of

http://dx.doi.org/10.5772/63446

two consecutive bending and torsion modes of blades. Structural analysis of composite blade value and safety factor (n_1) is calculated as follows:

$$n_1 = \frac{\omega_b}{\omega_\theta} = \frac{14.82}{10.63} = 1.39 \tag{3}$$

where $\omega_{(b)}$ and $\omega_{(\theta)}$ are bending and torsional frequencies, respectively. The torsional and bending modes of composite blade structure are shown in **Figures 7** and **8**. The reason for this choice is the lowest ratio between two successive bending and torsional modes. Obtained minimum safety factor is acceptable. Therefore, FEM shows that structural safety and aeroelastic stability are reliable.

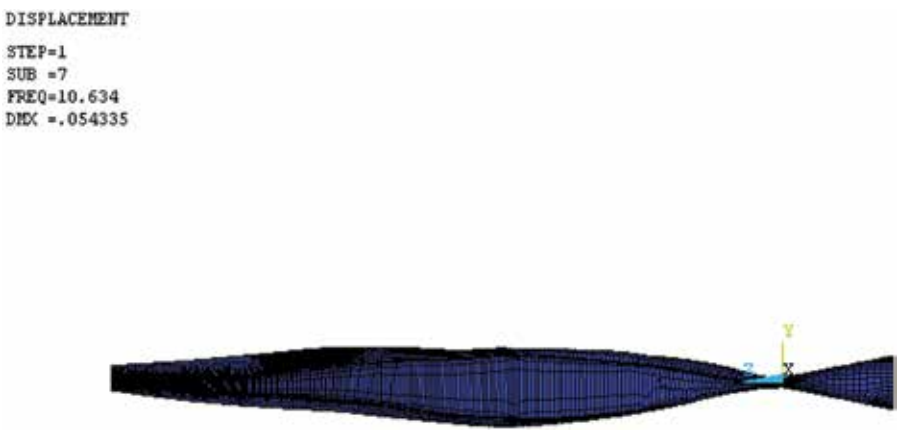

Figure 7. Torsion mode of the 660 kW composite wind turbine blade.

Figure 8. Bending mode following torsion mode of the 660 (kW) composite wind turbine blade.

5.2. Analytical aeroelastic of a blade

In this section, the two-dimensional analytical study of aeroelastic stability for composite wind turbine blade was carried out with two degrees of freedom. Flutter analysis was often performed using simple, spring restrained, and rigid wing models such as the one shown in **Figure 9**. In the later, the discrete springs would reflect the wing structural bending and torsional stiffnesses, and the reference point would present the elastic axis [24]. The points *P*, *C*, *Q*, and *T* refer to the reference point, the center of mass, the aerodynamic center, and the three-quarter-cord, respectively. The dimensionless parameters *e* and *a* determine the location of the point *C* and *P* when these parameters are zero, the point lies on the mid cord, and when they are positive/negative, the points lie toward the trailing/leading edge. Also, *b* is a reference of semi-chord of the lifting surface.

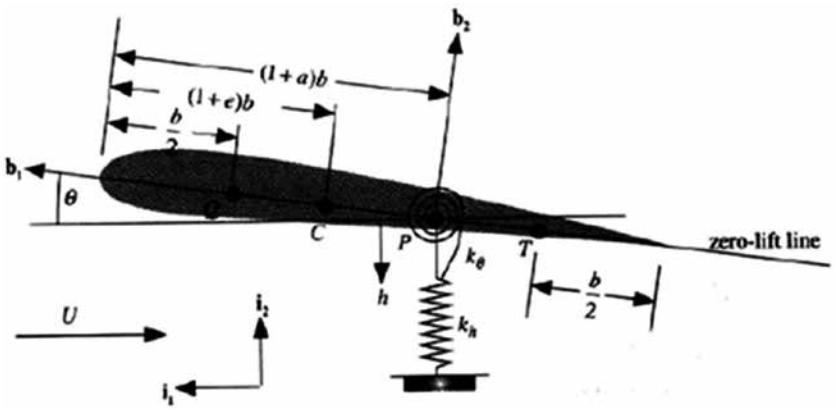

Figure 9. Two-dimensional aeroelastic modeling of airfoil with two-degree freedom.

The chordwise offset of the center of mass from the reference point is defined as follows:

$$x_\theta = e - a \tag{4}$$

The rigid plunging and pitching of the model is restrained by light, linear spring with spring constants k_h and k_θ. It is convenient to formulate the equations of motion from Lagrange's equations. To do this, one needs kinetic and potential energies as well as the generalized forces resulting from aerodynamic loading. The potential (*P*) and kinetic (*K*) energies are given by the following formula [24]:

$$\begin{aligned} P &= \frac{1}{2}k_h h^2 + \frac{1}{2}k_\theta \theta^2 \\ K &= \frac{1}{2}m v_c^2 + \frac{1}{2}I_c \dot{\theta}^2 \end{aligned} \tag{5}$$

where c is the mass center and I_c is the moment of inertia about c. In addition, m is mass and v_c is the velocity of mass center. The degrees of freedom h and θ are easily derived from the work done by the aerodynamic lift L, through a virtual displacement of point Q and the aerodynamic pitching moment about Q through a virtual rotation of the modal.

Using simplicity in Lagrange's formalism for the aerodynamics equation of motion can be presented as follows [24]:

$$\begin{aligned} m(\ddot{h} + bx_\theta\ddot{\theta}) + k_h h &= -L \\ I_P\theta + mbx_\theta\ddot{h} + k_\theta\theta &= b(0.5+a)L \end{aligned} \tag{6}$$

where L is Lagrangian and $I_P = I_C + mb^2x_\theta^2$. To simplify the formula, we introduce the uncoupled, natural frequencies at zero airspeed, represented by the following:

$$\omega_h = \sqrt{\frac{k_h}{m}}, \qquad \omega_\theta = \sqrt{\frac{k_\theta}{I_P}} \tag{7}$$

To introduce dimensionless variables to further simplify the problems, we consider the following four parameters:

$$r^2 = \frac{I_P}{mb^2} \quad \sigma = \frac{\omega_h}{\omega_\theta} \quad \mu = \frac{m}{\rho\ \pi\ b^2} \quad V = \frac{U}{b\omega_\theta} \tag{8}$$

where r is the dimensionless radius of gyration of the wing about the reference point P with $r^2 \succ x_\theta^2$; σ is the ratio of uncoupled bending to torsional frequencies, μ is the mass ratio parameter reflecting the relative importance of the model mass to the mass of the air affected by the model, and V is the dimensionless free stream speed of the air that is sometimes called the reduced velocity. The equations may be simplified as follows:

$$\begin{bmatrix} s^2+\sigma^2 & s^2x_\theta + \dfrac{2V^2}{\mu} \\ s^2x_\theta & s^2r^2 + r^2 - \dfrac{2V^2}{\mu}\left(\dfrac{1}{2}+a\right) \end{bmatrix} \begin{Bmatrix} \dfrac{\bar{h}}{b} \\ \bar{\theta} \end{Bmatrix} = \begin{Bmatrix} 0 \\ 0 \end{Bmatrix} \tag{9}$$

For a nontrivial solution to exist, the determinant of the coefficient matrix must be set equal to zero. There are two complex conjugate pairs of roots, say $s_{1,2} = {(\Gamma_{1,2} \pm i\Omega_{1,2})}\Big/_{\omega_\theta}$. For a given configuration and altitude, one must look at the behavior of the complex roots as functions of V and find smallest value of V to give divergent oscillations, whose value is $V_F = \frac{U_F}{b\omega_\theta}$, where U_F is the flutter speed.

For looking at flutter, we consider a specific section of a composite blade of wind turbines, defined by $a = 0.2$, $e = 0.1$, $\mu = 20$, $r^2 = 0.24$, and σ is obtained from numerical solution. Plots of the imaginary part of the roots versus V are shown in **Figure 10**. The modal frequency of critical torsional and bending modes is shown in **Figure 10**. In **Figure 10**, when $V = 0$, one expects the two-dimensionless frequencies to be close unity and σ represents pitching and plunging oscillations, respectively. Even at $V = 0$, these modes are lightly coupled because of the nonzero off-diagram term $x_{(\theta)}$ in the mass matrix. As V increases, the frequencies start to approach one another, and their respective mode shapes exhibit increasing coupling between plunge and pitch. Flutter occurs when the two modal frequencies come close, at which point the roots become complex conjugate pairs. Under this condition, both modes are highly coupled pitch-plunge oscillations. For this composite blade of wind turbine, the flutter speed is $V_F = U_F/b\omega_\theta = 3.306$, and the flutter frequency is $\Omega_F/\omega_\theta = 0.802$.

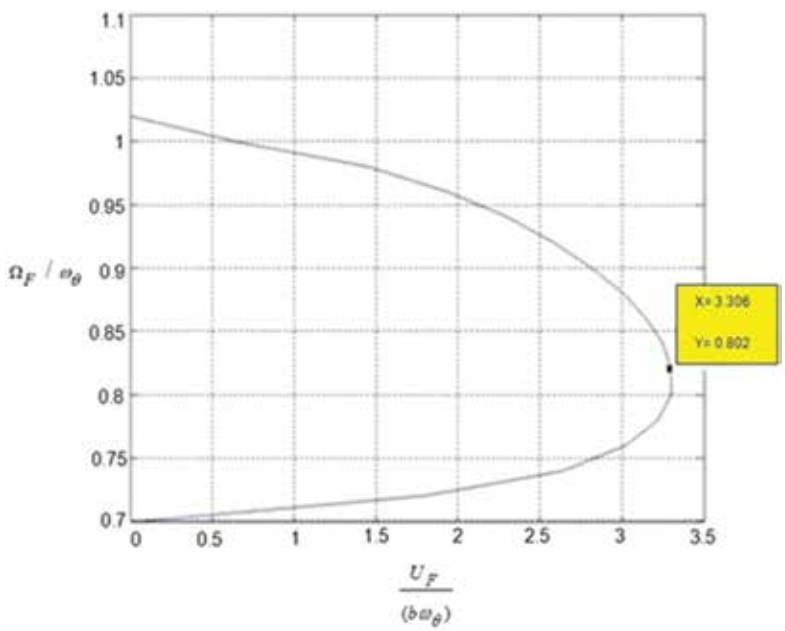

Figure 10. Modal frequency via V for critical torsional and bending modes.

According to the values of modal analysis and natural frequency of the torsion mode, the flutter speed is determined as follow:

$$U_F = 3.31 \times b\omega_\theta = 35 \, {}^{m}\!/_{s} \tag{10}$$

In Eq. (10), $b = 1$ is the half of chord length and $\omega_\theta = 10.63$. The relative real speed of the turbine performance is calculated as follows:

http://dx.doi.org/10.5772/63446

$$V = \sqrt{V_{rel}^2 + V_a^2} = 25.3 \, {}^{m}\!/_{s} \tag{11}$$

Given the flutter speed and the performance speed of the wind turbine, safety factor can be calculated as follows:

$$n_2 = \frac{U_F}{V} = 1.38 \tag{12}$$

Obtained safety factor is acceptable and shows the safety and aeroelastic stability of the structure in the performance and design of turbine blades.

6. Fatigue

One of the other basic topics for designing of the wind turbines specifically for the blades is fatigue considerations. The lifetime of a wind turbine blade is estimated about 20–30 years. This long lifetime bring some design constraints for the wind turbine blades which fall into the fatigue categories.

6.1. Accumulated fatigue damage modeling

One of the important issues in composites is fatigue. Shokrieh and Lessard [25] presented "generalized material property degradation technique," which is used for studying the fatigue. In this research, their technique is modified to simulate the laminated composite behavior under uni-axial fatigue loading. It means that by this model which is called "accumulated fatigue damage model", damage status at every level and the number of cycles from start of loading to sudden failure of the component are estimated and subsequently final fatigue life is predicted. Three different sections of this model are including stress analysis, damage estimation, and material properties degradation. Classical lamination plate theory (CLPT) is proper because the effect of edge will not occur due to placing the selected critical zone in a confined region. The flowchart of the accumulated fatigue damage is shown in **Figure 11**.

As depicted in **Figure 11**, in the first step, a proper model for stress analysis must be developed, which have defined different parameters including material properties, maximum and minimum fatigue load, maximum number of cycles, incremental number of cycles. In the second step, failure analysis is done so that if a sudden mode of failure exists, the material properties of the failed plies are changed according to the appropriate sudden material property degradation rules. Then, the stress and failure analyses are carried out again according to the new stiffness matrix of the FEM. In this step, if there is no sudden mode of failure, an incremental number of cycles is applied. The computer program stops if the number of cycles is greater than a preset total number of cycles. Otherwise, the gradual material property degradation rules are applied for changing the stiffness of all plies (of all elements).

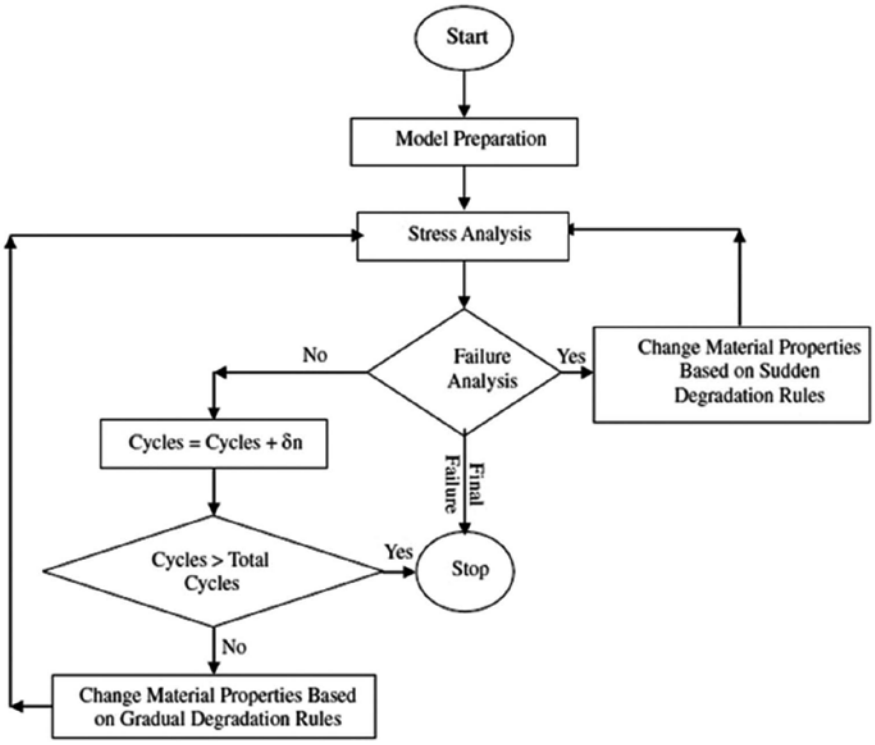

Figure 11. Flowchart of accumulated fatigue damage modeling.

The depicted loop is repeated until a failure occurs or the maximum number of cycles, which has been defined by the user, is reached. In this section, the stiffness degradation method is applied because one of the aims is decreasing the run-time of the model. In this method, remaining stiffness of an U-D ply under desired uni-axial state of stress and desired stress ratio can be calculated using the following equation which is a modified and improved form of Ye's model [26]:

$$E(n,\sigma,\kappa)=\left(1-\frac{\tilde{D}}{f(\sigma,\sigma_{ult})}\right)E_0 \tag{13}$$

where E_0, $E(n, \sigma, \kappa)$, and $\widetilde{D}$ are initial stiffness before start of fatigue loading, residual stiffness (as a function of number of cycles, applied stress, and stress ratio) and normalized damage parameter, respectively. It is necessary to mention that the role of stress is included in the amount of damage using $f(\sigma, \sigma_{ult})$ because amount of $\widetilde{D}$ does not depend on the applied stress level. A complete form of $f(\sigma, \sigma_{ult})$ was developed [25] based on available experimental data for carbon/epoxy (commercially called AS4/3501-6). A developed method is utilized for

damage estimation, which is called the normalized number of cycles, and it calculates D', which describes a relation between $\widetilde{D}$ and $\widetilde{N}$. Available experimental data show that normalized damage increases linearly from start of loading till $\widetilde{N}$ = 0.67 and after that the rate of damage increases non-linearly until final failure ($\widetilde{N}$ = 1). Therefore, the relation between $\widetilde{D}$ and $\widetilde{N}$ can be divided into two phases. All the linear and non-linear relations between $\widetilde{D}$ and $\widetilde{N}$ are presented for both phases [27] that in those relations, $\widetilde{N}$ is obtained using the following equation:

$$\widetilde{N} = \frac{\log(n) - \log(0.25)}{\log(N_f) - \log(0.25)} \tag{14}$$

where, n and N_f describe number of applied cycles and cycles to failure, respectively. N_f must be calculated using following relation [25]:

$$\frac{\ln(a/f)}{\ln\left[(1-q)(C+q)\right]} = A + B\log N_f \tag{15}$$

where

$$q = \sigma_m/\sigma_t \quad a = \sigma_a/\sigma_t \quad C = \sigma_c/\sigma_t \quad \sigma_m = \frac{(\sigma_{\max} + \sigma_{\min})}{2} \quad \sigma_a = \frac{(\sigma_{\max} - \sigma_{\min})}{2} \tag{16}$$

It is shown that in shear loading, the aforementioned equation can be modified to the following form [25]:

$$u = \log\left(\frac{\ln(a/f)}{\ln\left[(1-q)(C+q)\right]}\right) = A + B\log N_f \tag{17}$$

where u and f are curve fitting parameters, which have been obtained for AS4/3501 material [25].

6.2. Evaluation of accumulated fatigue damage model

The results have been calculated for a 0-degree unidirectional ply (U-D) of carbon/epoxy under tensile longitudinal fatigue loading, a 90-degree U-D ply of carbon/epoxy under tensile transverse fatigue loading and a cross-ply of carbon/ epoxy which are shown in **Figures 12–14**, respectively, and compared with the experimental results [25, 28, 29]. The results demonstrate that the presented model has appropriate performance.

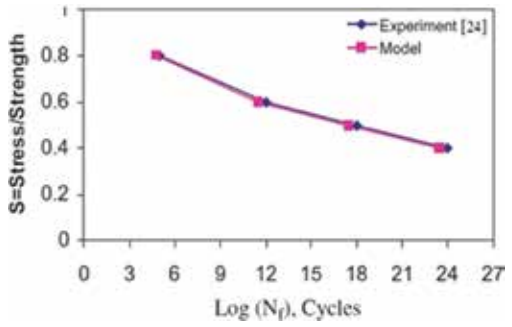

Figure 12. Experimental data and results of computer code for 0-degree ply.

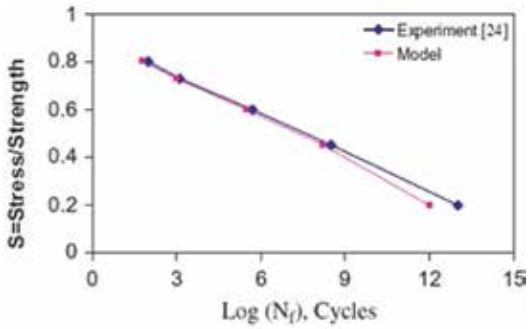

Figure 13. Experimental data and results of computer code for 90-degree ply.

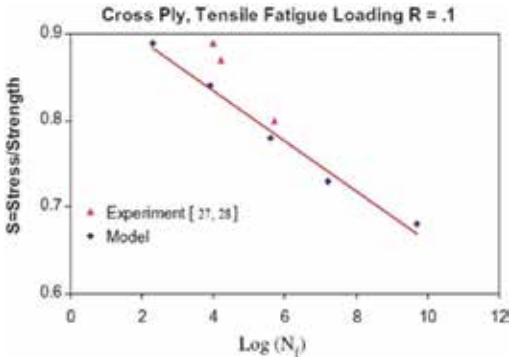

Figure 14. Experimental data and results of computer code for cross ply.

All equations and relations have been developed based on available experimental data for carbon/epoxy composites. Since normalized life curves for glass/epoxy were not available, a generic behavior was estimated based on the pattern of decreasing mechanical properties and strengths of carbon/epoxy. The only available criteria for the evaluation of aforementioned

generic fatigue behavior process are the mentioned criteria in Montana State University/ Department of Energy (MSU/DOE) fatigue database [30] for wind turbine blade application. In MSU/DOE, the behavior of involved composite materials in blade structures is defined by the following equation:

$$\sigma/\sigma_0 = 1 - b\log(N) \tag{18}$$

where σ, σ_0, and b are maximum applied stress, corresponding static strength in the same direction of applied stress and a parameter which varies for the different materials, respectively. In MSU/DOE, two magnitudes of "b" were presented which describe two boundaries of all curves. The upper and lower bounds refer to good and poor materials, respectively, which behave perfectly and weakly against fatigue. The values of "b" for different fatigue loading situations [30] are presented in **Table 6**.

Type of data	Extremes of normalized S-N fatigue data for fiberglass laminates		
Tensile fatigue data ($R = \sigma_{min} / \sigma_{max} = 0.1$)	Good materials (b =0.1)	Poor materials (b =0.14)	Normalization *UTS*
Compressive fatigue data (R = 10)	Good materials (b =0.07)	Poor materials (b =0.11)	Normalization *UCS*
Reversal fatigue data (R = –1)	Good materials (b =0.12)	Poor materials (b =0.18)	Normalization *UTS*

[a]Ultimate tensile strength.
[b]Ultimate compressive strength.

Table 6. Values of "b" for two bounds of good and poor materials (S-N data).

The results of tensile mode based on the generic method with good [30] and poor materials are indicated in **Figure 15**. It is found that the results are logical and the generic behavior is proper because the pre-preg materials have high quality and same volume of resin at all points containing non-woven fabrics.

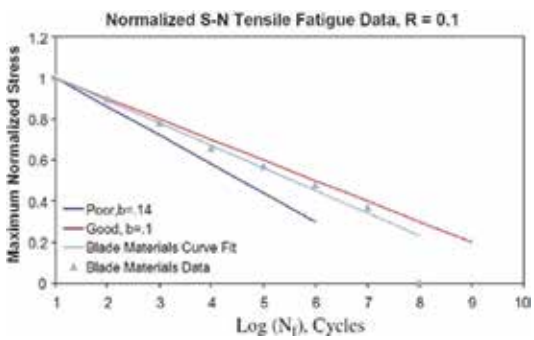

Figure 15. Results of computer code based on used generic method in comparison with good and poor material data from MSU/DOE database.

One of the most important advantages of using accumulated fatigue damage modeling is in its independence of layup configuration. Thus, it can be used for any configuration of fabrics, knowing behavior of involved U-D plies (full characterization of each configuration is not required).

6.3. Wind resource characterization

One of the most important issues for fatigue analysis is identification of governing wind patterns on the wind farm vicinity. The wind speed is never steady at any site because different parameters influence on it such as the weather system, the local land, and the height above the ground surface. Therefore, average wind speed should be obtained over a long term, for example, 10 or more years to raise the confidence in wind speed distribution. However, long-term measurements are expensive, and most projects cannot wait that long.

The "measure, correlate, and predict (MCP)" technique is used instead of long-term measurements so that short term, for example, one year is considered and data are compared with available long-term data of a near site. By this technique, the long-term annual wind speed at the site under consideration is obtained.

The Weibull function of Manjil (a city in the north of Iran), which can describe the wind speed variations over the period, was derived using metrological data in the following form [31]:

$$h(v) = \left(\frac{1.425}{9.3206}\right)\left(\frac{v}{9.3206}\right)^{(0.425)} e^{-\left(\frac{v}{9.3206}\right)^{1.425}} \tag{19}$$

where v and h(v) are wind speed and the corresponding probability of occurrence, respectively. This distribution is shown in **Figure 16**.

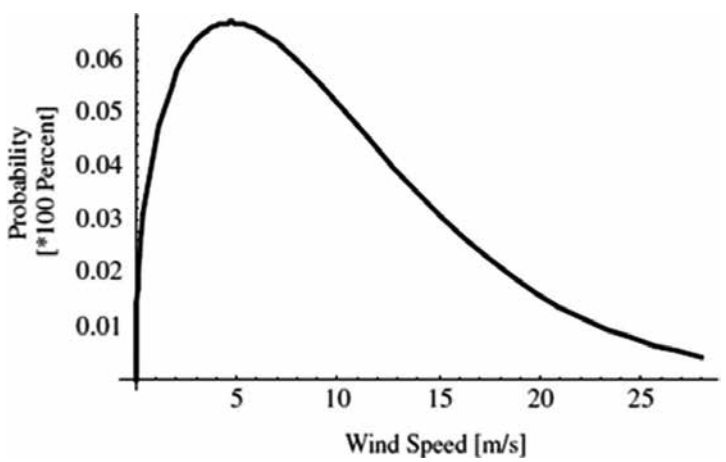

Figure 16. Weibull distribution function of Manjil.

6.4. Investigation on fatigue of the blade

There are different sources which produce cyclic loads on a wind turbine blade. Some of them are the variation of wind speed, annual gust, rotation of rotor, and variation of weight vector direction toward the local position of the blade [31]. The variation of wind speed and annual gust produces cyclic loads by changing the total amount of the load. Also, fluctuating load is produced by the rotation of rotor. In addition, the effect of wind shear, which arises from change of wind speed by change in height, causes cyclic loading. In the usual calculation, wind speed is measured at the hub center of rotor. So, the effect of wind shear is neglected because it has a negligible effect on the fatigue damage [18]. Therefore, this effect is not considered further in the design process. It has been proven that the wind shear effect acts in-phase with the weight vector.

The estimated lifetime of the blade by the computer code, which was executed 50 times, is shown in **Figure 17**. The results show that the maximum and minimum lifetimes are 24 and 18.66 years, respectively, and the average is 21.33 years. Further, 1.59 years are the standard deviation of the obtained results.

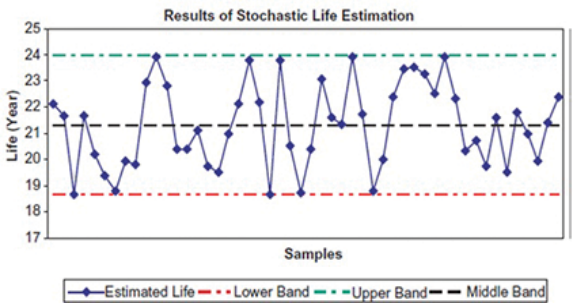

Figure 17. Predicted lifetime of the blade by computer code and for 50 runs.

7. Conclusion

In this chapter, the aerodynamic loading, design, static analysis, dynamic analysis, aeroelastic stability, and fatigue of composite wind turbine blades were considered. Aerodynamic loading with weight and the centrifugal loading to the blade was applied. Safety factor for failure in the composite model using Tsai-Wu failure criterion for the critical layer was obtained. In the FEM, using modal analysis and extracting natural frequencies and aeroelastic stability of structure, the safety factor was calculated and was equal to 1.39. In analytical method, the changes in natural frequencies of the system due to free stream speed were studied and flutter speed related to the coupling of bending and torsion was obtained. According to speed performance of turbine, safety factor of aeroelastic stability equivalent to 1.38 was calculated. Obtained safety factor was acceptable in all stages and indicates the stability and safety of composite blades structure in static, dynamic, and aeroelastic design. The accumulated fatigue

damage model was presented and applied based on CLPT. Furthermore, fatigue phenomenon was studied in the selected critical zone using accumulated fatigue damage modeling. The results of fatigue demonstrated that 24 and 18.66 years are the lower and upper limits, respectively. These results showed that the presented accumulated fatigue damage model was able to simulate the fatigue damage progress in a wind turbine composite blade. Considering the conservative nature of the employed technique, the investigated blade had 18.66 years in the worse situation and 24 years in the best situation.

Acknowledgements

The authors are grateful to the University of Kashan for supporting this work by Grant No. 463853/03.

Author details

Ahmad Reza Ghasemi* and Masood Mohandes

*Address all correspondence to: Ghasemi@kashanu.ac.ir

Department of Solid Mechanics, Faculty of Mechanical Engineering, University of Kashan, Kashan, Iran

References

[1] Jureczko M, Pawlak M, Mezyk A. Optimisation of wind turbine blades. Journal of Materials Processing Technology. 2005; 167, 463–471. doi:10.1016/j.jmatprotec. 2005.06.055

[2] Guo S. Aeroelastic optimization of an aerobatic aircraft wing structure. Aerospace Science and Technology. 2007; 11, 396–404. doi:10.1016/j.ast.2007.01.003

[3] Veers PS, Ashwill TD, Sutherland HJ, Laird DL, Lobitz DW. Trends in the design, manufacture and evaluation of wind turbine blade. Advances in Wind Energy. 2003; 6, 254–259. doi:10.1002/we.90

[4] Baumgart, A. A mathematical model for wind turbine blades. Journal of Sound and Vibration. 2002; 251, 1–12. doi:10.1006/jsvi.2001.3806

[5] Larsen JW, Nielsen SR. Nonlinear parametric instability of wind turbine wings. Journal of Sound and Vibration. 2007; 299, 64–82. doi:10.1006/jsvi.2001.3806

[6] Petrini F, Li H, Bontempi F. Basis of design and numerical modeling of offshore wind turbines. Structural Engineering and Mechanics. 2010; 36, 599–624. doi:10.12989/sem.2010.36.5.599

[7] Lee JW, Kim JK, Han JH, Shin HK. Active load control for wind turbine blades using trailing edge flap. Wind and Structures. 2013; 16, 263–278. doi:10.12989/was.2013.16.3.263

[8] Tenguria N, Mittal ND, Ahmed S. Structural analysis of horizontal axis wind turbine blade. Wind and Structures. 2013; 16, 241–248. doi:10.12989/was.2013.16.3.241

[9] Fung YC. An introduction to the theory of aeroelasticity. Dover Publications, INC, Mineola, New York; 1969.

[10] Joint aviation requirements, (JAR-23), Normal, Utility, Aerobatic and Commuter Category Aeroplanes, Joint Aviation Authorities, Hoofddorp, The Netherlands. March 1994.

[11] Shokrieh MM, Taheri-berooz F. Wing instability of a full composite aircraft. Composite Structures. 2001; 54, 335–340. doi:10.1016/S0263-8223(01)00107-6

[12] Baxevanou CA, Chaviaropoulos PK, Voutsinas SG, Vlachos NS. Evaluation study of a Navier–Stokes CFD aeroelastic model of wind turbine airfoils in classical flutter. Journal of Wind Engineering and Industrial Aerodynamics. 2008; 96, 1425–1443. doi:10.1016/j.jweia.2008.03.009

[13] Fazelzadeh SA, Mazidi A, Kalantari H. Bending-torsional flutter of wings with an attached mass subjected to a follower force. Journal of Sound and Vibration. 2009; 323, 148–162. doi:10.1016/j.jsv.2009.01.002

[14] Lee JW, Lee JS, Han JH, Shin HK. Aeroelastic analysis of wind turbine blades based on modified strip theory. J. Wind Eng. Ind. Aerod. 2012; 110, 62–69. doi:10.1016/j.jweia.2012.07.007

[15] Sutherland HJ. On the fatigue analysis of wind turbines. Sandia National Laboratories, Albuquerque, New Mexico; 1999.

[16] Mandel JF, Samborsky DD, Cairns DS. Fatigue of composite materials and substructures for wind turbine blades. Sandia National Laboratories, Albuquerque, New Mexico; 2002.

[17] Shokrieh MM, Rafiee R. Lifetime prediction of HAWT composite blade. In: 8th International Conference of Mechanical Engineering (ISME), Iran; 2004. p. 240.

[18] Noda M, Flay RGJ. A simulation model for wind turbine blade fatigue loads. Journal of Wind Engineering and Industrial Aerodynamics. 1999; 83, 527–40. doi:10.1016/S0167-6105(99)00099-9

[19] Germanischer Lloyd Rules and Guidelines Industrial Services, Part IV, Guideline for the Certification of Wind Turbines, Chapter 4, Load Assumptions, Hamburg, Germany, Edition 2010.

[20] Eggleston DM, Stoddard FS. Wind turbine engineering design. Springer, Van Nostrand Reinhold Co. Inc., New York, USA; 1987.

[21] Ghasemi AR, Jahanshir A, Tarighat MH. Numerical and analytical study of aeroelastic characteristics of wind turbine composite blades. Wind and Structures. 2014; 18, 103–116. doi:10.12989/was.2014.18.2.103

[22] Ghasemi AR, Tarighat MH. Aeroelastic analysis of composite wind turbines blades. Journal of Mechanical Engineering University of Tabriz. 2015; 44, 31–39.

[23] Tsai SW, Massard TN. Composites design (4th Ed.). Think Composites, Dayton, OH; 1984.

[24] Hodges DH, Pierce GA. Introduction to structural dynamics and aeroelasticity. Cambridge University Press, New York, USA; 2002.

[25] Shokrieh M, Lessard LB. Progressive fatigue damage modeling of composite materials, Part I: Modeling. Journal of Composite Materials. 2000; 34, 1056–80. doi: 10.1177/002199830003401301

[26] Ye L. On fatigue damage accumulation and material degradation in composite materials. Composite Science and Technology. 1989; 36, 339–50. doi: 10.1016/0266-3538(89)90046-8

[27] Shokrieh MM, Zakeri M. Evaluation of fatigue life of composite materials using progressive damage modeling and stiffness reduction. In: Proceedings of the 11th Annual Conference of Mechanical Engineering, Iran; 2003. p. 1256–1263.

[28] Charewics A, Daneil IM. Damage mechanics and accumulation in graphite/epoxy laminates. In: Hahn HT, editor. Composite Materials: Fatigue and Fracture. 1986; 247–288. doi:10.1520/STP19991S

[29] Lee JW, Daniel IM, Yaniv G. Fatigue life prediction of cross-ply composite laminated. In: Lagace PA, editor. Composite Materials: Fatigue and Fracture, ASTM International. 1989; 19–28. doi:10.1520/STP10406S

[30] DOE/MSU. Composite materials fatigue database. Sandia National Laboratories, Albuquerque, New Mexico; 2003.

[31] Shokrieh MM, Rafiee R. Lifetime prediction of HAWT composite blade. In: 8th International Conference of Mechanical Engineering (ISME), Iran; 2004. p. 240.

Chapter 2

A Review of Wind Turbine Yaw Aerodynamics

Daniel Micallef and Tonio Sant

Additional information is available at the end of the chapter

http://dx.doi.org/10.5772/63445

Abstract

The fundamental physics of HAWT aerodynamics in yaw is reviewed with reference to some of the latest scientific research covering both measurements and numerical modelling. The purpose of this chapter is to enable a concise overview of this important subject in rotor aerodynamics. This will provide the student, researcher or industry professional a quick reference. Detailed references are included for those who need to delve deeper into the subject. The chapter is also restricted to the aerodynamics of single rotors and their wake characteristics. Far wake and wind turbine to turbine effects experienced in wind farms are excluded from this review. Finally, a future outlook is provided in order to inspire further research in yawed aerodynamics.

Keywords: horizontal axis wind turbine, yaw, unsteady aerodynamics, wakes, rotors

1. Introduction: The relevance of wind turbine yaw aerodynamics

1.1. Wind turbine yaw fundamentals

A wind turbine converts the kinetic energy from the wind to electrical energy. The power which can be extracted is proportional to the cube of the wind speed. There is, however, a theoretical limit to the power which can be extracted from the turbine. This is known as the Betz limit. This limit was derived by Betz [1] to correspond to 59% of the maximum available power which can be extracted by the turbine. The efficiency of a wind turbine is called the power coefficient and is defined by the following:

$$C_P = \frac{P}{\frac{1}{2}\rho U_\infty^3 A} \tag{1}$$

where P is the turbine power, ρ is the density, U_∞ is the wind velocity and A is the rotor area. In practice, due to various practical reasons, only a fraction of the Betz limit can be exploited. Some reasons for this reduction in the overall efficiency of the turbines are mostly associated with the wind resource itself and include wind shear [2, 3], wind turbulence [4, 5], and yaw. In this chapter, we focus our attention on the latter for the case of a horizontal axis wind turbine (HAWT).

Yaw occurs when the wind direction is not perpendicular to the rotor plane. When the HAWT operates in yaw, the average power extracted by the turbine reduces as compared to the case when the wind is perpendicular to the rotor plane. This yawed flow situation is depicted in **Figure 1** where γ is the yaw angle. The blade will experience a varying relative velocity and angle of attack with azimuthal blade position, leading to an unsteady aerodynamics problem.

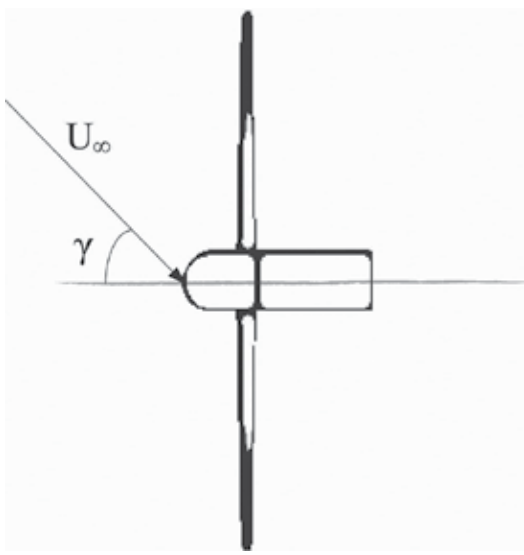

Figure 1. Wind turbine operating in yaw.

1.2. Relevance of studying yawed flows

Although modern wind turbines allow for various yaw mechanisms in order to align the turbine with respect to the incoming wind, the response to variations in wind direction is very slow. Consequently, the turbine will be in yaw during most of its operational time. Eggleston and Starcher [6] and Madsen et al. [7] show time series results of wind direction as observed from a sensor installed on two different experimental turbines in the field. A time series for

the wind yaw angle measured from the experimental turbines is shown in **Figure 2**. For the Tellus turbine (right figure), during a particular instant in time, the yaw angle increases and varies dramatically. The yaw angle can reach up to around 60°, depending on the wind flow characteristic on site.

While the yawed flow scenario presents an important and challenging problem, the basis of understanding the wind turbine aerodynamics is the axial flow case. The major challenges in the understanding of wind turbine flows are associated with the root and tip flows [8–10]. For an in-depth review of wind turbine aerodynamics, particularly for wind turbines operating in axial flow, the reader is referred to [11] and lately in [12].

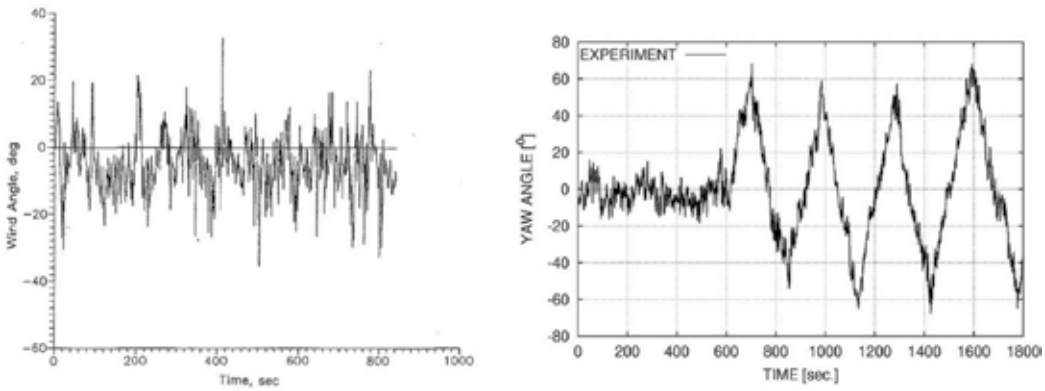

Figure 2. Time series of yaw angle during testing of (left) the Carter 25 turbine (wind direction sensor behind nacelle) [6] and (right) the Tellus turbine [7].

Unsteady aerodynamics inevitably results in unsteady loads which negatively affect the power quality and fatigue lifetime of wind turbines. Reference [13] provides a detailed overview of the various challenges in modelling wind turbines under unsteady conditions, including rotor yaw, given the lack of understanding of many aerodynamic phenomena associated with the wake structure developed behind the turbine and the dynamics of unsteady flows over the blade sections.

Wind turbines operating in wind farms are well known to suffer from significant aerodynamic interference losses, primarily due to the axial velocity deficit incurred by the wind flowing through the upstream turbines. The power output from full-scale turbines operating in large wind farms may be as low as 40% of a stand-alone turbine, depending on the turbine spacing as well as environmental flow conditions including the mean wind speed, turbulence intensity and atmospheric stability (see [14]). Yaw aerodynamics may eventually become more important for large offshore wind farm design, given the possibility of mitigating such wake losses by skewing the upstream turbine wake using smart rotor yaw control.

In this chapter, a review of the physics of HAWT aerodynamics in yaw is given by focusing on the aerodynamic phenomena of the near wake and the flow over the rotating blade sections. Far wake and turbine-to-turbine interference effects are excluded from this study. Further-

more, emphasis is made on single HAWT rotors operating in fixed yaw and under steady and uniform wind fronts. Reference is made to some of the latest scientific research in the field, including state-of-the-art wind tunnel measurements undertaken on model turbines under controlled conditions.

2. The blade element momentum (BEM) theory

The momentum conservation principle can be applied in order to be able to determine the wake inductions, and hence, the turbine blade loading and performance. In the blade element momentum (BEM) method, the blade is divided into a number of 2D elements. The momentum principle is then applied on aerodynamically independent annular elements. In doing so, a number of limitations and assumptions arise:

a. Inviscid flow.

b. Annular air elements are independent (no radial flow from one element to the next).

c. Aerofoil polars are generally based on 2D wind tunnel measurements.

d. The loading of the blades on the air is assumed not to vary with azimuth meaning that an infinite number of blades assumed. This must be resolved using tip loss correction methods.

e. The theory alone cannot be used for highly loaded rotors, where turbulent mixing is prevalent.

The velocity diagram for a particular blade element is shown in **Figure 3**. The relative velocity is given by the following:

$$V_{rel} = \sqrt{\left(U_{\infty} + V_{axial,ind}\right)^2 + \left(r \quad + V_{\theta,ind}\right)^2} \tag{2}$$

where $V_{axial,ind}$ is the axial wake-induced velocity (which would be opposing the freestream velocity), and $V_{\theta,ind}$ is the tangential wake-induced velocity. The inflow angle ϕ (indicated in **Figure 3**) can thus be found from:

$$tan\varphi = \frac{U_{\infty} + V_{axial,ind}}{r\Omega + V_{\theta,ind}} \tag{3}$$

from which the angle of attack becomes the difference between the inflow angle and the blade's pitch and twist angles (the sum of which is here represented by θ).

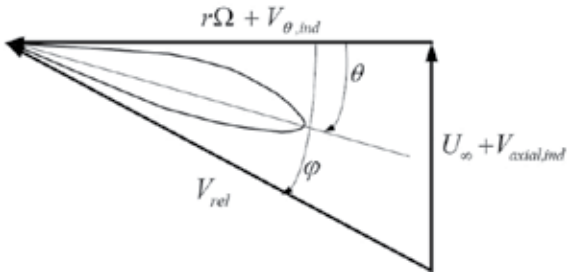

Figure 3. Velocity diagram for a blade section in axial flow at radius r. The blade section shown moves from left to right of the figure. Source: Micallef [19].

$$\propto = \varphi - \theta \tag{4}$$

From the aerofoil data, the normal and tangential force coefficients (with respect to the rotor plane) can be determined from the lift and drag coefficients (C_l and C_d) and the inflow angle ϕ as follows:

$$C_n = C_l cos\varphi + C_d sin\varphi \tag{5}$$

$$C_t = C_l sin\varphi - C_d cos\varphi \tag{6}$$

The induction factors defined as $a_1 = V_{axial,ind}/U_\infty$ and $a_2 = V_{\theta,ind}/r\Omega$ may then be determined applying the law of conservation of momentum in the axial and azimuthal directions by assuming that the momentum expressions are equal to the blade element expressions:

$$4a_1\left(1 - a_1\right)U_\infty^2 = \sigma V_{rel}^2 C_n \tag{7}$$

$$4a_2\left(1 - a_1\right)\Omega r U_\infty r = \sigma V_{rel}^2 C_t r \tag{8}$$

where a_1 and a_2 are the axial and tangential induction factors. σ is defined as the rotor local solidity:

$$\sigma = \frac{Bc}{2\pi r} \tag{9}$$

where c is the chord and B is the number of blades. This formulation does not include the effect of the finite number of blades. The most commonly used approach to deal with this problem

is to use the Prandtl tip loss factor reported [1]. In this formulation, Prandtl uses a disc representation to represent the wake effect and the finite number of blades. This is shown in **Figure 4**.

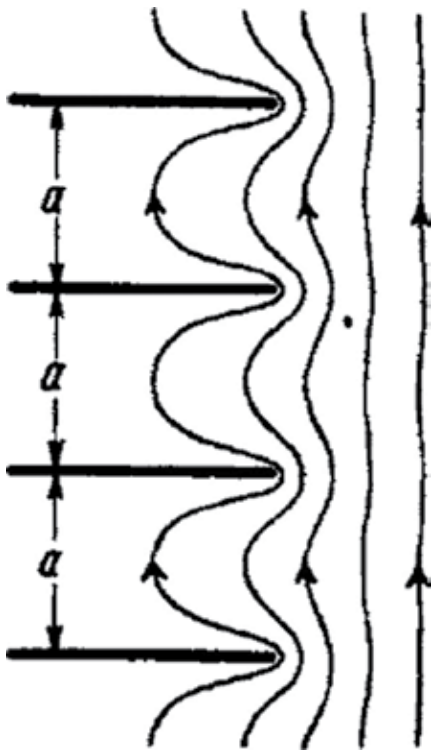

Figure 4. Prandtl tip loss model using a number of vorticity discs spaced apart by a distance a. Source: [1].

Prandtl came up with an analytical and implementable solution from a tip loss factor F of the following form:

$$F = \frac{2}{\pi} cos^{-1}\left(exp\left(-\frac{B(R-r)}{2R} \frac{\sqrt{(R)^2 + U_\infty^2 (1-a_1)^2}}{U_\infty (1-a_1)} \right) \right) \tag{10}$$

One way to account for tip loss is to modify Eqs. (13) and (14) to include the tip loss factor and re-arrange them for an iterative solution, as follows:

$$a_1 = \frac{1}{\frac{4Fsin^2\varphi}{\sigma C_n} + 1} \tag{11}$$

http://dx.doi.org/10.5772/63445

$$a_2 = \frac{1}{\frac{4Fsin\varphi cos\varphi}{\sigma C_t} - 1} \tag{12}$$

Various authors, such as in [15], assessed the validity of this model using a computational fluid dynamics (CFD) approach. While the accuracy of the Prandtl tip loss model is debatable, it nonetheless provides a simple solution to a complex problem and is still to date the most common method for accounting for a finite number of blades.

The algorithm for implementing the BEM theory can be found in various textbooks including [15–18]. Here, the one given in [19] is adapted:

1. Set $a_1 = a_2 = 0$.
2. Find the flow angle ϕ and hence the angle of attack α.
3. Calculate the tip loss factor from Eq. (10).
4. Read C_l and C_d from the 2D aerofoil polars.
5. The normal and tangential thrust coefficients C_n and C_t can be calculated from Eqs. (5) and (6).
6. New values for a_1 and a_2 can be established from Eqs. (17) and (18).
7. If a_1 and a_2 have converged below a defined tolerance, then move to the next step. Otherwise, repeat starting from step 2.
8. Compute the thrust and torque for the wind turbine rotor using the following:

$$T = B\int_{R_r}^{R} 4\pi\rho U_\infty^2 a_1\left(1-a_1\right) r dr \tag{13}$$

$$Q = B\int_{R_r}^{R} 4\pi\rho U_\infty \quad r a_2\left(1-a_1\right) r^2 dr \tag{14}$$

3. The BEM theory for yawed wind turbines

3.1. Modifications to the axial momentum theory

The linear momentum theory is modified for yawed wind turbines on the basis of Glauert's autogyro theory (see Glauert [20]). Only the normal wind flow component $U_\infty \cos\gamma$ is assumed to be affected by the presence of the actuator disc. It is assumed that this component changes to $U_\infty \cos\gamma + u$ at the disc and the resultant flow velocity here becomes

$$u' = \sqrt{U_\infty{}^2 sin^2\gamma + U_\infty{}^2 \left(cos\gamma - a\right)^2} \tag{15}$$

Glauert expresses the momentum equation for the axial thrust T on the rotor as

$$T = 2\rho AaU_\infty u' \tag{16}$$

The thrust parallel to the plane of the disc is zero as it is assumed that the flow component $U_\infty sin\gamma$ is left unperturbed by the rotor.

In yawed conditions, the wind speed and inflow relative to the moving blades change with azimuth angle. The velocity diagram for the blade at the top-most position is shown in **Figure 5**. The resultant velocities would hence be the following:

$$V_{axial} = U_\infty \cos\gamma - V_{axial,ind} \tag{17}$$

$$V_\theta = r\Omega + V_{\theta,ind} - U_\infty sin\gamma\, cos\phi \tag{18}$$

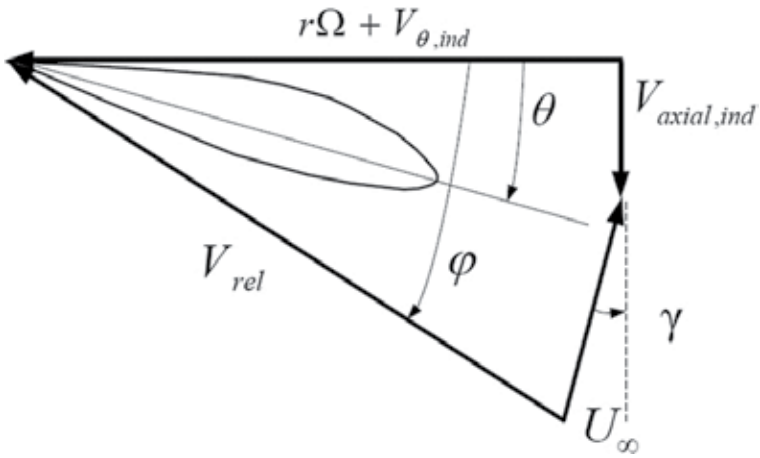

Figure 5. Velocity diagram for a blade section of a yawed rotor blade at radius r. The blade section is shown at the top most position and rotating clockwise. Source: [39].

Anderson showed, using a BEM approach that the power coefficient of a yawed turbine reduces with increasing yaw [16]. This hypothesis was later confirmed in [17, 18]. The results obtained by [18] for a 2- and 3-bladed rotor are compared with those found in [16, 17] in **Figure 6**. C_P is the power coefficient at a given yaw angle, while C_{Pmax} is that under axial conditions. The rotors which were used in these studies are different, and hence, a qualitative agreement was only obtained.

http://dx.doi.org/10.5772/63445

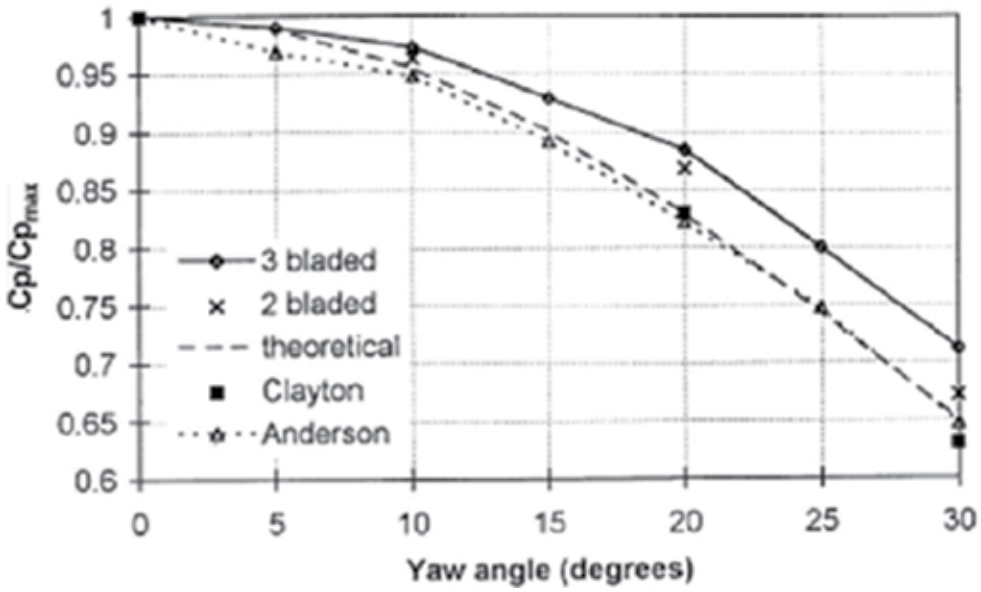

Figure 6. Power coefficient normalized by the maximum power coefficient (zero yaw) against yaw angle. Clayton and Filby considered a 3-bladed rotor while Anderson considered a 2-bladed rotor in his BEM analysis. The difference in results is primarily due to the different rotor geometries. The results, however, agree qualitatively (see [18]).

The ratio C_P/C_{Pmax} representing the loss in power due to rotor yaw may be approximated to $\cos^x(\gamma)$. The exponent x is often thought to be equal to 3; however, this is only valid if the axial induction distribution is small compared to $U_\infty \cos\gamma$ or the axial induction factor distribution is unchanged as a result of yaw. Recent wind tunnel measurements on the 0.9 m diameter 3-bladed model at NTNU have shown that the C_P/C_{Pmax} followed well the $\cos^3(\gamma)$ relation (see [21]). A different situation was observed in another measurement. In [22], it is reported that measurements involving both wind tunnel models and full-scale turbines tested at Vattenfall/FFA and DNW have indicated that the exponent x may vary between 1.8 and 5 for the NREL Phase VI rotor (see [23] pp. 181–183). Such studies have also consistently shown that the BEM theory over predicts the power at yawed conditions. This is possibly related to the limitations of the linear momentum equation modified for yawed flows [Eq. (16)].

Although yawed flow contradicts the fundamental assumption used in BEM of having radially independent annular elements, BEM models have still been used in yaw (refer to [24]). In order to correct for the asymmetric wake induction, a model was first developed in [25] in his work on the autogyro. Ignoring this correction will result in a zero restoring yawing moment, which has been shown experimentally to be unrealistic. Glauert proposed that the induction factor at the blades would take the following form:

$$a = a_1\left(1 + K\frac{r}{R}sin\phi\right) \tag{19}$$

where a_1 is the average induction factor, K is a function of yaw angle, r is the radial station in consideration, R is the rotor radius and ϕ is the azimuthal position of the rotor blade. Much of the efforts of the early experiments in yawed flow HAWTs were aimed at understanding the wake expansion and deflection. This enabled various improvements in the classical BEM techniques by improving the parameter K in the Glauert expression for the azimuthally varying induction [see Eq. (19)]. There are various models of the function K some of which are given here.

Coleman et al. [21]:

$$K = tan\left(\frac{\chi}{2}\right) \tag{20}$$

White and Blake [26]:

$$K = \sqrt{2}sin(\chi) \tag{21}$$

Pitts and Peters [27]:

$$K = \frac{15\pi}{32}tan\left(\frac{\chi}{2}\right) \tag{22}$$

Howlett [28]:

$$K = sin^2(\chi) \tag{23}$$

where χ is the skew angle; the angle between the wake and rotor axis. In the BEM formulation, this angle is defined as follows:

$$tan\chi = \frac{(U_\infty sin\gamma)}{(U_\infty cos\gamma - u_a)} \tag{24}$$

The K factors derived from the different models listed earlier are plotted in **Figure 7** to compare the differences. As can be seen, there are dramatic discrepancies between the results of various authors. Since this function will ultimately affect the varying inductions on the plane, knowledge of the induction field is also necessary to create sound models.

http://dx.doi.org/10.5772/63445

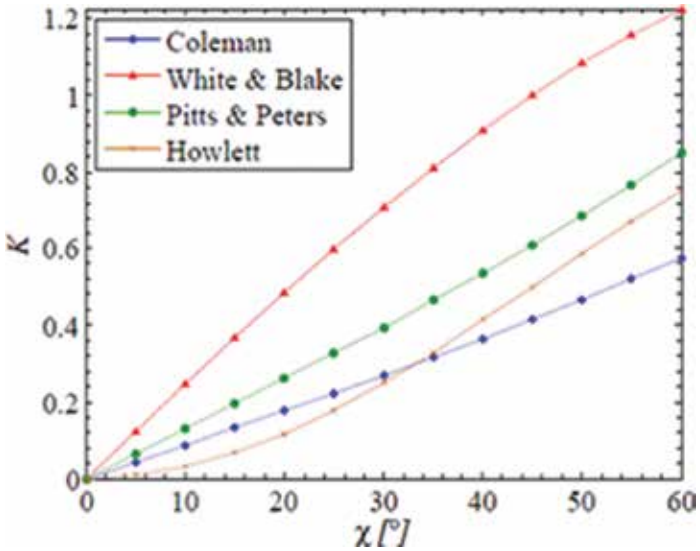

Figure 7. Comparison of the variation of K with χ as predicted by the different models.

Other engineering models were developed in the past years, some of which were examined against measurements in the EU JOULE Dynamic Inflow Projects (see [29, 30]). These models have been implemented in various BEM-based aeroelastic codes. One such model is that developed by Øye [31] and is similar to Glauert's model but introduces a radial variation in induction. The model was derived through a curve fitting procedure with results from an actuator disc model. The induced velocity distribution was found to depend on the radial location, azimuth angle and the wake skew angle:

$$a = a_1\left(1 + f_{2,tudk}\tan\frac{\chi}{2}\sin\varnothing\right) \tag{25}$$

$$f_{2,tudk} = \frac{r}{R} + 0.4\left(\frac{r}{R}\right)^3 + 0.4\left(\frac{r}{R}\right)^5 \tag{26}$$

The Glauert correction model [Eq. (19)] gives acceptable results towards the tip region of the blade where the sinusoidal variation of the induction is prevalent. However, the root region of the blade does not exhibit sinusoidal behaviour as was found in the experiments in [32]. Based on this same experiment, Schepers used Fourier series expansions to establish a model for yaw which models better the radial dependency of the induction variation with azimuth (see [33]). This is shown here for a particular radial station along the blade:

$$a = a_1\left(1 - A_1\cos\left(\varnothing - \varphi_1\right) - A_2\cos\left(2\varnothing - \varphi_2\right)\right) \tag{27}$$

where the amplitudes A_1 and A_2 and the phases ϕ_1 and ϕ_2 are curve fitting parameters, all functions of radial position. Also, Ref. [34] (pp. 403–405) recommends the inclusion of higher harmonics in BEM yaw modelling.

3.2. Unsteady aerofoil aerodynamics

As discussed earlier, yaw results in an asymmetric flow field where the relative velocity magnitude and direction (and hence angle of attack) both vary with time. Yawed HAWTs are for this reason naturally susceptible unsteady aerodynamic phenomena. Such phenomena give rise to hysteresis effects, even at small angles of attack for which the flow is fully attached. At high angles of attack however, dynamic stall leads to more pronounced hysteresis on both the lift and drag, with the resulting loads often exceeding that static loads significantly. A description of different dynamic stall models applied to wind turbines is presented in [35].

Dynamic stall on a rotating blade is more complex than that experienced in 2D flow conditions. Schreck (see [36, 37]) investigated the 3D dynamic stall processes on the NREL UAE Phase VI rotor through the analysis of blade surface pressure data and the local inflow angle when operating under yawed conditions. In the EU project 'Dynamic stall and 3D effects' coordinated by FFA, it was attempted to use the IEA Annex XVIII measurement to understand dynamic stall effects. An example is given in **Figure 8** for non-yawed conditions in the field. They show measurements of normal force coefficients at 68% span as function of angle of attack (around a low and a high angle of attack) on the Risø experiments, carried out on a 3-bladed, 19 m diameter turbine (see [38]). The angle of attack is derived from a local inflow angle as measured with a pitot probe and corrected for upwash. Hysteresis effects are visible at high angles of attack but in a very disorderly pattern.

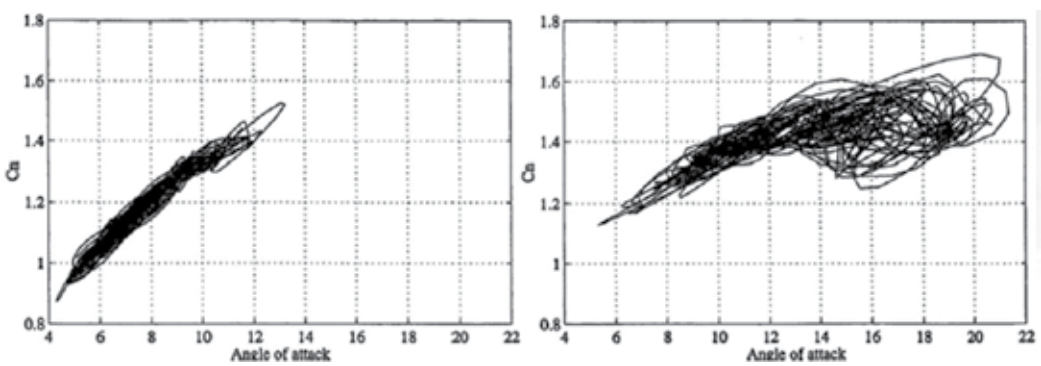

Figure 8. Measured normal force coefficient as a function of angle of attack measured at 68% span, low angle of attack series, and high angle of attack series are shown. Source: [38].

The reduced frequency k can be estimated as follows if the freestream velocity is assumed negligible compared to the rotational speed:

http://dx.doi.org/10.5772/63445

$$k = \frac{\Omega c}{2V_{rel}} \approx \frac{\Omega c}{2r\Omega} \approx \frac{c}{2r} \tag{28}$$

where c is the chord length, r is the radial location along the blade, Ω is the rotational speed, and V_{rel} is the relative velocity to the blade section. In situations where $k < 0.05$ can be considered steady or quasi-steady, values of $k = 0.1$ are typical for wind turbines in yaw. It is clear that this measure of unsteadiness is a function of the c/r ratio.

In [7], various models are used including a BEM approach (HAWC), an Navier-Stokes solver (EllipSys3D) and an actuator disc solver (HAWC3D) to find the local inflow angle (angle between local relative velocity and chord line) and angle of attack as well as the magnitude of the relative velocity and how it changes. Results are shown for the 91% station on the NREL UAE rotor in **Figure 9**. EllipSys3D results were very accurate as this model includes the effect of the wing geometry in its entirety, and hence, the local inflow angle was calculated. The other results, however, show quite a large difference since the models calculate the actual angle of attack. Despite the differences, the variation of angle of attack with azimuthal position is clear and leads to the unsteadiness that the yawed HAWT suffers from.

Lately, the loads on a yawed wind turbine have been established directly through stereo particle image (SPIV) measurements (see [39]) and reported in [40, 41], but these are limited to only one blade position, thus not allowing for establishing the time variation of the blade loads in yaw.

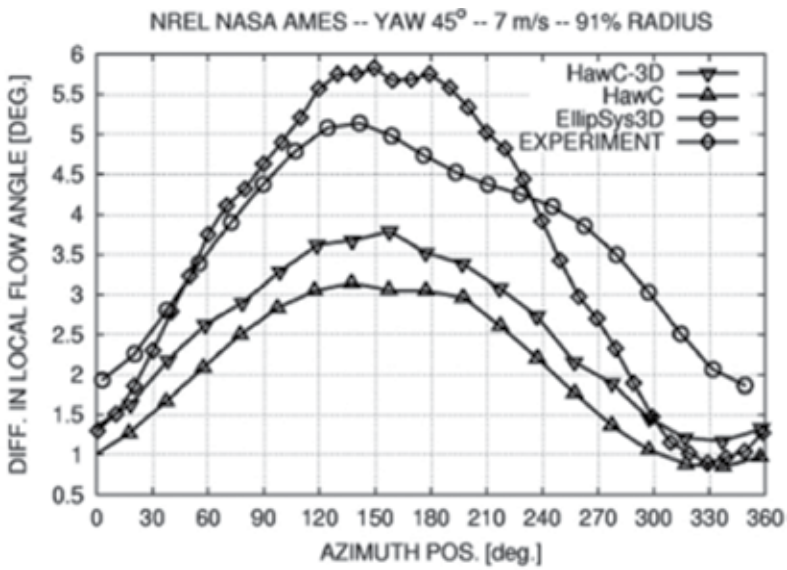

Figure 9. Local inflow angle for the NREL UAE rotor at 45° yaw and 7 m/s wind speed. Source: [7].

4. Wake characteristics

Experimental research has clearly demonstrated that in reality the wake of a wind turbine is by far more complex than that assumed in the BEM theory. It actually comprises helical vortex sheets, with one sheet originating from each individual rotating blade as illustrated in **Figure 10**. The circulation distribution in the vortex sheet originates from the bound circulation (Γ_B) developed at the blades. The wake circulation is composed of two vector components: trailing circulation (Γ_T) that is released from the blades in a direction normal to the trailing edges of the blades and is related to the spanwise variation of bound circulation ($d\Gamma_B/dr$); and shed circulation (Γ_S) that is released from the blades in a direction parallel to the blades' trailing edges and is related to the variation of bound circulation with time ($d\Gamma_B/dt$). The geometry of the vortex sheet emerging from each individual blade will change such that the edges roll-up (similar to that observed on a wind in linear flight) to form a strong tip vortex and root vortex.

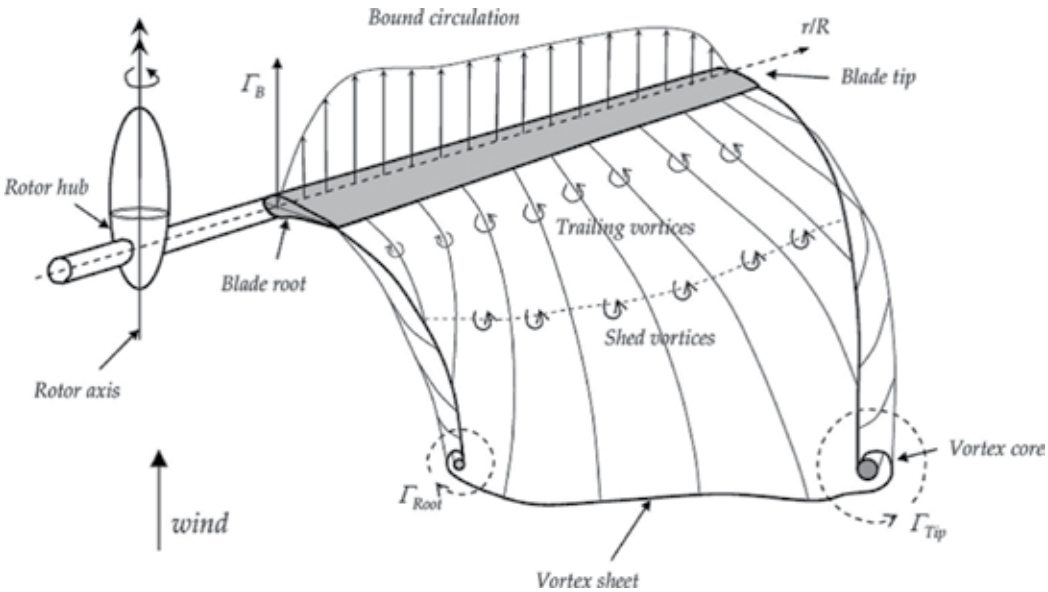

Figure 10. The formation of helical vortex sheet by a rotating wind turbine blade. Adapted from [38].

The helical wake of the turbine expands as a consequence of the slowdown of moving air. The higher the operating thrust coefficient, the higher the wake expansion. This has been shown by various researchers such as in [42, 43]. Tip vortices are easily noticeable in experiments on model rotors, even beyond one rotor diameter downstream. Smoke visualizations of tip vortices are shown in **Figure 11**. The root vortices are more difficult to track in experiments and have been only observed much closer to the rotor plane, as, for example, in the recent PIV measurements undertaken [39, 44]. It is most probable that the root vortex diffuses rapidly due to the interference effects of the turbine support structure.

In a yawed rotor, the blade sections have a geometric velocity component in a direction of the free wind speed resulting in the advancing and retreating effect. A variation in both the relative wind speed and angle of attack is experienced with the highest relative velocity reached by the advancing blade when it is vertical pointing upwards. Yawed conditions cause the wake to become skewed leading to an uneven distribution of induction at the rotor disc (see **Figure 12**). Measurements have shown that yawed wind turbines experience a restoring yawing moment. As noted in [23] (pp. 49–53), this moment is not generated by the advancing and retreating blade effect but by the skewed wake geometry which causes the trailing tip vorticity to be on average closer to the downwind side of the rotor plane.

Figure 11. Visualisation of the tip vortices for the experiment done under non-yawed conditions by [42].

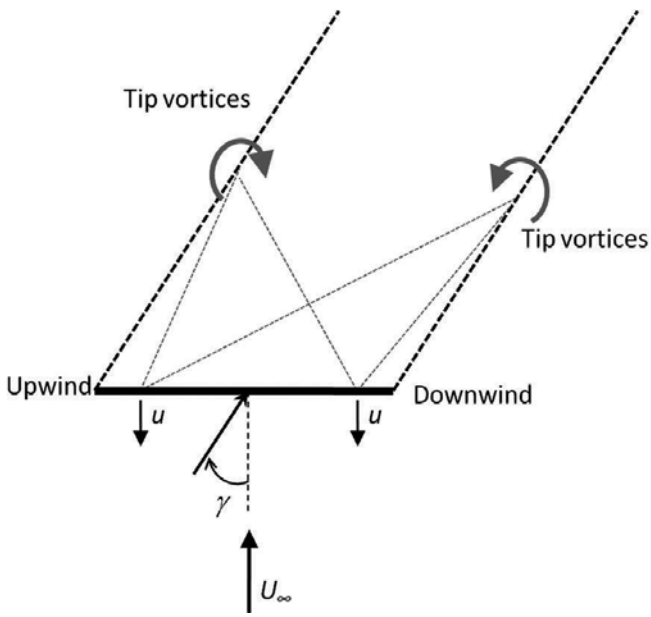

Figure 12. Unbalance in the induced velocity from the skewed wake under yawed conditions. Adapted from [23], (pp. 49).

Induced velocities on the upwind side or the rotor are hence lower, leading to large axial thrust loads on the blade sections here to develop a restoring yawing moment.

The influence of the skewed wake geometry on the induction at the rotor plane of yawed turbines was extensively studied in the EU JOULE Dynamic Inflow Projects (refer to Snel and Schepers [29, 30]). The implementation of advanced aerodynamic models based on vortex methods by Voutsinas et al. [45] and the acceleration potential technique by van Bussel [46, 47] has clearly indicated that, in addition to tip vorticity, root vorticity also has a considerable influence on the induction distribution at the rotor plane. However, root vorticity contributes to the generation of a destabilising yawing moment, hence opposing that induced by tip vorticity.

The axial thrust of a rotor with a finite yaw angle varies with azimuth and as a result, the expansion will vary along the azimuthal direction. This has been shown again by Grant et al. [48] and Haans et al. [49]. Some results are shown in **Figure 13**. As can be seen, there is a high expansion in the region where the rotor tip is pointing downwind and almost no expansion in the region where the rotor tip is pointing upwind. These results are coherent with the findings of [48]. The higher the yaw angle, the smaller the thrust coefficient, and hence, the smaller the expansion. Unfortunately, no empirical models have been proposed for the wake deformation in yaw. This would enable practical application in the design of wind turbine blades with applications in BEM or prescribed wake models. Haans et al. [49] have also derived the wake skew angle χ directly from the smoke visualizations of tip vortices at yaw angles equal to 15°, 30°, and 45°. This angle was found to be larger than the yaw angle at all tested blade pitch angles and tip speed ratios. It was observed that for each tested yaw angle, χ increased linearly with the measured axial thrust coefficient C_T (see **Figure 14**).

The analysis of wake development requires the use of velocity field measurements over a particular area. Due to this, techniques such as PIV must be used. Such measurements have been performed by [50] and in the MEXICO experiment (see [51]). More recent PIV measurements include those undertaken at TUDelft [39, 52], at NTNU [53] and at Monash University (see [44]). In the experiment by [50], PIV measurements were obtained at various blade azimuthal positions. With these measurements, the variation of the tip vortex circulation was calculated for yaw angles of +30° and -30° yaw as well as for the axial case. **Figure 11** from [50] shows various vorticity contour plots of the tip vortex at various blade azimuth phase angles and at various yaw angles. Information on the magnitude of vorticity is not present so only insight on the iso-vorticity lines can be gained. Soon after release, a 'vorticity tail' becomes apparent from the tip vortex for all cases particularly for yaw. The authors attribute the additional vorticity in these cases to the presence of additional shed vorticity in the wake of a yawed turbine due to the variation of bound vorticity with time. For the -30° yaw, the 'vorticity tail' is first located downstream since the measurement plane is in the upwind direction. For the +30° yaw, the 'vorticity tail' is pointing upwind since the measurement plane is in the downwind direction. As can be noticed, for the +30° yaw case, the vortex remains small. The trailing vorticity from the vortex sheet detaches itself and does not continue to feed into the tip vortex. This is the reason for the low circulation levels found in **Figure 11** of [50]. On the other hand for the -30° yaw case, the interaction between the trailing vorticity and the tip vortex

is more complex and is persistent up to 156° of azimuth blade position. The vortex becomes larger, and the circulation is similar to that found in the axial flow case.

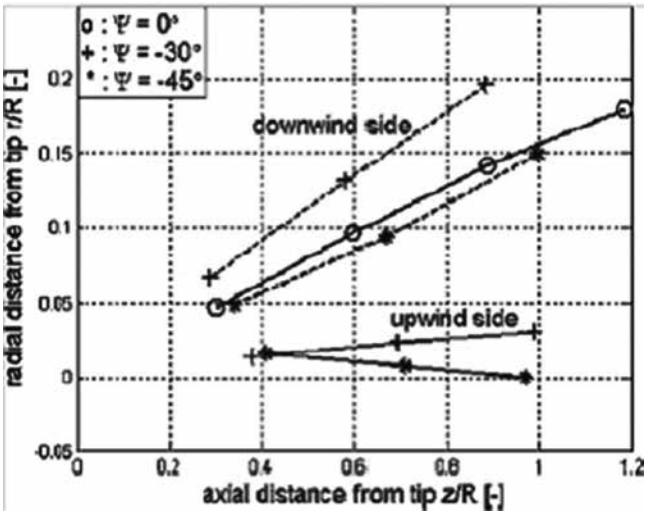

Figure 13. Wake pitch measurements: Source: [49].

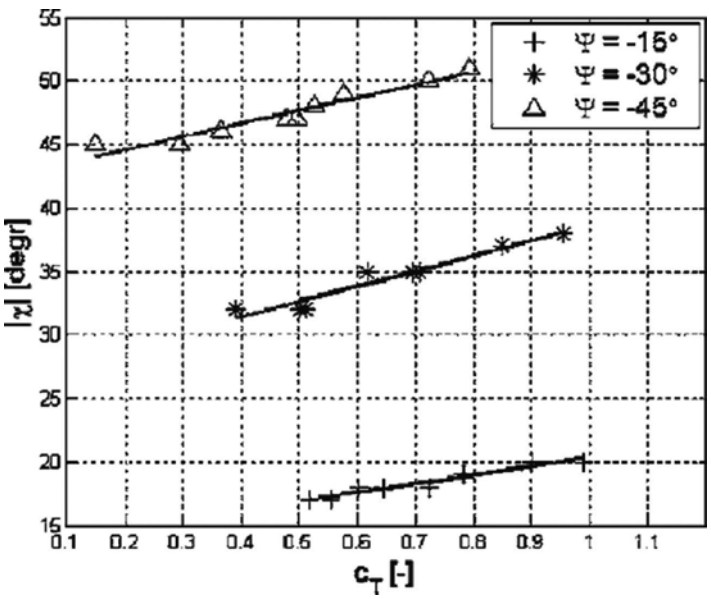

Figure 14. $|\chi_s|$ vs C_T for three yawed conditions. Source: [49].

In [54], the authors investigated the radial flows of the MEXICO rotor under both axial and yawed conditions. The investigation was based on both the experimental SPIV measurements

and numerical analysis using a 3D unsteady free-wake vortex model. The study found that the radial velocity increased by a factor of 2 when the turbine was yawed due to the in-plane freestream component. Under axial conditions, it was observed that a slight inboard convection of the tip vortex occurs. This phenomenon was also confirmed later on the more detailed SPIV measurements by Micallef on the TUDelft rotor (see [39]). In these more recent measurements, the tip vortex evolution could be clearly traced as a function of rotor azimuth angle. It could be noted that under yawed conditions, outboard motion of the tip vortex was delayed to a blade azimuth of 10°, even though a radial component equal to $U_\infty \sin\gamma$ was present.

5. Summary of research on HAWT rotors in yaw

A comprehensive summary of various experiments on HAWT rotors under both controlled and open field conditions is given in **Table 1**. **Table 2** includes references to various works covering the different aspects of HAWT aerodynamics in yaw discussed in this study.

Contributor	Year	Type	Rotor diameter	Blade	Variables	Information
Clayton and Filby, University College London	1982	HWA in the wake (for averages velocities and turbulence measurements) and power output	0.5 m (test section size not available)	3-bladed, no details of the chord, twisted NACA4415, tapered blades	Tip speed ratio, yaw angle, pitch angle	$1.4 \le \lambda \le 9.8$ $0° \le \gamma \le 40°$ $-15° \le \theta \le 15°$
Vestas Tjaereborg 2MW wind turbine	1983	Load measurement	61.1 m	3-bladed, tapered	N/A	Field experiment
NREL UAE Phase I–IV Experiments	1987	Blade pressure and load measurements	10 m	3-bladed, downwind, Constant chord, Twisted	N/A	Field experiment
Vermeer, TUDelft	1987	HWA	2.24 m	2-bladed, constant chord, twisted, NACA0012	Yaw angle	Max Re = 2:4e5
Bruining, TUDelft	1994	Blade pressure measurements	10 m	2-bladed, untapered,untwisted	Tip speed ratio, yaw angle	$4 < \lambda < 10$, 0:5e6 < Re < 1e6
Grant, Heriot-Watt University	1997	Smoke visualization and power output	0.9 m in open jet tunnel	2 and 3 blades, tapered	Yaw angle	$\lambda = 6:7$ 5:9e4 < Re < 1e5
Grant, Heriot-Watt	2000	PIV	0.9 m in open jet tunnel	3-bladed, tapered, untwisted but pitched, NACA4613, NACA3712	Yaw angle	$\lambda = 5:2$ $-30° \le \gamma \le 30°$

Contributor	Year	Type	Rotor diameter	Blade	Variables	Information
University				and NACA4611		
NREL UAE Phase VI Experiment	2000	Blade pressure measurements	10 m in, 4.4 m by 36.6 m wind tunnel	2-bladed, tapered, twisted, S809	Tip speed ratio, yaw angle	$1.5 \leq \lambda \leq 7.6$ $0° \leq \gamma \leq 60°$
Medici, KTH Mechanics	2005	HWA and load measurement	0.18 m in 1.2 m by0.8 m wind tunnel	2-bladed, tapered, untwisted, Gottingen417A	Freestream, tip speed ratio turbulence and yaw angle	$0° \leq \gamma \leq 60°$ $1.2e4 < Re < 3.4e4$
Maeda (field experiment), Mie University	2005	Blade pressure measurements and tuft visualization	10 m	3-bladed, tapered, twisted, DU and NACA aerofoils	Wind speed and yaw angle	$-45° \leq \gamma \leq 45°$ $3.5e5 < Re < 5.5e5$
Sant and Haans, TUDelft	2005–2006	HWA and smoke visualization	1.2 m in 2.24 m open-jet tunnel	2-bladed, constant chord, twisted, NACA0012	Yaw angle, pitch, tip speed ratio	$-45° \leq \gamma \leq 45°$ $Re \approx 1.7e5$
Maeda (tunnel experiment), Mie University	2007	Blade pressure measurements	2.4 m in 3.6 m open jet tunnel	3-bladed, tapered, twisted, DU91-W2-250, DU93-W-210 and NACA63-215	Yaw angle and tip speed ratio	$1.6 \leq \lambda \leq 6.5$ $0° \leq \gamma \leq 45°$ $Re \approx 2.1e5$
MEXICO Experiment	2007	Blade pressure measurements and PIV	4.5 m turbine in 9.5 m by 9.5 m open jet wind tunnel	3-bladed, tapered, twisted, DUW2-250, RisØ A1-21 and NACA64-418	Yaw angle, Tip speed ratio, pitch, Parked rotor	$0° \leq \gamma \leq 45°$ and $\gamma = \pm 45°$ (for PIV) $Re \approx 6.5e5$
Micallef, TUDelft	2011–2012	SPIV measurements	2 m turbine in octagonal open-jet tunnel of 3 m equivalent diameter	2-bladed, tapered, twisted, DU96-W180	Yaw angle and tip speed ratio	$\gamma = 0°$ and 30° $\lambda = 5$ (axial flow only) and 7 $Re \approx 3.6e5$
Krogstad and Adaramola, NTNU	2012	Power and load measurements, wake measurements using pitot-static probe and LDA	0.9 m turbine in a wind tunnel test-section 1.9 m by 2.7 m	3-bladed, tapered, twisted, S826	Freestream, yaw angle and tip speed ratio	$0° \leq \gamma \leq 50°$ $0.2e5 < Re < 5.0e5$

Table 1. Overview of experimental campaigns for HAWTs in axial and yawed flow.

Topic area	Experimental campaigns	Relevant literature
Gross performance	Clayton and Filby (University College London) Grant (Heriot-Watt University) Sant and Haans (TUDelft) Krogstad and Adaramola (NTNU)	Glauert [25], Clayton and Filby [17], Grant et al. [18], Haans et al. [49], Tongchitpakdee et al. [55], Krogstad et al. [53]
Wake geometry and development	Vermeer (TUDelft) Grant (Heriot-Watt University) Sant and Haans (TUDelft) MEXICO experiment Micallef (TUDelft) Krogstad and Adaramola (NTNU)	Øye [31], van Bussell [46, 47], Snel and Schepers [29, 30], Voutsinas et al. [45], Grant et al. [18, 48], Grant and Parkin [50], Hasegawa [56], Schepers [33], Vermeer [32, 43], Vermeer et al. [11], Mikkelsen [56], Haans et al. [49, 57, 58], Sezer-Uzol et al. [59], Schepers and Snel [51], Sant [34], Schepers et al. [23, 60], Sørensen et al. [61], Micallef et al. [52, 54], Micallef [39], Krogstad et al. [53], Sherry et al. [44]
Rotor aerodynamics	Bruining (TUDelft) Vermeer (TUDelft) Sant and Haans (TUDelft) Micallef (TUDelft) Krogstad and Adaramola (NTNU)	van Bussell [46, 47], Snel and Schepers [29, 30], Bruining [61], Schepers [23, 33, 60], Mikkelsen [62], Tongchitpakdee et al. [55], Haans et al. [49, 57, 63] Sezer-Uzol et al. [59], Sant [34, 64], Maeda et al. [65], Micallef et al. [52, 53], Micallef [39], Suzuki and Chattot [66], Krogstad et al. [53]
Aerofoil aerodynamics	Vestas Tjaereborg 2MW wind turbine Bruining (TUDelft) NREL UAE Phase I–IV Experiment NREL UAE Phase VI Experiment Maeda (Mie University)—field experiment Maeda (Mie University)—wind tunnel experiment MEXICO experiment	Voutsinas et al. [45], Bruining [67], Schreck et al. [36, 37, 68–70], Hand et al. [8], Madsen et al. [7], Johensen et al. [71], Tangler [72], Tongchitpakdee et al. [55], Maeda and Kawabuchi [73], Sezer-Uzol et al. [58], Sant [34], Breton et al. [74], Schmitz and Chattot [75], Shen et al. [76, 77], Schepers et al. [60], Schepers [23], Holierhoek et al. [35]

Table 2. Areas of research in yawed HAWT aerodynamics along with the experimental campaigns available and the relevant literature articles.

6. Conclusions and outlook

The fundamental physics of HAWT aerodynamics under yawed conditions has been discussed with reference to some of the latest works. Parallel research on helicopter rotor aerodynamics

has been shown to consist of a wealth of information which can be transposed to wind turbine rotor research. While no Mach number dependence would be expected for a HAWT rotor, the Reynolds number effect on the performance of aerofoils becomes very relevant since the currently available controlled experiments reproduce the rotor model on a much smaller scale.

It is clear that the current trend is towards the understanding of detailed flow fields around the blades. While various researchers have successfully utilized vortex methods and CFD to provide fundamental understanding of the flow, there is still the need for simple physical models which can be used in industry with little computational overhead. While BEM approaches utilize a number of engineering models to refine the representation of the physics, the fundamental assumptions in this theory ignore flow three-dimensionality. A simple approach such as BEM but which takes into account flow three-dimensionality would be very useful especially when dealing with the issue of yaw. More advanced issues such as 3D aerofoil aerodynamics have also been discussed and an overview of the most fundamental research questions which still need to be addressed has been given.

Knowledge of the complex 3D flow phenomena over wind turbine blades in yaw is still limited. New and more reliable models are necessary for modelling 3D aerofoil data to account for the combined effects of stall delay and unsteady flows. Better models are also necessary for modelling aerofoil data at the tip. The undertaking of more experiments under both controlled and open field conditions and with the latest sophisticated measurements techniques remains crucial for deepening the level of knowledge about the flow physics of yawed turbines.

As larger wind turbines rotors are being developed, especially for offshore deployment, rotor aerodynamics will play a more critical role to ensure a successful future for the wind energy industry. The design of larger wind turbine blades presents new challenges for engineers, making it more important to integrate more sophisticated and efficient aerodynamic models in design codes allowing fully coupled multi-physical simulation of entire wind turbine systems to solve complex fluid–structural interaction, control and cost optimisation problems. Further research in yaw aerodynamics should also cater for the latest technology development trends involving larger but more flexible blades and the implementation of smart control algorithms allowing to wind turbines in arrays to be controlled with a coordinated approach to minimise the negative impacts of aerodynamic turbine-to-turbine interactions on the energy yield from large wind farms.

Author details

Daniel Micallef[1*] and Tonio Sant[2]

*Address all correspondence to: daniel.micallef@um.edu.mt

1 Department of Environmental Design, Faculty for the Built Environment, University of Malta, Malta

2 Department of Mechanical Engineering, Faculty of Engineering, University of Malta, Malta

References

[1] Betz A (1919) *Schraubenpropeller mit Geringstem Energieverlust* (Dissertation, Gottingen Nachrichten, Gottingen)

[2] Dolan, D.S.L. and Lehn, P.W. (2006). Simulation model of wind turbine 3p torque oscillations due to wind shear and tower shadow. In *Power Systems Conference and Exposition, 2006. PSCE '06. 2006 IEEE PES*, Oct. 29 2006–Nov. 1 2006, pp. 2050–2057. doi: 10.1109/PSCE.2006.296240

[3] Micallef, D., Simao Ferreira, CJ., Sant, T. and Van Bussel, G.J.W. (2010). An analytical model of wake deflection due to shear flow. In *The 3rd EWEA Conference-Torque 2010: The Science of making Torque from Wind*, *Heraklion, Crete, Greece*, 28–30 June 2010.

[4] Rosen, A. and Sheinman, Y. (1994). The average output power of a wind turbine in a turbulent wind. *Journal of Wind Engineering and Industrial Aerodynamics*, 51(3):287–302. ISSN 0167-6105.

[5] Wagner, R., Antoniou, I., Pedersen, S.M., Courtney, M.S. and Jørgensen, H.E. (2009). The influence of the wind speed profile on wind turbine performance measurements. *Wind Energy*, 12:348–362. doi:10.1002/we.297

[6] Eggleston, D.M. and Starcher, K. (1990). A comparative study of the aerodynamics of several wind turbines using flow visualization. *Journal of Solar Energy Engineering*, 112:301–309.

[7] Madsen, H., Sørensen, N. and Schreck, S. (2003). Yaw aerodynamics analyzed with three codes in comparison with experiment. In *AIAA Paper 2003-519, 41st AIAA Aerospace Sciences Meeting and Exhibit*, Reno, Nevada.

[8] Hand, M., Simms, D., Fingersh, L., Jager, D., Cotrell, J., Schreck, S. and Larwood, S. (2001). Unsteady aerodynamics experiment phase VI: Wind tunnel test configurations and available data campaigns. Technical Report NREL/TP-500-29955, National Renewable Energy Laboratory, Colorado.

[9] Akay, B., Micallef, D., Simão Ferreira, C.J. and van Bussel, G.J.W. (2014). Effects of geometry and tip speed ratio on the HAWT blade's root flow. Journal of Physics: Conference Series 555 (2014) 012002; doi:10.1088/1742-6596/555/1/012002.

[10] Micallef, D., Ferreira, C.S., Sant, T., and Bussel, G.J.W. (2015). Experimental and numerical investigation of tip vortex generation and evolution on horizontal axis wind turbines. *Wind Energy.* doi:10.1002/we.1932

[11] Vermeer, L.J., Sørensen, J.N. and Crespo, A. (2003). Wind turbine wake aerodynamics. *Progress in Aerospace Sciences*, 98:467–510.

[12] Wang, T. (2012). A brief review on wind turbine aerodynamics. *Theoretical and Applied Mechanics Letters*, 2(6). Article 062001, ISSN 2095-0349.

[13] Leishman, J.G. (2002). Challenges in modeling the unsteady aerodynamics of wind turbines. *Wind Energy*, 5(11):85–132.

[14] Barthelmie, R., Frandsen, S., Rathmann, O., Hansen, K., Politis, E., Prospathopoulos, J., Schepers, J., Rados, K., Cabezon, D., Schlez, W., Neubert, A. and Heath, M. (2011). Flow and wakes in large wind farms: Final report for UpWind WP8. Technical Report Risø-R-1765(EN), Risø DTU, National Laboratory for Sustainable Energy.

[15] Hansen, M.O.L. and Johansen, J. (2004). Tip studies using CFD and comparison with tip loss models. *Wind Energy*, 7(4), October/December 2004, pp. 343–356.

[16] Anderson, M. (1979). Horizontal wind turbine in yaw. In *Proc. 1st BWEA Wind Energy Conference*, Cranfield University of Technology, pp. 68–77.

[17] Clayton, B. and Filby, P. (1982). Measured effects of oblique flows and change in blade pitch angle on performance and wake development of model wind turbines. In *Proc 4th BWEA Wind Energy Conference*, Cranfield Institute of Technology, UK.

[18] Grant, I., Parkin, P. and Wang, X. (1997). Optical vortex tracking of a horizontal axis wind turbine in yaw using laser-sheet, flow visualisation. *Experiments in Fluids*, 23(6): 513–519.

[19] Hansen, M. (2008). *Aerodynamics of Wind Turbines*, second edition. Earthscan., UK pp. 45–62.

[20] Glauert, H. (1926a). *The Analysis of Experimental Results in the Windmill Brake and Vortex Ring States of an Airscrew*. ARCR R&M 1026, Aeronautical Research Council (ARS), UK.

[21] Coleman, R., Feingold, A. and Stempin C.W. (1945). *Evaluation of the Induced Velocity Fields of an Idealized Helicopter Rotor.* NACA ARR L5E10, National Advisory Committee for Aeronautics (NACA), USA.

[22] Schepers, J.G. and Schreck, S. (2013). The importance of aerodynamics and the role of aerodynamic measurements, ECN-M-13-002, Energy Research Centre of the Netherlands. *Presented at the Science of Making Torque from Wind Conference*, Olderburg, Germany, 2012.

[23] Schepers, J.G. (2012). Engineering models in wind energy aerodynamics—Development, implementation and analysis using dedicated aerodynamic measurements. PhD thesis, Delft University of Technology. Available online from http://repository.tudelft.nl

[24] Burton, T., Sharpe, D., Jenkins, N. and Bossanyi, E. (2011). *Wind Energy Handbook.* John Wiley & Sons Ltd., West Sussex, UK. pp. 139–141.

[25] Glauert, H. (1926b). *A General Theory of the Autogyro*. ARCR R and M 1111, Aeronautical Research Council (ARS), UK.

[26] White, F. and Blake, B. (1979). Improved method of predicting helicopter control response and gust sensitivity. In *Proceedings of the 35th Annual Forum of the American Helicopter Soc.*, Washington, DC.

[27] Pitts, D. and Peters, D. (1981).Theoretical prediction of dynamic inflow derivatives. *Vertica*, 5:21–34.

[28] Howlett, J. (1981). *UH-60A Blackhawk Engineering Simulation Program: Vol 1: Mathematical Model*. NASA CR-66309, National Aeronautics and Space Administration (NASA), USA.

[29] Snel, H. and Schepers, J.G. (Ed.) (1994). *Joint Investigation of Dynamic Inflow Effects and Implementation of an Engineering Method*. Energy Research Centre of the Netherlands, Petten, the Netherlands, ECN-C-94-107.

[30] Snel H. and Schepers J.G. (Ed.) (1995). *Dynamic Inflow: Yawed Conditions and Partial Span Pitch Control*. Energy Research Centre of the Netherlands, Petten, the Netherlands, ECN-C-95-056.

[31] Øye, S. (1992). Induced velocities for rotors in yaw. In *Proceedings of the Sixth IEA Symposium*, ECN, Petten, The Netherlands.

[32] Vermeer, L. (1998). Wind tunnel experiments on a rotor model in yaw. In *Proceedings of the 12th symposium on Aerodynamics of Wind Turbines*, Lyngby, Denmark.

[33] Schepers, J. (1999). An engineering model for yawed conditions, developed on basis of wind tunnel measurements. In *Proceedings of the 37th Aerospace Sciences Meeting and Exhibit, AIAA-1999-39*, Reno, NV, USA.

[34] Sant, T. (2007). Improving BEM-based aerodynamics models in wind turbines design codes. PhD thesis, Delft University of Technology. Available online from http://www.tudelft.nl

[35] Holierhoek, de Vaal, J.B., van Zuijlen, A.H. and Bijl, H. (2013). Comparing different dynamic stall models. *Wind Energy*, 16(1):139–158.

[36] Schreck, S., Robinson, M., Hand, M. and Simms, D. (2000). HAWT dynamic stall response asymmetries under yawed flow conditions. In *Proceedings of the 36th ASME/AIAA Wind Energy Symposium*, Reno, Nevada.

[37] Schreck, S., Robinson, M., Hand, M. and Simms, D. (2001). Blade dynamic stall vortex kinematics for a horizontal axis wind turbine in yawed conditions. *Journal of Solar Energy Engineering*, 123(4):272–281.

[38] Schepers, J., Brand, A., Madsen, H., Stefanatos, N., Simms, D., Hand, M., Bruining, A., van Rooij, R., Shimizu, Y., Maeda, T. and Graham, M. (2001). IEA annex xiv/xviii, field rotor aerodynamics. In *Proceedings of the EWEC Conference*, Brussels.

[39] Micallef, D (2012c). 3D flows near a HAWT rotor: A dissection of blade and wake contributions. PhD Thesis, Delft University of Technology.

[40] del Campo, V., Ragni, D., Micallef, D., Akay, B., Diez, F.J. and Simão Ferreira, C.J. (2014). 3D load estimation on a horizontal axis wind turbine using SPIV. *Wind Energy*, 17:1645–1657. doi:10.1002/we.1658

[41] del Campo, V., Ragni, D., Micallef, D., Diez, F.J. and Ferreira, C.J.S. (2015). Estimation of loads on a horizontal axis wind turbine operating in yawed flow conditions. *Wind Energy*, 18:1875–1891. doi:10.1002/we.1794

[42] Alfredsson, P.-H. and Dahlberg, J.-A. (1981). *A Preliminary Wind Tunnel Study of Windmill Wake Dispersion in Various Flow Conditions*, The Aeronautical Research Institute of Sweden (FFA), Sweden. Technical Note AU-1499, Part 5.

[43] Vermeer, L. (2001). A review of wind turbine wake research at TUDELFT. In *A Collection of the 2001 ASME Wind Energy Symposium Technical Papers*, USA pp. 103–113.

[44] Sherry, M., Sheridan, J. and Jacono, D.L. (2013). Characterisation of a horizontal axis wind Turbine's tip and root vortices. *Journal Experiments in Fluids,* 54:1417.

[45] Voutsinas, S.G., Belessis, M.A. and Rados K.G. (1995). Investigation of the yawed operation of wind turbines by means of a vortex particle method. *AGARD-CP-552 FDP Symposium on Aerodynamics and Aeroacoustics of Rotorcraft*, Berlin, Germany.

[46] vanBussel, G. (1993). *The Acceleration Potential Models PREDICHAT/PREDICDYN Applied for Calculation of Axisymmetric Dynamic Inflow Cases, IW-93071R*, Delft University of Technology, the Neterlands.

[47] vanBussel, G. (1995). The aerodynamics of horizontal axis wind turbine rotors explored with asymptotic expansion methods. PhD thesis, Technische Universiteit Delft.

[48] Grant, I., Mo, M., Pan, X., Parkin, P., Powell, J., Reinecke, H., Shuang, K., Coton, F. and Lee, D. (2000). An experimental and numerical study of the vortex filaments in the wake of an operational, horizontal-axis, wind turbine. *Journal of Wind Engineering and Industrial Aerodynamics*, 23(6):513–519.

[49] Haans, W., Sant, T., van Kuik, G., and van Bussel, G. (2005). Measurement of tip vortex paths in the wake of a HAWT under yawed flow conditions. *Journal of Solar Energy Engineering*, 127(4):456–463.

[50] Grant, I. and Parkin, P. (1999). A DPIV study of the trailing vortex elements from the blades of a horizontal axis wind turbine in yaw. *Experiments in Fluids*, 28:368–376.

[51] Schepers, J.G. and Snel, H. (2007). *Model Experiments in Controlled Conditions (MEXICO)*, Energy Research Centre of the Netherlands, Petten, the Netherlands. ECN-E-07-042.

[52] Micallef, D., van Bussel, G.J.W., Ferriera, C.S. and Sant, T. (2012a). The origins of a wind turbine tip vortex. In *Proceedings from the Science of making Torque from Wind Conference*, Olderburg, Germany.

[53] Krogstad, P.Å. and Adaramola, M.S. (2012). Performance and near wake measurements of a model horizontal axis wind turbine. *Wind Energy*, 15(5):743–756.

[54] Micallef, D., van Bussel, G.J.W., Ferriera, C.S. and Sant, T. (2012b). An investigation of radial velocities for a horizontal axis wind turbine in axial and yawed flows. *Wind Energy*, 16(4):529–544.

[55] Tongchitpakdee, C., Benjanirat, S. and Sankar, L.N. (2005). Numerical simulation of the aerodynamics of horizontal axis wind turbines under yawed flow conditions. *Journal of Solar Energy Engineering,* 127(4):464–474.

[56] Hasegawa, Y. (1999). Numerical analysis of yawed inflow effects on a HAWT rotor. In *Proc. of 3rd ASME/JSME Joint Fluids Eng. Conf.*, FEDSM99-7820.

[57] Haans, W., Sant, T., van Kuik, G. and van Bussel, G. (2008). HAWT near wake aerodynamics, part I: axial flow conditions. *Wind Energy*, 11(3):19.

[58] Haans, W. (2011). Wind turbine aerodynamics in yaw, unravelling the measured rotorwake. PhD Thesis, Delft University of Technology. Available online from http://repository.tudelft.nl

[59] Sezer-Uzol, N. and Long, L.N. (2006). AIAA Paper 2006-0394. *Presented at AIAA Aerospace Sciences Meeting*, Reno, NV.

[60] Schepers, J.G., Boorsma, K., et al. (2011). *Final Report of IEA Task 29, Mexnext (Phase 1), Analysis of Mexico Wind Tunnel Measurements*. ECN-E-12-004, Energy Research Center of the Netherlands, ECN.

[61] Sørensen, N.N., Bechmann, A., Réthoré, P.-E. and Zahle, F. (2012). Near wake Reynolds-averaged Navier–Stokes predictions of the wake behind the MEXICO rotor in axial and yawed flow conditions. *Wind Energy.*, 17(1), 2014, p. 75–86. doi:10.1002/we.155

[62] Mikkelsen, R. (2003). Actuator disc methods applied to wind turbines. PhD thesis, Technical University of Denmark, Lyngby, Denmark.

[63] Haans, W., van Kuik, G. and van Bussel, G. (2007). Experimentally observed effects of yaw misalignment on the inflow in the rotor plane. *Journal of Physics: Conference Series*, 75:10.

[64] Sant, T., van Bussel, G. and van Kuik, G. (2009). Estimating the angle of attack from blade pressure measurements on the NREL Phase VI using a free wake vortex model: Yawed conditions. *Wind Energy*, 12:1–32.

[65] Maeda, T., Kamada, Y., Suzuki, J. and Fujioka, H. (2008). Rotor blade sectional performance under yawed inflow conditions. *Journal of Solar Energy Engineering*, 130:031018-1–031018-7.

[66] Suzuki, K. and Chattot, J.J. (2012). Unsteady hybrid Navier–Stokes/vortex model applied to wind turbine aerodynamics under yaw conditions. In *Proceedings from the*

Seventh International Conference on Computational Fluid Dynamics (ICCFD7), Big Island, Hawaii.

[67] Bruining, W. (1997). Aerodynamic characteristics of a 10 m diameter rotating wind turbine blade experimental results from the Delft University of Technology for the "Dynamic Stall and 3D Effects Project". IW95-084R, TU Delft, Institute of Wind Energy.

[68] Shreck, S. and Robinson, M. (2002). Rotational augmentation of horizontal axis wind turbine blade aerodynamic response. *Wind Energy Special Issue: Analysis and Modeling of the NREL Full-Scale Wind Tunnel Experiment*, 5(2–3):133–150.

[69] Schreck, S. and Robinson, M. (2005). Blade three-dimensional dynamic stall response to wind turbine operating condition. *Journal of Solar Energy Engineering,* 127(4):488–495.

[70] Schreck, S., Sant, T. and Micallef, D. (2010). Rotational augmentation disparities in MEXICO and UAE phase VI experiments. In *Proceedings from the Conference Science of Making Torque from Wind, Organised by the European Academy of Wind Energy*, Crete.

[71] Johansen, J. and Sørensen, N.N. (2004). Aerofoil characteristics from 3D CFD rotor computations. *Wind Energy*, 7(4):283–294.

[72] Tangler, J.L. (2004). Insight into wind turbine stall and post-stall aerodynamics. *Wind Energy*, 7(3):247–260.

[73] Maeda, T. and Kawabuchi, H. (2005). Surface pressure measurement on a rotating blade of field horizontal axis wind turbine in yawed conditions. *JSME International Journal*, 48:156–163.

[74] Breton, S.P., Coton, F.N. and Moe, G. (2008). A study on rotational effects and different stall delay models using a prescribed wake vortex scheme and NREL phase VI experiment data. *Wind Energy*, 11(5):459–482.

[75] Schmitz, S. and Chattot, J. (2009). Flow physics and stokes theorem in wind turbine aerodynamics. *Computational Fluid Dynamics,* 9:801–806.

[76] Shen W.Z., Hansen, M. and Sørensen, J. (2008). Determination of the angle of attack on rotor blades. *Wind Energy,* 12(1):91–98.

[77] Shen, W.Z., Hansen, M.O.L. and Sørensen, J.N. (2009). Determination of the angle of attack on rotor blades. *Wind Energy*, 12(1):91–98.

Chapter 3

Low-Noise Airfoil and Wind Turbine Design

Wei Jun Zhu, Wen Zhong Shen and
Jens Nørkær Sørensen

Additional information is available at the end of the chapter

http://dx.doi.org/10.5772/63335

Abstract

This chapter describes design and optimization of low-noise airfoil and wind turbines. The airfoils and wind turbine blades are designed with the objective of high-power performance. The aerodynamic noise is one of the important constraints for the optimization. The power coefficient of an airfoil is computed with the blade element momentum theory. The solution of the power coefficient is assumed to be maximized when the axial induction factor is 1/3. The airfoil noise is simulated with a semi-empirical model that requires airfoil boundary layer parameter as input. The airfoil and blade design process can be integrated such that the blade is designed with the desired airfoils. The results of three airfoil families and two rotor blades are presented, which are designed with the requirements of high-power performance and low-noise generation.

Keywords: cost of energy, design and optimization, low-noise wind turbine, wind turbine aeroacoustics, wind turbine aerodynamics

1. Introduction

Wind energy is one of the most attractive energy sources compared with the coal-based energy sources. In addition to the energy shortage, CO_2 emission is the worldwide concern of using conventional energy sources. Other types of air pollutants such as SO_x, NO_x and dust are becoming significant problems for some cities at densely populated areas. Also, as the size of wind turbine is getting larger, rotor noise has become a barrier for future development. For using wind energy, one of the major objectives in wind turbine airfoil design is to achieve a high aerodynamic performance that ensures wind turbine blade to operate with high-power performance. When it comes to social acceptance, the noise aspect becomes very important in

particular for onshore turbines, such that low-noise wind turbine design is an important competitive parameter. Therefore, the overall objective behind the design work is to make wind energy production more efficient, while at the same time lowering noise emission through gaining fundamental insight into the airfoil noise generation mechanisms.

The wind turbine noise regulation is restricted in Europe because it is more densely populated than many other countries outside EU. In Denmark, the noise limits for wind turbine in open area is 44 dB at a wind speed of 8 m/s and 42 dB at a wind speed of 6 m/s [1]. In addition, there is a low frequency limit (<20 dB) applied for wind turbine noise received inside a nearby house. Previous works on wind turbine airfoil design were aimed at high lift and high lift to drag ratio, such as the Wortmann FX 77-W-series airfoils [2] and the NREL airfoils [3, 4]. Later on, Björk [5, 6], Timmer and Van Rooij [7], Dahl and Fuglsang [8], and Fuglsang and Bak [9] made some significant contributions in designing wind turbine airfoils, and the designed airfoils were named with the institution's names (FFA, DU, and RISØ airfoils). Since 1990s, many researchers at Technical University of Denmark (DTU) have made advance research in designing wind turbine airfoils [8–12]. As the most important design objective, these wind turbine airfoils meet the demand of high lift to drag ratio and some of them are designed for low-noise emission [12].

To begin with airfoil and blade design, a profile shape can be described by the Joukowski transformation such that an airfoil shape can be represented by a series of trigonometric functions. Using this method, the DTU-LN1xx airfoils are designed [12]. Based on these airfoils, the LN2xx and LN3xx airfoil families are further developed. These airfoils are generated with a shape perturbation function that uses the LN1xx airfoils as baseline airfoils. All of these airfoils are noise constrained with a semi-empirical noise prediction model [13, 14]. To develop high-performance wind turbine blade, it is desired to have the airfoils designed for a specific blade. The above-mentioned LN2xx and LN3xx airfoils are designed for a 3 MW wind turbine and a 20 MW wind turbine, respectively. In the optimization process, the airfoils and blade design is integrated. The advantage is that the flow geometry over each rotor cross-section is optimized. A 2D blade element momentum (BEM) model is introduced during the optimization loop, which iteratively computes the local maximum C_p at each rotor cross-section.

This chapter is organized as follows: Section 2 introduces the 2D airfoil design method; Section 3 presents the airfoil and blade integrated design method; Section 4 presents results from aerodynamic and aeroacoustic simulations; and Section 5 concludes the work.

2. The 2D airfoil designs

In this section, the related design about the 2D airfoils is described. The Reynolds number, Mach number, angle of attack and surface roughness are flow-related parameters that need to be considered while applying the flow solver. The design objectives, constraints and some results are provided.

http://dx.doi.org/10.5772/63335

2.1. The flow conditions

The LN1xx, LN2xx and LN3xx airfoils are designed at Reynolds number around 1.6×10^6, 3×10^6 and 16×10^6, respectively, depending on the airfoil chord and radial location. According to the local flow at each blade section, the Mach number at each blade section also varies. To consider different flow conditions, the design angle of attack is between 3° and 10°. Numerical computations go through each angle of attack with a step of 1°. Such a wide range of angle of attack also takes into account the off-design condition. To model the airfoil roughness condition, the free transition simulation is based on the e^n model, where $n = 9$; the forced transition simulation is performed by giving the upper and lower transition points at 5% and 10% chords position, measured from the leading edge. The numerical tool Xfoil developed by Drela [15] is applied for airfoil boundary layer calculations. The code is used iteratively inside the optimization. The flow conditions, such as Reynolds number, angle of attack, Mach number and transition condition are written in an input script that is recognized by the Xfoil code.

2.2. The design variables

Although a number of functions can be used to describe airfoil shapes, however, it is imperative to choose proper functions to represent airfoil geometry. Ideally, an airfoil profile can be transformed into a near circle by the Joukowski transformation:

$$\varsigma = z + a^2 / z \tag{1}$$

where a = chord/4, ς and z are the complex variables in the airfoil plane and the near circle plane, respectively. The coordinate of z can be described as

$$z = a\exp(\varphi + \mathrm{i}\theta) \tag{2}$$

where ϕ is a function of θ. Using the concept of the Taylor series expansion, the function ϕ is expressed as [11]

$$\varphi(\theta) = \sum_{n}^{k=1}\left(a_k\left(1-\cos(\theta)\right)^k + b_k\sin^k(\theta)\right)\varphi(\theta) \tag{3}$$

where a_k and b_k are the design variables that determine airfoil shapes. By combining Eqs. (1), (2) and (3), an airfoil shape is represented by a series of trigonometric functions. Such a function is used for the design of LN1xx airfoils.

For the design of LN2xx and LN3xx airfoils, instead of creating a new airfoil shape from beginning, a shape perturbation function is applied to modify an existing airfoil. The idea of using such a function is to save computational time and inherit the shape from the previous airfoils that already have good performance. The shape perturbation function used for the upper surface is

$$\Delta y_{\mathrm{u,l}}(i) = \sum_{N}^{k=1} f_{\mathrm{u,l}}(k) P_{\mathrm{u,l}}(k,i) \tag{4}$$

where the subscripts u and l indicate upper and lower airfoil surfaces, respectively, i is the index of the x and y coordinates, and k is the index of the shape modes. The shape functions for each mode along the x-coordinate are

$$P_{\mathrm{u,l}}(k.i) = \sin^{\xi_{\mathrm{u,l}}}\left(\pi x_{\mathrm{u,l}}(i)^{g(k)}\right) \tag{5}$$

The amplitudes $f_{\mathrm{u,l}}$ are the design variables, and with the power factors $\xi_{\mathrm{u,l}}$ a total number of design points is dofs = 2*N + 2. g is a given vector which is the exponent of x. For example, the choice of g could be g = [0.1 0.2 0.3 0.5 1 3 5 8]. Because $x_{\mathrm{u,l}} \in [0, 1]$, Eq. (4) provides zero value at leading edge and trailing edge points. Therefore, the leading edge and the trailing edge are naturally fixed without being perturbed.

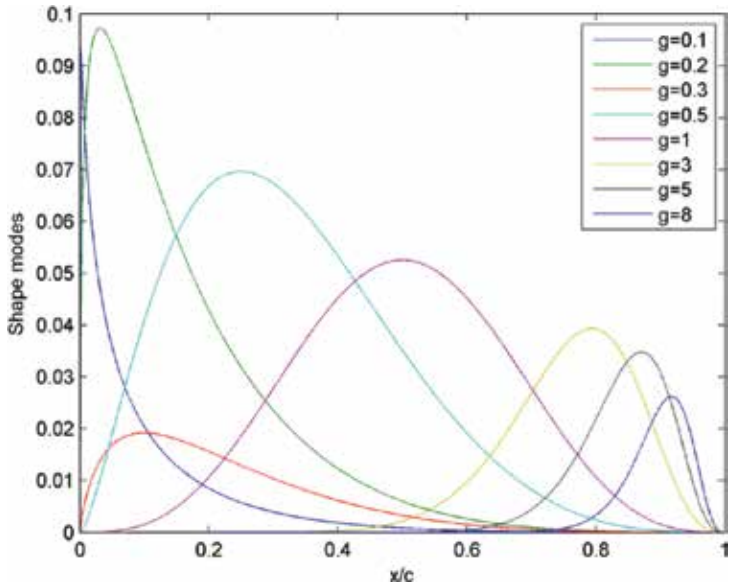

Figure 1. Example of the shape function.

Figure 1 shows an example of such shape perturbation function. It is possible to add more shape modes to put more focus at any chord-wise location. For example, adding more values around g = 0.1 leads to more detailed changes at the leading edge. The sum of the mode shapes will be added to the reference airfoil. At every iteration, the amplitude coefficients $f_{u,l}$ are updated until the final airfoil shape is found.

http://dx.doi.org/10.5772/63335

2.3. The objective

The design objective is the blending of power coefficient and rotor solidity such that

$$\text{Obj} = kC_p + (1-k)/\sigma \tag{6}$$

where $k = 0.5$ for airfoil section in the middle part of the blade. The k value shall be modified along the blade station while the solidity changes.

To obtain a good off-design property, the power coefficient is weighted between clean and rough conditions with the angle of attack ranging from $\alpha = 3°$ to $\alpha = 10°$:

$$C_p = w\sum_{10}^{\alpha=3} C_p^{\text{clean}} + (1-w)\sum_{10}^{\alpha=3} C_p^{\text{rough}} \tag{7}$$

By using a weighting factor$w$ for the clean and rough conditions, Eq. (7) indicates that the resulted power coefficient will be less sensitive to surface roughness and will keep high value over a wide range of AOAs.

2.4. The constraints

From the aerodynamic point of view, the lift and the lift to drag ratio are already included in the C_p calculations, which are defined as the objective. The main constraint is set for the leading edge roughness sensitivity such that ΔC_l is constrained between the clean and rough cases. In other words, the performance between clean and rough airfoils should be as small as possible. Another important constraint to design a low-noise airfoil is the sound pressure level (SPL) such that SPL< N (dB). To estimate the noise generated from an airfoil, a 2D version of the semi-empirical model was developed, which was originally developed by Brook et al. [13] using acoustic measurements for a NACA 0012 airfoil and improved by using the actual boundary layer quantities of individual airfoils. For more details about the noise prediction model, the reader is referred to [13, 14].

2.5. Optimization results

In **Figure 2**, airfoils with a relative thickness of 18, 21 and 24% are shown for each airfoil family. The LN1xx airfoil shapes are designed with the Joukowski transformation. The LN2xx airfoils are generated with the shape perturbation method based on the LN1xx airfoils. And the LN3xx airfoils are further optimized for higher Reynolds number based on the LN2xx airfoils. The advantage is that there are less three-dimensional effects due to curvature change along the blade span; in other words, the airfoils are designed to have smooth geometrical transition between each other.

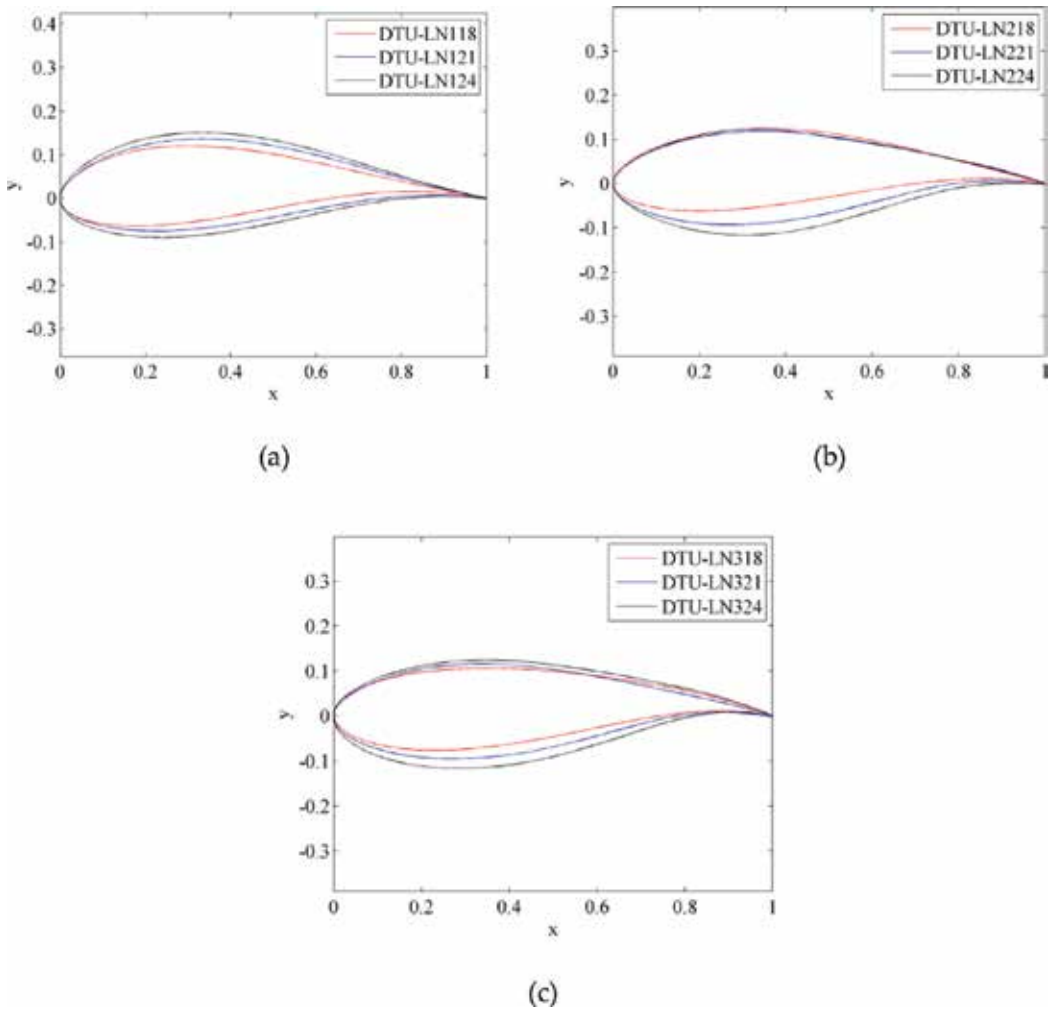

Figure 2. The airfoil families: (a) DTU-LN1xx; (b) DTU-LN2xx and (c) DTU-LN3xx.

3. The integrated design of airfoil and blade

The integrated design of airfoil family and blade can start from the BEM analysis of an airfoil section at a given blade station. The core of the analysis is the iterative computation of the power coefficient of a given airfoil during each step of optimization. The power performance has been used as a key reference number during design process [16], which is the most important measure of a rotor. With the aim of decreasing material cost, we introduce the rotor solidity as another parameter together with the power coefficient. In this analysis, we also involve the Prandtl's tip correction to the integrated design where the design of thin airfoils near the tip might be affected.

http://dx.doi.org/10.5772/63335

According to the 1D momentum theory, the solution of the power coefficient is maximized when the axial induction factor is $a = 1/3$, even though advanced computations show that the maximum power efficiency is obtained at slightly higher axial induction than $a = 1/3$. With this condition being valid, it can be shown that the power coefficient of an airfoil section can be written as

$$C_{\mathrm{p}} = \left[\left(1-a\right)^2 + x\left(1+a'\right)^2 \right] x C_{\mathrm{t}} \sigma \tag{8}$$

with the solidity defined as

$$\sigma = 2F\sin^2\left(\phi\right) / C_{\mathrm{n}} \tag{9}$$

where a and a' are the axial- and tangential-induced velocity interference factors, respectively, x is the local speed ratio, C_{t} and C_{n} are the tangential and axial force coefficients, respectively, σ is the rotor solidity, ϕ is the local flow geometry and F denotes the Prandtl's tip loss function.

As is known that the Prandtl's tip loss function corrects the assumption of a disk, therefore to consider rotors with a finite number of blades, the correction has to be implemented to the blade design as well as the airfoil design. Different tip loss functions can be used for such design purposes [17]. A well-known tip correction model proposed by Prandtl reads

$$F = 2\cos^{-1}\left(e^{-f}\right) / \pi \tag{10}$$

Where

$$f = B\left(R-r\right) / \left(2r\sin\phi\right) \tag{11}$$

In Eq. (8), not all of the variables have been explicitly known. An assumption made for the axial induction factor is that $a = 1/3$. Other parameters can be separated into two groups. Parameters in group 1 are the values that will not enter into the BEM iterations, such as the local speed ratio x, the local length of the blade r, the total length of blade R, the number of blades B and the airfoil normal and tangential force coefficients. To compute the tangential force (C_{t}) and normal force (C_{n}), the lift and drag coefficients, c_{l} and c_{d} from the airfoil computations, are needed during every iteration of airfoil optimization, such that

$$C_t = c_{\mathrm{l}}\left(\sin\phi - c_{\mathrm{d}} / c_{\mathrm{l}}\cos\phi\right) \tag{12}$$

$$C_n = c_l\left(\cos\phi + c_d / c_l \sin\phi\right) \tag{13}$$

The other group of the variables will be iteratively solved due to their dependency. These parameters are the power coefficient C_p, the flow angle ϕ and the tangential induction factor a'. The values of C_p, ϕ and a' are initialized with zero before the first BEM iteration. After several iterations, the highest C_p for the present flow condition is obtained. The process of finding maximum C_p is repeated for both clean and rough surface conditions. For each clean and rough surface condition, the angles of attack to be considered are from 3° to 10°. The surface roughness weighted C_p over a wide range of angles of attack is used as one of the airfoil design objectives. These procedures are repeated for each airfoil generation until the optimum airfoil is found.

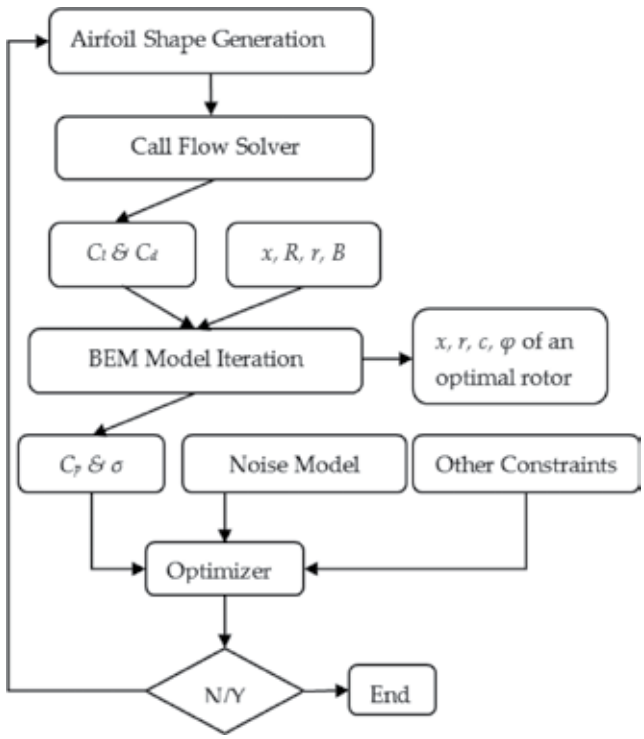

Figure 3. Flowchart of the integrated design method.

The integrated design process is summarized in **Figure 3**. As seen in the flowchart, the main loop goes through the airfoil shape optimization and the BEM iteration is inside the main loop. The BEM calculation is an important part of the integrated design concept that links the airfoil optimization with the optimal blade design. The BEM iteration requires input from airfoil aerodynamics, blade local speed ratio, etc. When the BEM converges, it writes an output to both the airfoil optimizer and results in a temporal optimal rotor (according to the temporally

obtained airfoil). The final optimal rotor is found when the airfoil optimizer finds a converged solution at each blade spanwise position.

4. Results and validations of airfoil and blade design

In this section, results are presented for both aerodynamics and aeroacoustics of airfoils and wind turbines. Several in-house developed models, Q^{3}UIC [18], EllipSys [19, 20] and BPM noise [14] programs, are used for design or cross comparisons.

4.1. Airfoil aerodynamics and noise

The pressure coefficient of the LN118 airfoil is simulated and compared with the wind tunnel measurements. With a wind speed of 60 m/s, the highest Reynolds number is achieved at about 2.1×10^6. In **Figure 4**, different models are compared with experiments. As seen from the comparisons, the three numerical methods, Xfoil, Q^{3}UIC and EllipSys can predict correctly C_p at angles of attack of 6.7°and 9.6°.

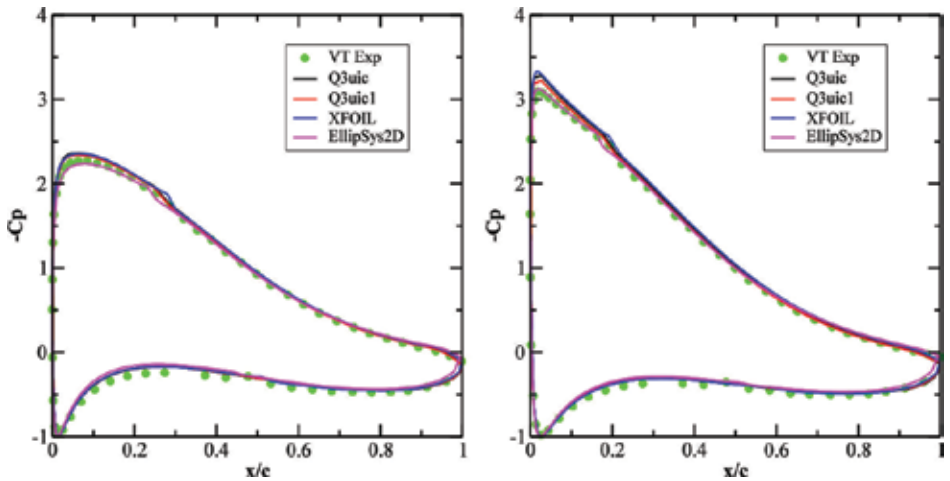

Figure 4. Comparisons of the surface pressure coefficient of a clean LN118 airfoil at Re = 2.1 × 10^6 and angles of attack of 6.7°(left) and 9.6°(right).

As shown in **Figure 5**, the sound pressure level is calculated at a reference point of 1.62 m away from the trailing edge and at 90° direction. The noise levels are compared for flows past the LN118 and NACA 64618 airfoils at a wind speed of 30 m/s. At a same lift coefficient of 0.52 (**Figure 5(a)**), the experiments show that the LN118 airfoil produces lower noise level below the frequency of 3000 Hz. Similar results are observed at a lift coefficient of 0.95 (**Figure 5(b)**). The noise prediction model is also shown to be compared with the measurement. As shown in the figure, the predicted airfoil noise slightly overpredicts the noise emission from both airfoils but the relative differences between the noise levels are found to be similar from

computation and experiment. From the predictions, the main differences between the two airfoils are seen in the frequency region below 500 Hz.

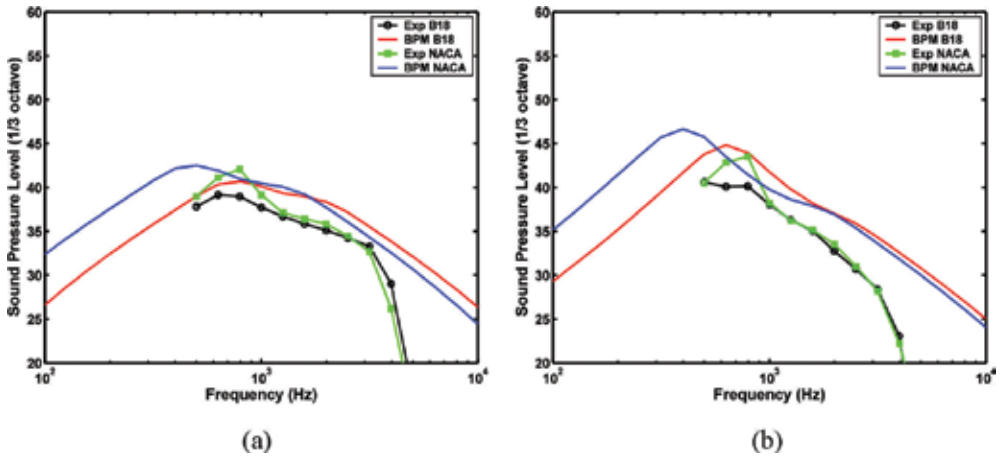

Figure 5. The measured and calculated 1/3-octave sound pressure level at a distance of 1.62 m and 90° direction from the LN118 airfoil and from the NACA 64618 airfoil at a wind speed of 30 m/s and $C_l = 0.52$ (a) and $C_l = 0.95$ (b).

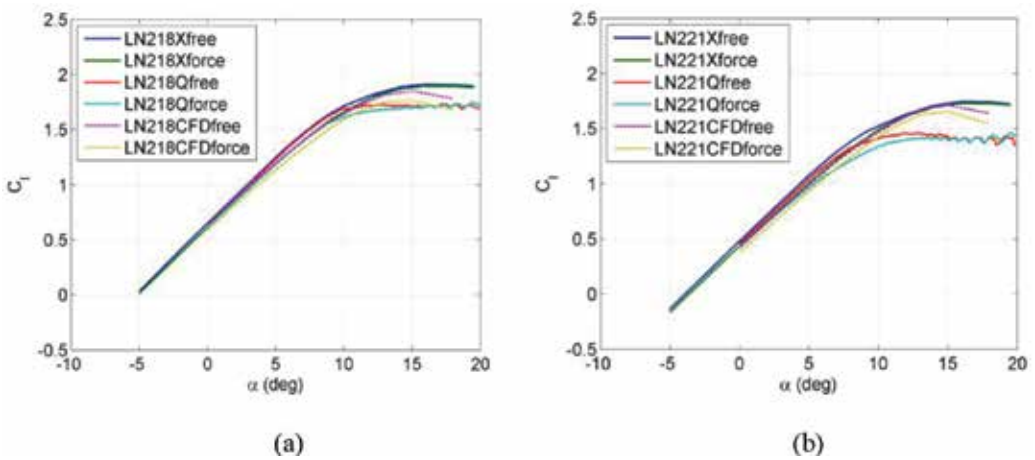

Figure 6. Comparisons of lift coefficient in free and force transition conditions using Xfoil, Q³UIC and EllipSys.

To show surface roughness sensitivity, we compute the lift coefficient of the LN218 and LN221 airfoils up to stall angle of attack with free and force transition models. In **Figure 6**, results from the Xfoil (Xfree/force), Q³UIC (Qfree/force) and EllipSys (CFDfree/force) are compared for the LN218 (**Figure 6(a)**) and LN221 (**Figure 6(b)**) airfoils. In the linear lift region, the results

are very similar. In the stall region, CFD (Computational Fluid Dynamics) results are in between Xfoil and Q^{3}UIC. It is important to see that the performance of the airfoils is very insensitive to the surface roughness.

4.2. Rotor aerodynamics and noise prediction

In this section, two of the newly designed in-house rotors are used for various simulations. The rotor sizes of the two wind turbines are 40 m and 130 m with the rated power of 3 MW and 20 MW, respectively. From the size of the two turbines, the design should have covered range of MW size wind turbines. The 3 MW wind turbine represents most of the existing commercial wind turbines. The design of the 20 MW wind turbine is more aimed at next 5–10-year development. To perform rotor simulations, the input of airfoil data to the BEM model is obtained from Xfoil calculations. By comparing the force distributions calculated from BEM (based on 2D airfoil data) and from CFD (based on full 3D flow), it is possible to identify the influence from the 2D design tools. **Figure 7** shows the platform of the 20 MW wind turbine blade; it is resulted from the iteration process as shown in **Figure 3**. An example of the full rotor CFD simulation for the 20 MW rotor is provided in **Figure 8**. This figure shows contour plots of the surface pressure coefficient and the individual pressure contours at the five designed blade sections, which represent the LN318, 21, 24, 27 and 30 airfoils.

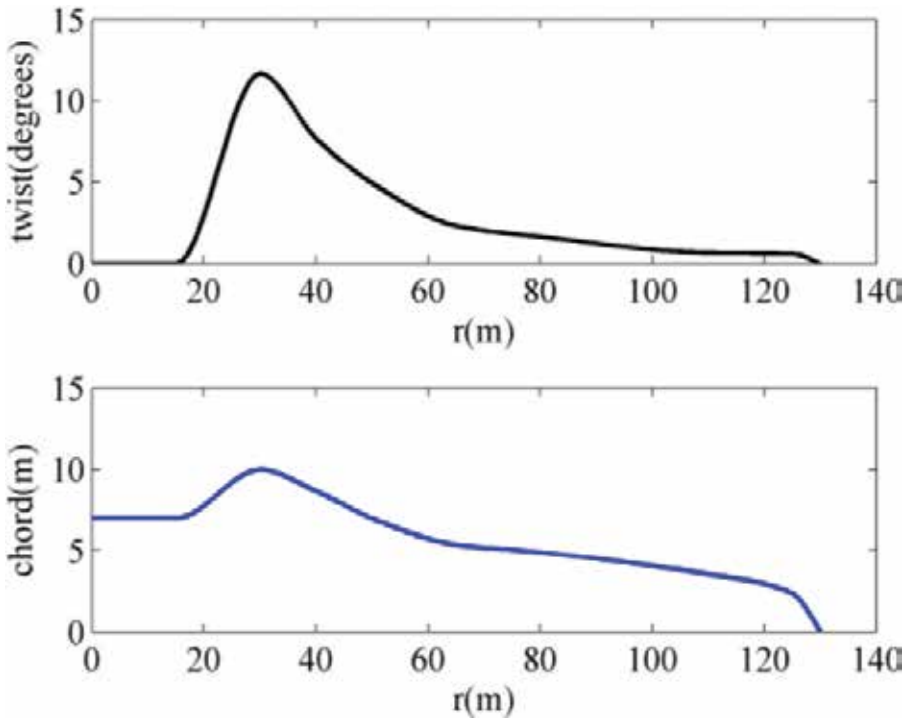

Figure 7. Plot blade twist and chord for 20 MW (airfoil family 2).

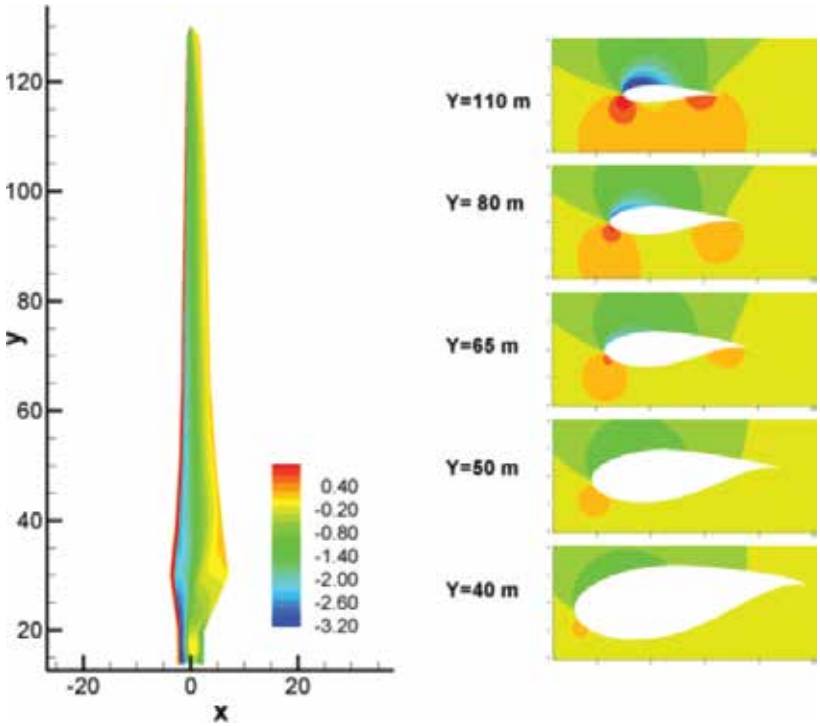

Figure 8. Contour plot of the surface pressure coefficient and pressure contour at five blade sections.

Since these airfoils are designed by integrating Xfoil and BEM methods, it will be interesting to compare pressure forces along each blade section using Xfoil and CFD. The pressure distribution at a blade section can be obtained after post-processing from the CFD calculation, for example, extracting the surface pressure from **Figure 8**. Since the BEM calculations already provide angles of attack along the blade, angles of attack are known for each blade spanwise location. Using these angles of attack to perform Xfoil simulation with a free transition model, the pressure coefficients are known from Xfoil. With the same free transition model and the same n-factor, the surface pressure obtained from Xfoil and CFD are compared at blade positions of Y = 80 m and Y = 40 m for the 20 MW rotor case. **Figure 10** reflects a few facts: (1) The BEM model performs very well, which provides accurate flow condition; (2) Xfoil is in well agreement with CFD prediction at the blade outer part; (3) Overprediction from the Xfoil code becomes evident at blade inboard part.

In **Figure 9**, the results from BEM and CFD are compared. It is noticed that the blade normal force (F_n) and the tangential force (F_t) obtained from CFD and BEM are close with each other, both for the 20 MW turbine (**Figure 9(a)**) and the 3 MW turbine (**Figure 9(b)**), respectively. It is found that CFD predicts slightly higher forces than BEM which is mostly observed from 40 m < r < 130 m (**Figure 9(a)**) and 15 m < r < 35 m (**Figure 9(b)**). Such kind of difference is often related to the rotational effect that has been modelled by CFD but not enough counted by BEM. The laminar boundary layer tends to be smaller while rotation is taking into effect, this leads

http://dx.doi.org/10.5772/63335

to a higher force in reality. For more accurate aerodynamic load prediction, the airfoil data should be corrected for rotational effect before applying to a BEM model. Overprediction of forces for thick airfoils and/or high angles of attack indicates the limitation of the Xfoil code. Although CFD simulation is much more accurate in most cases, it has not reached the stage so that it can be directly used as a design tool. Also, to better design or predict forces at blade inboard part, it is necessary to use some more sophisticated methods to remedy the existing engineering tools.

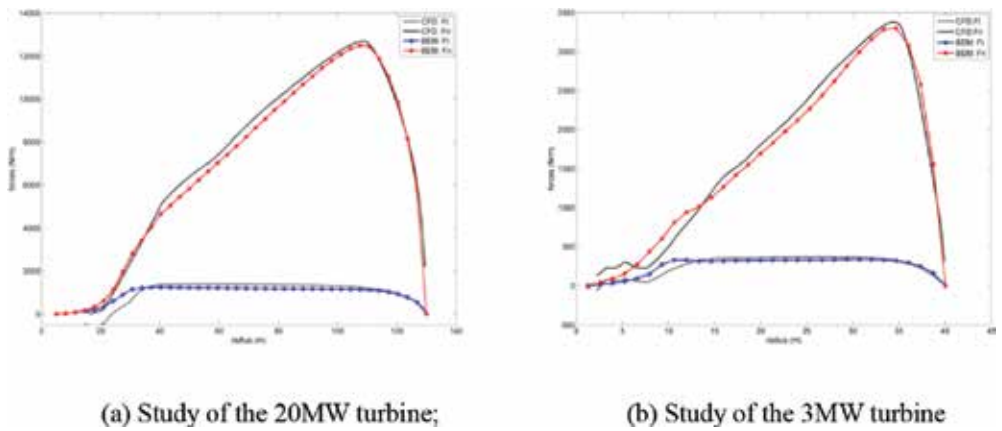

Figure 9. Simulated forces along blade for: (a) the 20 MW and (b) the 3 MW wind turbine at wind speed of 10 m/s.

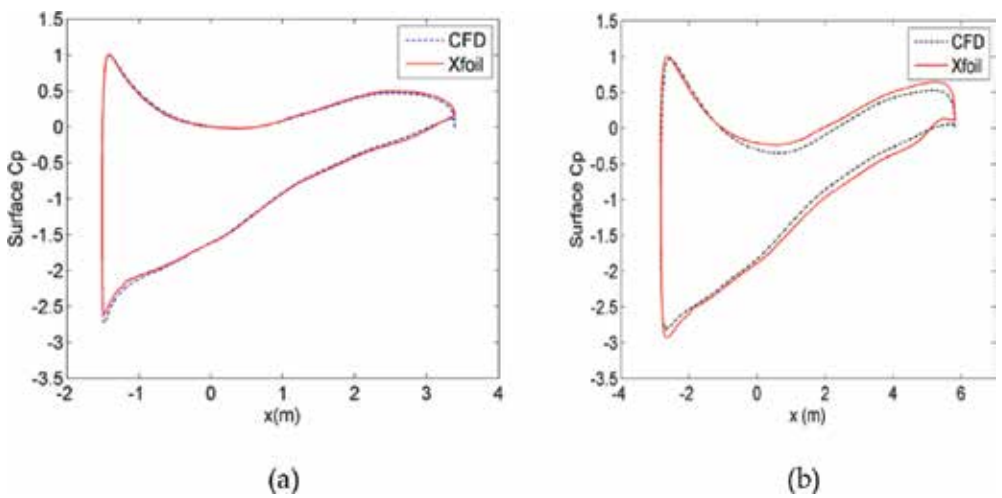

Figure 10. Surface pressure coefficients computed from CFD and Xfoil at $Y = 80$ m (a) and $Y = 40$ m (b).

The noise simulation for the two wind turbines is shown in **Figure 11**. The overall A-weighted sound pressure levels from the 20 MW wind turbine are 47.5 and 42.9 dBA for the 3 MW wind turbine. The individual noise mechanisms are similar, except that the 20 MW wind turbine has a lower peak frequency than the 3 MW wind turbine.

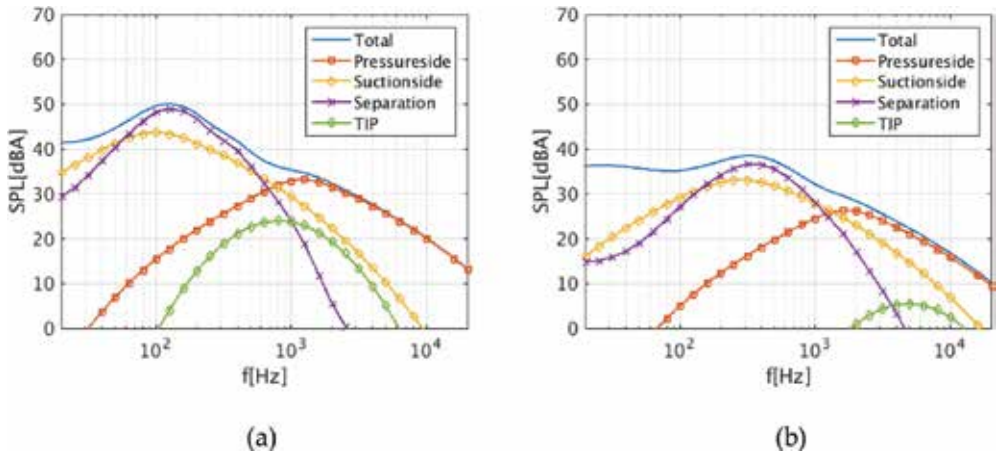

Figure 11. Wind turbine noise simulations: (a) 20 MW turbine (47.5 dBA) and (b) 3 MW turbine (42.9 dBA), measured at 200 m downstream at ground height of 2 m.

4.3. Further reduction of trailing edge noise

Even after the design of a low-noise blade, it is possible to further reduce noise from the trailing edge. This section briefly introduces the trailing edge serration as the additional add at the trailing edge. Several methods already exist for airfoil trailing noise simulation; however, models such as BPM and TNO [21] cannot be directly used for modelling noise with serrations. Based on the assumption of a flat plate, Howe [22] derived a noise prediction model for a saw-tooth trailing edge at zero angle of attack. In the model, the far-field noise spectrum is related to the aerodynamic pressure spectrum. However, theoretical prediction using Howe's theory does not fit well with some of the airfoil noise measurements in terms of overall noise magnitude. It is expected that advanced computational aeroacoustic (CAA) methods provide more accurate prediction of noise from a serrated trailing edge. In this study, the acoustic simulation method is the integrated representation of Ffowcs Williams-Hawkings (FW-H) acoustic analogy, more information related to the methods are referred in references [23, 24]. The acoustic solver is implemented in the in-house flow solver EllipSys3D. The unsteady turbulent flow over airfoil is solved by the large eddy simulation (LES) approach. The airfoil to be investigated is the LN118 airfoil. The surface mesh and the side view of the volume mesh are shown in **Figure 12**. The baseline LN118 airfoil is attached with serrations at the trailing edge.

http://dx.doi.org/10.5772/63335

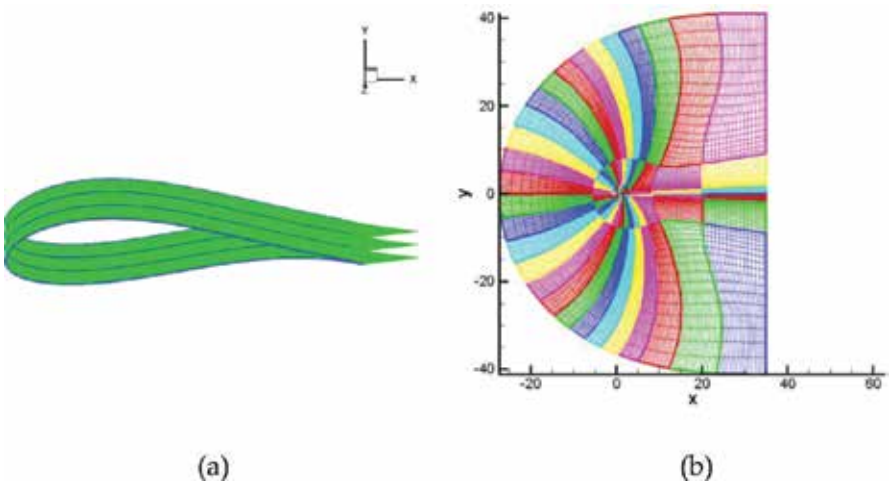

Figure 12. Mesh of the wall surfaces (a) and side view of mesh (b).

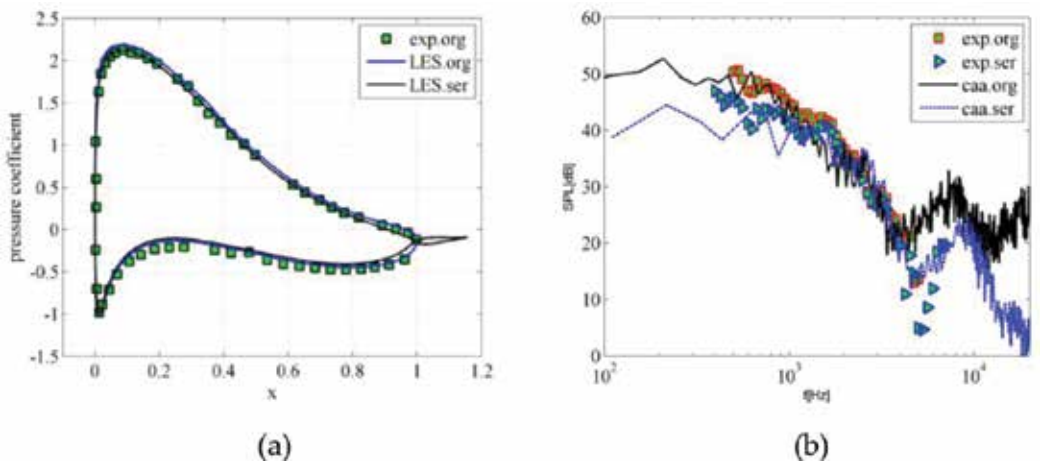

Figure 13. Comparisons of surface pressure (a) and noise spectra (b) against measurements at an angle of attack of 6°.

The wind speed used for the simulation is 45 m/s, the airfoil chord is 0.6 m, the serration length is 16.7% of the baseline airfoil chord and the wave number is 50% of the serration length. The surface pressure at angle of attack 6° is extracted from LES result. In **Figure 13**, the flow results from LES are first compared with the wind tunnel experiment. The results show very small difference with experiment either for the original LN118 airfoil or for the airfoil with serration. Only small difference is observed near the trailing edge. The results indicate that the serration does not provide a big influence on the airfoil aerodynamics. On the right side of **Figure 13**, the measured and simulated noise spectra are compared, which show some good agreement. The general trend from both results confirms the effect of the trailing edge serration.

5. Conclusion

In this chapter, the design of several airfoil families and wind turbine blades are introduced. Different aerodynamic and aeroacoustic tools are involved into the design and validation of the low-noise airfoil/blade design. The overall aerodynamic performance is good for all the airfoils. The noise emission is controlled by the optimization process. Large MW size wind turbine blade can be designed with integrated method where the power coefficient is significantly large while the noise level is restricted at low level. The noise spectrum is computed with semi-empirical model and CAA methods. The power and force are computed both by blade element momentum method and CFD with body-fitted mesh. Comparisons with measurements and other cross validations show that low-noise blade can be achieved, which still maintains high aerodynamic performance.

Author details

Wei Jun Zhu*, Wen Zhong Shen and Jens Nørkær Sørensen

*Address all correspondence to: wjzh@dtu.dk

Department of Wind Energy, Technical University of Denmark, Lyngby, Denmark

School of Hydraulic, Energy and Power Engineering, Yangzhou University, Yangzhou, China

References

[1] Bo Søndergaard. Noise and low frequency noise from wind turbines. In: Inter.noise 2014. Melbourne, Australia; November 2014. pp. 1–12.

[2] Thiele HM. Growian rotor blades: production development, construction and test. Report Number: NASA TM-77479; Publication data: Jul 01,1984.

[3] Tangler JL, Somers DM. Status of the special purpose airfoil families. In: Proceedings of WINDPOWER'87, San Francisco; 1987. pp. 3264.

[4] Tangler JL, Somers DM. NREL airfoil families for HAWT's. In: Proceedings of WINDPOWER'95, Washington, D.C.; 1995. pp. 117–123.

[5] Björk A. Airfoil design for variable rpm horizontal axis wind turbines. In: Proceedings of EWEC'89, Glasgow, Scotland; 1989.

[6] Björk A. Coordinates and calculations for the FFA-W1-xxx, FFA-W2-xxx and FFA-w3-xxx series of airfoils for horizontal axis wind turbines, Sweden, Stockholm; 1990.

[7] Timmer WA, Van Rooij R. Summary of the Delft university wind turbine dedicated airfoils. Journal of Solar Energy Engineering. 2003;125:488–496.

[8] Dahl KS, Fuglsang P. Design of the wind turbine airfoil family RISØ-A-XX. RISØ National Laboratory; Roskilde, Denmark; 1998 [RISØ-R-1024].

[9] Fuglsang P, Bak C. Development of the RISØ wind turbine airfoils. Wind Energy. 2004;7:145–162.

[10] Wang XD, Chen J, Shen WZ, Zhu WJ, Sørensen JN. Airfoils and methods for designing airfoils [P]. Application No. PCT/EP2010/056810, International patent application.

[11] Wang XD, Chen J, Shen WZ, Zhang S. Integration study on airfoil profile for wind turbines. Journal of China Mechanical Engineering. 2009;20(2):211–228.

[12] Chen JT, Zhu WJ, Fischer A, García NR, Madsen J, Chen J, Shen WZ. Design and validation of the high performance and low noise Chong Qing University and Technical University of Denmark LN1 airfoils. Wind Energy. 2014;17(12):1817–1833. DOI: 10.1002/we.1668.

[13] Brooks TF, Pope DS, Marcolini MA. Airfoil self-noise and prediction. Reference Publication 1218, National Aeronautics and Space Administration, USA; 1989.

[14] Zhu WJ, Heilskov N, Shen WZ, Sørensen JN. Modeling of aerodynamically generated noise from wind turbines. Journal of Solar Energy Engineering. 2005;127:517–528.

[15] Drela M. XFOIL: an analysis and design system for low Reynolds number airfoils. In: Conference on low Reynolds number aerodynamics, University of Notre Dame; 1989.

[16] Bak C. Research in aeroelasticity EFP-2006: key parameters in aerodynamic rotor design. RISØ National Laboratory, Roskilde, Denmark; 2007 [RISØ-R-1611(EN)].

[17] Shen WZ, Mikkelsen R, Sørensen JN. Tip loss corrections for wind turbine computations. Wind Energy. 2005;(8):457–475.

[18] Ramos García N, Sørensen JN, Shen WZ. A strong viscous–inviscid interaction model for rotating airfoils. Wind Energy. 2014;17(12):1957–1984. DOI: 10.1002/we.1677.

[19] Michelsen JA. Basis3D – a platform for development of multiblock PDE solvers. Technical Report AFM, Technical University of Denmark; Denmark: 1992.

[20] Sørensen NN. General purpose flow solver applied over hills. RISØ National Laboratory, Roskilde, Denmark; 1995 [RISØ-R-827(EN)].

[21] Parchen R. Progress report DRAW: a prediction scheme for trailing-edge noise based on detailed boundary-layer characteristics. TNO Rept. HAGRPT-980023 TNO Institute of Applied Physics, The Netherlands; 1998.

[22] Howe MS. Noise produced by a sawtooth trailing edge. Journal of the Acoustic Society of America. 1991;90(1):482–487.

[23] Ffowcs Williams JE, Hawkings DL. Sound generated by turbulence and surfaces in arbitrary motion. Philosophical Transactions of the Royal Society. 1969;264:321–342.

[24] Farassat F. Derivation of formulations 1 and 1A of Farassat. NASA/TM-2007-214853; 2007. http://ntrs.nasa.gov/archive/nasa/casi.ntrs.nasa.gov/20070010579.pdf

Chapter 4

Small Wind Turbines: Specification, Design, and Economic Evaluation

Jakub Bukala, Krzysztof Damaziak,
Krzysztof Kroszczynski, Jerzy Malachowski,
Tomasz Szafranski, Michal Tomaszewski,
Hamid R. Karimi, Krzysztof Jozwik,
Maciej Karczewski and Krzysztof Sobczak

Additional information is available at the end of the chapter

http://dx.doi.org/10.5772/62821

Abstract

In this work, we consider various aspects of small wind turbines' (SWTs) design and operation. First, an extensive literature study is presented by considering SWTs specification, market statistics, the smart grid, and the prosumer concepts as well as the most important parameters affecting the efficiency of wind turbines. Then, both the literature review and series of coupled numerical simulations investigating impact of the chosen design solutions on small wind turbine operation are performed. It allowed objective evaluation of different design approaches, which in turn enabled the systematic identification of actual limitations as well as the opportunities for specific design solutions of SWTs: horizontal axis wind turbines (HAWTs) and vertical axis wind turbines (VAWTs); the rotor position in relation to the tower (upwind vs. downwind); and diffusor-augmented wind turbine (DAWT). Additionally, an economic evaluation is carried with the use of an advanced numerical Weather Research & Forecasting (WRF) model. It is shown that auxiliary power generation using privately owned SWTs can be an economically viable option. Finally, a set of design goals for future SWTs is formulated based on the performed numerical analyses.

Keywords: Small wind turbine, Design, Economy, Evaluation, Market

1. Introduction

Small wind turbines (SWTs) are a distinct and separate group of devices developed within the wind energy sector. According to the IEC 61400-2 standard, SWTs are characterized by a rotor area of <200 m^2 and rated power below 50 kW [1]. Wind power plants in this category are generally designed for small and individual customers such as households, farms, weather stations, road signalization, and advertising systems. SWTs offer a promising alternative for many remote electrical uses where, given a set of site evaluation criteria, the wind resources can be identified as beneficial, both as stand-alone applications and in combination with other energy conversion technologies such as photovoltaic, small hydro or diesel engines.

The quantity of SWTs operating worldwide grows every year. In 2012, the total number of such devices was approximately 800,000 worldwide [2] with the growth of about 10%. The majority of SWTs (about 70%) are located in China, where the highest number of new installed units in 2012 was also noted. The second biggest market of SWTs is USA, where around 155,000 SWTs are operating at the time this document is prepared. In Europe, the leader is the United Kingdom: 23,500 units, followed by Germany: 10,000 units, Spain: 7020 units, and Poland: 3200 units. Total SWT generation capacity installed in 2012 was equal to around 678 MW (576 MW in 2011). The majority of world's capacity (85%) belongs to three countries: China (274 MW), USA (216 MW), and UK (83.7 MW). Unfortunately, developing countries play a minor role in small wind turbine industry. Electrical capacity growth in 2013 was small, with just 90 MW installed across Africa, for a cumulative total of 1255 MW. It is exceptionally regrettable considering enormous wind power potential (best around the coasts and in the eastern highlands of the African continent) [2]. A global forecast concerning SWTs installed capacity in years 2009–2020 is presented in **Figure 1**.

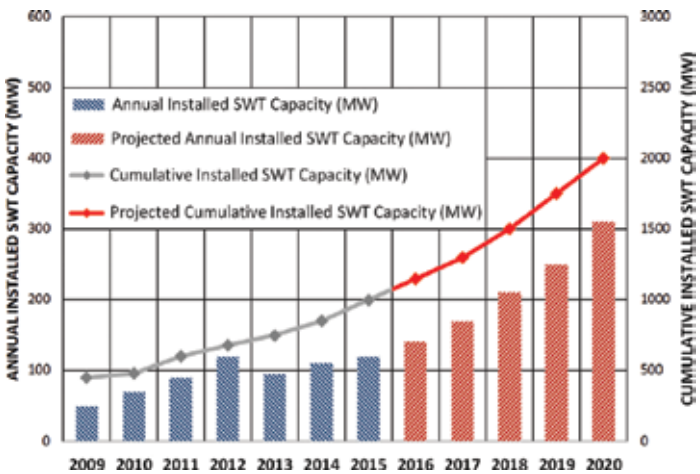

Figure 1. SWT installed capacity world market forecast for 2009–2020 [2].

http://dx.doi.org/10.5772/62821

The development and dissemination of SWTs involves great expectations in the field of eco-energy production. Some opinions suggest that without the dissemination of SWTs, the fulfillment of legal requirements for energy efficiency and energy production from renewable sources will be relatively difficult. In particular, in the developing countries, small wind turbine sector can efficiently contribute to provide electricity to millions of people in rural areas. In order to create a positive outcome, a big challenge awaits not only the authors of laws supporting investments in SWTs, but also engineers and scientists who should propose design solutions addressing the real issues found in the small wind turbine energy sector (aerodynamics: ill-optimized blade often using trends and observations from large HAWTs, poorly addressed issue of local wind resources abundance; structural: different nature of loads experienced by SWTs, little care given to weight optimization; conversion/control: seldom usage of active regulation methods, such as rpm control to expand operational margin of the SWTs, little attention given to match turbine's mechanical power capability with that of a generator; economic: lack of cost optimized SWTs) [3].

The wide prevalence of SWTs and the emergence of the so-called "prosumers" within the electrical grid (the Smart Grid concept) are believed to be one of the biggest factors changing the way that the power companies will deliver service over the next decade. This qualitative change may result in a reduction of transmission losses and make the electricity infrastructure more flexible and secure. The specialists agree that work on the design and architecture of the future grid is as important as the work on the technologies and products that would realize a smart grid vision, for example, SWTs being a part of electricity network [4]. The above motivates to devote more effort to the field of modern SWTs development.

In the small wind turbine market, the return on investment (ROI) is one of the most important factors determining the turbine's validity [5]. Having the above in mind, it has become a challenge for many designers and research facilities to develop a small wind turbine design which would be competitive with other renewable energy sources. For this to be possible, it would have to incorporate a number of factors: high efficiency, sufficient longevity, low installation, and maintenance costs. Having above in mind, it has been concluded that SWTs should be characterized by the lowest possible price, while maintaining relatively high efficiency as well as satisfying reliability and maintenance parameters.

2. SWT design solutions

This section presents both the literature investigation including manufactures data and independent expertise as well as series of coupled numerical simulations (computational fluid dynamics (CFD), Finite Element Method (FEM), multi-body), investigating impact of the chosen design solutions on small wind turbine operation. It allowed objective evaluation of different design approaches (advantages and disadvantages), which in turn enabled the systematic identification of actual limitations as well as the opportunities for specific design solutions of SWTs: horizontal axis wind turbines (HAWTs) and vertical axis wind turbines (VAWTs); the rotor position in relation to the tower (upwind vs. downwind); and the addition of a duct that encapsulates the rotor (diffusor-augmented wind turbine—DAWT).

2.1. Horizontal and vertical axis SWTs

Wind turbines in general can be divided into two major groups based on the position of rotor axis of revolution: HAWTs and VAWTs [6].

HAWTs are currently the vast majority of installed solutions worldwide. Consequently, close to 75% of SWTs are HAWTs. That is due to their high efficiency in relation to low installation and maintenance costs. Apart from the unconventional solutions and one- and two-bladed configurations, the classic three-bladed layout is the default choice with a 99% market share of all operating HAWTs [7]. Three blades is the lowest blade count which allows for easier management of centrifugal body forces. Some small turbines incorporate an increased amount of blades, which may improves aerodynamic efficiency slightly, but most often the added mass and material cost outweigh any benefits gained.

VAWTs are the earliest examples of harnessing the energy of the wind. These early machines were primarily based on a drag force as the mechanics to turn the turbine's working section. Some modern designs try to re-invent the concept, but the efficiency is generally unsatisfactory because of the limited tip speed ratio. Modern-day VAWTs most often use the aerodynamic principles of lift force to work, with Darrieus wind turbines being a good example. Some of the marketed advantages of VAWTs over the classic horizontal designs are as follows: easier maintenance thanks to the generator and the gearbox being placed near the ground, low cut-in wind speeds and no need for yaw mechanisms. In practice, maintenance and operational costs are similar because of the high loads on the bottom bearing, efficiency in converting wind kinetic energy into a mechanical power is relatively low for low wind speeds and response to an often changing wind direction dominated by turbulence is poor [7, 8]. Nevertheless, VAWTs are a popular choice for urban wind environments and are seeing some optimization research with advanced evolutionary algorithms aimed at raising the overall performance of these designs [9].

2.2. Shrouded SWTs

An interesting design solution for HAWT turbines is the addition of a circular duct that encapsulates the rotor. Such turbines have a number of commercial and scientific designations, such as DAWT, wind lens, compact wind acceleration turbine (CWAT). Attempts to add a shroud in order to stabilize and accelerate the flow through a turbine have been reported nearly 150 years ago. An invention proposed by Ernest Bollée, patented in 1868, was an American style multiblade wind turbine with a stator in the form of a shroud**.** After decades of stagnancy, shrouded turbines have seen a major interest increase in recent years with many academic and industrial centers proposing mechanically and aerodynamically optimized solutions which are said to be vastly superior to non-shrouded designs. The influence of the shroud on the air flow has been proven to be beneficial in numerous wind tunnel tests [10, 11], but little is available on the performance of such turbines in real outside conditions. What is more, the added diffusor is often expensive due to the amount of material used and the added mass puts more stress on the towers foundation and hinders the operation of the yaw system.

http://dx.doi.org/10.5772/62821

The concept of Framed Light Shell Diffuser (**Figure 2**) was created as an attempt to lighten the diffuser made of glass fiber composites which are the most commonly used materials for such applications nowadays. Geometrical shape of the diffuser was developed based on CFD simulations considering turbine efficiency optimization for low wind speed conditions. The authors focused on developing an overall structural design, as well as detailed technical solutions (stiffer struts, connecting rods, material forming issues). Subsequently, static structural finite element analysis was performed in order to assess the stiffness and stress distribution based on load conditions in the form of pressure field form the CFD analysis and gravitational forces. Obtained results lead to a conclusion that designed aluminum shell frame diffuser may be an alternative for the composite diffuser. Moreover, the developed structure is characterized by lower mass and comparable stiffness to its composite counterpart. It is worth mentioning that lighter diffusers allow use of lighter supporting structures, such as towers or guy-wired masts. This fact may contribute to lowering the overall costs of future SWTs and could be very beneficial for the privately owned small wind turbine market.

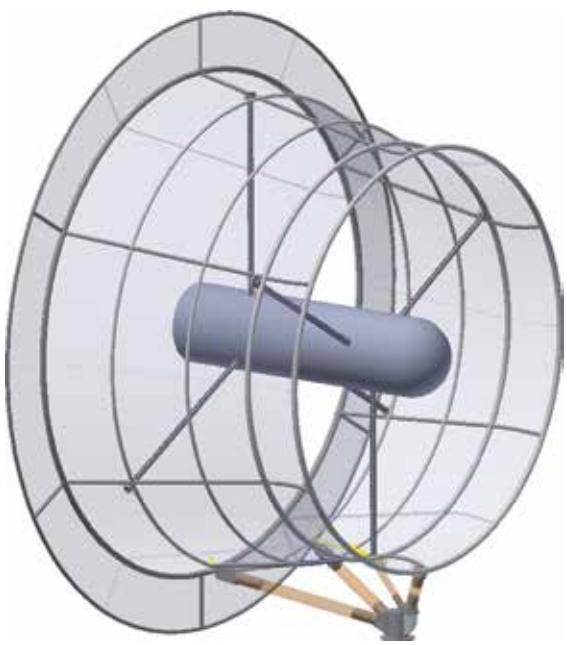

Figure 2. Framed Light Shell Diffuser concept for SWT.

2.3. Upwind vs. downwind SWTs

One of the fundamental distinguishing factors in horizontal wind turbines is the rotor position in relation to the tower (see **Figure 3**). Today market is dominated by upwind rotors: relative to the wind, their rotor is located in front of the tower (windward) (**Figure 3a**), while downwind rotors are behind the tower (leeward) (**Figure 3b**) [12].

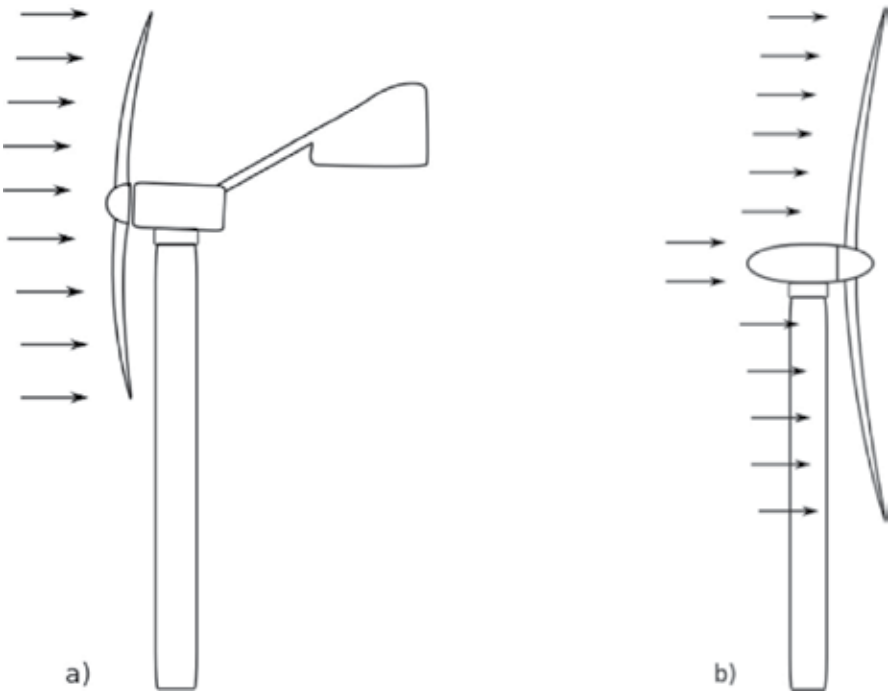

Figure 3. Upwind (a) and downwind (b) wind turbines.

In upwind design solution, the rotor is in the front of the unit (facing the wind) and it is characterized by higher efficiency due to the reduced tower impact on wind inducted at the working section. Unlike upwind, the downwind turbines experience a different inlet wind profile effectively changed by the development of a boundary layer on a nacelle and by the formation of wakes in the aerodynamic trail behind the mast. In upwind designs, the rotor needs to be made rather inflexible and placed at some distance from the tower to avoid collision. What is more, those are not self-aligning in the direction of the wind, and therefore, they need a tail vane or a yaw system to keep the rotor facing the wind.

In downwind turbines, the rotor is on the back side of the turbine (the lee side of the tower). Their main advantages are that they may be built without a yaw mechanism and the rotor may be made more flexible (since there is no danger of a tower strike). This may be an advantage both in regards to weight and the structural dynamics of the machine. Therefore, the basic advantage of the downwind machine is that theoretically, it may be built simpler and lighter than an upwind machine. Downwind turbines generally have lower aerodynamic efficiency, and the fluctuation in the wind power due to the rotor passing through the wind shade of the tower may give more fatigue loads on the turbine than those with an upwind design. Although the upwind type is more popular than the other one, the advantage that the downwind configuration can face the wind automatically makes them much more promising for SWTs due to its simplicity.

http://dx.doi.org/10.5772/62821

Using the methodology of aero-, servo-, elastic-coupled numerical analyses, the authors carried out analysis of small wind turbine behavior in terms of upwind vs. downwind SWT comparison. It is worth pointing out that the relative low cost of such research methods is a great advantage in comparison to real experiments (e.g., wind tunnel tests) [13].

The first set of the obtained results concerns the dynamic response of the simulated variants in terms of rapidly changing wind speed conditions. Case one was here the IEC 61400–1 direction-change condition [14]. Both considered turbine variants have proved to be capable of quick and precise nacelle turn during the changing direction, event and it can be stated that both design solutions work properly and similarly in this case. The upwind variant of the small wind turbine proves to have 5% higher efficiency than the downwind variant, which in turn resulted in a 13% higher energy output in economic analysis. For the 3 kW machine, the downwind variant should be at last 1200 USD cheaper than the upwind small wind turbine to be economically valid (by the application of lighter and cheaper materials, deflective blades, etc.); on the contrary, it is more likely to equip the small wind turbine in a tail vain having additional 1200 USD. The biggest disadvantage of the downwind design variant is the presence of significant fluctuations of momentums in rotor blades and forces on the top of turbine tower, which may cause a real danger of fatigue damage in the turbine construction as well as the risk of resonance [15].

2.4. Other SWTs designs

Other design solutions that can be found in SWT applications or concepts are, that is, as follows: two-blade, single-blade turbines with a counterweigh, multiblade rotors, Venturi design turbines, Magnus effect turbines, multi-rotor solutions, H-type turbines, Darrieus–Savonius hybrid, Tornado/Jet/Vortex/Spiral airfoil, Fuller's design (bladeless—Tesla like), Pawlak's design, airborne concepts, and other unconventional solutions.

The main driver for multiblade (up to three) turbine development is the fact that aerodynamic efficiency increases with the number of blades. Increasing the number of blades from one to two yields a six percent increase in aerodynamic efficiency, whereas increasing the blade count from two to three yields only an additional three percent in efficiency [16].

Extraction of wind energy by a single rotor leaves a substantial amount of power unrecovered. To use this remaining potential, a two-stage wind turbine was proposed. Contra-rotating wind turbines possessing two co-axial rotors can theoretically gain up to 40% more energy from a given swept area as compared to a single-rotor turbine. Contra-rotating turbines require a generator tailored for this system in order to avoid expensive and impractical placement of the second generator on rotor-nacelle assembly (RNA) to convert energy from the additional rotor. In fact, the twin shaft technology of co-axial rotors presents a possibility to increase the rotation speed of the electrical generator by summing up the relative velocities of the rotor and stator. The main drawbacks of two-stage turbines are an increased interaction between the rotors posing problems from aero-mechanical point of view and the additional costs associated with the installation of the second stage and a more sophisticated generator [17].

The Savonius rotor is a self-starting, high-torque wind turbine. It may be used alone or to jump start the Darrieus rotor, a high-efficiency rotor, but with a limited capability to initiate operation on its own. This combination is presented as an effective design that combines the advantages of both designs [18].

The Magnus effect is the commonly observed effect in which a spinning ball (or cylinder) curves away from its principal flight path (a force perpendicular to the direction of movement, acting on the rotating cylinder or other rotary body, moving relative to the fluid). This makes a range of potential advantages with respect to traditional blade wind turbine. Radial cylinder location is analogous to wind wheel blades with horizontal axe. The basic advantages are said to be seen at low, but the most repeated wind velocities 2–6 m/s, at which blade wind turbines are not effective [19].

2.5. SWT's blades

The blades are the components, which interact with wind and are designed to maximize the turbine efficiency. Blades are made from light materials, such as glass- or aluminum-based fiber-reinforced plastics, possessing good resistance to wear and tear. The fibers are incorporated in a matrix of polyester, epoxy resin, or vinyl ester constituting two shells kept together and strengthened by an internal matrix. The external surface of the blade is covered with a layer of colored gel to prevent ageing of composite material due to ultraviolet radiation [6, 7, 9].

A hollow shell corresponding to the defined blade envelope clearly provides a simple, efficient structure to resist flexural and torsional loads, and some blade manufacturers adopt this form of construction. The hollow shell structure defined by the airfoil section is not very efficient in resisting out-of-plane shear loads, so these are catered for by the inclusion of one or more shear webs oriented perpendicular to the blade chord.

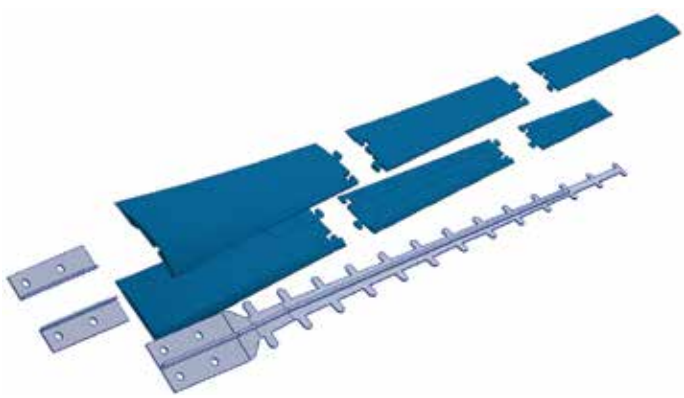

Figure 4. 3D printed ABS polymer-based SWT blade with a stiffening core made of steel.

Five different materials were considered in terms of turbine blade optimization: steel, aluminum alloy, glass fiber composite, carbon fiber composite, and ABS polymer for three-dimensional (3D) printing (**Figure 4**). Blades made of all listed materials have fulfilled the strength

http://dx.doi.org/10.5772/62821

criterion (stresses values generated by maximum loads did not crossed yield or fracture). Analysis revealed that the best material in terms of mass and stiffness is the carbon composite. Unfortunately, this material is very expensive and was opted with in order to keep SWT price reasonably low. Metal-based materials are characterized by very high stiffness, which reduces the blade tip deflection; however, the mass of the blade was too high in this case. What is more, a relatively high stiffness was a direct cause of relatively high stress values. Those values have raised justified questions on the fatigue toughness of the SWT. The ABS polymer is the cheapest and the lightest one of all mentioned. It is also the best choice from the manufacturing point of view. Unfortunately, it is also the most flexible material, producing high blade tip deflections even after the introduction of stiffening core made of steel (**Figure 5**).

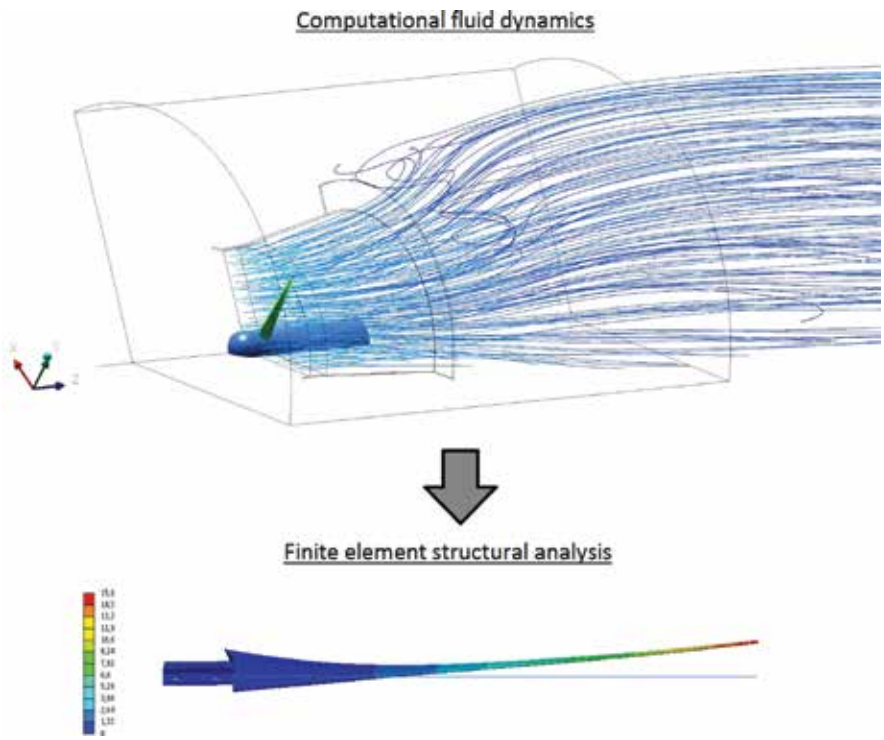

Figure 5. SWT blade deflection (ABS 3D printed coating with a steel core).

2.6. SWT's generators

SWTs are usually equipped with synchronous generators operating at variable angular speeds based on permanent magnets (e.g., neodymium magnets) [20]. It is a design solution which can contribute to meeting the requirements of efficient operation. Working principles of the variable speed generator determine many other aspects of the wind turbine operation including, for example, a tremendously increased annual energy production (AEP) in comparison with equal-power fixed pitch, fixed speed turbines.

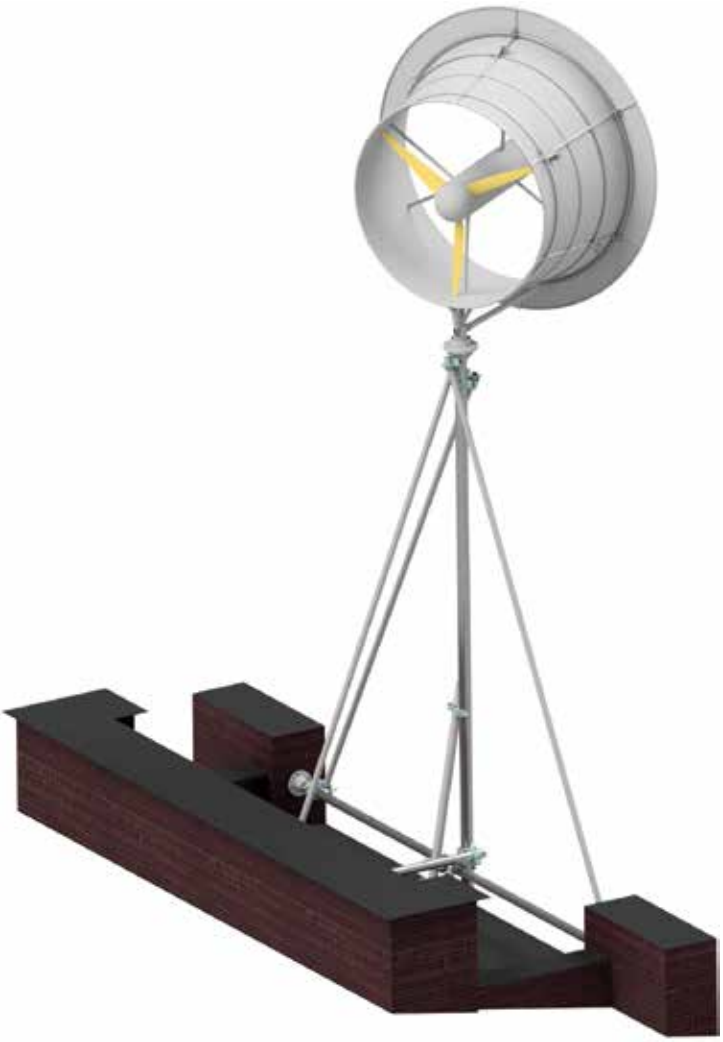

Figure 6. Roof-mounted SWT equipped with the diffuser.

SWTs typically operate in autonomous systems without connection to the grid, in which they directly power heating and other loads that do not require stable electric parameters, dictated by economic issues. Potential expenditure related to connecting the SWT to the electrical grid exceeds the usual financial benefits of possible income from selling energy produced. The other aspect is the fact that SWTs are generally simple devices and they are rarely equipped with sophisticated control systems such as blade pitch mechanisms.

This type of generator produces alternating current (AC), which must be rectified to direct current (DC) by means of a simple bridge rectifier. Similar to solar photovoltaic (PV) systems, the DC voltage allows the use of these turbines for battery charging. For in-battery charging systems, a charge controller is added to prevent the battery from overcharging. A dump load

http://dx.doi.org/10.5772/62821

is required to protect the inverter from overvoltage and to prevent the turbine from overspeeding [21].

2.7. SWT's supporting structures

The SWT is usually placed on a pole, preferably higher than 15 m, to lessen the impact of turbulent, sheared winds forming in close proximity to the ground. Utility-scale wind turbine towers are mostly of tubular type. In case of SWTs, tubular type towers are also popular; however, guyed lattice towers are also used. The tilt-up poles/towers are very popular since they are easy to install and offer good accessibility for maintenance and repair. Tubular towers are usually made of rolled steel, although sometimes reinforced concrete is used [9].

Rooftop-mounted turbines are yet another option. Such turbines are directly installed on a building. Both vertical and horizontal axis turbines can be mounted in such a way (**Figure 6**), but they might be subject to slightly different wind profiles being inducted at the rotor [21]. Particularly important for roof-mounted turbines is the identification of flow separations due to rooftop edges. Such flow structures not only influence the production efficiency but may be a source of unwanted loads that are difficult to control.

3. SWT's economic evaluation

The investment in SWTs is more often made by private individuals in order to partially fulfill residential household demand for electricity or to produce hot tap water. However, practice shows that a large portion of those who have decided to build a backyard wind turbine is disappointed with the actual amount of energy produced by it. This is mainly due to the promotion of inaccurate, overstated, or even incorrect information on the projected turbine's power output by manufacturers or installers. This reduces public confidence in the legitimacy of this sort of economic investment, thus slowing down the development of this industry sector [22, 23].

Numerical weather prediction (NWP) simulations over the span of year 2013, covering the whole area of Poland, were carried out. The purpose of these forecasts was to establish a reliable and accurate wind resource atlas for approximate AEP of small wind turbine systems. Long-term wind speed forecasting has been used with success for utility-scaled wind farms. This accounts not only for planned sites but also operational power plants, where weather forecasting is used constantly for setting up advanced control schemes or predicting suitable time windows for planned maintenance [24].

Calculation of meteorological parameters was performed using the non-hydrostatic mesoscale Weather Research & Forecasting (WRF) model. WRF is designed both for operational forecasting and atmospheric research use. It enables an atmospheric phenomena simulation for scales ranging from thousands of kilometers to single meters. The model contains several capabilities, important from the research point of view, such as: 3D data control with initial data and model results correction possibilities using aerological, radar and satellite measure-

ments; multilayer ground modeling; humidity cycle; vegetation; cloud cover and precipitation parameterization including water phase state; radiation transport processes; and boundary layer with turbulent vertical transport. These modules are responsible for the parameterization of physical phenomena occurring in the atmosphere. The boundary layer area of intensive surface radiative forcing and mechanical forcing is an important part of the simulated phenomena. Mechanical forcing is determined by orography, roughness, and cover. Radiative forcing is defined by albedo and thermal capacity of the surface. The parameters are determined by the ratio of land to water area; vegetation and its status; irradiation depending on location and inclination. Determination of these factors was of importance because the boundary layer close to the surface is the area associated with the presented studies.

The data used in the study covered the period of 1 year (01.01.2013-31.12.2013). The input data of the WRF came from the archive of the global forecast system (GFS). These were obtained from the National SOO Science and Training Resource Centre (NWS SOO/STRC). The model was run for each day and for each main synoptic term. Two grids with spatial resolution of 36 and 12 km were used. The simulation domain included a selected area of Europe as shown in **Figure 7**. Forecast modeling time was set equal to 24 h with a 1 h data sampling rate. Results for each 24-h period were obtained in a five-dimensional set of prognostic parameters fields. This set includes, among others: pressure values, geopotential, temperature, and three-dimensional wind fields [16]. Wind speed data averaged over a 60 min period have been said to be useful for long-term energy yield predictions for SWTs [25].

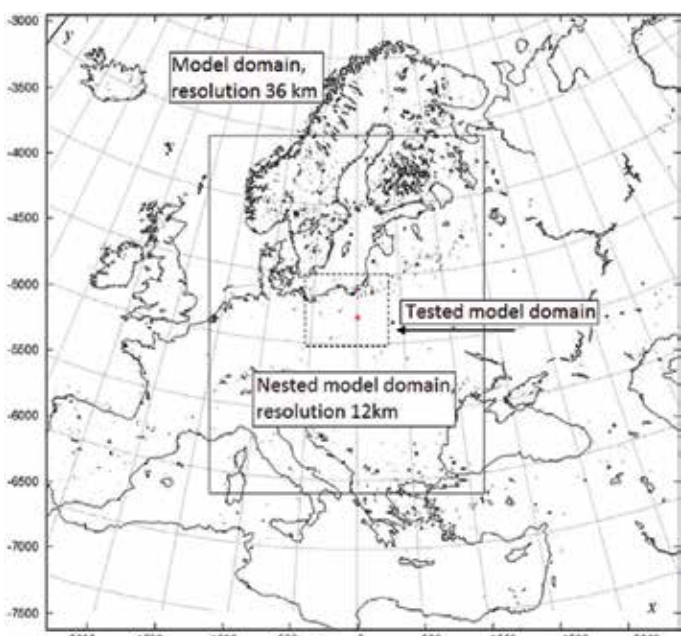

Figure 7. WRF model domains—36 and 12 km grid [23].

http://dx.doi.org/10.5772/62821

A randomly chosen location in model domain was a rural region neighboring a small town called Sokolow Malopolski in the Voivodship of Sub-Carpathia. It is characterized with rather typical rural wind speed conditions. Many of the houses built in the region are solitary and surrounded by open grass or farm fields, thus producing a suspected low ground roughness rate. Such households could potentially benefit from an auxiliary power or heating source in the form of a small wind turbine.

Calculations of the power output were performed using the following formula:

$$E = \sum_{i=1}^{n} \begin{cases} \frac{1}{2} A \rho_i \eta(v_i) v_i^3 h & P_r > \frac{1}{2} A \rho_i \eta(v_i) v_i^3 \\ P_r h & P_r \le \frac{1}{2} A \rho_i \eta(v_i) v_i^3 \end{cases} \quad (1)$$

where: E is the estimated total energy generated throughout the test period, n is the number of samples, h is the sample duration (1 h), v_i is the wind speed for sample i, A is the swept area of a given turbine, ρ_i is the air density for sample i, $\eta(v_i)$ wind turbine efficiency at given tip-speed ratio (TSR) and P_r is the turbine rated power.

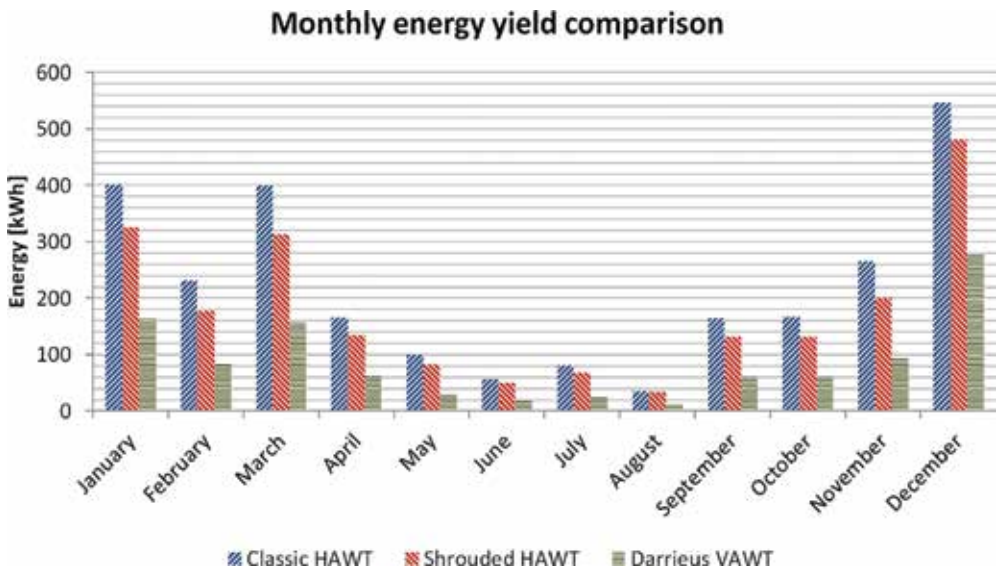

Figure 8. Monthly energy output for the chosen turbines [23].

3.1. HAWT, VAWT, and DAWT comparison

Three types of SWTs were chosen to be compared in terms of their productivity and cost-effectiveness. The first is a typical three-bladed HAWT design. The second is an aerodynamically complex, shrouded HAWT. The third is the Darrieus-type VAWT. All the turbine

characteristics, such as power curves, price, swept area, were taken from very popular, commercially proven designs. For the results to be meaningful, all the chosen turbines have a similar rated power of around 3 kW.

The outcome of the performed calculations is shown in **Figure 8** and compared in **Table 1**. When estimating the investment return period, the price for energy supplied (power supply) was established at 0.2 $/kWh. Maintenance and any additional costs associated with turbine operation are assumed to be the same for all three systems and are therefore neglected.

	Energy produced (kWh/year)	**ROI (years)**
Classic HAWT	2610	28+
Shrouded HAWT	2126	31+
Darrieus VAWT	1036	137+

Table 1. Chosen designs economic comparison [16].

The difference in monthly power generation is clearly visible with the majority of energy being produced during the windy winter months. Any needed maintenance or routine inspections should be carried out during calm summer months. Such a discrepancy in electricity generation raises the problem of continuous power supply.

For the chosen localization, the classic three-bladed HAWT proved to be the most cost-effective design of those taken into account, even though it had the lowest rated power. In theory, the advanced construction of the shrouded HAWT turbine allowed for a very high theoretical efficiency. In practice, because of its small rotor diameter it proved to be slightly inferior to the classic layout with a larger rotor. Moreover, the shroud is likely to put additional strain on the tower due to added mass and increased aerodynamic drag, possibly increasing the maintenance costs. Snowfall and icing of the shroud could lower the operational availability and introduce the need for deicing. The chosen Darrieus vertical wind turbine was the worst design in the terms of cost-effectiveness. Very high system costs and low efficiency in relation to rotor size led to the return period being unacceptably long [23].

3.2. Investigation of parameters influencing the efficiency of SWTs

Three cases will be carried out in order to find the factors which have the highest impact on the estimated electrical power generation. Case one investigates the difference between estimated one with a theoretical, constant efficiency turbine and a popular, commercially available, wind turbine using its power curve. The second case estimates the generated amount of energy based on three types of wind data for a randomly chosen site. In this case, calculations were performed using a yearly mean wind speed, discretized meteorological data and the Weibull wind speed distribution function. The third case shows the difference of estimated energy production for three tower heights: 10, 20, and 30 m [22]. Calculations of the power outputs were performed using formula (1.).

http://dx.doi.org/10.5772/62821

The turbine chosen for the analyses is the Evance R9000, which is a popular small wind turbine design with a high market share, especially in the UK. It is a 5 kW turbine, with a 5.5-m-radius rotor and a typical, of HAWTs, power curve [26]. Factors such as maintenance and down time were not taken into account. That is due to the fact that the goal for these calculations was to estimate small wind turbine sensitivity to operating parameters such as a tower height, efficiency, and wind data type with which the AEP forecast is modeled.

The estimated energy produced by the Evance R9000 amounted to 7551 kWh, assuming energy cost of 0.2 €/kWh, that is an equivalent of 1510 €. For a 5-year ROI period, without any maintenance or down time, the turbine would have to be priced at around 7500 €; however, in reality, such solutions are roughly priced at 36,500 €. Another aspect worth mentioning is that a yearly demand for energy of typical household is estimated at around 3–4 MWh. Thus, in theory, it would be possible to achieve energy independence. In practice, it would be nearly impossible (the problem arising from high fluctuation of the energy production throughout the year, mentioned in 3.1.1.).

Another very interesting way to present the obtained results is to draw an energy density function on top of the occurring wind speeds. **Figure 9** shows, in blue, the wind speed occurrence rates and, in red, the amount of energy generated from a specific wind speed by the Evance R9000 turbine during the whole year. The shift of the energy density function to the right in respect to wind speed curve is a direct result of the power equation, proportional wind speed cubed Equation (1).

Using Matlab computer software, the maximum likelihood estimate of the Weibull parameters has been established with the *wlbfit* function. The resultant Weibull probability density function is shown in **Figure 9**. Additionally, an arithmetic mean of the wind speed for the given location has been calculated and is equal to around 4.77 m/s. The yearly power generated has been again calculated using the obtained Weibull function and the mean wind speed with the standard Evance9000 power curve. A comparison of the estimated power production based on three different wind data types is presented in **Figure 10**. It is clearly visible that estimating the amount of wind power generation using an arithmetic mean of the wind speed is highly inaccurate. The predicted amount was 4420 kWh which is almost 70% off the amount of energy predicted using the direct method with accurate wind speed data. Energy production estimated with the Weibull function equaled 7932 kWh, which is 5% different from the result obtained using the direct method. This difference is small enough to prove the validity of using the Weibull or Rayleigh distributions for estimating small wind turbine energy production.

Five different calculations of estimated energy output were performed with five different small wind turbine characteristics. The first was performed with an artificial, constant value of 33%. Three characteristics were based on the Evance R9000 power curve including the original curve, one which is offset by +5% and another which is offset by −5% from the original distribution. The fifth one is a hypothetically proposed, small wind turbine curve which has increased efficiency in low wind speeds—STOW (**Figure 11**). The results of the performed calculations are presented in **Figure 12**.

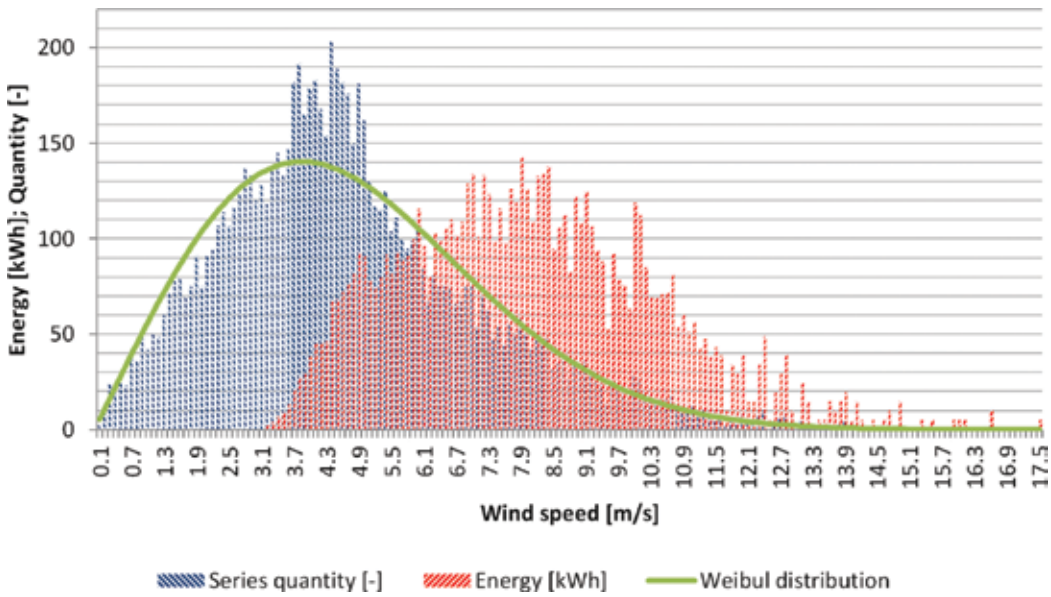

Figure 9. Wind speed distribution, energy distribution, and Weibull function fit (c = 5379; k = 2023) [22].

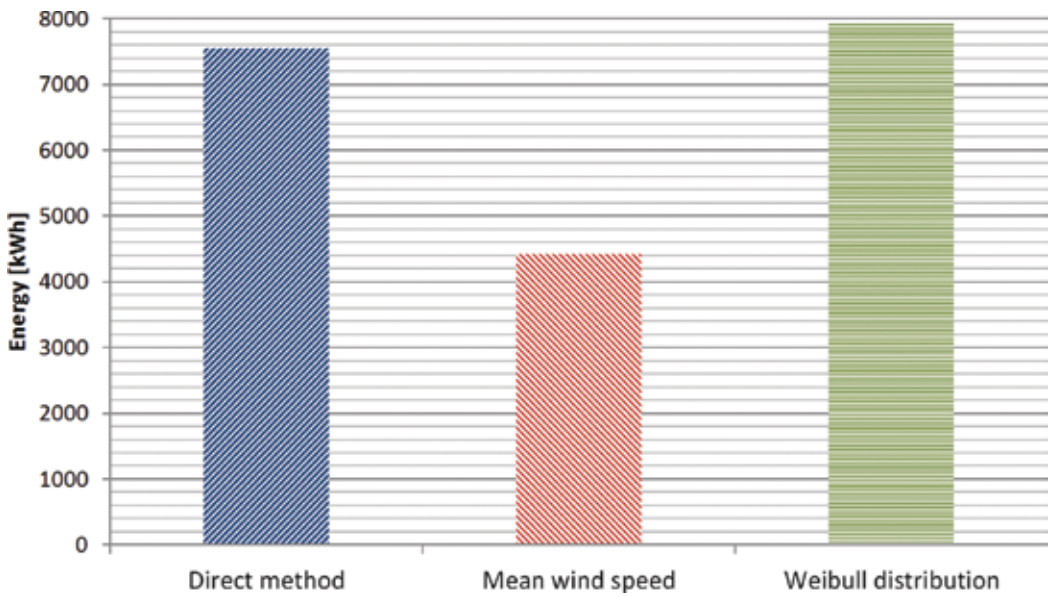

Figure 10. Energy production estimates based on three different wind speed data types [22].

http://dx.doi.org/10.5772/62821

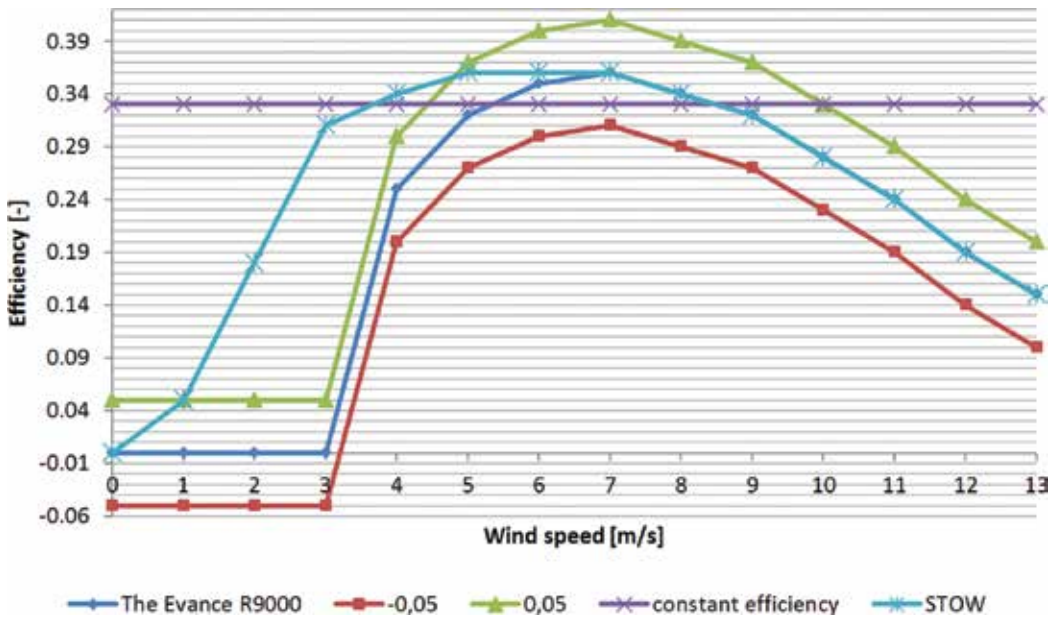

Figure 11. Efficiency curves used for the energy calculations [22].

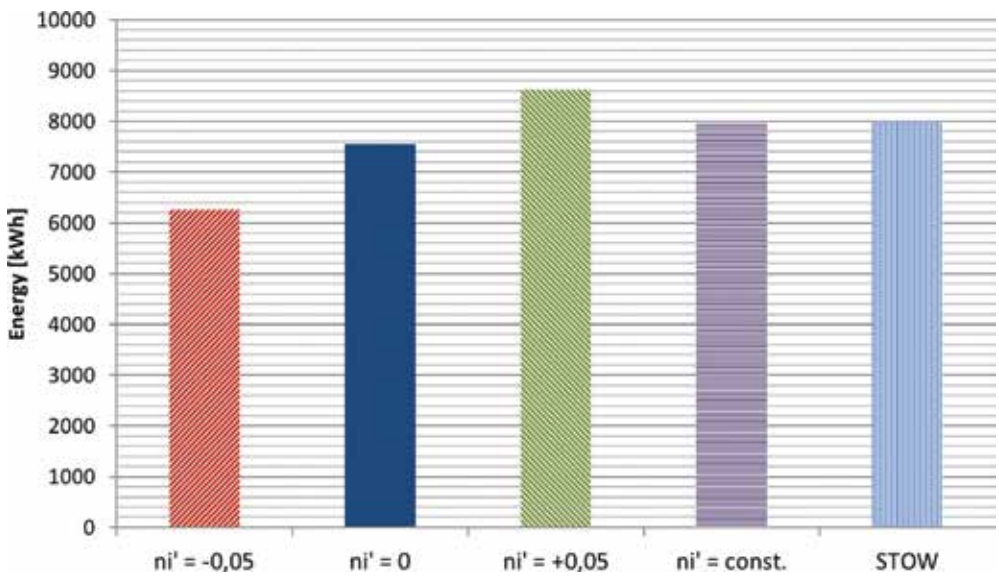

Figure 12. Energy produced by a 5 kW rated turbine with different efficiency curves; the series are tied to the curves presented in **Figure 11** [22].

The final investigated small wind turbine parameter was the tower height. Wind speed data were collected at 10 m height. Using the power law with the terrain dependent parameter α = 1/7, the wind speeds for the whole year have been recalculated for 20 and 30 m heights. The obtained wind speeds were used to estimate the produced power with the standard power curve and are presented in **Figure 13**.

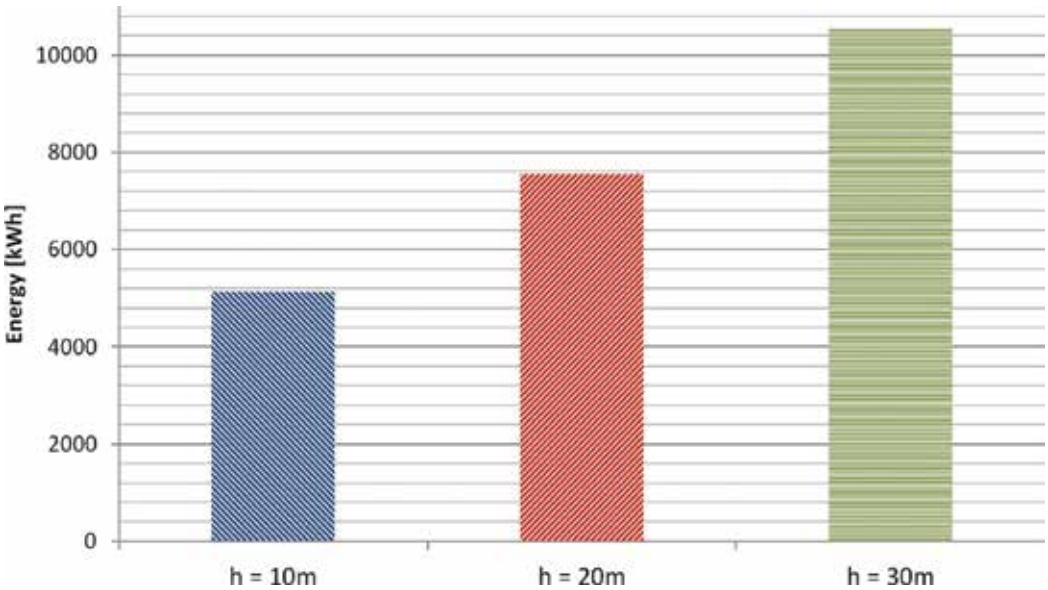

Figure 13. Estimated energy generated for different tower height variants (10, 20, and 30 m)—wind speed obtained with the empirical power law [22].

4. Summary

Auxiliary power generation using privately owned SWTs can be an economically viable option, but the price of design solutions available on the market is often unreasonably high. Due to the very long ROI period (even for popular and commercially proven designs), it is of great importance for those systems to be installed in areas with above average wind conditions.

Advanced and experimental solutions such as shrouded or VAWTs are an interesting concept, but real efficiency of such designs appears to be virtually equal or even lower to equivalent classic three-bladed turbines. Additionally, the overall size and weight of these systems are increased. This in turn forces the need for sturdier and more expensive towers.

Private investors interested in setting up a green auxiliary power system should be aware of the fact that wind turbines installed inland will be subjected to seasonally changing winds.

To avoid energy waste on AC/DC/AC conversion of electricity, it is advisable to use the generated power for water heating. The use of power banks greatly raises costs of the invest-

http://dx.doi.org/10.5772/62821

ment and is hazardous to the environment, as the used batteries are very difficult to recycle. With the windy winter months, no energy would be wasted as hot water is used constantly during this period of the year.

Most importantly, though, it has been shown that even a major increase in a turbine aerodynamic and overall efficiency will not provide as much additional power as an increased tower height. Aerodynamic optimization of the rotor, use of advanced, light materials, etc. will have a positive outcome in the turbines operation and power output; however, the increased costs of such solutions will undoubtedly result in the same or even longer ROI periods, based on the methodology presented herein. Taking into account all the above, in the authors' opinion, a major focus in developing new small wind turbine solutions should be paid to reducing the price of the final product and mounting the design on a tower as high as it is reasonably, from the aeromechanical and operational safety point of view, economically and legally possible. When establishing the final tower height, numerous aspects associated with it must be taken into account, such as, but not limited to: national construction law, mooring possibilities, space available on site, and the soil type. In short, it is more reasonable to invest in a robust and cheap turbine design and mount it on a high tower. Additionally, the authors' attention was also paid to the fact that optimizing a wind turbine for low speed conditions (4–5 m/s) is economically unjustified as such wind speed does not provide sufficient kinetic energy for the turbine.

Acknowledgements

The research leading to these results has received funding from the Polish-Norwegian Research Programme operated by the National Centre for Research and Development under the Norwegian Financial Mechanism 2009–2014 in the frame of Project Contract no. Pol-Nor/200957/47/2013.

Author details

Jakub Bukala[1*], Krzysztof Damaziak[1], Krzysztof Kroszczynski[1], Jerzy Malachowski[1], Tomasz Szafranski[1], Michal Tomaszewski[1], Hamid R. Karimi[2], Krzysztof Jozwik[3], Maciej Karczewski[3] and Krzysztof Sobczak[3]

*Address all correspondence to: jakub.bukala@wat.edu.pl

1 Military University of Technology, Warsaw, Poland

2 University of Agder, Grimstad, Norway

3 Lodz University of Technology, Lodz, Poland

References

[1] IEC 61400–2: Wind turbines—part 2: small wind turbines. International Electrotechnical Commission; 2013. doi: ISBN 978-2-8322-1284-4

[2] Gsänger S, Pitteloud J. Small Wind World Report 2014. WWEA; 2014

[3] Aresti L, Tutar M, Chen Y, Calay RK. Computational study of a small scale vertical axis wind turbine (VAWT): comparative performance of various turbulence models. Wind and Structures. 2013;17(6):647–670.

[4] Grijalva S, Umer Tariq M. Prosumer-based smart grid architecture enables a flat, sustainable electricity industry. IEEE; 2011. doi: ISBN 978-1-61284-220-2

[5] Woofenden I, Sargillo M. Is wind electricity right for you. Home Power. 2011;143:52–61.

[6] Gasch R, Twele J. Wind power plants: fundamentals, design, construction and operation, 2nd edition. Springer; Heidelberg 2012. doi: ISBN 978-3-642-22937-4.

[7] Burton T, Jenkins N, Sharpe D, Bossanyi E. Wind energy handbook. 2nd edition. John Wiley and Sons Ltd.; Chichester 2011.

[8] Bedon G, Castelli MR, Benini E. Optimization of a Darrieus vertical-axis wind. Renewable Energy. 2013;59:184–192.

[9] Technical Application Papers: Wind Power Plants. No 13 ed. ABB SACE e ABB S.p.A. L.V.; 2011.

[10] Ohya Y, Karasudani T. A shrouded wind turbine generating high output power. Energies. 2012;3(4):634–649.

[11] Olasek K, Karczewski M, Lipian M, Wiklak P, Jozwik K. Wind tunnel experimental investigations of a diffuser augmented wind turbine model. International Journal of Numerical Methods for Heat and Fluid Flow. Forthcoming. DOI (10.1108/HFF-06-2015-0246).

[12] Manwell JF, McGowan JG, Rogers AL. Wind energy explained: theory, design and application. Chichester: John Wiley & Sons; 2003.

[13] Kwansu K, Changhee L, Yong-Oon O, Ilhan K, Neungsoo Y, Insu P. Time-domain dynamic simulation of a wind turbine including yaw motion for power prediction. International Journal of Precision Engineering and Manufacturing. 2014;15(10):2199–2203.

[14] International Electrotechnical Commission. IEC 61400–2: Wind turbines—part 2: small wind turbines. 3.0 edition. IEC, Geneva 2013. doi: ISBN 978-2-8322-1284-4

[15] Bukala J, Damaziak K, Karimi HR, Malachowski J. Upwind vs downwind small wind turbine comparison—numerical analysis and economical evaluation. Journal of Wind Engineering & Industrial Aerodynamics. Forthcoming.

[16] Hau E, editor. Wind turbines fundamentals, technologies, applications, economics. 2nd edition. Springer; Heidelberg 2006. doi: ISBN 3-540-24240-6

[17] Iowa State University. Iowa State Engineers Study the Benefits of Adding a Second, Smaller Rotor to Wind Turbines [Internet]. March 6, 2015. Available from: http://www.news.iastate.edu/news/2015/03/06/dualrotorturbines [Accessed: February 10, 2016]

[18] T. Letcher, The Ohio State University, Columbus, OH. Small Scale Wind Turbines Optimized for Low Wind Speeds [Internet]. Available from: http://kb.osu.edu/dspace/bitstream/handle/1811/45531/hayes_proceedings_paper.pdf?sequence=1 [Accessed: February 10, 2016]

[19] Kozlov VV, Bychkov NM. Wind Turbine with Magnus Effect [Internet]. [Updated: 2011]. Available from: http://www.itam.nsc.ru/en/section/292/ [Accessed: February 10, 2016]

[20] Goudarzi N, Zhu WD. A review on the development of wind turbine generators across the world. International Journal of Dynamics and Control. 2013;1(2):192–202.

[21] Rolland S, Auzane B. The potential of small and medium wind energy in developing countries. Position Paper: Alliance for Rural Electrification; 2012.

[22] Bukala J, Damaziak K, Kroszczynski K, Krzeszowiec M, Malachowski J. Investigation of parameters influencing the efficiency of small wind turbines. Journal of Wind Engineering and Industrial Aerodynamics. 2015;146:29–38.

[23] Bukala J, Damaziak K, Karimi HR, Kroszczynski K, Krzeszowiec M, Malachowski J. Modern small wind turbine design solutions comparison in terms of estimated cost to energy output ratio. Renewable Energy. 2015;83:1166–1173.

[24] Al-Yahyai S, Charabi Y, Gastli A. Review of the use of Numerical Weather Prediction (NWP) Models for wind energy assessment. Renewable and Sustainable Energy. 2010;14(9):3192–3198.

[25] Elliott D, Infield D. An assessment of the impact of reduced averaging time on small wind turbine power curves, energy capture predictions and turbulence intensity measurements. Wind Energy. 2012;2(17):337–342.

[26] Small Wind Certification Council. Evance Summary Report. SWCC. 2013; pp. 10–27.

Chapter 5

Design of a Low-Cost Permanent Synchronous Machine for Isolated Wind Conversion Systems

Florin-Nicolae Jurca

Additional information is available at the end of the chapter

http://dx.doi.org/10.5772/62817

Abstract

The chapter deals with the theoretical analysis of two configurations of low-cost permanent synchronous generator (PMSG), suitable for small rating, direct driven applications, such as small- and microscale wind power plants. The first structure is a permanent magnet claw-pole synchronous generator (PMCPSG) to be used in an isolated microwind power plants with installed power around few hundred Watts. A permanent magnet synchronous machine with outer rotor (PMSMOR) is the second presented structure, suitable for small wind system with installed power between 2 and 5 kW. In order to obtain the optimal value of the main geometric dimensions of the generators, an optimization procedure, based on Hooke-Jeeves method, was implemented for all the considered structures.

Keywords: permanent synchronous machine, low-cost permanent magnet, small-scale wind power plants, direct-driven, optimization

1. Introduction

Wind turbines are widely used as a pollution-free and renewable source in order to supplement other electricity generators. Wind power technology has developed remarkably during the latest decade. Due to its flexibility, it can be used practically anywhere.

Small wind turbines have been used to generate electricity for rural farms or others remote buildings which do not have the possibility to connect to a main power supply. The increasing demand in recent years for clean and affordable energy will lead without doubt to a wider use of the small turbines for urban area.

The technology of the generator system in small wind turbine can be classified into direct drive and the geared technology concepts. The geared generator system has the advantages in terms of the cost, size, and weight. The direct-drive generator system is superior in terms of efficiency, reliability, and maintenance problem [1]. Because in direct drive generator technology is necessary a high number of poles, accordingly with a big weight, the permanent synchronous machine (PMS) have the advantages of comparing to other machines of being robust in construction, very compact in size, not requiring an additional power supply for magnetic field excitation [2]. One problem of this generator is the cost, especially when the permanent magnet is neodymium, because in the last years its price is continuously increasing. The solution is to use low-cost permanent magnets, such as ferrites and alnico. These materials are reasonably easy to find [3]. Usually, the performances of electrical machines with low-cost permanent magnets are lower comparative with the same machines using neodymium magnet. In order to keep the generator with low-cost permanent magnet feasible, more attention is necessary in design and optimization procedure. So, the challenge for small- and microscale wind power plants is to find a solution to maintain the lower costs of systems (e.g, generator) in conditions of reliability and the high value of efficiency.

This is the motivation of this research work. For that, two configurations of low-cost PMSG suitable for direct drive in wind power applications will be studied from the theoretical point of view.

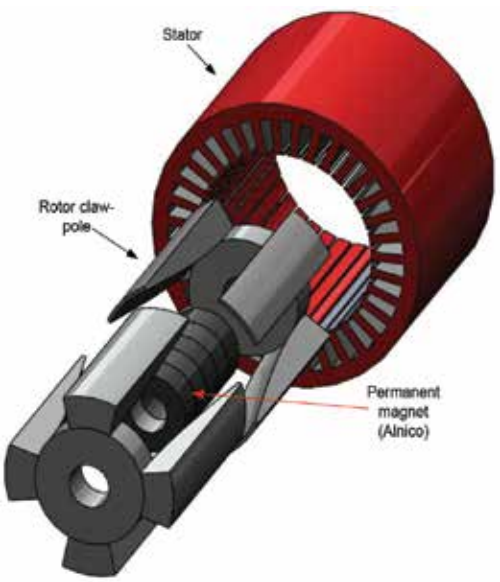

Figure 1. The PMCPSG topology.

The first structure is a permanent magnet claw-pole synchronous generator (PMCPSG) obtained usually from the conversion of an induction or a synchronous conventional machine (see **Figure 1**), suitable for isolated microwind power plants with installed power around few

http://dx.doi.org/10.5772/62817

hundred Watts. A permanent magnet synchronous machine with outer rotor (PMSMOR) is the second presented structure (see **Figure 2**), suitable for small wind system with installed power between 2 and 5 kW. Hence in this chapter, an exhaustive approach will be presented by going through all the phases in the development cycle of special topologies of low-cost permanent magnet synchronous machine.

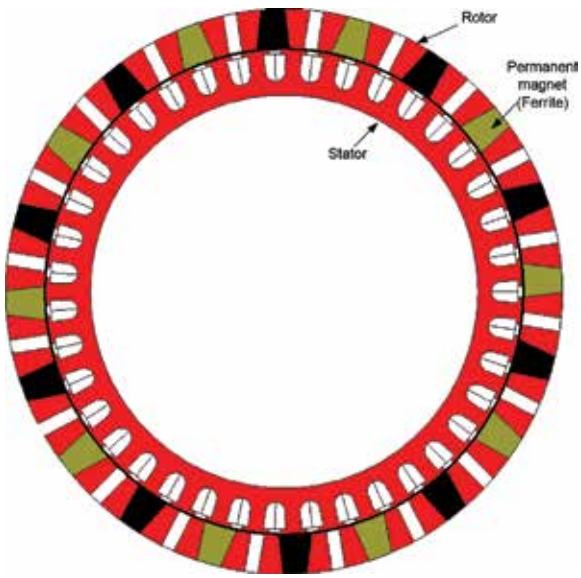

Figure 2. The PMSMOR topology.

2. Design and optimization of the studied electrical machines

2.1. Design of PMCPSG

The objective of the present subchapter was the design and optimization of a three-phase PMCPSG, driven by a small wind turbine with the following set of key parameter: s_N—180 apparent power (VA); rated phase voltage u_N—100 (V); rated speed n_N—750 rpm; pole pair number p—4; permanent magnet-type Alnico. In addition, several constraints must be met such as limited size, low weight, and low torque ripple content.

The analytical procedure includes the following topics: analysis of the specifications, selection of the topology and of the active and passive materials, dimensioning of the geometry, parameter and performance calculation, choice of the manufacturing technologies, and cost prediction.

For the given output power and operating speed, the PMCPSG main dimensions may be determined using the output power equation, based on specific magnetic and electric loads [4]. The inner stator diameter results as follows:

$$D_{is} = \sqrt[3]{\frac{60 \cdot S_N}{C \cdot n_N \cdot \lambda}} \tag{1}$$

with D_{is}—the stator inner diameter; C—machine constant; and λ—geometrical form factor. For PMGPSG, the machine constant could be written as:

$$C = \frac{\pi^3}{2\sqrt{2}} \cdot k_w \cdot \alpha_i \cdot A \cdot B_g \tag{2}$$

with A—electrical load (between 30 and 80 k_A/m for indirect air cooling); B_g—magnetic load (0.4…0.8 T for machines using Alnico); k_w—winding factor; and α_i—pole pitch coverage coefficient [the ratio between the rotor pole width (b_{pr}) and the rotor pole pitch(τ_r)] [4]. As a starting point, due to the special configuration of the rotor, the values for k_w (0.92… 0.966) and α_i (0.6…0.9) were chosen according to [4, 5] for a permanent magnet synchronous machine with rotor salient poles and single-layer fractional windings (see **Figure 3**).

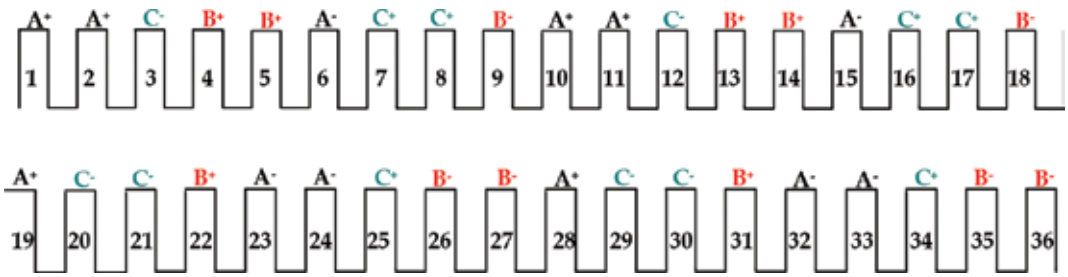

Figure 3. Stator winding of PMCPSG.

The lamination stack length results as follows:

$$l_{Fe} = \lambda \cdot D_{is} \tag{3}$$

Computation of the rotor outer diameter gives:

$$D_r = D_{is} - 2 \cdot g \tag{4}$$

with g—air-gap length.

Due to fault tolerance consideration and the fractional number of slots per pole and phase (q = 1.5), a single-layer fractional winding was chosen. The rms value of the phase electromotive force (emf) is given by [6]:

http://dx.doi.org/10.5772/62817

$$E_{ph\_rms} = \pi \cdot \sqrt{2} \cdot f \cdot k_w \cdot W_1 \cdot l_{Fe} \cdot \frac{\pi \cdot D_{is}}{2 \cdot p} \cdot B_{g\_av} \tag{5}$$

with w_1—number of turns per phase, p—number of pole pairs, and B_{g_av}—average magnetic load.

Starting from the geometric dimensions of the stator and the electrical parameters of the generator, we will obtain from the winding design algorithm, the winding connection diagram (see **Figure 3**), the number of turns per phase (W_1), the area of the wire cross section (S_c), the number of turns per slot (n_c), and the number of parallel current paths (a) [4].

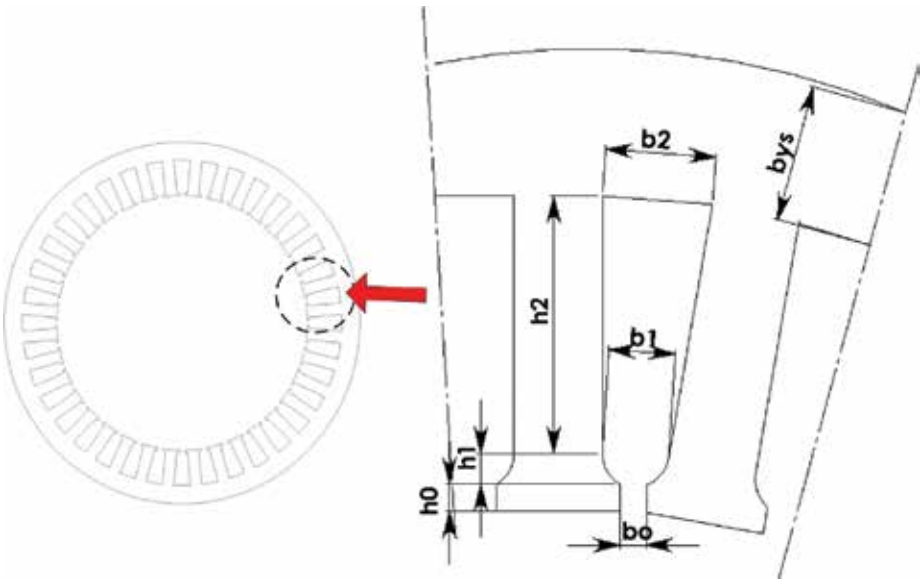

Figure 4. Stator slot geometry.

For the stator slot a trapezoidal cross section was chosen (see **Figure 4**). Its dimensions are derived from the slot area:

$$A_{slot} = \frac{n_c \cdot S_c}{k_{fill}} = b_0 \cdot h_0 + \frac{b_1 + b_0}{2} \cdot h_1 + \frac{b_2 + b_1}{2} \cdot h_2 \tag{6}$$

with k_{fill} = 0.36…0.55 and b_{ts}—the stator tooth width:

$$b_{ts} = \frac{\pi \cdot D_{is} \cdot B_{g\_av}}{Q_s \cdot B_{ts\_av}} \tag{7}$$

with B_{ts_av}—average flux density in stator tooth, usually between 0.8 and 1.2 T according to [5, 7]. Finally, choosing the values for the slot opening, tooth tip height, fixing wedge height [4], the stator slot, and tooth dimensions can be computed. The width of the stator yoke results as follows [6]:

$$b_{ys} = \frac{\pi \cdot D_{is} \cdot B_{g\_av}}{2 \cdot p \cdot B_{ys\_av}} \tag{8}$$

with B_{ys_av}—average flux density in stator yoke, usually between 0.6 and 1 T according to [5, 7].

Thus, the outer stator diameter results as follows:

$$D_{os} = D_{is} + 2 \cdot (h_{ts} + h_{ys}) \tag{9}$$

with h_{ts}—the stator tooth height and h_{ys}—the stator yoke height.

The rotor steel plate carrying 4 claw poles and its dimensions to be computed are shown in **Figure 5**.

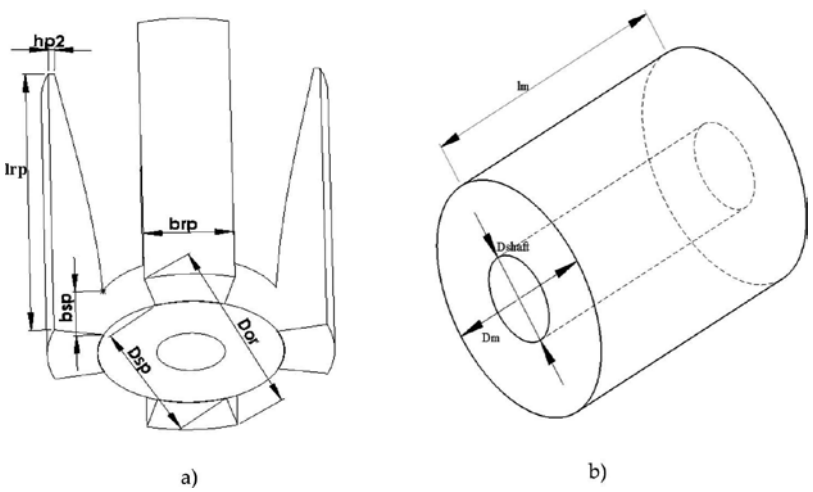

Figure 5. Rotor geometry: (a) claw-pole structure, (b) permanent magnet.

For reducing the leakage flux between two claw poles, the rotor claw-pole width value is given by:

$$b_{pr} = (0.6 \ldots 0.8) \cdot \tau_r \tag{10}$$

The height of the rotor pole tip:

http://dx.doi.org/10.5772/62817

$$h_{p2} = (2\ldots4)\cdot g \tag{11}$$

The length of the rotor pole should be smaller than the rotor length:

$$l_{rp} = (0.85\ldots0.95)\cdot l_{Fe} \tag{12}$$

As the permanent magnet will be accommodated between the two steel plates, its length can be computed as:

$$l_m = l_{Fe} - 2\cdot b_{sp} - 2\cdot b_{wedge} \tag{13}$$

with $b_{wedge} = 3.5$ mm.

Considering the average value of the magnetic field density in the air-gap, the average value of the magnetic field density in different parts of the machine (B_x) is calculated as [6]:

$$B_{x\_av} = \frac{k_x \cdot \pi \cdot D_{is} \cdot l_{Fe} \cdot B_{g\_av}}{2 \cdot p \cdot A_x} \tag{14}$$

with A_x the average area of the cross section of the x part of the machine (stator teeth and yoke, rotor claw poles, rotor steel plates, etc) and k_x a coefficient giving the percent of the air-gap magnetic field that is crossing the x part of the machine [8].

2.1.1. Steady-state parameters and losses computation of PMCPSG

The d-q model of the generator is characterized by the synchronous reactance' defined on direct and quadrature axis, X_d and X_q, respectively. The d-q reactance's are given as:

$$\begin{aligned} X_d &= \omega_1 \cdot L_d = \omega_1 \cdot \left(L_{md} + L_{s\sigma}\right) \\ X_q &= \omega_1 \cdot L_q = \omega_1 \cdot \left(L_{mq} + L_{s\sigma}\right) \end{aligned} \tag{15}$$

with ω_1 the rotor electrical speed, L_d and L_q the direct and quadrature axis corresponding synchronous inductances [8], given as the sum between the corresponding magnetizing inductances, L_{md} and L_{mq}, and the stator leakage inductance, $L_{s\sigma}$. Simplified formulae for the magnetizing inductances were derived as [8]:

$$L_{md} = L_m \cdot \frac{k_d \cdot k_f}{1 + k_{sd}}$$
$$L_{mq} = L_m \cdot \frac{k_q \cdot k_f}{1 + k_{sq}} \tag{16}$$

with L_m—the magnetizing inductance [8], k_d and k_q—the armature reaction coefficients, k_f—the form factor, and k_{sd} and k_{sq}—the saturation factors corresponding to direct and quadrature axis, respectively.

The magnetizing inductance of the three-phase PMCPSG was computed [4]:

$$L_m = \frac{3 \cdot D_{is}}{\pi \cdot p \cdot g_{ef}} \cdot \mu_0 \cdot l_{Fe} \cdot (k_w \cdot W_1)^2 \tag{17}$$

with g_{ef}—the effective air-gap, including the Carter factor [4]. The Carter factor was calculated considering both the stator and rotor Carter factors [9]. The expressions for the coefficients in [Eq. (16)] correspond to the ones presented in [10].

Stator leakage inductance was calculated for the stator slot geometry shown in **Figure 3** as the sum of four main components [4]: air-gap leakage inductance, slot leakage inductance, tooth tip leakage inductance, and end-winding leakage inductance. The phase resistance can be computed with the formula [4, 11].

$$R_s = \frac{W_1 \cdot l_c}{\sigma \cdot a \cdot S_c} \tag{18}$$

with l_c—average length of a turn in a coil and σ—conductivity of the conductor material.

Next, the losses and efficiency can be determined. The main losses of the PMCPSG [8] are as follows:

$$P_{losses} = P_{Joule} + P_{Fe} + P_{mech} \tag{19}$$

where P_{mech}— mechanical losses (can be approximated at 1%, as a starting point). Iron losses are the sum of hysteresis (P_{hyst}) and eddy current ($P_{eddy\_currents}$) for stator and rotor cores and the claw-pole surface (P_{scwp}) losses. The losses can be computed considering the general expression [4]:

$$P_{hyst/eddy\_currents} = C_{mat} \cdot f^{af} \cdot B^{aB} \cdot G$$
$$P_{scwp} = 2 \cdot p \cdot S_{cwp} \cdot k_{cp} \cdot f^{1.5} \cdot B_{g\_av}^2 \tag{20}$$

http://dx.doi.org/10.5772/62817

where a_f and a_B—material empirical constants than can be determinate from curve-fitting the losses for a wide range of "f" (frequency) and B values; k_{cp}—a factor dependent on the claw-pole material and machine Carter factor; and G—the weight of the considered part of the machine [6].

Thus, the efficiency of the machine can be written as:

$$\eta = \frac{P_N}{P_N + P_{losses}} \tag{21}$$

with $P_N = S_N \bullet cos\phi$.

After, the designing process, the following results have been obtained, see **Table 1**.

Parameter	PMCPSG
Output power (W)	150
Rated speed (rpm)	750
Phase voltage (V)	50
Number of phases (-)	3
Number of pole pairs (-)	4
Number of slots	36
Stator outer diameter (mm)	145
Stator inner diameter (mm)	95
Rotor pole width (mm)	29
Rotor pole length (mm)	105
Rotor pole base height (mm)	15
Steel plate radius (mm)	31
Rotor pole tip height (mm)	21
Permanent magnet diameter (mm)	60
Residual flux density—Alnico 8 (T)	0.9
Coercive force—Alnico 8 (kA/m) [11]	115
Rated current (A)	1
Losses (W)	81
Efficiency (%)	70

Table 1. Obtained results for the designed PMCPSG.

2.2. Design of PMSMOR

The dimensioning procedure was applied for the following set of key parameters: P_{out}—3 kW (estimated); rated phase voltage u_N—220 (V); rated speed n_N—500 rpm; pole pair number p—10.

By neglecting the leakage reactance and for a certain number of phases (m), phase current $i(t)$, and induced emf $e(t)$, we obtain the output power of an electrical machine [13]:

$$P_{out} = \eta \cdot \frac{m}{T} \cdot \int_{T}^{0} e(t) \cdot i(t)\, dt = \eta \cdot m \cdot k_p \cdot E_{max} \cdot I_{max} \tag{22}$$

where T is the period of one cycle of emf, E_{max} *is the* peak value of the emf, I_{max} *is* peak value of the phase current, k_p is the power coefficient, and η is the estimated efficiency. The peak value of the emf is expressed by introducing the electromotive force coefficient, k_E[13]:

$$E_{max} = k_E \cdot W_1 \cdot B_g \cdot D_g \cdot l_m \cdot \frac{f}{p} \tag{23}$$

with D_g—air-gap diameter.

By introducing a geometric coefficient, $k_L = L_m/D_g$, and a current coefficient (related to its wave form) $k_i = I_{max}/I_{rms}$, and defining the phase load ampere-turns:

$$A = \frac{2}{\pi} \cdot W_1 \cdot \frac{I_{rms}}{D_g} \tag{24}$$

it is possible to define the air-gap diameter of the machine [13]:

$$D_g = \sqrt[3]{\frac{2 \cdot p \cdot P_{out}}{\pi \cdot m \cdot A \cdot k_E \cdot k_i \cdot k_p \cdot k_L \cdot \eta \cdot B_g \cdot f}} \tag{25}$$

The height of the permanent magnet results as follows:

$$h_m = \frac{\pi \cdot D_{ir} \cdot B_g}{2 \cdot p \cdot B_m} \tag{26}$$

http://dx.doi.org/10.5772/62817

with $B_m = 0.405$ T (for permanent magnet type: ferrite) and interior diameter of rotor: $D_{ir} = D_g + g$.

Using Eq. (16), the dimensions of different parts of the rotor (permanent magnet width, rotor pole width, air barrier width) are calculated (see **Figures 6**, **7**). All the other stator geometric parameters will be computed based on air-gap diameter, as for conventional synchronous machine Thus, the performances of the generator will be determined with conventional equations [4]. All results after the designing process and the performances obtained are presented in **Table 2**.

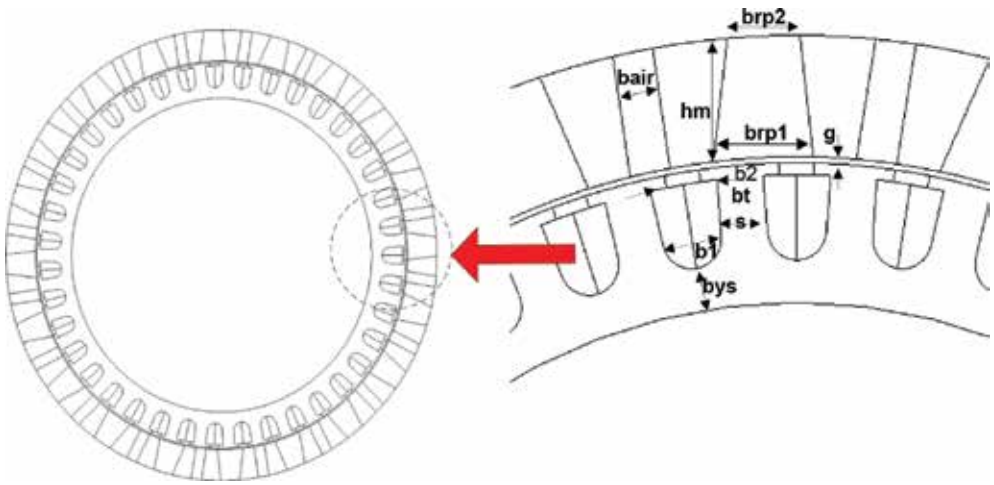

Figure 6. Stator and rotor geometry of PMSMOR.

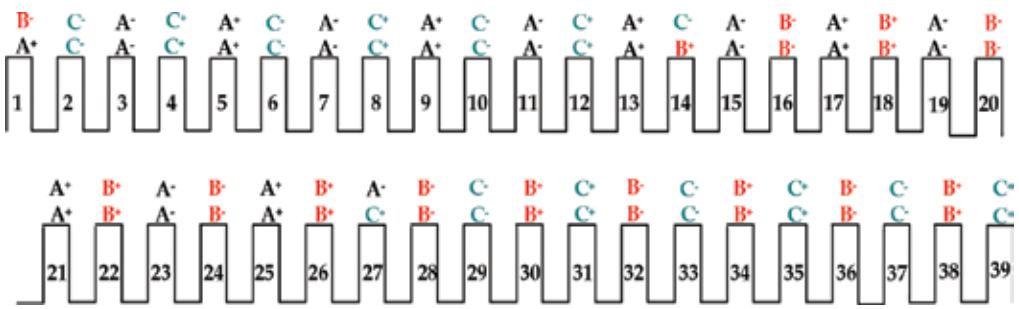

Figure 7. Stator winding of PMSMOR.

Parameter	PMSMOR
Output power (W)	3000
Rated speed (rpm)	500
Phase voltage (V)	220
Number of phases (-)	3
Number of pole pairs (-)	10
Number of slots	39
Stator outer diameter (mm)	248
Stator inner diameter (mm)	202
Rotor outer diameter (mm)	290
Rotor pole height (mm)	21
Rotor pole base width (mm)	5.2
Rotor pole top width (mm)	10.5
Permanent magnet base width (mm)	18
Permanent magnet top width (mm)	13
Residual flux density—Ferrite Y30BH (T)	0.405
Coercive force—Ferrite Y30BH (kA/m) [12]	230
Rated current (A)	5
Losses (W)	500
Efficiency (%)	86

Table 2. Obtained results for the designed PMSMOR.

2.3. Optimization of PMCPSG and PMSMOR

The influence of different geometrical dimensions on the PMCPSG and PMSMOR performances can be done by using 3D and 2D, respectively. Despite the fact that the results provided by finite element method (FEA) are accurate and can be very useful in for the optimization of the main geometric dimensions, this approach is highly time-consuming [6]. Hence, in order to reduce the time cycle and the number of iterations, a better solution is to use an optimization based on an analytical algorithm. Due to technological and cost constraints, two available stator laminations with the geometry given in **Figures 3** and **4**, respectively, and the dimensions given in **Tables 1** and **2**, respectively, were chosen.

The optimization of electric machine is a multivariable, nonlinear problem with constraints. To treat problems with constraints is necessary to transform them in unconstrained ones. This can be done, for example, by embedding the constraints in the objective function [6]. The so-called direct search optimization methods fulfill these requirements. Hooke-Jeeves, one direct search method, was selected for the optimization of the presented generators [6, 14]. The main steps in the optimization algorithm are as follows (see **Figure 8**): the choice of the optimization

http://dx.doi.org/10.5772/62817

variables, input of the constraints, the definition of the objective function, objective function calculation, the computation of the main parameters (geometrical and electromagnetic), and the visualization of the obtained result.

For the studied machine, a set of 4 variables (x_i, $i = 1…4$) for each structures were selected (see **Table 3**). In order to keep the topology, functional limits are set for each variable and specific constraints are set, together with a penalty coefficient for including in the objective function.

The following constraints were considered:

a. The output power has to be greater or equal to the design specified value.

b. The air-gap magnetic flux density has to be closed to the specified value.

c. The stator teeth magnetic flux density has to be closed to the specified value.

d. The stator lamination geometry remains unchanged.

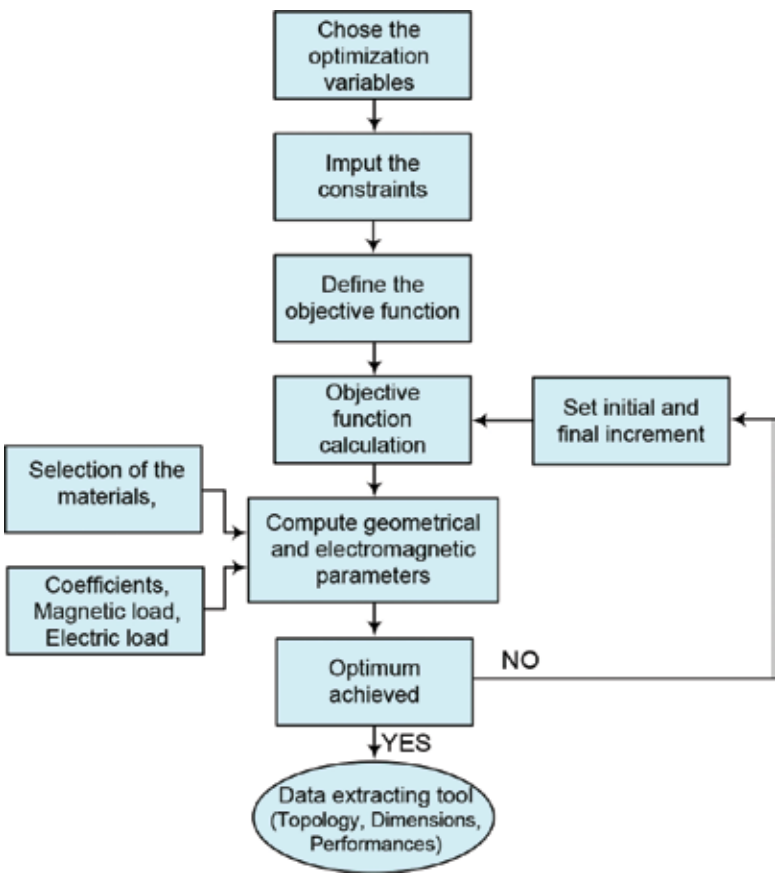

Figure 8. Optimization algorithm.

PMSMOR parameters	Initial value	Boundaries
Rotor pole width b_{rp} (mm)	29	[25.....35]
Rotor pole length l_{pr} (mm)	105	[55.....110]
Rotor pole base height h_{sp} (mm)	15	[10.....20]
Rotor pole to height h_{p2} (mm)	2.5	[1.....3.5]
PMSMOR parameters		
PM base width b_{rp1}(mm)	18	[14.....22]
PM top width b_{rp2}(mm)	13	[10.....16]
Height of the PM on magnetization direction h_m (mm)	21	[18.....23]
Rotor barrier width b_{air}(mm)	6	[5.....8]

Table 3. Optimization variables: initial values and boundaries.

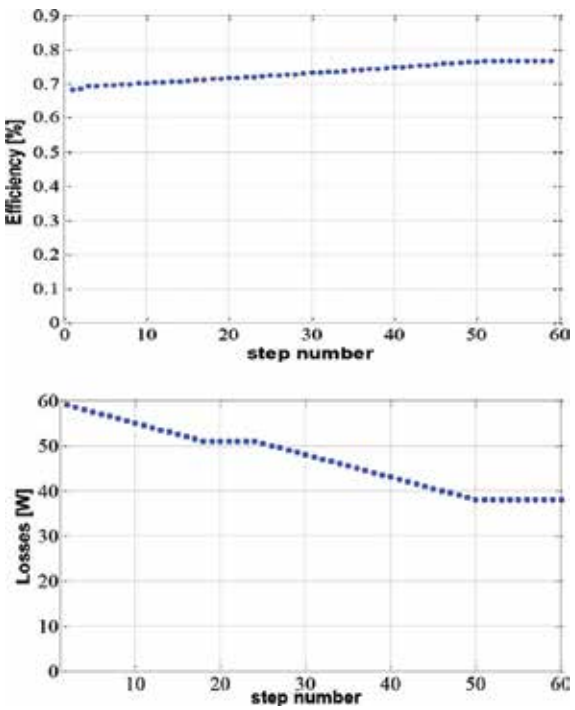

Figure 9. Optimization results of PMCPSG: efficiency and losses.

For the generators dedicated to microwind and small wind conversion systems, some optimization issues (objective functions) are important: low-cost, maximum generated voltage, and maximum efficiency. The maximum efficiency ($f_1(x_1)$) for the maximum generated voltage ($f_2(x_2)$) was selected as multi-objective optimization function. The chosen multi-objective function is mathematically expressed as [6]:

http://dx.doi.org/10.5772/62817

$$f(x_i) = w_1 \cdot f_1(x_i) + w_2 \cdot f_2(x_i) \tag{27}$$

The iterative process has reached its optimum after 60 steps, the simulation time being 1.26 s. The efficiency and the losses have been plotted in **Figure 9**, while the evolution of the geometric parameters of PMCPSG has been plotted in **Figure 10**. It can be seen that some parameters presented a low variation, but the length of claw pole presented a high variation around a mean value.

It is obvious that if the geometrical parameters will decrease, the iron losses will decrease too. This is the normal behavior; thus, the efficiency of the generator will increase. For the PMCPSG, the efficiency of the machine will increase with 8%.

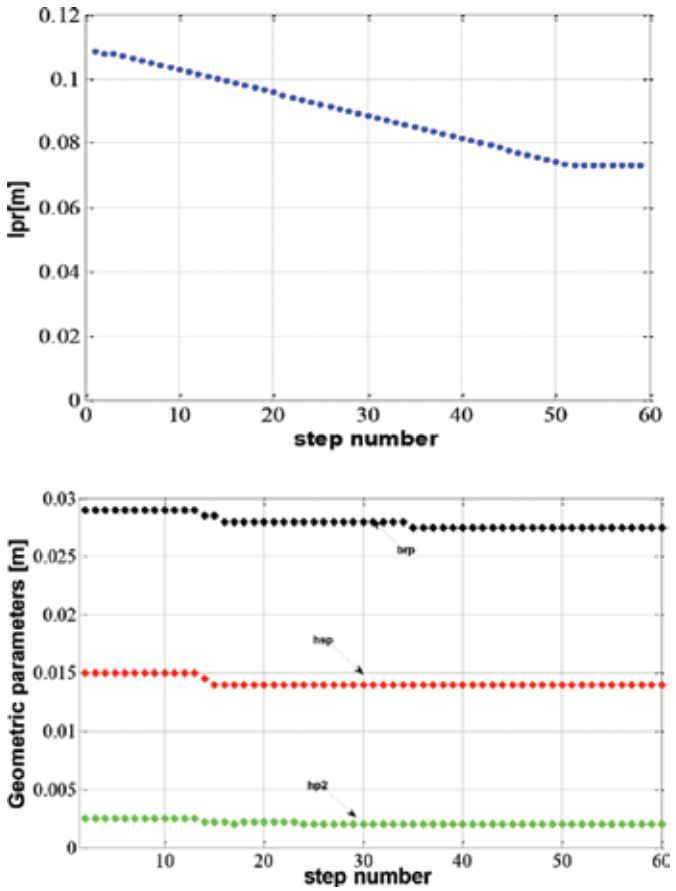

Figure 10. Optimization results of PMCPSG: evolution of geometrical parameters.

In **Figure 11**, the evolution of efficiency and losses of PMSMOR during the optimization process have been plotted. For this machine, the efficiency increase with decrease of losses due

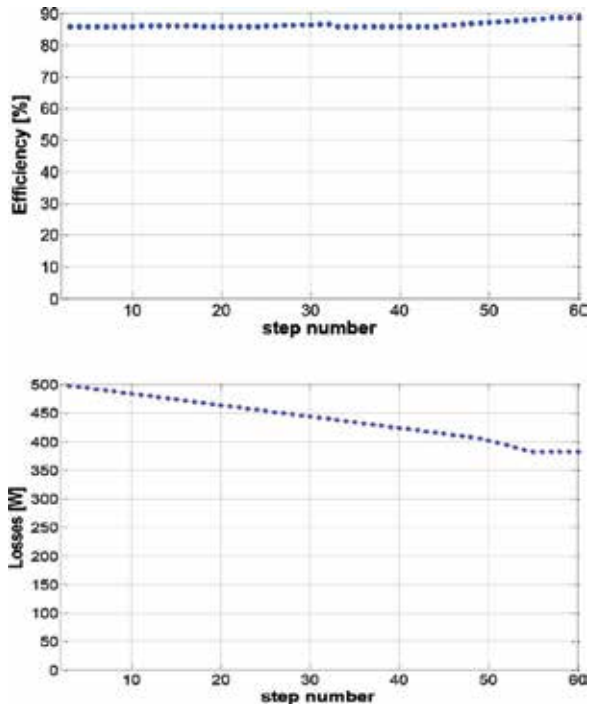

Figure 11. Optimization results of PMSMOR: efficiency and losses.

to changes of geometrical parameters is shown in **Figure 12**. Here, only the permanent magnet dimensions and rotor flux barrier width are presented as a sample. It can be seen that the value of geometrical parameters of permanent magnet is reduced, consequently barrier rotor width increased. The efficiency of the machine has globally increased with 3%.

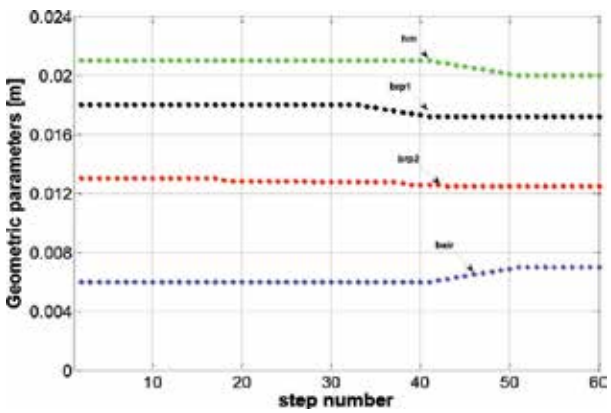

Figure 12. Optimization results of PMSMOR: evolution of geometrical parameters.

http://dx.doi.org/10.5772/62817

PMCPSG parameters	Initial value	Final value
Rotor pole width b_{rp} (mm)	29	27
Rotor pole length l_{pr} (mm)	105	60
Rotor pole base height h_{sp} (mm)	15	14
Rotor pole to height h_{p2} (mm)	2.5	2
Losses (W)	60	38
Efficiency (%)	0.695	0.78
PMSMOR parameters		
PM base width b_{rp1}(mm)	18	17
PM top width b_{rp2}(mm)	13	12.5
Height of the PM on magnetization direction h_m (mm)	21	20
Rotor barrier width b_{air}(mm)	6	7
Rotor outer diameter (mm)	290	288
Losses (W)	502	384
Efficiency (%)	85.8	89.1

Table 4. Main optimization results, at rated operating point, for both considered topologies.

The resume of the optimized results of the PMCPSG and PMSMOR are given in **Table 4**.

3. Magnetic field analysis of the studied electrical machines

The magnetic flux density distribution in the electrical machines' core is very important because this affects the voltage waveform, the iron losses, and the efficiency. The finite element method (FEM) is a simple, robust, and efficiently widely used method of obtaining a numerical approximate solution for a given mathematical model of the machine [6]. This analysis has been carried out by using Flux software (2D for PMSMOR and 3D for PMCPSG).

3.1. Magnetic field analysis of PMCPSG

Due to the complex three-dimensional structure of claw pole, the magnetic field inside the claw-pole generator needs to be treated as a 3D problem, using 3D module of Flux software [14]. In the case of 3D simulations, high memory resource of computer is necessary. However, they are much time-consuming. In order to reduce this, considering the symmetry of the machine structure, the analysis will be carried out for one pole pair. In the first steps of the analysis, the geometry of the structure was introduced and the mesh was generated. Next, if the previous steps are correct, the solution will be generated. After that, in post-processing stage, the data about magnetic behavior (map of flux density in the stator and rotor core, air-gap flux density distribution) and other performances (induced emfs, cogging torque, etc) of the generators will be computed [6].

The no-load regime for the rated speed was simulated, in order to present the maps of the magnetic flux density in the stator and rotor core (**Figure 13**).

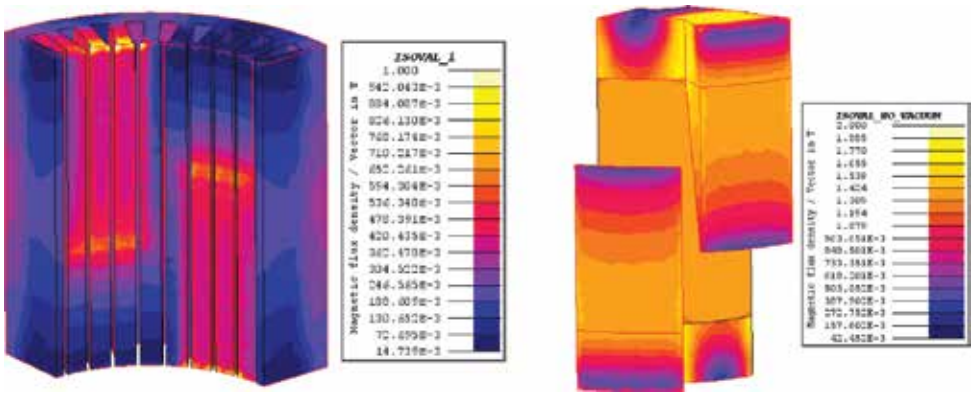

Figure 13. Magnetic flux density map in the stator an rotor core.

It has been observed that in **Figure 13**, the value of magnetic flux density is very close to the saturation level of the considered steel, especially at the base of the claw pole, where the direction of the flux density is changing. Since due to its complex three-dimensional structure, the rotor claws are usually press-formed out of solid metal or pressed in a die of iron powder [14], magnetic flux density distribution along the radial and axial length of the air-gap obtained in load condition are very useful in order to develop an optimum design in terms of low eddy current losses (**Figures 14**, **15**).

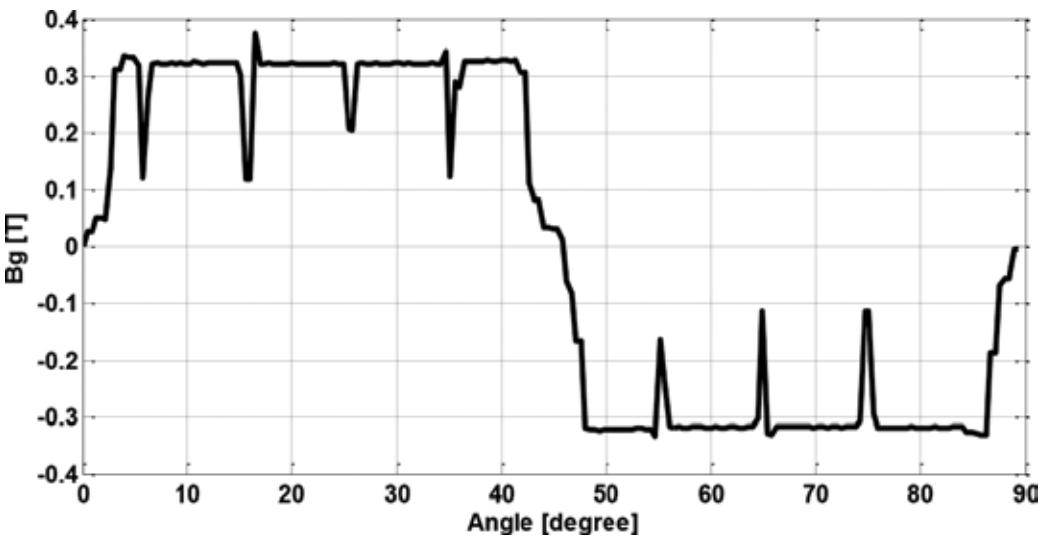

Figure 14. Magnetic field distribution along the radial air-gap.

http://dx.doi.org/10.5772/62817

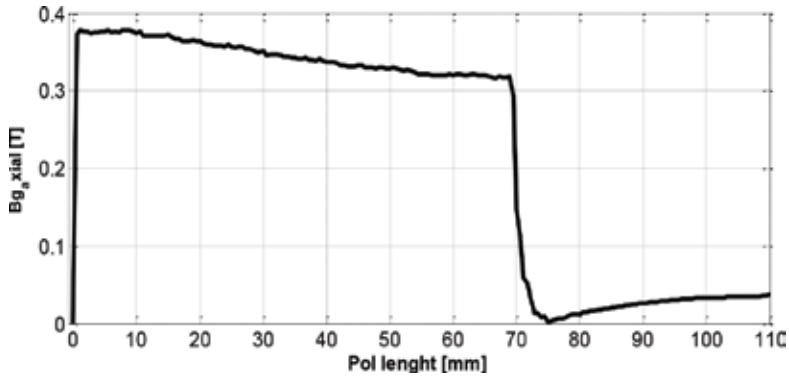

Figure 15. Magnetic field distribution along the axial air-gap.

The wave depicted in **Figure 14** shows maximum values when the air-gap is minimum and minimum values when the air-gap is maximum. As it can be noted that the flux density under each rotor pole has the same value, the peaks corresponding to the four stator teeth overlapped with one rotor pole.

The obtained voltage and axis torque in load condition are shown in **Figures 16** and **17**, respectively. It can be observed that the waveform of voltage is slightly deformed due to the shape of the claw poles. In this case, a further optimization of the shape of the claw poles can be achieved, but this involves a supplementary cost in manufacturing. For the structure of PMCPSG presented in this chapter, a supplementary optimization of the shape of the claw poles is not necessary in the context of the considered application (isolated microwind power plants with installed power around few hundred Watts).

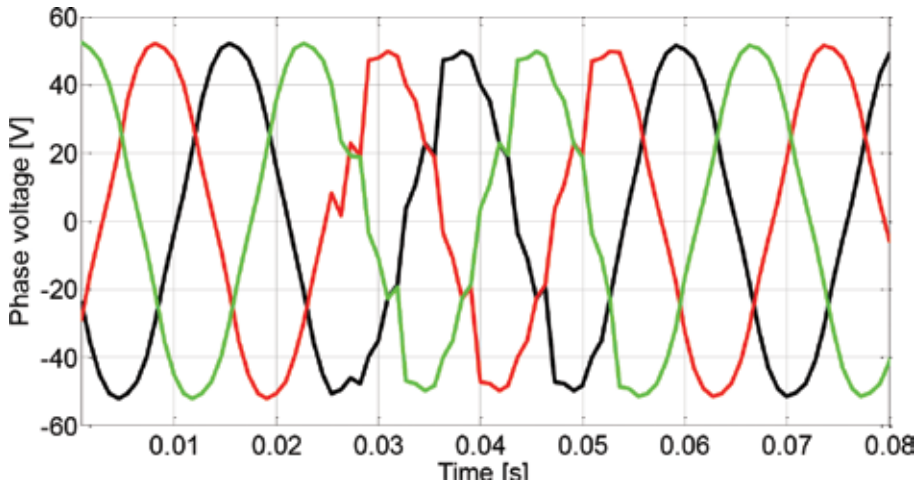

Figure 16. Computed voltage (rms value) in load condition.

The axis torque is obtained based on rated current (1 A). Also, the torque ripple is 15.7%. In this context, no strategy to reduce the torque ripple was adopted.

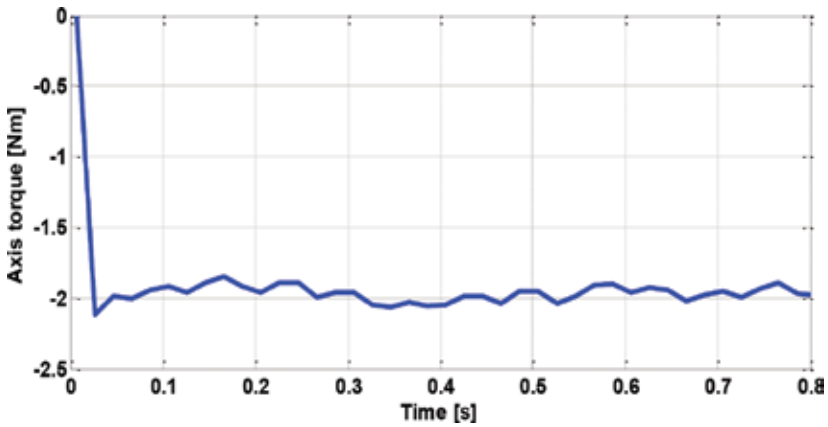

Figure 17. Axis torque in generator regime.

3.2. Magnetic field analysis of PMSMOR

Due to configuration of PMSMOR, the numerical computation has been carried out by using Flux 2D. In order to obtain the map of magnetic flux density distribution in the stator and rotor core and its distribution in air-gap the FEM analysis, in no-load condition, this generator regime is employed at rated speed (500 min^{-1}).

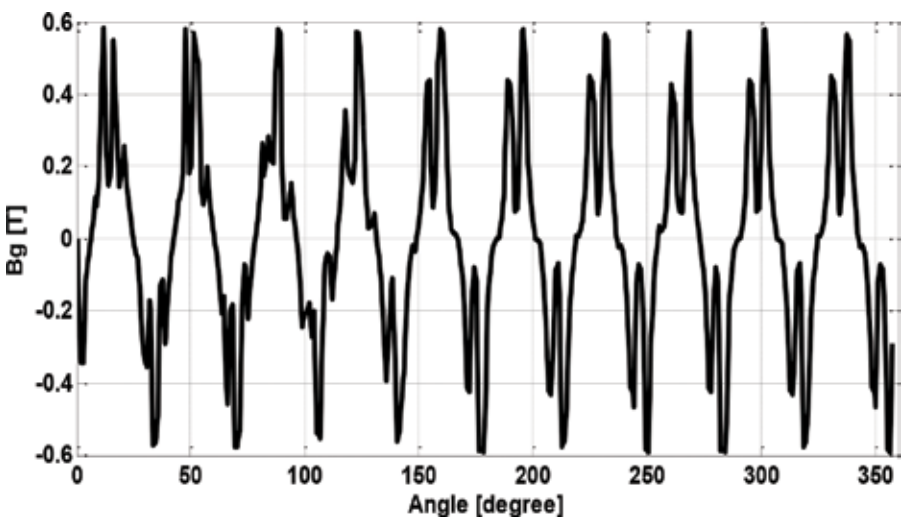

Figure 18. Magnetic field distribution in the air-gap.

http://dx.doi.org/10.5772/62817

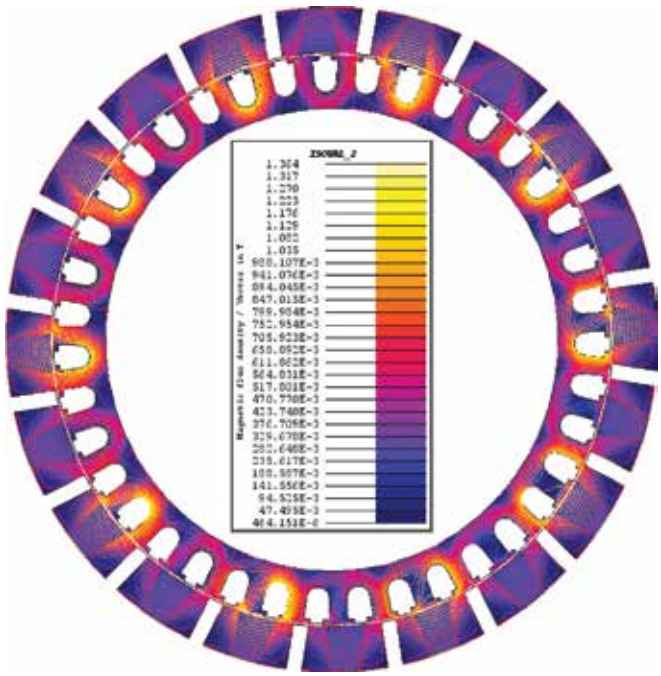

Figure 19. Flux density and field lines for studied PMSMOR.

The saturation level can be shown in **Figure 19**. It can be observed that the maximum value is almost 1.3 T in stator teeth. Because this value is below the maximum saturation level, more optimization can be performed in order to reduce the stator and rotor core.

In the next step of the simulation, the generator has been tested in load condition at rated power (3 kW) and speed.

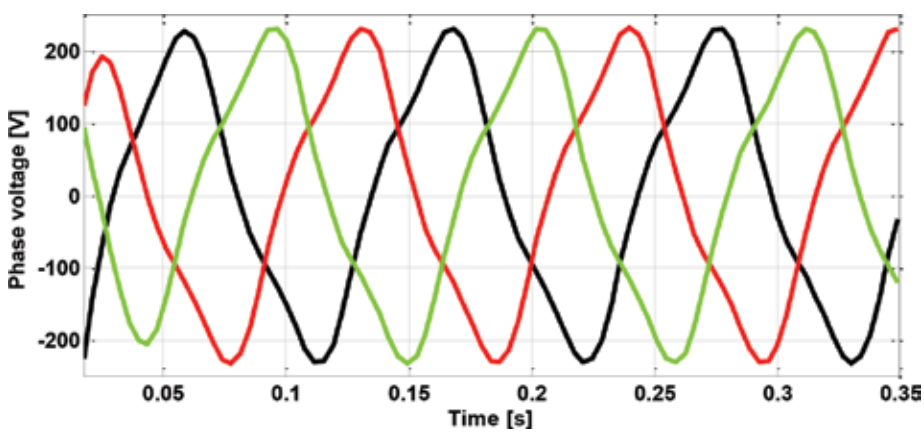

Figure 20. Computed voltage (rms value) at rated power.

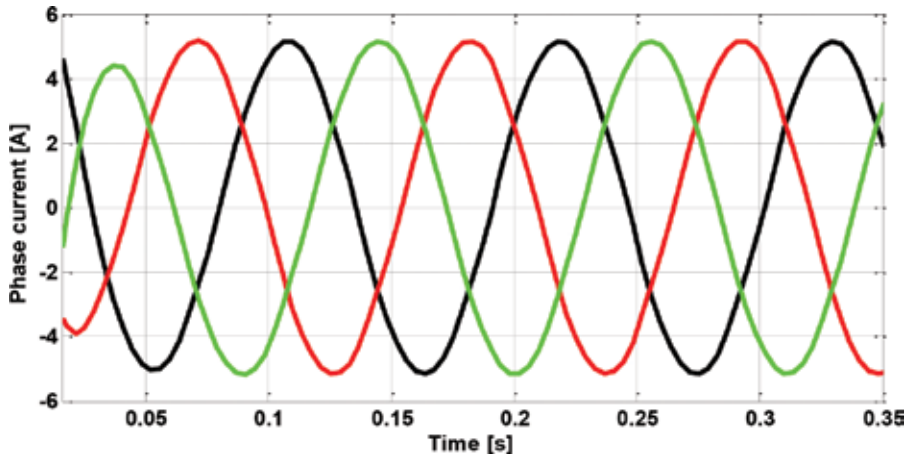

Figure 21. Computed current (rms value) at rated power.

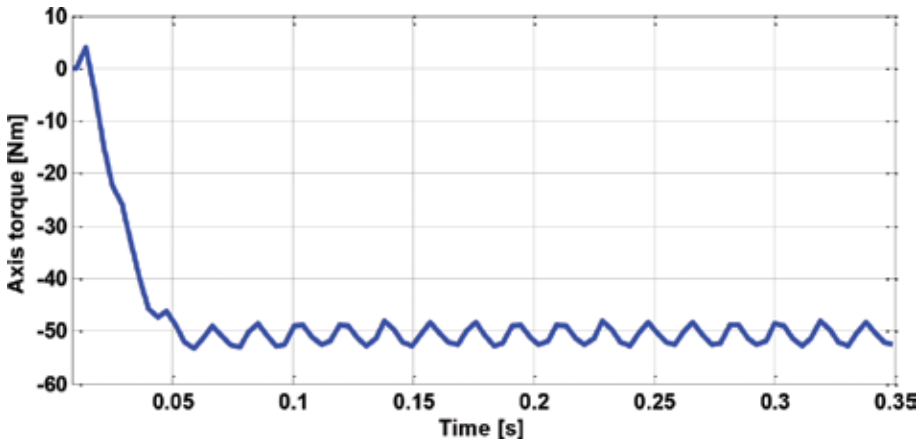

Figure 22. Axis torque in generator regime.

The generated phase voltage and obtained phase current using resistive load have been plotted in **Figures 20** and **21**, respectively. The average values of voltage and current are 223 V and 5.12 A, respectively, very close to the ones obtained from the analytical approach. The rated torque depicted in **Figure 22** is obtained for the rated current. Also, thanks to the proper winding–slots–poles combinations, the torque ripples are significantly reduced. In fact, the ratio of torque ripple is 6.6% (maximum at 52.5 Nm and minimum at 49.1 Nm).

3.3. Generators steady-state performances

In order to obtain the complete evaluation of performances of considered generators, an analysis in load condition was carried out for three different driven speeds for each generator.

http://dx.doi.org/10.5772/62817

3.3.1. Steady-state performances of PMCPSG

The simulation of PMCSPG has been performed for three different speeds: 500, 750, and 1000 rpm. The efficiency, the generated voltage, and the electric power have been computed, but the additional losses were neglected.

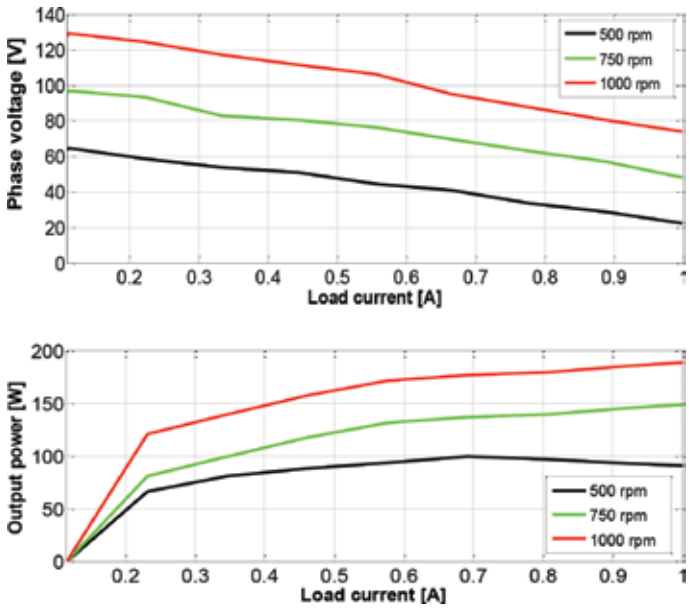

Figure 23. Steady-state performance of PMCPSG: phase voltage and output power.

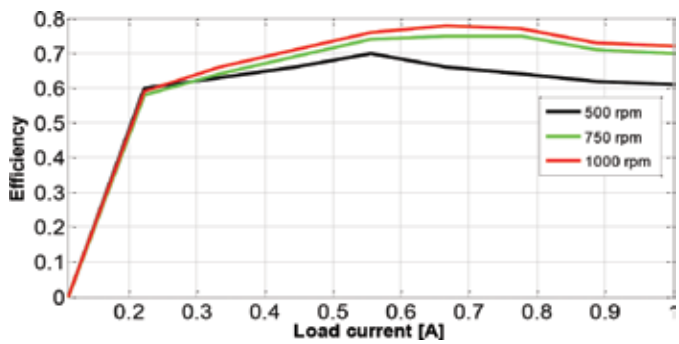

Figure 24. Steady-state performance of PMCPSG.

Figures 23 and **24**, respectively, show the steady-state performance (terminal voltage, output power, and efficiency) of the PMCPSG supplying a resistive load. The voltage–current characteristics are approximately linear from no load to rated load. Due to the rather high armature impedance, the voltage drop difference between no load and rated load is of 57% at

750 rpm. As it can be noted, for low speeds, the maximum efficiency occurs at rather low values of load current. For higher speeds, the load current for which the maximum efficiency is obtained is increasing.

3.3.2. Steady-state performances of PMSMOR

The simulation of PMSMOR has been performed for three different speeds: 250, 500, and 750 rpm.

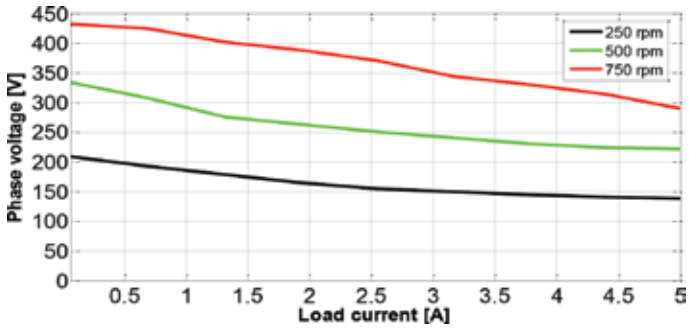

Figure 25. Performance of PMSMOR: phase voltage.

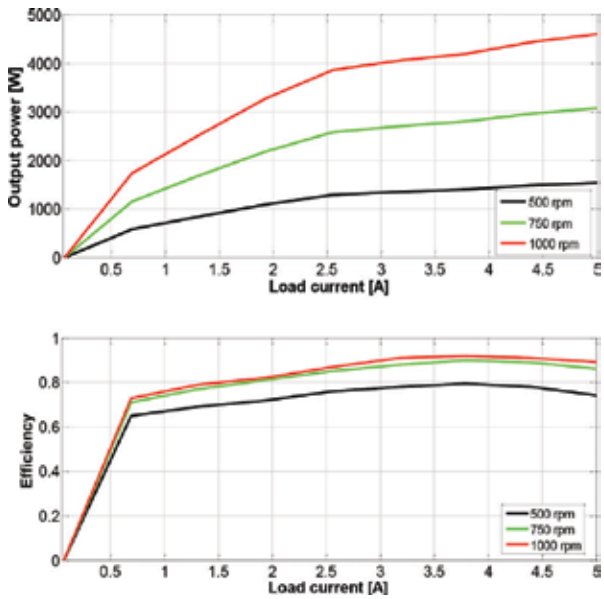

Figure 26. Performance of PMSMOR: output power and efficiency.

The voltage–current characteristics of PMSMOR are depicted in **Figure 25**. Also, the voltage drop difference between no load and rated load at 500 rpm is of 42%. The efficiency of the

http://dx.doi.org/10.5772/62817

generator can be shown in **Figure 26**. It can be observed that the maximum value is 0.92 for 3.62 A and 1000 rpm.

4. Conclusions

This chapter presents the main steps to be followed in the design of a low-cost permanent magnet synchronous machine suitable for small rating, direct driven applications, such as small- and microscale wind power plants. The analytical approach contains the major elements which need to be discussed. Detailed equations are presented for the calculation of geometrical parameters corresponding to the chosen special topologies of the rotor (claw pole and outer rotor). Also, the output performances (generated voltages, efficiency, losses) of the generators were computed. After preliminary design of the generators, the optimization procedure was performed using Hooke-Jeeves algorithm, in order to obtain the final topologies of the rotor in condition of maximum: efficiency, terminal voltage, and optimum weight.

The static performance of the machine, phase voltage, output power, and efficiency at different values of speed in order to obtain more detailed information, was studied through numerical analysis using Flux 3D for PMCSPG and 2D for PMSMOR.

Acknowledgements

This research work was supported by DEsign, Modellling and TESTing tools for Electrical Vehicles (DEMOTEST) project, in the frame of FP7 IAPP Marie Curie Actions.

Author details

Florin-Nicolae Jurca

Address all correspondence to: florin.jurca@emd.utcluj.ro

Department of Electrical Machines and Drives, Technical University of Cluj-Napoca, Cluj-Napoca, Romania

References

[1] Bang D, Polinder H, Shrestha G, Ferreira JA. Review of generator systems for direct-drive wind turbines. In: Proceedings of the European Wind Energy Conference and Exhibition (EWEC '08); 31 March 2008, Brussels, Belgium, p. 1800–1810.

[2] Camara MS, Camara MB, Dakyo B, Gualous H. Permanent magnet synchronous generator for offshore wind energy system connected to grid and battery-modelling and control strategies. Int J Renew Energy. 2015;2:386–393.

[3] Latoufis KC, Messinis GM, Kotsampopouls PC, Hatziargyriou ND. Axial flux permanent magnet generator design for low cost manufacturing of small wind turbines. Wind Eng. 2012;4:411–431. doi:10.1260/0309-524X.36.4.411.

[4] Pyrhonen J, Jokinen T, Hrabocova V. Design of rotating electrical machines. New York: Wiley; 2008. p. 538. doi:10.1002/9780470740095.

[5] Hendershot JR, Miller TJE. Design of brushless permanent-magnet motors. Oxford: Magna Physics Publishing and Clarendon; 1994. p. 584.

[6] Jurca FN, Martis C. Theoretical and experimental analysis of a three-phase permanent magnet claw-pole synchronous generator. IET Electr Power Appl. 2012; 6: 491–503. doi: 10.1049/iet-epa.2012.0075.

[7] Gieras JF. Permanent magnet motor technology. Design Appl. New York: M. Dekker; 1997.

[8] Jurca FN, Martis C. Claw-pole generator parameters and steady-state performances analysis. Int Rev Model Simul. 2013.

[9] Boldea I. Synchronous generators. Boca Raton: CRC Press Taylor&Francis. 2006. p. 444.

[10] Lundmark SKT. Application of 3-D computation of magnetic fields to the design of claw pole motors [thesis] Goteborg: Chalmers University of Technology, 2005.

[11] Hembach H, Gerling D. Beyer S. Estimation of boundaries for the claw-pole geometry in electrical water pump applications. In: Proceedings of the International Conference on Electrical Machines [ICEM '06]: 12–14 April 2007; Setubal, Portugal, 2007, p. 174–179.

[12] Permanent Magnet Datasheet [Internet]. http://www.eclipsemagnetics.com. Accessed: 2015-12-04.

[13] Fodorean D, Djerdir A, Viorel I.A, Miraoui A. A double excited synchronous machine for direct drive application-design and prototype test. IEEE Trans Energy Conv. 2007;22:656–665. doi:10.1109/TEC.2007.896279.

[14] Jurca F.N, Martis C, Birou I, Biro K, Analysis of permanent magnet claw-pole synchronous machine. In: Proceedings of the international conference on optimization of electrical and electronics equipment, [OPTIM '08]: 19–20 May 2008, Brasov, Romania, p. 75–80.

Chapter 6

Wind Turbine Design: Multi-Objective Optimization

Adam Chehouri, Rafic Younes, Adrian Ilinca and Jean Perron

Additional information is available at the end of the chapter

http://dx.doi.org/10.5772/63481

Abstract

Within the last 20 years, wind turbines have reached matured and the growing worldwide wind energy market will allow further improvements. In the recent decades, the numbers of research papers that have applied optimization techniques in the attempt to obtain an optimal design have increased. The main target of manufacturers has been to minimize the cost of energy of wind turbines in order to compete with fossil-fuel sources. Therefore, it has been argued that it is more stimulating to evaluate the wind turbine design as an optimization problem consisting of more than one objective. Using multi-objective optimization algorithms, the designers are able to identify a trade-off curve called Pareto front that reveals the weaknesses, anomalies and rewards of certain targets. In this chapter, we present the fundamental principles of multi-objective optimization in wind turbine design and solve a classic multi-objective wind turbine optimization problem using a genetic algorithm.

Keywords: wind turbine design, optimization, multi-objective, genetic algorithm, Pareto front

1. Introduction

The exhaustion of fossil-fuel reserves, stricter environmental regulations and the world's rising energy needs have led to the deployment of renewable and sustainable energy sources. Among these alternatives, wind energy is a promising technology and recorded the fastest growing installed alternative-energy production according to reference [1]. It is expected that by the year 2030, at least 20% of the United States energy will be supplied by onshore and offshore wind farms [1]. In the next decade and half, it is vital that authorities record a significant increase in

wind turbine installations and operability. Nevertheless, the prime conflict will continue to be the ongoing challenge to maintain a profitable and competitive cost of energy with fossil-fuel sources. Throughout the last 30 years, wind turbines have grown in size in order to reduce the cost of energy typically expressed in $/kWh. As a result, structural performance, durability requirements, safety hazards, transportation complications, noise and aesthetic pollutions all become issues that are more challenging for designers. Moreover, energy policies, international treaties, legislations and regulations set by governments have to be respected. For this reason, resolving the complex design problem of wind turbine design can be only achieved by *optimization* where an optimal solution is located. Many objective functions, design constraints, algorithms, tools and models have been proposed as will be discussed.

The rapid growth in the number of research papers on wind turbine design and optimization (**Figure 1**) during the last two decades highlights the status of the field of wind turbine optimization. In the past, some authors have compared the impact of different optimization objectives on the quality of the solution, others have reviewed the optimization algorithms, energy policies, economics, environmental impacts of wind turbines, but numerous researchers have proposed different optimization methodologies and resolution strategies. According to a study conducted by Chehouri et al. [2] in 2014, it was identified that less than 25% of the surveyed wind turbine optimization problems were solved using a multi-objective algorithm. In fact, solving such problems is not a straightforward task and often requires innovative techniques and algorithms. However, the main benefit is the ability to draw trade-off curves that reveal weaknesses and anomalies in the wind turbine design. For instance, it is very useful to pursue both minimum cost of energy and maximum annual energy production in the early stage of the design process.

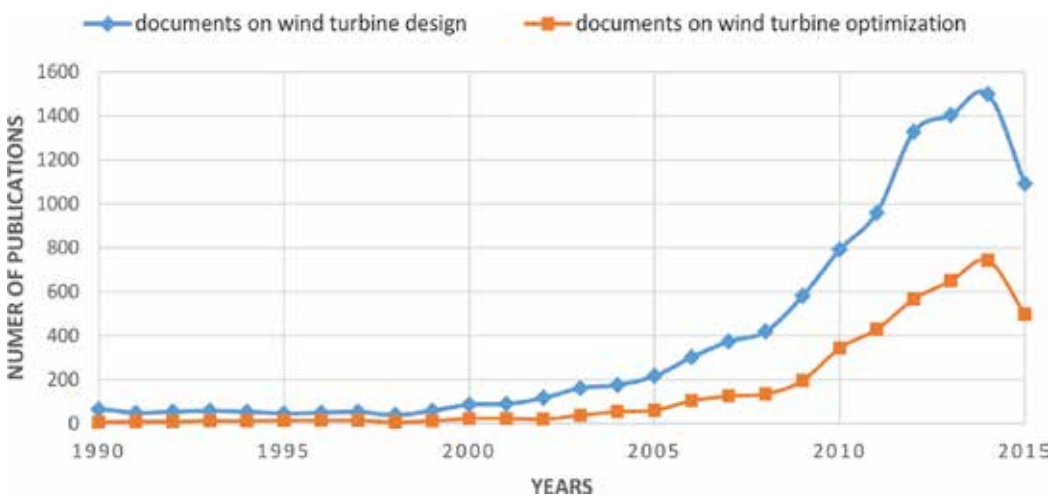

Figure 1. Number of published documents on wind turbine design in the last 40 years (reproduced from Scopus database).

http://dx.doi.org/10.5772/63481

Many authors carried a multidisciplinary study [3–12], where many objectives are considered in the design of wind turbines. The most common technique to combine conflicting functions (such as annual energy production and cost of energy) is by means of an appropriate set of weights. The variations that exist among these contradictory functions are essential for designers and therefore pursue to sketch the Pareto fronts.

In order to undertake the design of a horizontal wind turbine under multi-objective optimization (MOOP), there are numerous issues to be considered. The motif of this chapter is to present the fundamental principles of multi-objective optimization in the design of wind turbines. At the outset of this chapter in Section 2, we briefly discuss the fundamentals and terminology of multi-objective optimization. Section 3 highlights the objective functions that are used by designers. The design constraints that are enforced by wind turbine designers are enumerated in Section 4. We list the most relevant multi-objective optimization applied in wind turbine design in Section 5. The most common optimization algorithms used to solve multi-objective wind turbine optimization problems are examined in Section 6. Finally, a numerical example that demonstrates the resolution of a multi-objective design problem using a genetic algorithm (GA) is presented in Section 7.

2. Multi-objective optimization: state of art

2.1. Prologue

The term optimization refers to the finding of one or more feasible solutions, which correspond to extreme values of one or multiple objectives. Optimization methods are important in scientific experiments, particularly in engineering design and decision-making. When the problem is to find the optimal solution of one objective, the task is called *single-objective optimization*. There exist many algorithms that are gradient-based and heuristic-based that solves single-objective optimization problems. Beside deterministic search techniques, the field of optimization has evolved by the introduction of stochastic search algorithms that seek to find the global optimal solution with more ease. Among them, *evolutionary algorithms* (EAs) mimic nature's evolutionary principles and are now emerging as popular algorithms to solve complex optimization problems.

In engineering optimization, the designers are sometimes interested in finding one or more optimum solutions when dealing with two or more objective functions. This is known as *multi-objective optimization* and in fact, most real-world optimization problems involve multiple objectives. In this case, different solutions produce trade-offs or conflicting situations among the different objectives. Not enough emphasis is usually given to multi-objective optimization and there is a reasonable explanation for that. The majority of the methods that solve multi-objective optimization problems transform multiple objectives into a single function. Therefore, most of the efforts have been invested in improving the single-objective optimization algorithms. The studies concentrate on the conversion of multi-objective into single-objective problems, the convergence, constraint-handling approaches and the speed of these single-objective techniques.

Let us discuss the fundamental difference between single- and multi-objective optimization by taking two conflicting objective functions as examples. Obviously, each objective function possesses a unique and different optimal solution. For instance, if one is interested in buying a house, the decision-making has to take into consideration the cost and the comfort. If the buyer is willing to sacrifice comfort, they will get a house with the lowest price. However, if money is not an issue, then the buyer is able to afford a house with the best comfort. Between these two extremes, there exist many house choices at various costs and comfort. Now the big question is among these trade-offs, which solution is the best with respect to both objectives? Ironically, no house among the trade-off choices is the best with respect to both cost and comfort. Without any further information about these solutions (in our case example the houses), no solution from the set of trade-off can be said to be better than any other. This is the fundamental difference between a multi-objective and a single-objective optimization problem. From a practical standpoint, after a set of trade-off solutions are found, the user will use higher-level information to determine the convenient solution.

2.2. Multi-objective evolutionary algorithms

The classical way to solve multi-objective problems is to scalarize multiples objectives with a relative preference vector. Since only a single optimized solution can be found in one simulation, evolutionary algorithms shined as interesting methods to solve MOOP. The main reason is, unlike classical methods, EAs use a population of solutions in each iteration and therefore the outcome of an EA is a population of solutions. This ability to find multiple solutions in one single run made EAs an ideal approach to solve multi-objective optimization problems.

According to the available literature, the first real application of evolutionary algorithms in the determination of trade-off solutions for a MOOP was proposed in the doctoral dissertation of David Schaffer [13]. He developed the vector-evaluated genetic algorithm (VEGA), which demonstrated the ability of genetic algorithm to capture multiple trade-off solutions. Not much attention was given until another half a decade when David E. Goldberg published his book

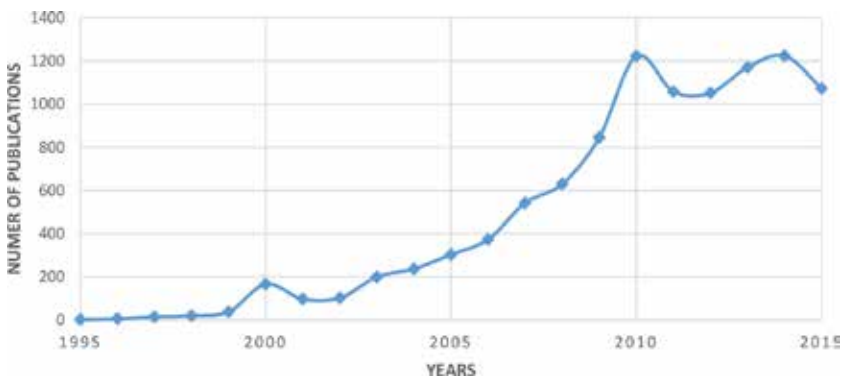

Figure 2. Number of published documents on multi-objective evolutionary algorithms.

http://dx.doi.org/10.5772/63481

in 1989 [14] on a multi-objective evolutionary algorithm (MOEA) using the concept of dominance. From the latter derived many MOEAs such as Srinivas and Deb's non-dominated sorting (NSGA) [15] and the niched Pareto GA by Horn et al. [16]. Other techniques different from the domination-based MOEAs were proposed by Kursawe in 1990 (Kursawe's diploidy approach [17]) and Hajela and Lin's weighted-based approach [18] just to name a few. It can be easily seen from **Figure 2** that the number of studies conducted on the topic of MOEA has increased well over the last two decades. In less than 10 years, the number of year-wise papers has tripled and it can be expected that the growth will continue as new studies, books, surveys, research papers and dissertations will be published.

2.3. Multi-objective optimization problems

A multi-objective optimization problem is composed of a number of objective functions, which are to be maximized or minimized. Similar to single-objective problems, the MOOP is subjected to a set of design constraints, which any optimal solution must satisfy. We can state the general form of a multi-objective optimization problem as follows:

$$\begin{aligned} &Minimize\ or\ Maximize\ f_m(\vec{x}), m = 1, 2 \ldots M \\ &Subject\ to\ g_j(\vec{x}) \geq 0\ j = 1, 2 \ldots J \\ &h_k(\vec{x}) = 0\ k = 1, 2 \ldots K \\ &\vec{x}_i^L \leq \vec{x}_i \leq \vec{x}_i^U\ i = 1, 2 \ldots N \end{aligned} \tag{1}$$

The solution $\vec{x}$ is a vector of n variables $\vec{x} = (x_1, x_2, \ldots x_n)^T$. Often, the user will restrict the design variables between lower and upper bounds $\vec{x}_i^L$ and $\vec{x}_i^U$, respectively. In the above problem, there is J inequality and K equality constraints that can be linear and/or non-linear functions. A solution $\vec{x}$ is said to be *feasible* when *all* the constraints ($J + K + 2N$) are satisfied. Because of the presence of M objective functions that need to be minimized and/or maximized, it is regularly convenient to apply the duality principle. The latter suggests that we can convert a maximization problem into a minimization one by multiplying the objective function by -1. This is a practical method because many optimization algorithms are developed to solve one type, for example, minimization problems. A major difficulty arises when any of the objective or constraint functions are non-linear, then the resulting MOOP becomes a non-linear multi-objective problem. Until now, the techniques to solve such problems do not have convergence proofs. Unfortunately, most real-world MOOPs are non-linear in nature and thus create a major challenge for scholars.

As stated earlier, the task in multi-objective optimization problems is to find a set of solution called the Pareto-optimal solution set, in which any two solutions must be non-dominated with respect to each other. In addition, any solution in the search space must be dominated by at least one point in the Pareto set. Therefore, the ultimate goal in multi-objection optimization is to find a set of solutions as close as possible to the Pareto-optimal front and as diverse as

possible. The concept of domination is used in most MOOP algorithms. Without going into deep details, a solution $\vec{x}_1$ is said to dominate $\vec{x}_2$ if both conditions are satisfied:

1. The solution $\vec{x}_1$ is no worse than $\vec{x}_2$ in all objectives.

2. The solution $\vec{x}_1$ is strictly better than $\vec{x}_2$ in at least one objective.

To gain more knowledge on the procedures to find the non-dominated set in a given set *P* of size *N*, the reader is referred to [8].

3. Objective functions

The objective function that wind turbine engineers have used in their designs has evolved in the last few decades. In the early 1980s, the focus was towards the maximization of the power coefficient (C_P), which represents the theoretical fraction of power in the wind that can be extracted by the wind turbine. The blade shapes achieved with this strategy presented blades with large root chords and high twists. Moreover, since the maximization of the power coefficient occurs for a particular tip-speed ratio, the designer's interests shifted towards an alternative optimization metric—maximization of the annual energy production (AEP). Unlike the previous objective function, the AEP is obtained from a range of time (e.g. 1 year) and the given wind-speed spectrum of the wind turbine site. As wind energy is unable to compete with fossil fuel, the main objective has progressed to the minimization of the cost of energy (COE). The difficulty is the definition of the COE, mainly outlining the total costs of the wind turbine components. An earlier approach to decrease the COE is to limit the blade weight by restricting the chord lengths. Nevertheless, the stability of the blade is strongly affected by the decrease of the weight. Consequently, a proper balance between mass and stability must be ensured during the design of the wind turbine blade.

3.1. Maximization of the annual energy production

The annual energy is obtained by the integration of the wind turbine power curve with a wind-speed distribution (e.g. Weibull) over the wind-speed spectrum from the cut-in to cut-out speed [Eq. (2)]. One of the reasons why this metric is chosen by designers is due to the absence of a reliable structural and cost model. On the other hand, if the cost of energy is insignificant to the manufacturers and consumers, the maximum energy production is assumed as

$$AEP = \int_{V_{\min}}^{V_{\max}} P(V) f(V) dV \tag{2}$$

P(V) is the power curve of the wind turbine, *f(V)* is the wind-speed distribution, $V_{\min}$ is the cut-in speed and $V_{\max}$ is the cut-out speed.

3.2. Minimization of the weight

Jureczko et al. [19] developed a numerical model of the wind turbine blade to perform a multi-criteria discrete-continuous optimization of wind turbine blades with the blade mass as the main objective function and the criteria's translated into constraints. Liao et al. [20] developed a multi-criteria-constrained design model with respect to minimum blade mass integrating a particle swarm optimization (PSO) algorithm using Federation Against Software Theft (FAST) [21]. Ning et al. [22] inspects the minimization of the turbine mass to AEP ratio as one of three examined objective functions. In a recent journal, Chen et al. [23] argue that a lighter blade mass will be beneficial to improve fatigue life based on requirements of the blade's strength and stiffness. Therefore, the minimum mass of the wind turbine blade was chosen as objective function.

4. Design constraints

Most engineering optimization problems include a set of equality and inequality constraints consisting of both linear and/or non-linear types. Generally, solving constrained optimization problems is more challenging than unconstrained systems. We have identified the most relevant constraints imposed by wind turbine blade designers as follows:

4.1. Ground clearance

A simple condition is set to prevent the collision of the blade with the ground.

4.2. Tip deflection

A constraint for the maximum tip deflection was included to ensure the local and global stability of the blade.

4.3. Shell and airfoil thickness

Some designers include a feasibility condition on the shell thickness and the surface of the airfoil to guarantee a proper trailing-edge separation.

4.4. Airfoil characteristics

In order to control the aerodynamic behaviour of the airfoil near stall, various constraints can be applied. For example, the absolute value of the slope beyond the stall angle can be regulated. Similarly, the coefficient of moment $C_{mc/4}$ and the ratio of the coefficient of lift and drag C_L/C_D can be constrained to limit the blade torsion and undesirable separation behaviour, respectively. Another technique to avoid abrupt stall is to enforce a transition condition on each of the suction and pressure sides.

4.5. Noise pollution

A major objection for wind turbines is the noise that it generates as the blades rotate. Most of the aerodynamic noise models are semi-empirical and origin from the tip-vortex/trailing-edge interaction, turbulent inflow or the trailing-edge thickness.

4.6. Stress

The wind turbine is subjected to a large number of loads and therefore its components will be exposed to high stresses. To constrain these stresses, particularly on the wind blades and gearbox, the designers add inequality constraints that relate the generated stresses and the ultimate permissible stresses.

4.7. Natural frequency

In order to prevent the occurrence of resonance, the natural frequency of the blade must be separated from the rotor's rotation harmonics. Therefore, many designers limit some natural frequencies ω between an admissible bound $[\omega_{low}; \omega_{upper}]$. Another method is to assume a safety gap factor between the rotor's rated speed and the natural frequency. The reader is referred to references [24, 25] where the optimal design is pursued with respect to the maximum frequency design criterion.

5. Wind turbine MOOP

Researchers began examining multi-objective optimization algorithms in the design of wind turbines only two decades ago. In 1996, Selig and Coverstone-Carroll [5] examined the maximization of the AEP with no or few constraints on the loads. A short year later, Giguère and Selig [3] presented a multidisciplinary optimization (MDO) for the blade geometry of horizontal axis wind turbines (HAWTs). A sharing function [26] is used to obtain the trade-off curve between cost and energy. Only the structure of the blades is considered; however, the effects of the rotor on the wind turbine components are accounted in the cost model. The form of the cost model is indicated as follows (Eq. (3)):

$$C_i = C_{ib}\left(c_i + (1-c_i)\left(\frac{P_i}{P_{ib}}\right)\right) \tag{3}$$

where $\boldsymbol{C}$ is the cost, $\boldsymbol{i}$ is the component, $\boldsymbol{c}$ is the cost factor (fixed portion of the total cost—cost factor of 20 % was used for the blades), $\boldsymbol{P}$ is the design parameters of importance for component $\boldsymbol{i}$ and subscripts ending with a $\boldsymbol{b}$ are baseline values.

Benini et al. [6] apply an MOEA for the design optimization of stall-regulated wind HAWT with a trade-off between the ratio of AEP per wind park area ($AEP_{density}$ to maximize) and the cost of energy (minimize). The idea behind using the first metric is that the number of turbines

http://dx.doi.org/10.5772/63481

that can be installed in a given area is inversely proportional to the square of the turbine radius. The MOEA handles the design parameters and searches for the optimal solutions following a set of Pareto concepts and basic principles of genetic programming [27, 28]. The authors choose the tip-speed, hub/tip ratio, and chord and twist distributions as their design variables. An assumption is made that the total turbine cost is reconstructed from the cost of the turbine blade alone, using the cost model from Eq. (4):

$$\mathrm{CoE} = \frac{\mathrm{TC} + \mathrm{BOS}}{\mathrm{AEP}} \mathrm{FCR} + \mathrm{OM} \tag{4}$$

where **TC** is the turbine cost, **BOS** the balance of station, **FCR** the fixed charge rate and **OM** the operation and maintenance costs.

In 2010, Grujicic et al. [10] developed a two-level optimization scheme to solve the MOOP. In the inner level, for a given aerodynamic design, the blade mass is minimized. In the outer level, a cost-assessment analysis is performed. This procedure is repeated until minimums are found for both the outer- and inner-level loops.

Kusiak et al. [9] introduced a data-driven approach to study the impact of turbine control on vibration. The authors developed a vibration prediction model using neural networks. Three objectives were included in the study (two vibrations and the power output), and a weighted sum of these objectives is minimized and set as follows (Eq. (5)):

$$\min\left(w_1 y_1(t) + w_2 y_2(t) + w_3 \frac{1}{y_3(t)} \right) \tag{5}$$

where $y_1(t)$ is the estimated vibration of the drive train, $y_2(t)$ the tower vibration model and $y_3(t)$ the estimated power output model.

In reference [29], Kusiak and Zheng present an approach to optimize the power factor and the power output of the wind turbine (bi-objective problem established by weights), using data-mining and evolutionary computation. The proposed approach generated optimized settings of the generator torque and the blade-pitch angle.

In the same year, Bottasso et al. [7] presented a thorough description of a multidisciplinary design optimization procedure. The authors assume that the weight is correlated to the cost. Since a reliable cost model is not offered to the public, no particular cost model was used. Instead of formulating a Pareto-optimal design problem, a combined cost was defined as the ratio of the annual energy production to the total weight. A two-stage sequential-constrained optimization algorithm was used to solve the constrained problem.

A year later, Wang et al. [11] presented a multi-objective algorithm. The power coefficient C_P at the design wind speed of 9 m/s and the blade mass are chosen as the optimization objectives. The two objectives can be formulated as follows (Eq. (6)):

$$f_1 = \max(\boldsymbol{C_p} \mid V = 9\,\mathrm{m.s^{-1}})$$
$$f_2 = \min \int_{R_{hub}}^{R} \boldsymbol{m}_i dr \tag{6}$$

Where C_p is the power coefficient, m_i is the radial mass distribution of the wind turbine blade, and R_{hub} and R are the hub radius and the blade length, respectively.

In the design of HAWTs, the most obvious feature is the rapid growth in the size of HAWT blades [30]; therefore, it is insufficient to perform an airfoil shape optimization by itself. Rather, the entire blade geometry must be taken into consideration. According to reference [12], a wind turbine blade airfoil should satisfy the following aerodynamic requirements:

1. High lift-to-drag ratio ($\boldsymbol{C}_{\mathrm{L}}/\boldsymbol{C}_{\mathrm{D}}$).
2. High lift coefficient $\boldsymbol{C}_{\mathrm{L}}$.
3. Good performance during the stochastic behaviour of the wind flow.
4. Low sensitivity to leading-edge roughness.

The reader is referred to references [31–33] for the design of more efficient wind turbine blade airfoils. Ju et al. [12] developed a robust design optimization (RDO) for the design of a new series of wind turbine airfoils by maximizing both the $\boldsymbol{C}_{\mathrm{L}}/\boldsymbol{C}_{\mathrm{D}}$ and $\boldsymbol{C}_{\mathrm{L}}$. They also completed a sensitivity analysis of the roughness at the leading edge associated with the geometry profile uncertainty.

Multidisciplinary optimization was far and widely recognized of having the potential of becoming the cutting edge of the future [34, 35]. Kim [36, 37] and Michelena [38] apply maximum length sequence (MLS) algorithms called the target-cascading methodology method, where multiple levels and interfacing between the levels are defined.

For offshore wind turbines, the environmental conditions are more severe and more considerations have to be taken into account. Designers aim for a more proficient use of the capacity of the very expensive electrical cables, foundation, installation and erection costs.

6. Algorithms

6.1. Introduction

The selection of the appropriate optimization algorithm is a critical undertaking in any engineering optimization problem that relies on the attributes of the design space and on the nature of the problem. The final results depend on the algorithm in terms of accuracy and local minima sensitivity. Throughout the years, the algorithms used to solve wind turbine design problems have matured. At the outset, most of the methods derived directly from the blade-element momentum (BEM) theory, typically from Wilson and Lissaman [39]. In the 1990s, Selig

and Coverstone-Carroll [5] were one of the originals to suggest a method based on GA for their wind turbine blade design tool. With the need to carry a multidisciplinary or multi-objective optimization design, Wood [40] and Sale et al. [41] simplified the MOOP into a single-objective question using a classical-weighted method. The approaches for solving conventional multi-objective design problems include:

- objective-weighted method
- hierarchical optimization method
- ε-constraint method
- goal-programming method.

It is important to highlight that all of the above algorithms convert the multi-objective problem into a single-objective problem. According to Ribeiro et al. [42], optimization algorithms can be categorized into two groups: gradient-based approaches (GBAs) and heuristic algorithms, whereas Endo [43] separates the optimization methods between genetic and non-genetic algorithms. In the last decades, in order to solve complicated optimization problems, evolutionary algorithms have been suggested such as:

- niched Pareto genetic algorithm (NPGA) [16]
- Pareto-archived evolution strategy (PAES) [44]
- strength Pareto evolutionary algorithm (SPEA) [45]
- neighbourhood cultivation genetic algorithm (NCGA) [46]
- non-dominated sorting genetic algorithm (NSGA)-II [47].

6.2. Meta-heuristic algorithms

Meta-heuristics are algorithms often inspired from nature, designed to replace or assist conventional solvers. This is a growing research field since the last few decades as meta-heuristics are now emerging as alternatives to the classical approaches.

An interesting fact can be drawn from the progress of the field of meta-heuristics and wind turbine optimization. In the recent years, wind energy showed an increase in the use of optimization methods such as linear programming, Lagrangian relaxation, quadratic programming and heuristic optimization (precisely genetic algorithm and particle swarm optimization) to name a few. However, it can be said that the gradient-based approaches and genetic algorithm are the two most popular optimization algorithms that have been applied in wind turbine design. The reason is quite simple, in the case of blade-geometry optimization, there is a large number of design variables, which are continuous (e.g. chord and twist distributions, blade pitch, etc.) and discrete (e.g. airfoil family, number of blades, etc.) at the same time. Moreover, some of these design variables are dependent from one another (e.g.

chord and twist), as well as competing objectives within the definition of the objective function (e.g. cost of energy).

GAs are the most popular evolutionary algorithms because of their robustness and reliability in wind turbine design problems. A genetic algorithm is an optimization method that mimics Darwin's principle of 'survival of the fittest' over a population of solutions (individuals) that evolves from one generation to another. It was originally proposed by Holland in 1975 [48]. Individuals with a large 'fitness' value have a superior probability to 'reproduce' in forming the new generation. Similar to a DNA chain, each individual is coded in one string and uses reproduction, crossover and mutation operators to direct the search over the generations. The usefulness of a GA is due to its robustness in multimodal design spaces. Likewise, GA explores non-linear, non-derivable, non-continuous domains and they are less sensitive to the initial domain.

7. Numerical example

In this section, we will solve a numerical example for the design of a wind turbine blade using a GA multi-objective optimization algorithm. The objective functions are the blade mass and the annual energy production. In order to calculate the mass, a structural model must be constructed. For the purpose of this study, a preliminary tool called Co-Blade [49] is used. As for the annual energy, WT-Perf [50] is introduced in the multi-objective platform to generate the AEP.

Co-Blade is a tool that helps designers to compute the structural properties of a wind turbine blade. It uses a combination of classical lamination theory (CLT) with an Euler-Bernoulli theory, and a shear-flow theory applied to composite beams is used to perform its analysis. This approach allows for a direct computation of the structural properties of a given blade, within several seconds of execution. The fitness function that Co-Blade minimizes is the blade mass penalitized by the maximum stress, buckling, deflection and the natural frequency. The design variables are the chord-wise width of the spar cap at the inboard and outboard locations, the thickness of the 'blade-root' material and the thicknesses of the laminas within the leading-edge panel (LEP), trailing-edge panel (TEP), spar cap and shear webs along the length of the blade. They are listed in **Table 1**.

At first, the blade is represented as a cantilever beam under flap-wise and edge-wise bendings, axial deflection and elastic twist. Additional coupling between bending, extension and torsion is accounted for, due to the offsets between the beam-shear centre, tension centre and centre of mass from the blade-pitch axis (**Figure 3**). The beam cross sections are assumed to be thin-walled, closed and single- or multicellular, and the periphery of each beam cross section is discretized as a connection of flat composite laminates.

Parameter	DESCRIPTION
w_cap_inb, w_cap_oub	Width of the spar cap normalized by the chord length at the INB_STN and OUB_STN blade stations
t_blade_root	Thickness of the 'blade-root' material at the INB_STN blade station
t_blade_skin1 …t_blade_skinN	Thickness of 'blade-shell' material at control points 1 through NUM_CP. The control points are equally spaced along the blade between the TRAN_STN and OUB_STN blade stations
t_cap_uni1 …t_cap_uniN	Thickness of 'spar-uni' material at control points 1 through NUM_CP
t_cap_core1 …t_cap_coreN	Thickness of 'spar-core' material at control points 1 through NUM_CP
t_lep_core1 …t_lep_coreN	Thickness of 'LEP-core' material at control points 1 through NUM_CP
t_tep_core1 …t_tep_coreN	Thickness of 'TEP-core' material at control points 1 through NUM_CP
t_web_skin1, t_web_skin2	Thickness of 'web-shell' material at the two control points located at INB_STN and OUB_STN
t_web_core1, t_web_core2	Thickness of 'web-core' material at the two control points located at INB_STN and OUB_STN.
w_cap_inb, w_cap_oub	Width of the spar cap normalized by the chord length at the INB_STN and OUB_STN blade stations
t_blade_root	Thickness of the 'blade-root' material at the INB_STN blade station
t_blade_skin1 …t_blade_skinN	Thickness of 'blade-shell' material at control points 1 through NUM_CP. The control points are equally spaced along the blade between the TRAN_STN and OUB_STN blade stations
t_cap_uni1 …t_cap_uniN	Thickness of 'spar-uni' material at control points 1 through NUM_CP
t_cap_core1 …t_cap_coreN	Thickness of 'spar-core' material at control points 1 through NUM_CP
t_lep_core1 …t_lep_coreN	Thickness of 'LEP-core' material at control points 1 through NUM_CP

Table 1. Design variable for Co-Blade.

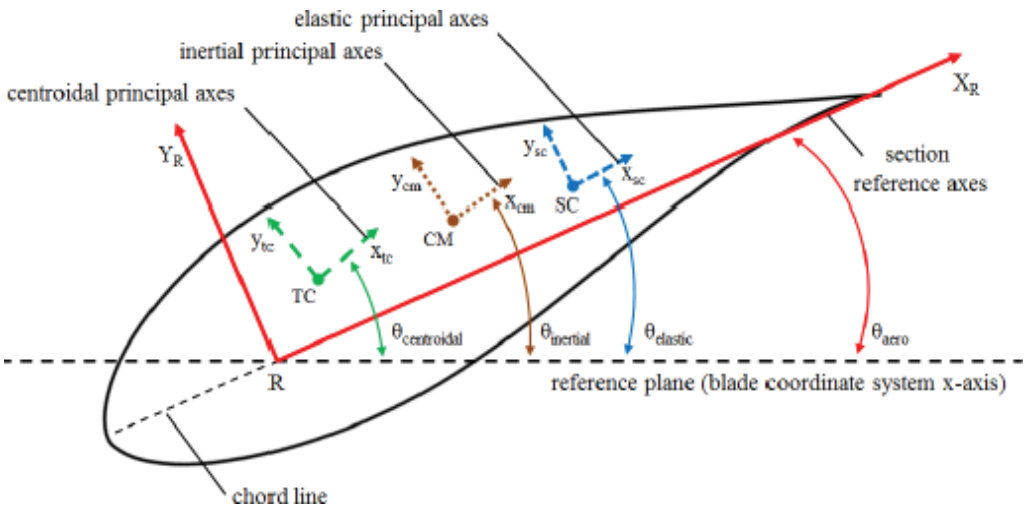

Figure 3. Orientation of the blade-axe systems [49].

In regard to Euler-Bernoulli beam theory, the beam cross sections are considered as heterogeneous and each of the material properties depends on the location in each cross section. The structural analysis at each discrete portion of the composite beam characterizes effective mechanical properties computed via classical lamination theory. Each discrete portion of the cross section then contributes to the global section properties of the composite beam (described further in references [51, 52]). Once the global cross-sectional properties are calculated, the deflections and effective beam axial stress (σ_{zz}) and the effective beam-shear stress (τ_{zs}) can be now computed under the assumptions of an Euler-Bernoulli beam (refer to references [51–53]). The calculation of τ_{zs}, the prediction of shear centre and torsional stiffness are based on a shear-flow approach, which is discussed in detail in reference [53]. Finally, by converting the distribution of effective beam stresses σ_{ZZ} and τ_{zs} into equivalent in-plane loads, the lamina-level strains and stresses in the principal fibre directions (ε_{11}, ε_{22}, γ_{12}, σ_{11}, σ_{22} and τ_{12}) can be evaluated using CLT.

As mentioned earlier, Co-Blade applies a penalized blade mass defined as the following (Eq. (7)):

$$\text{Minimize } f(\vec{x}) = \text{Blade Mass } x \prod_{n=1}^{8} \max(1, p_n)^2 \tag{7}$$

$$p_1 = \frac{\sigma_{11,max}}{\sigma_{11,fT}}$$

http://dx.doi.org/10.5772/63481

$$p_2 = \frac{\sigma_{11,min}}{\sigma_{11,fC}}$$

$$p_3 = \frac{\sigma_{22,max}}{\sigma_{22,fT}}$$

$$p_4 = \frac{\sigma_{22,min}}{\sigma_{22,fC}}$$

$$p_5 = \frac{\left|\tau_{12,max}\right|}{\tau_{12,y}}$$

$$p_6 = \left(\frac{\sigma}{\sigma_{buckle}}\right)^{\alpha} + \left(\frac{\tau}{\tau_{buckle}}\right)^{\beta}$$

$$p_7 = \frac{Tip\ Deflection}{Max\ Tip\ Deflection}$$

$$p_8 = max\left\{\frac{\min allowable\ diff.between\ rotor\ \ freq.and\ the\ blade\ natural\ \ freq.}{\left|\omega_m - \omega_{rotor}\right|}\right\},$$

$$m = 1,\ldots Modes$$

Subject to

$\vec{x}_{LB} \leq \vec{x} \leq \vec{x}_{UB}$ (lower and upper bounds)

$A\vec{x} \leq \vec{b}$ (linear constraint)

Before we describe our fitness function, let us briefly discuss the second half of the multi-objective algorithm, the aerodynamic tool that calculates the AEP.

WT-Perf uses blade-element momentum theory to predict the performance of wind turbines with good accuracy. Users must build an appropriate input file that consists of the following set of data (**Table 2**):

- Model configuration
- WT-Perf algorithm configuration
- Cavitation model
- Turbine data
- Aerodynamic data
- Input/output settings
- Analysis settings.

E_{11}	E_{22}	G_{12}	υ_{12}	ρ	**Material Name**
(Pa)	**(Pa)**	**(Pa)**	**(-)**	**(kg/m^3)**	**(-)**
2.80E + 10	1.40E + 10	7.00E + 09	0.4	1850	(blade-root)
2.80E + 10	1.40E + 10	7.00E + 09	0.4	1850	(blade-shell)
4.20E + 10	1.40E + 10	3.00E + 09	0.28	1920	(spar-uni)
2.60E + 08	2.60E + 08	2.00E + 07	0.3	200	(spar-core)
2.60E + 08	2.60E + 08	2.00E + 07	0.3	200	(LEP-core)
2.60E + 08	2.60E + 08	2.00E + 07	0.3	200	(TEP-core)
1.40E + 10	1.40E + 10	1.20E + 10	0.5	1780	(web-shell)
2.60E + 08	2.60E + 08	2.00E + 07	0.3	200	(web-core)

Table 2. Design variables for Co-Blade.

We have now defined two conflicting objective functions, the blade mass and the annual energy. Solving such MOOP can be achieved by the method of scalarizing. It consists of formulating a single-objective optimization problem such that optimal solutions to the single-objective optimization problem are Pareto-optimal solutions to the MOOP. A general formulation for a scalarization of a multi-objective optimization is given as (Eq. (8)):

$$\min \sum_{i=1}^{M} w_i f_i(\vec{x}) \tag{8}$$

where the weights of the objectives $w_i > 0$ are the parameters of the scalarization.

We propose to use the following fitness function to minimize the mass and maximize the annual energy production (Eq. (9)):

http://dx.doi.org/10.5772/63481

$$\min\left(\alpha\frac{M(\vec{x})}{M_0}+(\alpha-1)\frac{\mathrm{AEP}(\vec{x})}{\mathrm{AEP}_0}\right) \tag{9}$$

For a value of alpha near zero, the mass ratio is eliminated and the fitness function becomes $\min\left((\alpha-1)\frac{\mathrm{AEP}(\vec{x})}{\mathrm{AEP}_0}\right)$, which translates into the maximization of the normalized energy. Probably, for an alpha value close to 1, the energy ratio disappears and the problem is now a minimization of the mass. If we run the optimization problem for different values of alpha between 0 and 1, we can find Pareto-optimal solution to the MOOP. The reference mass and energy are taken, respectively, from the case study of alpha equals 0. The complete Pareto front is displayed in **Figure 4**.

Let us consider the following mechanical properties during the structural analysis. In our study, these properties are derived from Sandia 100-m blade SNL-100 [54]. **Table 3** lists the mechanical properties utilized in the structural design of the blade. Likewise, in **Table 2**, we list the configurations (input, model, turbine data and algorithm) for the input file required by the WT-Perf solver. The general flow chart of multi-objective optimization algorithm can be summarized in **Figure 5**. The complete inputs for the multi-objective optimization algorithm are listed in **Table 4**.

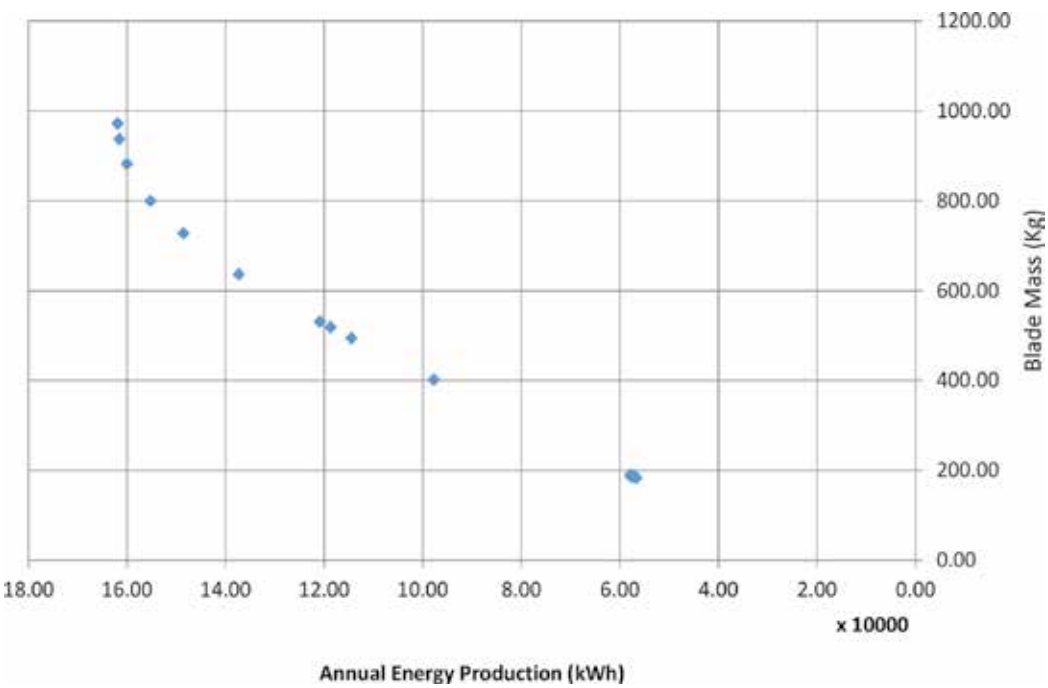

Figure 4. Pareto front for the given numerical example in Section 7.

Input configuration		
False	Echo:	Echo input parameters to '<rootname>.ech'?
True	DimenInp:	Turbine parameters are dimensional?
True	Metric:	Turbine parameters are Metric (MKS vs FPS)?
Model configuration		
1	NumSect:	Number of circumferential sectors.
1000	MaxIter:	Maximum number of iterations for induction factor.
1.00E + 06	ATol:	Error tolerance for induction iteration.
1.00E + 06	SWTol:	Error tolerance for skewed-wake iteration.
Algorithm configuration		
True	TipLoss:	Use the Prandtl tip-loss model?
True	HubLoss:	Use the Prandtl hub-loss model?
True	Swirl:	Include Swirl effects?
True	SkewWake:	Apply skewed-wake correction?
True	AdvBrake:	Use the advanced brake-state model?
True	IndProp:	Use PROP-PC instead of PROPX induction algorithm?
True	AIDrag:	Use the drag term in the axial induction calculation?
True	TIDrag:	Use the drag term in the tangential induction calculation?
Turbine data		
3	NumBlade:	Number of blades.
10	RotorRad:	Rotor radius (length).
0.5	HubRad:	Hub radius (length or div by radius).
0	PreCone:	Precone angle, positive downstream (deg).
0	Tilt:	Shaft tilt (deg).
0	Yaw:	Yaw error (deg).
30	HubHt:	Hub height (length or div by radius).
30	NumSeg:	Number of blade segments (entire rotor radius).

Table 3. Input file for WT-Perf.

http://dx.doi.org/10.5772/63481

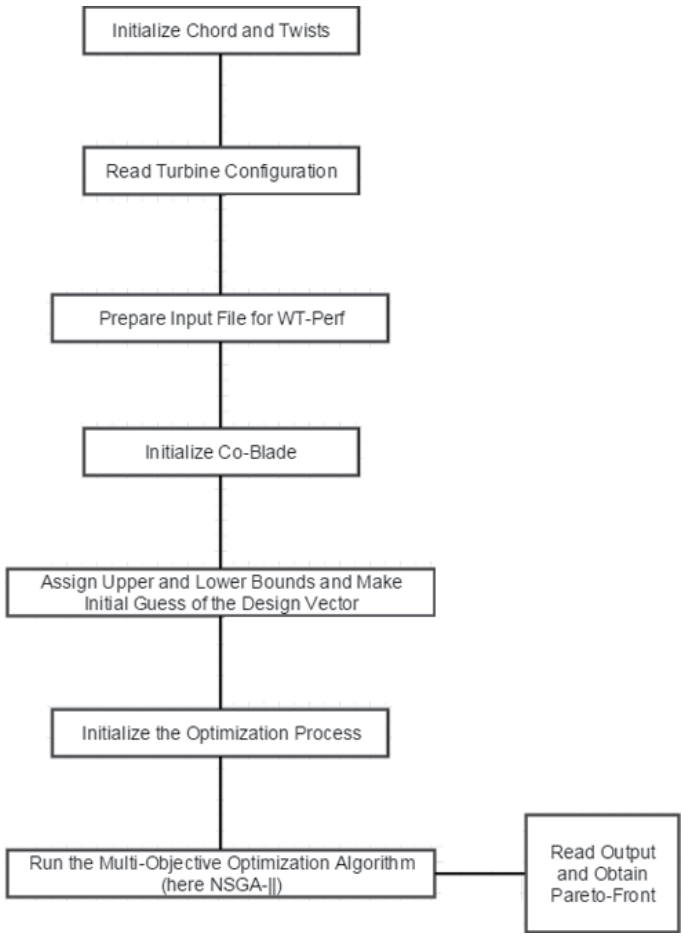

Figure 5. Flow chart of the multi-objective optimization algorithm.

WT-Perf settings		
1000	MaxIter:	Maximum number of iterations for induction factor.
1.00E-06	ATol:	Error tolerance for induction iteration.
1.00E-06	SWTol:	Error tolerance for skewed-wake iteration.
True	TipLoss:	Use the Prandtl tip-loss model?
True	HubLoss:	Use the Prandtl hub-loss model?
True	Swirl:	Include Swirl effects?
True	SkewWake:	Apply skewed-wake correction?
True	AdvBrake:	Use the advanced brake-state model?
True	IndProp:	Use PROP-PC instead of PROPX induction algorithm?

WT-Perf settings		
True	AIDrag:	Use the drag term in the axial induction calculation?
True	TIDrag:	Use the drag term in the tangential induction calculation?
3	NumBlade:	Number of blades.
0	Yaw:	Yaw error (deg).
30	HubHt:	Hub height (length or div by radius).
0.00001464	KinVisc:	Kinematic air viscosity
0	ShearExp:	Wind-shear exponent (1/7 law = 0.143).
False	UseCm:	Are Cm data included in the airfoil tables?
True	TabDel:	Make output tab-delimited (fixed-width otherwise).
True	KFact:	Output dimensional parameters in *K* (e.g. *kN* instead on *N*)
True	WriteBED:	Write out blade-element data to '<rootname>.bed'?
True	InputTSR:	Input speeds as TSRs?
'mps'	SpdUnits:	Wind-speed units (mps, fps, mph)
0	NumCases:	Number of cases to run. Enter zero for parametric analysis.
WS or TSR	RotSpd Pitch	Remove following block of lines if NumCases is zero.
3	ParRow:	Row parameter (1-rpm, 2-pitch, 3-tsr/speed).
1	ParCol:	Column parameter (1-rpm, 2-pitch, 3-tsr/speed).
2	ParTab:	Table parameter (1-rpm, 2-pitch, 3-tsr/speed).
True	OutPwr:	Request output of rotor power?
True	OutCp:	Request output of Cp?
True	OutTrq:	Request output of shaft torque?
True	OutFlp:	Request output of flap-bending moment?
True	OutThr:	Request output of rotor thrust?
0.0 0.0 0.0	PitSt, PitEnd, PitDel:	First, last, delta blade pitch (deg).
80 80 0.00	OmgSt, OmgEnd, OmgDel:	First, last, delta rotor speed (rpm).
Analysis options		
t	SELF_WEIGHT:	Include self-weight as a body force?
t	BUOYANCY:	Include buoyancy as a body force?
true	CENTRIF:	Include centrifugal force as a body force?
true	DISP_CF:	Apply correction factors to the beam displacements?
0	N_MODES:	Number of modes to be computed
50	N_ELEMS:	Number of blade finite elements to be used in the modal analysis

http://dx.doi.org/10.5772/63481

WT-Perf settings		
Optimization options		
t	OPTIMIZE:	Perform optimization of composite layup?
GS	OPT_METHOD:	Optimization algorithm for the optimization of composite layup
false	OPT_PITAXIS:	Optimize the pitch axis?
0.375	PITAXIS_VAL:	Pitch axis value outboard of max chord (ignored if OPT_PITAXIS = false)
3	INB_STN:	Inboard station where the leading- and trailing-edge panels, spar caps and shear webs begin
8	TRAN_STN:	Station where the root transition ends
28	OUB_STN:	Outboard station where the leading- and trailing-edge panels, spar caps and shear webs end
4	NUM_CP:	Number of control points between INB_STN and OUB_STN
false	READ_INITX:	Read the initial values for the design variables from INITX_FILE?
none	INITX_FILE:	Input file for the initial values of the design variables.
false	WRITE_STR:	Write structural input files at each function evaluation?
f	WRIT E_F_ALL:	Write the fitness value and penalty factors at each function evaluation?
f	WRIT E_X_ALL:	Write the design variables at each function evaluation?
f	WRITE_X_ITER:	Write the design variables at each iteration?
100	NumGens	Maximum number of generations for GA iterations
100	PopSize	Number of individuals per generation
1	EliteCount	Number of elite individuals per generation
0.5	CrossFrc	Fraction of individuals created by crossover
1.00E-06	GATol	Error tolerance for the GA fitness value
Environmental data		
1.225	FLUID_DEN:	Fluid density (kg/m^3)
9.81	GRAV:	Gravitational acceleration (m/s^2)
6.03	U_mean:	Long-term mean flow (m/s)
1.91	Weib_k:	Shape factor
6.8	Weib_c:	Scale factor
Blade data		
30	NUM_SEC:	Number of blade cross sections
10	BLD_LENGTH:	Blade length (m)
0.5	HUB_RAD:	Hub radius (m)

WT-Perf settings		
0	SHAFT_TILT:	Shaft tilt angle (deg)
0	PRE_CONE:	Precone angle (deg)
180	AZIM:	Azimuth angle (deg)
100	MAX_ROT	Maximum rotational speed (rpm)
10	MIN_ROT	Minimum rotational speed (rpm)
cosine	INTERP_AF:	Interpolate airfoil coordinates? (choose "none", "cosine", or "equal" with no quotation marks)
1	ElmSpc	Blade-element radial spacing (0 equal, 1 cosinus)
60	N_AF:	Number of points in interpolated airfoil coordinates (ignored
mats-Wind.inp	MATS_FILE:	Input file for material properties
0.13	RootTranSt	Start of root transition region
3	RootTranSt_index	Index of start of root transition region
0.288	RootTranEnd	End of root transition region
8	RootTranEnd_index	Index of end of root transition region
3 9 19 26 30	CP_Index	Index of control points (chord and twist)

Table 4. Input file for the multi-objective algorithm.

8. Conclusion

Within the last 20 years, wind energy conversion systems have reached maturity. The obvious growing worldwide wind energy market will culminate to further improvements. The continuous effort for the advancement in horizontal wind turbine performance strategies and techniques will result in additional cost reductions. The ultimate aim of any wind turbine manufacture is to design a wind turbine able to compete with fossil fuel. The number of research paper that applies optimization techniques in the attempt to reach an optimal blade design has demonstrated a significant increase in the recent decade alone. Despite the fact that a minimal cost of energy was chosen as the single main objective in most of the research papers, many have argued that it is more stimulating to evaluate the wind turbine design as an optimization problem consisting of more than one objective. Using multi-objective optimization algorithms, the designers are able to identify a trade-off curve called Pareto front that reveals the weaknesses, anomalies and rewards of certain targets. We can anticipate that future optimization problems will be set as multidisciplinary formulations. Consequently, solving such difficult optimization problem will require further developments in the optimization algorithm itself. Since traditional optimization techniques cannot overcome many of their drawbacks such as rapid divergence and sensitivity to the initial solution, population-based and nature-inspired algorithms will continue to emerge as worthy alternatives.

In this chapter, we presented the fundamental principles of multi-objective optimization in wind turbine design. We have identified the constraints and objective functions mostly targeted by designers. We briefly discussed the fundamentals and terminology of multi-objective optimization. The most common optimization algorithms used to solve multi-objective wind turbine optimization problems were presented. We highlighted the emergence of population-based techniques, particularly genetic algorithms. Finally, we showed the steps to solve a classic multi-objective wind turbine design problem using a genetic algorithm. The reader is referred to the following publications for further details [2, 55] concerning wind turbine optimization.

Author details

Adam Chehouri[1,2*], Rafic Younes[2], Adrian Ilinca[3] and Jean Perron[1]

*Address all correspondence to: adam.chehouri1@uqac.ca

1 Anti Icing Materials International Laboratory (AMIL), Université du Québec à Chicoutimi, Québec, Canada

2 Faculty of Engineering, Third Branch, Lebanese University, Rafic Harriri Campus, Hadath, Beirut, Lebanon

3 Wind Energy Research Laboratory (WERL), Université du Québec à Rimouski, Québec, Canada

References

[1] Lindenberg, S., B. Smith, and K. O'Dell, *20% wind energy by 2030.* 2008. National Renewable Energy Laboratory (NREL), US Department of Energy, Renewable Energy Consulting Services, Energetics Incorporated, United States.

[2] Chehouri, A., et al., *Review of performance optimization techniques applied to wind turbines.* Applied Energy, 2015. 142: p. 361–388.

[3] Giguere, P. and M.S. Selig, *Blade geometry optimization for the design of wind turbine rotors*. In Proceedings of AIAA/ASME Wind Energy Symposium. 2000. Reno, NV.

[4] Giguère, P., J. Tangler, and M. Selig, *Blade design trade-offs using low-lift airfoils for stall-regulated HAWTs.* Journal of Solar Energy Engineering, 1999. 121(4): p. 217–223.

[5] Selig, M.S. and V.L. Coverstone-Carroll, *Application of a genetic algorithm to wind turbine design.* Journal of Energy Resources Technology: Transactions of the Asme, 1996. 118(1): p. 22–28.

[6] Benini, E. and A. Toffolo, *Optimal design of horizontal-axis wind turbines using blade-element theory and evolutionary computation.* Journal of Solar Energy Engineering: Transactions of the Asme, 2002. 124(4): p. 357–363.

[7] Bottasso, C. L., Campagnolo, F., & Croce, A. (2012). Multi-disciplinary constrained optimization of wind turbines. *Multibody System Dynamics*, *27*(1), 21–53.

[8] Deb, K., *Multi-objective optimization using evolutionary algorithms*. Vol. 16, 2001. John Wiley & Sons, United States.

[9] Kusiak, A., Z.J. Zhang, and M.Y. Li, *Optimization of wind turbine performance with data-driven models.* IEEE Transactions on Sustainable Energy, 2010. 1(2): p. 66–76.

[10] Grujicic, M., et al., *Multidisciplinary design optimization for glass-fiber epoxy-matrix composite 5 MW horizontal-axis wind-turbine blades.* Journal of Materials Engineering and Performance, 2010. 19(8): p. 1116–1127.

[11] Wang, L., T.G. Wang, and Y. Luo, *Improved non-dominated sorting genetic algorithm (NSGA)-II in multi-objective optimization studies of wind turbine blades.* Applied Mathematics and Mechanics: English Edition, 2011. 32(6): p. 739–748.

[12] Ju, Y.P. and C.H. Zhang, *Multi-point robust design optimization of wind turbine airfoil under geometric uncertainty.* Proceedings of the Institution of Mechanical Engineers Part a: Journal of Power and Energy, 2012. 226(A2): p. 245–261.

[13] Schaffer, J.D., *Multiple objective optimization with vector evaluated genetic algorithms*. In Proceedings of the 1st international Conference on Genetic Algorithms. 1985. L. Erlbaum Associates Inc.

[14] Goldberg, D.E., *Genetic algorithms in search, optimization, and machine learning*. 1989. Addison-Wesley, Reading, MA.

[15] Srinivas, N. and K. Deb, *Multiobjective optimization using nondominated sorting in genetic algorithms.* Evolutionary Computation, 1994. 2(3): p. 221–248.

[16] Horn, J., N. Nafpliotis, and D.E. Goldberg. *A niched Pareto genetic algorithm for multiobjective optimization*. In Evolutionary Computation, 1994. IEEE World Congress on Computational Intelligence, Proceedings of the First IEEE Conference on. 1994. IEEE, Orlando, FL.

[17] Kursawe, F., A variant of evolution strategies for vector optimization, in *Parallel Problem Solving from Nature*. p. 193–197, 1990. Springer, 1st Workshop, PPSN I Dortmund, FRG.

[18] Hajela, P. and C.-Y. Lin, *Genetic search strategies in multicriterion optimal design.* Structural Optimization, 1992. 4(2): p. 99–107.

[19] Jureczko, M., M. Pawlak, and A. Mezyk, *Optimisation of wind turbine blades.* Journal of Materials Processing Technology, 2005. 167(2–3): p. 463–471.

[20] Liao, C.C., X.L. Zhao, and J.Z. Xu, *Blade layers optimization of wind turbines using FAST and improved PSO Algorithm.* Renewable Energy, 2012. 42: p. 227–233.

[21] Jonkman, J.M. and M.L. Buhl Jr, *FAST user's guide.* 2005. National Renewable Energy Laboratory, Golden, CO.

[22] Ning, A., R. Damiani, and P. Moriarty. *Objectives and constraints for wind turbine optimization*. In 31st ASME Wind Energy Symposium, United States. 2013.

[23] Chen, J., et al., *Structural optimization study of composite wind turbine blade.* Materials & Design, 2013. 46: p. 247–255.

[24] Maalawi, K.Y. and M.A. Badr, *Frequency optimization of a wind turbine blade in pitching motion.* Proceedings of the Institution of Mechanical Engineers Part a-Journal of Power and Energy, 2010. 224(A4): p. 545–554.

[25] Maalawi, K.Y. and H.M. Negm, *Optimal frequency design of wind turbine blades.* Journal of Wind Engineering and Industrial Aerodynamics, 2002. 90(8): p. 961–986.

[26] Goldberg, D.E. and J. Richardson. *Genetic algorithms with sharing for multimodal function optimization*. in *Genetic algorithms and their applications: Proceedings of the Second International Conference on Genetic Algorithms*. 1987. Lawrence Erlbaum, Hillsdale, NJ.

[27] Goldberg, D.E., *Genetic algorithms in search, optimization, and machine learning*. Vol. 412, 1989. Addison-Wesley, Reading, Menlo Park, CA.

[28] Schwefel, H.-P.P., *Evolution and optimum seeking: the sixth generation*. 1993. John Wiley & Sons, Inc., United States.

[29] Kusiak, A. and H.Y. Zheng, *Optimization of wind turbine energy and power factor with an evolutionary computation algorithm.* Energy, 2010. 35(3): p. 1324–1332.

[30] Li, J.Y., et al., *Aerodynamic optimization of wind turbine airfoils using response surface techniques.* Proceedings of the Institution of Mechanical Engineers Part a: Journal of Power and Energy, 2010. 224(A6): p. 827–838.

[31] Bizzarrini, N., F. Grasso, and D.P. Coiro, *Genetic algorithms in wind turbine airfoil design.* p. 14–17, 2011. EWEA, EWEC2011, Bruxelles, Belgium.

[32] Grasso, F., *Usage of numerical ptimization in wind turbine airfoil design.* Journal of Aircraft, 2011. 48(1): p. 248–255.

[33] Grasso, F. *Hybrid optimization for wind turbine thick airfoils*. In Proceedings of the 53rd AIAAJASME/ASCE/AHS/ASC Structures, Structural Dynamics and Materials Conference, AIAA Paper AIAA, Honolulu, Hawaii. 2012.

[34] Frank, P., et al. *A comparison of optimization and search methods for multidisciplinary design*. In American Institute of Aeronautics and Astronautics (AIAA) Symposium on MDO, Cleveland, OH, U.S.A. 1992.

[35] Alexandrov, N.M. and M.Y. Hussaini, *Multidisciplinary design optimization: state of the art*. Vol. 80, 1997. SIAM, United States.

[36] Kim, H.M., et al., *Target cascading in optimal system design.* Journal of Mechanical Design, 2003. 125(3): p. 474–480.

[37] Kim, H.M., et al., *Analytical target cascading in automotive vehicle design.* Journal of Mechanical Design, 2003. 125(3): p. 481–489.

[38] Michelena, N., et al., *Design of an advanced heavy tactical truck: a target cascading case study.* SAE Transactions, 2001. 110(2): p. 457–468.

[39] Wilson, R.E. and P.B. Lissaman, *Applied aerodynamics of wind power machines.* NASA STI/ Recon Technical Report N, 1974. 75: p. 22669.

[40] Wood, D., *Dual purpose design of small wind turbine blades.* Wind Engineering, 2004. 28(5): p. 511–527.

[41] Sale, D., J. Jonkman, and W. Musial, *Hydrodynamic optimization method and design code for stall-regulated hydrokinetic turbine rotors*. 2009. National Renewable Energy Laboratory, United States.

[42] Ribeiro, A.F.P., A.M. Awruch, and H.M. Gomes, *An airfoil optimization technique for wind turbines.* Applied Mathematical Modelling, 2012. 36(10): p. 4898–4907.

[43] Endo, M., *Wind turbine airfoil optimization by particle swarm method*. 2011. Case Western Reserve University, United States.

[44] Knowles, J. and D. Corne. *The pareto archived evolution strategy: a new baseline algorithm for pareto multiobjective optimisation*. In Evolutionary Computation, 1999. CEC 99. Proceedings of the 1999 Congress on. 1999. IEEE, Washington, DC.

[45] Kim, M., et al. *SPEA2+: improving the performance of the strength Pareto evolutionary algorithm 2*. In Parallel problem solving from nature-PPSN VIII. 2004. Springer, Birmingham, UK.

[46] Watanabe, S., T. Hiroyasu, and M. Miki. *NCGA: neighborhood cultivation genetic algorithm for multi-objective optimization problems*. In GECCO Late Breaking Papers. 2002.

[47] Deb, Kalyanmoy, Samir Agrawal, Amrit Pratap, and Tanaka Meyarivan. "A fast elitist non-dominated sorting genetic algorithm for multi-objective optimization: NSGA-II." In *Parallel problem solving from nature PPSN VI*, pp. 849–858. Springer Berlin Heidelberg, 2000.

[48] Holland, J.H., *Adaptation in natural and artificial systems: an introductory analysis with applications to biology, control, and artificial intelligence*. 1975. U Michigan Press, Oxford, England.

[49] Sale, D., *User's guide to co-blade: software for structural analysis of composite blades*. 2012. Northwest National Marine Renewable Energy Center, United States.

[50] Buhl, M.L., *WT_Perf user's guide.* 2004. National Renewable Energy Laboratory, United States.

[51] Rivello, Robert M. *Theory and analysis of flight structures*. McGraw-Hill College, 1969.

[52] Allen, D.H. and W.E. Haisler, *Introduction to aerospace structural analysis.* 1985.

[53] Bauchau, O.A. and J.I. Craig, *Structural analysis: with applications to aerospace structures*. Vol. 163. 2009. Springer, Germany.

[54] Griffith, D.T. and T.D. Ashwill, *The Sandia 100-meter all-glass baseline wind turbine blade: SNL100-00.* 2011. Informe Técnico, Sandia National Laboratories, United States.

[55] Chehouri, A., et al., *Optimal design for a composite wind turbine blade with fatigue and failure constraints.* Transactions of the Canadian Society for Mechanical Engineering, 2015. 39(2): p. 171.

Chapter 7

Methodology for the Low-Cost Optimisation of Small-Wind Turbines

Alberto Arroyo, Mario Manana, Pablo B. Castro,
Raquel Martinez, Ramon Lecuna and Juan Carcedo

Additional information is available at the end of the chapter

http://dx.doi.org/10.5772/63432

Abstract

The increasing use of small-wind energy has made it necessary to develop new methods that improve the efficiency of this technology. This is best done by considering the interaction between the various components, such as wind rotors, electrical generators, rectifiers and inverters, as opposed to studying the individual components in isolation.

Hence, this chapter describes a methodology to increase the efficiency of small-wind turbines (SWTs) equipped with an electrical machine, rectifier and inverter. To achieve this objective, capacitor banks will be connected between the electrical machine and the rectifier.

This methodology is motivated by two clear aims. The first one is to operate the SWT with its maximum power coefficient (C_p). The second one is to select the most suitable capacitor bank for each wind speed in order to optimise the energy supplied to the grid.

Keywords: capacitor, wind power generation, performance optimisation, Weibull distribution, renewable energy

1. Introduction

The fact that everyday more wind power is used demands the development of new technologies of electronic production and the improvement of existing ones. The humankind challenge will be, on the one hand, trying to satisfy the demands of the aforementioned energy and on the other, being respectful to the environment in order to stop the climate change that is taking place.

Thus, wind power is one of the energies that have been developed in order to satisfy this demand and be respectful to the environment. Recently, this energy has become one of the main sustainable sources used in developing countries.

The wind can generate electric power without producing undesirable pollutants associated with fossil fuels and nuclear energy. In addition, wind power is a potentially unlimited resource unlike fossil fuels and the elements used in nuclear power plants. Furthermore, wind power promotes a clear and sustainable energy future without the use of fossil fuel resources.

The wind industry promotes a clean and sustainable energy future distinct from the fossil resources. It is for this reason that the wind sector is the one which has experienced the biggest growth in recent years.

Historically, wind power was linked to windmills on land. However, nowadays, this trend is changing due to the discovery of the big benefits that these windmills would produce on the coast. Some of the main advantages of the off-shore farms are large usable wind power, the reduction of the visual impact and the reduction of mortality levels of birds.

Therefore, wind power is not new but one of the oldest energies together with the thermal energies. The wind, as a driving force is, was already used in olden days, for instance, to move the millstones that grind the wheat to produce flour. In the same way, ships were moved driven by the wind.

However, in the early 1980s, this type of renewable energy began to develop and is still being used. Since the year 2000, the wind power industry has been spreading all over the world, especially in Germany, the USA, Denmark and Spain. It is not necessary to go deeply into the issue but the main factor that produces such a development is the good wind condition found in those countries.

As mentioned earlier, the development of the modern turbines began from the 80s decade. Since then, the wind power sector has undergone a vertiginous increase; thus, nowadays, wind power has become one of the main supports of the worldwide economy.

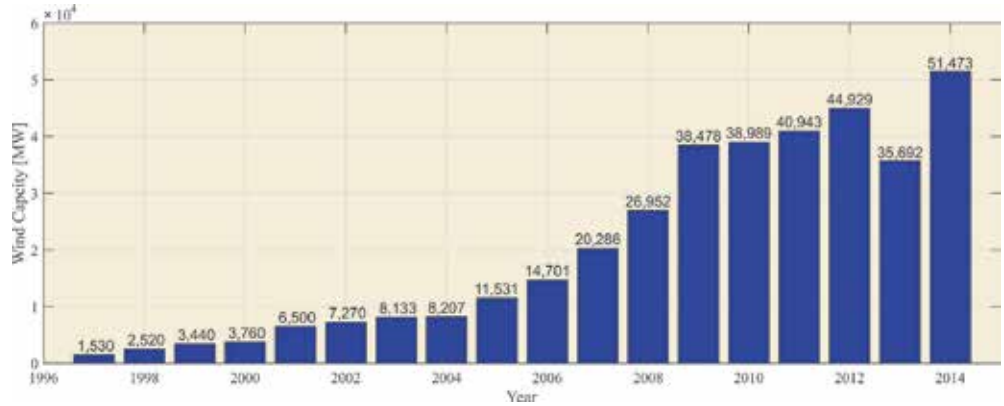

Figure 1. Global annual installed wind capacity 1997–2014. Adapted from reference [1].

http://dx.doi.org/10.5772/63432

According to the Global Wind Report created by the Global Wind Energy Council (GWEC), from 1996, the development of the world wind power has undergone a substantial increase. In 2010, this development was slowed down because of the crisis.

In **Figure 1**, variation of the global annual installed wind capacity in MW can be observed. In the aforementioned figure, it can be also observed how the crisis, as in all sectors, slowed down the development of the world installed power.

In **Figure 2**, the increase in the wind power that was produced worldwide, for several regions, can be perceived. It is important to take into account that the wind capacity development was different depending on the continent. It seems logical that in underdeveloped countries, there is a lower economic capacity to install this energy. Nevertheless, in 2014, a new increase in the wind capacity was produced.

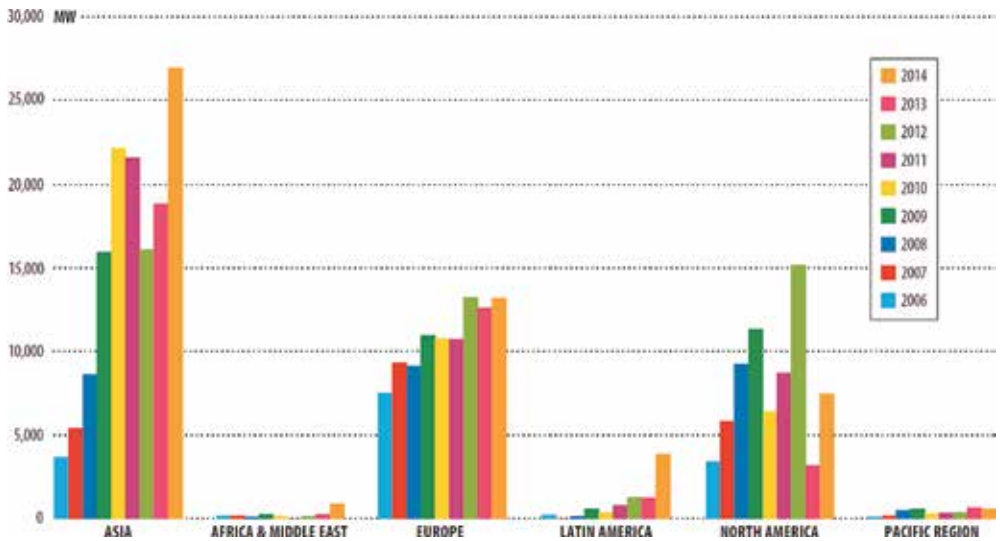

Figure 2. Annual installed wind capacity by region 2006–2014. Adapted from reference [1].

In the aforementioned figure, various details can be observed:

- First, the current power installed in Europe and North America was gradually increased until 2010, when it experienced the crisis.
- Second, the crisis has not influenced the wind power sector in Asia where the production even increased in 2010.
- Third, the installed power in Europe, Asia and North America is substantially higher than in other regions such as Latin America, Africa, the Middle East and the Pacific.
- Finally, it can be observed that in Latin America, Africa, Middle East and Pacific, production begins to increase gradually.

Although it is foreseen that the conventional installed wind power will continue to increase, sooner or later this growth will stop. Due to the fact that this moment is close in certain countries, the study, development and implementation of the small-wind energy will be a good point to continue working.

Although small-wind turbines (SWTs) do not supply as much power as bigger ones, their implementation has a wide range of possibilities because they can be located in other places such as roofs. In addition, they can work in isolated power systems and supply without any other means of alternative energy when the average wind speed allows it.

Of course, this option does not imply the total retirement of other types of energies such as the nuclear or thermal ones. However, this may imply the reduction in the amount of thermal and nuclear power stations in those places. In this way, each citizen may self-supply part of his daily energy. If a whole country is considered, the produced energy will be substantially reduced as well as the harmful effects on the environment. Both wind powers have been exhaustively studied, giving different kinds of settings.

The USA is the country with the largest development of the small-wind industry. In 2009, the USA had an installed wind capacity of 100 MW, and it has a prevision of exponential growth in the upcoming years. In the same continent, Canada has the aim of reaching 60 MW capacity.

In Europe, the country that has developed this energy the most is the UK due to the implementation of several strategies. These strategies establish that by 2050, 30–40% of the energy demand will be covered by microgeneration technologies.

In France and Italy, there is a trend for this type of energy with plans and decrees that enact the installation of small-wind power. Portugal strongly promotes this industry with the Decree 362/2oo7, where subsidies and bonuses for the small-wind energy producers are established. This makes a total difference with the traditional wind energy, unlike countries such as Spain.

In Spain, small-wind energy, despite its numerous advantages, is not developed enough due to legislative, economic, technological and social barriers. Despite its low development, the people in charge of this industry state that this renewable energy has great potential.

The key to increase the production and to decrease the costs is the development of new materials and new manufacturing techniques.

2. Description of the methodology

2.1. Introduction

This chapter presents a methodology to optimise the efficiency of SWTs. To test this methodology, it is necessary to create a model of the whole system. To optimise the system, two aspects are considered:

- The aerodynamic factor: The maximum power point tracker (MPPT) [2] is calculated to extract the maximum energy from the wind [3]. Using the MPPT and the SWT operating

http://dx.doi.org/10.5772/63432

surfaces, the optimal relationship between the continuous voltage of the rectifier and the grid power can be determined. This relationship must be set in the inverter, and it is known as the maximum power characteristic curve (MPCC).

- The capacitor bank effect: When a capacitor bank is connected, the armature reaction produces a magnetising effect in the electrical machine that is added to the magnetic field generated by the magnets. Therefore, a higher voltage at the machine terminals is generated [4, 5]. Then, before connecting a capacitor bank, some subjects have to be analysed. It must be verified that

○ The current increment, which produces the capacitor bank, does not damage the electrical machine windings. It should be noticed that if this methodology is used in a commercial SWT, the winding wire diameter cannot be changed. Thus, this current increment must be limited.

○ The magnetic saturation increment, which produces the capacitor bank, does not increase the iron losses too much.

2.2. Obtain the MPPT of an SWT

To be able to understand the calculation of MPCCs, you should first understand how the SWT operates. Thus, you will study the maximum power that can be extracted from the wind kinetic energy and the main characteristic parameters of the SWTs.

To perform this study, it is necessary to start from the beginning, the wind. As it is known, the wind is made up of particles in motion. In this way, when these particles find in their path an element (SWT blades) that can rotate about a shaft (either horizontal or vertical), they make it rotate. And if this shaft has got an electrical machine, the electricity is generated.

The air mass before passing through the SWT has got a kinetic energy. This kinetic energy can be expressed according to Eq. (1).

$$E_c = \frac{1}{2} m u^2 \tag{1}$$

where E_c is the air kinetic energy (J), m is the air mass (kg) and u is the air velocity (m/s).

The wind, in its path through SWT blades, suffers a decrease in its speed or what is the same a decrease in its kinetic energy. This lost kinetic energy is transformed, by means of the SWT blades, into mechanical energy. And the electrical generator transforms this mechanical energy into electrical energy [6].

To follow, a study of the air performance, when it passes through the SWT, will be made. This study led us to obtain an expression to calculate the maximum mechanical power that can be extracted from the wind. For this analysis, an air stream tube will be considered (**Figure 3**). This tube is formed by air lines in the laminar regime, parallel to the wind and with an axial symmetry.

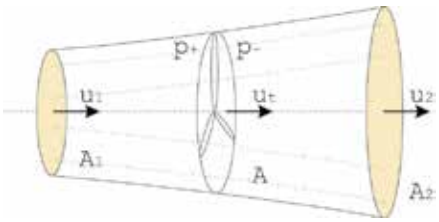

Figure 3. Airflow before and after wind turbine.

In the stream tube, the following parameters can be seen: air velocity at inlet of tube u_1 (m/s), air velocity at outlet of tube u_2 (m/s), air velocity in turbine u_h (m/s), air pressure before the turbine p_+ (Pa), air pressure after the turbine p_- (Pa), area at inlet of tube A_1 (m^2), area at outlet of tube A_2 (m^2) and area of the tube in turbine A (m^2).

Let us consider the mechanical power P_w extracted from wind as the loss of air kinetic energy due to its passage through the SWT, then the following equation can be obtained:

$$P_w = \Delta\varepsilon_c = \varepsilon_{c1} - \varepsilon_{c2} = \frac{1}{2}mu_1^2 - \frac{1}{2}mu_2^2 = \rho u_h \frac{\pi d^2}{4}\left(\frac{1}{2}u_1^2 - \frac{1}{2}u_2^2\right) \tag{2}$$

where E_{c1} is the kinetic energy at inlet of tube (J), E_{c2} is the kinetic energy at outlet of tube (J), ρ is the air density (kg/m^3) and d is the diameter of turbine blades (m).

Studying the Froude's theorem [6], it can be understood that the air average velocity in its passage through the stream tube is the arithmetic mean of u_1 and u_2. Thus:

$$u_h = \frac{u_1 + u_2}{2} \tag{3}$$

Eq. (3) can also be obtained as follows:

- The air velocity at inlet of tube u_1.
- The air velocity, as it approaches the turbine, is modified. In this way, its value will be u_1 minus an axial-induced velocity, which is known as u_a (**Figure 3**).

Consequently, it can be established that:

$$u_a = au_1 \tag{4}$$

$$u_h = u_1 - u_a \tag{5}$$

Or what is the same:

http://dx.doi.org/10.5772/63432

$$u_h = u_1(1-a) \tag{6}$$

Thus, the velocity u_2 will be:

$$u_2 = u_1(1-2a) \tag{7}$$

where a is the induced axial velocity coefficient, which is opposed to velocity u_1.

Thus, Eq. (2), (6) and (7) yield the following relation:

$$P_w = \frac{1}{2}\frac{\pi d^2}{4}\rho u_1^3(1-a)(1-(1-2a)^2) \tag{8}$$

The next step will be to derive Eq. (8) with respect to a and make it equal to zero. Then, the value of a, for which P_w is maximised, will be obtained.

$$\frac{\partial P_w}{\partial a} \rightarrow a = \frac{1}{3} \tag{9}$$

Thus, if a = 1/3 is replaced with Eq. (8), the following equation is obtained:

$$P_{w,max} = \frac{16}{27}\left(\frac{1}{2}\frac{\pi d^2}{4}\rho u_1^3\right) \tag{10}$$

Eq. (10) is usually expressed in a dimensionless way as the power coefficient (C_p):

$$C_p = \frac{P_w}{\frac{1}{2}\cdot\frac{\pi d^2}{4}\rho u_1^3} \tag{11}$$

Thus, C_p represents the percentage of power extracted from the wind kinetic energy. The maximum value that C_p might take is 16/27 = 0.593. This value is called *Betz limit* [7] and provides the maximum mechanical power P_w that can be extracted from wind kinetic energy, regardless of SWT type. In summary, no SWT will be able to extract more wind power than the *Betz limit* states.

The *Betz limit* is an upper limit. However, it does not mean that all SWTs can extract that upper limit. In fact, the *Betz limit* does not take into account several parameters that reduce this upper limit. Some of these parameters are aerodynamic roughness of blades due to their ageing, lost energy due to wake generated by the rotation, air properties, interference of blades, direction of SWT (ψ), pitch angle (β) and SWT shape.

In this way, C_p will be a function of the SWT diameter, wind speed, air density, air viscosity, blade roughness, SWT shape, SWT rotation speed and SWT angles.

Of all these parameters, the viscosity and the roughness can be initially ignored due to their small influence on the final results. The SWT orientation can be also ignored because the SWT is usually orientated in the wind direction. Furthermore, if you have a SWT-specific shape, it can also be assumed that C_p does not depend on it.

Thus, it is concluded that for this study C_p will be function of diameter d, wind speed u_h, SWT rotation speed ω and pitch angle β.

$$C_p = f(d, u_h, \omega, \beta) \tag{12}$$

Taking all this into account, it seems logical to think in a coefficient that includes all these parameters. This coefficient is the tip-speed ratio λ, and it is defined as:

$$\lambda = \frac{Speedo\ frotortip}{Windspeed} = \frac{\frac{\omega d}{2}}{u_h} \tag{13}$$

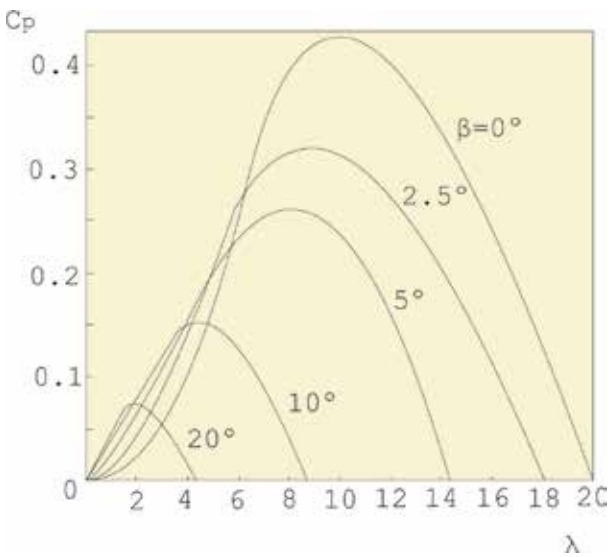

Figure 4. Typical family of curves $C_p(\lambda)$ for various values of β. Adapted from reference [6].

Figure 4 shows an example of the relationship $C_p(\lambda)$, for different values of β. Paying close attention to this figure, it can be seen that the maximum value of C_p is close to 0.4 and not to 0.593, as predicted by the *Betz limit*. This difference is due to the parameters that were not taken into account when the *Betz limit* was calculated, such as shape and interference of blades.

http://dx.doi.org/10.5772/63432

In addition, that figure also shows that for each value of β there is a value of λ that maximises C_p. It is important to understand this fact because MPCCs will be always defined in order to optimise the SWT electrical generation (working with the maximum value of C_p).

Other point to consider might be the influence of the SWT type on the relationship C_p (**Figure 5**). This figure allows us to identify the families of turbines that produce a higher value of C_p and consequently a higher efficiency. These families are one-bladed, two-bladed and three-bladed. That is the reason why the worldwide major manufacturers usually produce those types of turbines.

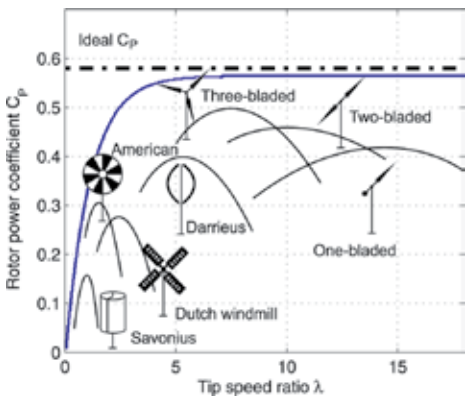

Figure 5. Typical family of curves $C_p(\lambda)$ for different SWT types.

Having explained all this, a simple study of forces occurring in SWT blades will be developed. In **Figure 6**, you can see that when the wind u_h hits a blade, a component u_g appears due to the displacement or blade rotation. The addition of these two components will result in the vector c.

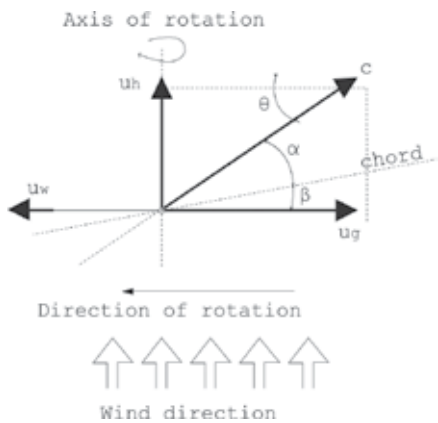

Figure 6. Velocities acting on a blade of a horizontal SWT.

On one hand, the wind component u_h will allow us to calculate the forces that arise on the blade at the turbine input. On the other hand, component c will allow us to do the same, but in this case, at the turbine output. Moreover, three angles will be defined: angle between the blade chord and c, called *attack angle* (α), angle between the rotation plane and c (θ) and angle between the blade chord and the rotation plane, called *pitch angle* (β).

The resultant force F (in its aerodynamic centre) will be used to calculate the SWT speed. That force will be obtained either with the SWT input wind u_h or with the SWT output wind c:

- Forces at the SWT input: In this case, the wind, which hits the blade at the input u_h, produces two kinds of forces: one in the direction of rotation axis F_{axial} and another in the perpendicular direction. This last one causes the SWT rotation F_{torque}. Adding F_{axial} and F_{torque}, the resultant force F will be obtained (**Figure 7**).
- Forces at the SWT output: In the other case, if the vector F is decomposed according to the direction of the apparent velocity c and its perpendicular, the drag force F_{drag} and the lift force F_{lift} will be obtained. The latter two forces are usually associated in a parameter, called L/D, where L is the lift force F_{lift} and D is the drag force F_{drag} (**Figure 7**).

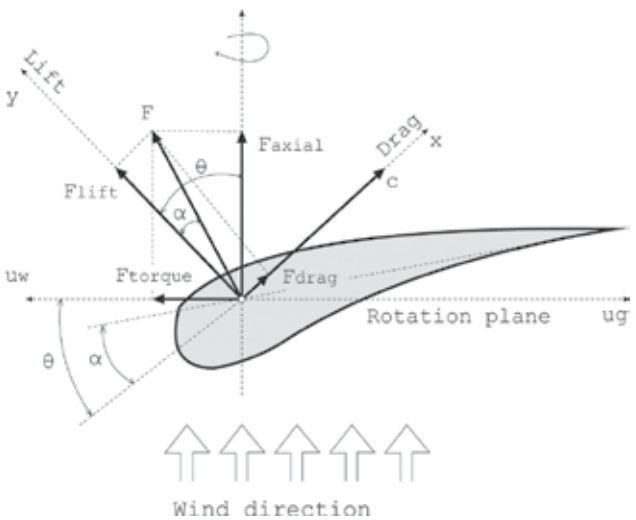

Figure 7. Forces acting on a blade of a horizontal SWT.

This parameter gives an idea of whether the blades are well designed or not. On one hand, the lower the value of L/D is, the greater the influence of F_{drag} will be and the lower the blade speed u_w will be. And on the other hand, the higher the value of L/D is, the greater the influence of F_{lift} will be and the higher the blade speed u_w will be.

Eq. (14) allows us to calculate an initial value of C_p. This relation assumes that C_p depends on λ, L/D and N (number of SWT blades). This equation is known as correlation of Wilson (1976) worldwide [8].

http://dx.doi.org/10.5772/63432

$$C_p = \frac{16}{27}\frac{\lambda}{\lambda + \frac{1.32 + \left(\frac{\lambda - 8}{20}\right)^2}{N^{2/3}}} - 0.57\frac{\lambda^2}{\frac{L}{D}\left(\lambda + \frac{1}{2N}\right)} \tag{14}$$

Although Eq. (14) is an expression that does not take into account many parameters, it will help us to achieve an initial power coefficient C_p. Once C_p is calculated, it will have to be reduced by means of a percentage. This reduction will help us to get a value of C_p which takes into account the rest of the parameters that were initially ignored. Thus, a value closer to the real one can be obtained.

Figure 8 shows an example obtained using Eq. (14), assuming $N = 3$. In the figure, it can be clearly seen, as it had been previously deduced from the study of wind forces, that higher values of L/D produce higher power coefficients C_p and therefore, higher mechanical powers P_w.

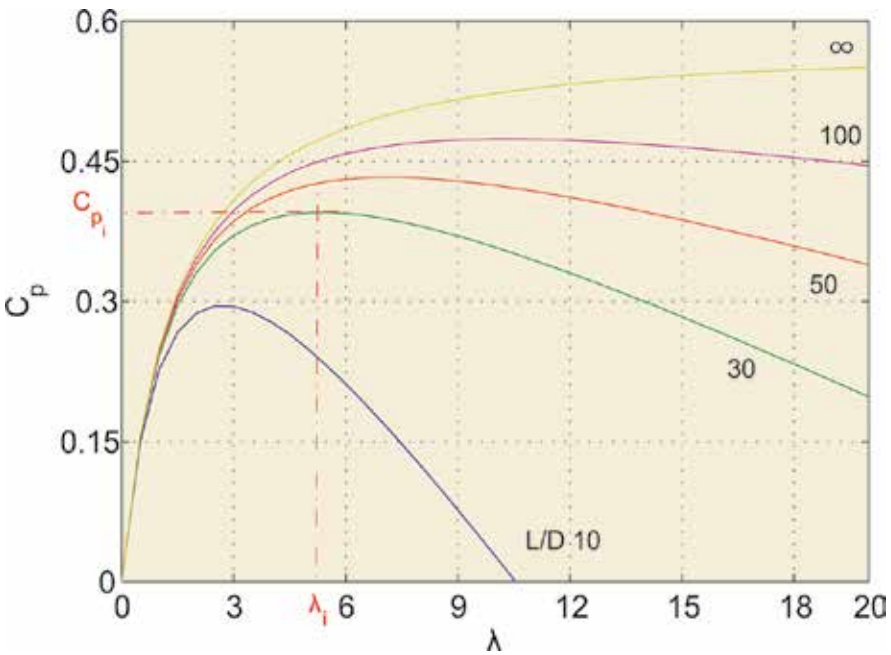

Figure 8. Example of C_p vs. λ for several values of L/D.

During the design of the SWT blades, you will have to make sure that the combination of the parameters λ and L/D produces a maximum value of C_p. That is the reason why a constant relation L/D along the entire blade is searched for. Therefore, it is easy to understand that each SWT will have its own relation L/D.

Eq. (11) and (14) yield the following relation:

$$P_w = \left(\frac{1}{2}\frac{\pi d^2}{4}\rho u_1^3\right)\left(\frac{16}{27}\frac{\lambda}{\lambda + \frac{1.32 + \left(\frac{\lambda - 8}{20}\right)^2}{N^{2/3}}} - 0.57\frac{\lambda^2}{\frac{L}{D}\left(\lambda + \frac{1}{2N}\right)}\right) \tag{15}$$

Using Eq. (15), the value of P_w can be obtained, for

- Constant values of N, d, ρ and L/D.
- Different values of n and u_h, where u_h is obtained from Eq. (6), and n is the SWT rotation speed (rpm) and can be obtained as,

$$n[rpm] = \omega\left[\frac{rad}{s}\right]\cdot\frac{60}{2\pi} \tag{16}$$

In the example of **Figure 9**, the relationship $P_w(n)$, for various wind speeds u_h, can be seen. Paying close attention to this figure and assuming a constant wind speed u_h, two conclusions can be drawn: (1) When the SWT rotation speed n increases, the mechanical power in the shaft P_w also does it and (2) P_w increases up to a maximum value from which it decreases.

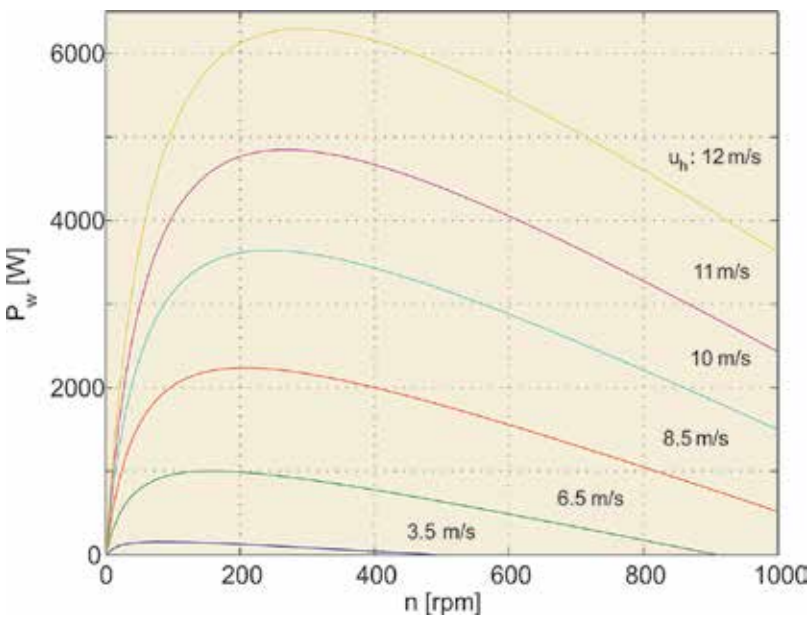

Figure 9. P_w vs. n for various wind speeds u_h and assuming $L/D = 30$.

http://dx.doi.org/10.5772/63432

Having explained this, it is easy to understand that if any change was introduced in the SWT, it should be studied whether this modification varies the value of λ or not. Analysing **Figure 8** and assuming $L/D = 30$, you can observe that for a value of $\lambda = \lambda_i$, the corresponding value C_{pi} is maximum. Thus, if some parameters of which are mentioned above are modified, it is very likely that the value of λ also varies, by moving either left or right. Therefore, the increase or decrease in λ causes a reduction in the power coefficient C_p and with it a drop in mechanical power P_w.

SWTs are designed in order to maximise the value of C_p. In this way, if any change is introduced into the system, it is important to verify that the tip-speed ratio λ remains constant. For this reason, all MPCCs that will be entered in the inverter are calculated in order to ensure a specific constant value of λ_i.

To get this value of λ_i, it is required that for all wind speeds u_{hi}, the SWT turns at a specific speed n_i. In other words, to get a maximum mechanical power P_{wi}, it will be necessary that

- The value of λ_i is constant.
- The value of λ_i provides the maximum power coefficient C_{pi} (**Figure 8**).

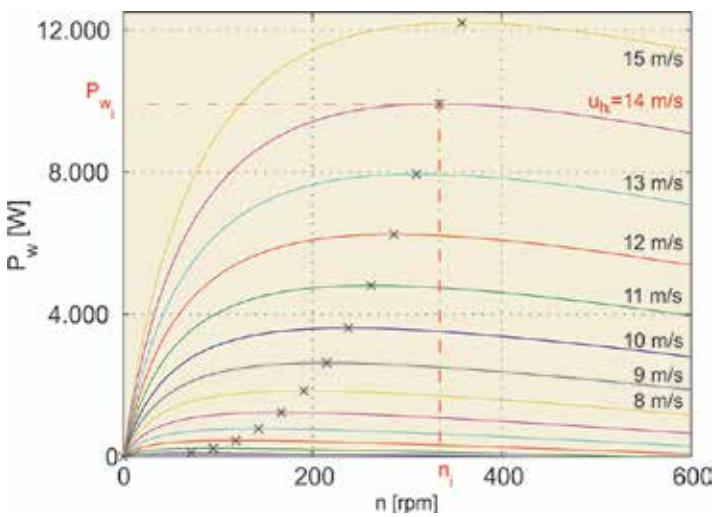

Figure 10. Maximum power point tracker (MPPT), assuming $L/D = 30$. P_w vs. n for several values of u_h.

The example of **Figure 10** shows the maximums of P_w for every wind speed u_h (highlighted points). Therefore, if a maximum mechanical power P_{wi} wants to be obtained for a specific wind speed u_{hi}, it will be necessary to turn the SWT to a particular rotation speed n_i.

If all these maximums are plotted in a new curve, the relationship $P_{w,max}(n)$ is obtained (**Figure 11**). This curve is known as the maximum power point tracker (MPPT).

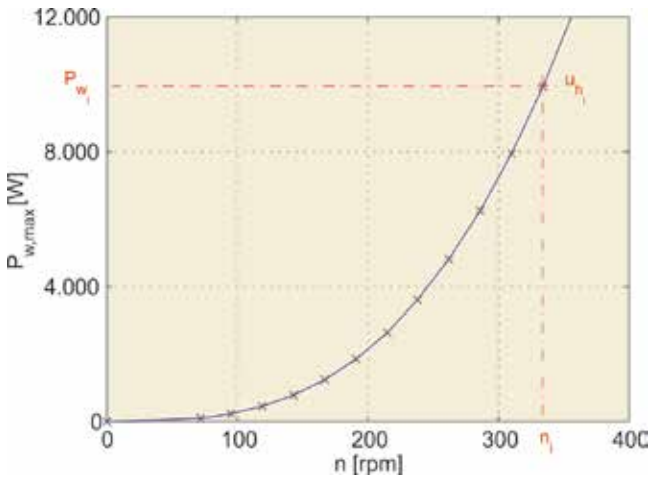

Figure 11. Maximum power point tracker (MPPT), assuming $L/D = 30$. Curve created with the maximums of P_w.

Figure 11 has the special characteristic that all its points provide a maximum value of P_w and consequently a maximum value of C_p. That is the reason why all the points have associated a constant value of λ.

Moreover, considering Eq. (17), which relates mechanical power P_w with torque T_w and with rotation speed ω, the optimal relationship between T_w and n can be also obtained. It will be known as maximum torque point tracker (MTPT; see e.g. in **Figure 12**):

$$P_w = T_w \omega \tag{17}$$

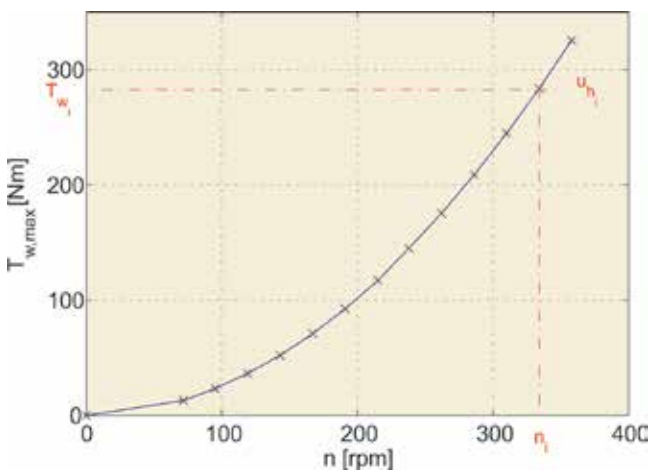

Figure 12. Maximum torque point tracker (MTPT), assuming $L/D = 30$.

http://dx.doi.org/10.5772/63432

2.3. Capacitor banks in an SWT

As it is known, if the electrical machine is working in the no-load test, it provides a rated voltage v_o at the output of the machine. Then, if an electrical load is connected to the machine output, the voltage v_o is reduced. This reduction is due to the emergence of a current in the armature winding that generates a voltage drop in that winding. Moreover, it also produces a magnetomotive force, which reacts with the magnetomotive force generated by the inductor. In this way, the air-gap magnetic flux is modified [5].

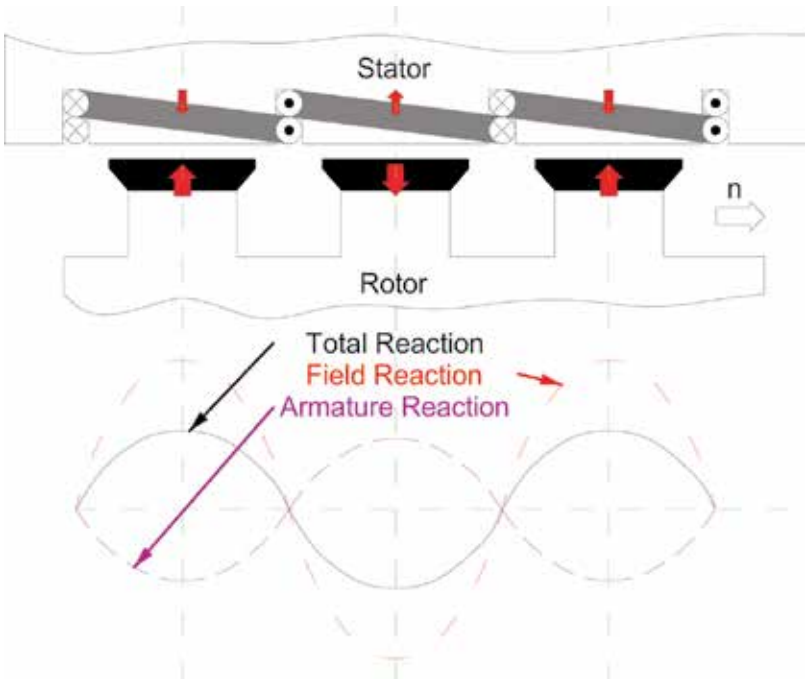

Figure 13. Magnetic field behaviour inside an electrical generator, connecting an inductive load.

Depending on the type of load that is connected to the output of the electrical machine, this effect may vary. On one hand, if an inductive load is connected to the electrical machine output, then the magnetomotive force caused by the armature reaction goes against the magnetomotive force caused by the inductor. This effect is known as the demagnetising effect (**Figure 13**).

On the other hand, if a capacitive load is connected to the electrical machine output, the opposite happens. The magnetomotive force caused by the armature reaction is additive to the magnetomotive force caused by the inductor. This effect is known as the magnetising effect (**Figure 14**).

Thus, an increase in the electrical machine magnetic field can be obtained by connecting a capacitor bank to the electrical machine output.

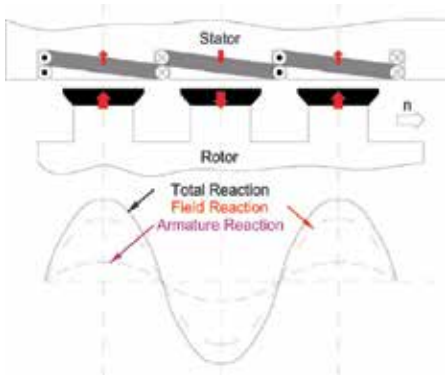

Figure 14. Magnetic field behaviour inside an electrical generator, connecting a capacity load.

2.4. Methodology for calculation of the optimal capacitor bank and the MPCCs

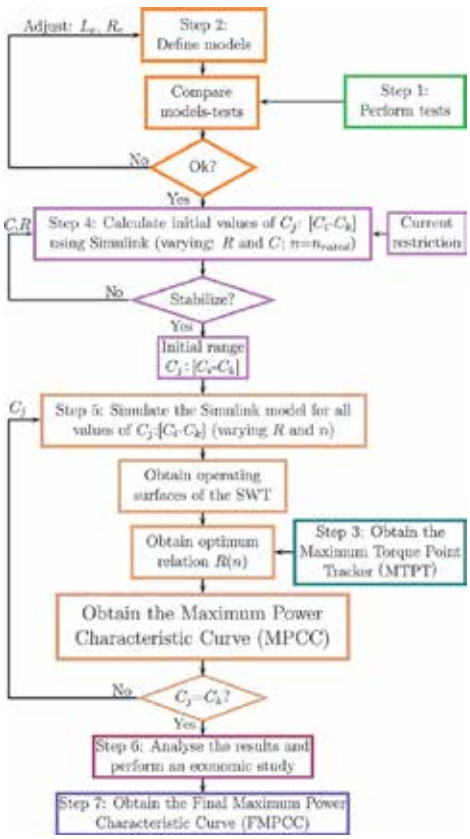

Figure 15. Flowchart of the methodology.

http://dx.doi.org/10.5772/63432

Figure 15 presents the flowchart for calculating the optimal capacitor bank and associated MPCC. The steps of the methodology are as follows:

Step 1: Perform several tests on the real SWT. At a minimum, a no-load test and a rated load test should be carried out.

Step 2: Define a system model.

A system model is needed in order to use the methodology presented here (i.e. using Matlab Simulink or using Finite Element Methods). Such a model makes it possible to analyse the SWT in detail and to evaluate its performance under various operating conditions.

The different parts of the SWT model are electrical machine, rectifier, grid power control (inverter and grid) and capacitor bank (**Figure 16**).

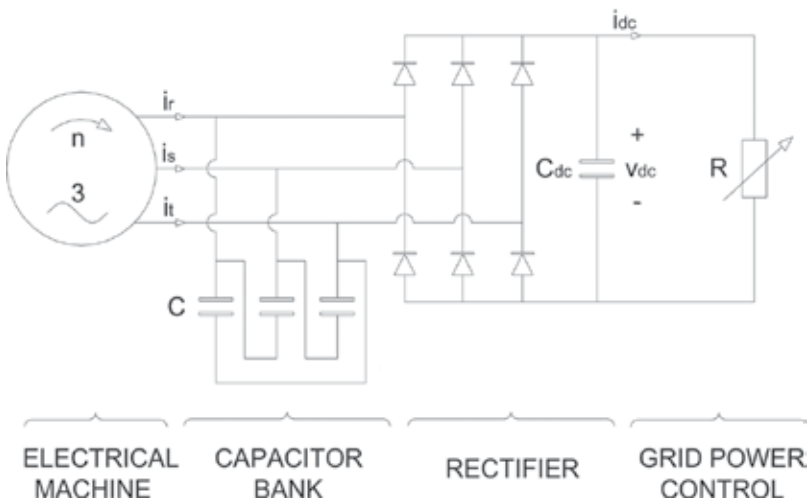

Figure 16. Wind power generation system.

Adjust model parameters by comparing simulation results with those obtained in Step 1. Thus, a reliable model of the system can be defined (**Figure 16**).

Step 3: Calculate the MTPT to extract the maximum power of the wind.

Using the SWT-rated parameters and Eq. (11) and (17), the optimal relationships $P_w(n)$ and $T_w(n)$ can be obtained (**Figures 11** and **12**).

Note that the MTPT must remain unchanged for every value of the variable resistor R. Therefore, MTPT in 3D can be represented as a parallel surface to axis R (**Figure 17**).

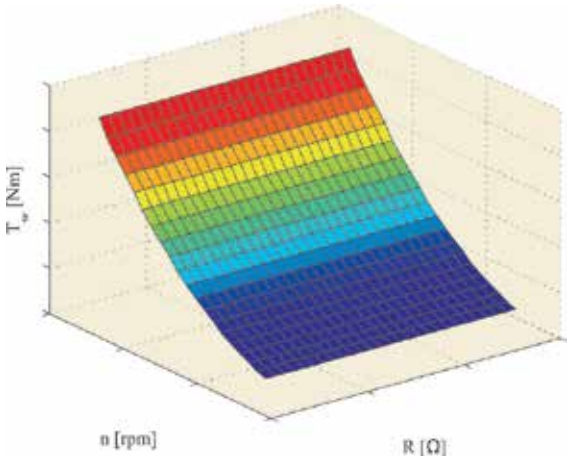

Figure 17. MTPT in 3D.

Step 4: Calculate a capacity range [C_i–C_k], which contains the optimal capacitor C.

In order to find this range, a simulation will be performed varying R and C for the SWT-rated speed. The initial ranges of R and C must be wide enough to effectively analyse the SWT performance.

Figure 18 indicates that by increasing the capacity C for each value of R, the power injected into the grid P_{grid} increases up to a maximum capacity C_{max}, from which point P_{grid} decreases. Thus, the value of C_{max} that maximises the P_{grid} is obtained.

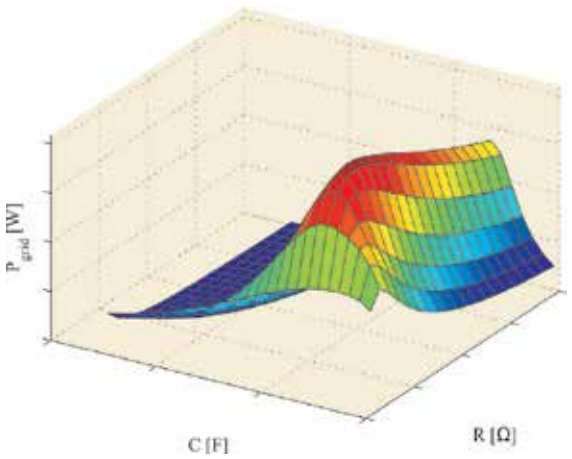

Figure 18. Grid power P_{grid} vs. resistor R and capacity C for the rated speed n_r.

However, the value of C_{max} must be controlled because it could also increase the current $i_{r,s,t}$ flowing into the electrical machine windings and thereby cause damage (**Figure 16**). Therefore,

http://dx.doi.org/10.5772/63432

it is important to know the winding wire diameter to determine the maximum current $i_{r,s,t,max}$ that can flow through the windings.

Once the value of $i_{r,s,t,max}$ is known, the capacity range [C_i–C_k] can be obtained by means of drawing a perpendicular surface to the axis $i_{r,s,t}$ (see an example in **Figure 19**).

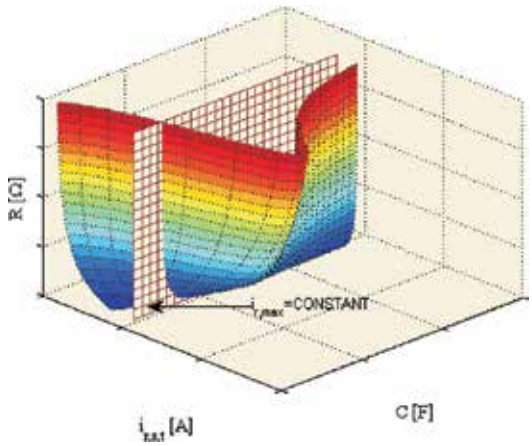

Figure 19. Relationship $R(C)$ not exceeding the restriction of $i_{r,s,t,max}$ and for the SWT-rated speed. Winding current $i_{r,s,t}$ vs. resistor R and capacity C.

By representing the intersection of both surfaces on the plane C–R (**Figure 20**), the capacity values that might be connected, for different values of the resistor R, can be determined. In this way, the current value that could damage the electrical machine will not be reached. So, the capacity range [C_i–C_k] is determined.

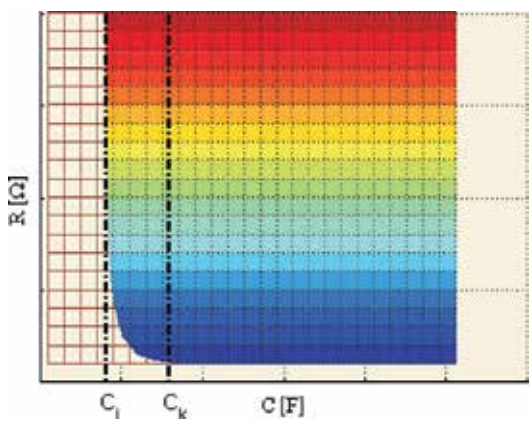

Figure 20. Relationship $R(C)$ not exceeding the restriction of $i_{r,s,t,max}$ and for the SWT-rated speed. Capacity C vs. variable resistor R.

Step 5: Obtain MPCCs for several values of C.

Perform simulations, varying n and R, for constant values of C within the range $[C_i–C_k]$. It should be borne in mind that the more the values of C you test, the more accurate the results will be. For each value of C, the following steps need to be performed:

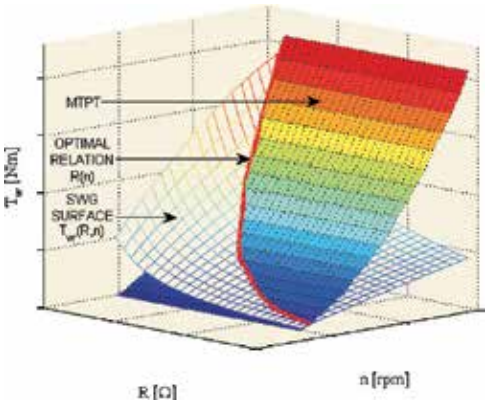

Figure 21. 3D Intersection between the MTPT and the SWT operating surface $T_w(R,n)$.

- **Step 5.1**: Use the system model to determine the SWT operating surface $T_w(R,n)$. Then, obtain the intersection of that surface with the MTPT (**Figure 21**). Thus, the relationship $R(n)$ for maximum mechanical power extraction from wind is given (**Figure 22**).
- **Step 5.2**: Project the optimal relationship $R(n)$ perpendicular to the R-n plane (**Figure 23**).
- **Step 5.3**: Use the model to determine the SWT operating surfaces $P_{grid}(R,n)$ (**Figure 23**) and $v_{dc}(R,n)$ (**Figure 24**). After that, derive the intersection of those SWT surfaces with the surface obtained in Step 5.2. In this way, the optimal relationships $P_{grid}(n)$ and $v_{dc}(n)$ will be determined.

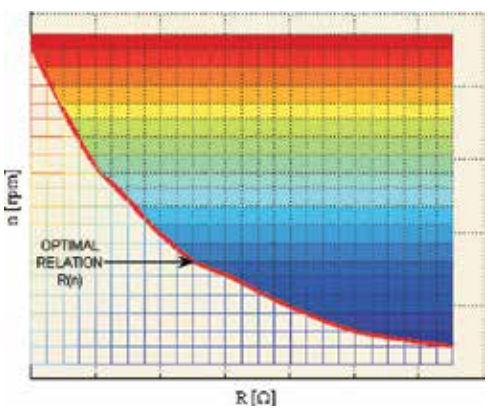

Figure 22. Intersection between the MTPT and the SWT operating surface $T_w(R,n)$. Optimal relationship $R(n)$.

http://dx.doi.org/10.5772/63432

- **Step 5.4**: Finally, combining the values of $P_{grid}(n)$ and $v_{dc}(n)$, the optimal relationship $P_{grid}(v_{dc})$, also known as the MPCC, can be easily determined (**Figure 25**).

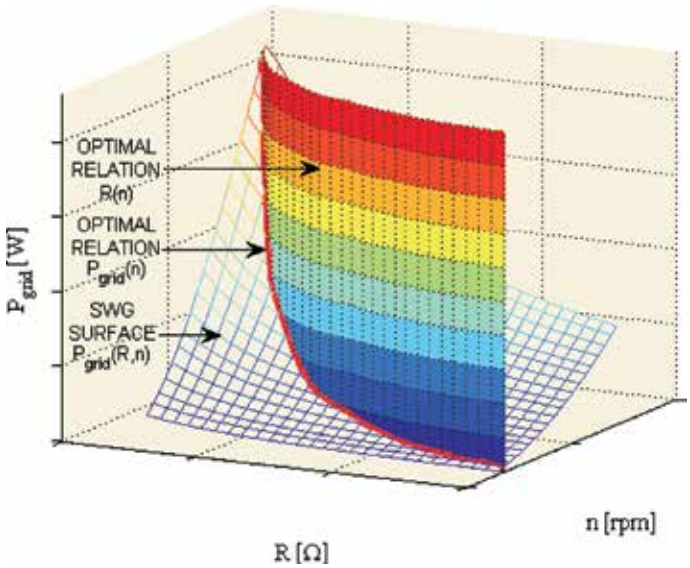

Figure 23. Three-dimensional intersection between the optimal relationship $R(n)$ and the SWT operating surface $P_{grid}(R,n)$.

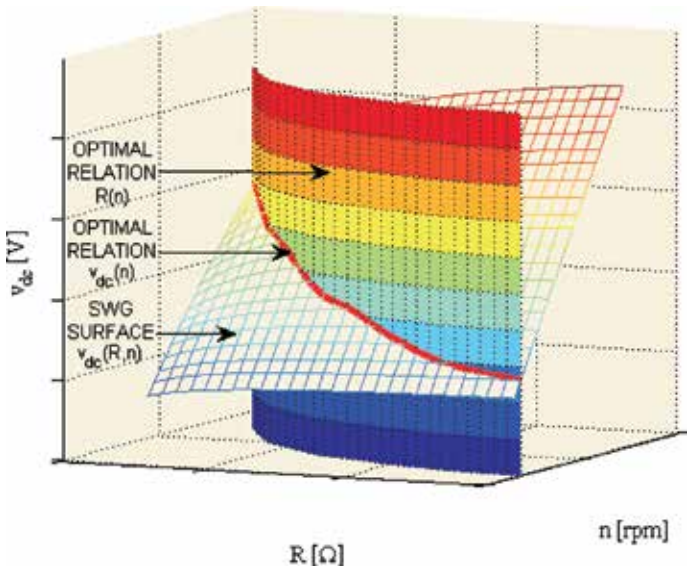

Figure 24. Three-dimensional intersection between the optimal relationship $R(n)$ and the SWT operating surface $v_{dc}(R,n)$.

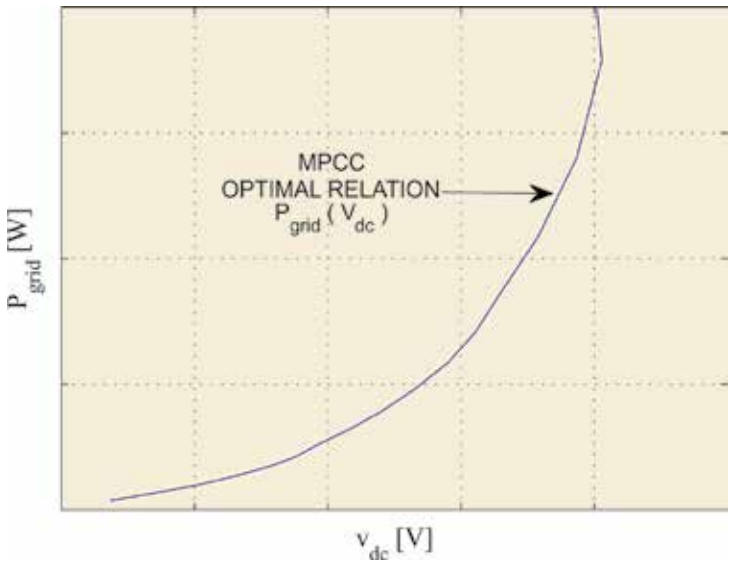

Figure 25. Maximum power characteristic curve (MPCC): grid power P_{grid} vs. rectifier DC voltage v_{dc}.

By repeating Steps 5.1 to 5.4 for each value of *C*, the additional MPCCs can be obtained.

Step 6: Analyse the results and perform an economic study.

To perform the analysis, the well-known Weibull distribution (WD) will be used [3, 9, 10]. This distribution is defined as:

$$W(u_h) = \frac{K}{u_h}\left(\frac{u_h}{u_m}\right)^K e^{-\left(\frac{u_h}{u_m}\right)^K} \tag{18}$$

where K is the shape parameter of the WD, and u_m is the average wind speed.

Wind Class	u_m (10 m)	u_m (50 m)
1	0–4.4	0–5.6
2	4.4–5.1	5.6–6.4
3	5.1–5.6	6.4–7
4	5.6–6	7–7.5
5	6–6.4	7.5–8
6	6.4–7	7–8.8
7	7–9.4	8.8–11.9

Table 1. Wind classification according to average speed. Adapted from reference [11].

http://dx.doi.org/10.5772/63432

Nevertheless, if this distribution is going to be used, certain features of the location where the SWT will be placed need to be known. The National Renewable Energy Laboratory (NREL) defines seven different wind classes (WC). The WC is a function of the average wind speed u_m and the height at which the SWT will be located with respect to the ground (10 or 50 m) [11]. These WCs can be seen in **Table 1**.

Figure 26 represents the WD (Eq. 18) for a value of $K = 1.9$ and for average wind speeds listed in **Table 1** (assuming a height of 10 m).

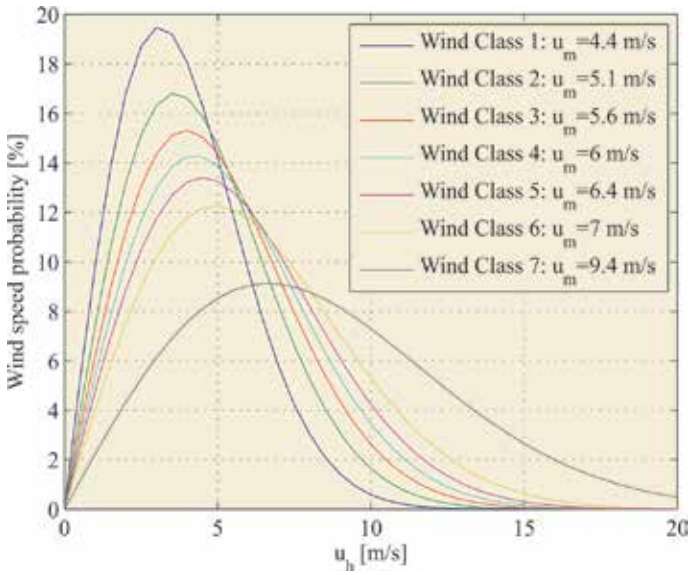

Figure 26. Weibull distribution for different WCs and a height of 10 m.

To compare the results obtained with different values of C, four parameters may be used: $P_d(u_h)$, E_{tot}, $\Delta\eta$ and $\Delta€$.

- $P_d(u_h)$ is the SWT power density and is defined as:

$$P_d(u_h) = W(u_h)\frac{P_{grid}(u_h)}{P_{rated}} \tag{19}$$

where P_{grid} (u_h) is the grid power for each wind speed u_h, and P_{rated} is the rated power of the SWT.

- E_{tot} is the annual total energy that can be produced by the SWT. It is obtained from the following equation:

$$E_{\text{tot}} = 8760\left[\frac{hours}{year}\right]\sum\left(W(u_h)P_{grid}(u_h)\right) \tag{20}$$

- $\Delta\eta$ represents the increment in annual total energy injected into the grid (E_{tot}) for different capacitor banks ($C = C_j$), as compared to the case without a capacitor bank ($C = 0$).

$$\Delta\eta = \frac{E_{tot,C=C_j} - E_{tot,C=0}}{E_{tot,C=0}} \tag{21}$$

$\Delta€$ represents the annual financial benefit obtained by using different capacitor banks ($C = C_j$), as compared to the case without a capacitor bank (C = 0).

$$\Delta€ = \left(E_{tot,C=C_j} - E_{tot,C=0}\right).Energycost\left[\frac{€}{kWh}\right] \tag{22}$$

Step 7: Obtain the final maximum power characteristic curve (FMPCC).

To determine the FMPCC, it is necessary to calculate, for each wind speed u_h, the capacity C that supplies the maximum grid power P_{grid}. Thus, the optimal relationship $C(u_h)$ is calculated. The FMPCC will be made up of sections of the MPCCs that were obtained for different values of C.

3. Conclusions

The increasing development of small-wind energy has made it necessary to study new methods that improve their efficiency. This chapter presents a methodology to increase the SWT efficiency by using a capacitor bank. This methodology will use an electrical model to simulate the system.

It has been shown that connecting different capacitor banks to the system modifies SWT performance and the MPCC. The power obtained from the SWT increases as a result of connecting capacitor banks and is only limited by the maximum current that can flow through the electrical machine windings.

It must be taken into account that it is necessary to know the location of the SWT and the associated average wind speed in order to connect the optimal capacitor bank.

The methodology described in this work could be used by electrical machine manufacturers to optimise the efficiency of SWTs [12] or to reduce the generator size because a new electrical machine with a capacitor bank would include the following modifications in order to obtain the same power: less copper (the capacitor bank decreases the current that flows through the electrical machine), smaller magnet size (magnetising effect of the capacitors) and fewer magnetic plates.

http://dx.doi.org/10.5772/63432

If these modifications are included in SWT design, manufacturing costs would decrease substantially and even more so in the case of higher WCs.

Nomenclature

a: Induced axial velocity coefficient.

A: Area of tube in turbine (m^2).

A_1 & A_2: Area at inlet and outlet of tube (m^2).

c: Apparent wind speed (m/s).

C: Capacitor (F).

d: Swept diameter of the SWT blades (m).

E_{c1} &E_{c2}: Kinetic energy at inlet and outlet of tube (J).

E_{tot}: Annual total energy extracted from SWT (kWh).

F: Resultant force on SWT blade (N).

F_{axial}: Axial force on SWT blade (N).

F_{torque}: Force that causes the turn of SWT blade (N).

F_{drag}: SWT drag force (N).

F_{lift}: SWT lift force (N).

$i_{r,s,t}$: Electrical machine phase current (A).

K: Shape parameter of the Weibull distribution.

m: Air mass (kg).

n: SWT rotation speed (rpm).

N: Number of SWT blades.

P_d: SWT power density (kWh).

P_{grid}: Electrical power injected to the grid (W).

P_{rated}: SWT-rated power (W).

P_w: Mechanical power extracted from wind (W).

p_+ &p_-: Air pressure before and after turbine (Pa).

R: Variable resistor (Ω).

T_w: Torque in the shaft of the SWT (Nm).

u: Wind speed (m/s).

u_1 &u_2: Wind velocity at inlet and outlet of tube (m/s).

u_a: Induced axial velocity (m/s).

u_g: Wind velocity due to rotation of blades (m/s).

u_h: Wind velocity in turbine (m/s).

u_m: Wind average speed of the Weibull distribution (m/s).

v_{dc}: DC voltage (V).

v_o: Rated voltage at the output of the electrical machine (V).

u_w: Linear velocity of SWT blades (m/s).

W: Weibull distribution.

α: Attack angle [°].

β: Pitch angle [°].

θ: Angle between the rotation plane and c [°].

λ: Tip-speed ratio.

ρ: Air density (kg/m^3).

ψ: {SWT orientation angle with respect to air (°).

ω: SWT angular speed (rad/s).

Author details

Alberto Arroyo*, Mario Manana, Pablo B. Castro, Raquel Martinez, Ramon Lecuna and Juan Carcedo

*Address all correspondence to: arroyoa@unican.es

University of Cantabria, Santanderm, Spain

References

[1] Pullen A. and Sawyer S. Annual Market Update 2010. Global Wind Report. Global Wind Energy; 2010, Brussels, Belgium.

[2] Kesraoui M., Korichi N., and Belkadi A. Maximum power point tracker of wind energy conversion system. Renewable Energy. 2011;36:2655–2662.

[3] Milivojevic N., Stamenkovic I., and Schofield N. Power and energy analysis of commercial small wind turbine systems. In: Industrial Technology (ICIT); 2010. p. 1739–1744.

[4] Fuchs E.F., Vandenput A.J., Holl J., and White J.C. Design analysis of capacitor-start, capacitor-run single-phase induction motors. Energy Conversion. 1990;5:327–336.

[5] Umans C., Fitzgerald S., and Kingsley A.E., editors. Electric Machinery. McGraw Hill; 2003, New York.

[6] Rodríguez S., Arnalte J.L., and Burgos J.C., editors. Electric systems of Electric Power Production. Spain: Editorial Rueda S.L.; 2003. 450 p.

[7] Kuik G.A.M., editor. The Lanchester Betz Joukowsky limit. Wind Energy. 2007;10:289-291. DOI: 10.1002/we.218

[8] Wilson R.E. and Lissaman B.S. Aerodynamic Performance of Wind Turbines. Office of Science. U.S. Department of Energy; 1976, United States.

[9] Sathyajith M., editor. Wind Energy. Fundamentals, Resource Analysis and Economics. Springer; 2006. The Netherlands. DOI: 10.1007/3-540-30906-3.

[10] Yu Z. and Tuzuner A. Wind speed modeling and energy production simulation with Weibull sampling. In: Power and Energy Society General Meeting. Conversion and Delivery of Electrical Energy in the 21st Century, IEEE; 2008. p. 1–6.

[11] Elliot D.L., Holladay C.G., Barchet W.R., Foote H.P., and Sandusky W.F., editors. Wind Energy Resource Atlas of the United States. Golden, CO: U.S. Department of Energy Pacific Northwest; 1986.

[12] Arroyo A., Manana M., Gomez C., Fernandez I., Delgado F., and Zobaa A. A methodology for the low-cost optimisation of small wind turbine performance. Applied Energy. 2013;104:1–9. DOI: 10.1016/j.apenergy.2012.10.068

Section 2

Control and Implementations In Wind Turbines

Chapter 8

Emulation of Wind Turbines

Diana Martinello, Emerson G. Carati,
Jean P. da Costa, Rafael Cardoso and
Carlos M. O. Stein

Additional information is available at the end of the chapter

http://dx.doi.org/10.5772/63448

Abstract

This chapter presents the modeling, simulation, and emulation for small wind turbine (WT) systems. The main objective of the emulation system is to reproduce the WT torque dynamic behavior in the generator shaft, which must be similar to one of real horizontal WTs used for distributed generation. The aerodynamic, mechanical, and electrical models for horizontal axis wind turbines (HAWTs) are presented in detail. The models are used for simulation analysis and emulation synthesis. The emulator consists a (i) computational platform, which is based on LabVIEW® environment and runs the model of the WT and (ii) an induction motor (IM) with AC power drive with torque control. The IM shaft is directly coupled with the real small wind generator and corresponding load. Experimental waveforms are also presented to demonstrate the functionality of the system.

Keywords: wind turbine, modeling, emulator, electrical generator, renewable energy, induction motor drive

1. Introduction

The increasing demand for electricity in addition to the need to minimize environmental problems such as global warming had led to the development of renewable sources for production of electricity in recent years. Among the alternative sources for power generation, wind-based generation is becoming increasingly common around the world, mainly due to government incentives and technological advances in recent years [1]. Thus, a worldwide growing number of large and small wind farms installed can be verified.

The design of wind to electricity conversion systems involves different kinds of generators, power electronics, and control, resulting in motivation for the development of numerous works. The analysis of the efficiency of a wind turbine (WT), based on an adequate simulation of its behavior, is an important step in the research and development of technologies for wind generation. A manufacturer needs tools and appropriate resources to test innovations and to evaluate their effects on the overall system. One possible and helpful tool uses a dedicated hardware and software that intends to emulate a real WT in a reduced scale. This tool is a so-called WT emulator.

A WT emulator uses a set of electrical machines (motor and generator) coupled by a shaft, driven by a converter, and controlled in real time by a computing environment in order to emulate different aerodynamic phenomena present in the rotor of a WT [2]. Therefore, using such a system, different control systems can be implemented and verified. In addition, WT emulators can be used as an educational tool in the study of the behavior of a real WT [3].

The emulation of a WT may be obtained by controlling the torque on the motor shaft. In reference [4], the reference torque for the motor is determined based on the wind speed applied to the turbine and on each mechanical shaft speed. This strategy has simple configuration and allows the validation of control strategies of converters connected to the generator side. However, the transient effects are disregarded, and only the steady-state conditions of the system are obtained.

There are several approaches for wind emulators that are used in different situations depending on the desired requirements. DC motors are used in the construction of wind emulators because of their great ease for implementation and due to their direct relationship between armature current and the torque produced by the machine, as shown in references [3] and [5]. However, they demand higher maintenance requirements and these are costly when compared to other electrical machines in the same power range. An emulation system based on an induction motor (IM) has a smaller size relative to the DC motor for a given power range and has lower cost. Emulators from IM are also described in references [6–8].

This chapter describes the development of an emulator of WTs. The emulator is composed of an IM coupled to the shaft of a permanent magnet synchronous generator (PMSG). The IM has an electrical drive system controlled in real time by a software developed in LabVIEW®. The interface between software and drive is performed by an instrumentation circuit and a data acquisition board PCI-2511. In the proposal, given the WT parameters and a specified wind speed the software module of emulator provides the necessary IM torque reference to emulate the desired turbine. A standard x86 personal computer with LabVIEW® executes the software module of wind emulator.

This chapter is organized as follows: Section 2 describes the mathematical modeling of WTs, including aerodynamic, mechanical, and electrical models. Section 3 presents a numerical analysis of horizontal axis WT using these models. Simulation waveforms are presented to show the turbine dynamics under typical wind conditions. Section 4 describes an emulator built using a LabVIEW® environment and IM drive system. The emulator experimental

http://dx.doi.org/10.5772/63448

evaluation is presented in Section 5. The waveforms of this evaluation are compared with simulation waveforms in Section 6, which concludes the chapter.

2. Mathematical model of wind turbines

A WT can be described using three mathematical models: aerodynamic, mechanical, and electrical model. The aerodynamic model is responsible to represent the energy conversion from a moving air mass at a certain speed, which creates the rotational movement of the turbine, into mechanical energy at the shaft of the generator. The mechanical power available reflects into the speed and torque of the shaft of the system. The electrical model describes the conversion of the mechanical torque into electrical energy at the generator output. This process is depicted in **Figure 1**.

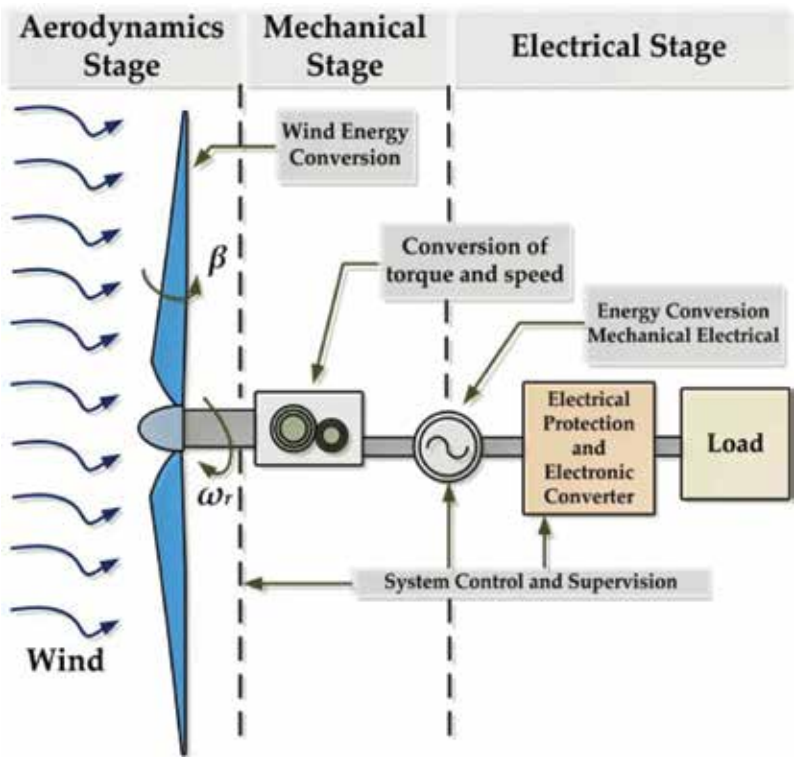

Figure 1. Energy conversion process for wind turbine.

In order to simulate/emulate a WT, it must obtain the three aforementioned mathematical models. From these models, given a wind profile, the mechanical torque and shaft speed that are used in the emulation stage can be obtained. The following topics present the mathematical modeling of a WT.

2.1. Aerodynamic model

The wind power that is converted into mechanical power at the turbine shaft is given by

$$P_T = \frac{\rho A V_w^3 C_p}{2} \tag{1}$$

where P_T is the mechanical power extracted by the wind turbine (W), ρ is the air density (1.225 kg/m^3 at sea level), A is the swept area (m^2), V_W is the wind speed (m/s), and C_p refers to the power coefficient. The aerodynamic characteristics and the orientation of a turbine relative to the wind flow result in its power efficiency. The value of *Cp* depends on the ratio speed of the blades and the wind. This ratio is known as tip speed ratio (TSR). Check reference [9] for more details of this conversion. The TSR is represented by λ and it is defined by

$$\lambda = \frac{\omega_r R}{V_W} \tag{2}$$

where R is the radius of the turbine swept area (m) and ω_r the angular velocity in the turbine shaft (rad/s).

For each WT model, the curves that relate C_p to different values of pitch angle (β) and TSR (λ) can be obtained from direct measurements of the turbine in operation. These curves are known as power curves, and they are useful in obtaining C_p for different points of operation of the turbine. The exact determination of C_p is not an easy task and demands complex mathematical models. Therefore, some approximations have been presented for the determination of C_p based on measurements of β and λ [10, 11]. An expression that is commonly used for determining C_p is

$$C_{p(\lambda,\beta)} = c_1\left(c_2\frac{1}{\lambda_i} - c_3\beta - c_4\right)e^{c_5\frac{1}{\lambda_i}} + c_6\lambda \tag{3}$$

$$\frac{1}{\lambda_i} = \frac{1}{\lambda + c_7\beta} - \frac{c_8}{1+\beta^3} \tag{4}$$

where c_1, c_2, …, c_8 are constants that depend on the aerodynamic characteristic of the turbine.

The torque developed by the turbine can be expressed as a function of wind speed that strikes the blades V_w, the power coefficient C_p, and the physical characteristics of the blades. A mathematical relationship is given by

http://dx.doi.org/10.5772/63448

$$T_T = \frac{1}{2\lambda}\rho A R V_w^2 C_{p(\lambda,\beta)} \tag{5}$$

According to Eq. (**5**), the torque developed in the shaft of a WT has a direct relationship with the wind speed. Since the wind has a stochastic behavior, it is expected to produce a resultant mechanical torque also with the stochastic profile.

2.1.1. Oscillatory effects of torque on wind turbines

Power source fluctuations in wind power systems are due to both a stochastic process that determines the wind speed at different time points and heights and a deterministic process. Deterministic processes on WTs are usually related to two aerodynamic effects called wind shear and tower shadow.

The wind shear phenomenon describes the variation of the wind speed ($V_{\omega s}$) that occurs at different heights [12] and its interaction with the turbine due to the rotation of the blades. Wind shear can be represented by the following equation [13]:

$$V_{\omega s} = V_W\left[\frac{R^2}{H}\frac{(\delta-1)}{8} + \frac{R^3}{H}\frac{\delta(\delta-1)(\delta-2)}{60}\cos\frac{\delta(\delta-1)(\delta-2)}{60}\cos 3\theta_b\right] \tag{6}$$

where H is the elevation of the rotor hub (m), δ is defined as an empirical coefficient of shear which varies in the range $0.1 < \delta < 1$, θ_b angular position to the blades (degrees) also called azimuthal angle.

The tower shadow effect is the change in wind speed due to the presence of the turbine tower [12]. Due to proximity between the blades and the tower of structure, wind flowing around the tower causes oscillations in the mechanical elements acting on the blades as well as on the mechanical torque developed on its axis. This effect can be modeled as presented in reference [13], that is,

$$V_{ts} = \frac{V_W}{3R^2}\sum_{b=1}^{3}\left[\frac{a^2}{\sin^2\theta_b}\ln\left(\frac{R^2\sin^2\theta_b}{x^2}+1\right) - \frac{2aR^2}{R^2\sin^2\sin^2\theta_b + x^2}\right] \tag{7}$$

where a is the tower radius (m) and x is the average distance between the tower and the blade (m).

Therefore, combining both effects results in the equivalent wind velocity V_{eq} given by

$$V_{eq}(t,\theta) = V_{ws} + V_{ts}. \tag{8}$$

Incorporating the shear and tower shadow effects, the total torque T_T developed by a WT is expressed by

$$T_T = \frac{\rho A R V_W C_{p(\lambda,\beta)}}{\lambda}\left(\frac{V_W}{2} + V_{eq}(t,\theta)\right). \tag{9}$$

In order to observe the impact of the aforementioned effects, consider two WTs with characteristics given in **Table 1**.

Parameters	Small turbine: 2.2 kW	Midsize turbine: 850 kW
Wind rated speed (V_W)	12 m/s	12 m/s
Mechanical nominal speed (ω_r)	630 rpm	26 rpm
Rotor radius (R)	1.23 m	26 m
Shear coefficient (δ)	0.1	0.3
Tower radius (a)	0.4 m	1.5 m
Tower height (H)	6 m	86 m
Blade tip away until half tower (x)	1.5 m	3.8 m

Table 1. Specifications of wind turbines.

The tower wind shear effect and the shadow effect for two turbines of different size are presented in **Figures 2** and **3**, respectively. Note that these effects are more pronounced for a midsized turbine, compared with the effects for a small one.

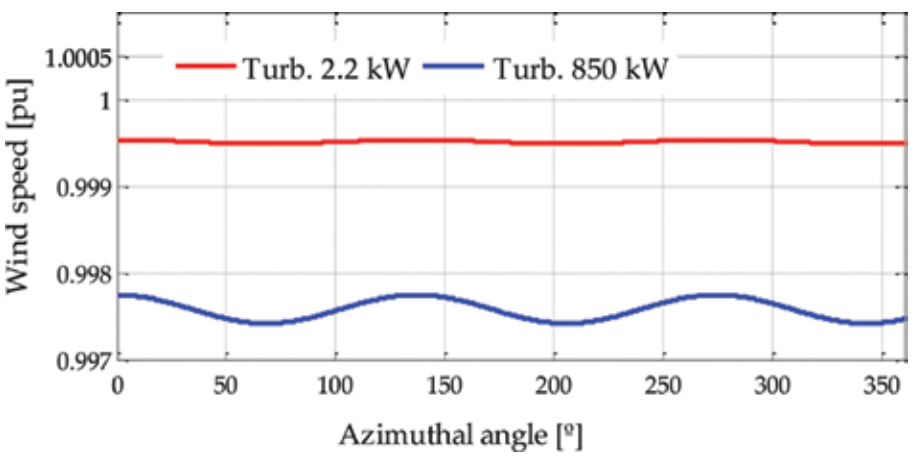

Figure 2. Wind shear effect of different wind turbines.

http://dx.doi.org/10.5772/63448

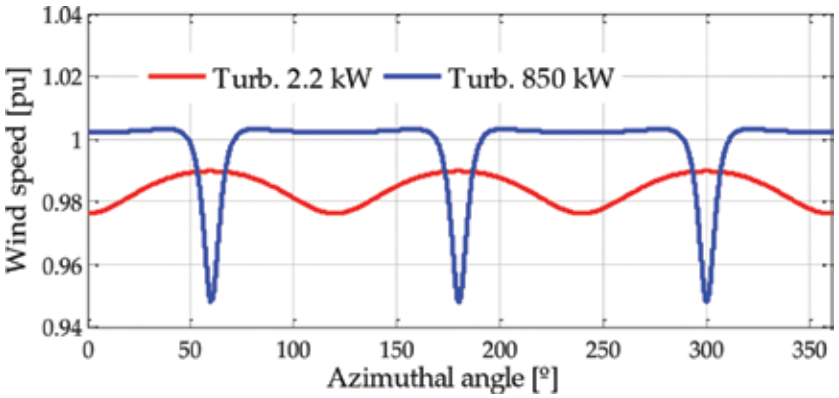

Figure 3. Tower shadow effect of different wind turbines.

The above-mentioned analysis shows that the tower shadow effect has greater impact on the resulting speed of the turbine than the wind shear effect. The tower shadow effect is responsible for an offset in the resulting torque. In addition, small turbines are less susceptible to oscillatory effects of wind than the midsize turbines.

2.2. Mechanical model

The mechanical dynamics of a WT can be modeled by two rotating masses, which represent the rotor of the WT and the generator shaft. The connection between them can be made with a gearbox or with direct coupling. Damping and torsion are also considered in the model as shown in **Figure 4**.

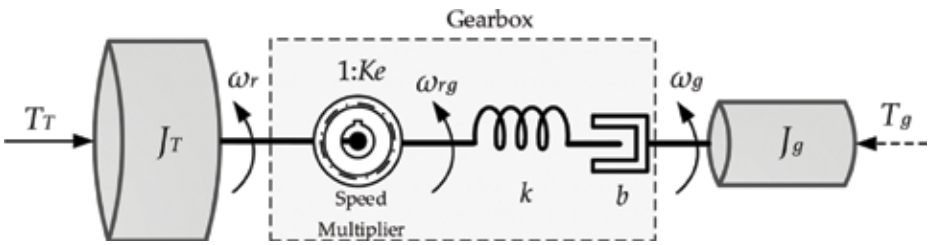

Figure 4. Mechanical model of wind turbine with generator.

The parameters presented in **Figure 4** are described below:

- J_T: Moment of inertia of the WT;
- J_g: Moment of inertia of the generator;
- T_T: Torque of the turbine, as a function of wind speed and power coefficient;
- T_g: Torque of the electrical generator, as a function of output electrical power;
- ω_r: Rotational speed of the turbine;

- ω_{rg}: Rotational speed of the turbine seen from the generator ($K_e \cdot w_r$);
- ω_g: Rotational speed of the generator;
- k: Torsion constant of the connection shaft;
- b: Damping coefficient of the shaft;
- K_e: Speed multiplication ratio.

Thus, the equations for the mechanical model of the WT are

$$\begin{aligned} T_{gT} &= K_e^{-1} \cdot T_T \\ \omega_{rg} &= K_e \cdot \omega_r \\ J_{gT} &= J_g + K_e^{-2} \cdot J_T \end{aligned} \tag{10}$$

where T_{gT} is the turbine torque seen by the generator and J_{gT} is the combined moment of inertia of the WT with the generator.

In most cases, for small WTs (that operate in a power range up to 10 kW) the dynamics of the axis are neglected, such as torsion and damping. In this situation, the equation regarding the mechanical model of the system becomes

$$T_{gT} - T_g = J_{gT} \frac{d}{dt}\left(\omega_{rg}\right). \tag{11}$$

2.3. Electrical model

Considering V_d, V_q and I_d, I_q as the voltages and currents of the stator of a PMSG represented in the synchronous reference frame [14], the electrical power of the generator is given by

$$P_e = \frac{3}{2}\left(V_d i_d + V_q i_q\right). \tag{12}$$

The electrical dynamic equations of the PMSG are expressed by

$$\begin{aligned} V_d &= R_s i_d - \omega_e L_q i_q + L_d \frac{di_d}{dt} \\ V_q &= R_s i_q + \omega_e \left(L_d i_d + \psi_{pm}\right) + L_q \frac{di_q}{dt} \end{aligned} \tag{13}$$

where ω_e is the angular velocity of the reference frame ($\omega_e = N_p\, \omega_g$), N_p is the number of pole pairs, L_d and L_q are the inductances of the stator winding in the synchronous reference frame,

http://dx.doi.org/10.5772/63448

R_s is the stator resistance, and ψ_{pm} is the flux constant of the generator rotor. The electrical torque (T_g) of the generator is expressed by

$$T_g = \frac{3}{2}\frac{Np}{2}\left(\psi_{pm} i_q + \left(L_d - L_q\right) i_d i_q\right) \tag{14}$$

3. Numerical simulation of the wind turbine

Based on the WT models presented in Section 2, an application was developed to simulate the behavior of a wind generator system. The simulator was developed in Matlab/Simulink® and was used for purposes of comparison with the waveforms of the emulator that was also developed for experimental analysis.

Figure 5 shows the block diagram that implements the dynamic behavior of a WT. The wind velocity and pitch angle are user inputs to the aerodynamic model. These inputs as well as the rotor speed are used to compute the power coefficient and the turbine torque. From the turbine torque and generator torque, the rotor speed is obtained. Then, the electrical model applies the load characteristic to obtain voltages, currents, and generator torque.

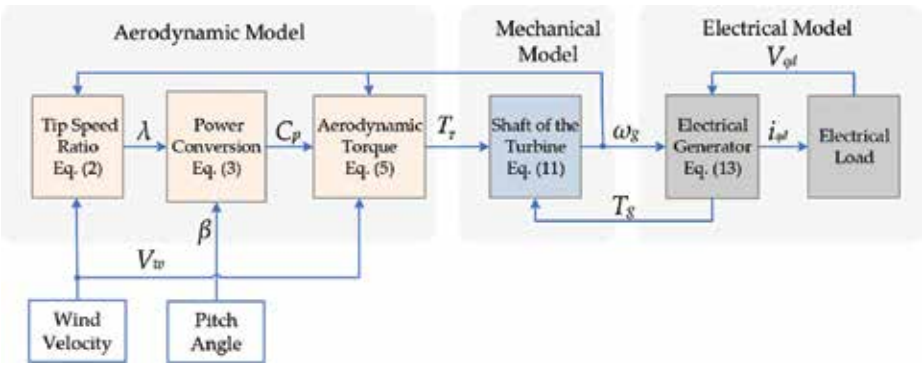

Figure 5. Block diagram of the wind turbine mathematical model for simulation implementation.

A 2.2-kW horizontal axis WT was considered as an example for the evaluation of dynamic behavior. The specifications of the aerodynamic model of the turbine are presented in **Table 1**, while the specifications of the mechanical model are given in **Table 2**.

Total turbine inertia (J_{gT})	2.29 kgm^2
Gearbox (K_e)	1200/630 = 1.9

Table 2. Parameters of mechanical model.

Due to the high-speed characteristics of the generator, the simulated WT incorporates a gearbox. The inertia of the turbine is obtained according to reference [15], and a resistive load used to terminals PMSG connected to "Δ". Torsion and damping are neglected.

The generator used is a PMSG that corresponds to the machine used in the experimental setup. The parameters of the PMSG were obtained by experimental tests and are described in **Table 3**.

Rated power	2.2 kW
Speed rotation	1200 rpm (125.5 rad/s)
Number of pole pairs	3
Moment of inertia	0.0084 kgm^2
Stator resistance (R_s)	1.455 Ω
Axis inductance (L_d,L_q)	1.97 mH; 2.59 mH
Permanent flux (ψ_{pm})	0.205 Wb
Resistive load (R)	7.4 Ω

Table 3. Parameters of PMSG.

The system operates at variable speed without control for maximum power extraction. Therefore, the system will only provide maximum energy to the load at the nominal operation

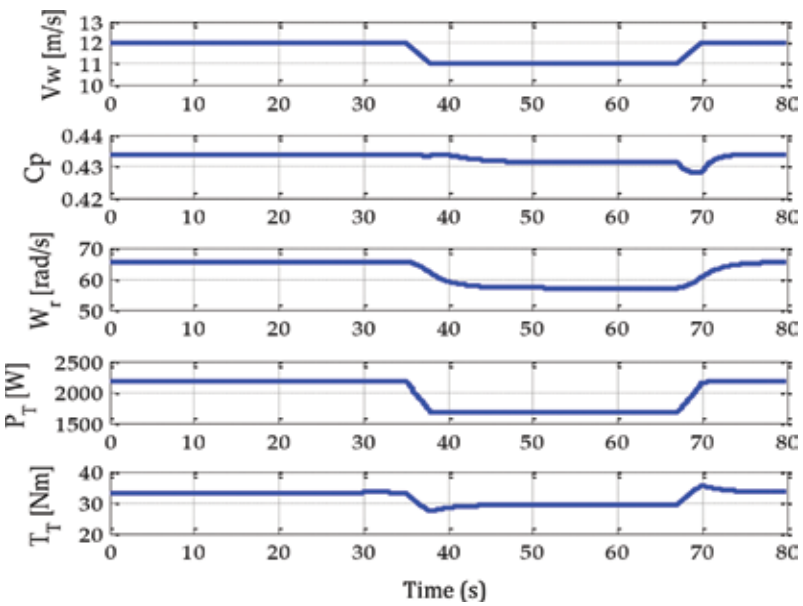

Figure 6. Aerodynamic quantities for a 2.2 kW turbine and wind speed changing from 12 to 11 and back to 12 m/s.

http://dx.doi.org/10.5772/63448

point. Thus, the analysis of the system starts at the nominal operating point with a wind speed of 12 m/s. After 35 s, the wind speed is reduced to 11 m/s using a ramp profile. At 67 s, the wind velocity is increased using a ramp profile up to the rated speed of 12 m/s. **Figure 6** describes the aerodynamic behavior of the simulated turbine.

In **Figure 6**, the variation in the wind speed results in a reduction of the mechanical power delivered to the generator around 25% (from 2.2 kW to 1.6 kW). The nominal torque of the turbine corresponds to 33.3 Nm. However, the torque seen by the generator is 17.5 Nm due to the gearbox speed ratio *Ke*. Due to the wind speed variation, the torque delivered to the shaft of the generator has a reduction of 9.7% (from 17.5 Nm to 15.8 Nm). The variation of the point of operation provides a small change in *Cp* value. The *Cp* changed from 0.434 to 0.431.

The turbine was also simulated at different points of operation that considered a variation in the wind speed from 12 to 10 m/s. The results are depicted in **Figure 7**.

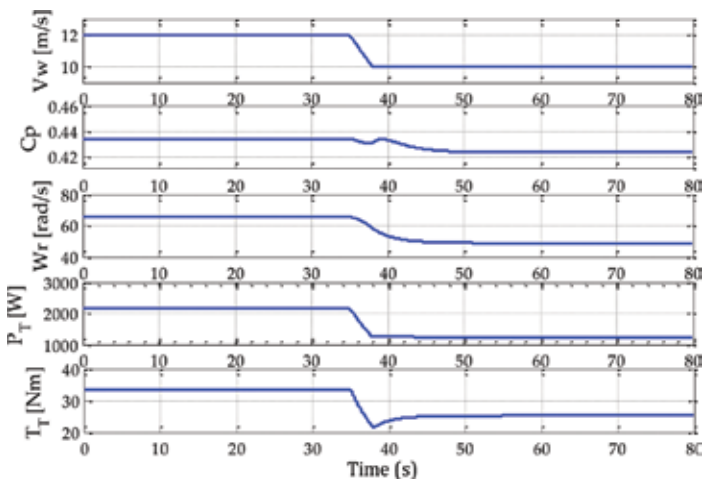

Figure 7. Aerodynamic quantities for a 2.2-kW turbine with a variation in the wind speed from 12 to 10 m/s.

As can be seen in **Figure 7**, even with a small wind speed variation of 2 m/s, the power coefficient is sensibly reduced. Moreover, the power absorbed by the turbine presents a larger reduction, around 40%. The simulation waveforms obtained in this section will be used to verify the emulator dynamics in the next section.

4. Emulation of the wind turbine

To develop a WT emulator, the setup is divided into two subsystems. The first one is a graphical user interface (GUI) running in a PC. The GUI was developed using LabVIEW® environment and uses an input-output card to communicate with the hardware setup. The second subsystem is an IM drive that emulates the WT following the dynamics evaluated by the software.

The software emulator developed in LabVIEW® incorporates the aerodynamic mathematical model presented in Section 2 and provides the necessary dynamic variables, such that the hardware is able to emulate the intended WT. Using the GUI, the user can provide parameters to the mathematical model. These input parameters include:

- Wind speed characteristics;
- Turbine parameters;
- IM parameters;
- Speed and torque signal specifications.

From input parameters, the software emulator acquires the rotational speed (ωr) of the IM shaft to compute the turbine torque that must be developed on the shaft of the motor-generator set. The software converts both acquired IM torque and speed to the turbine nominal values (per-unit conversion) before using the aerodynamic emulator. After computing the turbine torque, the software converts it back to the IM nominal base, such that it is used as reference torque (T_T*) by IM drive.

Figure 8. Emulator interface—wind turbine specifications screen.

4.1. Software implementation

The software has two tabs in the top of the main screen. The "Specifications" is the interface where the user inputs the parameters of the WT to be emulated. This screen is shown in **Figure 8**. The second tab, named "Signals Generated - Power – Torque" presents, graphically and in

http://dx.doi.org/10.5772/63448

real time, the dynamic characteristics of the emulated turbine. The dynamic characteristics are obtained from the model of the turbine. The mechanical quantities of the system are also shown. Torque and speed sensors installed on the experimental setup provide these quantities. To improve visualization, the quantities are presented in per-unit (pu) values. The user defines the base values in the "Specifications" tab. **Figure 9** shows the screen used to show the emulated variables in real time.

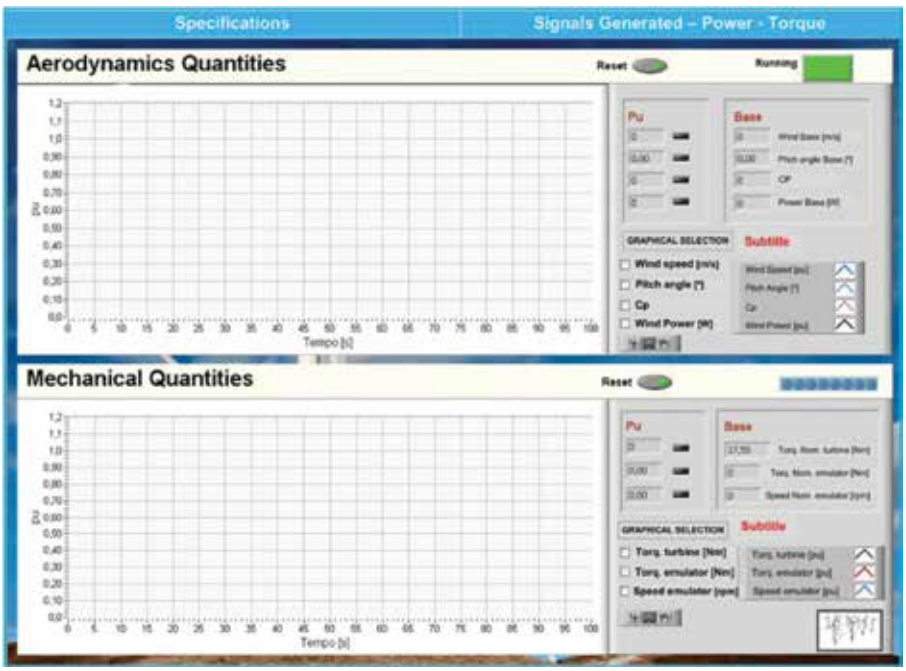

Figure 9. Emulator interface—screen used to present the generated signals.

4.2. Implementation of the drive system

The emulator drive is built using a motor-generator set based on IM-PMSG machines controlled in real time by the software platform. In addition, the drive can be designed to be flexible to receive future hardware upgrades or modifications and to be controlled by a high-level software. In this way, it is capable to emulate different WTs or even to use a new IM-PMSG set, such that it requires the user to inform the new parameters of the system in the GUI.

Since it is monitoring and controlling the system, a computing environment is responsible to provide the torque reference signal (T_T*) according to mechanical speed (ωr) measure, and a wind speed to be emulated. The nominal torque (1 pu) to be emulated on the motor shaft corresponds to a load of 16.6 Nm. An acquisition board PCI-2511 performs the hardware-software interface circuit. Afterward, a digitally controlled PWM inverter is used as the IM drive. Moreover, to perform the drive, different approaches can be used. Either a commercial

IM drive system (CFW 11) or a DSP/microcontroller user programmable controller with a three-phase PWM inverter are possible choices.

The proposed emulator is a horizontal axis wind turbine (HAWT) with rated power of 2.2 kW. Hence, the nominal power of the IM-PMSG was defined as 3 kW. The IM has eight pole pairs, while the PMSG has four pole pairs. A torque transducer (T22WN) measures the mechanical torque signal developed in the shaft of the machines, which employs VK20A (commercial board) and TCB (user developed) conditioning boards to be read by PCI2511. An absolute encoder (AC58) measures the speed of the motor-generator shaft, which is read by the software through the PCI2511 and a SCB conditioning board (user developed).

Since the mechanical characteristics of the system are given by the IM-PMSG connection, the software obtains the real dynamic speed on the shaft of the machines. The rotational speed is one of the input variables for the aerodynamic model used to determinate TSR. The electrical system for wind system is composed of the real PMSG-load set. **Figure 10** shows the representation of the experimental emulator.

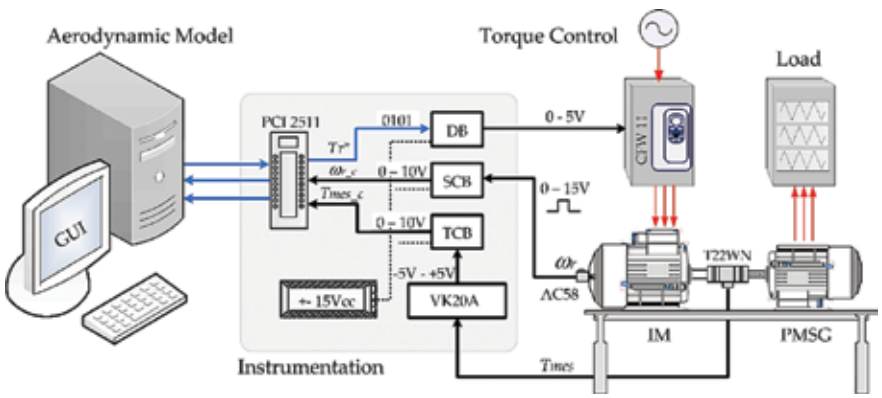

Figure 10. Representation of the wind turbine emulator experimental setup.

5. Emulator experimental evaluation

The emulator performance was analyzed considering two scenarios:

– Scenario 01: The emulation of the real system is carried out for different values of the operation curve of the WT, according to different wind speed profiles;

– Scenario 02: The emulation considers the wind turbulence, like steps and wind ramps.

Initially, the system is subject only to the aerodynamic conditions imposed by the wind speed changes. The emulator activation occurs after 20 s, due to torque control restrictions of the CFW11 drive. This drive requires the motor start at least 30% of its torque nominal. During the first 20 s, the setup operates in open-loop, in order to establish a constant speed in the shaft.

http://dx.doi.org/10.5772/63448

Then, the system starts to operate in closed-loop, where the mechanical speed dynamics feds the WT model implemented in the computing environment.

In the first scenario, the analyzed operating points correspond to wind speeds of 10, 11, and 12 m/s. **Figure 11** shows the behavior of the WT for emulator running when the wind speed changes from 12 to 11 m/s at 43 s. After 94 s the variation of the wind speed occurs from 11 to 12 m/s, and at 135 s the execution of emulated system considers a wind step 12 to 10 m/s. As can be seen in **Figure 11**, when the wind speed V_w is reduced from 12 to 11 m/s, the power coefficient is not significantly affected (0.43), such that the absorbed power is reduced as V_w^2 and rotor speed and turbine torque are reduced as V_w. On the other way, when V_w diminishes from 12 to 10 m/s, the power coefficient also significantly decreases (under 0.4), and the absorbed power drops to 50%.

Figure 11. Operating dynamics for wind turbine emulation system.

Figures 12 and **13** show the waveforms of the real-time voltage and line current measured with a digital 1 GS/s oscilloscope in terminals of the PMSG for a resistive load. In these figures, the electrically generated quantities (voltage and current) vary according to the absorbed power when wind speed changes in **Figure 11**. A large transitory drop in generated quantities can be noted when wind speed changes from 12 to 10 m/s. This drop is due to the dynamics of the turbine torque reference and the IM drive (CFW 11) characteristics.

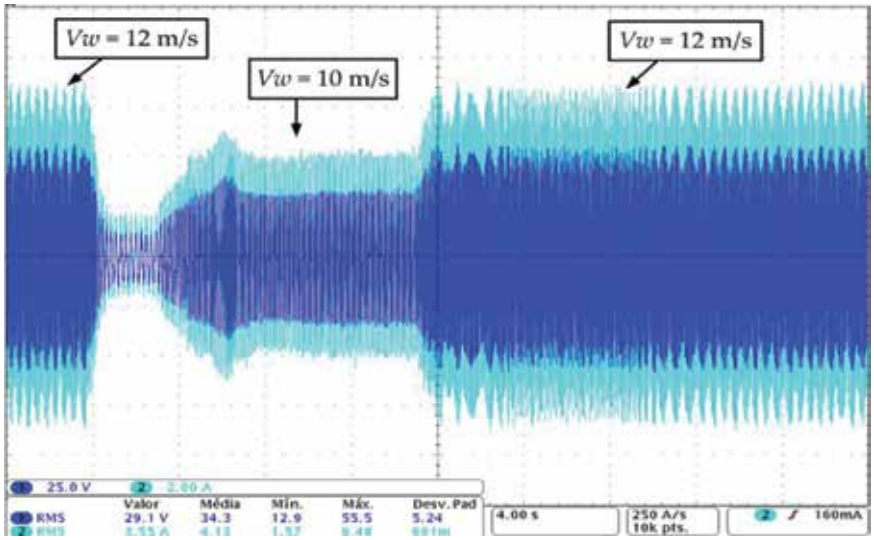

Figure 12. Voltage and electric current in the PMSG terminals for V_w changes from 12 to 10 m/s.

Figure 13. Voltage and electric current in the PMSG terminals for V_w changes between 12 and 10 m/s.

In order to check the response of the emulator in turbulence behavior within the nominal limits of the WT, the second scenario presents ramp conditions for wind speed. As can be seen in **Figure 14**, the setup exhibits high performance with significant variations in mechanical quantities, especially when drop variations occur in wind speed.

http://dx.doi.org/10.5772/63448

Figure 14. System emulator for the scenario with wind speed ramps.

It is possible to note the well working of system emulation considering consistent aerodynamic and mechanical quantities wind speed variation. In addition, due to the inertia of the turbine, rotational speed at the mechanical shaft does not respond instantaneously to changes in wind speed. The variation of the mechanical power available on the shaft of the turbine is 0.6 pu, corresponding to 1.3 kW. The *Cp* behavior shows greater variation during transitory, after the end of the wind ramp. After the transitory, *Cp* reaches its nominal value for 10 m/s wind speed. The variation of the mechanical torque on the turbine shaft is 0.4 pu, corresponding to 7 Nm. Since the mechanical torque in the shaft of IM-PMSG has also a variation of 0.4 pu, it features the same dynamics between the emulated system and the simulated one. Comparing the results from Simulink and LabVIEW is easy to note; the curves are very close. Small differences are present in mechanical torque since the simulator and the emulator drive applies different scales.

The performance analysis of the laboratory arrangement confirms that the emulator holds similar aerodynamic and mechanical dynamics to simulation models. In this way, the emulator can be used to design power converters as well as to check turbine dynamics in different generator/load arrangements.

6. Conclusion

This chapter presented the main steps for the implementation of a WT emulator through the torque control of an IM. First, it describes the simulation models and their verification. The simulator environment developed in Simulink/Matlab® can be used to analyze models and

check the emulator dynamics. Also, it presents the main concepts for building an emulator using LabVIEW, an IM drive, and an electrical generator.

An experimental evaluation presents emulator waveforms, which are compared with simulated ones in order to check emulator dynamics. Considering simulation and experimental waveforms for different wind conditions and their effects on several aerodynamic and mechanical variables, it is possible to validate the algorithm for WT emulation.

The described system permits a number of studies, such as

- design of power converters and correspondent control loops;

- implementation of the generator control to extract maximum wind power;

- implementation of computer platforms for other models of WTs, as well as for vertical axis WTs;

- an educational tool to teach main concepts of WTs and power conversion.

Acknowledgements

The authors acknowledge FINEP, CAPES, SETI, CNPq, and Fundação Araucária for scholarships and funding.

Author details

Diana Martinello, Emerson G. Carati*, Jean P. da Costa, Rafael Cardoso and Carlos M. O. Stein

*Address all correspondence to: emerson@utfpr.edu.br

Post-Graduation Program in Electrical Engineering, PPGEE, Federal University of Technology —Paraná, Pato Branco, PR, Brazil

References

[1] GWEC: Global Wind Energy Council [dissertation, in Portuguese]. Global Wind Report – Annual Market Update [Internet]. March 2014. Available from: http://www.gwec.net/wp-content/uploads/2015/03/GWEC_Global_Wind_2014_Report_LR.pdf [Accessed: December 2015].

[2] Han B., Lee H., Yoon D. Hardware simulator development for PMSG wind power system. In: Power & Energy Society General Meeting, 26–30 July 2009, Calgary, AB, IEEE; 2009. p. 1–6. DOI: 10.1109/PES.2009.5275770

[3] Kouadria S., Belfedhal S., Meslem Y., Berkouk E.M. Development of real time wind turbine emulator based on DC motor controlled by hysteresis regulator. In: Renewable and Sustainable Energy Conference, 7–9 March 2013, Ouarzazate, IEEE; 2013. p. 246–250. DOI: 10.1109/IRSEC.2013.6529649

[4] Rocha V.R. Experimental bench for wind turbine emulation [dissertation, in Portuguese]. Rio de Janeiro, Brasil; 2008. 80 p. Available from: http://www.pee.ufrj.br/teses/textocompleto/2008042802.pdf [Accessed: December 2015].

[5] Ovando R.I., Aguayo J., Cotorogea M. Emulation of a low power wind turbine with a DC motor in Matlab/Simulink. In: Power Electronics Specialists Conference, 17–21 June 2007, Orlando, FL, IEEE; 2007. p. 859–864. DOI: 10.1109/PESC.2007.4342101

[6] Tammaruckwattana S., Ohyama K. Experimental verification of variable speed wind power generation system using permanent magnet synchronous generator by wind turbine emulator. In: IECON 2012 – 38th Annual Conference on IEEE Industrial Electronics Society, 25–28 Oct. 2012, Montreal, QC, IEEE; 2012. p. 5827–5832. DOI: 10.1109/IECON.2012.6389131

[7] Nye J.M., de la Bat J.G., Khan M.A., Barendse P. Design and implementation of a variable speed wind turbine emulator. In: 2012 XXth International Conference on Electrical Machines (ICEM), 2–5 Sept. 2012, Marseille, IEEE; 2012. p. 2060–2065. DOI: 10.1109/ICElMach.2012.6350166

[8] Xie Z., Zhang X., Yang S., Cao R. A dynamic wind turbine simulator of the wind turbine generator system. In: 2012 Second International Conference on Intelligent System Design and Engineering Application (ISDEA), 6–7 Jan. 2012, Sanya, Hainan, IEEE; 2012. p. 967–970. DOI: 10.1109/ISdea.2012.549

[9] Ackermann T., editor. Wind power in power systems, 1st ed. John Wiley – Sons. West Sussex, England. April 2005. 742 p.

[10] Slootweg J.G., Polinder H., Kling W.L. Representing wind turbine electrical generating systems in fundamental frequency simulations. IEEE Transactions on Energy Conversion. 2003;18(4):516–524. DOI: 10.1109/TEC.2003.816593

[11] Silva K.F. Control and integration of wind farms to the power grid using doubly fed induction generators [thesis]. University of São Paulo – USP; 2006. 270 p.

[12] Thresher R.W., Wright A.D., Hershberg E.L. A computer analysis of wind turbine blade dynamic loads. Journal of Solar Energy Engineering. 1986;108(1):17–25. DOI: 10.1115/1.3268046

[13] Dolan D.S.L., Lehn P.W. Simulation model of wind turbine 3p torque oscillations due to wind shear and tower shadow. In: Power Systems Conference and Exposition, 29

Oct 2006–1 Nov 2006; Atlanta, GA, IEEE; 2006. p. 2050–2057. DOI: 10.1109/PSCE.2006.296240

[14] Bernardes A.T. Analysis and control of permanent magnet synchronous generator applied to wind energy conversion system [dissertation, in Portuguese]. Federal University of Santa Maria – UFSM; 2009. 192 p. Available from: http://cascavel.ufsm.br/tede/tde_arquivos/7/TDE-2009-10-23T120114Z-2296/Publico/BERNARDES, THIAGO ARAUJO.pdf [Accessed: December 2015].

[15] Tielens P., De Rijcke S., Srivastava K., Reza M., Marinopoulos A., Driesen J. Frequency support by wind power plants in isolated grids with varying generation mix. In: Power and Energy Society General Meeting; 22–26 July 2012; San Diego, CA, IEEE; 2012. p. 1–8. DOI: 10.1109/PESGM.2012.6344690

Chapter 9

A Maximum Power Point Tracking Control Algorithms for a PMSG-based WECS for Isolated Applications: Critical Review

Karim Belmokhtar, Hussein Ibrahim and
Mamadou Lamine Doumbia

Additional information is available at the end of the chapter

http://dx.doi.org/10.5772/63803

Abstract

This chapter deals with a comprehensive overview study of the direct-driven (DD) permanent magnet synchronous generator (PMSG) for wind-energy generation system for stand-alone applications. The dynamic model of PMSG is presented, and different maximum power point tracking (MPPT) algorithms have been realized in the aim to compare their performance. A comparison of performances of the conventional P&O MPPT and the fuzzy logic P&O (FLC P&O) MPPT is presented. Control technique for the presented system is presented and analyzed for the generator side converter. The simulation results carried out using Matlab/Simulink software show the effectiveness of the wind turbine control system.

Keywords: wind-energy conversion system, PMSG, MPPT, energy storage, direct-drive, direct torque control.

1. Introduction

Wind power is an important renewable energy resource, which has known a great growth in the last two decades [1-4]. This had led to reduced cost comparative to the conventional fossil energy resources. Nowadays, diesel generators are still the main source of energy in remote areas [5-9]. In stand-alone applications, small wind turbines provide a very attractive source of renewable energy. Wind turbines contribute to decrease stress on the grid, reduce pollution [10], and save on fuel costs by reducing or eliminating the need for diesel generators. These diesel generators consume a lot of polluting fuel, and their high operation and maintenance

costs can result in substantial additional costs if installed in a remote location, where the fuel transport and refueling is a complex mission [6, 8, 11, 12]. In addition, wind turbine in autonomous applications can be installed anywhere the wind resource is abundant and there is no access to the grid, while the grid connection is very expensive [13-17] or is not authorized or is difficult due to the different official approvals [18]. Nevertheless, in case of hybrid wind-diesel systems, a more complex control is required to accomplish an effective power management [18, 19].

Several structures of wind turbine systems are proposed in the literature, and their classification can be based on point of view of the type of generators, or a rotational speed, and the type of power control techniques which is used. Comparatively to the fixed speed type, the variable speed operation type permits to reach a high energy gain (20–30% more energy than the fixed speed operation [20]), reduce stresses, and increase efficiency and power quality [21-24]. In the variable speed wind turbine, to achieve a power flow control, a high efficiency through a maximum power point tracking (MPPT) techniques or a high quality of a delivered power, a (partial or full scale) power converters are needed [18]. In the fixed speed wind turbine, the squirrel-cage induction machine is commonly used, and no electronic interface is required [25, 26]. Asynchronous and synchronous machines are the most common generators used in variable speed wind turbine systems, where it is possible to operate in wide range of rotation speed with respect to the used generators and power converters types [18].

In the other hand, when considering the drive system, and when the generator is coupled to the turbine's shafts via a gearbox, the turbine is classified into the geared systems. The turbine is classified into direct-drive (DD) or gearless systems when the generator is directly coupled to the turbine's shaft [18, 22, 27]. The cost, weight, and maintenance of mechanical transmission needs give a serious limitation on the pursuit of increased power [22, 28]. Indeed, the DD type has many advantages such as a lower maintenance cost, noise reduction, and smaller size [22]. As a consequence, the correct selection of type of generator with regard to the wind conditions is essential to capture the maximum wind energy [18]. Typically, the geared generators cover a speed range of much lower about 20 to 60 rpm and much higher poles, (*e.g.*, about 50 to 300 poles) [28]. In order to avoid the excitation requirement of the generators in remote locations, it has been established that the permanent magnet (PM) machines are more suitable [18, 29-31]. The key technologies of small-scale wind turbine are listed in [32], where the PM machine is addressed as the competitive solution for stand-alone applications [33, 34].

This work focuses on overview study of a DD PMSG used in remote areas power systems, since it is the most usually used generator in small-scale wind turbines [18, 32]. PMSG has many advantages such as its high efficiency, improved thermal characteristics due to the absence of magnetic losses, a solid structure of its field, a high power per weight ratio, and an improved dynamic stability [35-39]. The PM generators can easily provide power without undergoing the process of voltage accumulation, and there is no risk of loss of excitation. In addition, the application of PM machines as wind turbine generators has grown rapidly due to the development of power electronics and permanent magnet materials [22, 40]. An overall configuration of the wind-energy conversion system (WECS) based on DD PMSG is shown in **Figure 1**. It contains the mechanical part (aerodynamics, gearless drive train) and the electrical

http://dx.doi.org/10.5772/63803

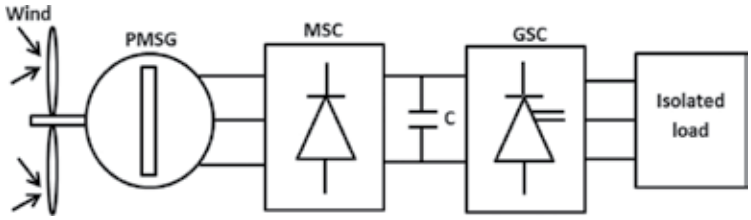

Figure 1. Configuration of the direct-driven PMSG wind-energy conversion system.

part (PM generator, full-scale converters). In this work, each element of the WECS is presented and detailed. The power converters topologies for the direct-driven PM generator system are widely discussed in the literature [18, 22, 41, 42] and highlighted in this chapter.

A field orientation control (FOC) algorithm, which is the advanced scheme, is the most used technique in AC machine control applications such as a PMSG wind-generation system [43, 44]. However, FOC technique has many drawbacks, such as high parameter dependence, and requires much computational resources. Furthermore, using mechanical speed sensors or observers is required to achieve FOC applications. Indeed, the rotor position is needed to give both current and voltage coordinates transformation [45]. On the other hand, a direct torque control (DTC), which is introduced in the mid-1980s [46, 47], is the new concept in WECSs and has many improvements in comparison with the FOC, such as the elimination of the current

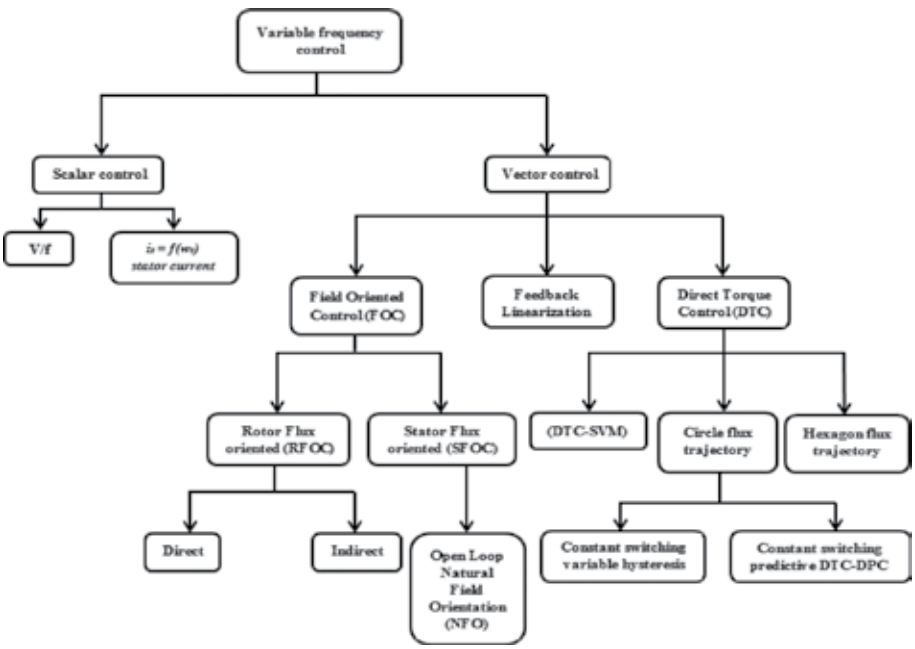

Figure 2. Classification of the PMSG control techniques [54, 55].

control loops, reduce the physical parameters sensitivity, intrinsic sensorless operation, and it is easy to implement in variable speed strategies [48]. Then, the DTC is more appropriate in WECS applications than the conventional FOC technique [49, 50]. The standard DTC technique based on switching table is already employed in commercial wind power generation systems using PMSG products. Some works have used a different DTC techniques such as space vector modulation (DTC-SVM) and a standard DTC in wind-energy systems, and the conclusion is that a DTC is very well appropriated [49, 51-53]. The different variable frequency control techniques of PMSG can be classified as shown in **Figure 2**. However, DTC presents some drawbacks such as the difficulty to control both torque and flux at very low speed, variable switching frequency operation and high torque and current ripple, and high noise level at very low speed [48].

This chapter is organized as follows. A dynamic model of WECS based on axial flux (AF) PMSG and its control are presented in Section 2. In Section 3, a simulation results are presented and analyzed. Finally, a conclusion based on the analysis of performance of different MPPT algorithms is given in Section 4.

2. PMSG Modeling Control system

2.1. Modeling of Wind Turbine

Generally, wind turbines are characterized by two parameters: tip speed ratio (λ) and power coefficient (Cp). The tip speed ratio is defined as follows:

$$\lambda = \frac{R\,\Omega}{v} \tag{1}$$

where R is the radius of the wind turbine aerodynamic rotor in meters Ω is rotational speed of rotor in rad/s, and v presents wind linear velocity in m/s.

The mechanical power harvested by the wind turbine, which is given by the usual cube law, can be calculated as follows:

$$p_{mec} = \frac{1}{2}\rho\pi R^2 C_p(\lambda,\beta)v^3 \tag{2}$$

where ρ is the air density at the turbine in kg/m^3, and Cp designates the fraction of power available in the wind that is converted into mechanical power. Cp has a theoretical maximum value of 0.593, the Betz limit [56, 57], and basically, it depends on the tip speed ratio λ, and the blade pitch angle, β, can be expressed as follows [58]:

http://dx.doi.org/10.5772/63803

$$C_p(\lambda,\beta) = 0.5\left(\frac{116}{\lambda_i} - 0.4\beta - 5\right)e^{-\frac{21}{\lambda_i}} \tag{3}$$

with

$$\lambda_i = \left(\frac{1}{\lambda + 0.08\beta} - \frac{0.035}{\beta^3 + 1}\right)^{-1} \tag{4}$$

Figure 3. illustrates the characteristic curves of the power coefficient obtained from (3). In the aim to extract the maximum available wind power by the wind turbine at a certain speed, the operating point of the turbine must be kept in the λ_{opt} area. Consequently, a maximum power point tracking (MPPT) algorithm, which is detailed below, is needed to control the rotational rotor velocity of the turbine and maintains it at the maximum power.

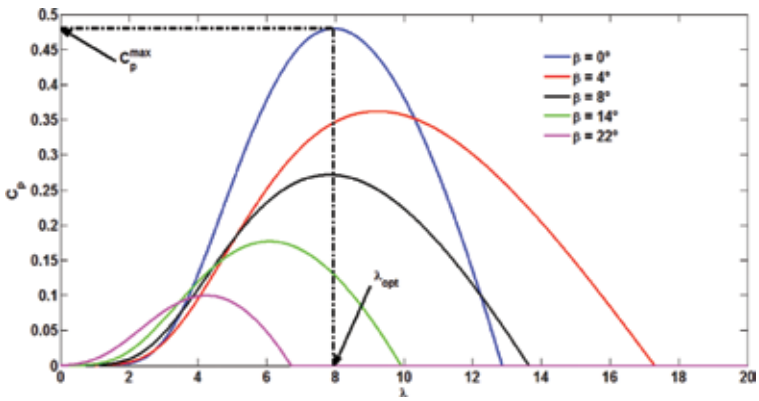

Figure 3. Power coefficient curves versus tip speed ratio for different blade angles.

2.2. Modeling of PMSG

In the aim to define the PMSG control system, its dynamic model is required. The model of the generator is derived by the projection of its equations on a reference coordinate system rotating synchronously with the magnet flux. In order to reach a synchronization between the *dq* rotating reference frame and the *abc* three-phase frame, a phase-locked loop (PLL) is used [59].Then, a dynamic model of the surface mounted PMSG is expressed as follows:

$$\begin{cases} v_{ds} = R_s\, i_{ds} + L_s \dfrac{di_{ds}}{dt} - \omega \psi_{qs} \\ v_{qs} = R_s\, i_{qs} + L_s \dfrac{di_{qs}}{dt} + \omega \psi_{ds} \end{cases} \tag{5}$$

where Ls and Rs are, respectively, the generator inductance and resistance, *w* is the electrical generator speed, and Ψ_{ds} *and* Ψ_{qs} are d-axis and q-axis magnet flux, respectively, which are expressed as follows:

$$\begin{cases} \psi_{ds} = L_s i_{ds} + \varphi \\ \psi_{qs} = L_s i_{qs} \end{cases} \tag{6}$$

where Φ is the magnet flux. Then, the electrical model of PMSG in the synchronous reference frame can be expressed as follows:

$$\begin{cases} \dfrac{di_{ds}}{dt} = \dfrac{1}{L_s}\left(-R_s i_{ds} + \omega L_s i_{qs} + v_{ds}\right) \\ \dfrac{di_{qs}}{dt} = \dfrac{1}{L_s}\left(-R_s i_{qs} - \omega L_s i_{ds} - \omega\varphi + v_{qs}\right) \end{cases} \tag{7}$$

The electromagnetic torque of the nonsalient poles of PMSG is written as follows:

$$T_{em} = \frac{3}{2} p\, \varphi i_{qs} \tag{8}$$

where p is the number of pole pairs of the generator. Eq. (8) shows that the generator torque can be controlled directly via the q-axis current of the stator.

The mechanical dynamics model of the considered wind turbine system can be defined by the following expression:

$$J_T \frac{d\omega_r}{dt} + f\,\varphi_r = T_T - T_{em} \tag{9}$$

where T_T represents the mechanical torque, J_T is the moment of inertia, f is the coefficient of friction, and ω_r is the mechanical speed, which is related to the electrical rotating ω as follows:

$$\omega = p\,\omega_r \tag{10}$$

2.3. Different structures of DD PMSG-based wind turbine system

For remote area applications, different topologies of PMSG-based WECS and their control techniques are presented in order to demonstrate their efficient performance [18]. In [60], a diode bridge rectifier and boost DC-DC converter is controlled in order to extract the maximum power by controlling the duty cycle of the IGBT switch. In addition, a controlled voltage source

http://dx.doi.org/10.5772/63803

inverter (VSI) is used to control both voltage amplitude and frequency on the load side. The results have shown that the proposed control strategy gives a good performance in both transient and steady-state cases. However, these performances can be enhanced by taking into account the use of energy storage systems. An experimental study of a voltage control strategy focused only to compensate harmonic due the using a nonlinear load in autonomous application are presented and analyzed in [61]. In [62], the same structure studied in [60] is analyzed under unbalanced load, with the addition of battery as energy storage device and its DC-DC reversible converter, with an addition of hydrogen storage in [63]. A dump load is used to balance power between wind generator, battery, and primary load through a controllable switch such as IGBT. Hysteresis band current control (HBCC), voltage-oriented control (VOC), and flux-oriented control (FOC) are used to control machine side converter, in order to regulate DC-link voltage in [64]. It has demonstrated that VOC and FOC control strategies give a small THD in comparison with the HBCC. Therefore, the estimation of the field improves the performance of VOC, making FOC better compared to VOC. However, in this work, the optimization of wind power generation, such as MPPT strategy, has not been taken into account. After presentation and discussion of some works dealing with autonomous PMSG-based WECSs, we present in the next section their typical topologies.

Figure 4(a). illustrates the PMSG wind turbine system used three-phase bridge diode rectifier as generator side converter (GSC) and a voltage source converter as GSC in (b).

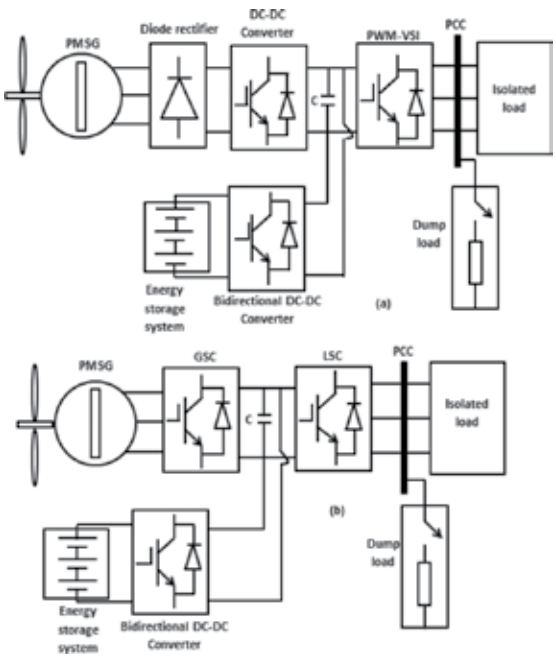

Figure 4. DD PMSG-based stand-alone WECS: (a) bridge diode rectifier as MSC and (b) voltage source converter as MSC.

In remote area applications, due to the intermittent and randomness nature of wind, energy storage system (ESS) is required. Therefore, a bank of batteries is used as an ESS in order to ensure continuity of the power system. Indeed, in the case where production is higher than demand, the batteries are charged through the bidirectional DC-DC converter. In the other hand, when production is less than demand, the batteries provide the difference between consumption and production. Dump load is used in case of surplus power, and the batteries are fully charged. Note that for this application, hydrogen storage system (HSS) can be a good alternative to meet production and demand power. Indeed, the electrolyzer is used to store the excess power as hydrogen, which will be used to regenerate electricity via fuel cell when production is less than demand.

There are also other configurations of PMSG-based WECS for remote applications, with the integration of other sources, and using of power electronics. **Figure 5** shows the structure of the hybrid power system (HPS) with the main DC bus structure. An ESS is connected to the DC bus, which can contribute to regulate the DC voltage. A PV array and diesel genset are used to reduce the overall cost of the system and the optimization of renewable energy sources penetration rate. **Figure 6** represents the simplified block diagram of the HPS with a main AC bus structure.

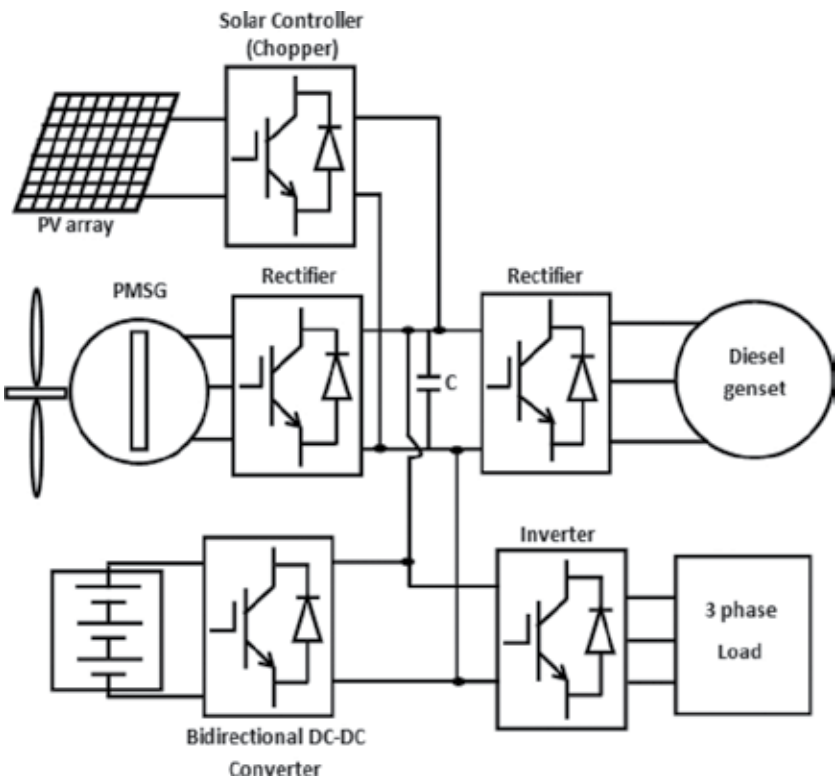

Figure 5. PMSG-based WECS with the DC main structure.

http://dx.doi.org/10.5772/63803

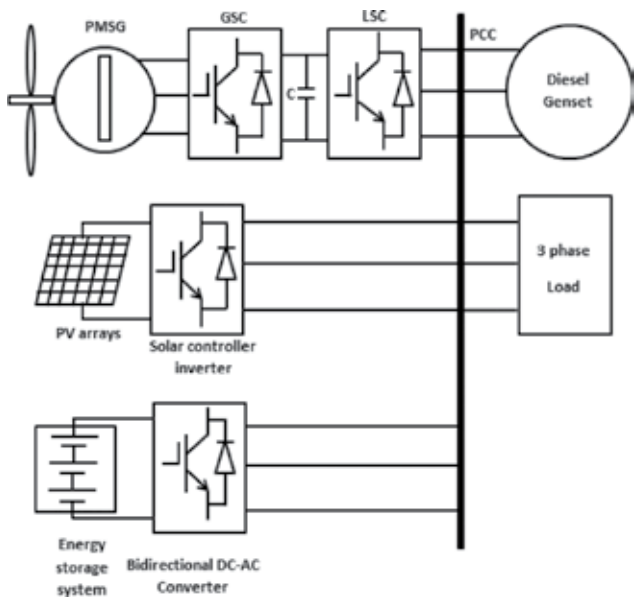

Figure 6. PMSG-based WECS with the AC main structure.

2.4. Control of PMSG

A global scheme of DD PMSG control scheme is illustrated in **Figure 7**, where two controlled PWM VSI, GSC and LSC, are used. These back-to-back converters are controlled in the aim to improve the captured wind power and increase the system performance by adjusting the power factor [44, 65]. The GSC is controlled to maximize the extraction of wind power. Indeed, vector control law associates space vector modulation (SVM) and maximum power point tracking (MPPT) algorithm is used to maximize the provided power under varying wind speed condition.

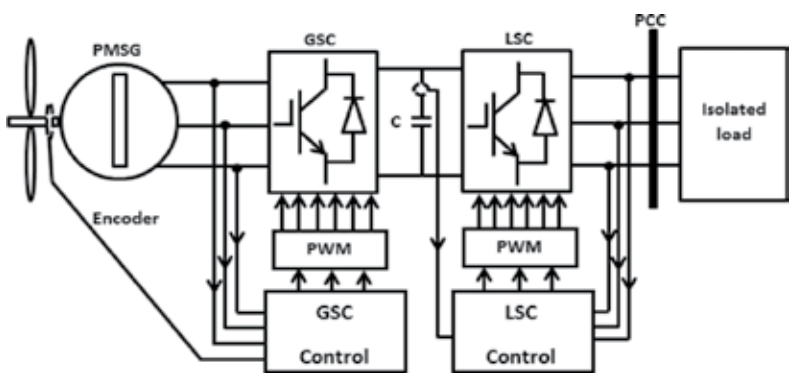

Figure 7. DD PMSG control scheme.

2.4.1. Generator Side Converter (GSC) Control

The detailed scheme of GSC control is illustrated in **Figure 8**, where the FOC by mean of vector control is applied. The FOC strategy consists of two outer and inner control loops. An outer loop is applied to regulate the optimal rotor speed, which is given by the MPPT algorithm. The inner loops consist of rotor current control in the aim to improve the performance of the system.

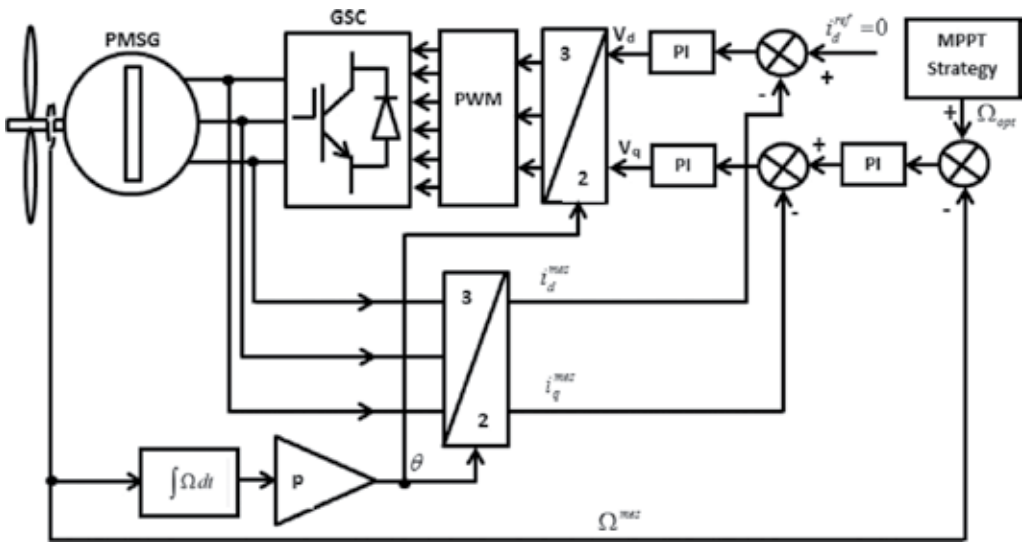

Figure 8. Detailed scheme of FOC applied to the GSC.

The optimal speed of the generator is determined by MPPT algorithm according to the wind speed variation in order to track the optimum point of power. The controller of speed generates the reference of quadratic axis rotor current, where the direct axis rotor current reference is kept at zero. There are commonly four MPPT algorithms for WECS listed in the literature, which can be used for the control of PMSG WECS. Indeed, the MPPT controller dependent on power electronics converter configuration is used.

a) *Tip Speed Ratio (TSR) technique*

In order to guarantee the maximization of the extraction of the energy, the TSR is kept constant at its optimal value regardless of wind speed. This method requires the direct and constant measure of wind speed, which is impossible in reality and increases the cost of the overall system [66-70]. Then, some research have make interest on wind speed estimation to improve the reliability of the control system. Neural network technique has been used in [71], to estimate the wind speed. Other methods based on using signals, which are easy to measure to estimate wind speed [72] or with fuzzy logic technique [73-75], are used to estimate wind speed. The diagram block of TSR control is illustrated in **Figure 9**.

http://dx.doi.org/10.5772/63803

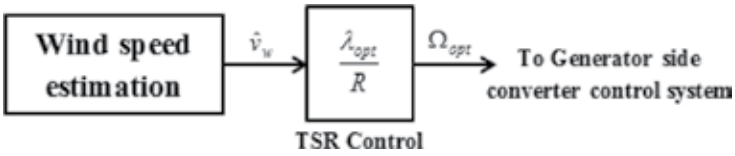

Figure 9. Detailed scheme of FOC applied to the GSC.

b) *Hill Climbing Searching (or Perturb & Observe) technique*

The P&O algorithm, which is the sensorless mathematical optimization approach to seek the optimum local point for a given function, is widely used in the literature in order to extract the maximum energy [2, 76-81]. Nevertheless, this technique has many drawbacks such as mechanical stress due to the constant perturbations [82] and permanent fluctuation around the optimal point [66, 83], especially with medium and large inertia wind turbine. In [84, 85], additional control strategies have been added to a basic P&O algorithm in order to resolve the problems listed above. However, some disadvantages such as the response to fast variations of the wind speed are still persisting. In the other hand, it is not easy to choose step size: A large step size means a fast response but generates more oscillations around the optimum point, and then, efficiency is reduced, where the small step size increases stability and efficiency but makes lower convergence of the control [78, 86]. Accordingly, the performance of these algorithms is particularly low in case of strong changes in wind speed, which is the case of most wind turbines. Then, the development of new algorithms including these issues is required. The P&O control principle is depicted in **Figure 10**. In [78], it has been reported the absence of difference of the wind power resulting from the variation of the wind speed and those resulting from the change in the previous perturbation.

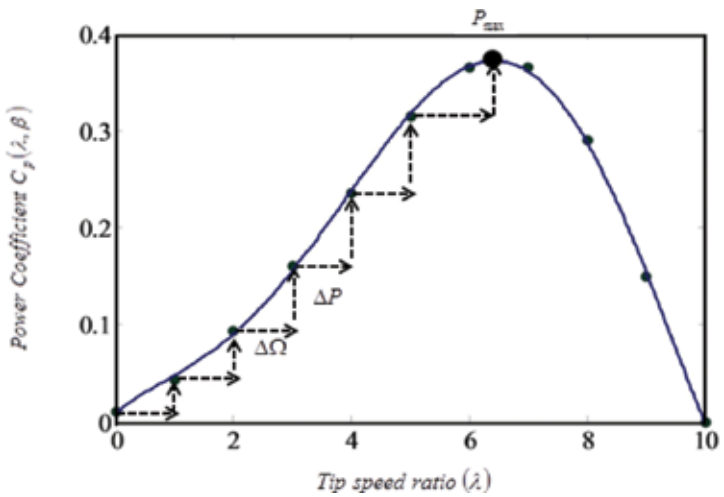

Figure 10. P&O control principle.

Some studies [76-78] have proposed a modified step-size algorithms in order to improve efficiency and the precision of the conventional P&O algorithms.

c) *Power Signal Feedback (PSF) Control technique*

The PSF control technique requires the knowledge of the optimum power curve of wind turbine (see **Figure 11**) as function of the rotor speed, which is obtained from experimental tests. Then, the recorded data for maximum output power and the corresponding rotor speed must be implemented in a lookup table [86-88]. The measured rotor speed is used to provide the optimal power to extract as shown in **Figure 12**. In [88], the optimum power depends on the rotor speed and the output DC voltage is used to calculate the optimum power [79].

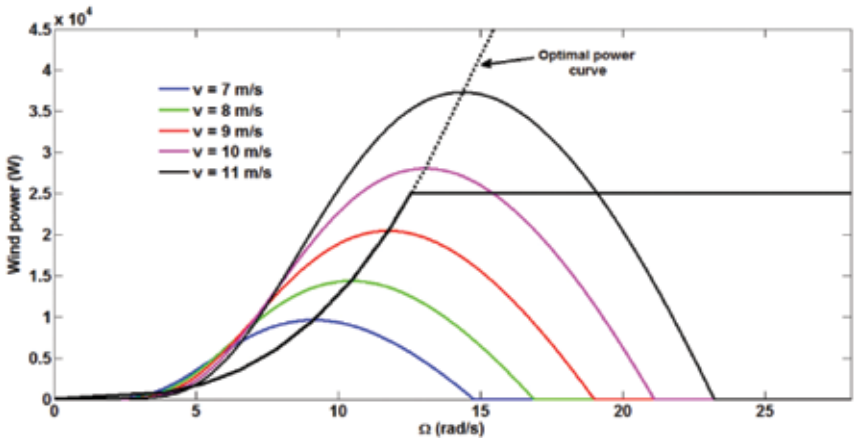

Figure 11. Wind power curve as function of the rotor speed for different wind speed.

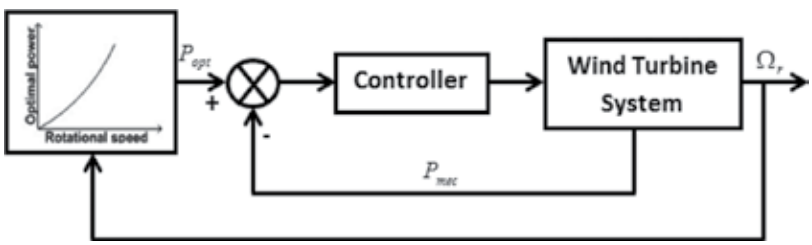

Figure 12. Block diagram of PSF control algorithm to track the optimum power point.

d) *Optimal Torque Control (OTC)*

The principle of the OTC strategy consists of the adjusting of the generator's speed according to a maximum power reference torque for a given wind speed (see **Figure 13**) [89]. Indeed, to ensure the maximum capture of the available wind power, the TSR must be kept at its optimal value (λ_{opt}). The characteristic torque as function of rotor speed is shown in **Figure 14**.

http://dx.doi.org/10.5772/63803

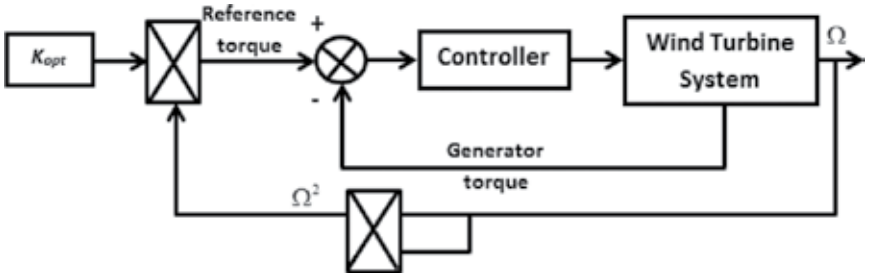

Figure 13. Block diagram of OTC control algorithm to track the optimum point.

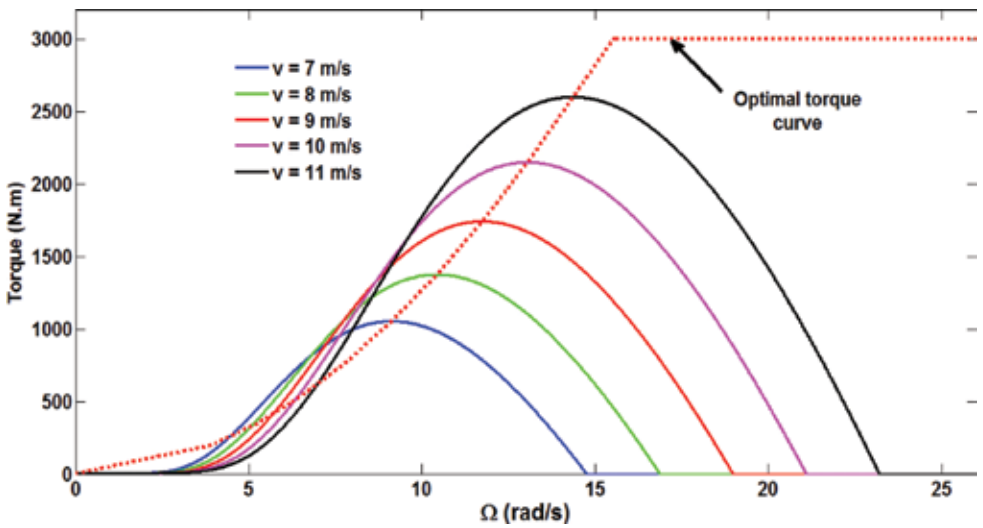

Figure 14. The characteristic torque as function of rotor speed for different wind speed.

By replacing the wind speed expression from eq. (1) in eq. (2), we can get the following expression:

$$p_{mec} = \frac{1}{2}\rho\pi R^5 C_p(\lambda,\beta)\frac{\Omega^3}{\lambda^3} \tag{11}$$

If TSR is maintained at its optimal value (λ_{opt}), the previous relation is expressed as follows:

$$p_{mec}^{opt} = \frac{1}{2}\rho\pi R^5 C_p^{opt}(\lambda,\beta)\frac{\Omega^3}{\lambda_{opt}^3} \tag{12}$$

If we consider that the wind power is equal of the product of torque and speed, the optimal torque can be written as follows:

$$T_{mec}^{opt} = \frac{1}{2}\rho\pi R^5 C_p^{opt}(\lambda,\beta)\frac{\Omega^2}{\lambda_{opt}^3} = K_{opt}\Omega^2 \tag{13}$$

where

$$K_{opt} = \frac{1}{2}\rho\pi R^5 \frac{C_p^{opt}(\lambda,\beta)}{\lambda_{opt}^3} \tag{14}$$

The OTC method is simple to analyze, easy to implement, and efficient since the measured wind speed is not required achieving the maximum power generation. Nevertheless, in case of strong and fast change of wind speed, the response is low. Indeed, no direct measurement of wind speed allows not reflect the rapid change in the value of the reference torque.

2.4.2. Load Side Converter Control

The main objective of load side converter (LSC) control is to maintain the DC-link voltage, Vdc, constant regardless the amount and direction of the active power, and the power factor by adjusting the amount of the reactive power. Then, the requirements of unit power factor can also be reached. In order to achieve the control, voltage and current on load side and the DC-link voltage are measured. Since the load voltage-phase angle is needed to accomplish the vector oriented control (VOC) of LSC, phase-locked loop (PLL) is used to track the load voltage vector [90].

In this study, a DC-link voltage and a unit power factor control are applied. Since we focus our work essentially on the analysis of MPPT's performances, the scheme used in this work was given in several papers [91–95].

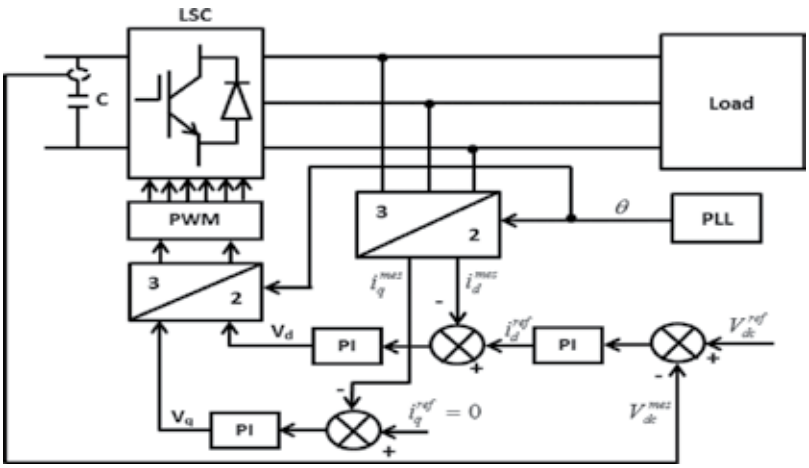

Figure 15. Block diagram of vector control of LSC.

http://dx.doi.org/10.5772/63803

Figure 15 illustrates the overall control scheme of the LSC. The control of the DC-link voltage and the power quality is also reached by current regulation on a synchronously rotating reference frame.

The output voltage signals, which are generated from the current controllers, are used by the space vector pulse width modulation SVPWM module to produce the IGBT gate control signals to drive the LSC. Moreover, to increase the transient performance of the inner current loops, the *d-q* decoupled current control through vector control is applied.

The proportional-integral (PI) controllers are used in both outer and inner control loops, and their gains are determined by trial and error method.

3. Simulation results and discussions

In order to achieve a comparative analysis of different MPPT algorithms, we consider an isolated application of direct-drive wind turbine driving a PMSG as shown in **Fig. 7** and **8**. The WTG represents a 14 kW variable-speed wind turbine equipped with a 12.5 kW PMSG. An isolated and balanced three-phase resistive load is connected to the LSC and draws a variable active power from the wind power system. The parameters of the WTG are given in Appendix.

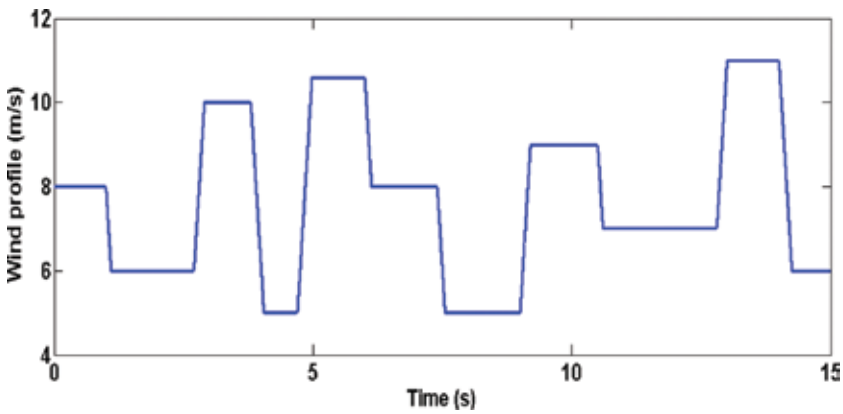

Figure 16. Wind speed profile

To validate the effectiveness and the dynamic of the PMSG control via GSC, some simulations are carried out using Matlab/Simulink software program. **Figure 16** illustrates the wind speed profile that incident on the wind turbine, while **Figure 17** shows the performance of the generator speed control. As we can see, the measured rotor speed tracks with a good accuracy the reference optimal value, since the tracking error is kept less than ± 1.5% all the time. Wind power and electrical power provided by the PMSG are depicted in **Figure 18**. The instantaneous generator currents are indicated in **Figure 19**. The variation of the power coefficient (C_p) with the wind speed is kept at its optimum value as shown in **Figure 20**.

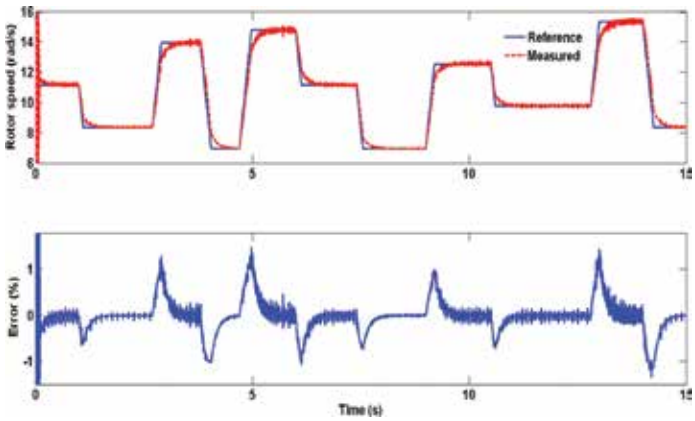

Figure 17. Generator speed control performance.

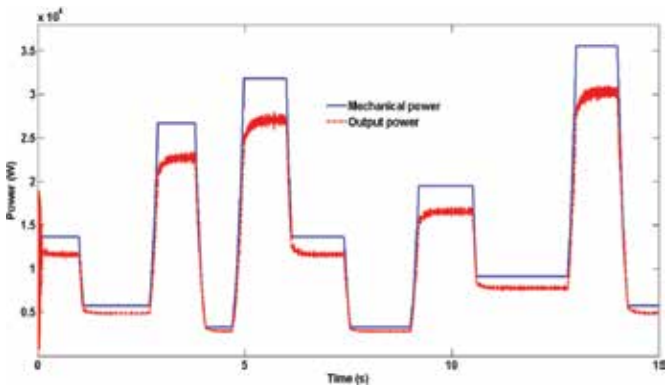

Figure 18. Wind power and output electrical power.

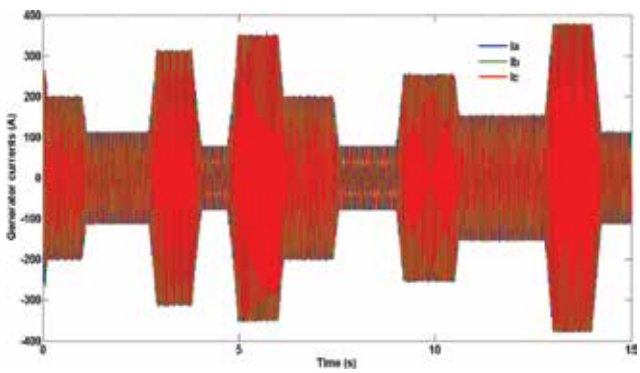

Figure 19. Three-phase currents of the PMSG.

http://dx.doi.org/10.5772/63803

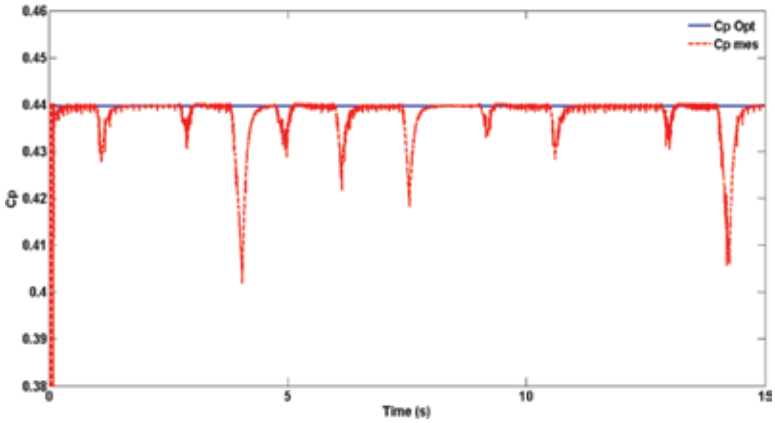

Figure 20. Power coefficient.

Subsequently, a comparative analysis of the performance of a new MPPT P&O strategy based on fuzzy logic techniques, which is known to be an excellent tool for modeling and management of nonlinear systems and the conventional P&O MPPT, is presented. The control strategy of the fuzzy logic is based on an expert human operator to interpret a situation and initiate its appropriate command action. Generally, a controller based on fuzzy logic has two inputs and provides a control action. For FLC P&O, inputs are quantized into 5 levels represented by a set of linguistic variables: negative big (NB), negative (NS), zero (Z), positive (PS), and positive big (PB). The fuzzy rules base formulation of FLCP&O is shown in **Table 1**. These rules are chosen to perform the optimization of wind generation capture as follows: (i) When the input signals are far from the optimal point, the output of the FLCP&O provides a big step size; (ii) when the inputs are close to the optimum point, the output is set to a small value of step size; and (iii) once the inputs are close to the optimum point, then the step size is set to zero. In this article, we use the min and max operators as t-norm and t-conorm, respectively. Triangular membership functions are used, principally due to their efficiency and high-performance computing. The membership adopted for both inputs and output variables is illustrated in **Figures 21** and **22**, respectively.

Step size		***ΔPower***						
		NB	***N***	***Z***	***P***	***PB***		
ΔSpeed			*NB*	*NB*	*N*	*Z*	*P*	*PB*
N	*NB*	*N*	*Z*	*P*	*PB*			
Z	*NB*	*N*	*Z*	*P*	*PB*			
P	*NB*	*N*	*Z*	*P*	*PB*			
PB	*NB*	*N*	*Z*	*P*				

Table 1. Fuzzy rules base formulation of FLCP&O.

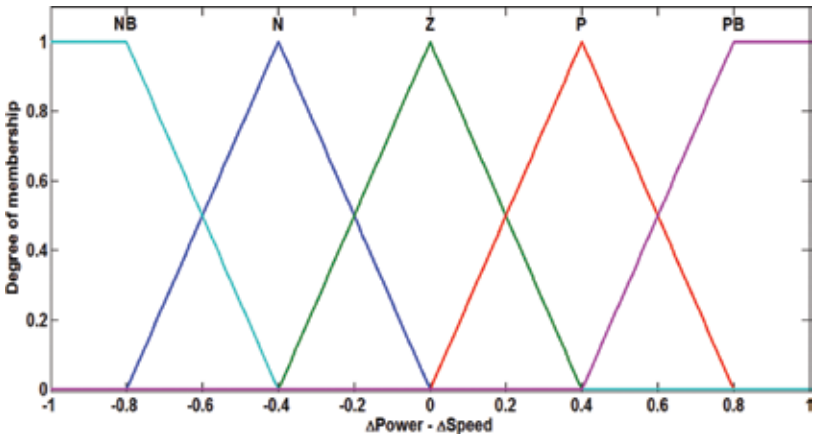

Figure 21. Membership functions of the inputs variables.

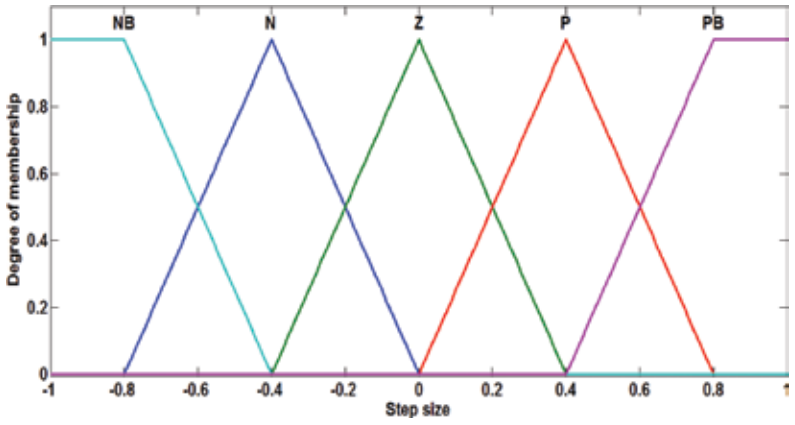

Figure 22. Membership functions of the output variables.

The main drawback of this conventional P&O MPPT is the calculation of step size. Indeed, a major step modification allows a faster convergence of the system, but increases the oscillation around the optimal point. On the other hand, a small step size reduces the oscillations, but it makes the system slower to reach the optimal point, especially in case of rapid changes of wind speed. Fuzzy logic provides an adaptive step size, and its value depends on the distance between the current point and the optimal point. Indeed, if the actual point is very near to the optimum point, the variation is not very larger, thereby increasing the speed of convergence, and while the actual point is nearby the optimum point, step size decreases avoiding oscillation around the optimal point. **Figure 23** shows the profile wind speed. **Figure 24** depicts the performance of new FLCP&O and the conventional P&O MPPT listed in [70]. As we can see, the new FLCP&O strategy (black dashed curve) is almost confused with the optimal value (red curve). The variation of the step size for both P&O MPPT is illustrated in **Figure 25**.

http://dx.doi.org/10.5772/63803

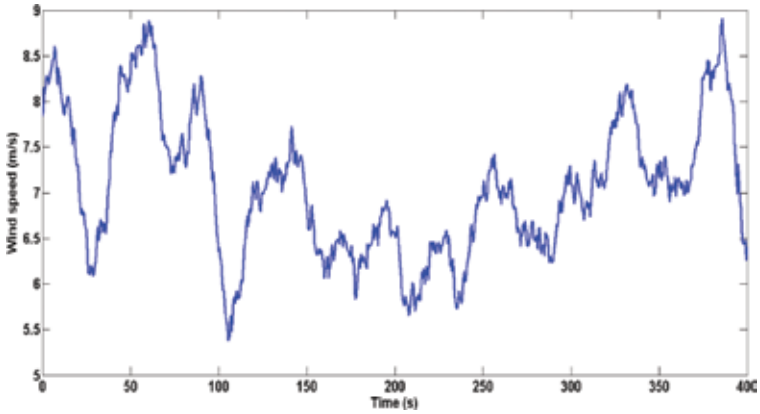

Figure 23. Profile of wind speed.

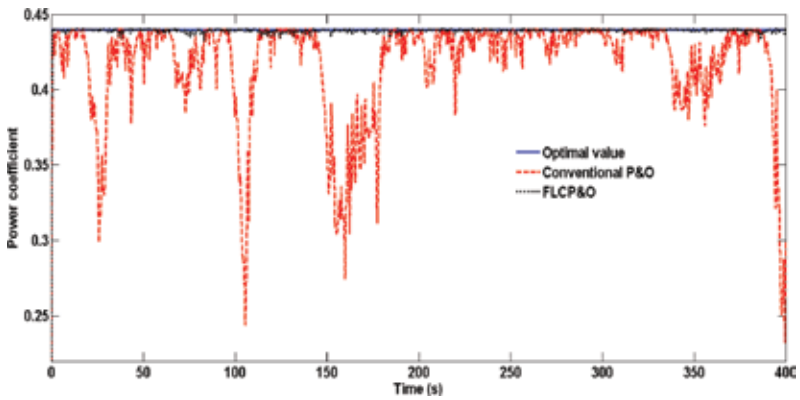

Figure 24. Comparison of the performances of a new FLP&O and the conventional P&O MPPT.

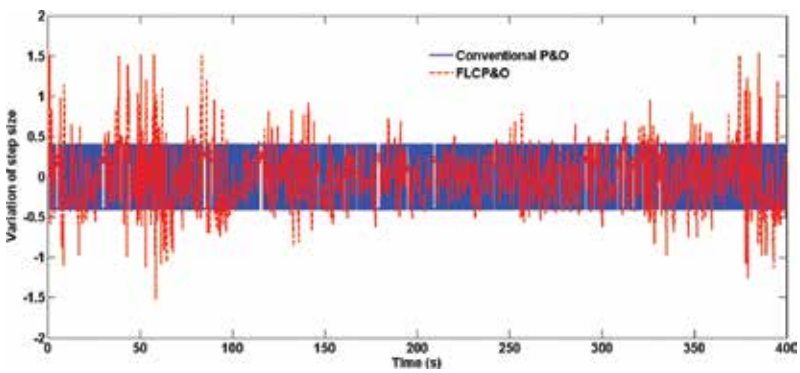

Figure 25. Variation of the step size for both P&O MPPT algorithms.

After showing the effectiveness and the dynamics of the proposed control strategy system, the assessment of the performance of the different MPPT algorithms is achieved. The comparison of the values of the power coefficient for different MPPT algorithms is depicted in **Figure 26**. As we can see, the FLCP&O provides the best performances versus OTC MPPT and PFS MPPT methods.

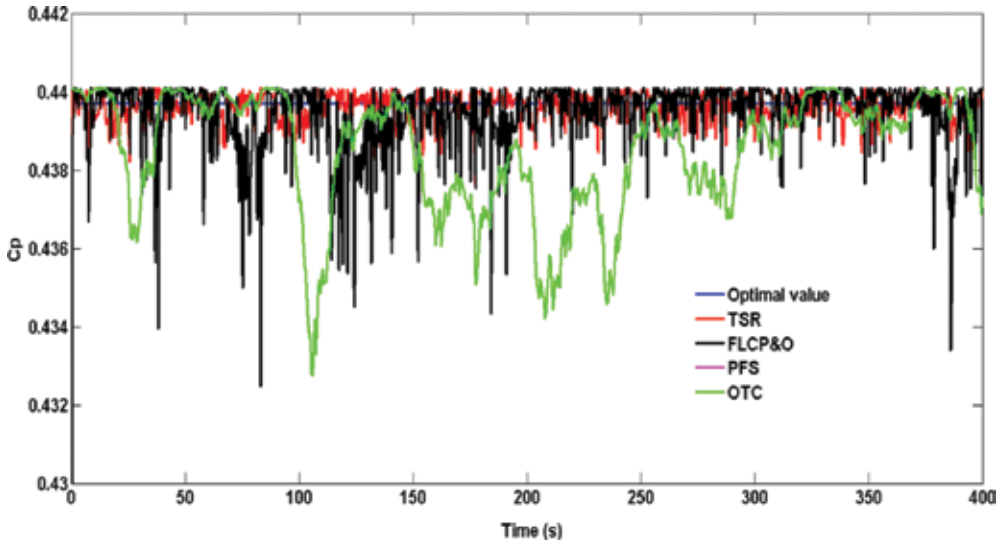

Figure 26. Comparison of the power coefficient for different MPPT methods.

4. Conclusion

In this work, a comparative study of different MPPT algorithms is presented. Firstly, the effectiveness and dynamics of the strategy control to extract maximum power, which is implemented using Matlab/Simulink/SimPower dynamic simulation system, are performed. The simulation results demonstrate that the proposed control strategy provides best performances in both transient and steady states. Thereafter, a new P&O MPPT algorithm based on fuzzy logic techniques, which provides a variable step size, was presented. The performances of this novel algorithm were compared to those of the algorithm presented in conventional literature. This new approach allows obtaining a power coefficient, where its value is very close to the maximum value.

After that, a comparative study between a MPPT algorithms applied to the DD-PMSG has been accomplished. The comparison of their performances is presented and analyzed. It is seen that the new sensorless FLCP&O gives a best performance with comparison to the OTC and PFS MPPT methods. Moreover, this approach is independent to the aerodynamic characteristics of the turbine unlike the OTC and PFS MPPT methods.

http://dx.doi.org/10.5772/63803

Nomenclature

Acronyms	Signification	Acronyms	Signification
AF	Axial flux	PMSG	Permanent Magnet Synchronous Generator
DD	Direct-Drive	PLL	Phase-Locked Loop
DTC	Direct Torque Control	P&O	Perturb and Observe
ESS	Energy Storage System	PSF	Power Signal Feedback
FLC	Fuzzy Logic Controller	PWM	Pulse Width Modulation
FOC	Field Orientation Control	SVM	Space Vector Modulation
GSC	Grid Side Converter	TFPM	Transverse Flux Permanent Magnet
HBCC	Hysteresis Band Current Control	THD	Total Harmonic Distortion
HPS	Hybrid Power System	VSI	Voltage Source Inverter
IGBT	Insulate Gate Bipolar Transistor	VOC	Voltage-Oriented Control
LSC	Load Side Converter	WECS	Wind-energy Conversion System
MPPT	Maximum Power Point Tracking	WTG	Wind Turbine Generator
OTC	Optimal Torque Control		

Greek letters	Signification
λ	Tip Speed Ratio (TSR)
ρ	Air Density [kg/m^3]
β	Blade Pitch Angle
Φ	The Magnet Flux [Wb]

Appendices

Wind turbine parameters

Rated power [kW]	14
Cut-in wind speed [m/s]	5
Cut-off wind speed [m/s]	25
Rated wind speed [m/s]	12
Rotor radius (R) [m]	2.5
λ_{opt}	8.1

PMSG parameters

Rated power [kW]	12.5

Number of pairs poles	8
Rs [Ω]	0.5
Ls [mH]	0.5
Moment of inertia (J) [kg/m^2]	10
Rated rotor speed [rad/sec]	314

Author details

Karim Belmokhtar[1*], Hussein Ibrahim[1] and Mamadou Lamine Doumbia[2]

*Address all correspondence to: kbelmokhtar@eolien.qc.ca

1 TechnoCentre éolien, Gaspé, Québec, Canada

2 University of Quebec at Trois-Rivieres, 3351, Rue des Forges, Trois-Rivières, Québec, Canada

References

[1] Hu, Yu., and Pablo. Solana. "Optimization of a hybrid diesel-wind generation plant with operational options." *Renewable Energy* 51 (2013): 364-372.

[2] Abdullah, M. A., et al. "A review of maximum power point tracking algorithms for wind energy systems." *Renewable and Sustainable Energy Reviews* 16.5 (2012): 3220-3227.

[3] Saidur, R., et al. "A review on global wind energy policy." *Renewable and Sustainable Energy Reviews* 14.7 (2010): 1744-1762.

[4] Beltran, Brice, Tarek Ahmed-Ali, and Mohamed El Hachemi Benbouzid. "High-order sliding-mode control of variable-speed wind turbines." *IEEE Transactions on Industrial Electronics* 56.9 (2009): 3314-3321.

[5] Uhlen, Kjetil, B. A. Foss, and O. B. Gjosaeter. "Robust control and analysis of a wind-diesel hybrid power plant." *IEEE Transactions on Energy Conversion* 9.4 (1994): 701-708.

[6] Chedid, Riad B., Sami H. Karaki, and Chadi El-Chamali. "Adaptive fuzzy control for wind-diesel weak power systems." *IEEE Transactions on Energy Conversion* 15.1 (2000): 71-78.

[7] Sharma, Pawan, and T. S. Bhatti. "Performance investigation of isolated wind–diesel hybrid power systems with WECS having PMIG." *IEEE Transactions on Industrial Electronics* 60.4 (2013): 1630-1637.

http://dx.doi.org/10.5772/63803

[8] Ross, Michael, et al. "Energy storage system scheduling for an isolated microgrid." *IET Renewable Power Generation* 5.2 (2011): 117-123.

[9] Fidalgo, J. N., JA Peças Lopes, and Vladimiro Miranda. "Neural networks applied to preventive control measures for the dynamic security of isolated power systems with renewables." *IEEE Transactions on Power Systems* 11.4 (1996): 1811-1816.

[10] Misak, Stanislav, and Lukas Prokop. "Off-grid power systems." *Environment and Electrical Engineering (EEEIC), 2010 9th International Conference on*. IEEE, 2010.

[11] Sharma, Pawan, Waldemar Sulkowski, and Bjarte Hoff. "Dynamic stability study of an isolated wind-diesel hybrid power system with wind power generation using IG, PMIG and PMSG: A comparison." *International Journal of Electrical Power & Energy Systems* 53 (2013): 857-866.

[12] Brunarie, Joöl, et al. "Delivering cost savings and environmental benefits with hybrid power." *INTELEC 2009-31st International Telecommunications Energy Conference*. IEEE, 2009.

[13] Kaldellis, John K., ed. *Stand-Alone and Hybrid Wind Energy Systems: Technology, Energy Storage and Applications*. Elsevier, 2010.

[14] El Mokadem, M., et al. "Maximum wind power control using torque characteristic in a wind diesel system with battery storage." *Recent Developments of Electrical Drives*. Netherlands: Springer, 2006, 385-396.

[15] AWEA. *Wind-Diesel Systems Architecture Guidebook*, American Wind Energy Association, 1991, 1-41.

[16] Hunter, Ray, and George Elliot. *Wind–Diesel Systems: A Guide to the Technology and Its Implementation*. Cambridge University Press, 1994.

[17] Sebastián, R., and R. Peña Alzola. "Simulation of an isolated wind diesel system with battery energy storage." *Electric Power Systems Research* 81.2 (2011): 677-686.

[18] Alnasir, Zuher, and Mehrdad Kazerani. "An analytical literature review of stand-alone wind energy conversion systems from generator viewpoint." *Renewable and Sustainable Energy Reviews* 28 (2013): 597-615.

[19] Alnasir, Zuher, and Mehrdad Kazerani. "An analytical literature review of stand-alone wind energy conversion systems from generator viewpoint." *Renewable and Sustainable Energy Reviews* 28 (2013): 597-615.

[20] Mukund, R. Patel. "Wind and solar power systems." (1999).

[21] Van Hulle, F. J. L. *Large Scale Integration of Wind Energy in the European Power Supply: Analysis, Issues and Recommendations: Executive Summary*. European Wind Energy Association, 2005.

[22] Khater, Faeka, and Alaa Omar. "A review of direct driven PMSG for wind energy systems." *Journal of Energy and Power Engineering* 7.8 (2013).

[23] Spee, R., and S. Bhowmik. "Wind turbines. Encyclopedia of Electrical Engineering." (1999).

[24] Muller, Set, M. Deicke, and Rik W. De Doncker. "Doubly fed induction generator systems for wind turbines." *IEEE Industry Applications Magazine* 8.3 (2002): 26-33.

[25] Chen, Zhe, Josep M. Guerrero, and Frede Blaabjerg. "A review of the state of the art of power electronics for wind turbines." *IEEE Transactions on Power Electronics* 24.8 (2009): 1859-1875.

[26] Haque, M. H. "Evaluation of power flow solutions with fixed speed wind turbine generating systems." *Energy Conversion and Management* 79 (2014): 511-518.

[27] Shrestha, Ghanshyam, et al. "Structural flexibility: A solution for weight reduction of large direct-drive wind-turbine generators." *IEEE Transactions on Energy Conversion* 25.3 (2010): 732-740.

[28] Kim, Seul-Ki, and Eung-Sang Kim. "PSCAD/EMTDC-based modeling and analysis of a gearless variable speed wind turbine." *IEEE Transactions on Energy Conversion* 22.2 (2007): 421-430.

[29] Sivachandran, P., P. Venkatesh, and N. Kamaraj. "A review of wind energy based decentralized power generation systems with new developments in India." *International Journal of Energy and Environment* (2007): 1563-1362.

[30] Gowda, S. Deve, and S. Raja Pandian. "Simulation of simple standalone wind energy system." *2006 India International Conference on Power Electronics*. IEEE, 2006.

[31] Haraguchi, Hiroshi, Shigeo Morimoto, and Masayuki Sanada. "Suitable design of a PMSG for a small-scale wind power generator." *Electrical Machines and Systems, 2009. ICEMS 2009. International Conference on*. IEEE, 2009.

[32] Liang, Wei, and Weiguo Liu. "Key technologies analysis of small scale non-grid-connected wind turbines: A review." *2010 World Non-Grid-Connected Wind Power and Energy Conference*. IEEE, 2010.

[33] Orlando, Natalia Angela, et al. "A survey of control issues in PMSG-based small wind-turbine systems." *IEEE Transactions on Industrial Informatics* 9.3 (2013): 1211-1221.

[34] Mirecki, Adam, Xavier Roboam, and Frdric Richardeau. "Architecture complexity and energy efficiency of small wind turbines." *IEEE Transactions on Industrial Electronics* 54.1 (2007): 660-670.

[35] Saleh, S. A., M. A. S. K. Khan, and M. A. Rahman. "Steady-state performance analysis and modelling of directly driven interior permanent magnet wind generators." *IET Renewable Power Generation* 5.2 (2011): 137-147.

http://dx.doi.org/10.5772/63803

[36] Mauricio, Juan Manuel, et al. "Frequency regulation contribution through variable-speed wind energy conversion systems." *IEEE Transactions on Power Systems* 24.1 (2009): 173-180.

[37] Benelghali, Seifeddine, et al. "Experimental validation of a marine current turbine simulator: Application to a permanent magnet synchronous generator-based system second-order sliding mode control." *IEEE Transactions on Industrial Electronics* 58.1 (2011): 118-126.

[38] Hauck, Matthieu, et al. "Operation of grid-connected cross-flow water turbines in the stall region by direct power control." *IEEE Transactions on Industrial Electronics* 58.4 (2011): 1132-1140.

[39] Kim, Hong-Woo, Sung-Soo Kim, and Hee-Sang Ko. "Modeling and control of PMSG-based variable-speed wind turbine." *Electric Power Systems Research* 80.1 (2010): 46-52.

[40] Chan, T. F., and L. L. Lai. "An axial-flux permanent-magnet synchronous generator for a direct-coupled wind-turbine system." *IEEE Transactions on Energy Conversion* 22.1 (2007): 86-94.

[41] Chen, Zheng, et al. "Analysis of converter topological structure for direct-drive wind power system with PMSG." *Power System Technology (POWERCON), 2010 International Conference on*. IEEE, 2010.

[42] Baroudi, Jamal A., Venkata Dinavahi, and Andrew M. Knight. "A review of power converter topologies for wind generators." *Renewable Energy* 32.14 (2007): 2369-2385.

[43] Morimoto, Shigeo, Masayuki Sanada, and Yoji Takeda. "Wide-speed operation of interior permanent magnet synchronous motors with high-performance current regulator." *IEEE Transactions on Industry Applications* 30.4 (1994): 920-926.

[44] Chinchilla, Monica, Santiago Arnaltes, and Juan Carlos Burgos. "Control of permanent-magnet generators applied to variable-speed wind-energy systems connected to the grid." *IEEE Transactions on Energy Conversion* 21.1 (2006): 130-135.

[45] Xu, Z., et al. "Direct torque and flux control of the converters for a permanent magnet wind power generation system." *Electric Power and Energy Conference (EPEC), 2010 IEEE*. IEEE, 2010.

[46] Takahashi, Isao, and Toshihiko Noguchi. "A new quick-response and high-efficiency control strategy of an induction motor." *IEEE Transactions on Industry Applications* 5 (1986): 820-827.

[47] Depenbrock, Manfred. "Direct self-control (DSC) of inverter-fed induction machine." *IEEE Transactions on Power Electronics* 3.4 (1988): 420-429.

[48] Casadei, Domenico, et al. "FOC and DTC: Two viable schemes for induction motors torque control." *IEEE Transactions on Power Electronics* 17.5 (2002): 779-787.

[49] Bouwer, Pieter. *Modelling, Design and Implementation of a Small-Scale, Position Sensorless, Variable Speed Wind Energy Conversion System Incorporating DTC-SVM of a PMSG Drive with RLC Filter*. Diss. Stellenbosch: Stellenbosch University, 2013.

[50] Xu, Z., T. Pang, and Dianguo Xu. "Instantaneous torque control of a permanent magnet wind power generator without a position sensor." *Electrical Machines and Systems, 2008. ICEMS 2008. International Conference on*. IEEE, 2008.

[51] Busca, Cristian, et al. "Control of Permanent Magnet Synchronous Generator for large wind turbines." *2010 IEEE International Symposium on Industrial Electronics*. IEEE, 2010.

[52] Kwon, Jeong Min, et al. "Optimal power extraction algorithm for DTC in wind power generation systems." *2008 IEEE International Conference on Sustainable Energy Technologies*. IEEE, 2008.

[53] Inoue, Yukinori, Shigeo Morimoto, and Masayuki Sanada. "Output maximization using direct torque control for sensorless variable wind generation system employing IPMSG." *Power Electronics and Motion Control Conference, 2008. EPE-PEMC 2008. 13th*. IEEE, 2008.

[54] Cirrincione, Maurizio, Marcello Pucci, and Gianpaolo Vitale. "Power Converters and AC Electrical Drives with Linear Neural Networks (Energy, Power Electronics, and Machines)." (2012).

[55] Wilamowski, Bogdan M., and J. David Irwin, eds. *Power Electronics and Motor Drives*. CRC Press, 2016.

[56] Ragheb, Magdi, and Adam M. Ragheb. *Wind Turbines Theory—The Betz Equation and Optimal Rotor Tip Speed Ratio*. INTECH Open Access Publisher, 2011.

[57] Kirke, Brian, and Leo Lazauskas. "Variable pitch Darrieus water turbines." *Journal of Fluid Science and Technology* 3.3 (2008): 430-438.

[58] Chichester, S. H. "Grid integration of wind energy conversion systems." (1999).

[59] Chung, S-K. "Phase-locked loop for grid-connected three-phase power conversion systems." *IEE Proceedings-Electric Power Applications* 147.3 (2000): 213-219.

[60] Haque, Md E., Michael Negnevitsky, and Kashem M. Muttaqi. "A novel control strategy for a variable speed wind turbine with a permanent magnet synchronous generator." *Industry Applications Society Annual Meeting, 2008. IAS'08. IEEE*. IEEE, 2008.

[61] Fatu, Marius, et al. "Novel motion sensorless control of stand-alone permanent magnet synchronous generator (PMSG): Harmonics and negative sequence voltage compensation under nonlinear load." *Power Electronics and Applications, 2007 European Conference on*. IEEE, 2007.

[62] Bhende, C. N. "Stand-alone wind energy supply system." *Power Systems, 2009. ICPS'09. International Conference on*. IEEE, 2009.

http://dx.doi.org/10.5772/63803

[63] Bhende, C. N., Shivakant Mishra, and Siva Ganesh Malla. "Permanent magnet synchronous generator-based standalone wind energy supply system." *IEEE Transactions on Sustainable Energy* 2.4 (2011): 361-373.

[64] Kendouli, F., et al. "High performance PWM converter control based PMSG for variable speed wind turbine." *2012 First International Conference on Renewable Energies and Vehicular Technology*. IEEE, 2012.

[65] Brahmi, Jemaa, Lotfi Krichen, and Abderrazak Ouali. "A comparative study between three sensorless control strategies for PMSG in wind energy conversion system." *Applied Energy* 86.9 (2009): 1565-1573.

[66] Kazmi, Syed Muhammad Raza, et al. "Review and critical analysis of the research papers published till date on maximum power point tracking in wind energy conversion system." *2010 IEEE Energy Conversion Congress and Exposition*. IEEE, 2010.

[67] Patel, Mukund R. *Wind and Solar Power Systems: Design, Analysis, and Operation*. CRC Press, 2005.

[68] Quincy, W. *Maximum Wind Energy Extraction Strategies Using Power Electronic Converters*. Diss. PhD. dissertation, Univ. of New Brunswick, Canada, 2003.

[69] Zhang, Jianzhong, et al. "Pitch angle control for variable speed wind turbines." *Electric Utility Deregulation and Restructuring and Power Technologies, 2008. DRPT 2008. Third International Conference on*. IEEE, 2008.

[70] Thongam, Jogendra Singh, and Mohand Ouhrouche. *MPPT Control Methods in Wind Energy Conversion Systems*. INTECH Open Access Publisher, 2011.

[71] Li, Hui, K. L. Shi, and P. G. McLaren. "Neural-network-based sensorless maximum wind energy capture with compensated power coefficient." *IEEE Transactions on Industry Applications* 41.6 (2005): 1548-1556.

[72] Xu, Zhiqiang, Qinghua Hu, and Mehrdad Ehsani. "Estimation of effective wind speed for fixed-speed wind turbines based on frequency domain data fusion." *IEEE Transactions on Sustainable Energy* 3.1 (2012): 57-64.

[73] Xin-Fang, Zhang, Xu Da-Ping, and Liu Yi-Bing. "Adaptive optimal fuzzy control for variable speed fixed pitch wind turbines." *Intelligent Control and Automation, 2004. WCICA 2004. Fifth World Congress on*. Vol. 3. IEEE, 2004.

[74] Simoes, M. Godoy, Bimal K. Bose, and Ronald J. Spiegel. "Fuzzy logic based intelligent control of a variable speed cage machine wind generation system." *IEEE Transactions on Power Electronics* 12.1 (1997): 87-95.

[75] Prats, M. A. M., et al. "Improving transition between power optimization and power limitation of variable speed, variable pitch wind turbines using fuzzy control techniques." *Industrial Electronics Society, 2000. IECON 2000. 26th Annual Confjerence of the IEEE*. Vol. 3. IEEE, 2000.

[76] Koutroulis, Eftichios, and Kostas Kalaitzakis. "Design of a maximum power tracking system for wind-energy-conversion applications." *IEEE Transactions on Industrial Electronics* 53.2 (2006): 486-494.

[77] Kesraoui, M., N. Korichi, and A. Belkadi. "Maximum power point tracker of wind energy conversion system." *Renewable Energy* 36.10 (2011): 2655-2662.

[78] Kazmi, Syed Muhammad Raza, et al. "A novel algorithm for fast and efficient speed-sensorless maximum power point tracking in wind energy conversion systems." *IEEE Transactions on Industrial Electronics* 58.1 (2011): 29-36.

[79] Wang, Quincy, and Liuchen Chang. "An intelligent maximum power extraction algorithm for inverter-based variable speed wind turbine systems." *IEEE Transactions on Power Electronics* 19.5 (2004): 1242-1249.

[80] Johnson, Kathryn E., et al. "Control of variable-speed wind turbines: Standard and adaptive techniques for maximizing energy capture." *IEEE Control Systems* 26.3 (2006): 70-81.

[81] Xia, Yuanye, Khaled H. Ahmed, and Barry W. Williams. "A new maximum power point tracking technique for permanent magnet synchronous generator based wind energy conversion system." *IEEE Transactions on Power Electronics* 26.12 (2011): 3609-3620.

[82] González, L. G., et al. "Maximum-power-point tracking with reduced mechanical stress applied to wind-energy-conversion-systems." *Applied Energy* 87.7 (2010): 2304-2312.

[83] Kortabarria, Iñigo, et al. "A novel adaptative maximum power point tracking algorithm for small wind turbines." *Renewable Energy* 63 (2014): 785-796.

[84] Duan, Rou-Yong, Chung-You Lin, and Rong-Jong Wai. "Maximum-power-extraction algorithm for grid-connected PMSG wind generation system." *IECON 2006-32nd Annual Conference on IEEE Industrial Electronics*. IEEE, 2006.

[85] Narayana, Mahinsasa, et al. "Generic maximum power point tracking controller for small-scale wind turbines." *Renewable Energy* 44 (2012): 72-79.

[86] Barakati, S. Masoud, Mehrdad Kazerani, and J. Dwight Aplevich. "Maximum power tracking control for a wind turbine system including a matrix converter." *IEEE Transactions on Energy Conversion* 24.3 (2009): 705-713.

[87] Tan, Kelvin, and S. Islam. "Optimum control strategies in energy conversion of PMSG wind turbine system without mechanical sensors (vol 19, pg 399, 2004)." *IEEE Transactions on Energy Conversion* 19.3 (2004): 654-654.

[88] Barakati, Seyed Masoud. "Modeling and controller design of a wind energy conversion system including a matrix converter." (2008).

[89] Wang, Quincy, and Liuchen Chang. "An intelligent maximum power extraction algorithm for inverter-based variable speed wind turbine systems." *IEEE Transactions on Power Electronics* 19.5 (2004): 1242-1249.

http://dx.doi.org/10.5772/63803

[90] Tang, Chun. *Analysis and Modelling of the Effects of Inertia and Parameter Errors on Wind Turbine Output Power*. Diss. 2010.

[91] Wu, Bin, et al. *Power Conversion and Control of Wind Energy Systems*. John Wiley & Sons, 2011.

[92] Yuan, Xibo, and Yongdong Li. "Control of variable pitch and variable speed direct-drive wind turbines in weak grid systems with active power balance." *IET Renewable Power Generation* 8.2 (2014): 119-131.

[93] Ganti, Vijay Chand, et al. "DFIG-based wind power conversion with grid power leveling for reduced gusts." *IEEE Transactions on Sustainable Energy* 3.1 (2012): 12-20.

[94] Liu, Changjin, et al. "DC-voltage fluctuation elimination through a DC-capacitor current control for DFIG converters under unbalanced grid voltage conditions." *IEEE Transactions on Power Electronics* 28.7 (2013): 3206-3218.

[95] Li, Shuhui, et al. "Optimal and direct-current vector control of direct-driven PMSG wind turbines." *IEEE Transactions on Power Electronics* 27.5 (2012): 2325-2337.

[96] Qiao, Wei, et al. "Wind speed estimation based sensorless output maximization control for a wind turbine driving a DFIG." *IEEE Transactions on Power Electronics* 23.3 (2008): 1156-1169.

[97] Spooner, E., A. C. Williamson, and G. Catto. "Modular design of permanent-magnet generators for wind turbines." *IEE Proceedings-Electric Power Applications* 143.5 (1996): 388-395.

[98] Svechkarenko, Dmitry, Juliette Soulard, and Chandur Sadarangani. "A novel transverse flux generator in direct-driven wind turbines." *Proc. Nordic Workshop on Power and Industrial Electronics*. 2006.

[99] Grauers, Anders. *Design of Direct-Driven Permanent-Magnet Generators for Wind Turbines*. Diss. School of Electrical and Computer Engineering, Chalmers University of Technology, 1996.

[100] Dubois, Maxime Roger Joseph. *Optimized Permanent Magnet Generator Topologies for Direct-Drive Wind Turbines*. TU Delft, Delft University of Technology, 2004.

[101] Weh, H., H. Hoffmann, and J. Landrath. "New permanent magnet excited synchronous machine with high efficiency at low speeds." *Proc. Int. Conf. Electrical Machines.* Vol. 3. 1988.

[102] Henneberger, G., and M. Bork. "Development of a new transverse flux motor." *New Topologies for Permanent Magnet Machines (Digest No: 1997/090), IEE Colloquium on*. IET, 1997.

[103] Anpalahan, Peethamparam, Juliette Soulard, and Hans-Peter Nee. "Design steps towards a high power factor transverse flux machine." *Proc. European Conf. on Power Electronics and Applications*. 2001.

[104] Lu, K. Y., et al. "Modeling and power factor analysis of a single phase surface mounted permanent magnet transverse flux machine." *Power Electronics and Drive Systems, 2003. PEDS 2003. The Fifth International Conference on*. Vol. 2. IEEE, 2003.

[105] Zhang, Chun, et al. "An improved scheme of fuzzy direct torque control of transverse flux permanent-magnet machine⋆." *Journal of Computational Information Systems* 8.1 (2012): 125-133.

[106] ZHENG, Xue-qin, et al. "Design of TFPM digital control system." *Journal of Jimei University (Natural Science)* 3 (2008): 009.

[107] Bang, D., et al. "Review of generator systems for direct-drive wind turbines." *European Wind Energy Conference & Exhibition, Belgium*. 2008.

[108] Hansen, L. H., Helle, L., Blaabjerg, F., Ritchie, E., Munk-Nielsen, S., Bindner, H. W., ... & Bak-Jensen, B. (2002). *Conceptual survey of generators and power electronics for wind turbines*.

[109] Henneberger, G., and M. Bork. "Development of a new transverse flux motor." *New Topologies for Permanent Magnet Machines (Digest No: 1997/090), IEE Colloquium on*. IET, 1997.

[110] Harris, M. R., G. H. Pajooman, and SM Abu Sharkh. "Performance and design optimisation of electric motors with heteropolar surface magnets and homopolar windings." *IEE Proceedings-Electric Power Applications* 143.6 (1996): 429-436.

[111] Dubois, M. R., H. Polinder, and J. A. Ferreira. "Comparison of generator topologies for direct-drive wind turbines." *Proceedings of NORPIE'00* (2000): 22-26.

[112] Rang, Yuqi, Chenglin Gu, and Huaishu Li. "Analytical design and modeling of a transverse flux permanent magnet machine." *Power System Technology, 2002. Proceedings. PowerCon 2002. International Conference on*. Vol. 4. IEEE, 2002.

[113] Huang, Surong, Jian Luo, and Thomas A. Lipo. "Analysis and evaluation of the transverse flux circumferential current machine." *Industry Applications Conference, 1997. Thirty-Second IAS Annual Meeting, IAS'97., Conference Record of the 1997 IEEE*. Vol. 1. IEEE, 1997.

[114] Hasubek, B. E., and E. P. Nowicki. "Two dimensional finite element analysis of passive rotor transverse flux motors with slanted rotor design." *Electrical and Computer Engineering, 1999 IEEE Canadian Conference on*. Vol. 2. IEEE, 1999.

[115] Njeh, A., A. Masmoudi, and A. Elantably. "3D FEA based investigation of the cogging torque of a claw pole transverse flux permanent magnet machine." *Electric Machines and Drives Conference, 2003. IEMDC'03. IEEE International*. Vol. 1. IEEE, 2003.

[116] Lu, K. Y., et al. "Modeling and power factor analysis of a single phase surface mounted permanent magnet transverse flux machine." *Power Electronics and Drive Systems, 2003. PEDS 2003. The Fifth International Conference on*. Vol. 2. IEEE, 2003.

http://dx.doi.org/10.5772/63803

[117] Li, Shuhui, et al. "Optimal and direct-current vector control of direct-driven PMSG wind turbines." *IEEE Transactions on Power Electronics* 27.5 (2012): 2325-2337.

[118] Masmoudi, Ahmed. "On the attempts to optimize the performance and cost-effectiveness of TFPM drives: A crucial challenge for the automotive industry." *European Transactions on Electrical Power* 15.6 (2005): 481-495.

[119] Li, Shuhui, et al. "Optimal and direct-current vector control of direct-driven PMSG wind turbines." *IEEE Transactions on Power Electronics* 27.5 (2012): 2325-2337.

Chapter 10

Wind-Driven Self-Excited Reluctance Generator for Rural Electrification

Ayodeji S.O. Ogunjuyigbe, Temitope R. Ayodele,
Bukola B. Adetokun and Adisa A. Jimoh

Additional information is available at the end of the chapter

http://dx.doi.org/10.5772/62738

Abstract

This chapter presents the dynamic performance of an isolated wind-driven self-excited reluctance generator (WDSERG) for rural electrification application. The performances of the machine under conditions of constant wind speed, varying wind speed, constant load, and varying loads are analysed and presented. The modelling and simulation have been carried out using MATLAB-Simulink. A step-wise procedure clearly set forth for the Simulink implementation of the wind-driven machine forms the balance of this work, which can be a good teaching aid. The result shows that with the variations in the connected loads, the output frequency of SERG remains constant, which makes it a good alternative for rural electrification.

Keywords: self-excited reluctance generator, rural electrification, wind speed, MATLAB-Simulink, dynamic performance

1. Introduction

The age-long exploitation of fossil fuel has resulted into attendant global warming, which has become the single largest environmental threat globally. An attempt to mitigate the effects of climate change due to the burning of fossil fuels and to meet the increasing energy demand has informed multi-dimensional researches into the harnessing of renewable energy sources for power generation. Thus, exploration of renewable energy sources such as hydro, solar, wind, and geothermal energies has gained global attention [1, 2].

Distributed generation is also receiving a rapt attention over centralized generation due to cost of transmission, particularly to rural areas which are mostly remote and isolated from the urban regions. The underlying issues involved in such distributed generation includes energy conversion, control, and integration . A number of electrical machines can be used for the electromechanical energy conversion, each with its attendant merits and demerits [3, 4].

The use of self-excited induction generator (SEIG) in isolated wind turbine energy conversion has gained prominence in recent years. This is largely due to its inherent advantages over the conventional synchronous generator, which includes simple, brushless, rugged, and robust construction with squirrel cage rotor, relatively low initial and maintenance cost, self protection against excessive overload, and short-circuit contingencies [5]. In addition, SEIGs require no external direct current (DC) supply for excitation and voltage regulation, and they have better transient performances [6]. On the other hand, the major drawbacks of SEIG are poor voltage and frequency regulations under varying prime mover speed and loading conditions. Its output frequency and generated voltage are dependent on the speed of the prime mover, hence a need for frequency and voltage stabilizing and control circuits, which invariably increases the installation cost [7, 8].

Another self-excited machine that can also provide a good and competitive potential for wind energy conversion for rural electrification is the self-excited reluctance generator (SERG). Three-phase SERG has almost all the advantages of SEIG. An additional advantage of SERG is the fact that it has constant output frequency in spite of varying loading conditions and excitation capacitances. Another desirable advantage of SERG is that of enhanced steady state performances and relatively high efficiency over a wide range of operation [9].

In view of its shortcomings, SEIG suffers in terms of changes in both magnitude and frequency of the generated voltage under various loads. A salient-pole or segmental pole rotor SERG without dc excitation has been proposed to decrease such problem [10].

This chapter therefore focuses on the harnessing of wind energy for electric power generation in rural areas using SERG. A detailed mathematical model of energy conversion with SERG suitable for the dynamic and transient analysis of the machine is presented. The model is utilised to build an investigative simulation tool in the MATLAB-Simulink environment. The advantages of SERG over SEIG are shown in the simulation results.

Also, a typical model of a wind turbine is developed and integrated to that of the SERG to obtain a complete network for the wind-driven self-excited reluctance generator (WDSERG). The complete model was used to simulate the WDSERG. Different scenarios of wind speed and load conditions were investigated to determine the process of voltage build-up and voltage collapse. Simulation results of the SERG driven by a wind turbine are presented in the concluding section of this chapter.

2. Wind turbine model

Wind energy is one of the most prominent renewable energy sources on earth. In recent years, there has been a marked growth in the harnessing of this resource for electricity generation.

http://dx.doi.org/10.5772/62738

The installed power increased from 7.5 GW in 1997 to more than 194 GW in 2010 globally [11]. This brought about a corresponding increase in the size and power ratings of turbines, with rotor diameters of more than 100 m and power ratings ranging from kilowatts to megawatts. The obvious need for off-grid distributed generation is another reason for the increasing demand for the design, construction, and operation of wind energy conversion systems. The mechanical output power of the turbine (in Watts) is given by:

$$P_m = \frac{1}{2} C_p(\lambda, \beta) \rho A v_w{}^3 \tag{1}$$

where C_p is the performance coefficient of the turbine, λ is the tip speed ratio (TSR), β is the blade pitch angle, ρ is density of air in Kg/m^3, A is the turbine swept area in m^2, and v_w is the wind speed in m/s. The performance coefficient (C_p) of the turbine is a measure of how much mechanical power can be derived from the wind, that is, the aerodynamic efficiency of the turbine. It represents the fraction of the wind's kinetic energy that is converted into mechanical energy. It is a function of the tip-speed ratio (λ) and blade pitch angle (β) given by:

$$C_p(\lambda, \beta) = C_1 \left(\frac{C_2}{\lambda_1} - C_3 \beta - C_4 \right) e^{\frac{-C_5}{\lambda_1}} + C_6 \lambda \tag{2}$$

Where

$$\lambda_1 = \frac{\left(\beta^3 + 1\right)(\lambda + 0.08\beta)}{\beta^3 - 0.028\beta - 0.035\lambda + 1} \tag{3}$$

The coefficients C_1 to C_6 are C_1=0.5176; C_2=116; C_3=0.4; C_4=5; C_5=21; C_6=0.0068. The TSR is the ratio of the turbine blade linear speed to the wind speed

$$\lambda = \frac{\omega_t \mathrm{R}}{v_w} \tag{4}$$

where ω_t is the rotor blade tip speed in rad/s, and R is the radius of the turbine blade. The mechanical torque developed by the wind turbine is given as:

$$T_m = \frac{P_m}{\omega_t} = \frac{0.5 C_p(\lambda, \beta) \rho A v_w{}^3}{\omega_t} \tag{5}$$

The turbine power characteristics for different values of wind speeds and for the specified blade pitch angle (β) are shown in **Figure 1**:

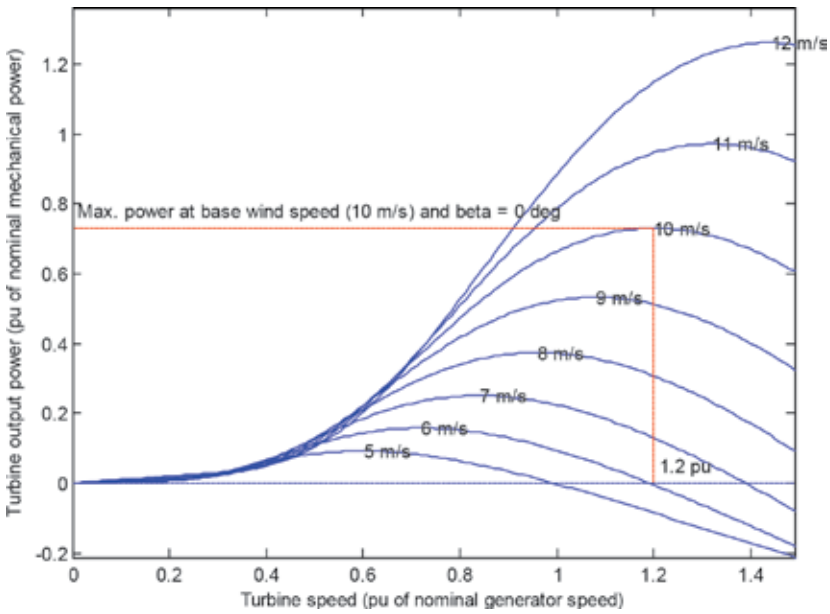

Figure 1. Turbine Power Characteristics for different values of wind speed.

3. The reluctance machine

Although reluctance machine has been known as early as induction machine, it has received minimal attention due to its relatively poor overall performance. Its earliest operations were largely in the motor mode for special applications [12, 13]. These applications include electric clocks, textile drives, synchronous switches drives, and the more sophisticated applications in nuclear reactors to position control rods with exact precision and reliability [14, 15]. However, since early 1960s, [14] and others started to study the theory and performance of poly-phase reluctance machines, and this paved way for an extensive study of the machine. Most of the studies carried out were however concentrated on the reluctance motor, until early 1980s when it was reported that the reluctance machine can also be operated as a SERG [16].

The reluctance machine is made up of a stator similar to that of the induction machine, and the rotor is basically a squirrel-cage induction machine rotor modified in order to have saliency in its magnetic circuit, which enhances the production of reluctance torque [14]. In order to ensure self-starting, the machine is provided with squirrel-cage rotor bars or damper cage windings. The principle of operation of the reluctance machine is based on the existence of varying air-gap reluctance, such that the opposition to the passage of magnetic flux is a minimum along an axis called the direct axis, and a maximum along an electrically perpen-

http://dx.doi.org/10.5772/62738

dicular axis, called the quadrature axis. The rotor is thus said to be magnetically anisotropic [15]. The tendency of the direct axis to align itself with the axis of the rotating magnetic field provided by the stator forms the basis for the operation of this machine.

Unlike induction machines, the motion of the rotor can be perfectly latched under the influence of the rotating magnetic field of the stator such that the rotor runs with the same speed of the stator's field. Thus, reluctance machine is a synchronous machine. This is a major advantage of the reluctance machine. Regardless of variations in the supply voltage and the load, the reluctance motor would run at synchronous speed. It is well-known that the output power of a reluctance machine increases with the ratio of the direct-axis inductance (or reactance) to the quadrature-axis inductance (or reactance) (L_d/L_q or X_d/X_q). Therefore, several attempts have been made to increase the L_d/L_q ratio [13]. To improve the overall performance of the reluctance machine, there have been improvements in electromagnetic designs which have brought about different rotor geometrical configurations. Because of these improved designs, the reluctance machine can compete favourably with the well-established induction machine [13]. Some of the rotor configurations include conventional salient pole rotor, segmented rotor, axially laminated anisotropic (ALA) rotor, flux-guided or flux-barrier rotor, and transversely laminated (TLA) rotor [13]. These have their different advantages and limitations.

3.1. Self-excited reluctance generator

The growing interest to harness renewable energy sources has informed the use of self-excited machines for energy conversion. Like the induction machine, the reluctance machine can also be used as a SERG driven by a prime mover. The self-excitation is initiated when suitable capacitors are connected across its stator terminals. As the rotor rotates, the residual flux in the rotor induces a small amount of electromotive force in the stator windings. With suitable capacitors connected across the stator terminals, a small amount of current flows in the stator windings which then increases the magnetic flux in the machine. The voltage then builds up in this manner until the magnetic core becomes saturated. Thus, these two conditions must be satisfied for self excitation and voltage build-up to occur [17]: (i) the rotor must have sufficient residual magnetism and (ii) the capacitance value must be adequate. The magnetizing inductance is a major factor for voltage buildup and stabilization of generated voltage for unloaded and loaded conditions.

4. Modelling of the self-excited reluctance generator

In this chapter, the following simplifying assumptions have been made.

i. Only the d-axis magnetizing inductance is affected by magnetic saturation.

ii. Core loss is negligible.

iii. Negligible space harmonics in the air-gap flux and time harmonics in the electromotive force and current waveforms.

4.1. Voltage equations

The equations of a reluctance machine can be obtained from those of the wound field synchronous machine with the field winding terms omitted [18, 19]. In rotor reference frame, the voltage equation for a synchronous reluctance generator with no rotor conductor can thus be written as follows:

$$v_{qs} = -r_s i_{qs} + \omega_r \lambda_{ds} + p\lambda_{qs} \tag{6}$$

$$v_{ds} = -r_s i_{ds} - \omega_r \lambda_{qs} + p\lambda_{ds} \tag{7}$$

$$\lambda_{qs} = -L_q i_{qs} \tag{8}$$

$$\lambda_{ds} = -L_d i_{ds} \tag{9}$$

$$L_q = L_{ls} + L_{mq} \tag{10}$$

$$L_d = L_{ls} + L_{md} \tag{11}$$

where: v_{qs} (v_{ds}) is the q-axis (d-axis) stator voltage, i_s is the stator current, r_s is the stator resistance, L_q (L_d) is the q-axis (d-axis) stator inductance, L_{mq} (L_{md}) is the q-axis (d-axis) stator mutual inductance, L_{ls} is the stator leakage inductance, λ_{qs} (λ_{ds}) is the q-axis (d-axis) stator flux linkage, ω_r is the rotor speed and p is the differential operator denoting $\frac{d}{dt}$.

The *q-d* equivalent circuit of the reluctance generator without a damper winding in the rotor as obtained from equations (6) to (9) is shown below. Since a generator is under consideration here, the direction of the stator current is taken to be out of the machine stator terminals.

4.2. Electromagnetic torque equation

The electromagnetic torque developed by the generator may be written as:

$$T_e = \left(\frac{3}{2}\right)\left(\frac{P}{2}\right)\left[\lambda_{ds} i_{qs} - \lambda_{qs} i_{ds}\right] \tag{12}$$

If we substitute (8) and (9) into (12), we obtain:

http://dx.doi.org/10.5772/62738

$$T_e = \left(\frac{3}{2}\right)\left(\frac{P}{2}\right)\left[\left(L_q - L_d\right) i_{qs} i_{ds}\right] \tag{13}$$

Where P is the number of poles on the SERG rotor. With the assumed current direction into the stator, this torque expression is positive for generator action and negative for motor action.

4.3. Coupling equation

A system of gears contained in a gearbox system is required to convert the lower rotational speeds on the wind turbine side to a high rotor speed on the generator side, for electrical energy production. The gear ratio is the ratio of the generator speed to the tip speed of the turbine blade.

Therefore, the coupling equation, which represents the swing equation of the generator is given as:

$$p\omega_r = \frac{P}{2J_T}\left(T_m - T_e - \frac{2}{P} B\omega_r\right) \tag{14}$$

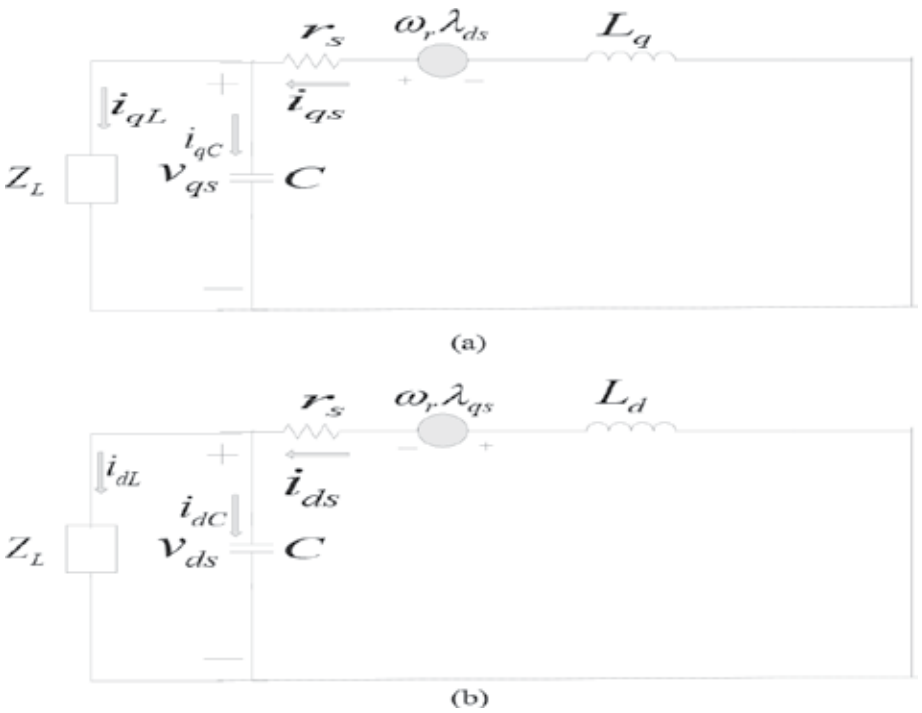

Figure 2. Rotor reference frame equivalent circuit of a self-excited reluctance generator. (a) q-axis (b) d-axis.

where B is the friction constant of the system. The wind turbine is represented as a single lumped inertia, J_T, in equation (14). This includes the inertial masses of the turbine blades, the gearbox, and the generator, referred to the generator side.

4.4. Excitation capacitance and load model

The stator terminals are connected to a capacitance bank in parallel with the load. The equations that relate the terminal voltages with the stator currents and load currents are presented in the following equations. Looking into the equivalent circuit of **Figure 2**, the nodal equation at the stator-capacitor-load terminals is obtained using Kirchoff's Current Law as:

$$i_{dC} = i_{ds} - i_{dL} \tag{15}$$

$$i_{qC} = i_{qs} - i_{qL} \tag{16}$$

i_{dC} (i_{qC}) and i_{dL} (i_{qL}) are the *d*-axis(*q*-axis) currents drawn by the excitation capacitors and the load respectively.

A general representation of the excitation capacitance in rotor reference frame is given in matrix form as:

$$\begin{bmatrix} i_{qC} \\ i_{dC} \end{bmatrix} = \begin{bmatrix} pC & \omega_r C \\ -\omega_r C & pC \end{bmatrix} \begin{bmatrix} V_{qL} \\ V_{dL} \end{bmatrix} \tag{17}$$

whereupon, the voltages are expressed as:

$$pV_{qL} = -\omega_r V_{dL} + \frac{i_{qs} - i_{qL}}{C} \tag{18}$$

$$pV_{dL} = \omega_r V_{qL} + \frac{i_{ds} - i_{dL}}{C} \tag{19}$$

Taking the load as a typical RLC, a general balanced RLC load model can be represented by:

$$V = iR + L\frac{di}{dt} + \frac{1}{C}\int idt \tag{20}$$

R_L , L_L , and C_L respectively represents the resistance, inductance, and capacitance of the load.

The RL load model can be obtained from (20) and it is expressed in rotor reference frame as:

http://dx.doi.org/10.5772/62738

$$i_{qL} = \int \frac{1}{L_L}\left[V_{qL} - i_{qL}R_L - \omega_r L_L i_{dL}\right]dt \tag{21}$$

$$i_{dL} = \int \frac{1}{L_L}\left[V_{dL} - i_{dL}R_L + \omega_r L_L i_{qL}\right]dt \tag{22}$$

5. Simulation of the WDSERG

A 2 hp (1.5 KW), 4-pole, 60 Hz machine with the parameters obtained from [20], and [21] is used for the simulation in this chapter. The parameters are given in **Table 1**.

Machine rating			**Tbase**	**Ibase(abc)**	r_s	L_q	**J**
Horsepower	Volts	Rpm	Nm	Amps	Ohms	H	Kgm^2
2	120	1800	7.9577	4.1667	3.77	0.081	0.1

Table 1. Reluctance machine parameters.

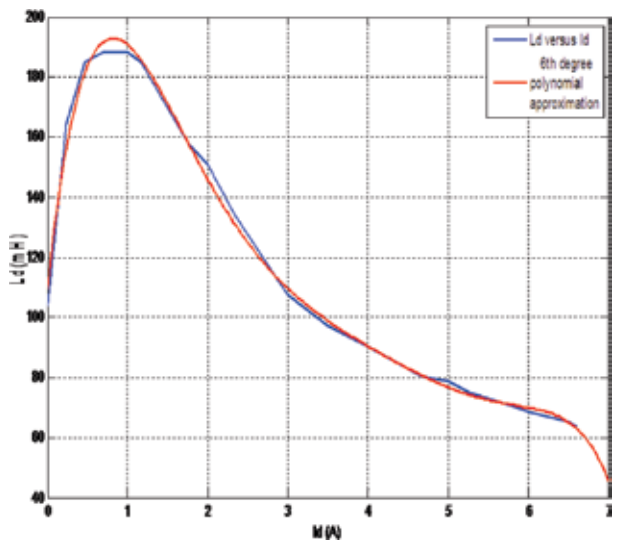

Figure 3. d-axis magnetising characteristic.

The magnetising characteristics of the machine is given by the L_d-I_d curve shown in **Figure 3**. A 6^{th} order curve fitting polynomial has been used to approximate the relationship. This enables the saturation effect to be taken into consideration.

The polynomial is given as:

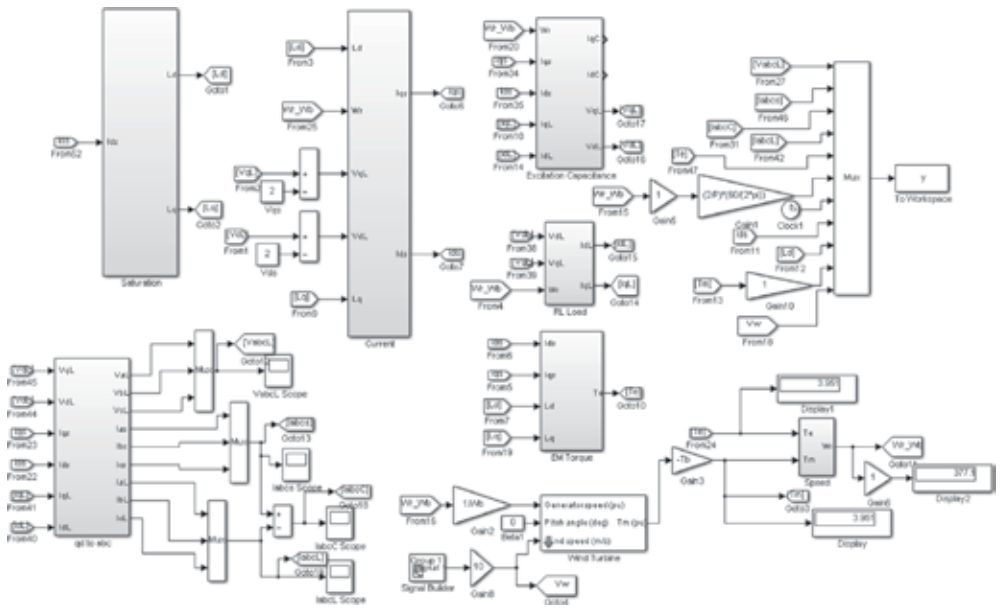

Figure 4. Complete WDSERG model in MATLAB-Simulink.

$$L_d = -0.10007 i_d{}^6 + 2.3788 i_d{}^5 - 22.52 i_d{}^4 + 107.06 i_d{}^3 - 259.15 i_d{}^2 + 253.62 i_d + 109.44 \tag{23}$$

5.1. MATLAB-Simulink implementation

The equations derived in the previous sections are arranged in forms suitable for simulation. For the purpose of clarity, the voltage equations have been rearranged below. By substituting equations (8) and (9) into (6) and (7) respectively, the currents can be expressed as:

$$i_{qs} = \frac{-\lambda_{qs}}{L_q} = -\int \frac{1}{L_q}\left[V_{qs} + r_s i_{qs} + \omega_r L_d i_d\right] dt \tag{24}$$

$$i_{ds} = \frac{-\lambda_{ds}}{L_d} = -\int \frac{1}{L_d}\left[V_{ds} + r_s i_{ds} - \omega_r L_q i_q\right] dt \tag{25}$$

The detailed MATLAB-Simulink model developed and utilised to simulate WDSERG is presented in the following **Figures 4** to **12**.

The model is made up of the different subsystems (saturation, current, excitation capacitance, EM torque, *qd* to *abc*, speed, wind turbine) as shown in **Figure 4**. The details in the saturation

http://dx.doi.org/10.5772/62738

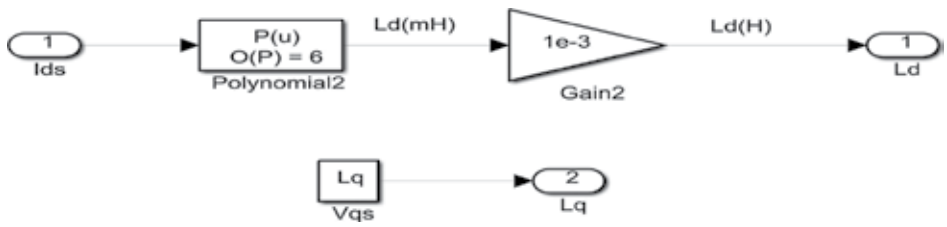

Figure 5. Saturation Subsystem.

subsystem is shown in **Figure 5**. This implements the magnetising characteristic approximated by equation (23), while **Figure 6** shows the details in the current subsystem and it implements equations (24) and (25). The shunt excitation capacitance is implemented by the details of the subsystem shown in **Figure 7**. The implementation of the RL load model derived from equations (21) and (22) is shown in **Figure 8**, while **Figures 9** and **10** respectively shows the electromagnetic torque and generator speed subsystems.

The inverse transformation (*qd* to *abc*) subsystem shown in **Figure 11** transforms the *qd* stator-load-capacitor terminal voltages, stator, capacitor, and load currents into machine (abc) variables. The wind turbine model in MATLAB-Simulink implementation is shown in **Figure 12**.

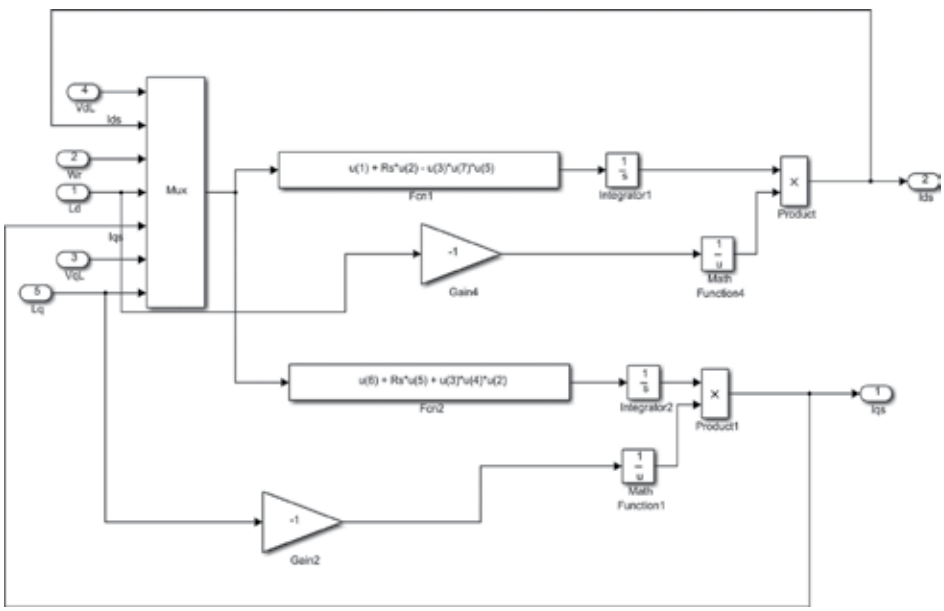

Figure 6. Current Subsystem.

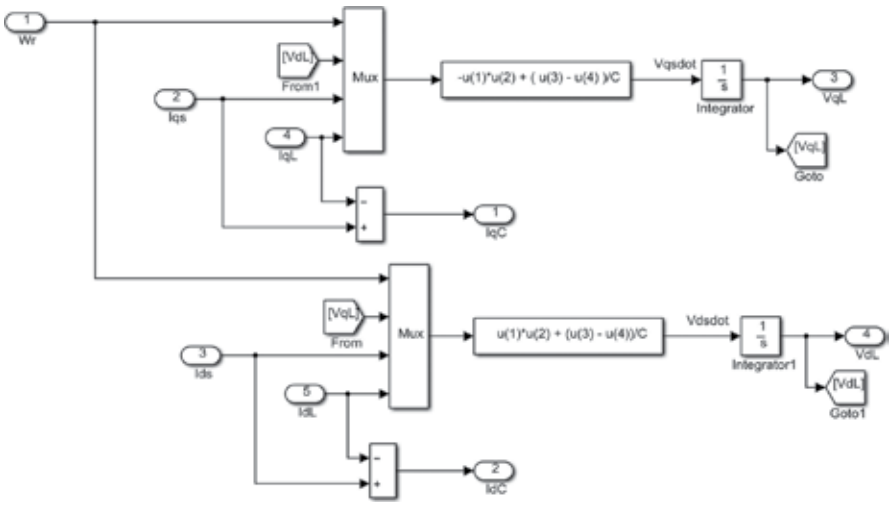

Figure 7. Shunt Excitation Capacitance Subsystem.

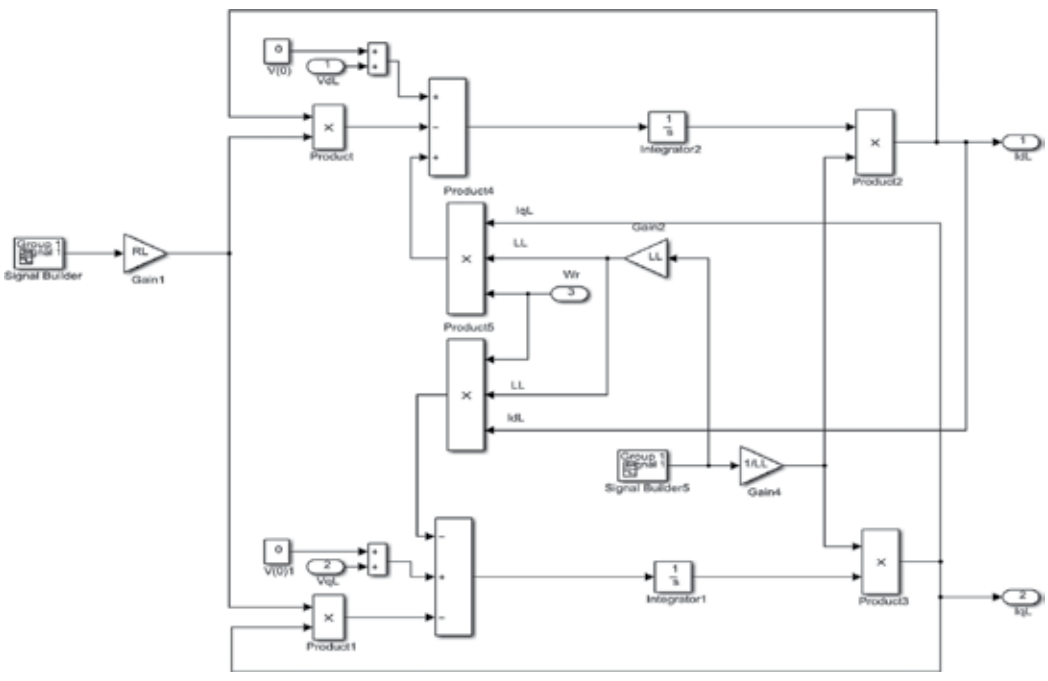

Figure 8. RL Load Subsystem.

http://dx.doi.org/10.5772/62738

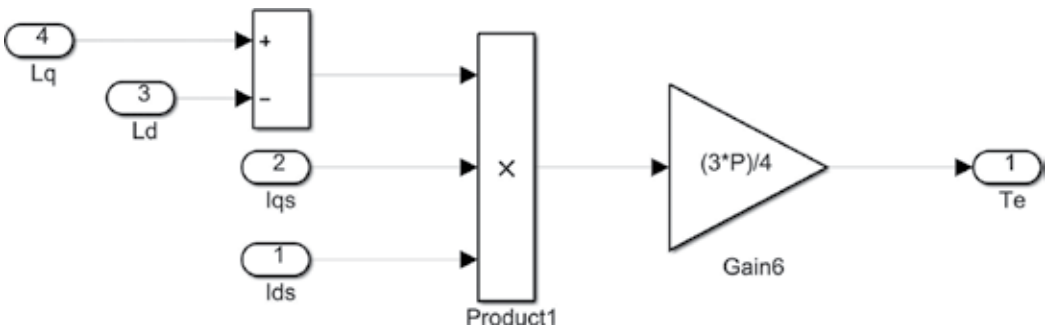

Figure 9. Electromagnetic Torque Subsystem.

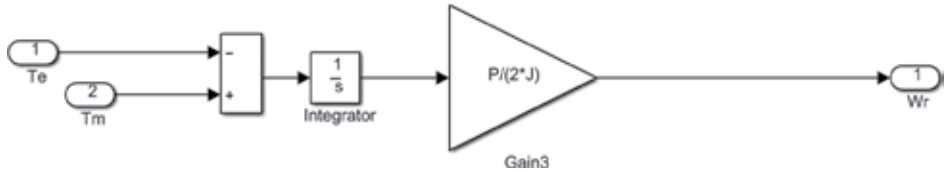

Figure 10. Rotor Speed Subsystem.

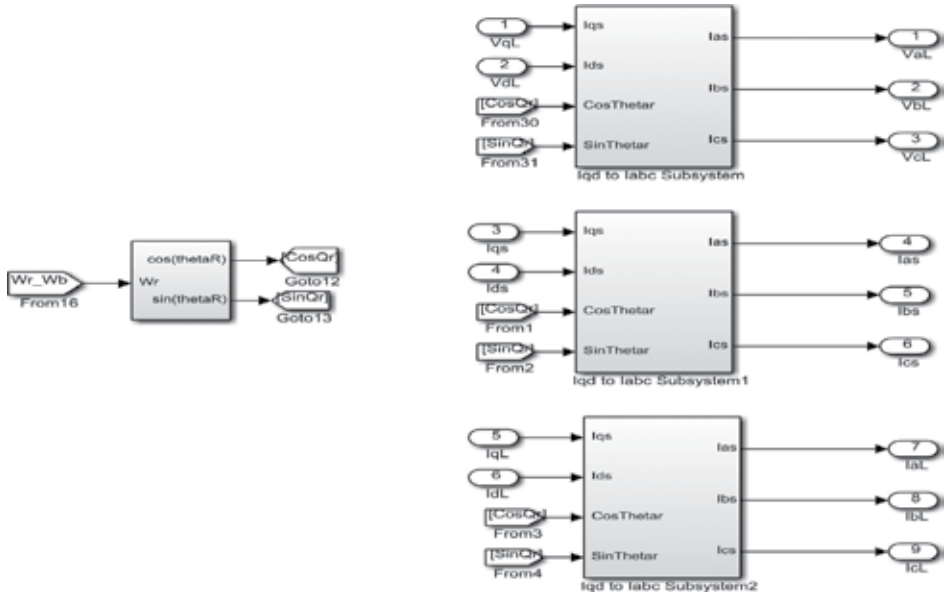

Figure 11. *qd* to *abc* subsystem.

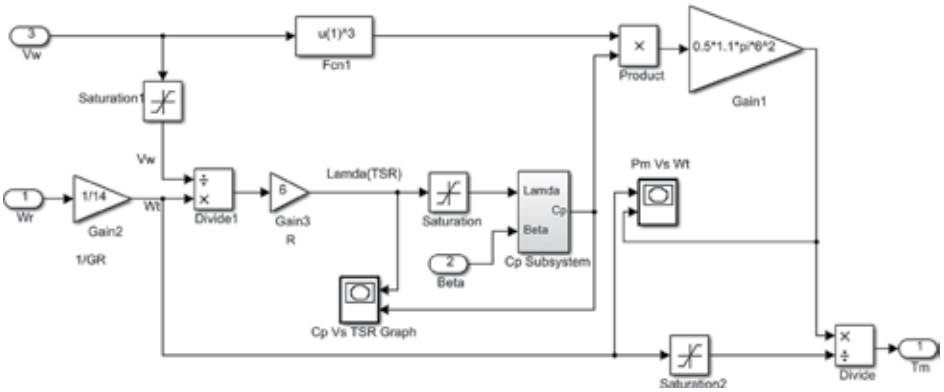

Figure 12. Wind Turbine Model.

6. Simulation result

The simulation has been done using MATLAB-Simulink to observe the performance of the system under the following conditions:

a. Constant wind speed

b. Wind Speed Variation

c. Load variations

The stator terminals are connected to a balanced star-connected capacitance bank of $85\mu F$ per phase. It has been mentioned earlier, that for a successful excitation and voltage build up, there must be a sufficient residual emf. This has been represented in the simulink model by an assumed value of 2 V.

A no load condition can be simulated using a very large value of R and L (**Figure 13**). Under this condition, the terminal impedance is so high that it can be regarded as an open circuit. The result of the simulation under this condition is shown in **Figure 13**. The stator phase current is about 10.33 A, while the load current is practically equal to zero (0.000035 A). The electromagnetic torque developed, which is equal to the wind turbine torque rises to a steady value of 3.707 Nm.

6.1. WDSERG performance at constant wind speed

The performance of the WDSERG under a constant wind speed of 10 m/s and an RL load (R = 400 Ohms; L = 30 mH) is shown in **Figure 14**. The wind turbine torque rose to a steady value of 0.7611 Nm. As the wind torque is applied, the generator speed quickly rises to the synchronous speed of 1800 rpm. The electromagnetic torque developed by the machine closely matches the wind torque, which invariably leads to a constant SERG speed.

http://dx.doi.org/10.5772/62738

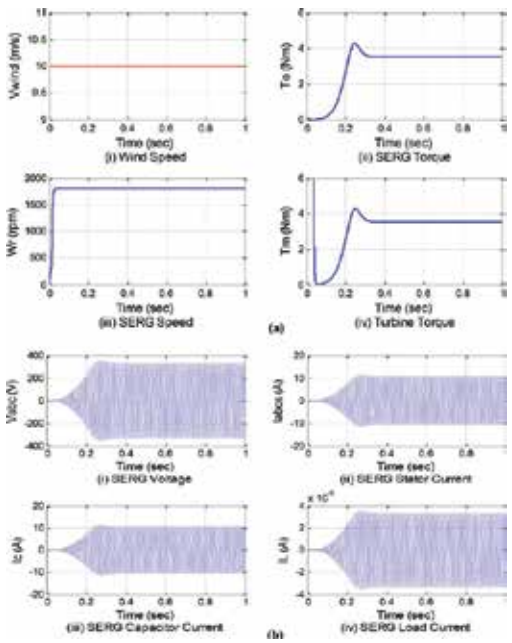

Figure 13. WDSERG At Vwind = 10m/s at No load (R = 10Megaohms; L = 30H).

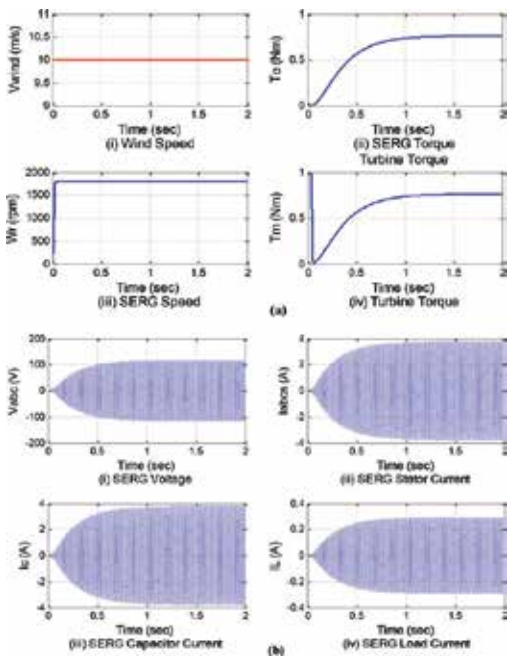

Figure 14. WDSERG At Vwind = 10m/s with R = 400ohms; L = 30mH.

It is observed that a WDSERG would perform smoothly with a constant wind speed profile.

6.2. WDSERG performance at varying wind speed

This scenario is analysed in two possible cases of decrease in wind speed and increase in wind speed as follows:

6.2.1. Decrease in wind speed

The dynamic response of the wind-driven SERG when the wind speed suddenly falls to 8 m/s for an RL load of 400 Ohms, 30 mH. The wind torque and the electromagnetic torque also falls suddenly from an initial value of 0.7611 Nm to a value of 0.3656 Nm. As the wind speed falls, the generator speed also falls from the synchronous value of 377 rad/s (1800 rpm) to 301.9 rad/s (1441.5 rpm).

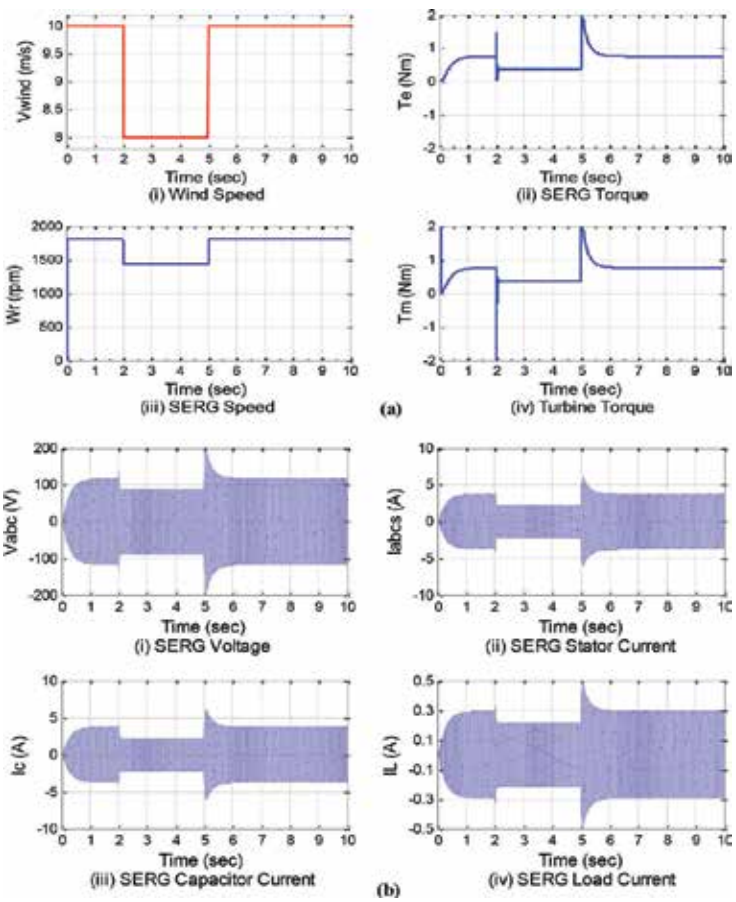

Figure 15. Dynamic response of the WDSERG when the wind speed suddenly falls to 8m/s.

http://dx.doi.org/10.5772/62738

Under this input condition, the generated voltage falls from a value of 118 V to a new value of about 100 V. The machine continues in this new values until 5 s when the wind speed was suddenly returned to 10 m/s. Thus, a decrease in the wind speed tends to reduce the generated voltage (**Figure 15**).

6.2.2. Increase in wind speed

In **Figure 16**, with an RL load of 400 Ohms, 30 mH, and an excitation capacitance of $85\mu F$, the wind speed is suddenly increased to a value of 10.2 m/s at 2 s and then dropped back to 10 m/s at 4 s. The figure shows that as the wind speed is increased by this small value, the generated voltage suddenly falls from a value of 118 V to about 25 V. This shows that in this particular case, the generated voltage of the wind-driven SERG tends to collapse at an increased wind speed. For the value of $85\mu F$ excitation capacitance, the SERG could not be operated with a

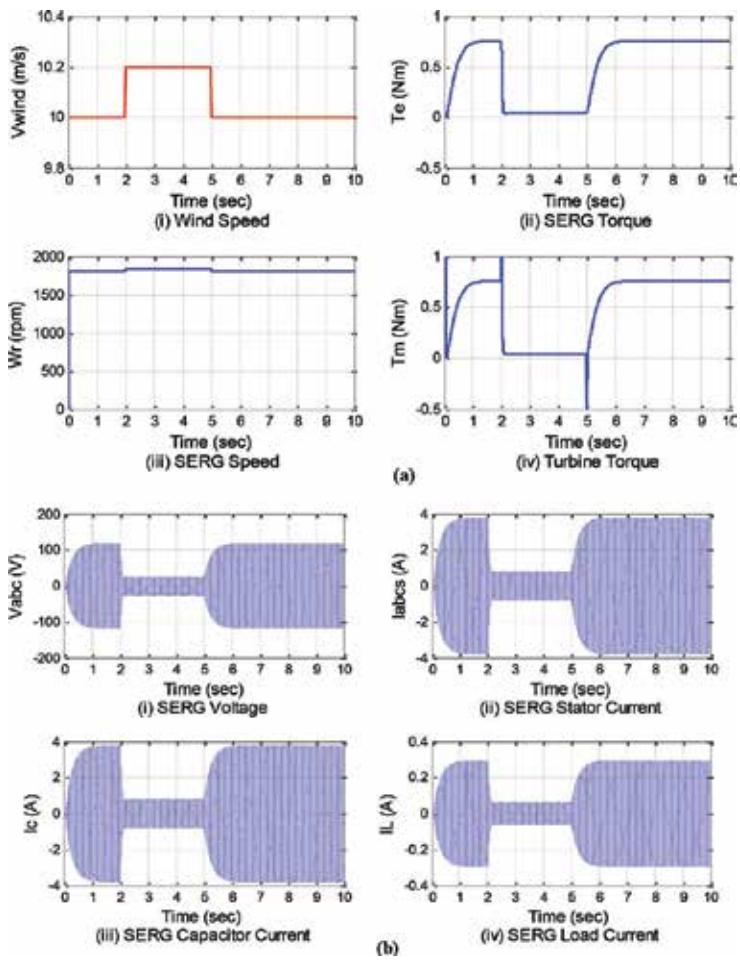

Figure 16. Dynamic response of the WDSERG when the wind speed suddenly rises to 10.2m/s.

reasonable voltage build up at wind speeds above 10 m/s, as this produces a generator speed greater than the rated synchronous speed. However, a reasonable voltage build-up is observed when the excitation capacitance is reduced accordingly. This shows that the excitation capacitance requirement reduces as the wind speed increases. This result therefore shows an inverse relationship between excitation capacitance and rotor speed. For $85\mu F$ excitation capacitance, **Figure 16** shows the wind torque and the electromagnetic torque falling to a very low value (0.041 Nm) at 2 s when the wind speed rises to 10.2 m/s and the torque rises again at 4 s when the wind speed decreases sharply back to 10 m/s to attain the initial steady value of 0.7611 Nm. However, at a selected lower capacitance value, the WDSERG voltage builds up appreciably at 12 m/s. Thus, a well-designed pitch-control mechanism for the wind turbine is necessary to operate the WDSERG at higher wind speeds with a fixed excitation capacitance, such that the torque developed by the wind speed is not above the value required to drive the generator at rated speed. Alternatively, the SERG can be provided with wind-following excitation.

6.3. SERG performance under load variations

A scenario of an overloaded condition was simulated using an effective load impedance which reduced in steps from 400 Ohms to 200 Ohms at 2 s to 100 Ohms at 4s then to 80 Ohms at 6 s and finally back to 400 Ohms. The result of the simulation is illustrated in **Figure 17**. It is observed that at t = 2s, when the load suddenly changes to 200 Ohms, there is a remarkable fall in the voltage level. The generated voltage continues to fall at 4 s and at 6 s until it rapidly falls toward zero as a result of overload. This illustrates that at an overloaded condition, the generator will suffer voltage collapse. The voltage builds up again at 8 s when the load changes back to its initial impedance value.

The performance of the WDSERG under varying loads is shown in **Figure 18**. When the RL load suddenly changes from 400 Ohms, 35 mH to 300 Ohms, 105 mH at 3 s, and then changes back to the initial RL values at 6 s, the following are observed:

(a) At 3 s, the drive torque and hence the electromagnetic torque falls from a value of 0.8216 Nm to a new steady state value of 0.6181 Nm. This consequently leads to a reduction in both the stator voltages and currents. The voltage dropped from about 123 V to a steady value of 101 V, and the stator current falls from about 4 A to about 3.2 A. However, during this period the load current increases slightly due to an increase in load inductance. When the RL value is suddenly increased again at 6 s, the voltage and current rises back to their initial values.

In spite of the sudden increase and decrease in the load, the speed of the SERG remains constant at 1800 rpm, and hence the frequency. Thus, there is a constant output frequency regardless of the variations in load. This is unlike the SEIG, whose voltages and frequency are heavily affected by varying loading conditions [22]. It is obvious also that though the WDSERG voltage output varies with the load, this variation may not be as severe compared to the SEIG.

http://dx.doi.org/10.5772/62738

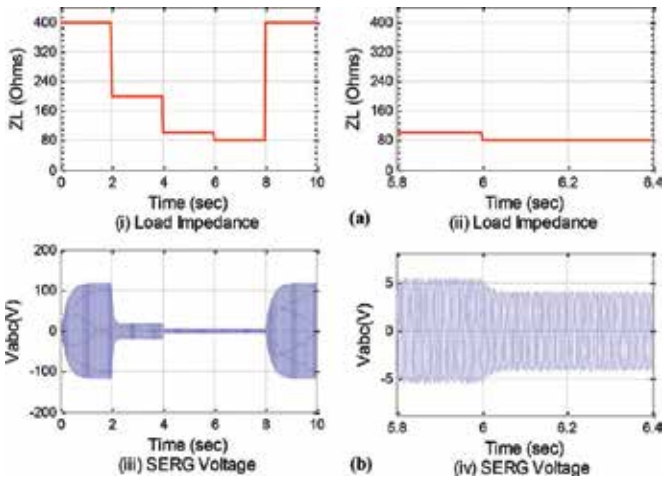

Figure 17. Voltage Collapse of the WDSERG.

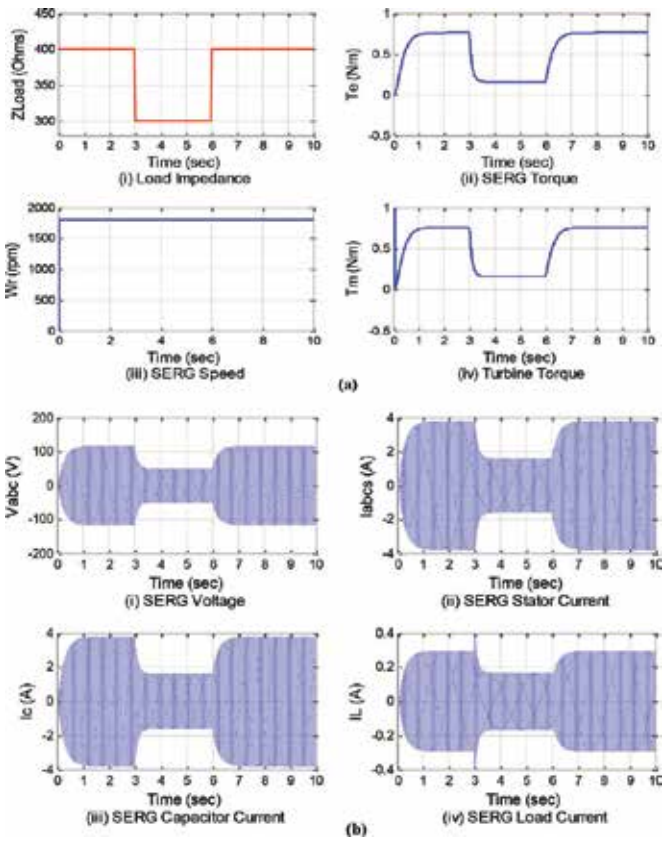

Figure 18. Dynamic response of the WDSERG under sudden increase and decrease in the RL load at Vwind = 10m/s.

7. Conclusion

The dynamic performance of a wind-driven SERG has been analysed and presented under conditions of constant wind speed, varying wind speed, and varying load. A step-by-step procedure for the MATLAB-Simulink implementation has been clearly presented.The results show that the generated voltage slightly falls with increasing load, and requires an increase in excitation capacitance within the stable operating limits to maintain a constant generated voltage. A wind-driven SERG will however operate at constant output frequency regardless of the load variations at its output terminals. This makes the SERG a good candidate for wind power application in rural electrification.

Author details

Ayodeji S.O. Ogunjuyigbe[1*], Temitope R. Ayodele[1], Bukola B. Adetokun[1] and Adisa A. Jimoh[2]

*Address all correspondence to: a.ogunjuyigbe@ui.edu.ng

1 Power Energy Machines and Drives (PEMD) Research Group, Department of Electrical and Electronic Engineering, University of Ibadan, Nigeria

2 Electrical Engineering Department, Tshwane University of Technology, Pretoria, South Africa

References

[1] T. R. Ayodele and A. S. O. Ogunjuyigbe, "Wind energy resource, wind energy conversion system modelling and integration: a survey," *International Journal of Sustainable Energy,* vol. 34, pp. 657–671, 2015.

[2] N. H. Malik and S. E. Haque, "Steady state analysis of an isolated self-excited induction generator," *IEEE Transactions on Energy Conversion,* vol. 1, pp. 133–139, 1986.

[3] K. Idjadarene, D. Rekioua (ZIANI), T. Rekioua, and A. Tounzi, "Performance of an isolated induction generator under unbalanced loads," *IEEE Transactions on Energy Conversion,* vol. 25, 2010.

[4] T. R. Ayodele, A. S. O. Ogunjuyigbe, and O. O. Akinola, "Optimal location, sizing, and appropriate technology selection of distributed generators for minimising power loss using genetic algorithm," *Journal of Renewable Energy,* vol. 2015, pp. 1–9, 2015.

[5] A. I. Alolah, "Capacitance requirements for three-phase self-excited reluctance generator," *IEE Proceedings on Generation, Transmission and Distribution,* vol. 138, pp. 193–198, 1991.

[6] S. C. Kuo and L. Wang, "Analysis of isolated self-excited induction generator," *IEEE Proceedings on Generation, Transmission and Distribution,* vol. 149, pp. 90–97, 2002.

[7] Y. H. A. Rahim, J. E. Fletcher, and N. E. A. M. Hassanain, "Performance analysis of salient-pole self-excited reluctance generators using a simplified model," *IET Renewable Power Generation,* vol. 4, pp. 253–260, 2010.

[8] F. M. El-Khouly and A. M. Osheiba, "Brushless induction and reluctance generators with DC excitation: experimental verification," *Electric Power Components and Systems,* vol. 32, pp. 839–853, 2004.

[9] W. S. Abu-Elhaija, "Capacitance requirement of single-phase self-excited reluctance generator using eigenvalues criterion," in *Proceedings on IEEE PES Transmission and Distribution Conference & Exposition (TD 2005-000019)*, Dallas, Texas, pp. 21–25, 2006.

[10] A. L. Mohamadein, Y. H. A. Rahim, and A. S. Al-Khalaf, "Steady state performance of self-excited reluctance generators," in *IEE Proceedings on Electric Power Apparatus*, 293–298, 1990.

[11] O. O. Mengi and I. H. Altas, "Fuzzy logic control for a wind/battery renewable energy production system," *Turkish Journal of Electrical Engineering & Computer Sciences,* vol. 20, 2012.

[12] M. H. Nagrial and M. A. Rahman, "Operation and characteristics of self-excited reluctance generator," in *Proceedings of IEEEIAS Annual Meeting*, 55–58, 1988.

[13] A. S. O. Ogunjuyigbe and A. A. Jimoh, "On the development and performance of reluctance machine," *International Review of Automatic Control (I.RE.A.CO),* vol. 5, 316–326, 2012.

[14] P. J. Lawrenson and L. A. Agu, "Theory and performance of polyphase reluctance machines," *Proceedings of IEE,* vol. 111, 1435–1445, 1964.

[15] L. U. Anih, E. S. Obe, and S. E. Abonyi, "Modelling and performance of a hybrid synchronous reluctance machine with adjustable Xd/Xq ratio," *IET Electric Power Applications,* vol. 9, 171–182, 2015.

[16] F. E. Abdel-Kader, "The reluctance machine as a self-excited generator," *Electric Machines and Power Systems,* vol. 10, 141–148, 1985.

[17] A. Kishore, R. C. Prasad, and B. M. Karan, "MATLAB SIMULINK based DQ modeling and dynamic characteristics of three phase self excited induction generator," in *Progress in Electromagnetics Research Symposium*, Cambridge, USA, 312–316, 2006.

[18] P. Krause, O. Wasynczuck, and S. Sudhoff, *Analysis of Electric Machinery and Drive System*, John Wiley & Son Publication, 2002.

[19] D. W. Novotny and T. A. Lipo, *Vector Control and Dynamics of AC Drives,* Clarendon Press, Oxford, 1996.

[20] I. Boldea, Z. X. Fu, and S. A. Nasar, "High-performance reluctance generator," in *IEE Proceedings-B*, 124–130, 1993.

[21] M. Enache, C. Nica, and S. Ivanov, "Aspects regarding modelling of reluctance synchronous motors," in *6th International Conference on Electromechanical and Power Systems*, Chisinau, Rep. Moldova, 126–129, 2007.

[22] L. Wang and Y. Wang, "Characteristics of a self-excited reluctance generator as affected by sudden connection and disconnection of an induction motor load," in *IEEE International Conference on Power System Technology*, 1998.

Chapter 11

Control and Estimation of a Variable Pitch Wind Turbine for Maximum Power Point Tracking

Ranjan Vepa

Additional information is available at the end of the chapter

http://dx.doi.org/10.5772/62723

Abstract

In this chapter, the design of a nonlinear rotor-side controller is described for a variable pitch wind turbine based on nonlinear, H_2 optimal control theory. The objective is to demonstrate the synthesis and application of a maximum power point tracking (MPPT) algorithm. In the case of a variable pitch wind turbine, the blade collective pitch angle is controlled to ensure that the turbine is not overloaded. In the case of such turbines the blade pitch may be treated as unknown input and the actual pitch angle is estimated in real time from torque measurements. The algorithm uses a non-linear estimation technique and maximizes an estimate of the actual power transferred from the turbine to the generator. It is validated by simulating the wind-turbine's dynamics. It is shown that the MPPT algorithm performs within prescribed error bounds both in the case when no disturbances are present, as it is an indicator of the validity of the algorithm and in cases when significant levels of wind disturbances are present.

Keywords: control system, Kalman filtering, nonlinear estimation, nonlinear filters, simulation, state estimation, induction generators, tracking, tracking filters, wind power generation

1. Introduction

The extraction and regulation of the power from the wind by a wind turbine followed by the capture of this power by a generator has been the subject of several recent research investigations. The use of a doubly fed induction generator (DFIG) is one of most popular options for large-scale electromechanical conversion of wind power to electrical power. The DFIG employs a two-sided controller, a rotor-side controller (RSC) to control the speed of operation and the reactive power, and a grid-side controller (GSC) using a grid-side voltage source converter

which is responsible for regulating the DC link voltage as well as the stator terminal voltage. The rotor-side controller is expected to (i) minimize or regulate the reactive power and hold the stator output voltage frequency constant by a form of current control, (ii) regulate the rotor speed to maintain stable operation, and (iii) alter the speed set point to ensure maximum wind power capture. The role of the grid-side controller is to ensure regulation of the DC voltage bus, and thereby indirectly control the stator terminal voltage. In the case when the generator is feeding an AC-grid, it can be designed to control the power factor. In a typical system, the stator phase voltages and the stator, rotor, and grid phase voltages are assumed to be measured. It is usual to connect the grid-side converter to the grid via chokes to filter the current harmonics. An AC-crowbar is generally included to avoid DC-link over-voltages during grid faults.

It is well known [1] that only a fraction of the power available in the wind is captured by a wind turbine. There is further reduction in the actual power converted to useful power by the generator. The fraction of the power captured by the wind turbine, which is theoretically limited by the so called Betz limit (about 58%), known as the power coefficient is primarily a function of the tip speed ratio, and is usually less than a certain peak value which is about 45% [1]. Maximum energy conversion is possible when the turbine operates at an optimum tip speed ratio which depends on the variation of the power coefficient with respect to the tip speed ratio. The relationship between the power coefficient and the tip speed ratio can be best determined experimentally. In the case of most of the current horizontal axis wind turbines operating at optimum speed, this can be accomplished by indirect control of the rotational speed. The indirect control of the speed is realized by directly controlling the reaction torque of the electric generator [2]. When the principal variables can all be measured, then one could employ one of a large number of maximum power point tracking (MPPT), algorithms have developed. The concept of maximum power point tracking was first introduced in the design of solar panels for spacecraft in the 1970s with the objective of maximizing the power transfer from the photo-voltaic power sources.

In a recent paper [3], the design of a nonlinear rotor-side controller for a wind turbine generator was developed based on nonlinear, H_2 optimal control theory. The objective was to demonstrate the synthesis of a maximum power point tracking (MPPT) algorithm for transferring the maximum power from the turbine to the generator. In the case of a doubly fed induction generator, it was essential that the rotor-side controller and the MPPT algorithm are synthesized concurrently as the nonlinear perturbation dynamics about an operating point is either only just stable or unstable in most real generators. The algorithm uses a non-linear estimation technique and maximizes an estimate of the actual power transferred from the turbine to the generator. It is validated by simulating the wind-turbine's dynamics. In ref. [3], the estimation method was based on the unscented Kalman filter (UKF) and compared with the traditional extended Kalman filter (EKF). The implementation of the algorithm required modelling the real wind velocity profiles from a broadband white noise generator, and by using low order spectrum shaping filters that are derived from approximations of the Kaimal wind velocity spectrum. The simulation was completely executed in the MATLAB environment. The simulation was based on executing the UKF estimator as well as numerically integrating step by step, in parallel, the process model with the feedback controller included in the dynamic

http://dx.doi.org/10.5772/62723

model, about the steady equilibrium solution without linearizing the dynamics. The MPPT algorithm was successfully demonstrated in cases when significant levels of wind disturbances are present. In particular the actual power transferred is compared with maximum available power in the wind, and it is shown in ref. [3] that the maximum power is transferred from the wind to the generator by the turbine.

When applying this algorithm to a real wind turbine, it was found that for purposes of ensuring that the turbine was not overloaded, the collective pitch angle of the turbine's blades could be controlled so as to be able to limit the maximum power captured by the wind turbine. When the pitch of the blades is controllable there are two control inputs to consider. While the blade pitch angle can be used to regulate the capture of the power from the wind by the wind turbine rotor, controlling the generators reaction torque allows for the power to be smoothly converted into electrical energy. For such variable pitch wind turbine, it was found that in order to implement the algorithm developed in ref. [3], it was essential to either measure the blade pitch angle or the torque on the turbine shaft, which is then used to estimate the true wind turbine aerodynamic torque and the blade pitch angle. In the latter case only a model of the closed loop collective pitch angle dynamics is essential. As there were no other benefits of measuring the blade pitch angle, the second option was preferred. The blade pitch angle was then considered as an unknown input to the torque, and it was estimated from the measurements.

In this chapter the modified MPPT algorithm, in the presence of unknown inputs to the aerodynamic torque, is successfully demonstrated both in the case when no disturbances were present, as it is a prerequisite for successful implementation, and in cases when significant levels of wind disturbances are present.

2. The electro-mechanical model of a wind turbine

There have been a number of papers on the subject of modelling of a wind turbine driving an induction generator under turbulent or stochastic wind conditions [4–7]. In this section the electro-mechanical model used in this study which is identical to the model used in ref. [3], is briefly summarized.

2.1. The mechanical model

The mechanical model of the wind turbine is described by,

$$J_{eq} d\omega_m / dt + B_{eq}\omega_m = T_{wt} - T_{mel} \tag{1}$$

where, as defined in ref. [3], ω_m is the mechanical speed of the generator shaft, T_{wt} is the torque extracted by the turbine from the wind, T_{mel} is the mechanical equivalent of the electromagnetic load torque, J_{eq} is the equivalent total inertia of the generator shaft and B_{eq} is the equivalent total friction coefficient. The electromagnetic load torque $T_{mel} = (P/2)T_{el}$ is a linear function of the number of poles P and may be estimated from the electromagnetic reaction torque of the

electric generator per pole pair T_{el}. The torque extracted by the wind turbine T_{wt} is related to the total power absorbed by the turbine from the wind which may respectively be expressed as,

$$T_{wt} = P_w / \omega_m$$

and

$$P_w = \frac{1}{2}\rho\left(\pi R^2\right)C_p(\lambda)U^3 \tag{2}$$

In the above expression ρ is the density of the air at the hub of the turbine, R is the rotor radius, $C_p(\lambda)$ is a power coefficient which is a function of $\lambda = R\omega_m/U$, the tip speed ratio and U is the wind velocity. Thus, the mean torque may be expressed as,

$$T_{wt} = \rho\left(\pi R^3\right)C_q(\lambda)U^2/2,$$

$$C_q(\lambda) = C_p(\lambda)/\lambda. \tag{3}$$

There are several approximations [8, 9] of $C_p(\lambda)$ in use and a typical approximation in terms of the blade collective pitch angle θ is given by,

$$C_p = 0.22\left(\frac{116}{\lambda_i} - 0.4\times\theta - 5\right)e^{-12.5/\lambda_i}, \tag{4a}$$

$$\frac{1}{\lambda_i} = \frac{1}{\lambda + 0.08\theta} - \frac{0.035}{1+\theta^2} \tag{4b}$$

Typically depending on the approximation used the maximum power coefficient varies over the range, $0.44 \le C_p(\lambda)_{\max} \le 0.492$ and the corresponding tip speed ratio varies over the range, $6.9 \le \lambda_{\max} \le 8.8$.

2.2. The dynamics and control of the pitch angle

The dynamics of variable pitch wind turbine blades plays a key role in the capture and regulation of the power from the wind by the wind turbine rotor. In the case of a horizontal axis wind turbine, there are up to five blades which are assumed to be equi-spaced and to lie with the plane of the rotor disc. The most popular choice for most variable pitch wind turbines

http://dx.doi.org/10.5772/62723

is a three bladed rotor. The dynamics of a variable pitch wind turbine blade can be expressed either in a frame that is fixed in the blade or in a frame that is fixed to the rotor disc. It is convenient to represent the aerodynamic forces in a frame fixed to the blade, while the wind inputs and gusts are more easily represented in a frame fixed to the rotor disc plane. In most practical horizontal wind turbine designs, the rotor disc plane usually aligns itself normal to the wind direction. Thus both frames of reference are used in the dynamical analysis of wind turbines and are transformed from one to the other as and when this is required.

The rotor dynamic model is typically described in terms of non-dimensional quantities so that the general rotor configurations can be analyzed without the need to specify the size. Because of the similarity between the mechanical designs of the rotor for a helicopter, the development of the model closely follows the methodology outlined by Padfield [10] and Fox [11]. The important rotor blade properties of interest are the aerodynamic forces and moments acting on the individual blades, as well as the rotor thrust and torque which are related to the blade forces. Each blade is assumed to be fully controllable in pitch with the root of the blade offset from the rotor axis. The Lock number is an important non-dimensional aerodynamic parameter, and is used to characterize the rotor dynamics parameters. The aerodynamically coupled flap-pitch equations of motion of a single blade are derived in a rotating frame as function of the azimuth angle. To derive the equations of motion of all the blades as a single unit, the coefficients in the equations may be expressed in terms of the so called multi-blade coordinates. This is done by expanding all trigonometric functions such as products of sine and cosine functions as the sums of relevant sine and cosine terms. Thus the fixed frame equations of motion obtained by applying multi-blade coordinate transformations will represent the dynamics of the rotor disc containing N blades. The model of the inflow dynamics is based on the finite state approximation developed by Pitts and Peters [12]. The wind is responsible in generating the primary moment acting on the rotor resulting in a rotor torque, which produces the dominant component of the moment about the rotor shaft axis, which is converted into electrical energy by the generator. This torque can be obtained by integrating the moments of the in-plane aerodynamic pressure distribution acting on the blades about the shaft axis.

Broadly, the approaches to pitch control may be classified into two groups. In a direct pitch controlled system, the controller monitors the wind-turbine's power output at every sampling instant. When the power output exceeds an upper bound, the blade pitch is altered to lower the power generated by the turbine. Increasing the pitch attitude generally reduces the power output. When the maximum power output of the turbine is within the safe operating limits, the pitch angle is reduced to zero.

The second approach to pitch control involves operating the wind turbine with the blades pitched at angle just below the stall angle. The geometry of the blade profile and twist, however are aerodynamically tailored to ensure that when the induced wind speed is high, the angle of attack also increases and the blade begins to stall. The stalling of the lift generated restricts the magnitude of the lift generated and consequently the power generated is also limited. In an actively stall controlled turbine, the pitch of the blade is maintained just below the critical stall angle as long as the power generated by the wind turbine is within the safe operating limits, and increased beyond the critical value when it is desired to stall the generation of lift

on the blade. Thus, when the generator is overloaded, the controller will pitch the blades in the opposite direction from what a pitch controlled machine does, in order to make the blades go into an increased state of stall.

The approximation to $C_p(\lambda)$ given by equations (4a) and (4b) are only valid or small increments in the blade pitch angle, and do not include the influence of blade stall. For this reason, in this work, we consider only a pitch controlled wind-turbine. To model the blade dynamics, it is first required to model the open loop dynamics. Once the open loop pitch dynamics is obtained, it is assumed that an appropriate feedback law is designed. Thus, what is important is the closed loop dynamics of the pitch angle which is represented by a reduced, first order model of the form,

$$\tau \frac{\partial \theta(t)}{\partial t} + \theta(t) = \theta_{demand} \tag{5}$$

Thus the discrete dynamics of the pitch angle may be expressed as,

$$\theta_{k+1} - \theta_k = \frac{\Delta t}{\tau}\left(\theta_{demand} - \theta_k\right) \tag{6}$$

The model may be used to design control laws for both active pitch controlled and active stall controlled wind-turbines. The demanded blade pitch angle θ_{demand}, is set by the unconstrained minimization of the square of the error between the desired output power and the actual power generated by the wind turbine rotor.

To design an active stall controller, the first step is to model the section lift and drag coefficients of the blade when the section angle of attack exceeds the stall angle. Modes of both the section lift and drag coefficients of the blade when the section angle of attack exceeds the stall angle have been presented by Tangler and Kocurek [13] and by Tangler and Ostowari [14] based on a model developed by Viterna and Corrigan [15]. These are then substituted into the expression for the power coefficient developed on the basis of the blade element momentum theory (see for example Vepa [16], Section 4.4.1). Once the expression for the power coefficient is found, the commanded blade angle is found by requiring the error between the actual power generated, estimated from the power coefficient, and the maximum power is a minimum.

2.3. The nonlinear dynamic electro-mechanical model

The basic equations of the dynamics of the doubly fed induction machine can be established as done in ref. [3], by considering the equivalent circuit of a single stator phase and a single rotor phase and the mutual coupling between the stator and rotor phases. The voltage vector consisting of the voltages applied to each stator and rotor phases is related to the voltage drops across the resistances of these phases and the rate of change of the fluxes linking the stator and rotor phases. The fluxes in turn are related to the current vector via a matrix of inductances

http://dx.doi.org/10.5772/62723

which are not constant but period functions of time with the period equal to the rotor's electrical speed, $\omega_e = P\omega_m$, which is the product of the number of pole pairs, P and the rotor's mechanical speed, ω_m. When all of the stator and rotor quantities are transformed to a stationary frame (the d–q frame) using the standard Park-Blondel transformation, in terms of the stator's and rotor's voltage oscillation frequencies ω_s and ω_r respectively, the dynamic equations reduce to a set of four with constant coefficients as derived in ref. [3]. Moreover $\omega_r = \omega_s - \omega_e$ can be found by measuring ω_s and ω_e, and is also the slip frequency. (The ratio $s = \omega_r/\omega_s$ is the slip.)

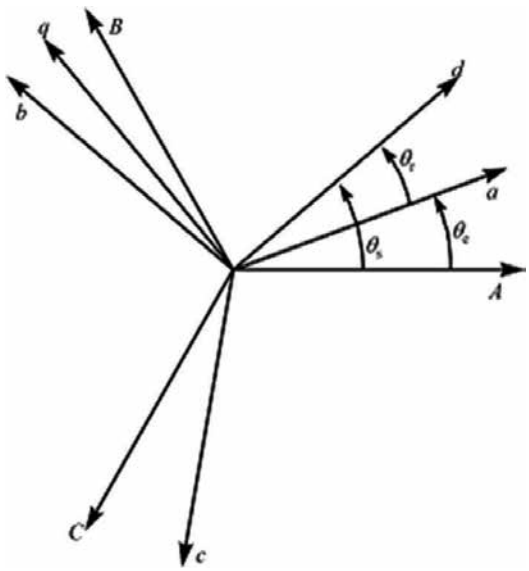

Figure 1. Relationships between the d–q frame and the stator and rotor phases.

The phase angles relating the directions of the d–q frame and the phase angles of the first of the three stator phases, A, B, and C, θ_s and the first of the three rotor phases, a, b and c, θ_r satisfy the relation $\theta_r = \theta_s - \theta_e$ where θ_e is the rotor's electrical angle as illustrated in **Figure 1**. In modeling the stator of DFIG, the generator convention that positive direction of electromagnetic torque is in the direction opposing to the direction of rotation is used, while in modeling the rotor of DFIG the motor convention is used. The dynamic equivalent circuit of generator in synchronous rotating reference frame, the d–q frame, is used to set up the model equations.

The dynamical equations of the DFIG relating the voltages in the stator and rotor and in the d–q frame to the currents, fluxes and the flux rates are,

$$v_{ds} = R_s i_{ds} + \frac{d\varphi_{ds}}{dt} - \omega_s \varphi_{qs}\ , v_{qs} = R_s i_{qs} + \frac{d\varphi_{qs}}{dt} + \omega_s \varphi_{ds}\ , \tag{7a}$$

$$v_{dr} = R_r i_{dr} + \frac{d\varphi_{dr}}{dt} - \omega_r \varphi_{qr} \ , v_{qr} = R_r i_{qr} + \frac{d\varphi_{qr}}{dt} + \omega_r \varphi_{dr} \tag{7b}$$

The stator fluxes are related to the stator and rotor currents in the *d–q* frame as,

$$\varphi_{ds} = L_s i_{ds} + L_m i_{dr} \ , \varphi_{qs} = L_s i_{qs} + L_m i_{qr} \tag{8a}$$

The rotor fluxes are related to the stator and rotor currents in the *d–q* frame as,

$$\varphi_{dr} = L_r i_{dr} + L_m i_{ds} \ , \varphi_{qr} = L_r i_{qr} + L_m i_{qs} \tag{8b}$$

In the above equations, as defined in ref. [3], L_s,L_r,R_s, and R_r, are respectively the self-inductances and resistances of the stator and rotor windings. The quantity L_m is the mutual inductance between a stator and a rotor phase when they are fully aligned with each other.

At the stator terminals, the active and reactive components of the power are given by,

$$P_s = v_{ds} i_{ds} + v_{qs} i_{qs} \ , Q_s = v_{qs} i_{ds} - v_{ds} i_{qs} \tag{9a}$$

At the rotor terminals, the active and reactive components of the power are given by,

$$P_r = v_{dr} i_{dr} + v_{qr} i_{qr} \, , Q_r = v_{qr} i_{dr} - v_{dr} i_{qr} \tag{9b}$$

The active and reactive powers exchanged by the generator and the grid are respectively the sum of the active and reactive components of the power at the stator and rotor. The electromagnetic reaction torque may be expressed as,

$$T_{el} = \left(\varphi_{ds} i_{qs} - \varphi_{qs} i_{ds} \right) \tag{10}$$

Assuming that the stator flux is stationary in the *d–q* frame and neglecting the stator's resistive voltage drop $v_{ds} = 0$. Hence the q – component of the stator voltage may be expressed as, $v_s = v_{qs}$. Assuming further that a grid-side controller is in place and choosing a stator-flux oriented reference frame, the *d*-axis is aligned with the stator flux linkage vector, φ_s; thus $\varphi_{ds} = \varphi_s$ and $\varphi_{qs} = 0$. From equations (8a) and (7a), i_{ms} is defined by,

$$\varphi_s = L_s i_{ds} + L_m i_{dr} = \frac{1}{\omega_s} \left(v_{qs} - R_s i_{qs} \right) \equiv L_m i_{ms} \tag{11a}$$

http://dx.doi.org/10.5772/62723

Thus, from equations (8a),

$$L_s i_{ds} = L_m \left(i_{ms} - i_{dr} \right), L_s i_{qs} = -L_m i_{qr} \tag{11b}$$

Eliminating i_{ds} and i_{qs} from equations (7b) and (8b) it can be shown that, the rotor flux components are,

$$\varphi_{dr} = L_r \left(\frac{L_s L_r - L_m^2}{L_s L_r} \right) i_{dr} + \frac{L_m^2}{L_s} i_{ms} \ , \ \varphi_{qr} = L_r \left(\frac{L_s L_r - L_m^2}{L_s L_r} \right) i_{qr} \tag{11c}$$

The electromagnetic reaction torque given by equation (10) and the reactive power at the stator terminal given by the second of equations (9a) may also be expressed in terms of i_{ms} as,

$$T_{el} = \varphi_s i_{qs} = -L_m^2 i_{ms} i_{qr} / L_s \ , \tag{12a}$$

$$Q_s = v_{qs} i_{ds} - v_{ds} i_{qs} = \omega_s \varphi_s i_{ds} = \omega_s L_m^2 i_{ms} \left(i_{ms} - i_{dr} \right) / L_s \tag{12b}$$

Defining the mutual inductance coupling coefficient σ as,

$$\sigma = \left(L_s L_r - L_m^2 \right) / L_s L_r \tag{13}$$

and using equations (11c) with $v_{ds} = 0$ and $v_s = v_{qs}$ the rotor voltage equations given by the equations (7b) are expressed as,

$$v_{dr} = R_r i_{dr} + \sigma L_r \frac{di_{dr}}{dt} - \sigma s \omega_s L_r i_{qr} \tag{14a}$$

$$v_{qr} - s \frac{L_m}{L_s} v_s = \left(R_r + s \frac{L_m^2}{L_s^2} R_s \right) i_{qr} + \sigma L_r \frac{di_{qr}}{dt} + \sigma s \omega_s L_r i_{dr} \tag{14b}$$

The total reactive power is $Q = Q_r + Q_s$ where Q_s is given by equations (11a) and (12b), with $v_{ds} = 0$ and $v_s = v_{qs}$. Thus the total reactive power is,

$$Q = v_{qr} i_{dr} - v_{dr} i_{qr} + \omega_s \frac{L_m^2}{L_s} \times \left(\frac{v_s}{\omega_s L_m} + \frac{R_s}{\omega_s L_m} i_{qr} \right) \left(\frac{v_s}{\omega_s L_m} + \frac{R_s}{\omega_s L_m} i_{qr} - i_{dr} \right) \tag{15}$$

The definitions of the resistances and inductances and their typical values assumed in this chapter are listed in **Table 1**.

P	**Number of poles**	**6**
R_s	Stator resistance	0.95 Ω
L_s	Stator inductance	94 mH
L_m	Magnetizing inductance	82 mH
R_r	Rotor resistance	1.8 Ω
L_r	Rotor inductance	88 mH
V_a	Stator phase voltage	380 V
	Grid frequency	50 Hz
	Nominal mechanical rotor speed	100 rads/sec
	Rated maximum power	100 kW

Table 1. Definitions and typical values assumed for the generator's parameters.

In steady state, assuming that,

$$v_{dr} = v_{dr}^0,\ v_{qr} = v_{qr}^0,\ i_{dr} = i_{dr}^0,\ i_{qr} = i_{qr}^0,\ s = s^0, \tag{16}$$

where the superscript '0' refers to the steady-state condition, and subtracting the steady-state components from (14a) and (14b), the electro-mechanical perturbation equations are obtained. The perturbation states, inputs and variables are defined as:

$$\begin{gathered}\Delta v_{dr} = v_{dr} - v_{dr}^0,\ \Delta v_{qr} = v_{qr} - v_{qr}^0,\ \Delta i_{dr} = i_{dr} - i_{dr}^0,\ \Delta i_{qr} = i_{qr} - i_{qr}^0, \\ \Delta s = s - s^0 = -\frac{\Delta\omega_e}{\omega_s},\ \Delta\omega_e = \omega_e - \omega_e^0.\end{gathered} \tag{17}$$

Given that $T_{wt} = T_{wt}^0$ in steady-state and that $\Delta T_{wt} = T_{wt} - T_{wt}^0$, $\Delta\omega_e$ satisfies the equation,

$$J_{eq}\frac{d\Delta\omega_e}{dt} + B_{eq}\Delta\omega_e = \frac{P}{2}\left(\Delta T_{wt} - \frac{P}{2}T_{el} + \frac{P}{2}T_{el}^0\right) \tag{18}$$

Using equation (11a) and introducing the steady state and perturbation variables, the expression for the electromagnetic torque is,

http://dx.doi.org/10.5772/62723

$$T_{el} = T_{el}^0 - \frac{L_m^2}{L_s}\left(\frac{v_s}{\omega_s L_m} + \frac{R_s}{\omega_s L_s}\left(2i_{qr}^0 + \Delta i_{qr}\right)\right)\Delta i_{qr} \tag{19}$$

The wind turbine perturbation torque $\Delta T_{wt}(U, \omega_e) = \left(T_{wt}(U, \omega_e) - T_{wt}\left(U_0, \omega_e^0\right)\right)$, is a function of two variables, the wind speed U, and the rotor speed ω_e. Given that the wind speed, $U = U_0 + \Delta u_f$ is the sum of a mean component, U_0 and a fluctuating component, Δu_f, the wind turbine perturbation torque can be considered to be made of two components,

$$\Delta T_{wt}\left(U, \omega_e\right) = \left(T_{wt}\left(U, \omega_e\right) - T_{wt}\left(U_0, \omega_e\right)\right) +$$

$$\left(T_{wt}\left(U_0, \omega_e\right) - T_{wt}^0\left(U_0, \omega_e^0\right)\right) = \Delta T_{wt}\big|_{\omega_e} + \Delta T_{wt}\big|_{U=U_0} \tag{20}$$

where the first component is evaluated at the current rotor speed, ω_e and the second at the mean wind speed, U_0. Hence, without making any assumptions that the perturbations are small, the equation for mechanical motion, equation (18), may be expressed as,

$$J_{eq}\frac{d\Delta\omega_e}{dt} = \left(\frac{P}{2}\frac{\Delta T_{wt}}{\Delta\omega_e}\bigg|_{U=U_0} - B_{eq}\right)\Delta\omega_e +$$

$$\frac{P^2}{4}\frac{L_m^2}{L_s}\left(\frac{v_s}{\omega_s L_m} + \frac{R_s}{\omega_s L_s}\left(2i_{qr}^0 + \Delta i_{qr}\right)\right)\Delta i_{qr} + \Delta T_{wt}\big|_{\omega_e} \tag{21}$$

while the electrical machine perturbation equations are,

$$\sigma L_r \frac{d\Delta i_{dr}}{dt} = -\sigma L_r i_{qr}\Delta\omega_e - R_r\Delta i_{dr} + \sigma s^0\omega_s L_r\Delta i_{qr} + \Delta v_{dr} \tag{22a}$$

$$\begin{aligned}\sigma L_r \frac{d\Delta i_{qr}}{dt} = +&\left(\sigma L_r i_{dr} + \frac{L_m^2}{\omega_s L_s^2}R_s i_{qr}\right)\Delta\omega_e - \sigma s^0\omega_s L_r\Delta i_{dr} \\ &-\left(R_r + s^0\frac{L_m^2}{L_s^2}R_s\right)\Delta i_{qr} + \Delta v_{qr}\end{aligned} \tag{22b}$$

Assuming that

$$\Delta v_{dr} = \Delta v_{dr}^{+} + \sigma L_r i_{qr} \Delta\omega_e - R_r^{+} \Delta i_{dr} + \sigma s^0 \omega_s L_r \Delta i_{qr} \ , \tag{23}$$

equations (21) and (22) may be partially decoupled, and (22a) may be treated independently. Thus the complete non-linear equations for the perturbation states used for the design of the nonlinear rotor-side controller may be expressed in state space form as,

$$\frac{d}{dt}\begin{bmatrix} \Delta\omega_e \\ \Delta i_{qr} \end{bmatrix} = \mathbf{A}\begin{bmatrix} \Delta\omega_e \\ \Delta i_{qr} \end{bmatrix} + \frac{1}{\sigma L_r}\begin{bmatrix} 0 \\ 1 \end{bmatrix}\Delta v_{qr} + \begin{bmatrix} 1 \\ 0 \end{bmatrix}\alpha_u \tag{24a}$$

where

$$\alpha_u = \left(\Delta T_{wt} / \Delta u_f\Big|_{\omega_e} / J_{eq}\right)\Delta u_f \tag{24b}$$

is the disturbing angular acceleration on the rotor due to wind speed fluctuating component and **A** is a matrix of functional coefficients.

R	**Wind turbine blade disc radius**	**6 m**
	Number of blades	3
U_0	Nominal wind speed	10 m/s
P_n	Wind power at nominal wind speed	~10 kW
	Gearbox ratio	10
J_{eq}	Rotor inertia	40 kgm^2
B_{eq}	Viscous friction coefficient	0.07 Nms/rad
	Cut-in wind speed (m/s)	3.5 m/s

Table 2. Definitions and typical values of the wind turbine parameters.

The modeling of the turbulent wind component and the control of wind turbine is based entirely on [3] and will not be repeated here. The complete characteristics of the wind turbine are summarized in **Table 2**.

3. The measurements and nonlinear state estimation

The dynamic model of the wind turbine that must be employed for purposes of state estimation is not only not linear but also involves the estimation of large dynamic signals. The Kalman filter which was formulated in the 1960s is primarily applicable to linear systems. To overcome the limitations imposed by the requirement of linearity, it was subsequently, empirically,

http://dx.doi.org/10.5772/62723

extended and applied to nonlinear systems. A number of approaches such as the extended Kalman filter (EKF) have been proposed in the literature to extend the application of the traditional Kalman filter for nonlinear state estimation. However, the stability of these extended formulations is not guaranteed unlike the linear Kalman filter. Thus the EKF may diverge if the consecutive linearizations are not a good approximation of the linear model over the entire uncertainty domain. Nonetheless the EKF provides a simple and practical approach to dealing with essential non-linear dynamics.

The UKF has been proposed by Julier, Uhlmann, and Durrant-Whyte [17], and used in ref. [3]. It can overcome the limitations of applying the Kalman filter to nonlinear systems. The UKF based on the unscented transformation of the statistics of a random variable. It provides a method of calculating the mean and covariance of a random variable undergoing a non-linear transformation $\mathbf{y} = \mathbf{f}(\mathbf{w})$. In the main, the method is used to construct a set of *sigma vectors* and propagate them through the non-linear transformation. The mean and covariance of the transformed vector are approximated as a weighted sum of the transformed *sigma vectors* and their covariance matrices. The details may be found in the paper by Julier and Uhlmann [18].

As in ref. [3], given a general discrete nonlinear dynamic system in the form,

$$\mathbf{x}_{k+1} = \mathbf{f}_k\left(\mathbf{x}_k, \mathbf{u}_k^{ui}, \mathbf{u}_k\right) + \mathbf{w}_k,\ \mathbf{z}_k = \mathbf{h}_k\left(\mathbf{x}_k, \mathbf{u}_k\right) + \mathbf{H}_k\mathbf{u}_k^{ui} + \mathbf{v}_k \tag{25}$$

where $\mathbf{x}_k \in R^n$ is the state vector, $\mathbf{u}_k^{ui} \in R^{uk}$ is the unknown input vector, $\mathbf{u} \in R^r$ is the known input vector, $\mathbf{z}_k \in R^m$ is the output vector at time k. $\mathbf{w}_k$ and $\mathbf{v}_k$ are, respectively, the disturbance or process noise and sensor noise vectors, which are assumed to Gaussian white noise with zero mean and are also assumed to be independent of each other. We have tacitly assumed that the unknown input is related to the measurements linearly. Furthermore, $\mathbf{Q}_k$ and $\mathbf{R}_k$ are assumed to be the covariance matrices of the process noise sequence, $\mathbf{w}_k$ and the measurement noise sequence, $\mathbf{v}_k$ respectively. The joint unscented transformation of the states and unknown inputs by the nonlinear function $\mathbf{f}_k\left(\mathbf{x}_k, \mathbf{u}_k^{ui}, \mathbf{u}_k\right)$ is denoted as, $\mathbf{f}_k^{UT} = \mathbf{f}_k^{UT}\left(\mathbf{x}_k, \mathbf{u}_k^{ui}, \mathbf{u}_k\right)$, the unscented transformation of the states by the nonlinear function $\mathbf{h}_k(\mathbf{x}_k, \mathbf{u}_k)$ is denoted as $\mathbf{h}_k^{UT} = \mathbf{h}_k^{UT}(\mathbf{x}_k, \mathbf{u}_k)$ while the transformed covariance matrices and cross-covariance are respectively denoted as, $\mathbf{P}_k^{ff} = \mathbf{P}_k^{ff}\left(\hat{\mathbf{x}}_k, \hat{\mathbf{u}}_k^{ui}, \mathbf{u}_k\right)$, $\mathbf{P}_k^{hh-} = \mathbf{P}_k^{hh}\left(\hat{\mathbf{x}}_k^-, \mathbf{u}_k\right)$ and $\mathbf{P}_k^{xh-} = \mathbf{P}_k^{xh-}\left(\hat{\mathbf{x}}_k^-, \hat{\mathbf{u}}_k^{ui}, \mathbf{u}_k\right)$. In the above unscented transformations $\mathbf{u}_k$ is a deterministic variable while $\mathbf{u}_k^{ui}$ is a stochastic variable which is dealt with by augmenting the state vector $\mathbf{x}_k$ to $\left[\mathbf{x}_k^T \quad \mathbf{u}_k^{ui\,T}\right]^T$ for obtaining $\mathbf{f}_k^{UT}$. We have chosen to use the scaled unscented transformation proposed by Julier [19], as this transformation gives one the added flexibility of scaling the sigma points to ensure that the covariance matrices are always positive definite. The unknown input UKF estimator can then be expressed in a compact form based on the original derivation for the linear case by Pan, Su, Wang, and Chu [20]. The state time-update equation, the propagated covariance, the Kalman gain, the state estimate, and the updated covariance are respectively given by,

$$\hat{\mathbf{x}}_k^- = \mathbf{f}_{k-1}^{UT}\left(\hat{\mathbf{x}}_{k-1}, \hat{\mathbf{u}}_{k-1}^{ui}, \mathbf{u}_{k-1}\right) \tag{26a}$$

$$\hat{\mathbf{P}}_k^{x-} = \mathbf{P}_{k-1}^{ff} + \mathbf{Q}_{k-1} \tag{26b}$$

$$\hat{\mathbf{P}}_k^{zz} = \left(\hat{\mathbf{P}}_k^{hh-} + \mathbf{R}_k\right), \mathbf{K}_k = \hat{\mathbf{P}}_k^{xh-}\left(\hat{\mathbf{P}}_k^{zz}\right)^{-1} \tag{26c}$$

$$\hat{\mathbf{P}}_k^{uu} = \left(\mathbf{H}_k^T\left(\hat{\mathbf{P}}_k^{zz}\right)^{-1}\mathbf{H}_k\right)^{-1}, \hat{\mathbf{P}}_k^{xu} = -\mathbf{K}_k\mathbf{H}_k\hat{\mathbf{P}}_k^{uu} \tag{26d}$$

$$\mathbf{M}_k = \hat{\mathbf{P}}_k^{uu}\mathbf{H}_k^T\left(\hat{\mathbf{P}}_k^{zz}\right)^{-1}, \hat{\mathbf{u}}_k^{ui} = \mathbf{M}_k\left[\mathbf{z}_k - \mathbf{h}_k^{UT}\left(\hat{\mathbf{x}}_k^-\right)\right] \tag{26e}$$

$$\hat{\mathbf{x}}_k = \hat{\mathbf{x}}_k^- + \mathbf{K}_k\left[\mathbf{z}_k - \mathbf{h}_k^{UT}\left(\hat{\mathbf{x}}_k^-\right) - \mathbf{H}_k\hat{\mathbf{u}}_k^{ui}\right], \tag{26f}$$

$$\hat{\mathbf{P}}_k^{x} = \hat{\mathbf{P}}_k^{x-} - \mathbf{K}_k\left(\hat{\mathbf{P}}_k^{zz} - \mathbf{H}_k\hat{\mathbf{P}}_k^{uu}\mathbf{H}_k^T\right)\mathbf{K}_k^T, \tag{26g}$$

$$\hat{\mathbf{P}}_k = \begin{bmatrix} \hat{\mathbf{P}}_k^{x} & \hat{\mathbf{P}}_k^{xu} \\ \left(\hat{\mathbf{P}}_k^{xu}\right)^T & \hat{\mathbf{P}}_k^{uu} \end{bmatrix} \tag{26h}$$

It is possible to estimate the unknown inputs only when the matrix product $\mathbf{H}_k^T\hat{\mathbf{P}}_k^{zz}\mathbf{H}_k$ is invertible. Equations (26a)–(26h), which are referred to as unscented Kalman filter equations with unknown inputs, are used to estimate all the states of the system when only a limited combination of states are measured. Equations (26) are in the same form as the traditional unscented Kalman filter in the absence of the unknown inputs and the traditional extended Kalman filter. Thus, higher order non-linear models capturing significant aspects of the dynamics may be employed to ensure that the Kalman filter algorithm can be implemented to effectively estimate the states in practice.

4. The MPPT outer loop controller

Several algorithms for achieving maximum power tracking and control have been proposed for a number of power systems [21, 22]. There have been a number of MPPT controllers proposed recently for wind turbines based on maximizing the net power captured by the generator [23–26]. A recent book on the topic has covered the optimal control based strategies

http://dx.doi.org/10.5772/62723

quite extensively [27]. There have also been a few methods based on some form of optimal estimation of the wind speed [28]. A nonlinear controller based MPPT method has also been applied to wind turbines [29]. Several of the optimal control strategies may be efficiently implemented for a wind turbine provided that highly reliable non-linear estimation algorithms are used to estimate the states of the wind turbine in operation. In this section, one such approach is briefly outlined and implemented as in ref. [3]. The system now includes the independently controlled variable pitch blades while in ref. [3], only a turbine with fixed blades was considered.

It is assumed that the induction machine is controlled in a manner so as to ensure variable-speed operation over a wide range input conditions, so it is possible to exercise direct control of the system's tip speed ratio. The wind power captured by the wind-turbine is estimated from the state estimates by the equation, $\hat{P}_w = \hat{T}_{wt}\hat{\omega}_m$ where $\hat{T}_{wt}$ is an estimate of the turbine torque and $\hat{\omega}_m$ is an estimate of the mechanical speed. The wind turbine torque may be estimated from the mechanical equation of the shaft rotation by using (1) to develop the equation for the electrical speed ω_e, to give T_{wt}. However, since the pitch angle is not generally known, the wind turbine torque is estimated at the current estimate of the pitch angle and compared with either the measurement of the wind turbine torque or an estimate of the measurement. This process facilitates the update of the estimate of the pitch angle in the first instance. Once the blade pitch angle is updated, the wind turbine torque is estimated at the updated value of the blade pitch angle. With the updated estimate of the wind turbine torque the algorithm for estimating the rotor frequency for maximum power is essentially identical to the method in ref. [3] and briefly summarized in the next paragraph.

The wind turbine torque T_{wt} is a weighted linear combination of T_{el}, $d\omega_e/dt$, and ω_e. When $\hat{P}_w$ is maximum,

$$\frac{d}{d\hat{\omega}_m}\hat{P}_w \equiv \hat{P}_w' = \hat{\omega}_m\left(\frac{d\hat{T}_{wt}}{d\hat{\omega}_m} + \frac{\hat{T}_{wt}}{\hat{\omega}_m}\right) = 0 \tag{27a}$$

The condition for maximum power capture is,

$$\hat{T}_{wt} / \hat{\omega}_m = -d\hat{T}_{wt} / d\hat{\omega}_m \tag{27b}$$

Thus the instantaneous torque speed ratio or the *instantaneous impedance* is equal to the negative of the incremental torque to incremental speed ratio or the *incremental impedance*. This is frequency dependent and is determined when the wind power input is a maximum. It follows that in the nonlinear perturbation equations,

$$\left.\frac{\Delta T_{wt}}{\Delta\omega_e}\right|_{U=U_0} = -\frac{T_{wt}}{\omega_e} \tag{28}$$

In evaluating $\Delta T_{wt}/\Delta u_f|_{\omega_e}$, the wind turbine torque perturbation due to a change in the wind speed, the power coefficient, $C_p(\lambda)$ is assumed to be a maximum.

To determine the rotor frequency at which maximum power is extracted from the wind by the turbine, the rotor frequency is assigned an initial value $\omega_p^0=\omega_{r0}$ and updated at regular time intervals. The update is filtered, driven by an estimate obtained by using the Newton-Raphson formula at each time step *k*, and given by,

$$\omega_p^{k+1} = \omega_p^k + \Delta_k,\ \Delta_{k+1} = \Delta_k + \left(u_k - \Delta_k\right)dt/\tau_{fu} \tag{29a}$$

$$u_k = K_\omega \frac{\hat{P}_{k-1}^{'}\left(\omega_p^{k-1} - \omega_p^{k-2}\right)}{\left(\hat{P}_{k-1}^{'} - \hat{P}_{k-2}^{'}\right)},\ \hat{P}_k^{'} = \hat{\omega}_m^k \frac{d\hat{T}_{wt}^k}{d\hat{\omega}_m^k} + \hat{T}_{wt}^k \tag{29b}$$

The frequency ω_p^k is the estimated rotor frequency at the maximum power point. The optimum time constant $\tau_{fu} \approx 0.04$ and the update gain, $K_\omega \approx 0.27$ were empirically determined after several simulation runs. The turbine torque and its derivative with respect to the estimated mechanical rotor speed $\hat{\omega}_m$ must be evaluated accurately in order to ensure that the turbine operates at the peak power. The turbine torque peaks at a speed slightly less than the speed at which the turbine power is a peak. The full control law for maximum power point tracking takes the form,

$$\omega_r = \omega_p^k \tag{30}$$

where ω_p^k is given by (29a).

5. Typical simulation-based results

To make the comparisons easy and to draw meaningful conclusions, the same example as the one considered in ref. [3] is also considered here with the exception that, in the case considered here, the blade pitch angle was assumed to be independently controlled. The initial equilibrium conditions were deliberately chosen so the nonlinear perturbation dynamics of the turbo-generator about the initial operating point were not stable. So the initial feedback controller was obtained by adopting the LQR-based methodology of Vepa [3] and using a model evaluated at the initial perturbation. Measurements of the rotor speed and the rotor *d–q* currents were generated by adding a random error with zero mean and a specified variance to the simulated outputs. All the perturbation states were estimated using both the UKF and the traditional EKF methodologies. **Figure 2** illustrates the simulated electrical speed of the generator, which is thrice the mechanical speed, for a time step, $dt = 0.001$ s and compared with

http://dx.doi.org/10.5772/62723

the UKF and EKF estimates over a time frame of 20,000 time steps or 20 seconds in real time. The maximum error between the curves is less than 0.2%.

Figure 3 compares the electrical speed error in the measurement, with estimates of it obtained by using the UKF and the EKF. To make the comparison we have zoomed-in over a time frame of the first 50 time steps. Quite clearly the UKF estimate converges rapidly to the measurement while the EKF estimate fluctuates in the vicinity of the measurement. From the comparisons shown in **Figure 3**, the superiority of the UKF over the EKF can be deduced. For purposes of maintaining clarity, all the other results corresponding to the EKF estimates are not shown in the figures.

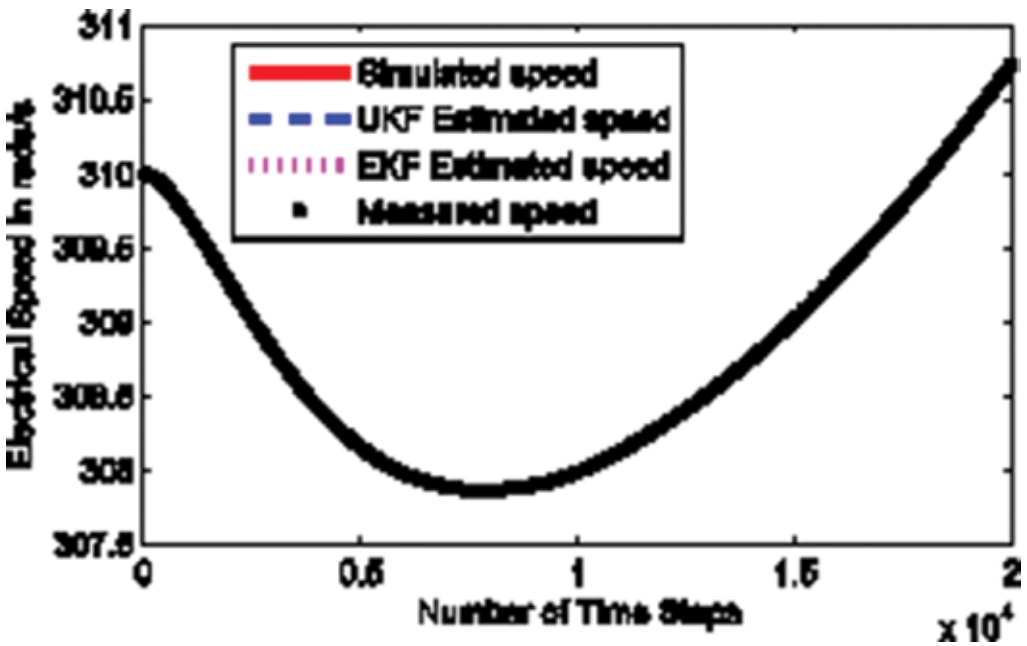

Figure 2. Simulated electrical speed (in rads/s) response of the DFIG generator compared with the measurement, the UKF and the EKF estimates.

Using this algorithm repeatedly has accentuated the need for making accurate electrical speed rate measurements and estimates. The electrical speed rate estimation was done using measurements of the electrical speed rate. From the previously estimated electrical speed and independently processing the measured electrical speed rate in another first order mixing filter, the estimates of the electrical speed are continuously updated. This approach provides precise estimates of the speed rate and facilitates the accurate estimation of the torque absorbed by the turbine from the wind. **Figure 4** shows the corresponding power transferred from the wind to the generator over the first 20,000 time steps and compared with maximum available wind power at that particular maximum magnitude of the wind speed and zero blade pitch angle.

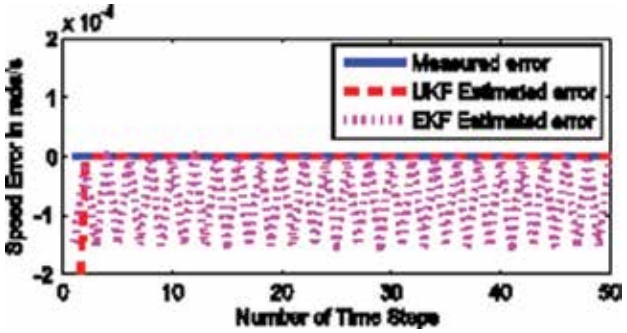

Figure 3. Comparison of the measured and UKF and EKF estimated electrical speed (in rads/s) errors corresponding to **Figure 2**.

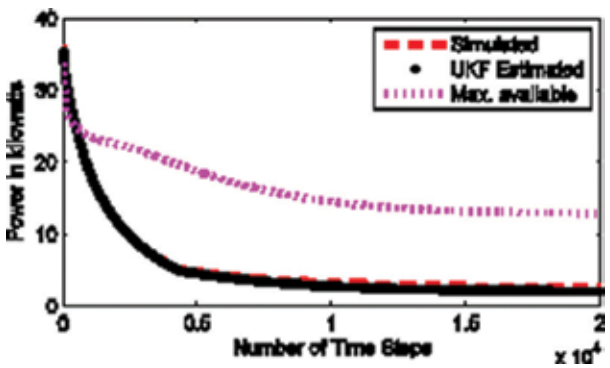

Figure 4. Wind power transferred to the generator over the first 20,000 time steps and compared with maximum available wind power.

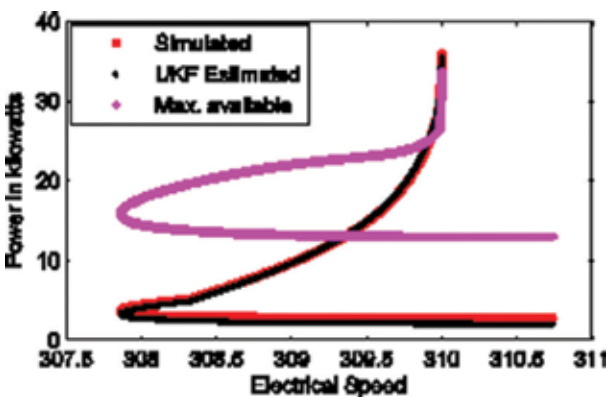

Figure 5. Turbine power characteristic over the operating speeds in rad/s.

http://dx.doi.org/10.5772/62723

Figure 5 illustrates the power speed characteristic corresponding to **Figure 4**. From **Figures 4** and **5**, it may be observed that the power transferred by the turbine from the wind to the generator tracks the maximum available wind power. **Figures 6** and **7** illustrate the corresponding torque on the generator and the torque-electrical speed characteristic. Also shown on these figures is the torque corresponding to the maximum available power.

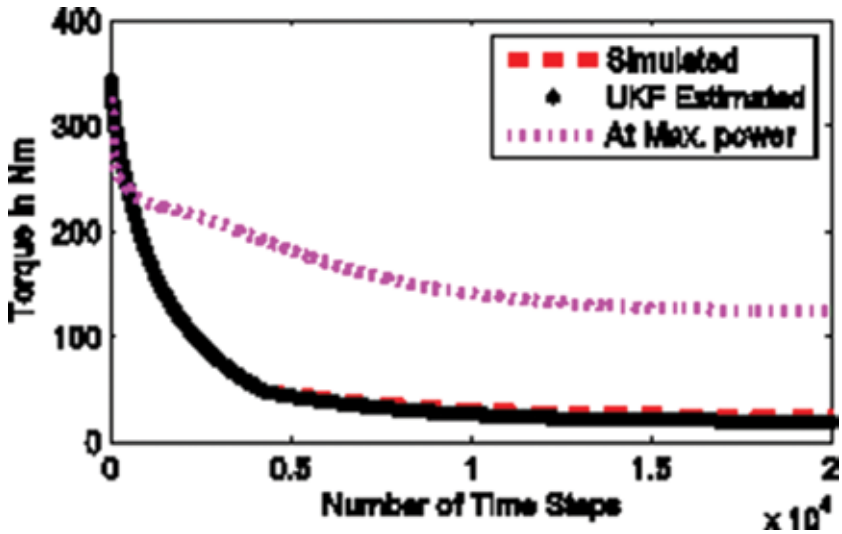

Figure 6. Turbine torque over the first 20,000 time steps and compared with the torque at the maximum available wind power.

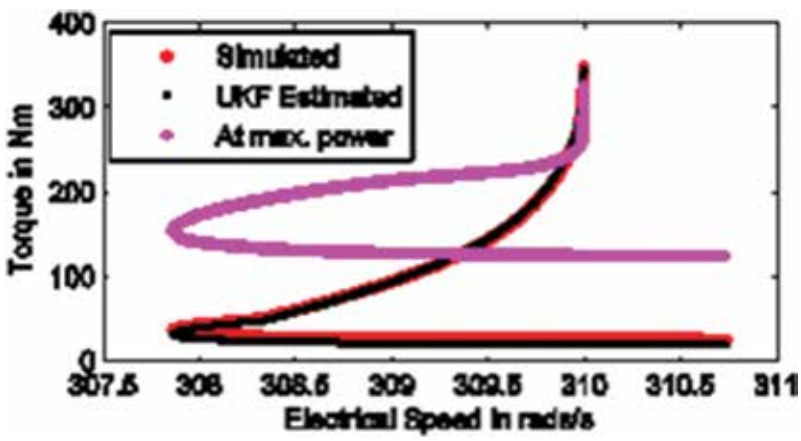

Figure 7. Turbine torque characteristic over the operating speeds in rad/s.

Figure 8 shows the growth of the estimated blade pitch angle and compared with the simulated blade pitch angle.

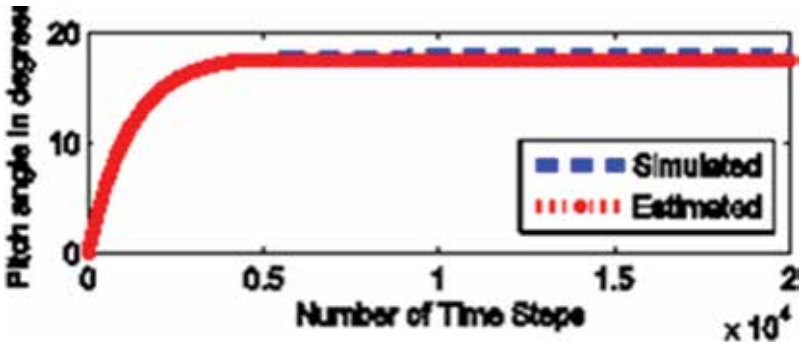

Figure 8. Estimated and simulated blade pitch angles compared.

6. Discussion and conclusions

In this chapter, a nonlinear UKF is used to provide the rotor-side control inputs and also in a tracking controller that ensures that the desired maximum power operating point is exactly tracked. As in ref. [3], the uncontrolled DFIG is unstable. Thus this necessitates the use of a stabilizing controller prior to implementing a MPPT filter. The MPPT filter tracks the maximum power point as the power is transferred from the wind to the turbine. The rotor-side control laws are synthesized by employing a H_2 optimal control law as described in ref. [3]. The MPPT filter is proposed and validated using non-linear UKF and EKF based estimation techniques. Thus an estimate of the actual power transferred from the turbine to the generator is maximized. It is shown that the MPPT filter can operate alongside the controller for regulating the blade pitch angle. The state estimation method is based on the UKF which is compared with the traditional EKF and is shown to be superior. The validation of the algorithm is carried out by simulating real wind velocity profiles from a white noise generator and using low order spectrum shaping filters that are derived from approximations of the Kaimal wind velocity spectrum. The MPPT algorithm is successfully demonstrated in the case significant levels of wind disturbances present and with the independently controlled variable pitch blades.

The advantages of using stochastic optimal control theory and nonlinear optimal control are discussed in ref. [3]. In this chapter it has been demonstrated that the MPPT control filter which acts as an outer-loop controller, continuously seeks to maximize the power absorbed by the wind turbine while the inner loop estimator continuously estimates and updates the states including the blade pitch angle (which was held fixed in ref. [3]). The MPPT control filter included a feedback signal estimated using the Newton-Raphson formula at each time step, just as in ref. [3]. One can estimate the wind power captured by the turbine and it indicates that the filter is seeking to operate within 5–9% of the simulated operating maximum power point by controlling the speed of the rotor after a 0.5 s delay, which allows the UKF to estimate the states and the unknown blade pitch angle without a significant error and to eliminate the

http://dx.doi.org/10.5772/62723

influence of power transients. The maximum available power in the wind is computed, as in ref. [3], by assuming that the wind is frozen at its maximum magnitude before it encounters the blades and the deterministic formula for the maximum power coefficient $C_p(\lambda)_{\max}$, is used to calculate it. In steady state the estimated maximum turbine power was generally uniformly less than the maximum available power, the difference being accounted for by the losses due to the finite and variable blade pitch angle, and the losses due to viscous frictional torques.

Finally the MPPT algorithm, based on the nonlinear state estimation using the UKF, is shown to perform, even when the blade pitch angles are dynamically varied and the introduction of the blade dynamics does not cause any additional instabilities when compared with the case of fixed blades considered in ref. [3]. The maximum power transfer achieved is less than in ref. [3], unless the blade is assumed to be fixed with the pitch angle set at zero.

Author details

Ranjan Vepa

Address all correspondence to: r.vepa@qmul.ac.uk

School of Engineering and Material Science, Queen Mary University of London, London

References

[1] Burton T, Sharpe D, Jenkins N, Bossanyi E. Wind Energy Handbook. John Wiley & Sons Ltd, England, 2001.

[2] Connor B, Leithead WE. Investigation of fundamental trade-off in tracking the Cpmax curve of a variable speed wind turbine. In: Proceedings of the 12th British Wind Energy Conference, 1993. pp. 313–317.

[3] Vepa R. Nonlinear, optimal control of a wind turbine generator. IEEE Transactions on Energy Conversion, 2011; 26(2):468–478.

[4] Fan L, Yin H, Miao, Z. On active/reactive power modulation of DFIG-based wind generation for inter-area oscillation damping. IEEE Transactions on Energy Conversion, 2011; 26(2):513–521.

[5] Shree KHP, Ram Kumar SVJ. Decoupled control of active and reactive powers of DFIG with cascaded SPWM converters. International Journal of Engineering Science and Technology, 2011; 3(10):7540–7545.

[6] Dendouga A, Abdessemed R, Bendaas ML, Chaiba A. Decoupled active and reactive power control of a doubly fed induction generator (DFIG). In: Proceedings of the 15th

Mediterranean Conf. on Control and Automation, Athens, Greece, July 27–29, 2007, Paper No. T26-004.

[7] Peresada S, Tilli A, Tonielli A. Power control of a doubly fed induction machine via output feedback. Control Engineering Practice, 2004; 12:41–57.

[8] Rosas P. Dynamic influences of wind power on the power system (PhD Thesis). Technical University of Denmark: Ørsted Institute, Section of Electric Power Engineering, March 2003.

[9] Slootweg JG, de Haan SWH, Polinder H, Kling WL. General model for representing variable speed wind turbines in power systems dynamics simulations. IEEE Transactions on Power Systems, 2003; 18(1):144–151.

[10] Padfield GD. Helicopter Flight Dynamics, Blackwell Science Ltd, Oxford, 1996.

[11] Fox ME. Blade mounted actuation for helicopter rotor control (MSc thesis). Boston: Massachusetts Institute of Technology, June 1993. pp. 83–125.

[12] Pitts DM, Peters DA. Theoretical predictions of dynamic-inflow derivatives. Vertica, 1981; 5:21–34.

[13] Tangler JL, Kocurek JD. Wind turbine post-stall airfoil performance characteristics guidelines for blade-element momentum methods. In: Proceedings of the 43rd AIAA Aerospace Sciences Meeting and Exhibit, Reno, Nevada, January 10–13, 2005, NREL/CP-500-36900.

[14] Tangler JL, Ostowari C. Horizontal axis wind turbine post stall airfoil characteristics synthesization. In: DOE/NASA Wind Turbine Technology Workshop, Cleveland, Ohio, May 1984, SERI/TP-257-4400, UC Category 261, DE91002198.

[15] Viterna LA, Corrigan RD. Fixed pitch rotor performance of large horizontal axis wind turbines. In: DOE/NASA Workshop on Large Horizontal Axis Wind Turbines, Cleveland, Ohio, July 1981.

[16] Vepa R. Wind power generation and control. In: Dynamic Modelling Simulation and Control of Energy Generation, Lecture Notes in Energy Series No. 20, Springer Verlag, London, 2013, Chapter 4.

[17] Julier SJ, Uhlmann J, Durrant-Whyte HF. A new method for the nonlinear transformation of means and covariances in filters and estimators. IEEE Transactions on Automatic Control, 2000; 45(3):477–482.

[18] Julier SJ and Uhlmann JK. Unscented filtering and nonlinear estimation. Proceedings of the IEEE, 2002; 92:401–422.

[19] Julier SJ. The scaled unscented transformation. In: Proceedings of the American Control Conference, 2002; 6:4555–4559.

[20] Pan S, Su H, Wang H, Chu J. The study of joint input and state estimation with Kalman filtering. Transactions of the Institute of Measurement and Control, 2011;33(8):901–918; doi:10.1177/0142331210361551.

[21] Hohm DP, Ropp ME. Comparative study of maximum power point tracking algorithms. Progress in Photovoltics: Research and Applications, 2003; 11(1):47–62.

[22] Yu GJ, Jung YS, Choi JY, Kim GS. A novel two-mode MPPT control algorithm based on comparative study of existing algorithms. Solar Energy, 2003;76:455–463.

[23] Bhowmik S, Spee R, Enslin JHR. Performance optimization for doubly fed wind power generation systems. IEEE Transactions on Industry Applications, 1999; 35(4):949–958.

[24] Qiao W, Gong X, Qu L. Output maximization control for DFIG wind turbines without using wind and shaft speed measurements. In: IEEE Energy Conversion Congress and Exposition, 2009, ECCE 2009. DOI: 10.1109/ECCE.2009.531613, pp. 404–410.

[25] Koutroulis E, Kalaitzakis K. Design of a maximum power tracking system for wind-energy-conversion applications. IEEE Transactions on Industrial Electronics, 2006; 53(2):486–494.

[26] Kawabe I, Morimoto S, Sanada M. Output maximization control of wind generation system applying square-wave operation and sensorless control. In: Power Conversion Conference, Nagoya, Japan, April 2007; 1:203–209.

[27] Munteanu I, Iuliana-Bratcu A, Cutululis N-A, Ceanga, E. Optimal control of wind energy systems: towards a global approach. Advances in Industrial Control, Springer, 1st Edition, 2008; 5:109–128.

[28] Abo-Khalil AG, Lee D-C. MPPT control of wind generation systems based on estimated wind speed using SVR. IEEE Transactions on Industrial Electronics, 2008; 55(3):1489–1490.

[29] Boukhezzar B, Siguerdidjane H. Nonlinear control of variable speed wind turbines without wind speed measurement. In: Proceedings of the 44th IEEE Conference on Decision and Control, Seville, Spain, December 12–15, 2005, pp. 3456–3461.

Chapter 12

Standard Calculation of Fault Current Contribution of Doubly Fed Induction Generator-Based Wind Turbine

Ahmed El-Naggar

Additional information is available at the end of the chapter

http://dx.doi.org/10.5772/63450

Abstract

The fault current contribution of the doubly fed induction generator-based wind turbines (DFIG-WTs) is dictated by a combination of factors, including the electrical parameters of the machine and the controller configuration of the converters. A detailed manufacturer-based simulation model for DFIG-WT was used for detailed analysis of the controller influences on short-circuit parameters. Based on the analysis, new approximate expressions of the short-circuit parameters were introduced and a new mathematical model of the short-circuit current were developed. The mathematical models and the expressions were later validated using nonlinear optimization for parameter extraction. Subsequently, a new method was introduced for fault current contribution calculation in a simple and reliable way similar to IEC-60909. The method is based on linearization and a newly introduced correction factor that takes the influence of the controller into account. Finally, the new introduced method was tested on a small wind farm and the results show better accuracy in comparison with IEC-60909.

Keywords: DFIG-WT, short-circuit, transient impedance, fault, time constant

1. Introduction

Until 1998, the majority of the installed wind turbines were of fixed speed type [1]. It is a cheap and simple technology but with many inherent disadvantages. Yet, these never created any unmanageable difficulties until the introduction of grid codes. The wind turbine technology has since developed rapidly in order to match the stipulated requirements as well as to optimize energy yields, efficiency, and overall costs. The commercial wind turbine concepts can generally be classified into fixed speed, limited variable speed, and variable-speed turbines. Variable-

speed wind turbines can also be classified based on the location of the converter as partial or full-scale power electronic converter. Whether a turbine uses geared drive or direct-drive can be used as further criterion for classification [1, 2].

Currently, the doubly fed induction generator-based wind turbine (DFIG-WT) is the dominating concept [3]. In this setup, a DFIG is used as shown in **Figure 1**, where the stator is directly connected to the grid and the rotor is linked through a partially rated power electronic converter to enable variable-speed operation. The dynamic speed range is dependent on the size of the frequency converter. A typical rating for the latter is 25–30% of the generator capacity leading to a typical speed range of ±30% around the synchronous speed [2]. The frequency converter also allows for the slip power to be fed into the. Moreover, it allows for reactive power compensation and smooth grid connection. The multistage gearbox as well as the slip rings is still inevitable to have some drawbacks, such as heat dissipation from friction, increase need for maintenance and audible noise.

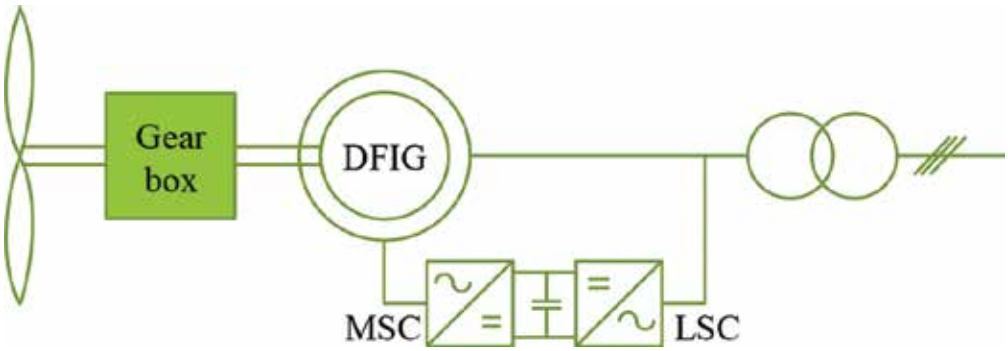

Figure 1. Layout of variable-speed DFIG-WT.

2. Modeling of DFIG-WT

The role of the DFIG is to convert the mechanical power captured by the rotor blade from the wind into electrical power, while the voltage source converter (VSC) generates the required rotor and DC voltages in relation to the control signals.

2.1. Modelling of VSC circuit

Power electronics converters are used for power flow control in variable-speed drives during steady state and dynamic periods. In DFIG-WT, the back-to-back low voltage two-level converter shown in **Figure 2** is commonly used owing to its simplicity [4]. Additionally, it allows for power generation in sub- and super-synchronous mode, active and reactive power control, and harmonic compensation [5].

http://dx.doi.org/10.5772/63450

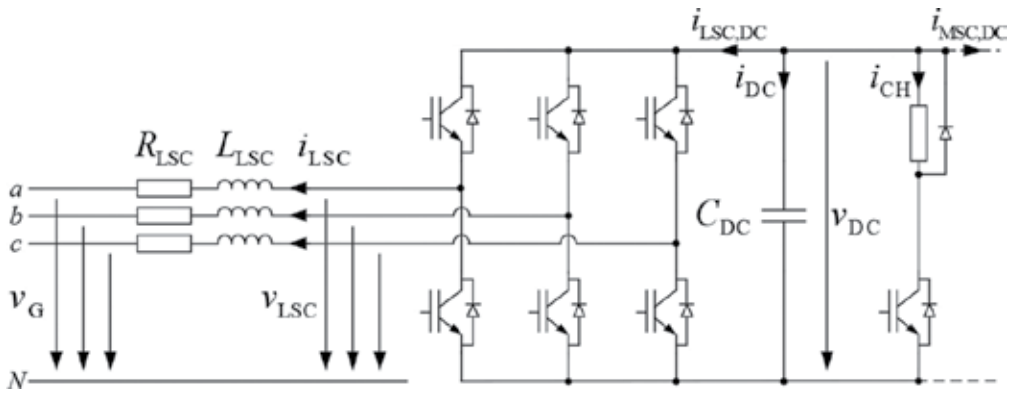

Figure 2. Two-level voltage source converter.

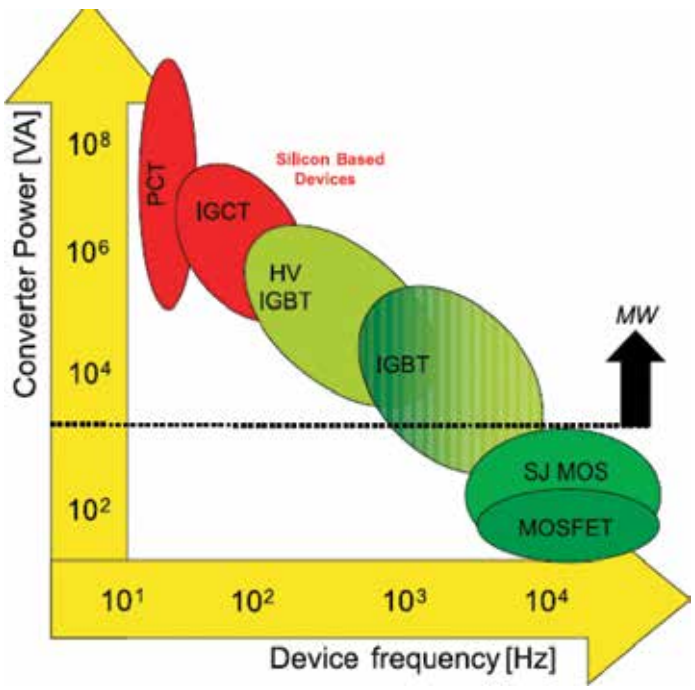

Figure 3. Switching frequency ranges of semiconductor devices [7].

The IGBT is the dominating semiconductor device used in converter systems for DFIG-WT. It offers turn-on and turn-off capability; thus, allowing full controllability over a wide range of switching frequencies. The switching frequency is determined by the switching losses, which limits the upper limit to approximately 5 kHz, and the harmonic generation, which limits the lower limit to approximately 500 Hz as depicted in **Figure 3**. The IGBT is a combination of a bipolar junction transistor (BJT) and MOSFET placed monolithically on the same silicon wafer

to combine the qualities of both devices [6]. Therefore, the IGBT can be modeled as a BJT driven by a MOSFET, where the IGBT properties are influenced by the parasitic elements of the IGBT structure as shown in the equivalent circuit of **Figure 4**. The physical interpretation and designations of the parasitic elements of the IGBT equivalent circuit are evident in [7].

The switching process of the IGBT is very fast, which requires very small simulation time steps (0.1–1 ns) to achieve high accuracy in the results. Such small simulation time steps will result in high-computational effort for the simulation of a full wind turbine system, correspondingly more for wind farms. An alternative method to increase the simulation time step and reduce the computational effort is to replace the semiconductor devices by ideal switches. The implementation of ideal switches allows the investigation of harmonics generation and interactions with the filter circuits.

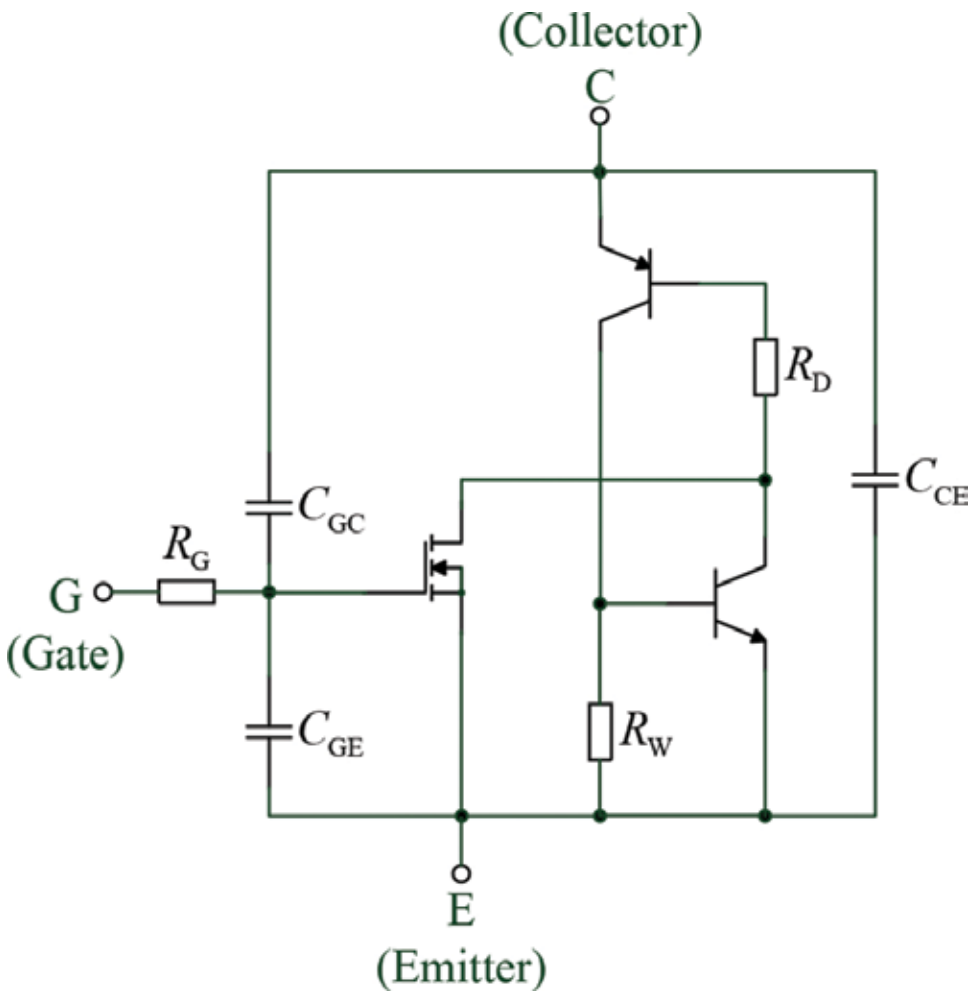

Figure 4. Equivalent circuit diagram of IGBT.

http://dx.doi.org/10.5772/63450

2.2. DC circuit

The DC circuit as shown in **Figure 2** consists of a DC capacitor and braking chopper. The DC capacitor is used to suppress the interfering voltages originating from the rectification process and to prevent fast and large oscillations in the DC voltages, while the braking chopper is used to protect the IGBT against high DC bus voltages that may occur during fault conditions. The value of DC capacitor is chosen based on the time constant required to charge the capacitor from zero to the rated voltage if supplied by the nominal power. This time constant is given by the following:

$$\tau = \frac{1}{2}\frac{C_{\mathrm{DC}} V_{\mathrm{DC,N}}^2}{S_{\mathrm{N}}} \tag{1}$$

where $V_{\mathrm{DC,N}}$ is the nominal DC voltage and S_{N} is the wind turbine nominal power.

It should be noted that from now on, all the relations will be expressed in per unit quantities expressed by small character rather than capital one as in Eq. (1).

The DC capacitor time constant is usually set between 5 and 10 ms to satisfy low ripple and overvoltage in the DC voltage and to allow for fast active and reactive power.

The differential equation describing the DC voltage neglecting the losses is given by the following:

$$\frac{\mathrm{d}v_{\mathrm{DC}}}{\mathrm{d}t} = \frac{1}{c_{\mathrm{DC}}} \cdot i_{\mathrm{DC}} = \frac{1}{c_{\mathrm{DC}}}\left(-i_{\mathrm{LSC,DC}} - i_{\mathrm{MSC,DC}} - i_{\mathrm{CH}}\right) = \frac{1}{c_{\mathrm{DC}} \cdot v_{\mathrm{DC}}}\left(-p_{\mathrm{LSC}} - p_{\mathrm{MSC}} - p_{\mathrm{CH}}\right) \tag{2}$$

where

$$p_{\mathrm{CH}} = \begin{cases} 0 & \text{, if chopper off} \\ \dfrac{v_{\mathrm{DC}}^2}{r_{\mathrm{CH}}} & \text{, if chopper on} \end{cases} \tag{3}$$

2.3. Generator

The voltage equation of the DFIG using machine variables shown in **Figure 5**, assuming identical stator and rotor windings, and uniformly distributed three phase windings whose axes displaced 120 may be expressed as follows:

$$\begin{bmatrix} v_{\mathrm{S,abc}} \\ v_{\mathrm{R,abc}} \end{bmatrix} = -\begin{bmatrix} r_{\mathrm{S,abc}} & 0 \\ 0 & r_{\mathrm{R,abc}} \end{bmatrix}\begin{bmatrix} i_{\mathrm{S,abc}} \\ i_{\mathrm{R,abc}} \end{bmatrix} - \frac{\mathrm{d}}{\mathrm{d}t}\begin{bmatrix} \psi_{\mathrm{S,abc}} \\ \psi_{\mathrm{R,abc}} \end{bmatrix} \tag{4}$$

The flux linkages maybe expressed for magnetically linear system as follows:

$$\begin{bmatrix} \psi_{\mathrm{S,abc}} \\ \psi_{\mathrm{R,abc}} \end{bmatrix} = \begin{bmatrix} l_{\mathrm{S,abc}} & l_{\mathrm{M,abc}} \\ l_{\mathrm{M,abc}} & l_{\mathrm{R,abc}} \end{bmatrix} \begin{bmatrix} i_{\mathrm{S,abc}} \\ i_{\mathrm{R,abc}} \end{bmatrix} \tag{5}$$

All the relations stated in Eqs. (4) and (5) are in p.u. quantities, where all the parameters and variables are normalized on the machine rated power and voltage as a base. Additionally, all the rotor variables are referred to the stator windings using the stator–rotor turns ratio. The assumption that the machine operating point remains in the linear range and the windings are identical is a simplification that is not satisfied for all type of studies. However, it is adequate for behavior prediction in most applications [8].

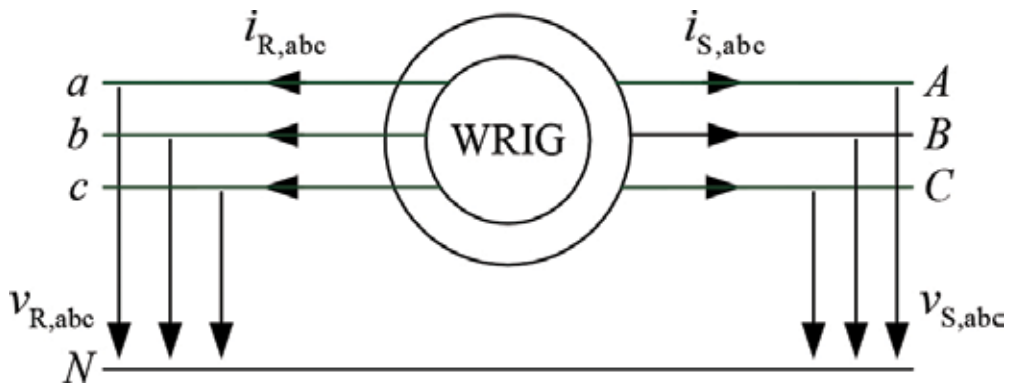

Figure 5. Doubly fed induction generator with measured quantities.

It is usually desirable to express the machine variables as a space vector with arbitrarily chosen reference frame. The space vector model of the DFIG in a fixed reference frame is as follows:

Voltage equations:

$$\begin{aligned} \underline{v}_{\mathrm{S}}^{\angle 0} &= -r_{\mathrm{S}}\underline{i}_{\mathrm{S}}^{\angle 0} - s\underline{\psi}_{\mathrm{S}}^{\angle 0} \\ \underline{v}_{\mathrm{R}}^{\angle 0} &= -r_{\mathrm{R}}\underline{i}_{\mathrm{R}}^{\angle 0} - \left(s - \mathrm{j}\omega_{\mathrm{R}}\right)\underline{\psi}_{\mathrm{R}}^{\angle 0} \end{aligned} \tag{6}$$

Flux equations:

$$\begin{aligned} \underline{\psi}_{\mathrm{S}}^{\angle 0} &= l_{\mathrm{S}}\underline{i}_{\mathrm{S}}^{\angle 0} + l_{\mathrm{M}}\underline{i}_{\mathrm{R}}^{\angle 0} \\ \underline{\psi}_{\mathrm{R}}^{\angle 0} &= l_{\mathrm{R}}\underline{i}_{\mathrm{R}}^{\angle 0} + l_{\mathrm{M}}\underline{i}_{\mathrm{S}}^{\angle 0} \end{aligned} \tag{7}$$

Electromagnetic torque:

http://dx.doi.org/10.5772/63450

$$t_{\mathrm{el}} = \mathrm{Im}\left\{\underline{\psi}_{\mathrm{S}} \cdot \underline{i}_{\mathrm{S}}^{*}\right\} = \mathrm{Im}\left\{\underline{\psi}_{\mathrm{R}} \cdot \underline{i}_{\mathrm{R}}^{*}\right\} \tag{8}$$

Equation of motion:

$$2H_{\mathrm{R}} \frac{\mathrm{d}\omega_{\mathrm{R}}}{\mathrm{d}t} = T_{\mathrm{Aero}} - T_{\mathrm{El}} \tag{9}$$

Eqs. (6)–(9) constitute the full-order model (FOM) of the DFIG used for dynamic simulations.

The analysis of the transient response as well as control of the DFIG requires the transfer function of the DFIG currents, which can be derived from FOM after some mathematical manipulation as follows:

Stator current:

$$\begin{aligned}\underline{i}_{\mathrm{S}}^{\angle 0} &= \frac{-\left(r_{\mathrm{R}} + \left(s - \mathrm{j}\omega_{\mathrm{R}}\right)l_{\mathrm{R}}\right)l_{\mathrm{M}}\underline{v}_{\mathrm{S}}^{\angle 0} + sl_{\mathrm{M}}^{2}\underline{v}_{\mathrm{R}}^{\angle 0}}{s^{2}\sigma l_{\mathrm{S}}l_{\mathrm{R}} + s\left(l_{\mathrm{R}}r_{\mathrm{S}} + l_{\mathrm{S}}r_{\mathrm{R}} - \mathrm{j}\omega_{\mathrm{R}}\sigma l_{\mathrm{S}}l_{\mathrm{R}}\right) + r_{\mathrm{S}}\left(r_{\mathrm{R}} - \mathrm{j}\omega_{\mathrm{R}}l_{\mathrm{R}}\right)} \\ &= \underline{G}_{\mathrm{SZ}}\underline{v}_{\mathrm{S}}^{\angle 0} + \underline{G}_{\mathrm{SW}}\underline{v}_{\mathrm{R}}^{\angle 0}\end{aligned} \tag{10}$$

Rotor current:

$$\begin{aligned}\underline{i}_{\mathrm{R}}^{\angle 0} &= \frac{\left(s - \mathrm{j}\omega_{\mathrm{R}}\right)l_{\mathrm{R}}l_{\mathrm{M}}\underline{v}_{\mathrm{S}}^{\angle 0} - \left(r_{\mathrm{S}} + sl_{\mathrm{S}}\right)l_{\mathrm{R}}\underline{v}_{\mathrm{R}}^{\angle 0}}{s^{2}\sigma l_{\mathrm{S}}l_{\mathrm{R}} + s\left(l_{\mathrm{R}}r_{\mathrm{S}} + l_{\mathrm{S}}r_{\mathrm{R}} - \mathrm{j}\omega_{\mathrm{R}}\sigma l_{\mathrm{S}}l_{\mathrm{R}}\right) + r_{\mathrm{S}}\left(r_{\mathrm{R}} - \mathrm{j}\omega_{\mathrm{R}}l_{\mathrm{R}}\right)} \\ &= \underline{G}_{\mathrm{RZ}}\underline{v}_{\mathrm{S}}^{\angle 0} + \underline{G}_{\mathrm{RW}}\underline{v}_{\mathrm{R}}^{\angle 0}\end{aligned} \tag{11}$$

where $\sigma = 1 - \frac{l_{\mathrm{M}}^{2}}{l_{\mathrm{S}}l_{\mathrm{R}}}$ is the leakage coefficient.

The frequency response of stator and rotor currents to stator and rotor voltages is shown in **Figures 6** and **7**, respectively. In the low frequency range (0–1 Hz), the frequency response to stator voltage has high magnitude, while the response to the rotor voltage shows negative magnitudes. This is because in the low frequency range (setting the Laplace operator to zero) the rotor circuit is seen from the stator side as closed circuit and the stator impedance becomes purely resistive, while the rotor impedance becomes infinite as seen from the rotor. On the other hand, in the frequency range around the rotor speed (setting the Laplace operator to $\mathrm{j}\omega_{\mathrm{R}} = \mathrm{j}1.2\omega_{0}$), the phenomena is reversed, where the rotor is seen from the stator side as an open circuit, while the rotor impedance becomes purely resistive as seen from the rotor.

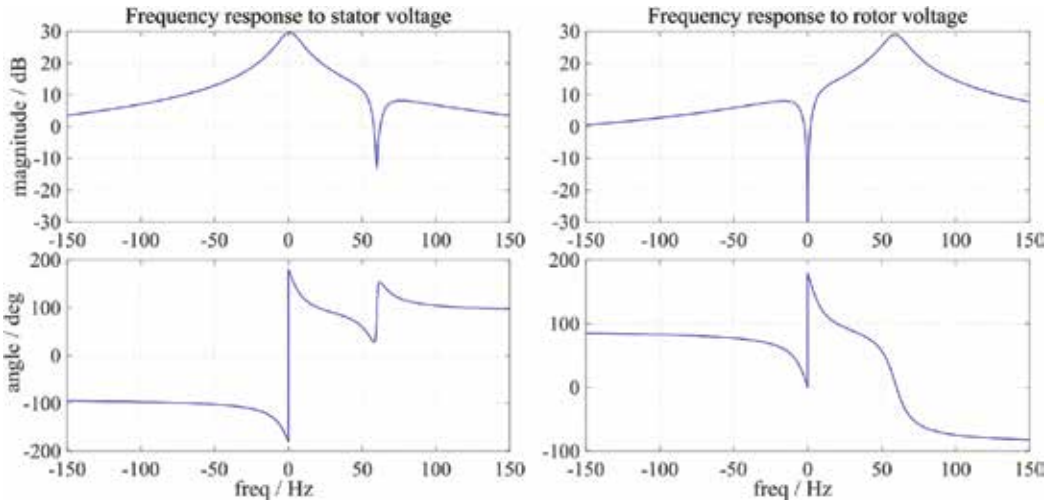

Figure 6. DFIG stator frequency response.

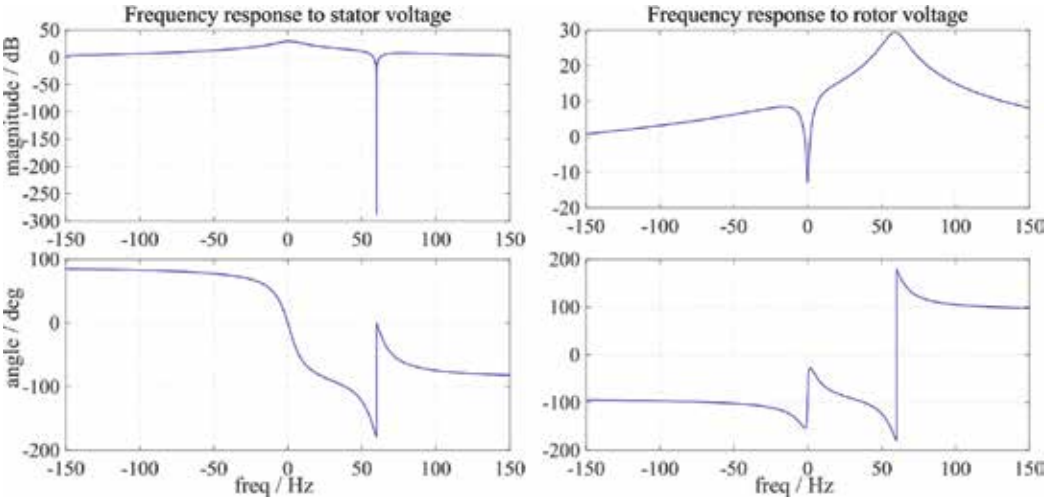

Figure 7. DFIG rotor frequency response.

3. Fault current contribution analysis

Knowledge of fault current contribution of the wind power plants is crucial for power system design and protection system setting. According to analyses in various studies [9–12], it was assumed that the fault current contribution of the DFIG-WT is dictated only by its electrical parameters. Yet, this would be true if only the crowbar protection circuit was engaged directly

http://dx.doi.org/10.5772/63450

upon fault occurrence. However, the crowbar operation is no longer desired due to the long deactivation period which leads to loss of controllability and incompatibility with the currently applicable fault ride through specific requirements. Under such configuration when no crowbar exists and full controllability is still in place, the fault current contribution of the DFIG-WT is dictated by a combination of factors, including the electrical parameters of the machine and the controller configuration of the converters [13].

The fault current contribution of the DFIG is the sum of both the machine and the line side converter (LSC) contributions. Usually, the DFIG contribution dominates, but it will be shown later that the response of the LSC is too fast and the reactive current capability of the LSC is utilized for grid voltage support during faults [13]. Therefore, the LSC contribution cannot be ignored. The fault response of the DFIG-WT will be separately analyzed for both the DFIG and LSC, starting from their natural responses till their responses with the full controller.

3.1. LSC natural fault response

Assuming a linear inductor and neglecting the switching behavior of the converter, the voltage equation of the LSC, based on the configuration of **Figure 2**, in fixed reference frame is given by the following:

$$\underline{v}_{\mathrm{LSC}}^{\angle 0} = \underline{v}_{\mathrm{G}}^{\angle 0} + (r_{\mathrm{LSC}} + sl_{\mathrm{LSC}})\underline{i}_{\mathrm{LSC}}^{\angle 0} \tag{12}$$

Rearranging Eq. (12) yields the transfer function of the LSC current as follows:

$$\underline{i}_{\mathrm{LSC}}^{\angle 0} = \frac{\underline{v}_{\mathrm{LSC}}^{\angle 0} - \underline{v}_{\mathrm{G}}^{\angle 0}}{r_{\mathrm{LSC}} + sl_{\mathrm{LSC}}} = \underline{G}_{\mathrm{LSC}}(s) \cdot (\underline{v}_{\mathrm{LSC}}^{\angle 0} - \underline{v}_{\mathrm{G}}^{\angle 0}) \tag{13}$$

Solving the Eq. (13) for a step change in the grid voltage yields:

$$\underline{i}_{\mathrm{LSC}}^{\angle 0}(t) = \frac{\Delta\underline{v}_{\mathrm{LSC}}^{\angle 0} - \Delta\underline{v}_{\mathrm{G}}^{\angle 0}}{r_{\mathrm{LSC}} + \mathrm{j}\omega_0 l_{\mathrm{LSC}}} e^{-\frac{r_{\mathrm{LSC}}}{l_{\mathrm{LSC}}}t} + \underline{i}_{\mathrm{LSC,ss}}^{\angle 0} \tag{14}$$

According to Eq. (14), the fault response of the LSC current is similar to the natural response of an RL-circuit, with a steady state fault current $\underline{i}_{\mathrm{LSC,ss}}^{\angle 0}$ and a DC decaying current of a magnitude dependent on the change of grid and LSC voltages and a time constant determined by the choke parameters.

3.2. LSC fault response with feed-forward control

The LSC voltage as well as the steady state current is dependent on the controller configuration and the internal set-points. Therefore, a proper analysis of the LSC fault response requires the converter control equation to be plugged into Eq. (13).

The current control loop of the LSC converter is based on a feed-forward term and a PI-controller to compensate for measurement uncertainties. The feed-forward term is found by replacing the Laplace operator in the transfer function by the operating frequency. Accordingly, the resulting controller becomes

$$\underline{v}_{\mathrm{LSC}}^{\angle v_{\mathrm{G}}} = \left(k_{\mathrm{P}} + \frac{k_{\mathrm{I}}}{s} \right) \left(\underline{i}_{\mathrm{LSC,ref}}^{\angle v_{\mathrm{G}}} - \underline{i}_{\mathrm{LSC}}^{\angle v_{\mathrm{G}}} \right) + \underline{v}_{\mathrm{G}}^{\angle v_{\mathrm{G}}} + \underline{z}_{\mathrm{LSC}} \underline{i}_{\mathrm{LSC}}^{\angle v_{\mathrm{G}}} \tag{15}$$

Figure 8 shows the resulting inner current control loop considering the input measurement delays and the converter dead time. The transfer function of the input measurement filter and the PWM converter dead time as a PT1 delay element and a first-order Padé approximation is, respectively, as follows:

$$\begin{aligned} G_{\mathrm{meas}}(s) &= \frac{1 + \mathrm{j}\omega_0 \tau_{\mathrm{meas}}}{1 + \tau_{\mathrm{meas}} s} \\ G_{\mathrm{dt}}(s) &= \frac{-s(2\tau_{\mathrm{dt}} + \mathrm{j}\omega_0) + 2\mathrm{j}\omega_0 \tau_{\mathrm{dt}} + 4\tau_{\mathrm{dt}}^2}{s(2\tau_{\mathrm{dt}} - \mathrm{j}\omega_0) - 2\mathrm{j}\omega_0 \tau_{\mathrm{dt}} + 4\tau_{\mathrm{dt}}^2} \end{aligned} \tag{16}$$

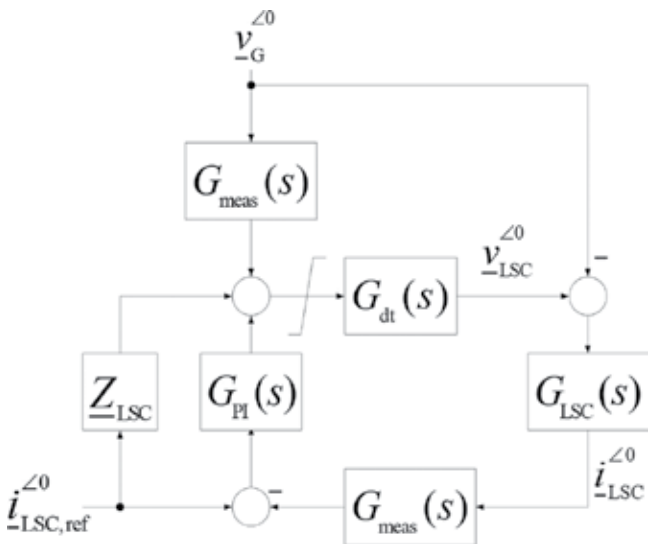

Figure 8. LSC converter inner current control loop.

http://dx.doi.org/10.5772/63450

The closed-loop transfer function of the LSC current according to **Figure 8** is given by the following:

$$\underline{i}_{\mathrm{LSC}}^{\angle 0} = \frac{G_{\mathrm{dt}}(s)\cdot(G_{\mathrm{PI}}(s)+\underline{z}_{\mathrm{LSC}})\,\underline{i}_{\mathrm{LSC,ref}}^{\angle 0} + \left(G_{\mathrm{dt}}(s)\cdot G_{\mathrm{meas}}(s)-1\right)\underline{v}_{\mathrm{G}}^{\angle 0}}{1+G_{\mathrm{LSC}}^{-1}(s)+G_{\mathrm{dt}}(s)\cdot G_{\mathrm{meas}}(s)\cdot G_{\mathrm{PI}}(s)} \tag{17}$$

The characteristic polynomial of Eq. (17) is of fifth order, which can be solved in radicals, only if the sixth-degree resolvent possesses a rational solution (Galois Theory) [14]. Solving the quartic function as given in [15, 16] would result in highly complex formula. However, if both $G_{\mathrm{meas}}(s)$ and $G_{\mathrm{dt}}(s)$ are neglected, considering that their time constants are in order of few hundreds of μs, the transfer function would be reduced to a quadratic function given by the following:

$$\underline{i}_{\mathrm{LSC}}^{\angle 0} = \frac{(s-\mathrm{j}\omega_0)\left(\frac{1}{\tau_{\mathrm{kp}}}+\mathrm{j}\omega_0\right)+\frac{1}{\tau_{\mathrm{ki}}}}{s^2+s\left(\frac{1}{\tau_{\mathrm{kp}}}-\mathrm{j}\omega_0\right)+\frac{1}{\tau_{\mathrm{ki}}}-\mathrm{j}\frac{\omega_0}{\tau_{\mathrm{kp}}}}\,\underline{i}_{\mathrm{LSC,ref}}^{\angle 0} \tag{18}$$

where $\tau_{\mathrm{kp}}=\frac{l_{\mathrm{LSC}}}{r_{\mathrm{LSC}}+k_{\mathrm{P}}}$, $\tau_{\mathrm{ki}}=\frac{l_{\mathrm{LSC}}}{k_{\mathrm{I}}}$ and $k_{\mathrm{I}}=\frac{\mathrm{k_P}}{\tau_{\mathrm{I}}}$.

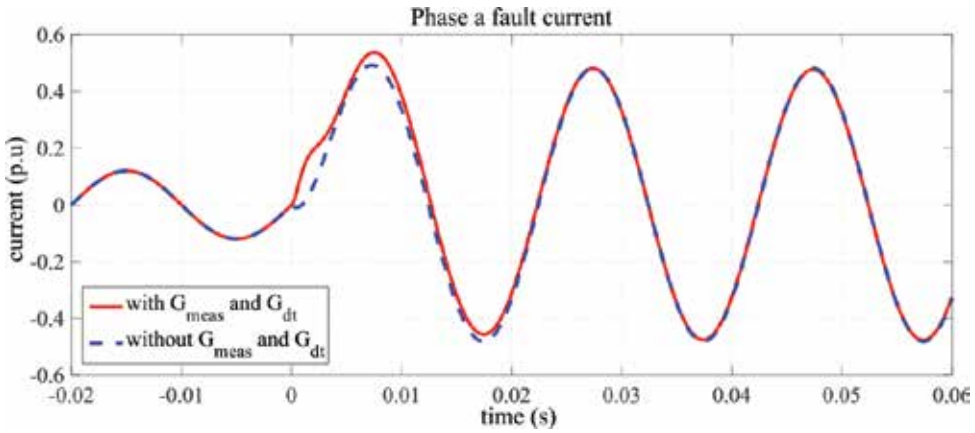

Figure 9. Influence of measurement and dead-time delays on LSC short-circuit current.

Figure 9 illustrates the small influence of neglecting $G_{\mathrm{meas}}(s)$ and $G_{\mathrm{dt}}(s)$ on the short-circuit current of the LSC. This simplification resulted in a full rejection of the disturbance quantity $\Delta \underline{v}_{\mathrm{G}}^{\angle 0}$, and the resultant response would only be dictated by the change in the reference tracking quantity $\Delta \underline{i}_{\mathrm{LSC,ref}}^{\angle 0}$, which will result in two transient currents that decay with time constants

and frequencies that can be found by solving the general quadratic formula [17] of the characteristic polynomial in Eq. (18) as follows:

$$\begin{aligned}\frac{1}{\tau_{DC}}+j\omega_{DC}&=-\frac{1}{2\tau_{kp}}+j\frac{\omega_0}{2}-\sqrt{(\frac{1}{2\tau_{kp}}+j\frac{\omega_0}{2})^2-\frac{1}{\tau_{ki}}}\\ \frac{1}{\tau_{AC}}+j\omega_{AC}&=-\frac{1}{2\tau_{kp}}+j\frac{\omega_0}{2}+\sqrt{(\frac{1}{2\tau_{kp}}+j\frac{\omega_0}{2})^2-\frac{1}{\tau_{ki}}}\end{aligned} \tag{19}$$

According to Eq. (19), the time constants and frequencies are dependent on the line choke and the PI-controller parameters. The later are usually tuned to result in over-damped response, which means that one of the two transient currents decreases much faster than the other with a time constant nearly equal to τ_{kp} and negligible frequency, while the other has a dynamic coefficient that approaches zero. Consequently, both transient currents can be ignored and it can be considered that the output current tracks the reference current directly without any dynamics. This is evident in **Figure 10**, which shows the tracking behavior of the output current. Therefore, it could be concluded that the LSC behaves as a current source with the reference current as a set-point.

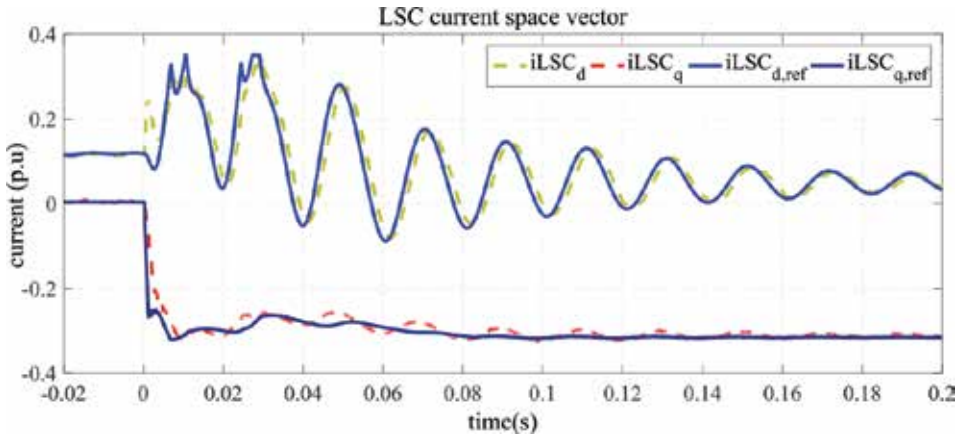

Figure 10. LSC short-circuit current space vector.

3.3. DFIG natural fault response

The characteristic polynomials in Eqs. (10) and (11) are identical and of second order. This implies that the short-circuit current of the stator and rotor will contain two decaying transient currents and that decay with the same time constants and Eigen frequencies but with different magnitudes for the stator and rotor. Those time constants and Eigen frequencies are found by solving the general quadratic formula in the same manner as in Eq. (19). However, that would result in complex formulas as given in [13]. An alternative method is to use the singular

http://dx.doi.org/10.5772/63450

perturbation to separate the fast and slow dynamics from one another, which yields the following expressions:

$$\frac{1}{\tau_{DC}} - j\omega_{DC} \approx \frac{r_S\left(r_R - j\omega_R l_R\right)}{l_S\left(r_R - j\omega_R \sigma l_R\right)}, \frac{1}{\tau_{AC}} - j\omega_{AC} \approx \frac{r_R\left(r_S + j\omega_0 l_S\right)}{l_R\left(r_S + j\omega_0 \sigma l_S\right)} - j\omega_R$$
$$\underline{z}'_{S1} \approx r_S + j\omega_0 l_S \frac{\left(r_R - j\omega_R \sigma l_R\right)}{\left(r_R - j\omega_R l_R\right)}, \underline{z}'_{R1} \approx r_R + j\left(\omega_0 - \omega_R\right) l_R \frac{\left(r_S + j\omega_0 \sigma l_S\right)}{\left(r_S + j\omega_0 l_S\right)} \tag{20}$$

Finally, the natural fault current response of the DFIG can be expressed as follows:

$$\underline{i}_{S1}^{\angle 0}(t) \approx \underline{i}_{S1,ss}^{\angle 0} - \frac{\Delta \underline{v}_{S1}^{\angle 0}}{\underline{z}'_{S1}} e^{-\left(\frac{1}{\tau_{DC}} - j\omega_{DC}\right)t} + \frac{j\omega_0 l_M \Delta \underline{v}_{R1}^{\angle 0} - r_R\left(\frac{1}{\sigma} - 1\right)\Delta \underline{v}_{S1}^{\angle 0}}{\underline{z}'_{R1}} e^{-\left(\frac{1}{\tau_{AC}} - j\omega_{AC}\right)t} \tag{21}$$

Figure 11 shows the resultant transient and steady state currents of DFIG natural fault response.

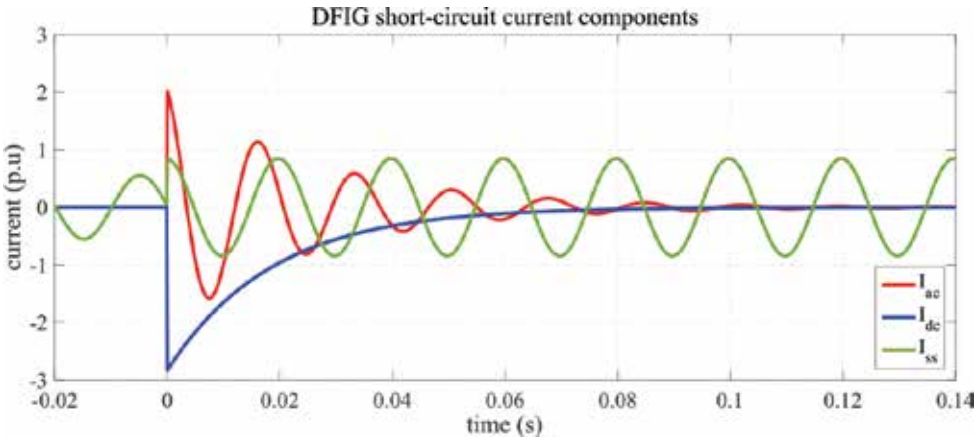

Figure 11. DFIG natural short-circuit current components.

3.4. DFIG fault response with feed-forward control

The DFIG closed-loop controller has the same structure as the LSC, where the current control loop is dependent on a feed-forward term derived from rotor voltage equation and a PI-controller to compensate for steady state errors. Accordingly, the resultant controller becomes

$$\begin{aligned}\underline{v}_{\mathrm{R}}^{\angle\nu_{\mathrm{S}}} &= -\left(r_{\mathrm{R}} + \mathrm{j}s_{\mathrm{G}}\omega_0\sigma l_{\mathrm{R}}\right)\underline{i}_{\mathrm{R}}^{\angle\nu_{\mathrm{S}}} + s_{\mathrm{G}}\frac{l_{\mathrm{M}}}{l_{\mathrm{S}}}\underline{v}_{\mathrm{S}}^{\angle\nu_{\mathrm{S}}} - \left(k_{\mathrm{P}} + \frac{k_{\mathrm{I}}}{s}\right)\left(\underline{i}_{\mathrm{R,ref}}^{\angle\nu_{\mathrm{S}}} - \underline{i}_{\mathrm{R}}^{\angle\nu_{\mathrm{S}}}\right) \\ &= -\underline{G}_{\mathrm{FFI}}\underline{i}_{\mathrm{R}}^{\angle\nu_{\mathrm{S}}} + \underline{G}_{\mathrm{FFV}}\underline{v}_{\mathrm{S}}^{\angle\nu_{\mathrm{S}}} - \underline{G}_{\mathrm{PI}}\left(\underline{i}_{\mathrm{R,ref}}^{\angle\nu_{\mathrm{S}}} - \underline{i}_{\mathrm{R}}^{\angle\nu_{\mathrm{S}}}\right)\end{aligned} \tag{22}$$

The structure of the DFIG inner current control loop is shown in **Figure 12** with the transfer function of $G_{\mathrm{meas}}(s)$ and $G_{\mathrm{dt}}(s)$ which are the same as for LSC. The closed-loop transfer function of the DFIG stator current then becomes

$$\underline{i}_{\mathrm{S}}^{\angle 0} = \frac{N_1(s)\underline{i}_{\mathrm{R,ref}}^{\angle 0} + N_2(s)\underline{v}_{\mathrm{S}}^{\angle 0}}{1 + D(\mathrm{s})} \tag{23}$$

where

$$\begin{aligned}D(s) &= G_{\mathrm{RR}}(s)\cdot G_{\mathrm{dt}}(s - \mathrm{j}\omega_{\mathrm{R}})\cdot(\underline{G}_{\mathrm{FFI}} - G_{\mathrm{PI}}(s)\cdot G_{\mathrm{meas}}(s - \mathrm{j}\omega_{\mathrm{R}})) \\ N_1(s) &= -G_{\mathrm{SR}}(s)\cdot G_{\mathrm{PI}}(s)\cdot G_{\mathrm{dt}}(s - \mathrm{j}\omega_{\mathrm{R}}) \\ N_2(s) &= D(s)\cdot(G_{\mathrm{DVR}}(s) - G_{\mathrm{DVS}}(s)) + G_{\mathrm{SR}}(s)\cdot \\ &\quad G_{\mathrm{dt}}(s - \mathrm{j}\omega_{\mathrm{R}})\cdot G_{\mathrm{meas}}(s)\cdot\underline{G}_{\mathrm{FFV}} + G_{\mathrm{DVS}}(s)\end{aligned} \tag{24}$$

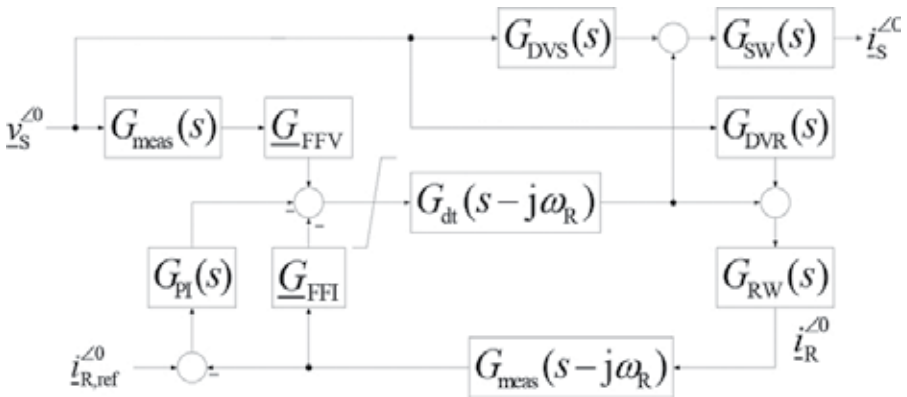

Figure 12. Schematic of DFIG inner current-control loop structure.

The characteristic polynomial in Eq. (23) is of seventh order, which cannot be solved by radicals because the quartic function is highest degree polynomial that can be solved in radicals. Rather iterative methods, for instance, Newton Raphson can be used for finding the roots.

Figure 13 shows the frequency response of the DFIG stator current, from which it can be concluded that there exist two Eigen frequencies that lie around the operating frequency. Additionally, the measurement and dead-time delays do not influence the response except in the high-frequency region and only in the response to the reference tracking quantity.

http://dx.doi.org/10.5772/63450

Consequently, neglecting both $G_{meas}(s)$ and $G_{dt}(s)$ would not result in significant difference in the dynamic response of the DFIG. This is evident in **Figure 14**, which shows the behavior of the stator current with and without considering $G_{meas}(s)$ and $G_{dt}(s)$.

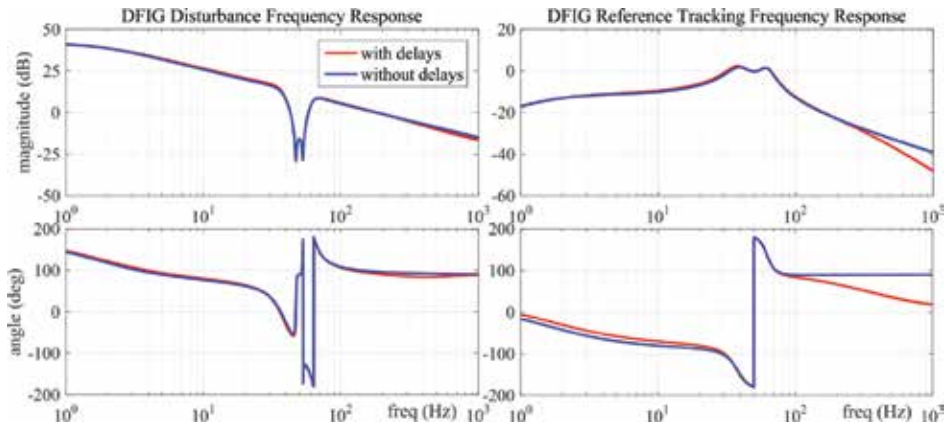

Figure 13. Frequency response of DFIG stator current.

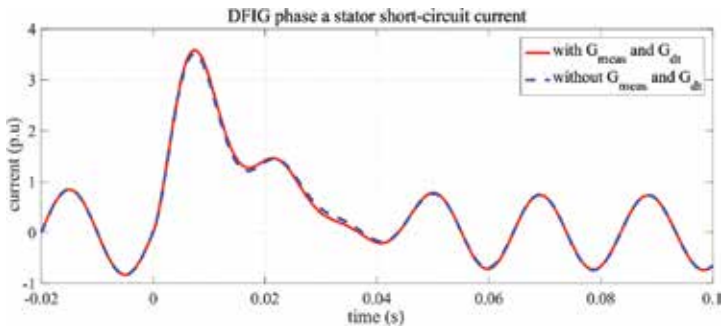

Figure 14. Influence of measurement and dead-time delays on DFIG short-circuit current.

Neglecting $G_{meas}(s)$ and $G_{dt}(s)$ will result in a third order transfer function given by the following:

$$\underline{i}_S^{\angle 0} = \frac{-\left(\left(s-\mathrm{j}\omega_0\right)\left(k_P + l_R\left(s-\mathrm{j}\omega_0\right)\right)+k_I\right)\underline{v}_S^{\angle 0} - \mathrm{j}\omega_0 l_M\left(k_P\left(s-\mathrm{j}\omega_0\right)+k_I\right)\underline{i}_{Ref}^{\angle 0}}{\left(k_P\left(s-\mathrm{j}\omega_0\right)+k_I\right)\left(r_S+\mathrm{j}\omega_0 l_S\right)+l_R\left(s-\mathrm{j}\omega_0\right)\left(s-\mathrm{j}\omega_0\right)\left(r_S+\mathrm{j}\omega_0\sigma l_S\right)} \tag{25}$$

The time constants and Eigen frequencies of Eq. (25) can be found by solving the general cubic formula [13]. However, this would result in complex formulas [18], and an easier way is to again apply singular perturbation as before which would result in more relaxed formulas as follows:

$$\begin{aligned}
&\frac{1}{\tau_{DC}} - j\omega_{DC} \approx \frac{r_S\left(\omega_0^2 l_R - k_I + j\omega_0 k_P\right)}{l_S\left(\omega_0^2 \sigma l_R - k_I + j\omega_0 k_P\right)} \\
&\frac{1}{\tau_{AC,12}} - j\omega_{AC,12} \approx \frac{k_P\left(r_S + j\omega_0 l_S\right)}{2l_R\left(r_S + j\omega_0 \sigma l_S\right)} - j\left(\omega_0 \pm \sqrt{\frac{k_I\left(r_S + j\omega_0 l_S\right)}{l_R\left(r_S + j\omega_0 \sigma l_S\right)}}\right) \\
&\underline{z}'_S \approx r_S + j\omega_0 l_S \frac{\left(\omega_0^2 \sigma l_R - k_I + j\omega_0 k_P\right)}{\left(\omega_0^2 l_R - k_I + j\omega_0 k_P\right)}
\end{aligned} \tag{26}$$

Finally, the fault current response of the DFIG with feed-forward control can be expressed as follows:

$$\underline{i}_S^{\angle 0}(t) \approx \underline{i}_{S,ss}^{\angle 0} - \frac{\Delta \underline{v}_S^{\angle 0}}{\underline{z}'_S} e^{-\left(\frac{1}{\tau_{DC}} - j\omega_{DC}\right)t} + \left(\frac{\Delta \underline{v}_S^{\angle 0}}{\underline{z}'_S} - \frac{j\omega_0 l_M \Delta \underline{i}_{Ref}^{\angle 0}}{r_S + j\omega_0 l_S}\right)\left(\frac{e^{-\left(\frac{1}{\tau_{AC1}} - j\omega_{AC1}\right)t} + e^{-\left(\frac{1}{\tau_{AC2}} - j\omega_{AC2}\right)t}}{2}\right) \tag{27}$$

where the steady state current is given by the following:

$$\underline{i}_{S,ss}^{\angle 0} = \frac{j\omega_0 l_M \underline{i}_{Ref}^{\angle 0} + \underline{v}_S^{\angle 0}}{r_S + j\omega_0 l_S} \tag{28}$$

The resultant transient short-circuit current components from Eq. (27) in comparison with the transient current from simulation are shown in **Figure 15**.

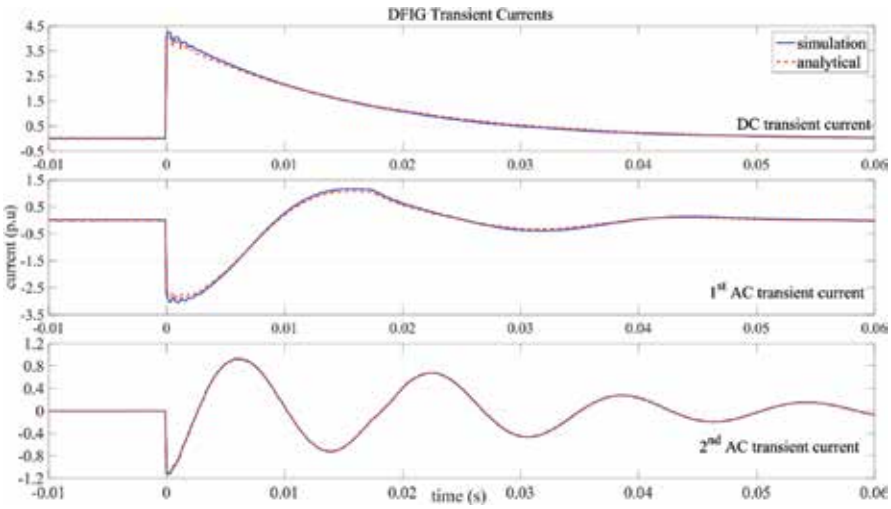

Figure 15. DFIG stator short-circuit current transient components.

http://dx.doi.org/10.5772/63450

4. Standard method for calculation of DFIG-WT fault current contribution

The fault current contribution of the DFIG-WT can be directly calculated through electromagnetic transient (EMT) calculation. However, this would be inconvenient in large network with large number of machines due to the high-computational effort required. Therefore, the calculation methods offered in IEC-60909 are usually used. This is attributed to its simplicity and reliable procedures, which are based on equivalent voltage source calculation and correction factors that offer sufficient accuracy.

The procedures for fault current calculation according to IEC-60909 are as follow:

$$I''_{\mathrm{k}} = \frac{cU_{\mathrm{n}}}{\sqrt{3}Z''} \qquad i_{\mathrm{p}} = \sqrt{2}\kappa I''_{\mathrm{k}} \tag{29}$$

where I''_k is the initial symmetrical short-circuit current, i_{p} is the peak short-circuit current, c is the voltage correction value, Z'' is the sub-transient impedance, and κ is a term that accounts for the exponential decay of the current and is given by the following:

$$\kappa = 1.02 + 0.98e^{-3R/X} \tag{30}$$

IEC-60909 offers three different methods for R/X ratio calculation in meshed networks, viz.:

Method A: the factor κ is calculated based on Eq. (30) taking the smallest ratio of R/X in all branches.

Method B: The R/X ratio is calculated from the equivalent impedance seen from the short-circuit location. A correction value 1.15 modifies the factor κ to cover inaccuracies caused using $R_{\mathrm{k}}/X_{\mathrm{k}}$ ratio from network reduction with complex impedances.

Method C: The equivalent impedance seen from short-circuits location is calculated assuming f_{c} = 20Hz, then the R/X ratio is calculated by the following:

$$\frac{R}{X} = \frac{R_{\mathrm{c}}}{X_{\mathrm{c}}} \cdot \frac{f_{\mathrm{c}}}{f} \tag{31}$$

Although IEC-60909 offers a fast and reliable method for fault current calculation, it is not adequate for calculation of fault currents from DFIG-WT; because it assumes a constant transient/internal voltage [19]. However, in DFIG-WT, the controller reacts fast upon fault occurrence and manipulates the internal voltage in order to comply with the grid codes, and consequently influence the short-circuit quantities in accordance with Eqs. (26) and (27).

4.1. Influence of PI-controller on the short-circuit current quantities

According to Eqs. (26) and (27), the PI-controller has a great influence on the behavior of the DFIG stator. In order to validate those expressions and examine their influences, the different transient current components are extracted from the simulated fault current by means of nonlinear optimization which minimizes the objective function:

$$\min_{x} \sum_{i} \left(F\left(x, xdata_i\right) - y_i \right)^2 \tag{32}$$

where y_i is the simulated short-circuit current, and $F(x)$ is the proposed solution, which was considered to be a summation of the four current components proposed in Eq. (27) described by the following:

$$\begin{aligned} i_S(t) = {} & \left|i_{S,ss}\right| \sin\left(\omega_0 t + \varphi_0\right) + \left|i_{DC}\right| e^{-\frac{t}{\tau_{DC}}} \sin\left(\omega_{DC} t + \varphi_{DC}\right) + \\ & \left|i_{AC1}\right| e^{-\frac{t}{\tau_{AC1}}} \sin\left(\omega_{AC1} t + \varphi_{AC1}\right) + \left|i_{AC2}\right| e^{-\frac{t}{\tau_{AC2}}} \sin\left(\omega_{AC2} t + \varphi_{AC2}\right) \end{aligned} \tag{33}$$

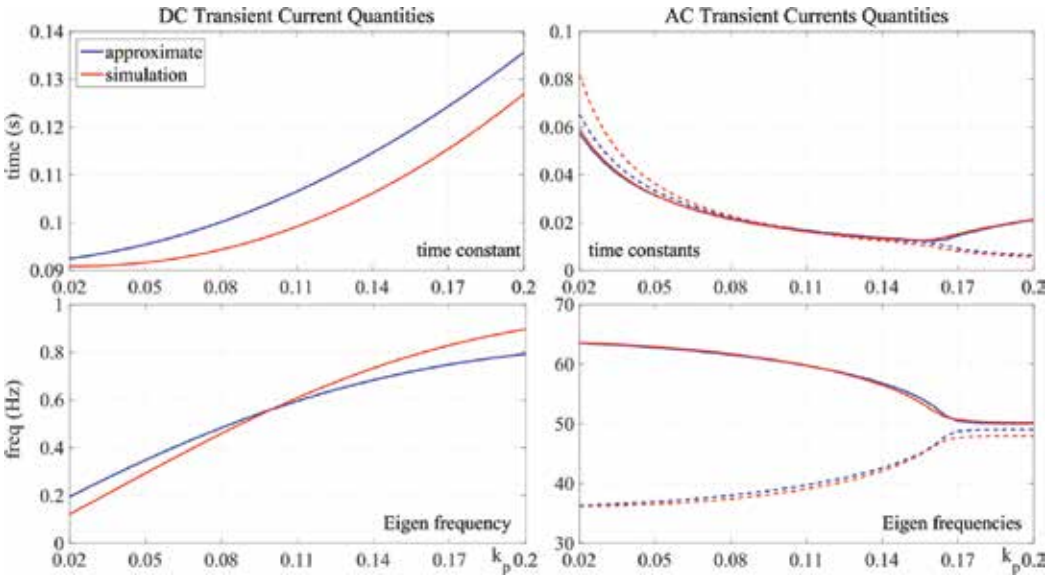

Figure 16. Influence of the proportional gain on time constants and Eigen frequencies.

Figures 16–18 show the influence of the PI-controller on the short-circuit current components, and the following could be concluded:

- the expressions given in Eqs. (26) and (27) tally with the simulation results with small errors;

http://dx.doi.org/10.5772/63450

- the integral gain does not have great influence on the peak values of the short-circuit current because it does not influence the time constants significantly;
- the IEC-60909 method does not consider the controller parameters and therefore does not offer accurate results.

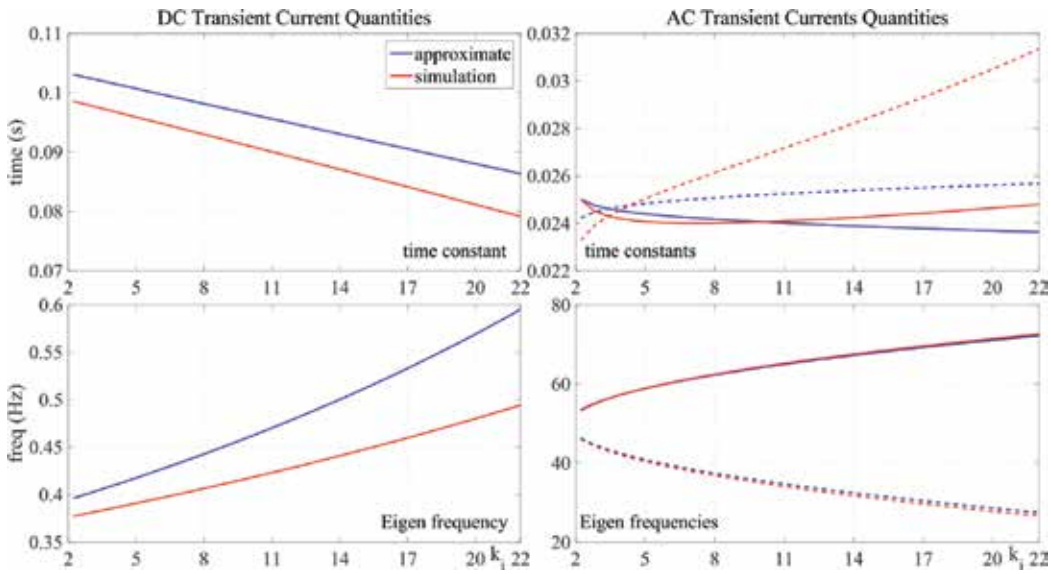

Figure 17. Influence of the integral gain on time constants and Eigen frequencies.

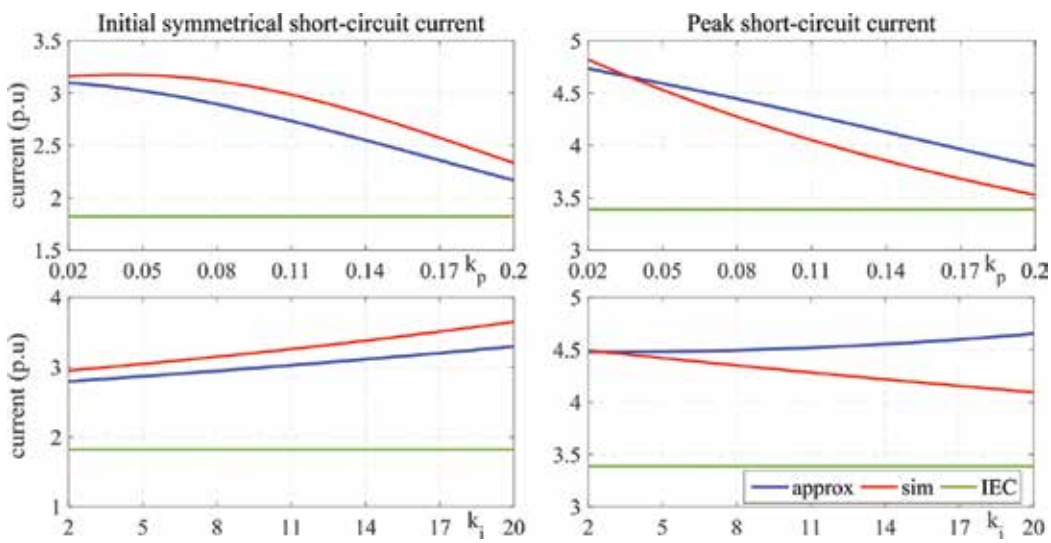

Figure 18. Influence of the PI-controller on short-circuit current values.

4.2. Standard calculation methods

As shown already, the integral gain does not influence the peak current values as well as the time constants. For sake of simplicity, it can be ignored and the Eqs. (26) and (27) can be reduced to the following:

$$\begin{aligned}
&\frac{1}{\tau_{DC}} - \mathrm{j}\omega_{DC} \approx \frac{r_S\left(k_P - \mathrm{j}\omega_0 l_R\right)}{l_S\left(k_P - \mathrm{j}\omega_0 \sigma l_R\right)}, \frac{1}{\tau_{AC}} - \mathrm{j}\omega_{AC} \approx \frac{k_P\left(r_S + \mathrm{j}\omega_0 l_S\right)}{l_R\left(r_S + \mathrm{j}\omega_0 \sigma l_S\right)} - \mathrm{j}\omega_0 \\
&\underline{z}'_S \approx r_S + \mathrm{j}\omega_0 l_S \frac{\left(k_P - \mathrm{j}\omega_0 l_R\right)}{\left(k_P - \mathrm{j}\omega_0 \sigma l_R\right)} \\
&\underline{i}_S^{\angle 0}(t) \approx \underline{i}_{S,ss}^{\angle 0} - \frac{\Delta \underline{v}_S^{\angle 0}}{\underline{z}'_S} e^{-\left(\frac{1}{\tau_{DC}} - \mathrm{j}\omega_{DC}\right)t} + \left(\frac{\Delta \underline{v}_S^{\angle 0}}{\underline{z}'_S} - \frac{\mathrm{j}\omega_0 l_M \Delta \underline{i}_{Ref}^{\angle 0}}{r_S + \mathrm{j}\omega_0 l_S}\right) e^{-\left(\frac{1}{\tau_{AC}} - \mathrm{j}\omega_{AC}\right)t}
\end{aligned} \tag{34}$$

Expressing the short-circuit current in phasor form yields the following:

$$\begin{aligned}
i_S(t) = &\left|i_{S,ss}\right| \sin\left(\omega_0 t - \varphi_0 + \varphi_U\right) \\
&+ \left|i_{DC}\right| e^{-\frac{t}{\tau_{DC}}} \sin\left(\omega_{DC} t + \varphi_{DC} - \varphi_U\right) \\
&+ \left|i_{AC}\right| e^{-\frac{t}{\tau_{AC}}} \sin\left(\omega_{AC} t - \varphi_{AC} + \varphi_U\right)
\end{aligned} \tag{35}$$

Eq. (35) is not similar to the IEC-60909 method for peak value calculation as given in Eq. (29) because the proposed current model contains three components. In order to similarize, the current model to model of IEC-60909 linearization of the proposed current model can be applied.

Ignoring the phase difference in the same manner as IEC-60909 and equating the peak current of Eq. (35) with the one from IEC-60909 in Eq. (29) yields the following:

$$\begin{aligned}
&\left|i_{S,ss}\right| + \left|i_{AC}\right| e^{-\frac{t_p}{\tau_{AC}}} + I'_k e^{-\frac{t_p}{\tau_{DC}}} = I'_k\left(1 + e^{-3\frac{R}{X}}\right) \\
&c_{ss} I'_k + \left(1 + c_{ref}\right) I'_k e^{-\frac{t_p}{\tau_{AC}}} + I'_k e^{-\frac{t_p}{\tau_{DC}}} = I'_k\left(1 + e^{-3\frac{R}{X}}\right) \\
&c_{ss} + \left(1 + c_{ref}\right) e^{-\frac{t_p}{\tau_{AC}}} + e^{-\frac{t_p}{\tau_{DC}}} = 1 + e^{-3\frac{R}{X}}
\end{aligned} \tag{36}$$

http://dx.doi.org/10.5772/63450

where $t_p \approx 0.01$s is the time instant for the occurrence of the peak, $c_{ss} = |i_{S,ss} + i_{LSC,ss}| / I'_k$ and $c_{ref} = -\left| \frac{j\omega_0 l_M \Delta i^{\angle 0}_{.Ref}}{r_S + j\omega_0 l_S} + \Delta i^{\angle 0}_{.LSC,Ref} \right| / I'_k$.

Applying Taylor expansion of the exponential parts and neglecting the higher-order terms yields the equivalent *R*/*X* ration of the DFIG-WT as follows:

$$
\begin{aligned}
& c_{ss} + c_{ref}\left(1 - \frac{t_p}{\tau_{AC}}\right) - \frac{t_p}{\tau_{AC}} - \frac{t_p}{\tau_{DC}} \approx -3\frac{R}{X} \\
& c_{cont} = 0.033\left(\frac{t_p}{\tau_{AC}} - c_{ss} - c_{ref}\left(1 - \frac{t_p}{\tau_{AC}}\right)\right) \\
& \frac{R}{X} \approx c_{cont} + \frac{r_S}{\omega_0 \sigma l_S}
\end{aligned}
\tag{37}
$$

The correction factor c_{cont} is newly introduced to account for the influential behavior of the controller on the short-circuit current. It can be directly calculated if all controller parameters are known. Otherwise, it can be calculated using measurement. Using of measurement to estimate c_{cont} is preferred as it offers better and more accurate values because not all controller parameters or structures follow what has been introduced here and they vary from manufacturer to manufacturer. Additionally, the measurement would account for the deviation of the transient impedance from the one offered by the manufacturer and to the deviation in the time occurrence of the peak value from the one offered by IEC-60909 and to the error in the linearization process.

4.3. Validation of the calculation method

The test network in **Figure 19** is used to validate the proposed calculation method. A manufacturer provided simulation model of DFIG-WT (real-world parameters are used, so that the results reflect the real dynamic behavior as closely as possible) is implemented and the ratings of the DFIG-WT are found in the Appendix.

The test networks consists of a wind farm that contains 10 DFIG-WTs connected via two winding step-up transformer to 20 kV medium voltage point of common coupling (PCC) designated as K10. The PCC is connected by a medium voltage cable of length 13 kM to the main bus K11, which is connected to the 110 kV high-voltage bus K12 by two windings step-up transformer. Three different short-circuits were applied at K10, K11, and K12, and the values of the short-circuit current using the proposed method and IEC-60909 were calculated and compared to the simulation results **Tables 1–3**.

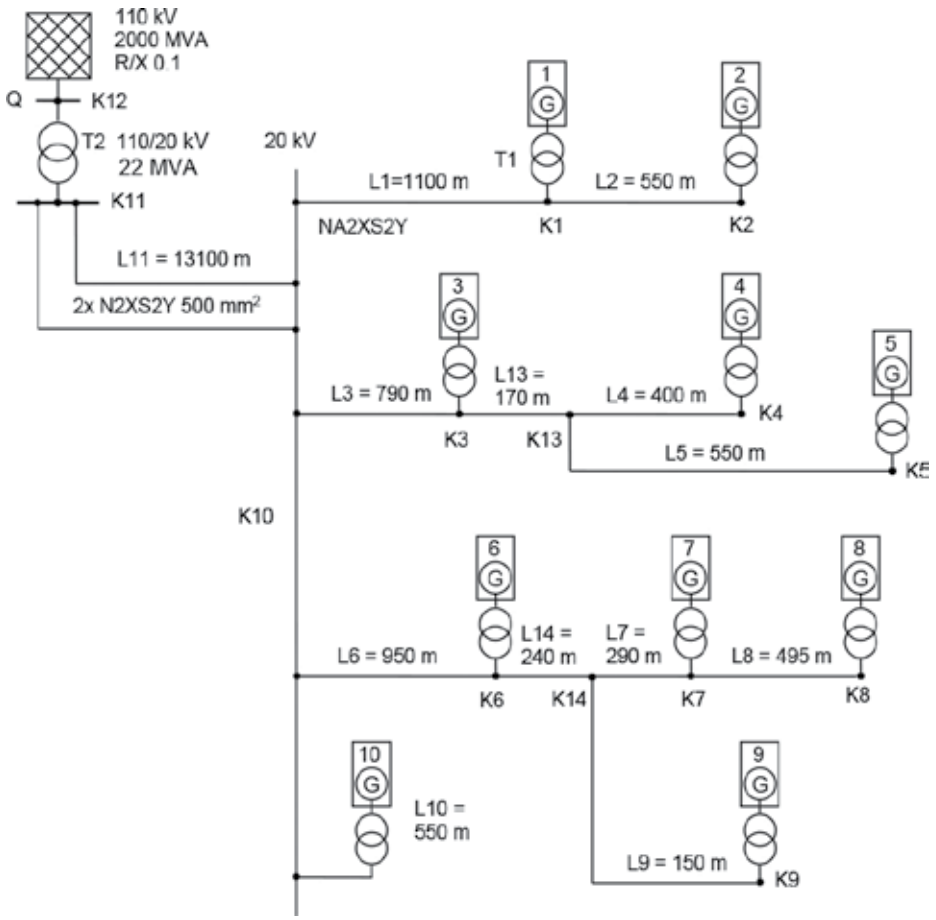

Figure 19. Simulation network.

R/X	**K 10**	**K 11**	**K 12**
IEC-60909	0.23	0.1	0.1
New method	0.296	0.16	0.11

Table 1. R/X ratio as seen from K 10, K 11, and K 12.

I''_k **(kA)**	**K 10**						**K 11**			**K 12**		
	L10	**L6**	**L3**	**L1**	**L11**	**K10**	**L11**	**T2**	**K11**	**T2**	**Grid**	**K12**
IEC-60909	0.22	0.87	0.66	0.44	3.67	5.86	1.82	5.45	7.23	0.25	10.5	10.75
New method	0.26	1.01	0.77	0.51	3.7	6.2	2.06	5.45	7.5	0.28	10.5	10.78

Table 2. Initial symmetrical short-circuit current at K 10, K 11, and K 12.

i_p (kA)	K 10						K 11			K 12		
	L10	L6	L3	L1	L11	K10	L11	T2	K11	T2	Grid	K12
IEC-60909 C	0.47	1.86	1.4	0.94	7.8	12.5	4.5	13.4	17.8	0.63	25.8	26.4
IEC-60909 B	0.54	2.1	1.6	1.1	9	14.3	5	15.1	20.0	0.72	29.7	30.4
New method	0.4	1.6	1.2	0.8	8.1	11.1	3.4	14.3	16.1	0.5	25.9	26.1
Simulation	0.4	1.6	1.2	0.79	7.1	11	3.3	12.6	15.4	0.5	25.62	26

Table 3. Peak short-circuit current at K 10, K 11, and K 12.

5. Conclusion

The fault current contribution of DFIG-WTs is dictated by a combination of factors, including the electrical parameters of the machine and the converter controller configuration. A detailed analysis of the DFIG-WT fault response was introduced considering all controller parameters and configurations.

It was shown that ignoring delays introduced by the measurement and PWM converter do not lead to significant difference in the dynamic response of both DFIG and LSC. Additionally, the simplification led to full dynamic rejection of the disturbance quantity in the LSC current response and reduced order model of the DFIG stator current.

The analysis of the fault response of the LSC showed that the dynamics of the LSC current are too fast and of small magnitude and can safely be ignored. Consequently, the LSC fault response can be modeled as a current source with the reference currents as a set-point. On the other hand, the analysis of the fault current response of the DFIG showed that the PI-controller has a great influence on the dynamics of the current. Therefore, approximate expressions were provided for the short-circuit parameters which agree well with the values estimated from simulation.

The simplified and reliable procedures for short-circuit current calculation offered by IEC-60909 is not suitable for DFIG-WT and may lead to overdesign of circuit breakers and bus bars as well as improper setting of protective relays. Therefore, a new standard and simple method for calculation of fault current contribution of DFIG-WT was introduced to overcome the deficiency of the IEC-60909 but with the same procedures. The method was derived by reducing the proposed current model by ignoring the integral gain, which was already shown that it does not influence the time constants and consequently the peak value, then using Taylor expansion of the exponential terms to estimate the equivalent R/X ratio, where a new correction factor named controller factor was introduced. The newly introduced correction factor considers the influencing behavior of the controller and its various configurations and can be estimated based on measurement.

In order to validate the efficiency of the new method, a small wind farm of 10 DFIG-WTs was implemented using a detailed manufacturer-based model. Three-phase short-circuits were

applied at three different places and the results from IEC-60909, and the proposed method were compared to the results from the simulation. The comparison showed that the proposed method offers very accurate results in comparison with IEC-60909 especially when the short-circuit locations were near the DFIG-WTs.

6. Appendix

$$\begin{aligned} &V_S = 690\,\mathrm{V},\ V_R = 1.7\,\mathrm{kV},\ r_S = 0.00206\,\Omega,\ l_S = 0.0027\,\mathrm{H} \\ &r_R = 0.00607\,\Omega,\ l_R = 0.0027\mathrm{H},\ l_M = 0.0026\,\mathrm{H},\ \mathrm{Pole\,Pairs} = 2 \\ &V_{DC} = 1100\,\mathrm{V},\ c_{DC} = 0.038\,\mathrm{F}\ \ \mathrm{chopper\,on\,/\,off} = 1.07\,/\,1.04\,V_{DC} \end{aligned} \tag{38}$$

Author details

Ahmed El-Naggar

Address all correspondence to: ahmed.elnaggar@uni-due.de

Institute of Electrical Power Systems, University of Duisburg-Essen, Duisburg, Germany

References

[1] H. Polinder, "Overview of and trends in wind turbine generator systems," in *2011 IEEE Power and Energy Society General Meeting*, 2011, pp. 1–8.

[2] H. Li and Z. Chen, "Overview of different wind generator systems and their comparisons," *IET Renew. Power Gener.*, vol. 2, no. 2, pp. 123–138, 2008.

[3] F. Blaabjerg and K. Ma, "Future on power electronics for wind turbine systems," *IEEE J. Emerg. Sel. Top. Power Electron.*, vol. 1, no. 3, pp. 139–152, 2013.

[4] O. Anaya-Lara, N. Jenkins, J. Ekanayake, P. Cartwright, and M. Hughes, *Wind Energy Generation: Modelling and Control*, 1. Auflage. Chichester, U.K: John Wiley & Sons, 2009.

[5] M. Z. B. Sujod, "Advanced converter control techniques for improving the performances of DFIG based wind turbines," Ph. D Dissertation, Electrical Power System, Duisburg-Essen, Duisburg, Germany, 2014.

[6] N. Mohan, T. M. Undeland, and W. P. Robbins, *Power Electronics: Converters, Applications, and Design*, 3. Auflage. Hoboken, NJ: John Wiley & Sons, 2002.

http://dx.doi.org/10.5772/63450

[7] A. Wintrich, U. Nicolai, W. Tursky, and T. Reiman, *Application Manual Power Semiconductors*, 2nd ed. Nuremberg, Germany: SEMIKRON International GmbH, 2015.

[8] *The Induction Machines Design Handbook*, 2nd ed. Boca Raton, FL: CRC Press, 2009.

[9] E. Muljadi, N. Samaan, V. Gevorgian, J. Li, and S. Pasupulati, "Short circuit current contribution for different wind turbine generator types," in *2010 IEEE Power and Energy Society General Meeting*, 2010, pp. 1–8.

[10] P. Karaliolios, A. Ishchenko, E. Coster, J. Myrzik, and W. Kling, "Overview of short-circuit contribution of various Distributed Generators on the distribution network," in *Universities Power Engineering Conference, 2008. UPEC 2008. 43rd International*, 2008, pp. 1–6.

[11] J. Morren and S. W. H. de Haan, "Short-circuit current of wind turbines with doubly fed induction generator," *IEEE Trans. Energy Convers.*, vol. 22, no. 1, pp. 174–180, 2007.

[12] G. Pannell, D. J. Atkinson, and B. Zahawi, "Analytical study of grid-fault response of wind turbine doubly fed induction generator," *IEEE Trans. Energy Convers.*, vol. 25, no. 4, pp. 1081–1091, 2010.

[13] C. Feltes, "Advanced Fault Ride Through Control of DFIG Based Wind Turbines Including Grid Connection Via VSC-HVDC," Ph. D Dissertation, Electrical Power System, Duisburg-Essen, Duisburg, Germany, 2012.

[14] F. Klein, *Lectures on the Ikosahedron and the Solution of Equations of the Fifth Degree*. London: Trübner & Co., 1888.

[15] D. S. Dummit, "Solving solvable quintics," *Math. Comput.*, vol. 57, no. 195, pp. 387–401, 1991.

[16] V. S. Adamchik and D. J. Jeffrey, "Polynomial transformations of tschirnhaus, bring and jerrard," *SIGSAM Bull.*, vol. 37, no. 3, pp. 90–94, 2003.

[17] W. H. Press, B. P. Flannery, S. A. Teukolsky, and W. T. Vetterling, *Numerical Recipes in FORTRAN 77: Volume 1, Volume 1 of Fortran Numerical Recipes: The Art of Scientific Computing*, 2nd ed. Cambridge England; New York: Cambridge University Press, 1992.

[18] A. El-Naggar and I. Erlich, "Analysis of fault current contribution of Doubly-Fed Induction Generator Wind Turbines during unbalanced grid faults," *Renew. Energy*, vol. 91, pp. 137–146, 2016.

[19] A. El-Naggar, C. Feltes, and I. Erlich, "R/X ratio influence on short circuit current of doubly-fed induction generator based wind turbines," in *2013 IEEE Power and Energy Society General Meeting (PES)*, 2013, pp. 1–5.

Chapter 13

Active Flow Control of Wind Turbine Blades

Victor Maldonado

Additional information is available at the end of the chapter

http://dx.doi.org/10.5772/63480

Abstract

Active flow control is a technique to improve the fluid dynamics of an aerodynamic body utilizing an active actuator and energy input. Much progress on the application of active flow control techniques for wind turbine blades has been accomplished in the last decade. The main focus has been on regulating unsteady aerodynamic blade loads and vibration by controlling the flow locally along the blade. The trailing edge flap and synthetic jet actuator have emerged among the most effective actuators for wind turbines. This chapter gives an overview of active flow control techniques, with a specific focus on the application and use of the piezoelectric synthetic jet for vibration reduction of small-scale wind turbine blade models tested in a wind tunnel. Using the techniques presented, the global flow field over the blade was altered such that flow separation was mitigated. Consequently, this resulted in a significant decrease in the vibration of the blade. Particle image velocimetry (PIV) was used to quantify the flow field over the blade. Using synthetic jets, the flow over the blade was either fully or partially reattached, depending on the angle of attack. Current and future research in this field has evolved to understanding and controlling realistic 3D vortex flows typical of actual wind turbines utilizing scaled-down rotor platforms. To this end, the author presents the design and operation of a rotor test tower with custom blades embedded with synthetic jet actuators aimed at investigating multi-scale blade tip vortex interaction and breakdown that may lead to blade vibration and noise reduction.

Keywords: active flow control, wind turbines, synthetic jets, load, vibration control

1. Introduction

As the desire to harvest more energy from the wind by increasing the rotor diameter of modern wind turbines continues, wind turbine manufacturers seek to implement techniques that reduce blade load fluctuations and structural vibration. The use of variable-speed and individual blade

pitch control rotors (used in most modern large-scale turbines) offers an efficiency increase by allowing the turbine to operate closer to its maximum aerodynamic performance at a wider range of wind speeds, thus extracting more energy from the wind.

Active flow control is a method to selectively manipulate the flow field around certain portions of the blade in response to the local wind conditions in order to bring about a desirable effect. Active flow control requires external energy or auxiliary power; therefore, the benefit of the technique (e.g., in terms of increase in power output or blade lifetime) must offset the external energy or additional capital/maintenance costs required for flow control. There are various examples of active flow control devices, for example; trailing edge flaps or microtabs for laboratory scale non-rotating wind turbine blades [1–4] and large-scale industry wind turbines [5–11], or trailing edge synthetic jets for circulation control [12], air-jet vortex generators on the surface of the blade [13], and plasma actuators to control aerodynamic loading and separation [14, 15]. Two of the most common types of actuators are the piezoelectric synthetic jet and the dielectric barrier discharge or plasma actuator. The former utilizes a piezoelectric disk as a diaphragm to ingest and expel air surrounding a cavity at high frequency, and the latter ionizes the air surrounding two electrodes such that the air is accelerated through an electric field. In the active flow control methods that follow, we focus our discussion on piezoelectric-based synthetic jet actuators.

Much of the work on synthetic jet actuators has focused largely on control of separation on fixed-pitch (non-rotating) blades. Separation control is achieved by exploiting the narrow-band receptivity of the separating shear layer and the upstream boundary layer to external actuation [16]. Oster and Wygnanski [17] and Roberts [18] showed that the actuation can affect the global flow field by modifying the evolution and interactions of the large-scale vortical structures. These modifications can lead to a Coanda-like deflection of the separating shear layer toward the surface [19] such that the layer vortices are advected downstream in close proximity to the surface. This approach has been implemented, with varying degrees of success and different actuation means, to restore aerodynamic performance of stalled airfoils and flaps [20–21]. In particular, Seifert et al. [19] and Wygnanski [22] argued that the actuation is most effective when its period scales with the advection time over the length of the flow domain downstream of separation as measured by the reduced frequency F^+. Therefore, when the separation domain scales with the characteristic length of an aerodynamic body, the (dimensionless) actuation frequency can couple to, and even drive the shedding frequency in the near wake. The possibility of coupling between (nominally) time-periodic shedding of coherent vortices and the separated shear layer in the absence of actuation is intriguing because such feedback between the near-wake instabilities and the separating shear layer is even more pronounced in the presence of actuation, thereby amplifying the unsteady component of the global aerodynamic forces. The approach of coupling the actuation frequency to instabilities relies explicitly on the narrow-band receptivity of the separating shear layer to a control input that is effective within a limited spatial domain immediately upstream of separation. Furthermore, when the flow is not separated, the effectiveness of this approach diminishes.

Another approach to control the flow is based on fluidic modification of the apparent aerodynamic shape of lifting surfaces using integrated synthetic jets that are driven at high

frequencies (i.e., much larger than the characteristic frequencies of the flow); this approach was presented by Amitay and Glezer [23] Thus, it does not necessarily rely on coupling to global flow instability and therefore can be applied over a broader range of flow conditions [24, 25]. Furthermore, this approach can accommodate broader band control algorithms when more complex actuation waveforms are used such as the pulse modulation technique [26, 27]. The modification of aerodynamic characteristics of an unconventional airfoil with synthetic jets [27] has demonstrated that flow separation at high angles of attack can be mitigated or altogether suppressed by appropriate dynamic tailoring of the apparent surface curvature (and thus the distribution of the stream-wise pressure gradient) in advance of the onset of separation.

Some studies have attempted to take a classical feedback control approach to controlling the flow and its desired performance advantage. The modeling and closed-loop control of fluid flow is widely recognized as a challenging multidisciplinary effort [28] requiring expertise in fluid dynamics, sensor and actuator design, and modeling and control design. In the literature, three primary strategies exist for closed-loop control of fluid flow [29] (i) a model-independent approach based on empirical controller tuning, (ii) a full-order optimal control solution based on the solution of the Navier-Stokes equation, and (iii) approaches based on reduced-order models. To achieve reliable performance and robustness, the model-independent approach is not appropriate. For implementation in real time, a full-order solution is computationally impractical. Much current literature relates to the reduced-order approach to flow modeling. A variety of approaches have been taken to develop reduced-order models; these include the representation of the flow system by linear transfer functions [30] using system identification techniques to obtain experimental transfer function model [31, 32] and proper orthogonal decomposition (POD) [33] performed with experimental particle image velocimetry (PIV) data on a model wind turbine array [34] and most recently on a wind turbine blade in dynamic stall [35].

The goal of this chapter is to present to the reader some of the most common experimental active flow control techniques familiar to the author and new developments in the field. It is by no means an exhaustive or detailed review; rather it serves to acquaint the reader with the basic knowledge and significance of active flow control for wind turbine blades.

2. Experimental techniques

The experimental techniques utilized to conduct research in active flow control of wind turbines can be classified into three broad categories: (i) the wind turbine blade design and fabrication, (ii) the active flow control technique (e.g., synthetic jets or plasma actuators), and (iii) the equipment and facilities required to analyze the characteristics or behavior of the blade. We begin our treatment with a general description of the techniques utilized to design and fabricate turbine blades, and then focus our attention on rapid prototyping techniques with a specific example of wind turbine blade model fabricated from stereolithography and tested inside a wind tunnel. The instrumentation of these blades with piezoelectric-based synthetic

jet actuators and sensors is also discussed. Additional equipment to quantify some physical phenomena, typically the fluid dynamics of the blade to evaluate the effectiveness of the flow control is also required. This is normally accomplished by testing the wind turbine blade inside a wind tunnel where the upstream flow conditions are known and can be controlled. The most common experimental techniques including the use of wind tunnel facilities to test the performance of wind turbines blades are examined below.

2.1. Wind turbine blade design and fabrication

Modern wind turbine blades are created with a combination of computer design tools (e.g., computer-aided design (CAD) and computational fluid dynamics) and advanced composite materials and fabrication techniques [36]. The scale and application of the blade are very important in determining the exact materials and fabrication process. The majority of consumer- and utility-scale wind turbine blades utilized to generate electric power are manufactured from composite materials such as carbon fiber. Their high strength-to-weight ratio translates into an ability to withstand high load conditions with low rotational inertia. This key characteristic contributes to the manufacture of increasingly large wind turbine rotor diameters, which is a trend in the wind energy industry to reduce the cost of energy to compete with traditional fossil fuels.

Wind turbine blades that we can refer to as experimental and sometimes not utilized to generate electric power are often manufactured from a variety of rapid prototyping techniques and materials. The scale of these blades is relatively small, and custom-design requirements are needed. The main design considerations for blades utilizing active flow control include (i) modularity to assemble/disassemble the blade in multiple sections with a common core spar, (ii) accessibility and features to mount the actuators and sensors, and (iii) mounting mechanism of the blade. Design modularity is an important feature for experimental blade design that is considered in the conceptual design and solid CAD modeling stage. Utilizing active flow control and measuring the fluid dynamics of an original blade may prompt new insight into how changes in the design or geometry of the flow control actuator can improve the behavior or aerodynamics of the blade. As the blade is fabricated in modules, redesigning and rapid prototyping a new module with different design features is easier and more cost-effective than creating a new blade. Multiple blade modules also make it easier to access and manipulate the blade when applying actuators and sensors, which are placed in precise locations. For these reasons, the combination of CAD modeling and rapid prototyping are ideal tools to develop experimental wind turbine blades. Finally, we must consider how the blade will be mounted and design the proper mechanism or adapter. In most cases, the blade will be tested inside of a wind tunnel where the blade may be mounted to a load cell or pitching mechanism to change the pitch angle.

An example of an experimental wind turbine blade model developed by the author is shown in **Figure 1**. It contains an S809 airfoil profile, which is an airfoil developed by the National Renewable Energy Laboratory (NREL) for wind turbine operation [37]. The geometry of the blade includes a span of 0.457 m and a taper ratio of 0.688 (the tip chord divided by the root chord) where the root chord is 0.203 m. The model was designed in the Unigraphics CAD

http://dx.doi.org/10.5772/63480

package and is modular; it contains four modules with three additional removable surfaces to access the piezoelectric disk actuators. The modules and surfaces screw into a common aluminum spar. The model is rapid prototyped with a stereolithography technique with a material tensile strength of about 65 MPa. The blade contains a total of 14 synthetic jet-based piezo-actuators: 4 closest to the root and 5 in the middle and tip portions of the blade as shown. The synthetic jet orifices have a width of 0.75 mm and a length of 10 mm and are located at chord-wise location of x/c of 0.318 parallel to the blade leading edge. Each synthetic jet is individually controlled and driven with a 20-mm piezo disk. The optimum piezo-actuation frequency of 2100 Hz was determined from calibration discussed in the next section. Finally, the blade contains two strain gauges (in a Wheatstone bridge arrangement for increased sensitivity) mounted at the root to measure the blade tip deflection amplitude and frequency.

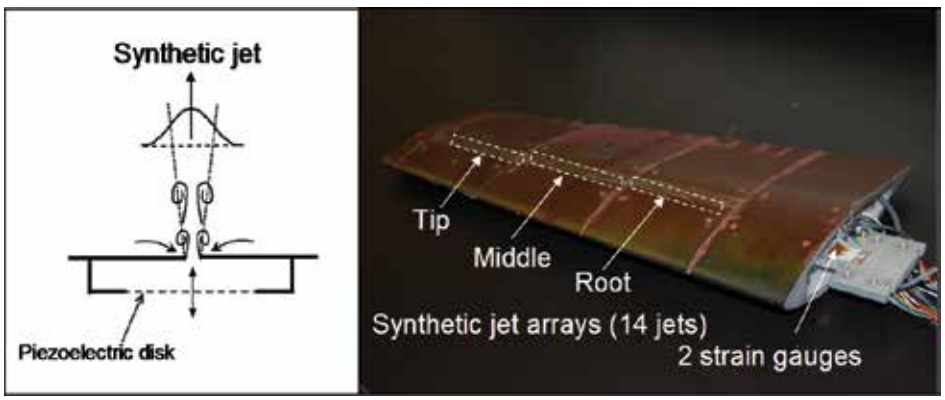

Figure 1. Experimental S809 wind turbine blade model and synthetic jet schematic.

2.2. Active flow control techniques

There are various types of actuators utilized to manipulate or control the flow field of wind turbine blades. We can classify most of them into two main categories: fluidic actuators and moving surface actuators. Moreover, both of these types of actuators can be applied near the leading edge or trailing edge of the airfoil, where their effect is markedly different as shown in **Figure 2**. Actuators mounted on the trailing edge of the blade manipulate the airfoil circulation, Γ thereby changing the lift per unit span, L' according to the Kutta-Joukowski theorem; $L' = \rho V \Gamma$. This can result in an increase or decrease in the lift coefficient compared to the baseline for a wide range of angle of attack, α, such that a change in lift coefficient, ΔC_L, bounds the baseline value as depicted in **Figure 2a**. On the other hand, actuators such as synthetic jets mounted near the airfoil leading edge are effective only for a small range of angles of attack; typically when the flow has separated in the vicinity of the synthetic jet. In these cases, active flow control is able to delay stall by partly reattaching the mean flow, thereby increasing the baseline stall angle of attack and maximum lift coefficient by ΔC_L, as shown in **Figure 2b**. More specifically, the separating shear layer shown schematically in **Figure 2c** at a certain shedding frequency is receptive to synthetic jet actuation at actuator input frequencies

at least an order of magnitude higher. The interaction between the synthetic jet and cross-flow creates a localized recirculation bubble that imparts momentum to the separating boundary layer causing the flow to reattach to the surface as shown schematically in **Figure 2d**.

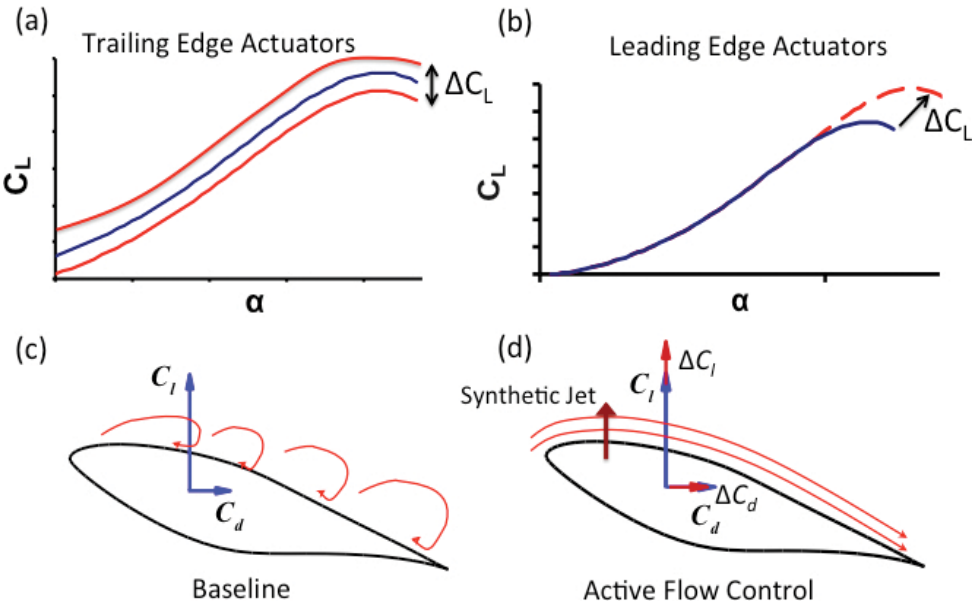

Figure 2. Active flow control modes on lift: (a) trailing edge actuators, (b) leading edge actuators, (c) baseline, and (d) active flow control.

When this occurs, there is a finite increase in lift coefficient and a decrease in drag coefficient, C_d (reduction in pressure or separation drag), which improves the aerodynamic efficiency of the blade as measured by the lift-to-drag ratio.

Plasma or dielectric barrier discharge actuators are characterized by very short response times and low power consumption. The main drawback is that they require very large AC voltage amplification and amplifiers in the range of 10–25 kV. In addition, they typically produce lower electric wind velocities compared to piezoelectric-based synthetic jets. Moving surface actuators include such devices as active microtabs, trailing edge flaps/gurney flaps, and vortex generators. Typically, they are the driven by electromechanical means, whether it might be a servo motor or piezoelectric materials. The advantages of these actuators are that they have a considerable effect on the flow to change the aerodynamic properties (i.e., lift and drag) of an airfoil. However, they generally rely on more complex lower bandwidth mechanical actuation compared to fluidic actuators, and they may be considered as a lower research-oriented approach. Fluidic actuators include steady or unsteady blowing/suction devices and synthetic jet actuators. **Figure 3** displays schematics for three of the most common types of active flow control actuators: (i) plasma actuator, (ii) trailing edge flap, and (iii) piezo-based synthetic jet. We concentrate our discussion on the principle of operation for piezoelectric disk-based synthetic jets actuators.

http://dx.doi.org/10.5772/63480

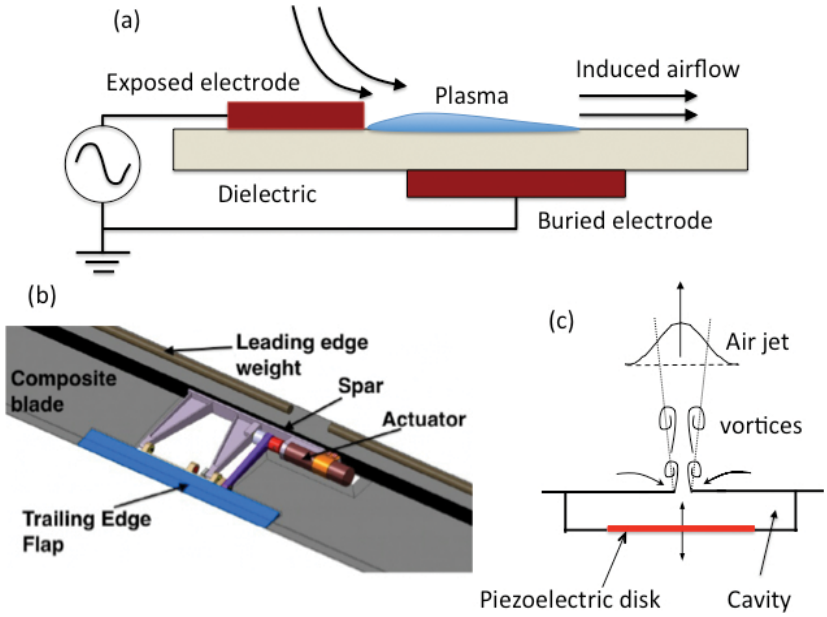

Figure 3. Active flow control actuator schematics: (a) plasma actuator, (b) trailing edge flap, and (c) piezoelectric synthetic jet actuator.

2.3. Piezoelectric synthetic jet actuator

The synthetic jet contains zero-net-mass flux and is synthesized by the time-harmonic formation and subsequent interactions of a train of vortex pairs that are formed at the edge of the orifice by the motion of a piezoelectric disk mounted in a sealed cavity. During the piezo upstroke, fluid is ejected from the cavity. The flow separates at the edge of the orifice forming a vortex sheet that rolls into a vortex pair and moves away from the orifice under its self-induced velocity [38]. During the piezo downstroke moving away from the orifice, the vortex pair has emanated sufficiently away from the orifice and is unaffected by the ambient fluid that is drawn into the cavity. The synthetic jet therefore imparts nonzero mass and impulse momentum for each vortex pair that is produced. The strongest vortex trains are produced when the piezo disk is driven at resonance with a certain optimum frequency determined via calibration with a hot-wire anemometer. The calibration process is depicted in the flowchart of **Figure 4**. An electronic signal generator is utilized to generate a sinusoidal signal of varying frequency. Depending on the piezo characteristics and cavity volume and geometry, the optimum driving frequency may be in the range of 1–2 kHz. The output channel of the signal generator is connected to the input channel of a piezo amplifier to amplify the voltage to a functional range for the piezoelectric disk. For most piezo disks, this voltage should not exceed 50 V in order to avoid damaging the piezo. The output of the piezo amplifier channel is then connected to the two piezo disk terminals while mounted to the cavity location on the wind turbine blade. Mounting the piezo disk is an important consideration; in order to create maximum momentum transfer, the piezo must be mounted semirigidly. In other words, the

piezo should be bonded with a flexible silicon-based sealant to allow maximum vertical deflection while also ensuring there is no air leaks around the perimeter of the piezo disk.

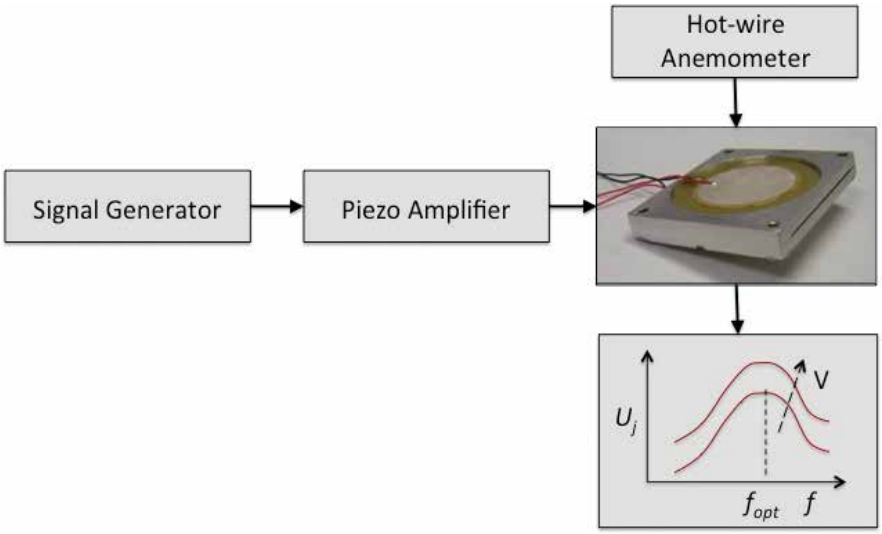

Figure 4. Synthetic jet actuator calibration process.

A hot-wire anemometer is utilized to measure the synthetic jet velocity, U_j, for a range of frequencies. The sensing element of the hot-wire probe is carefully placed in the middle of the orifice at the jet exit plane. The frequency of the sinusoidal signal is incrementally adjusted from a relatively low frequency with a step-size of about 50 Hz. As the frequency is increased, the velocity measured is observed to exhibit a somewhat linear relationship and gradually taper and reach a maximum at the optimum frequency, then decrease monotonically. This frequency is said to produce the maximum synthetic jet velocity, which is desired for most effective flow control performance. The calibration above should be repeated for several values of input piezo voltage. As **Figure 4** suggests, the synthetic jet velocity increases with higher voltage for a given frequency input. For modern piezo-based synthetic jet actuator techniques, jet velocities of 30 m/s and higher are possible.

The strength of a synthetic jet relative to the free-stream flow is quantified using the momentum coefficient, C_μ, defined as

$$C_\mu = \frac{nI_j}{\frac{1}{2}\rho U_\infty^2 A_w} \tag{1}$$

where U_∞ is the blade area, ρ is the air density, and n is the number of synthetic jets activated. I_j is the time-average jet momentum calculated only during the blowing portion of the actuation cycle, defined as

$$I_j = \frac{1}{\tau}\rho A_{sj}\int_0^{\tau} u_j^2(t)\,dt \tag{2}$$

where τ is the synthetic jet outstroke time (half the input frequency period), A_{sj} is the area of the synthetic jet orifice, and $u_j(t)$ is the centerline velocity at the jet exit plane. The time-average jet momentum is defined only for the outstroke part of the cycle. The centerline velocity is determined experimentally with a hot-wire anemometer.

2.4. Wind turbine blade techniques

Wind turbine blade models are typically tested inside a wind tunnel or outdoors where the atmospheric boundary layer (ABL) provides the inflow conditions. The advantage of a wind tunnel is that the inflow conditions can be controlled, whereas the ABL inflow conditions (such as velocity profile and turbulence intensity) cannot be changed; they are variable and must be measured prior to performing flow control on the blade. In this section, we focus on wind tunnel testing, which is the natural experimental tool of choice when investigating the fluid dynamics of novel flow control techniques or blade designs.

The wind tunnel experiments related to the wind turbine blade of **Figure 1** were conducted in an open-return low-speed wind tunnel. The test section has an 80 cm x 80 cm cross-section and is 5 m long. The wind tunnel is capable of achieving speeds up to 50 m/s and a turbulence level of less than 0.25%. The wind turbine blade model was mounted to one of the sidewalls of the test section on a pitch actuator capable of generating static blade pitch angles of attack, as well as unsteady angle of attack motions by prescribing a dynamic pitch waveform. The motion controller was implemented in xPC Target, a real-time operating system from Mathworks for control development. The blade pitch actuator is a DC-motor–based system with an optical encoder for position feedback, enabling angular position to 0.01°. The flow over the wind turbine blade must be quantified in terms of the Reynolds number, which is a non-dimensional parameter that relates the inertial forces of the blade relative to the viscous forces. The distinction must be made whether the flow is likely to be laminar, transitional, or turbulent. The actual flow depends on factors such as airfoil or blade surface finish, steadiness of the flow, and absence of disturbances. Generally speaking however, flat plate laminar flow can be expected for Reynolds numbers below 500,000, transitional flow in the range of 500,000 to one million, and fully turbulent flow for Reynolds numbers above one million. The Reynolds number based on blade chord is defined as

$$Re_{c'} = \frac{U_\infty c'}{\nu} \tag{3}$$

where ć is the mean aerodynamic chord of the blade and ν is the air kinematic viscosity. For the blade model of **Figure 1** tested in the wind tunnel with experimental results presented in the next section, the Reynolds numbers were in the range of between 71,000 and 238,000. This flow can be considered as laminar flow.

The blade model was instrumented with a pair of strain gauges to measure blade structural vibration by quantifying its unsteady tip deflection. The strain gauges were surface mounted on the upper and lower surfaces of the blade's aluminum spar near the root. This created a Wheatstone half-bridge, where each gauge produced an equal but opposite magnitude strain, resulting in improved resolution of the strain reading. The strain gauges were oriented in the span-wise direction to capture the bending movements of the model (i.e., the deflections that are correlated to the roll moment). The voltage output from the strain gauges due to span-wise bending was correlated to the deflection at the tip. First, the voltage output was calibrated to the tip deflection by manually loading the blade with multiple equal weights (at the tip) and measuring its deflection. A second-order curve of the tip deflection as a function of voltage was then fitted to the data points and was integrated into the code to generate the time histories of the tip deflection.

2.4.1. Particle image velocimetry

PIV is an optical method of flow diagnostics utilized in experimental fluid dynamics research. It is utilized to obtain instantaneous velocity measurements and related turbulence properties in fluids. The fluid is seeded with small tracer particles designed to follow the flow and faithfully represent the flow dynamics. Together with a laser source to illuminate the particles and one or two charge-coupled device (CCD) cameras to take a pair of images of the particles in a fluid, the motion of the particles can be tracked to compute the velocity of the flow being studied.

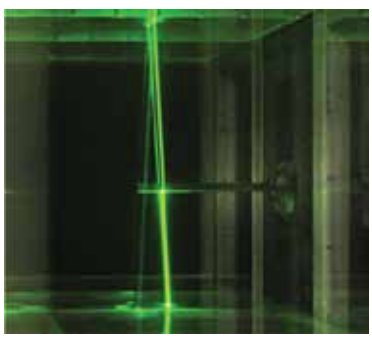

Figure 5. Measuring the flow with PIV on a wind turbine blade model.

The flow field over the suction surface of the blade was measured using PIV at a span-wise location of $y/b = 0.47$ (about mid span) coinciding with the middle of a synthetic jet orifice to capture maximum flow control effectiveness. The PIV system consists of a 1376 x 1040 pixel resolution thermoelectrically cooled 12-bit CCD camera, a pair of pulsed 120 mJ Nd:YAG lasers, and a programmable timing unit. In the present experiments, 2-D PIV data were acquired where a single CCD camera was mounted on a computer-controlled three-axis traverse. The laser light sheet was emitted from a free-moving optical arm and a laser head with variable lenses that can be positioned at any location along the outside of the test section.

With this arrangement, precise positioning of the laser light sheet was obtained. **Figure 5** is a photograph of the wind turbine blade tested during the PIV measurements; notice the vertical laser sheet, which emanates from top to bottom utilizing laser optics.

A smoke generator (model Magnum 800 made by Martin Manufacturing PLC) was used together with water-based fluid to provide droplets in the order of a few micrometers in diameter to serve as flow tracers. The smoke was introduced into the tunnel via the wind tunnel fan's air filter. The stream-wise and cross-stream velocity components (*U, V*) were computed from the cross-correlation of pairs of successive images with 50% overlap between the interrogation domains. For the time-averaged velocity vector fields, 250 image pairs were processed using an advanced multi-pass method where the initial and final correlation passes were 64 x 64 pixels and 32 x 32 pixels, respectively. The camera was mounted at a perpendicular distance of approximately 1 m to the laser light sheet, such that the distance between pixels is up to 125 μm. The maximum velocity (30.48 m/s) corresponds to an average displacement of approximately 8 pixels with an error of ±0.1 pixels, which corresponds to a maximum error of ±1.25% of the free-stream velocity (±0.38 m/s at the maximum speed).

2.4.2. Load cell and surface pressure measurements

Active flow control for wind turbine blades is often applied as a technique to regulate the aerodynamic loads of the blade. These unsteady loads lead to blade structural vibration due to periodic flow separation on some portion of the blade. The most direct and accurate manner to measure blade loads (e.g., lift and drag) is to mount the blade on a multi-axis load cell or force transducer. The load cell is typically mounted onto a pitch actuator to change the blade angle of attack. The pitch actuator is then fixed to the sidewall of the wind tunnel test section. Force data are collected with a modern data acquisition (DAQ) hardware and software such as Labview from National Instruments. When selecting a load cell and taking force measurements, care must be taken to obtain sufficient resolution in the measurement by estimating the maximum lift and drag generated (using an analytical approach) and the expected changes in these forces due to active flow control which are small in comparison.

Surface pressure measurements are made to acquire the pressure distribution around the suction and pressure surfaces of the blade. This technique normally involves placing an array of pressure ports distributed along the chord on the surface of the blade at a certain span-wise location(s). The pressure ports are connected on the inside of the blade to small flexible tubes, which are routed to exit the blade and test section. The pressure difference between a given pressure tap and the reference free-stream pressure inside the wind tunnel is measured using a pressure scanner transducer with around 32 channels for good pressure distribution resolution and subsequent normal force coefficient calculation. The objective of this method is to calculate the pressure coefficient at each pressure tap location for each test free-stream velocity and angle of attack. The pressure distributions can then be utilized to compute the normal and tangential force coefficients with numerical integration schemes. The lift and drag coefficients of the blade are finally calculated via a trigonometric relation of these coefficients with the angle of attack. It must be stated that calculating the lift and drag coefficients with this technique is only valid and reasonably accurate for small to moderate angles of attack,

where the flow is still globally attached to the surface of the blade and the velocity is fairly steady in order to obtain a valid pressure tap measurement. Moreover, a more accurate method to calculate the drag coefficient would be to measure the velocity deficit and thus momentum loss at the wake of the blade (typically about one chord length behind the blade trailing edge) utilizing a pressure rake or traversing a pitot tube across the wake.

3. Experimental results

The experimental methods discussed above were utilized to analyze various aspects of the performance of wind turbines blades. In this section, we describe some of the main research findings, which have been published by the author in various journals and conference proceedings. Perhaps some of the earliest work on the feasibility of piezoelectric synthetic jets for active flow control of wind turbine blades was reported by Maldonado et al. (2011) [39, 40], with a subsequent paper focusing on the S809 airfoil [41], which is the basis for the results presented below.

3.1. Structural vibration control

A wind turbine blade exhibits various levels of structural vibration due to prime factors as incoming flow conditions (e.g., wind speed level, turbulence) and flow separation on different portions of the blade. Flow separation induces structural vibration of the blade at its structural resonance or natural frequency; the more severe the flow separation, the larger the amplitude of vibration will be. Active flow control was utilized as a technique to partially reattach the flow at post-stall angles of attack. The effect of the synthetic jets on the structural vibration is presented in **Figure 6a** at a Reynolds number of 1.85 x 105 and angle of attack of α = 16.5°. The time histories of the blade tip deflection with and without flow control are presented. For the

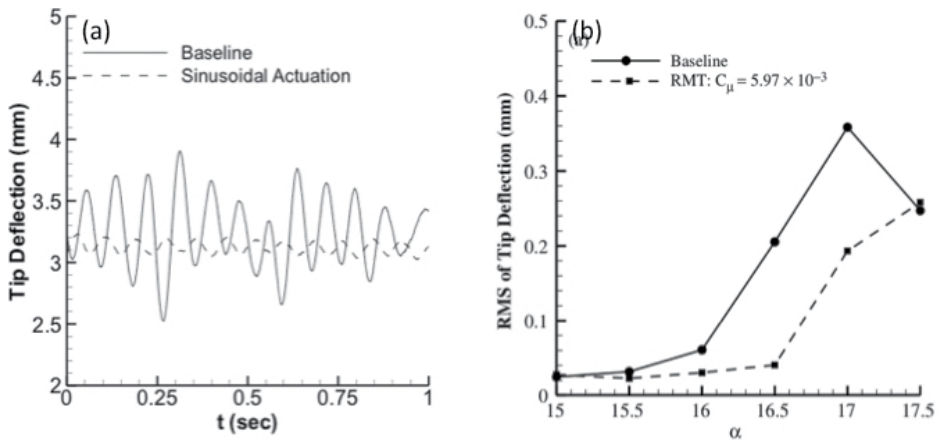

Figure 6. (a) Unsteady blade tip deflection and (b) RMS of blade tip deflection.

http://dx.doi.org/10.5772/63480

controlled case, the momentum coefficient of each synthetic jet is $C_\mu = 5.97 \times 10^{-3}$, where all 14 synthetic jets on the S809 blade of **Figure 1** were activated together. Without flow control, the blade vibrates at its fundamental structural resonance frequency, f_{struc} of around 6 Hz about its mean tip deflection of about 3.25 mm and average peak-to-peak amplitude of 0.8 mm. When the synthetic jets are activated, the peak-to-peak amplitude is reduced to about 0.13 mm; a reduction factor of 6 in the amplitude of vibration. The root mean square (RMS) of tip deflection as a function of the angle of attack is shown in **Figure 6a**. Flow control is effective in reducing vibration for a small range of post-stall angles of attack between 15° and 17.5°, where maximum vibration reduction occurs at 16.5° corresponding to the tip deflection time history of **Figure 6a**.

The effect of flow control on the structural vibration was also evaluated by computing the power spectral density (PSD) content as a function of frequencies present in the blade shown in **Figure 7a**. Without flow control, there is a noticeable peak at the structural frequency, f_{struc} of the blade. Using actuation, there is a reduction in all frequencies below 30 Hz. Furthermore, the magnitude of the structural peak decreases about an order of magnitude from the baseline level. This implies that the energy associated with the structural frequency vibration of the blade has greatly reduced. Another aspect of flow control is the ability to achieve proportional control of the blade tip deflection. This can be obtained by varying the momentum coefficient of the synthetic jets (i.e., their strength). **Figure 7b** presents the effect of the momentum coefficient on the PSD structural peak, where all the synthetic jets were activated. The figure clearly shows that proportional control of the tip deflection is achieved by simply varying the momentum coefficient.

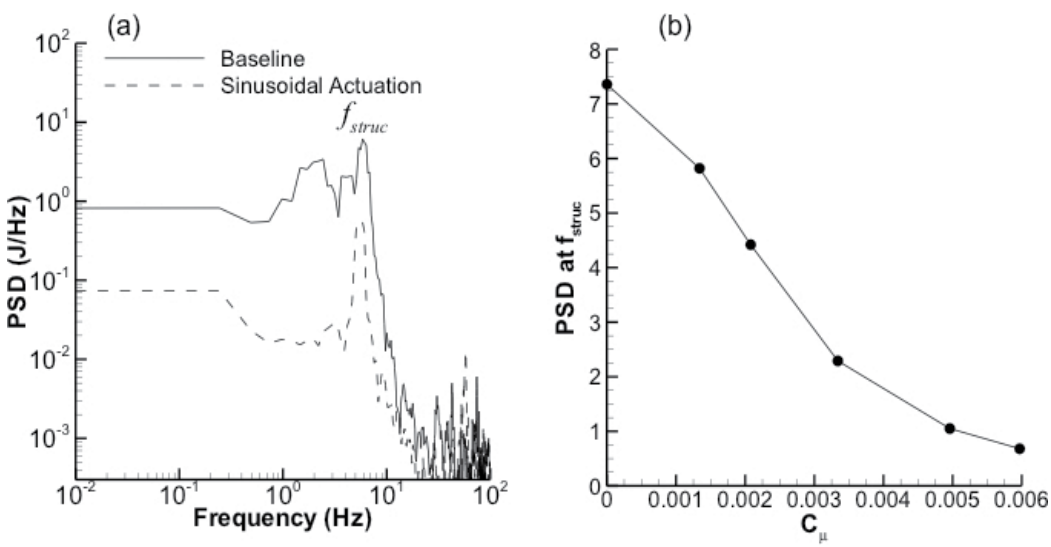

Figure 7. Power spectral density: (a) as a function of frequency and (b) power spectral density of structural vibration as a function of jet momentum coefficient.

3.2. PIV flow field measurements

Activation of the synthetic jets yields profound effects on the vibration of the blade due to flow reattachment. In order to quantify the ability for flow control to delay flow separation, 2-D PIV measurements of the mean global flow on the suction surface of the blade were conducted and are presented in **Figures 8** and **9** for the baseline and forced ($C_\mu = 5.97 \times 10^{-3}$) cases, respectively. The PIV plane was placed at $y/b = 0.47$, in the middle of a synthetic jet orifice for maximum control effectiveness. **Figures 8** and **9** present superimposed span-wise vorticity contours and streamlines for α = 15°, 15.5°, 16°, 16.5°, 17°, and 17.5°. Without flow control, the stream-wise

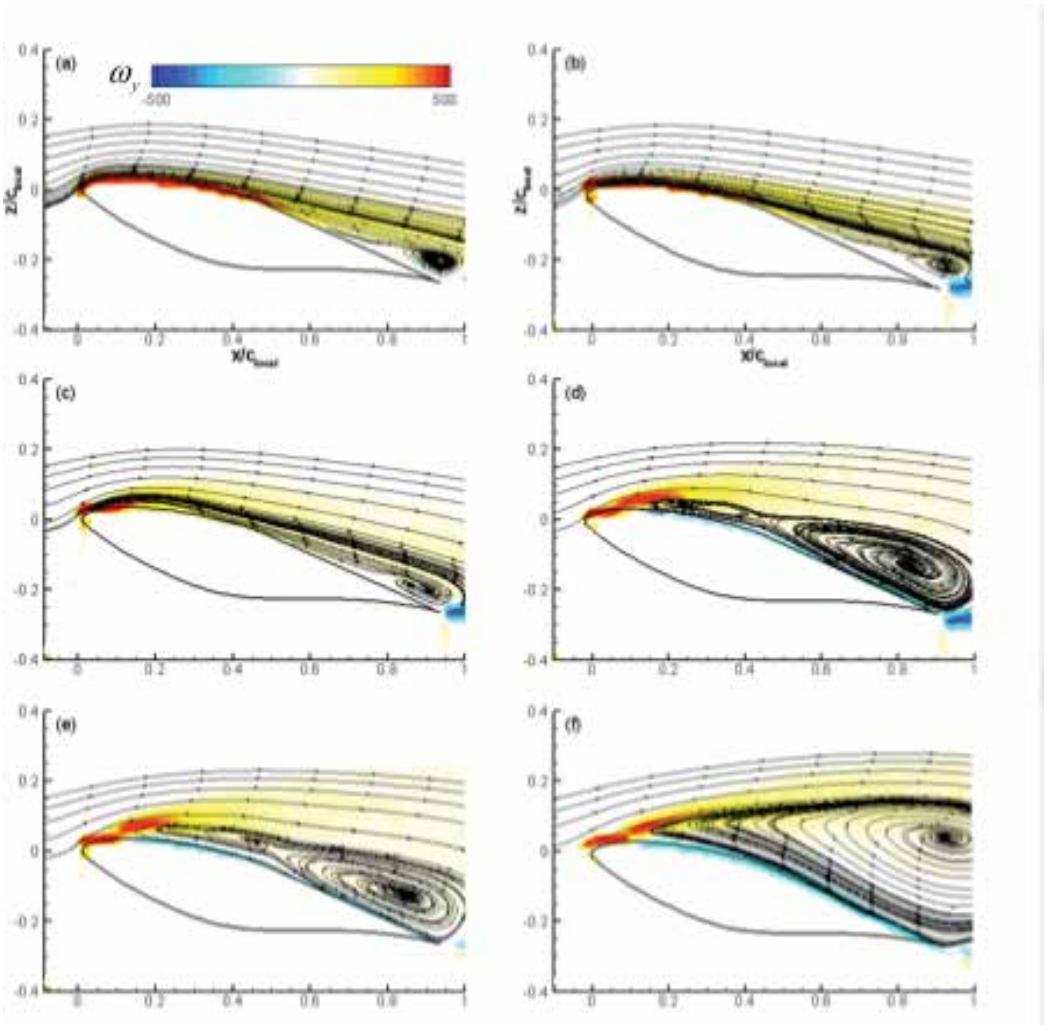

Figure 8. Superimposed span-wise vorticity and streamlines for the baseline case at $y/b = 0.47$ and $Re = 1.85 \times 10^5$. α = 15°(a), 15.5°(b), 16°(c), 16.5 °(d), 17°(e), and 17.5°(f).

http://dx.doi.org/10.5772/63480

and cross-stream extent of the separated flow increase as the angle of attack increases; this explains the increase of the RMS of tip deflection with angle of attack.

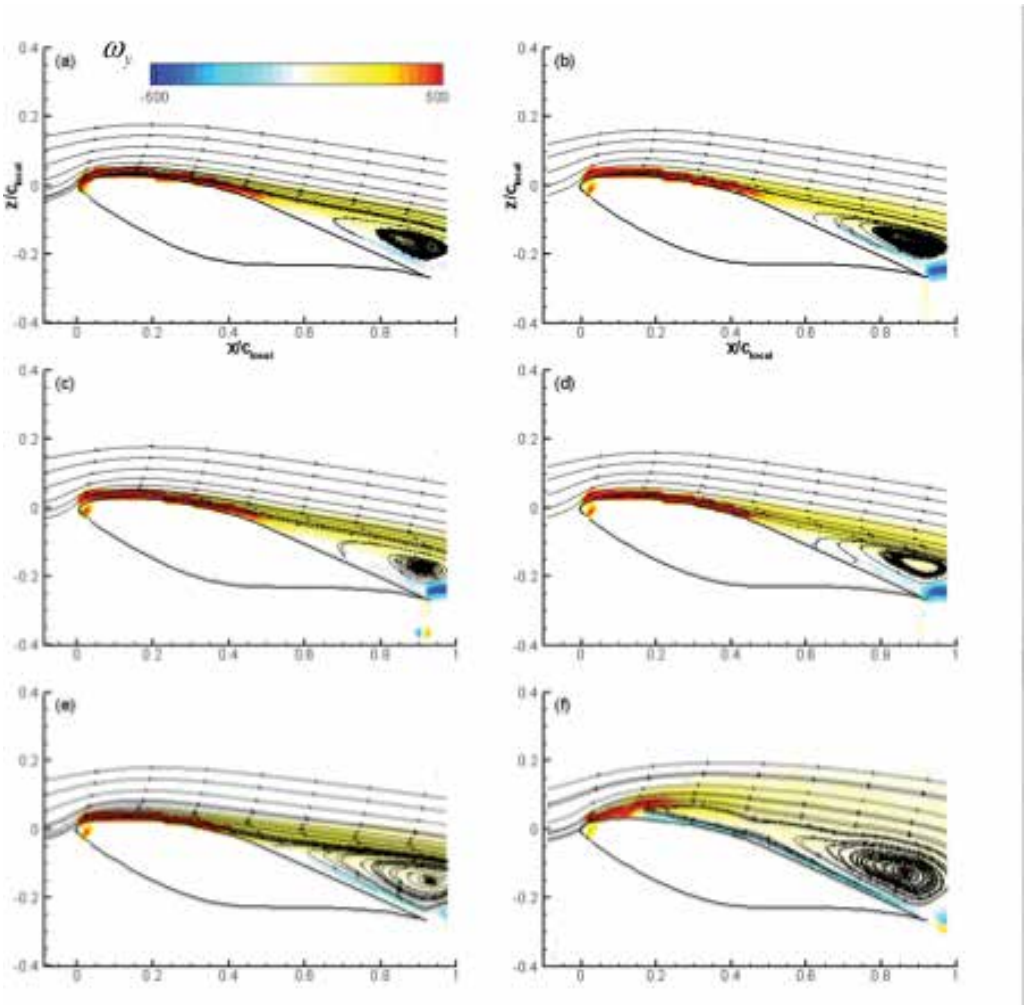

Figure 9. Superimposed span-wise vorticity and streamlines for the forced case at $y/b = 0.47$ and $Re = 1.85 \times 10^5$. $\alpha = 15°$ (a), 15.5°(b), 16°(c), 16.5 °(d), 17°(e), and 17.5°(f).

When flow control is applied (**Figure 9**), the flow field at $\alpha = 15°$ and 15.5° (**Figure 9a** and **(b)**, respectively) is very similar to the baseline; thus, there is minimal effect on the tip vibrations at these angles of attack as seen in **Figure 6b**. However, as the angle of attack increases, the degree of flow separation is significantly reduced when flow control is applied (**Figure 9c–f**). These results qualitatively help explaining the trends in **Figure 6b**, where the RMS of tip deflection stays almost constant for the forced case up to $\alpha = 16.5°$, while for the baseline case there is a sharp increase in RMS values. This is directly related to the extent and severity of the

flow separation and reattachment. At higher angles of attack (i.e., α = 17° and 17.5°, **Figure 9e** and **(f)**, respectively), flow control is able to significantly reduce the flow separation. It is reasonable to conclude that the reduction in the extent of flow separation is predominantly responsible for reducing structural vibration of the blade.

4. Frontiers of active flow control research

The majority of the work in active flow control has been conducted with stationary and non-rotating wind turbine blades in order to simplify the interaction of the external cross-flow and the synthetic jet, leading to an understanding of the flow physics. In the process, the capabilities of flow control in the context of improving fluid dynamic and aerodynamic performance have been largely determined. The next logical step for investigators is to develop active flow control techniques for complex vortex-dominated flows, representative of actual rotating wind turbines blades and rotors. Some recent studies for rotating wind turbines include the use of a trailing edge flap [42] and other studies have been implemented on rotating blades for dynamic stall on helicopters [43, 44].

The author has recently embarked on establishing a research program for rotating wind turbine blades at the University of Texas at San Antonio. A rotor test tower facility was designed and constructed to investigate various wind turbine flow control topics of interest ranging from wake turbulence evolution and downstream impact, blade tip vortex breakdown, blade structural vibration/noise reduction, and energy capture efficiency. One of the fundamental concerns of wind farms is that wind turbines suffer from electric power loss due to the wake interaction of successive rows of wind turbines. The tip vortices generated from wind turbine blades are highly turbulent wake structures that may extend many rotor diameters downstream and reduce the power output and shortens the lifetime of the rotor of downstream turbines. For full-wake conditions, power losses of downstream turbines can be 30–40%, and when averaged over different wind directions, losses of 5–8% are reported [45]. The author's current project seeks to advance the understanding of vortex structure formation and breakdown on a small-scale wind turbine utilizing synthetic jets. Novel active flow techniques based on the methods presented earlier are used with an a priori understanding of the flow physics. Particle image velocimetry is utilized to experimentally measure coherent vortex structures and their turbulence characteristics to identify the most energetic scales that are susceptible to synthetic jet excitation and breakdown. The author theorizes that the larger scales can be "broken-down" into smaller turbulence scales with lower turbulent kinetic energy and strength, such that the adverse impact of the tip vortex on the inflow conditions and operation of a downstream turbine is mitigated. It is also believed that the amplitude of structural vibration of the blades is also diminished by the breakdown of large turbulent scales, which have a greater role in influencing blade resonance at its natural frequency.

http://dx.doi.org/10.5772/63480

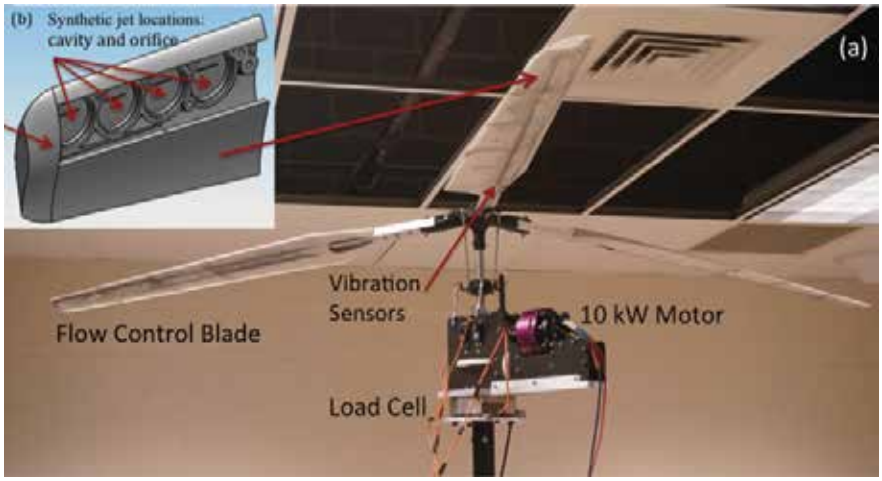

Figure 10. Rotor test tower facility for active flow control research.

The upper portion of the rotor test tower showing a rotor instrumented with synthetic jet slots is shown in **Figure 10a**. The rotor is powered by a 10-kW electric motor with a high-torque geared down transmission and collective/cyclic blade pitch capability mounted on a six-component load cell to measure rotor thrust and torque. A hall-effect sensor and magnet on the rotating shaft allow measurement of the rotor rotational velocity. The rotor shown contains a diameter of 2.41 m and the blades were custom designed in CAD with an S809 airfoil section and zero twist distribution. The blade has a span of 1.06 m and tapers down from a root chord of 0.178 m to a tip chord of 0.0889 m. A unique feature is the modular design of the blades; they are fabricated with additive manufacturing in sections to allow for modification to the blades, that is, changes to the geometry and/or location of the synthetic jet orifices. The tip section of the blade with four piezoelectric disk slots is shown in **Figure 9b**. The blade contains a total of 20 piezoelectric disk actuators and rectangular orifices placed at the quarter chord (0.25 c) of the airfoil as shown in the blade prototype of **Figure 11**.

Figure 11. S809 wind turbine blade prototype with synthetic jet actuators.

A 24-conductor slip ring is mounted to the rotor hub and transfers electrical signals between the synthetic jet actuators on the rotating blades and the stationary piezoelectric amplifier.

Finally, a high-power 10 kW supply powers the motor, and a National Instruments data acquisition system with Labview integrates the hardware for sensor measurements and actuator control.

Preliminary rotor thrust and torque measurements have been obtained in the Winter of 2015 for the baseline case without flow control at low rotor rotational velocities and blade pitch angles. The objective of these measurements was to validate operation of the tower and to observe tower vibration response for safe operation. Further experiments include the thrust, torque, and blade vibration measurements with and without flow control, as well as phase-locked stereoscopic (three velocity components) PIV flow measurements over the top suction surface of the blade and synthetic jets. The goal is to first characterize and understand the vortex flow nature of the rotor before attempting to perform flow control to influence and breakdown the turbulent vortex scales.

5. Conclusions

The wind energy industry is benefiting from the development of active flow control actuators and techniques to restore performance in wind turbines. As wind turbine rotor diameters continue to grow in order to reduce the cost of energy, the industry will require localized flow control along the blades to regulate unsteady blade loads and fatigue stress. This is critical in order to extend the life of the blades and other gearbox components. While some flow control technology such as trailing edge tabs have been demonstrated for aerodynamic load control in laboratories and large-scale field wind turbines, other flow control techniques and theories are still strictly being researched in the laboratory. This includes most notably the use of piezoelectric and plasma synthetic jet actuators for the control of vortex flow in rotating blades, blade tip vortex breakdown for vibration/noise reduction and to reduce wake turbulence levels for downstream wind turbines, and finally advanced closed-loop flow control techniques with blade sensors that adapt to the local flow conditions. Such concepts will be demonstrated in large-scale field turbines in the future, and wind energy will undoubtedly continue to be a growing source of renewable energy and an integral component of the US energy portfolio.

Author details

Victor Maldonado

Address all correspondence to: victor.maldonado@utsa.edu

Department of Mechanical Engineering, University of Texas at San Antonio, One UTSA Circle, San Antonio, Texas, USA

References

[1] D.T. Yen, C.P. Van Dam, R.L. Smith, and S.D. Collins, "Active load control for wind turbine blades using MEM translational tabs," 39th AIAA/ASME, Salt Lake City, Utah, 2001.

[2] D.T.Y. Nakafuji, C.P. van Dam, J. Michel, and P. Morrison, "Load control for wind turbines – a non-traditional microtab approach," 40th, AIAA/ASME, Indianapolis, Indiana, 2002.

[3] J.P. Baker, K.J. Standish, and C.P. van Dam, "Two-dimensional wind tunnel and computational investigation of a microtab modified S809 airfoil," 43rd AIAA/ASME, Tucson, Arizona, 2005.

[4] R. Chow, and C.P. van Dam, "Computational investigations of deploying load control microtabs on a wind turbine airfoil," 45th AIAA/ASME, Reno, Nevada, 2007.

[5] S. Joncas, O. Bergsma, and A. Beukers, "Power regulation and optimization of offshore wind turbines through trailing edge flap control," *2005* ASME Wind Energy Symposium, Reno, Nevada, 2005.

[6] N. Troldborg, "Computational study of the Riso-B1-18 airfoil with a hinged flap providing variable trailing edge geometry," *Wind Engineering*, 2005; 29: 89–113.

[7] P.B. Andersen, M. Guanaa, C. Bak, and T. Buhl, "Load alleviation on wind turbine blades using variable airfoil geometry," European Wind Energy Conference, Athens, 2006.

[8] S. Basualdo, "Load alleviation on wind turbine blades using variable airfoil geometry," *Wind Engineering*, 2005; 29: 169–182.

[9] C. Bak, M. Gaunaa, P.B. Andersen, T. Buhl, P. Hansen, K. Clemmensen, and R. Moeller, "Wind tunnel test on wind turbine airfoil with adaptive trailing edge geometry," 45th AIAA Aerospace Sciences Meeting and Exhibit, Reno, 2007.

[10] M. Gaunaa, "Unsteady 2D potential-flow forces on a thin variable geometry airfoil undergoing arbitrary motion," Technical Report Risø-R-1478(EN), Risø, 2006.

[11] T. Buhl, M. Gaunaa, C. Bak, "Potential of load reduction using airfoils with variable trailing edge geometry," *Journal of Solar Energy Engineering*, 2005; 127: 503–516.

[12] C. Tongchitpakdee, S. Benjanirat, and L.N. Sankar, "Numerical studies of the effect of active and passive circulation enhancement concepts on wind turbine performance," *Journal of Solar Energy Engineering*, 2006; 128: 432–444.

[13] T. Vronsky, "High performance cost-effective large wind turbine blades using air-jet vortex generators," ETSU W/41/00541/REP, 2000.

[14] R.C. Nelson, T.C. Corke, H. Othman, M.P. Patel, S. Vasudevan, and T. Ng, " A smart wind turbine blade using distributed plasma actuators for improved performance," 46th AIAA Aerospace Sciences Meeting, Reno, 2008.

[15] M.L. Post and T.C. Corke, "Separation control using plasma actuators: dynamic stall vortex control on oscillating airfoil," *AIAA Journal*, 2006; 44: 3125–3135.

[16] C.M. Ho and P. Huerre, "Perturbed free shear layers," *Annual Review of Fluid Mechanics*, 1984; 16: 365–424.

[17] D. Oster and I.J. Wygnanski, "The forced mixing layer between parallel streams," *Journal of Fluid Mechanics*, 1982; 123: 91–130.

[18] F.A. Roberts. "Effects of periodic disturbances on struc- ture of mixing in turbulent shear layers and wakes," PhD Thesis, California Institute of Technology, Pasadena, California, 1985.

[19] A. Seifert, T. Bachar, D. Koss, M. Shepshelovich, and I. Wygnanski, "Oscillatory blowing: a tool to delay boundary-layer separation," *AIAA Journal*, 1993; 31: 2052–2060.

[20] K.H. Ahuja and R.H. Burrin, "Control of flow separation by sound," AIAA-84-2298. AIAA/NASA 9th Aeroacoustics Conference, Williamsburg, VA, 1984; 15p.

[21] D. Neuberger and I. Wygnanski, "The use of a vibrating ribbon to delay separation on two dimensional airfoils. Proceedings of Air Force Academy Workshop in Unsteady Separated Flow, Colorado Springs, CO, 1987.

[22] I. Wygnanski, "Some observations affecting the control of separation by periodic excitation," *AIAA Paper* 2000-2314, 2000.

[23] M. Amitay and A. Glezer, "Role of actuation frequency in controlled flow reattachment over a stalled airfoil," *AIAA Journal*, 2002; 40: 209–216.

[24] M. Amitay, M. Horvath, M. Michaux, and A. Glezer, "Virtual aerodynamic shape modification at low angles of attack using synthetic jet actuators," *AIAA Paper* 2001-2975, 2001.

[25] Amitay M, Glezer A. Controlled transients of flow reattachment over stalled airfoils. *International Journal of Heat and Fluid Flow*, 2002; 23: 690–699.

[26] M. Amitay and A. Glezer, "Flow transients induced on a 2-D airfoil by pulse-modulation actuation," *Experiments in Fluids*, 2006; 40: 329–331.

[27] M. Amitay, D.R. Smith, V. Kibens, D.E. Parekh, and A. Glezer, "Modification of the aerodynamics characteristics of an unconventional airfoil using synthetic jet actuators," *AIAA Journal*, 2001; 39: 361–370.

[28] T.R. Bewley, "Flow control: new challenges for a new Renaissance," *Progress in Aerospace Sciences*, 2001; 37: 21–58.

[29] K. Cohen, S. Siegel, and T. McLaughlin, "Control issues in reduced-order feedback flow control," *AIAA Paper* 2004-0575, 2004.

[30] C.W. Rowley, D.R. Williams, T. Colonius, R.M. Murray, D.G. MacMartin, and D. Fabris, "Model-based control of cavity oscillations," Part II. *AIAA Paper* 2002-0972, 2002.

[31] L.N. Cattafesta, S. Garg, and M. Choudhari, "Active control of flow-induced cavity response," *AIAA Paper* 1997-1804, 1997.

[32] L.N. Cattafesta, S. Garg, M.A. Kegerise, and G.S. Jones, "Experiments on compressible flow-induced cavity oscillations," *AIAA Paper* 1998-2912, 1998.

[33] G. Berkooz, P. Holmes, and J.L. Lumley, "The proper orthogonal decomposition in the analysis of turbulent flows," *Annual Review of Fluid Mechanics*, 1993; 25: 539–575.

[34] R.B. Cal and M. Gibson, "Proper orthogonal decomposition of a wind turbine array boundary layer," 6th AIAA Theoretical Fluid Mechanics Conference, Honolulu, HW, 2011.

[35] M. Melius, R.B. Cal, and K. Mulleners, "Dynamic stall of an experimental wind turbine blade," *Physics of Fluids*, 2016; 28: 034103.

[36] D.S. Berry, "Blade system design studies phase 2: final project report," Sandia Report, SAND2008-4648, 2008.

[37] D.M. Somers, "Design and experimental results for the S809 airfoil," NREL/SR-440-6918, 1997

[38] A. Glezer and M. Amitay, "Sythetic jets," *Annual Review of Fluid Mechanics*, 2002; 34: 503–529.

[39] V. Maldonado, J. Farnsworth, W. Gressick, and A. Amitay, "Active control of flow separation and structural vibrations of wind turbine blades," *Wind Energy*, 2010; 13: 221–237.

[40] V. Maldonado, J. Farnsworth, W. Gressick, and M. Amitay, "active enhancement of wind turbine blades performance", 27th AIAA/ASME Wind Energy Symposium, 2008, Reno, NV.

[41] Maldonado, V., Boucher, M., Ostman, R., and Amitay, M., "Active vibration control of a wind turbine blade using synthetic jets," *International Journal of Flow Control*, 2010; 1: 4.

[42] M.J. Balas and N. Li, "Adaptive flow control of rotating wind turbine blades based on the Beddoes-Leishman model using trailing-edge flaps", AIAA Guidance, Navigation, and Control Conference, AIAA SciTech (AIAA 2016-0624), San Diego, California.

[43] H. Mai, G. Dietz, W. Geissler, K. Richter, J. Bosbach, H. Richard, and K. De Groot, "Dynamic stall control by leading-edge vortex generators," *Journal of the American Helicopter Society*, 2008 January; 53(1), pp. 26-36.

[44] P. Martin, J. Wilson, J. Berry, T.C. Wong, M. Moulton, and M. McVeigh, "Passive control of dynamics stall," 26th AIAA Applied Aerodynamics Conference, Honolulu, Hawaii, 2008.

[45] R.J. Barthelmie, S.T. Frandsen, N.M. Nielsen, S.C. Pryor, P.E. Rethore, and H.E. Jørgensen, "Modelling and measurements of power losses and turbulence intensity in wind turbine wakes at Middelgrunden offshore wind farm," *Wind Energy*, Vol. 10(6), pp. 517-528, 2007.

Chapter 14

Experimental Investigation of Power Requirements for Wind Turbines Electrothermal Anti-icing Systems

Oloufemi Fakorede, Hussein Ibrahim,
Adrian Ilinca and Jean Perron

Additional information is available at the end of the chapter

http://dx.doi.org/10.5772/63449

Abstract

Atmospheric icing effects is a critical issue for wind farms in Nordic regions; it is responsible for production losses, shortens the equipment's lifetime, and increases safety risks. Electrothermal anti-icing is one of the existing techniques of ice mitigation, and its energy consumption for wind turbines has been numerically investigated over the years but never fully validated experimentally in the literature. In this work, we aimed to determine the energy consumption for anti-icing systems based solely on experimental investigations. Our methodology is to quantify the energy required to protect a custom-built NACA 0012 airfoil from ice buildup in a wind tunnel. The results are extrapolated to a full-scale wind turbine.

Keywords: wind turbines, anti-icing, ice mitigation systems, energy consumption, electrothermal anti-icing systems

1. Introduction

To perform anti-icing, knowing the energy required to prevent ice buildup on the wind turbine's blade is the most important parameter for a wind farm operator. It can be used to select the most suitable ice protection system for a given site and to decide whether or not to operate wind turbines during icing events. There are a few softwares, primarily designed for aeronautics, such as LEWICE, TURBICE, and FENSAP-ICE based on computational fluid dynamics (CFD) methods that can be used for modeling anti-icing for wind turbine blades. They require a certain level of expertise to be used. However, more importantly, there are very

few research results in the literature for anti-icing experiments on full-scale wind turbines. These results are essential for validation and improvement of existing numerical models.

Our approach is to experimentally investigate the power requirement for anti-icing on a NACA 0012 airfoil partially equipped with resistive heaters and instrumented with fluxmeters and thermocouples. Based on wind tunnel measurements, correlations are developed between the anti-icing energy flux and the airflow wind speed for a given temperature and liquid water content. Finally, under some assumptions, we use these correlations to evaluate the anti-icing power requirements for a full-scale wind turbine. Our experiments have been conducted in the icing wind tunnel of the Anti-icing Materials International Laboratory at the University of Québec at Chicoutimi.

2. Wind turbine Icing

Ice accretion on wind turbine blades can affect both the energy production and the lifetime of the wind turbine. Ice accumulation on blades reduces wind turbine power due to airfoil shape alteration and increased surface roughness [1]. This disrupts the airflow, increases drag, and reduces lift [2, 3, 4]. In severe meteorological conditions, ice accretion on the blades can cause downtime for days or weeks at a time [5]. An imbalanced ice load on the blades can increase their vibrations and reduce the wind turbine's lifetime [6, 7]. Also, ice blocks fall represent a risk for both staff and facilities in the vicinity. In certain cases, the ice on the blade can delay the stall causing a power surge that can damage components and cause fires [8]. In areas subjected to frequent icing events, an ice mitigation strategy is mandatory in order to reduce production losses [9, 10].

To overcome the effects of icing, wind farm operators have generally two solutions. The first is to stop the wind turbine during icing events. With this strategy, the turbines must remain stopped until there is no more ice on the blades; this can have a strong impact on the profitability of a wind plant if icing events are frequent because the recovery time is often very long. The second alternative is to install an ice protection device. Several more or less complex approaches and technologies have been implemented over the years in wind farms. Currently, wind turbines designed to be much better adapted to cold climate regions and equipped with ice protection systems are available in the market.

Ice protection systems can be regrouped in two categories: anti-icing and de-icing. Anti-icing systems prevent ice buildup at the surface of the blade while de-icing systems remove accumulated ice from the surface of the blade [11].

There are several types of ice protection systems using various technologies for mitigating ice accretion on wind-turbine blades. These technologies can be passive (ice-phobic/hydrophobic coatings, thermal coatings such as black paint, etc.) or active (antifreeze coolants, pneumatic and expulsive techniques, hot air injection, resistive heaters, microwaves or infrared heating, etc.) [12, 13]. Heating the wind turbine's blade is currently the most efficient protection technique against ice accretion. It can be achieved by driving hot air inside the blade or by

http://dx.doi.org/10.5772/63449

installing resistive heaters on or in the blade. Driving hot air along a high diameter rotor results in important energy loss. Besides, retrofit is not possible with the hot air system. Therefore, resistive heaters installed on the outer surface of the blade seems to be the most suitable technique for most applications.

3. Methodology

There are two anti-icing systems using resistive coatings. The first one consists in heating the surface enough to evaporate the impinging droplets; it is the evaporative anti-icing. This technique requires a lot of energy, and the effects of the heat on the blade lifetime are unknown at this time. The second approach consists in heating the droplets enough to avoid accretion both on impact and during runback; it is the wet running anti-icing. This approach requires transferring an additional energy to the droplet in order to prevent the freezing when it streams along the blade. Our experimentation is based on the second approach.

For the experimental work, we use a rectangular NACA 0012 airfoil blade with a constant section of 0.254 m and length of 0.381 m. The airfoil is covered with resistive heaters and instrumented with fluxmeters and thermocouples. For various airflow wind speeds, temperatures, and liquid water contents, we measure the heating energy required to maintain the airfoil surface temperature at 5°C determined as a threshold for keeping the runback water in liquid form. The data are processed to find correlations that will help to extrapolate the anti-icing energy consumption of an operating full-scale wind turbine blade.

4. Fundamentals of power requirements

4.1. Sensible heating

The sensible heating is the energy required to heat up the impinging droplets in order to keep them in a liquid state. Part of this energy serves to heat up the runback water and avoid secondary icing. If we assume that the droplets are heated from their initial temperature to the surface temperature, the sensible heating can be expressed by

$$\dot{q}_{\text{sens}} = \dot{q}_{\text{imp}} = \dot{m}_{\text{imp}} \cdot C_{p,w} \left(T_{\text{s}} - T_{\infty} \right) \tag{1}$$

The impinging mass flow of droplets is the amount of water per unit of time and surface that can be caught by the airfoil. It is also known as the intensity of ice accretion and identified according to the formula [14]:

$$\dot{m}_{imp} = V \cdot LWC \cdot E \tag{2}$$

The collection efficiency E can be taken as the average of local collection efficiencies around the airfoil.

4.2. Kinetic heating

Kinetic heating is the gain of energy due to the velocity of the droplets and is given by [15]

$$\dot{q}_{kin} = \dot{m}_{imp} \frac{V_{\infty}^{\ 2}}{2} \tag{3}$$

4.3. Convective energy loss

The convective heat loss is given by [15]

$$\dot{q}_{conv} = h\left(T_s - T_{\infty}\right) \tag{4}$$

The convective heat transfer coefficient h is an averaged value. It is usually computed at the tip of the blade section (highest distance from the nacelle).

4.4. Evaporative energy loss

Even if the anti-icing strategy does not consist in the evaporation of the impinging droplets, the heat at the airfoil surface is high enough to evaporate a fraction of the impinging water. The evaporated heat loss can be estimated with [15]

$$\dot{q}_{evap} = \frac{0.622 \cdot h \cdot 2.5 \cdot 10^6}{C_{p,a} \cdot L_{evap}^{\ 2/3} \cdot p_{\infty}^{0}} 27.03 \cdot \left(T_s - T_{\infty}\right) \tag{5}$$

4.5. Aerodynamic heating

Aerodynamic heating is due to the friction between the droplet and the air [16]:

$$\dot{q}_{aero} = h \frac{r_c V_{\infty}^{\ 2}}{2C_{p,a}} \tag{6}$$

with

http://dx.doi.org/10.5772/63449

$$r_c = \begin{cases} \left(\frac{C_{p,a}\mu}{k_a}\right)^{\frac{1}{2}} = Pr^{1/2} & \left(laminar\,boundary\right) \\ \left(\frac{C_{p,a}\mu}{k_a}\right)^{\frac{1}{3}} = Pr^{1/3} & \left(turbulent\,boundary\right) \end{cases} \tag{7}$$

4.6. Energy balance

The energy balance equation is given by

$$\left|\dot{q}_{anti}\right| + \left|\dot{q}_{aero}\right| + \left|\dot{q}_{kin}\right| = \left|\dot{q}_{conv}\right| + \left|\dot{q}_{sens}\right| + \left|\dot{q}_{evap}\right| \tag{8}$$

5. Experimental investigations

5.1. Icing wind tunnel

AMIL's icing wind tunnel is a closed-loop, low-speed, refrigerated wind tunnel which is able to operate at negative temperatures. The refrigeration system is capable of varying the air temperature between −20 and 20°C by passing it through a 1.6 m × 1.6 m heat exchanger powered by a compressor and a glycol pump. A fan connected to a motor allows for an empty section to reach flow rates up to 31 kg/s at an air temperature of 22°C.

The icing wind tunnel has two test sections. The smaller one measure 0.5 m wide by 0.6 m high and can be used to perform experiments at wind speeds up to 37 m/s at ambient temperature. The second test section is 0.91 m wide by 0.76 m high and can reach wind speeds up to 86 m/

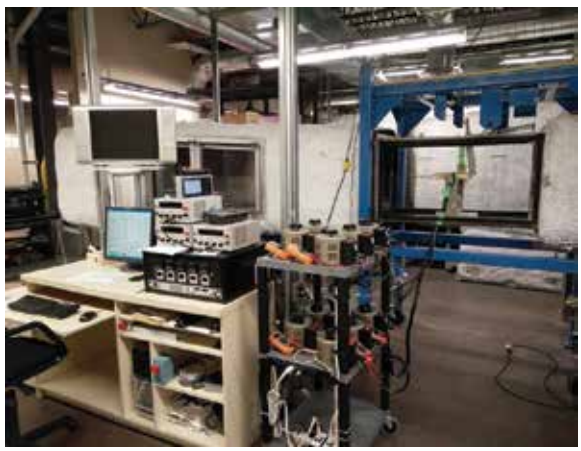

Figure 1. Experimental setup in the small section of the icing wind tunnel.

s at ambient temperature. Experiments in this study have been done using the small section (**Figure 1**).

5.2. Experimental setup

The airfoil has been made of 2.54-mm-thick fiberglass resin. It is equipped with 10 resistive heaters pasted on the external surface of the upper surface (**Figure 2**).

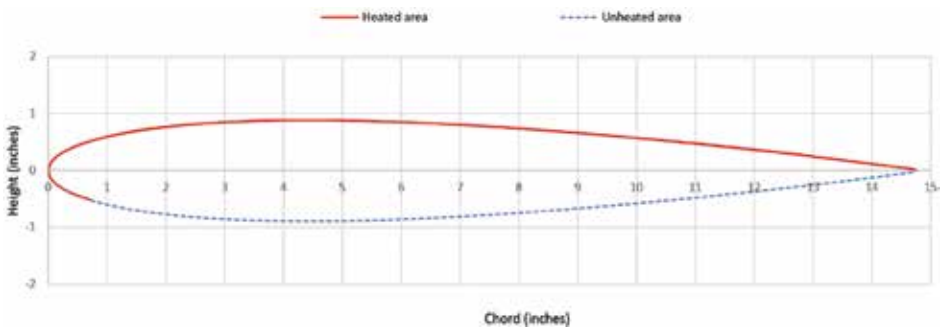

Figure 2. Resistive heater distribution along the experimental airfoil.

A thermocouple is placed between the surface of the airfoil and each resistive heater. Another thermocouple is placed inside the airfoil right under the external thermocouple. In addition, a fluxmeter is pasted above each resistive heater; these fluxmeters give the outgoing energy flux and an additional indication of the surface temperature. Each heater is powered individually by an independent power source. The setup has a total of 20 thermocouples, 10 fluxmeters, 10 resistive heaters, and 10 power sources (**Figure 3**).

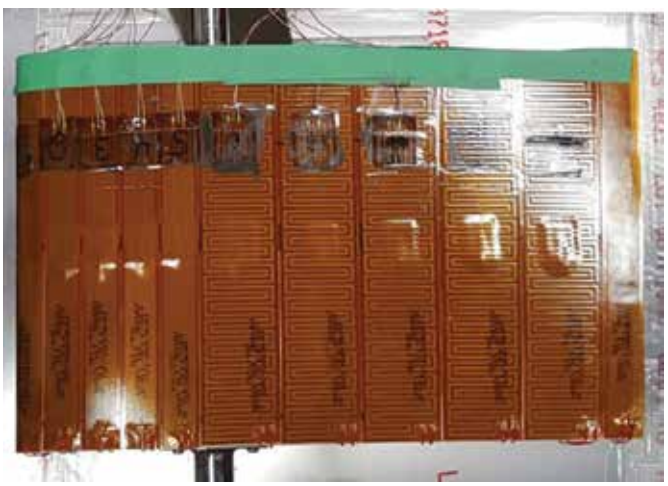

Figure 3. Upper view of the NACA0012 airfoil.

http://dx.doi.org/10.5772/63449

5.3. Energy consumption

We have conducted 30 experiments at five different wind speeds (10, 15, 20, 25, and 30 m/s), two different temperatures (−10 and −15°C), and three different values of liquid water content. The surface temperature in each experiment has been fixed to 5°C and the angle of attack is 0°.

For the first set of experiments, there was no precipitation (dry air):

$$\dot{q}_{anti\_exp} = \dot{q}_{dry} \tag{9}$$

These experiments quantified the convective effects. **Figure 4** shows the variation of $\dot{q}_{\mathrm{dry}}$ with the airflow wind speed.

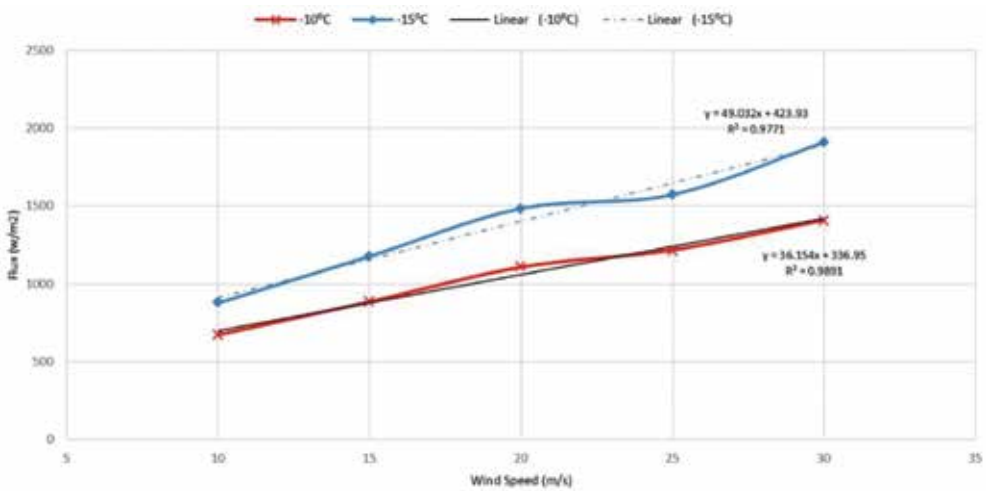

Figure 4. $\dot{q}_{\mathrm{dry}}$variation with the wind speed (LWC = 0 g/m^3).

In the second set of experiments, we fixed the airflow temperature to −10°C and added water droplets to the airflow (wet air):

$$q_{\mathrm{anti\_exp}} = \dot{q}_{\mathrm{dry}} + \dot{q}_{\mathrm{wet}} \tag{10}$$

The different values of liquid water contents experimented are 0.3 and 0.9 g/m^3. **Figure 5** shows the variation of $\dot{q}_{\mathrm{wet}}$ with the airflow wind speed.

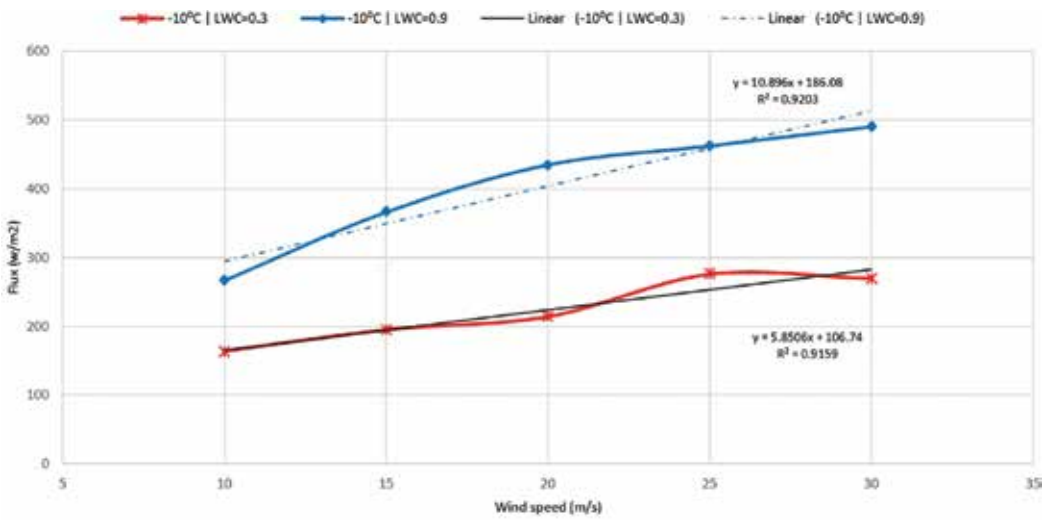

Figure 5. $\dot{q}_{wet}$variation with the wind speed (LWC = 0.3 g/m^3 and LWC = 0.9 g/m^3) at temperature −10°C.

Finally, we repeat the wet experiments for an airflow temperature of −15°C. **Figure 6** shows the variation of $\dot{q}_{wet}$ with the airflow wind speed.

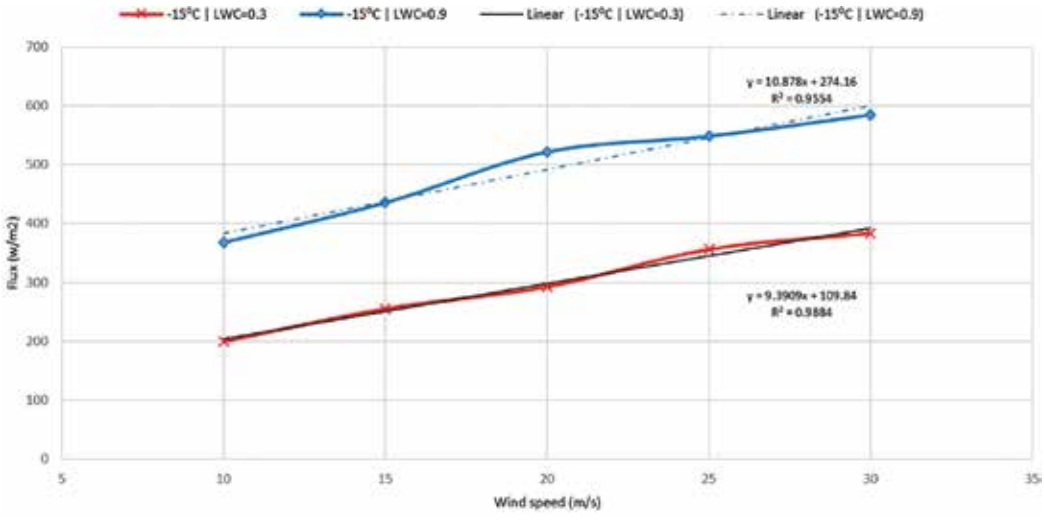

Figure 6. $\dot{q}_{wet}$ variation with the wind speed (LWC=0.3 g/m^3 and LWC=0.9 g/m^3) at temperature −15°C.

The graphs of $\dot{q}_{wet}$ and $\dot{q}_{dry}$, between the ranges of 10 and 30 m/s, can be approximated by linear functions with a very good precision. Thus, under those conditions, we can deduce the following correlations for required anti-icing energy flux.

http://dx.doi.org/10.5772/63449

	LWC = 0 g/m³	LWC = 0.3 g/m³	LWC = 0.9 g/m³
$T = -10°C$	$\dot{q}_{anti} = 36.154 \cdot V + 336.95$	$\dot{q}_{anti} = (36.154 \cdot V + 336.95) + (5.8506 \cdot V + 106.74)$	$\dot{q}_{anti} = (36.154 \cdot V + 336.95) + (10.896 \cdot V + 186.08)$
$T = -15°C$	$\dot{q}_{anti} = 49.032 \cdot V + 336.95$	$\dot{q}_{anti} = (49.032 \cdot V + 336.95) + (9.3909x + 109.84)$	$\dot{q}_{anti} = (49.032 \cdot V + 336.95) + (10.878 \cdot V + 274.16)$

Table 1. Experimental anti-icing flux correlations.

6. Extrapolation to a full-scale wind turbines

To extrapolate the results presented in the previous section to a full-scale wind turbine, we do the following assumptions:

- Linear approximations of $\dot{q}_{wet} = f(V)$ and $\dot{q}_{dry} = f(V)$ are good for wind speeds between 30 and 80 m/s.
- The turbulence effects around the experimental setup and the wind turbine on site are similar.
- The wind turbine is composed of NACA 0012 blades (3) at an angle of attack of 0°.
- The efficiency of the experimental setup is the same as the efficiency of the anti-icing device installed on the wind turbine.

6.1. Chord distribution

The chord distribution is based on the NREL 5MW reference wind turbine for offshore development [17]. We defined the chord distribution used in our study as follows:

	r/*R*	Chord/*R*
-	0.00	0.02
Zone 1 (hub)	0.02	0.02
Zone 2	0.05	0.06
Zone 3	0.19	0.07
Zone 4	0.26	0.08
Zone 5	0.96	0.03
Zone 6	1.00	0.02

Table 2. Blade discretization.

The graphical normalized chord distribution is shown in **Figure 7**.

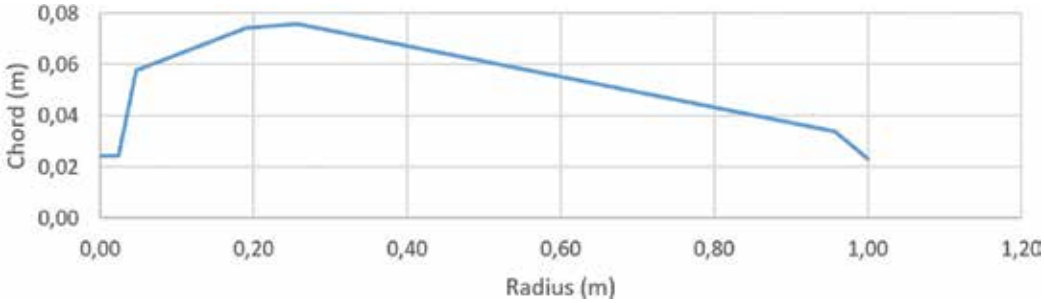

Figure 7. Chord distribution for a 1-m-long blade.

6.2. Wind speed distribution

The relative airflow wind speed V along the blade is given by

$$V(r) = \sqrt{V_{\infty}^{2} + (r\omega)^{2}} \tag{11}$$

with

$$\omega = \frac{V_{\infty} \cdot \lambda}{R} \tag{12}$$

				Tair = −10°C		
				LWC 0 g/m³	**LWC 0.3 g/m³**	**LWC 0.9 g/m³**
	Radius (m)	Tip speed ratio	Output (KW)	Anti-icing power (KW)		
ENERCON E40	20	5.8	600	130	466	529
Vestas V47	23.5	4.3	660	149	538	612
Vestas V66	33	4.6	1650	300	1100	1250
Vestas V80	40	4.66	2000	450	1630	1850
Vestas V90	45	5.05	3000	600	2160	2460
Vestas V100	50	4.68	2750	710	2550	2910
Vestas V120	60	6.5	4500	1260	4250	5120

Table 3. Extrapolated anti-icing power requirements at −10°C.

http://dx.doi.org/10.5772/63449

6.3. Results

For each zone of the blade determined in Section 6.1, we compute the average value of $\dot{q}_{anti}$ by integrating its expression (**Table 1**) with respect to the radius r. The anti-icing power requirement for each zone is found by multiplying the average $\dot{q}_{anti}$ by the zone's surface (for both intrados and extrados). The total power anti-icing for the wind turbine is summation of the anti-icing power for each zone multiplied by the number of blades. The extrapolation results for seven wind turbines [18–22] are presented in **Tables 3** and **4**.

				Tair = −15°C		
				LWC 0 g/m³	**LWC 0.3 g/m³**	**LWC 0.9 g/m³**
	Radius (m)	Tip speed ratio	Output (KW)	Anti-icing power (KW)		
ENERCON E40	20	5.8	600	173	625	682
Vestas V47	23.5	4.3	660	198	718	792
Vestas V66	33	4.6	1650	400	1470	1620
Vestas V80	40	4.66	2000	600	2180	2400
Vestas V90	45	5.05	3000	800	2900	3170
Vestas V100	50	4.68	2750	940	3410	3750
Vestas V120	60	6.5	4500	1680	6080	6600

Table 4. Extrapolated anti-icing power requirements at −15°C.

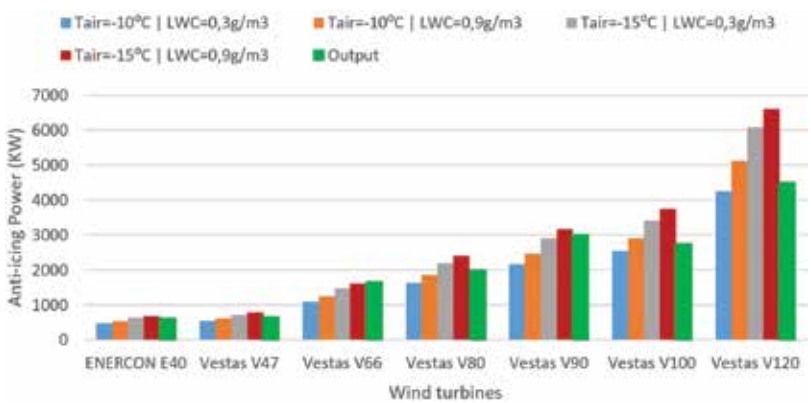

Figure 8. Histogram of the extrapolated anti-icing power requirements.

At first glance, we note that the anti-icing power consumption is sometimes higher than the nominal output power of the wind turbine (**Figure 8**). In such conditions, stopping the wind turbines is a better alternative. Plotting the anti-icing energy in terms of the percentage of the

nominal output power (**Figure 9**) showed that the anti-icing operation consumes more than 50% of the nominal output power.

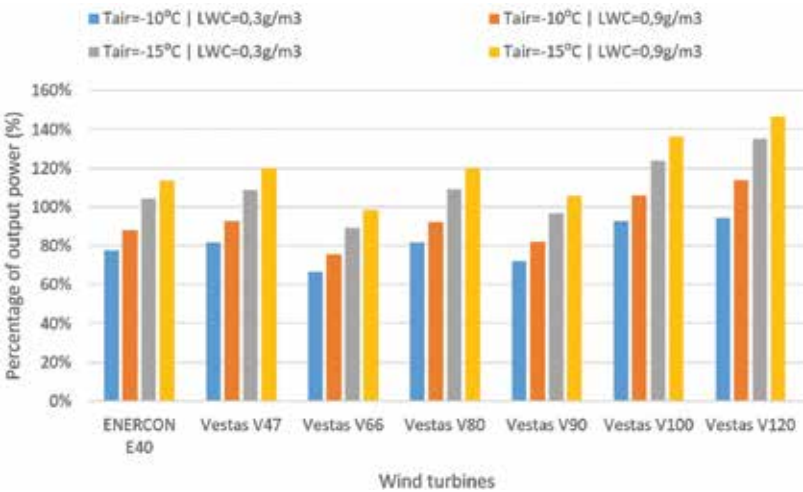

Figure 9. Power requirements in percentage of the nominal output power.

Figure 10. Fraction of Q_{dry} and Q_{wet} in the anti-icing power consumption.

Figure 10 displays the fraction of Q_{dry} and Q_{wet} in the anti-icing energy. It shows that Q_{dry} is at most 30% of the total anti-icing energy. It also means that the convective effects are approximately 30%, and the rest of the energy is lost to the water droplets.

7. Conclusion

In this chapter, we have introduced the effects of the icing on wind turbines and investigated the anti-icing power requirements of a full-scale wind turbine. Our methodology was to build a section of NACA 0012 airfoil covered externally by resistive heaters and instrumented with thermocouples and fluxmeters. We assembled the airfoil and conducted anti-icing tests in the Anti-icing Materials International Laboratory wind tunnel. The measured data have been used to establish correlations between the anti-icing energy and the airflow wind speed around the airfoil. Under some reasonable assumptions, we used these correlations to estimate the anti-icing power consumption for full-scale wind turbines.

The extrapolated power consumption showed that the anti-icing consumed a considerable amount of energy that can exceed the nominal output of the wind turbine itself. In reality, the anti-icing power consumption should be higher than the values that we extrapolated because

- The NACA 0012 is slimmer than the wind turbines airfoil.
- The wind turbine angle of attack is above 0°.

Thus, the blades collect more water droplets and consume more energy. Nevertheless, the work presented in this chapter proves that anti-icing for wind turbines is not a viable solution to mitigate icing effects. The correlation presented in this chapter can also be used for anti-icing on heated flat surfaces.

Given that wind turbines are designed to be more robust and to be able to withstand significant ice loads, then the de-icing seems to be a more promising strategy. This work is the first part of a project on the estimation and control of mass and heat transfers during the anti-icing and de-icing of wind turbines. The project, motivated by the need of the wind industry, answers some issues related to anti-icing strategy and its feasibility. The results are useful for the choice, design, and control of de-icing/anti-icing systems.

8. Abbreviations and acronyms

AMIL: Anti-Icing Materials International Laboratory

CFD: computational fluid dynamics

$\dot{m}_{imp}$: impingement water, kg

E: collection efficiency

C_p: heat capacity, J/(kg K)

NACA: National Advisory Committee for Aeronautics

Q: heating power, W

$\dot{q}$: heating flux, W/m^2

$\dot{q}_{anti}$: anti-icing energy, W/m^2

T_s: surface temperature, K
T_∞: free stream temperature, K
V_∞: free stream velocity, m/s
V: relative stream velocity, m/s
LWC: liquid water content, kg/m^3
h: thermal convection coefficient, W/(m K)
r_c: recovery factor
L_{evap}: latent heat of evaporation, J/kg
$\dot{q}_{dry}$: experimental convective heating, W/m^2
$\dot{q}_{wet}$: experimental water heating, W/m^2
$\dot{q}_{anti\_exp}$: experimental anti-icing energy, W/m^2
$\dot{q}_{sens}$: sensible heating, W/m^2
$\dot{q}_{imp}$: impinging droplet heating, W/m^2
$\dot{q}_{kin}$: kinetic heating, W/m^2
$\dot{q}_{conv}$: convective energy, W/m^2
$\dot{q}_{evap}$: evaporative energy, W/m^2
$\dot{q}_{aero}$: aerodynamic heating, W/m^2
p_∞^0: atmospheric pressure, Pa
k_a: thermal conductivity of air, W/(m K)
μ: dynamic viscosity, kg/(m s)
Pr: Prandtl number
R: blade radius, m
λ: tip speed ratio
ω: rotor velocity, rpm
$\dot{q}_{anti}$: anti-icing energy (W/m^2)
NREL: National Renewable Energy Laboratory

Author details

Oloufemi Fakorede[1], Hussein Ibrahim[2], Adrian Ilinca[3*] and Jean Perron[1]

*Address all correspondence to: Adrian_Ilinca@uqar.ca

1 University of Quebec at Chicoutimi, 555 boulevard de l'Université, QC, Canada

2 TechnoCentre éolien, 70 rue Bolduc, Gaspé, QC, Canada

3 University of Quebec at Rimouski, 300 allée des ursulines, Rimouski, QC, Canada

References

[1] E. Sagol, M. Reggio and A. Ilinca, Issues concerning roughness on wind turbine blades, vol. 23, Renewable and Sustainable Energy Reviews, 2013, pp. 514–525.

[2] W. J. Jasinski, S. C. Noe, M. S. Selig and M. B. Bragg, Wind turbine performance under icing conditions, Journal of Solar Energy Engineering, 1998, vol. 120, no 1, pp. 60–65.

[3] O. Fakorede, J. Perron, A. Ilinca and H. Ibrahim, Modelling ice accretion and its effects on wind turbine blades, Wind turbines: types, design and efficiency, ISBN: 978-162-808-891-5, NY: Nova Science Publishers, Inc., 2013.

[4] P. Suke, Analysis of heating systems to mitigate ice accretion on wind-turbine blades (Master's thesis of Applied Science in Engineering). Hamilton, Ontario: McMaster University; January 2014.

[5] M. Homola, Impacts and causes of icing on wind turbines, Navrik University College Report, 2005.

[6] P. Frohboese and A. Anders, Effects of icing on wind turbine fatigue loads, vol. 75, I. Publishing, Ed., Journal of Physics: Conference Series (Vol. No. 1, p. 012061), 2007.

[7] N. Dalili, A. Edrisy and R. Carriveau, A review of surface engineering issues critical to wind turbine performance, vol. 13(2), Renewable and Sustainable Energy Reviews, 2009, pp. 428–438.

[8] B. Tammelin, M. Stuke, H. Seifert and S. Kimura, Icing effect on power production of wind turbines, Proceedings of the BOREAS IV Conference, Finland, 1998.

[9] C. Hochart, G. Fortin, J. Perron and A. Ilinca, Wind turbine performance under icing conditions, vol. 11, Wind Energy, 2008, pp. 319–333.

[10] M. Dimitrova, H. Ibrahim, G. Fortin, A. Ilinca and J. Perron, Software tool to predict the wind energy production losses due to icing, Electrical Power and Energy Conference (EPEC), 2011 IEEE, Winnipeg, MB, 2011, pp. 462–467.

[11] C. Mayer, A. Ilinca, G. Fortin and J. Perron, Design characteristics of electro-thermal deicing systems for wind turbine blades based on wind tunnel studies, vol. 17, International Journal of Offshore and Polar Engineering, 2007, pp. 182–188.

[12] O. Parent and A. Ilinca, Anti-icing and de-icing techniques for wind turbines: Critical review. Cold regions science and technology, 2011, vol. 65, no 1, p. 88–96.

[13] A. Ilinca, Analysis and Mitigation of Icing Effects on Wind Turbines, Wind Turbines, Dr. Ibrahim AlBahadly (Ed.), ISBN: 978-953-307-221-0, InTech. 2011.

[14] L. Makkonen, Estimating intensity of atmospheric ice accretion on stationary structures, vol. 20, Journal of Applied Meteorology, 1981, pp. 595–600.

[15] G. Fortin, J. Laforte and A. Ilinca, Heat and mass transfer during Ice accretion on aircraft wings with an improved roughness model, vol. 45, International Journal of Thermal Sciences, 2006, pp. 595–606.

[16] F. Villalpando, M. Reggio and A. Ilinca, Numerical study of flow around an iced wind turbine airfoil, vol. 6(1), Engineering Application of Computational Fluid Mechanics, pp. 39–45, 2012.

[17] L. Battisti, Wind turbines in cold climates: icing impacts and mitigation systems, ISBN: 978-3-319-05191-8, Switzerland: Springer International Publishing, 2015.

[18] O. Meier and D. Scholz, A Handbook Method for the Estimation of Power Requirements for Electrical De-Icing Systems. Deutscher Luft-und Raumfahrtkongress,

Hamburg, 2010. DocumentID: 161191. [Online]. Available: http://MOZART.Prof-Scholz.de [Accessed: 09 May 2016]

[19] J. Jonkman, S. Butterfield, W. Musial, and G. Scott, Definition of a 5-MW Reference Wind Turbine for Offshore System Development, NREL/TP-500-38060, Golden, CO: National Renewable Energy Laboratory, February 2009. DOI: 10.2172/947422

[20] P. Gipe, Wind energy basics: a guide to home and community-scale wind-energy systems, ISBN: 978-160-358-227-8, VT: Chelsea Green Publishing, 2009.

[21] Vestas, V120-4.5 MW Offshore leadership, Denmark: Vestas Wind Systems A/S, 2008. [Online]. Available: NRG Systems, http://www.nrg-systems.hu/dok/en/V120_UK.pdf [Accessed: 09 May 2016]

[22] Vestas, V100-2.75 MW The future for low wind sites, Denmark: Vestas Wind Systems A/S, 2008. [Online]. Available: NRG Systems, http://www.nrg-systems.hu/dok/en/V100_UK.pdf [Accessed: 09 May 2016]

[23] Vestas, V90 3.0 MW, Denmark: Vestas Wind Systems A/S, 2016. [Online]. Available: Direct Industry, https://www.vestas.com/en/products/turbines/v90-3_0_mw [Accessed: 09 May 2016]

[24] Vestas, V80-2.0 MW Versatile megawattage, Denmark: Vestas Wind Systems A/S, 2012. [Online]. Available: Vestas, http://pdf.directindustry.com/pdf/vestas/v80-20-mw-brochure/20680-53605.html [Accessed: 09 May 2016]

Edited by Abdel Ghani Aissaoui and Ahmed Tahour

Renewable energies constitute excellent solutions to both the increase of energy consumption and environment problems. Among these energies, wind energy is very interesting. Wind energy is the subject of advanced research. In the development of wind turbine, the design of its different structures is very important. It will ensure: the robustness of the system, the energy efficiency, the optimal cost and the high reliability. The use of advanced control technology and new technology products allows bringing the wind energy conversion system in its optimal operating mode. Different strategies of control can be applied on generators, systems relating to blades, etc. in order to extract maximal power from the wind. The goal of this book is to present recent works on design, control and applications in wind energy conversion systems.

ISBN 978-953-51-6664-1

Photo by Ian Dyball / iStock

IntechOpen